Far-infrared optical properties and molecular interactions

Barker, Colin

FAR-INFRARED OPTICAL PROPERTIES

AND MOLECULAR INTERACTIONS

A THESIS

SUBMITTED TO THE

UNIVERSITY OF DURHAM

by

COLIN BARKER, B. Sc.

(HATFIELD COLLEGE)

for the degree of

DOCTOR OF PHILOSOPHY

September 1977

DECLARATION

The work described in this thesis was carried out by me in the Chemistry Department of the University of Durham, between August 1972 and September 1975.

I declare that this work has not been accepted in substance for any degree, and is not being concurrently submitted in candidature for any degree.

Signed Colin Baker

J Haywood

Dated 20/9/77

ABSTRACT

The far-infrared absorption spectra of solutions of tetra-n-alkylammonium salts have been studied in benzene, chloroform, carbon tetrachloride and tetrahydrofuran, as a function of concentration, temperature, solute and solvent. The absorption profile has been computer fitted to the sum of 3 component bands, and the variation of band centre, half-band width, area and intensity with concentration, temperature, solute and solvent has been studied. The spectral features, and their variation with the parameters above, have been shown to be consistent with the absorptions arising from ion-ion vibrations, ion aggregate 'librational' absorptions and fluctuating electrical fields, due to 'effective' dipole-induced dipole interactions. The observed intensities were seen to be reproduced for model geometries and effective aggregate dipoles, which agreed well with those obtained from dielectric relaxation measurements. It was concluded that the higher degree of ion-clustering in the solutions leads to severe restrictions on the movement of both solute and solvent species. It is proposed that some solvent molecules may be trapped within the ionic cluster. The absorptions of more polar systems have been compared with the non-polar systems. Computer programmes have been developed to compute refractive index data from interferograms obtained with a Michelson interferometer operated in the dispersive mode. The experimental and computational procedures have been tested by determining the refractive index of polytetrafluoroethylene sheets in the far-infrared. Methods for the computation of intensities from refractive index values have been developed, and the intensities for the 202 cm^{-1} band of polytetrafuoroethylene obtained by both dispersive and non-dispersive methods have been compared. A cell has been designed, constructed and tested, which can be used to measure the refractive index of liquids and solutions in the far-infrared region. This cell has been incorporated into a Beckman-RIIC Ltd. FS-720 interferometer, as an extra (dispersive) module.

Acknowledgements

Thanks are due, firstly, to the Science Research Council for a CASE Award Studentship in conjunction with Beckman-RIIC Ltd., which provided financial support during the period of study. Further thanks go to Prof. W.J. Orville-Thomas , Department of Chemistry, Salford University, for the loan of a modular cube interferometer, and to Prof. D.H. Martin and Dr. Peter Ade for their assistance in setting up the cooled bolometer detector.

I would like to thank Mr. Tony Scott and Mr. Bob McKenzie of Beckman-RIIC Ltd. for their extensive help in the design and construction of the refractive index cell, and Mr. Bob Brown, Mr. George Rowe and Mr. Billy Nelson for their many electronic modifications to my equipment.

Thanks are also due to Mr. Bob Coult for performing the Karl-Fischer Titrations, and to Mr. Brian Lander, and the staff of the Durham University Computer Unit, for their assistance in solving my computing problems.

Finally, I would like to offer my sincere thanks to my supervisor, Dr. J. Yarwood, whose constant and unending enthusiasm acted as a great encouragement throughout the duration of the work.

Thank you, to you all.

Colin Barker, London, August 1977.

CONTENTS

PART A Instrumental and theory

Chapter 1 Basic principles of far-infrared interferometric spectroscopy

1.1 Introduction 6

1.2 The delay principle 7

1.3 The Michelson interferometer 9

1.4 Derivation of the basic integral equation for Fourier transform spectroscopy 11

1.5 Beam-splitter operation 18

1.6 Advantages and disadvantages of Fourier transform spectroscopy 21

Chapter 2 Description of the instrument and peripherals 25

2.1 Basic instrument 25

2.2 Sources 27

2.3 The Golay detector 27

2.4 Moiré system 30

2.5 Golay amplifier and demodulator 31

2.6 Analogue to digital converter 31

2.7 Interferogram output 32

2.8 Experimental beam-splitter characteristics 32

2.9 Filtering 37

2.10 Reproducibility of non-ratioed spectra 39

2.11 Vacuum system 39

2.12 Liquid cell 42

2.13 Variable temperature control 49

2.14 Cooled germanium bolometer 52

Chapter 3 Computation of the spectrum and data handling 73

3.1 Computation of the spectrum from the interferogram function 73

3.2 Comparison of the theoretical and experimental resolution obtained using the FS-720 interferometer and the programme FTRAN4 93

PART B Ionic solvation studies

Chapter 4 Far-infrared studies of tetra-n-alkylammonium salts in various solvents 113

4.1 Introduction to ionic solvation work 114

4.2 Tetra-n-butylammonium chloride in benzene 116

4.2.1 Effect of concentration 118

4.2.2 Effect of water 135

4.2.3 Time dependence 140

4.2.4 Effect of temperature 142

4.2.5 Solid solution spectra 145

4.2.6 Studies of benzene internal modes 155

4.3 Tetra-n-butylammonium bromide in benzene 163

4.3.1 Effect of concentration 166

4.4 Tetra-n-pentylammonium and tetra-n-heptylammonium chlorides in benzene 169

4.5 Tetra-n-butylammonium chloride in carbon tetrachloride 175

4.6 Tetra-n-butylammonium bromide in carbon tetrachloride 184

4.7 Tetra-n-butylammonium chloride in chloroform 185

4.8 Tetra-n-butylammonium bromide in chloroform 192

4.9 Tetra-n-butylammonium iodide in chloroform 192

4.10 Tetra-n-butylammonium nitrate in chloroform 195

4.11 Tetra-n-butylammonium perchlorate in chloroform 195

4.12 Tetra-n-butylammonium chloride in tetrahydrofuran 199

4.13 Indications for the presence of a high frequency component in the overall absorption profile 202

Chapter 5 Computer fitting to spectral profiles for tetra-n-alkylammonium salts 214

5.1 Band fitting theory 214

5.2 Preliminary fits and precision tests 219

5.3 3 pure Gauss components fit for tetra-n-butylammonium chloride in benzene. Effect of concentration 216

247
5.4 3 pure Gauss components fit for tetra-n-butylammonium chloride in chloroform
5.5 3 pure Gauss components fit for tetra-n-butylammonium chloride in carbon tetrachloride. Effect of concentration 263
5.6 3 pure Gauss components fit for tetra-n-butylammonium chloride in benzene. Effect of temperature 288
5.7 Fitting for the tetra-n-butylammonium bromide in benzene system 301
5.8 Summary of the fits for tetra-n-butylammonium chloride/solvent systems 310
Chapter 6 Further studies of ionic solvation 316
6.1.1 Pure benzene solvent spectra 316
6.1.2 Pure toluene solvent spectra 328
6.2 Pure chloroform solvent spectra 330
6.3 Pure carbon terachloride solvent spectra 339
6.4 Lithium perchlorate in tetrahydrofuran spectra 339
6.5.1 Sodium iodide in acetone spectra 345
6.5.2 Sodium iodide in acetone mid-infrared spectra 353
6.6 Silver perchlorate in benzene and toluene spectra 355
6.7 Summary
Chapter 7 Discussion of the ionic solvation studies 364
7.1 Historical introduction to the theory of solvation 364
7.2 Previous far-infrared studies and interpretations 367
7.3 Aims of this work in terms of interpretation 382
7.4 Assignment of bands 383
7.4.1 Introduction 383
7.4.2 120 cm^{-1} band 385
7.4.3 80 cm^{-1} band 396
7.4.4 180 cm^{-1} band 403
7.5 Indications as to the structure of the near-ion environment 406
PART C Dispersive far-infrared studies
Chapter 8 Solid phase refractive index measurements 409

8.1 Theory of refractive index measurements 409

8.2 Programming to obtain phase and refractive index values 415

8.3 Reproducibility and precision of refractive index spectra 441

8.4 Intensity calculations from refractive index values 447

8.4.1 Theory for intensity calculations 447

8.4.2 Preliminary intensity calculations for 0.0083 cm teflon 457

8.4.3 More sophisticated fitting techniques for intensity calculations 457

8.5 Advantages and disadvantages of intensity determinations from refractive index data 467

Chapter 9 Liquid phase refractive index measurements 471

9.1 Previous work 471

9.2 Viability tests for the refractive index cell 474

9.3 Design and construction of the refractive index cell 480

9.4 Use of the refractive index cell 489

9.5 Preliminary results 493

REFERENCES 504

APPENDICES

A1 Listings of computer programmes and input data 514

A1.1 FTRAN4 Fourier transformation programme 514

A1.2 DCH0690 Dispersive Fourier transformation programme 528

A1.3 DCH0623 Refractive index programme 540

A1.4 GPLOT3 Spectra plotting programme 547

A1.5 RIINTEN Intensities from refractive index programme 553

A2 Papers

A2.1 Journal of the Chemical Society, Faraday Transactions II, 71, 1322 (1975). 566

A2.2 Faraday Symposium 11 - 11/11 (Dec. 1976). 574

PART A

INSTRUMENTAL AND THEORY

CHAPTER 1

BASIC PRINCIPLES OF FAR-INFRARED INTERFEROMETRIC SPECTROSCOPY

1.1 Introduction

Spectroscopy in its broadest sense may be defined as the study of the interactions of electromagnetic radiation with matter. This interaction can be harnessed to provide useful properties of atoms, molecules and macroscopic bodies, which can then help in formulating relationships between a substances microstructure and its macroscopic or observable properties. At present we are far from the ultimate aim of the physical sciences, where a mathematical formulation of the forces within a molecule and within an ensemble of molecules, would enable us to calculate all the physical properties of a substance. With this goal in mind this thesis describes work performed in a study of far-infrared optical properties (particularly in the liquid phase) determined by the use of a Michelson interferometer.

In the liquid phase the far-infrared optical properties are important because the spectroscopic properties of the molecules depend upon the interactions of the molecules with each other. In a pure liquid the interaction can only be with other 'like' molecules, whereas in a solution interactions can take place between both 'like' solute molecules or with surrounding solvent molecules. All the physical and chemical properties of the molecules in the liquid are influenced to some extent by these interactions, but the spectroscopic properties are also determined by the internal vibrations of the individual molecules themselves. Thus the spectroscopic properties can be used to study the bulk properties of a liquid or solution, and also to study the individual molecules making up the liquid or solution. By studying the internal modes of the molecules in the system it is possible to discover the effects of the environment on the molecule. This enables deductions to be made concerning the structure of the liquid phase.

Measurements of optical constants are important since it has been shown (1) that the internal and intermolecular processes can be distinquished by the different dispersions of refractive index which occur in the region of maximum absorption. We hoped that such refractivity

functions would give information regarding the processes involved in the low-frequency absorption of liquids. Absorptions in various liquid systems have been thought of as arising from three mechanisms. Firstly, as a result of residual motion of molecules which is known as the Poley-Hill resonance phenomenon (2-4). Secondly, from translation movements of the molecule producing collision-induced effects (5-7). Thirdly, from Debye dipole relaxation (ref. 8, pps. 177-187). These mechanisms for absorption will be discussed further in chapter 7 in the light of the experimental observations.

To make the refractive index measurements a cell had to be constructed to enable the liquid sample to be contained in one arm of the interferometer used for such measurements. The design, construction and testing of this cell was to be the main objective of the study. However difficulties were experienced in the construction of such a cell and the majority of the experimental work on the liquid systems was conducted with the interferometer in the conventional, symmetric mode.

This chapter introduces the background theory for interferometric spectroscopy. Firstly, the reasons for using an interferometer, rather than conventional dispersion systems, is discussed. The interferometer is then described and the relevent mathematics developed to indicate how the spectrum can be obtained from the interference pattern.

1.2 Why use interferometers?

To answer this question we need to return to the basics of spectroscopy. In an absorption experiment the sample under investigation is placed in a path of radiation, between a suitable source and detector. A spectrum is a plot of the power absorbed by the sample as a function of frequency. Radiation is a time-dependent fluctuating electromagnetic field, which, according to Fourier (9), can be resolved into an infinite number of pure cosine and sine waves of differing frequencies. Therefore the spectrum, being the plot of the power of the component waves lying between frequency ν and $\nu + \partial\nu$ as a function of the frequency, is the Fourier Transform of the

temporal fluctuations of the electromagnetic field.

In the far-infrared region, by convention usually taken as the region of the spectrum between 3 and 500 cm^{-1} (3333 and 20 μm), one is limited by the available sources being incoherent (black body) sources, and the only available detectors giving a d.c. output proportional to the mean power of the total incident radiation. Since the source is broad-band then the Fourier components of the radiation are all scrambled and have to be unscrambled before they reach the detector. One technique for unscrambling the Fourier components is based upon the delay principle (10).

The simplest device utilising the delay principle is the prism, as was demonstrated by Newton when he observed the splitting of the visible portion of the suns rays into their spectral components by spatial separation. If a parallel beam of monochromatic light is incident upon one of the inclined faces of a prism, then the emerging beam can be condensed to a point image by use of a lens. The emerging beam has been deviated by the prism from its original path by an angle dependent upon the refractive index of the prism. The infinite number of rays into which the beam of light is divided by the inclined faces have all travelled different pathlengths within the prism. Interference between the beams will be constructive at only one angle of deviation, and destructive at all other angles. If light containing two components of different frequencies is incident upon the prism then the two components will have different deviations, since the refractive index depends upon the frequency due to dispersion effects, and will form images at different points on the image plane if the light emerging from the prism is brought to a focus by use of a lens, so that interference can occur. Thus a spatial separation of the spectral components has been obtained, and a detector can be used to obtain a plot of power within a small frequency increment against the frequency, which is known as the spectrum.

A diffraction grating similarly utilises the delay principle. When parallel, monochromatic light is incident upon a grating of narrow

strips of perfectly transmitting regions separated by regions which are totally opaque, then the light emerging from the grating at a particular angle can be focused to a point by a lens. The intensity in the image plane shows strong maxima and minima dependent upon the angle of the rays emerging from the grating. A grating produces a large number of maxima when irradiated with monochromatic light and these maxima are referred to as orders of the grating. If the grating is irradiated with polychromic light then for all orders of the grating greater than zero the different frequencies are imaged to different points in the same order. Thus a spectrum is produced for each order of the grating. The diffraction grating is thus an interferometer utilising a finite number of beams, whereas the prism is an interferometer utilising an infinite number of beams.

If the band-width of radiation incident upon a diffraction grating is large then the spectra produced from one order will overlap spectra from another order and much confusion can arise. Decreasing the number of beams will thus assist in interpretation of the spectral record. If the delay principle is to be employed then the minimum number of beams possible is two, and this is the number found in the Michelson interferometer.

1.3 The Michelson interferometer

In a Michelson interferometer (see fig. 1.1) incoherent radiation from the source, S falls upon a beam-splitter, B, inclined at 45^{o} to the beam, where part of the radiation is reflected and part is transmitted. These two beams travel to the mirrors, M_1 and M_2, which are set at 90^{o} to the beam, and hence the two beams return along their respective paths and are recombined at the beam-splitter and interference occurs. The two beams are once again divided by the beam-splitter and a beam of light is incident on the detector, D. The intensity of the light beam incident on the detector is determined by the path-difference introduced between the two beams before interference occurs. The path-difference is introduced by translating one of the mirrors in a direction parallel to the beam incident upon it. Varying

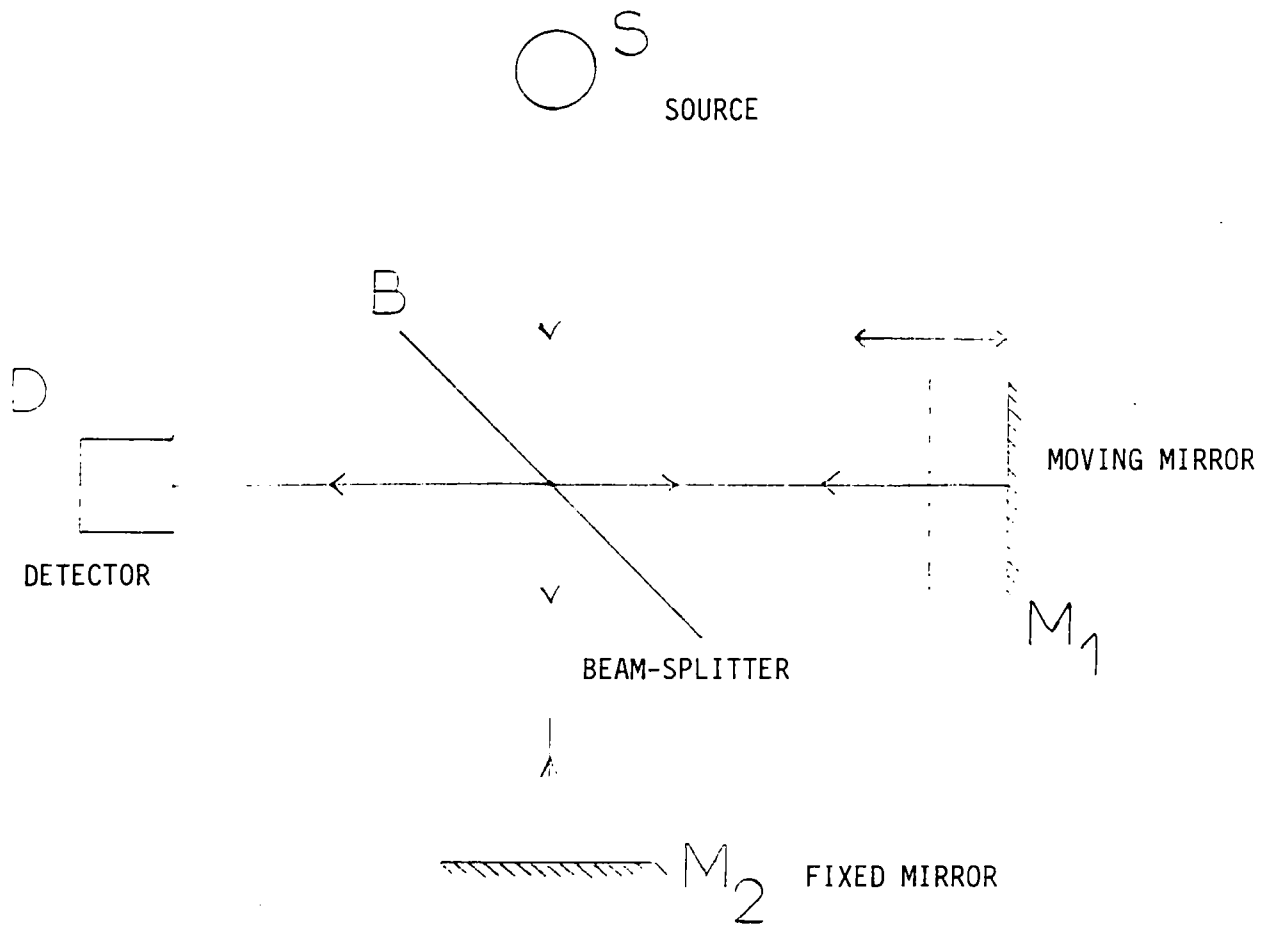

FIG. 1.1 TWO BEAM MICHELSON INTERFEROMETER

degrees of interference are produced for different frequencies depending upon the optical path-difference between the beams reflected from the two mirrors. The balanced position, where there is no optical path-difference between the beams, and where interference for all frequencies is completely constructive is called the 'Grand Maximum'. The Michelson interference fringes have cylindrical symmetry and the interference pattern produced at the detector is thus a series of concentric rings. The system is set up so that the detector measures only the intensity of the central fringe of the interference pattern. Fig. 1.2 shows a typical interference function, or interferogram, for optical path-differences of -0.4 to +0.4 cm for broad-band radiation between 10 and 250 cm^{-1}.

1.4 Derivation of the basic integral equation for Fourier Transform Spectroscopy.

The intensity of the beam reaching the detector is determined by considering the Fourier components of the recombined light beams. For one Fourier component in a beam of light the electric field vector amplitude E(t) at time t is given by:

$$E(t) = E\cos(2\pi\nu t) \qquad 1.1$$

where ν is the frequency (Hz)

E is the electric vector amplitude at time t = 0.

Let us consider one Fourier component for the two recombined beams at time t, where the second beam has travelled an extra optical path-difference x. The resultant electric field amplitude, $E_R(t)$ is given by:

$$E_R(t) = E\cos(2\pi\nu t) + E\cos(2\pi\nu t + 2\pi\nu x/c) \qquad 1.2$$

where c is the velocity of light.

Eqn. 1.2 assumes that when two beams superimpose then the resultant electric vector is the sum of the electric vectors in the two beams. The equation further assumes that the two beams have equal amplitudes. This will be the case for symmetric Fourier Transform Spectroscopy providing that the efficiencies of transmission and reflection at the beam-splitter are

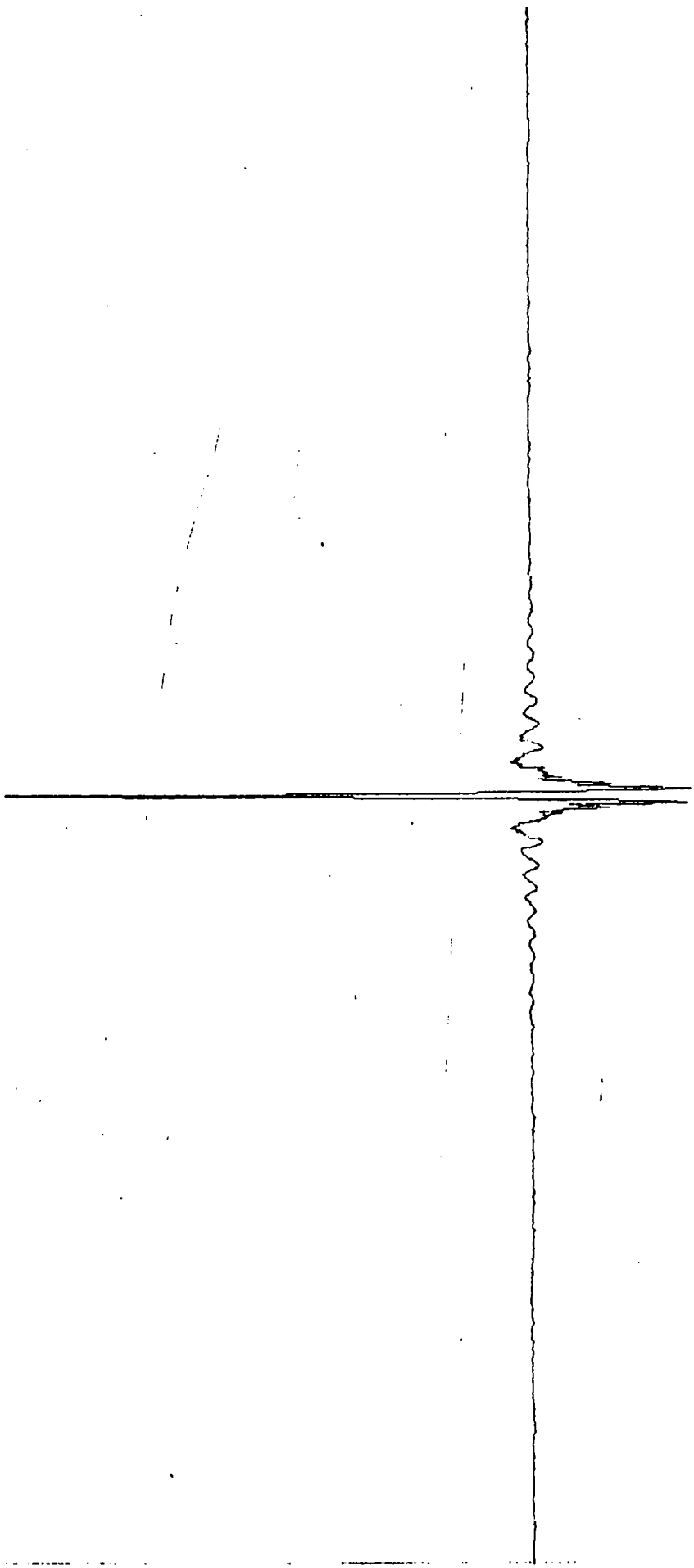

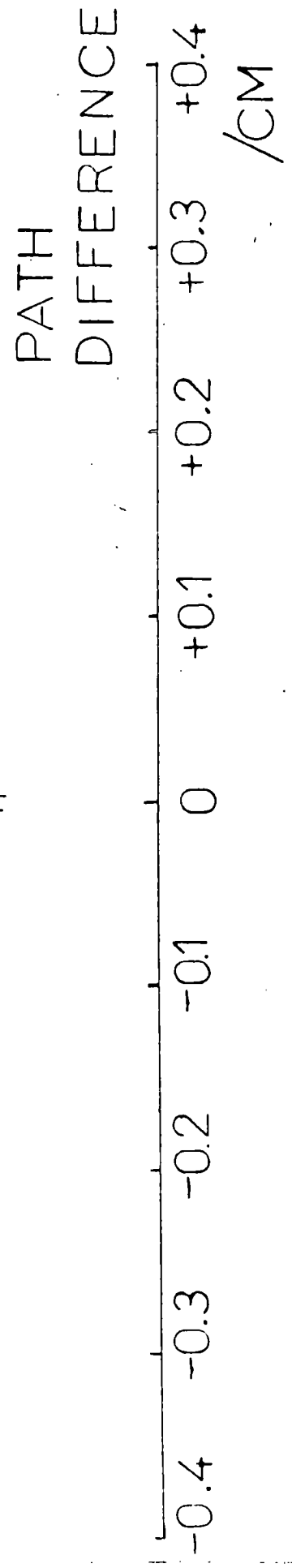

FIG 1.2 TYPICAL INTERFEROGRAM

equal, and also that the reflectivities of the two mirrors are equal. The amplitudes of the two beams will not be equal in the case of Asymmetric Fourier Transform Spectroscopy, where the sample is placed in one beam only, and not in the recombined beam as for Symmetric Fourier Transform Spectroscopy (see chapter 8).

If eqn. 1.2 is now expressed in terms of wavenumbers, i.e. writing $\bar{\nu} = \nu/c$ it becomes:

$$E_R(t) = E\{\cos(2\pi\nu t) + \cos(2\pi\nu t + 2\pi\bar{\nu}x)\} \qquad 1.3$$

The mean intensity at the image point is given by the time average of the square of the electric vector amplitudes for each Fourier component:

$$E_R^2(t) = E^2\{\cos(2\pi\nu t) + \cos(2\pi\nu t + 2\pi\bar{\nu}x)\}^2 \qquad 1.4$$

Since $\cos A + \cos B = 2\cos\{(A+B)/2\}.\cos\{(A-B)/2\}$

$$E_R^2(t) = 4E^2\{\cos(2\pi\nu t + \pi\bar{\nu}x).\cos(\pi\bar{\nu}x)\}^2 \qquad 1.5$$

The time average of the term $\cos^2(2\pi\nu t + \pi\bar{\nu}x)$ will be a constant and hence the time average can be written:

$$E_R^2 = (\text{constant}).E^2\cos^2(\pi\bar{\nu}x) \qquad 1.6$$

Equation 1.6 gives the spectral intensity due to one Fourier component. If a source emitting light of continuous spectrum from zero to infinite frequency is considered then all the intensity values δI for the individual components have to be summed. Thus we have:

$$\delta I = E_R^2 = (\text{constant}).E^2\cos^2(\pi\bar{\nu}x) \qquad 1.7$$

$$\int_0^\infty \frac{\delta I}{\delta\bar{\nu}}.\delta\bar{\nu} = I(x) = \int_0^\infty E_R^2.\delta\bar{\nu} \qquad 1.8$$

$$I(x) = (\text{constant}).\int_0^\infty E^2.\cos^2(\pi\bar{\nu}x).\delta\bar{\nu} \qquad 1.9$$

Where $I(x)$ is the total intensity arriving at the detector for an optical path-difference x. $I(x)$ is in fact the interferogram function.

The spectral intensity can be related to the square of the electrical vector amplitude as shown by Strong (ref. 11, p47).

$$S(\bar{\nu},x) = \tfrac{1}{2}ck_0E^*(\bar{\nu},x).E(\bar{\nu},x) \qquad 1.10$$

where $\int_0^\infty E^*(a) = \int_0^\infty E(-a)$

Eqn. 1.10 can be rewritten as:

$$S(\bar{\nu},x) = (\text{constant}).E^*(\bar{\nu},x).E(\bar{\nu},x) \qquad 1.11$$

where $S(\bar{\nu},x)$ is the spectral function.

Since the electrical vector amplitude is a real quantity, E_R is Hermitian (ref. 12, p 35) and hence:

$$\int_0^\infty E^*(\bar{\nu},x) = \int_0^\infty E(\bar{\nu},x)$$

$$\text{and } S(\bar{\nu},x) = (\text{constant}).E^2(\bar{\nu},x) \qquad 1.12$$

Using this relationship in eqn. 1.9 gives:

$$I(x) = (\text{constant}).\int_0^\infty S(\bar{\nu}).\cos^2(\pi\bar{\nu}x).\delta\bar{\nu} \qquad 1.13$$

now since $\cos^2 x = \frac{1}{2}(1+\cos 2x)$

$$I(x) = (\text{constant}).\tfrac{1}{2}\int_0^\infty S(\bar{\nu}).(1+\cos 2\pi\bar{\nu}x).\delta\bar{\nu} \qquad 1.14$$

Eqn. 1.14 is the autocorrelation function for the radiation incident at the detector. Now we can write

$$I'(x) = I(x) - \tfrac{1}{2}\int_0^\infty S(\bar{\nu}).\delta\bar{\nu} \qquad 1.15$$

We now have a modified interferogram function $I'(x)$. To understand clearly the relationship between $I'(x)$ and $I(x)$ it is necessary to consider the interferogram function $I(x)$ at large optical path-differences, i.e. when x in eqn 1.14 approaches infinity. The $\cos(2\pi\bar{\nu}x)$ term will oscillate very rapidly and will average zero. Hence for infinite x eqn. 1.14 becomes:

$$I(\infty) = (\text{constant}).\tfrac{1}{2}\int_0^\infty S(\bar{\nu}).\delta\bar{\nu} \qquad 1.16$$

Eqn. 1.15 can thus be rewritten as:

$$I'(x) = I(x) - I(\infty) \qquad 1.17$$

Thus we are subtracting the constant level of the interferogram at large path-differences from the interferogram function $I(x)$, leaving only the modulating interferogram function $I'(x)$. Substituting eqn. 1.15 into eqn. 1.14 gives:

$$I'(x) = (\text{constant}).\int_0^\infty S(\bar{\nu}).\cos(2\pi\bar{\nu}x).\delta\bar{\nu} \qquad 1.18$$

Thus we have a relationship between the modulating interferogram and the spectral intensity function $S(\bar{\nu})$. All that remains is to discover a method for retrieving $S(\bar{\nu})$ from eqn. 1.18.

If f(t) represents a quantity that varies with time then f(t) can be analysed into an integral sum of harmonic oscillations over a continuous range of frequencies (13). This can be represented by the pair of equations:

$$F(\omega) = \int_{-\infty}^{\infty} f(t).e^{-j\omega t}.\delta t \qquad 1.19$$

$$f(t) = \frac{1}{2\pi}\int_{-\infty}^{+\infty} F(\omega).e^{j\omega t}.\delta\omega \qquad 1.20$$

from eqn. 1.19:

$$F(\omega) = \int_{-\infty}^{+\infty} f(t).(\cos(\omega t) - j\sin(\omega t))\delta t \qquad 1.21$$

now $\omega = 2\pi\nu = 2\pi\bar{\nu}c$ and t = distance/speed = $1/c$

Thus $\frac{\delta t}{\delta l} = 1/c \qquad \delta t = \delta l/c$

$$F(2\pi\bar{\nu}c) = \int_{-\infty}^{+\infty} \frac{1}{c} f(l)\{\cos(2\pi\bar{\nu}l) - j\sin(2\pi\bar{\nu}l)\}.\frac{\delta l}{c} \qquad 1.22$$

$$F(\bar{\nu}) = \frac{1}{2\pi c^3}.\int_{-\infty}^{+\infty} f(l).\{\cos(2\pi\bar{\nu}l) - j\sin(2\pi\bar{\nu}l).\delta l \qquad 1.23$$

now $\omega = 2\pi\bar{\nu}c \qquad \frac{\delta\omega}{\delta\bar{\nu}} = 2\pi c$

from eqn. 1.20

$$\frac{1}{c} f(l) = \frac{2\pi c}{2\pi}\int_{-\infty}^{+\infty} F(2\pi\bar{\nu}c).\{\cos(2\pi\bar{\nu}l) + j\sin(2\pi\bar{\nu}l)\} \qquad 1.24$$

$$f(l) = 2\pi c^3\int_{-\infty}^{+\infty} F(\bar{\nu}).\{\cos(2\pi\bar{\nu}l) + j\sin(2\pi\bar{\nu}l)\} \qquad 1.25$$

The Fourier pair relating wavenumber and distance are thus:

$$F(\bar{\nu}) = \int_{-\infty}^{+\infty} f(l).\{\cos(2\pi\bar{\nu}l) - j\sin(2\pi\bar{\nu}l)\}.\delta l \qquad 1.26$$

$$f(l) = \int_{-\infty}^{+\infty} F(\bar{\nu}).\{\cos(2\pi\bar{\nu}l) - j\sin(2\pi\bar{\nu}l)\}.\delta\bar{\nu} \qquad 1.27$$

Clearly a change of integration limits is necessary before comparisons can be made between eqns. 1.18 and 1.27. Using the relation derived by Bell (ref. 12, p. 36):

$$\int_{-\infty}^{+\infty} b(\bar{\nu}).e^{j2\pi\bar{\nu}x}.\delta\bar{\nu} = 2\int_{0}^{\infty} Re\{b(\bar{\nu}).e^{j2\pi\bar{\nu}x}\}.\delta\bar{\nu} \qquad 1.28$$

$$\text{thus } \int_{-\infty}^{+\infty} S(\bar{\nu}).\{\cos(2\pi\bar{\nu}x) - j\sin(2\pi\bar{\nu}x)\} = 2\int_{0}^{\infty} S(\bar{\nu}).\cos(2\pi\bar{\nu}x).\delta\bar{\nu} \qquad 1.29$$

Therefore eqn. 1.18 can be rewritten as:

$$I'(x) = (\text{constant}).\int_{-\infty}^{+\infty} S(\bar{\nu}).\cos(2\pi\bar{\nu}x).\delta\bar{\nu} \qquad 1.30$$

By comparing eqn. 1.30 with eqn. 1.27 and using the other half of the Fourier pair eqn. 1.26 it can be seen that the spectral function $S(\bar{\nu})$ is obtainable by the Fourier Transformation of the modified interferogram function $I'(x)$.

$$S(\bar{\nu}) = (\text{constant}).\int_{-\infty}^{+\infty} I'(x).\cos(2\pi\bar{\nu}x).\delta x \qquad 1.31$$

To obtain a spectrum it is only necessary to repeat the Fourier Transformation using eqn. 1.31 for each wavenumber in the frequency range of interest. To give a spectrum over a usable frequency range the calculations are far too complex and tedious to carry out by hand, but they are easily handled by a high speed digital computer. The Michelson interferometer must therefore be coupled to, or be associated with, a computer to give a useful submillimetre spectrometer. Fig. 1.3 gives a schematic representation of a complete spectrometer.

Normally the proportionality constant in eqn. 1.31 is omitted. This is permissible since ratioed spectra of sample to background are recorded, the ratioing process aleviating the need to know the value for the constant. If a non-ratioed spectrum is recorded then the spectrum is represented on a normalised transmission scale, where normalisation takes place to peak transmission within the frequency range of interest, making the proportionality constant of purely academic interest. Eqn. 1.31 is thus replaced by:

$$S(\bar{\nu}) = \int_{-\infty}^{+\infty} I'(x).\cos(2\pi\bar{\nu}x).\delta x \qquad 1.32$$

or by using eqn. 1.17:

$$S(\bar{\nu}) = \int_{-\infty}^{+\infty} \{(I(x) - I(\infty)).\cos(2\pi\bar{\nu}x)\}.\delta x \qquad 1.33$$

Fourier Transform Spectroscopy can thus be seen to be a troublesome, indirect method to measure a spectrum, which, nevertheless, has to be employed in the submillimetre-wave region, where sources do not emit much radiation, since it is less wasteful of the radiation that is present. To emphasize the need for optimal use of available radiation in the far-infrared it is a sobering thought that less than 1 part in 10^4 of the total

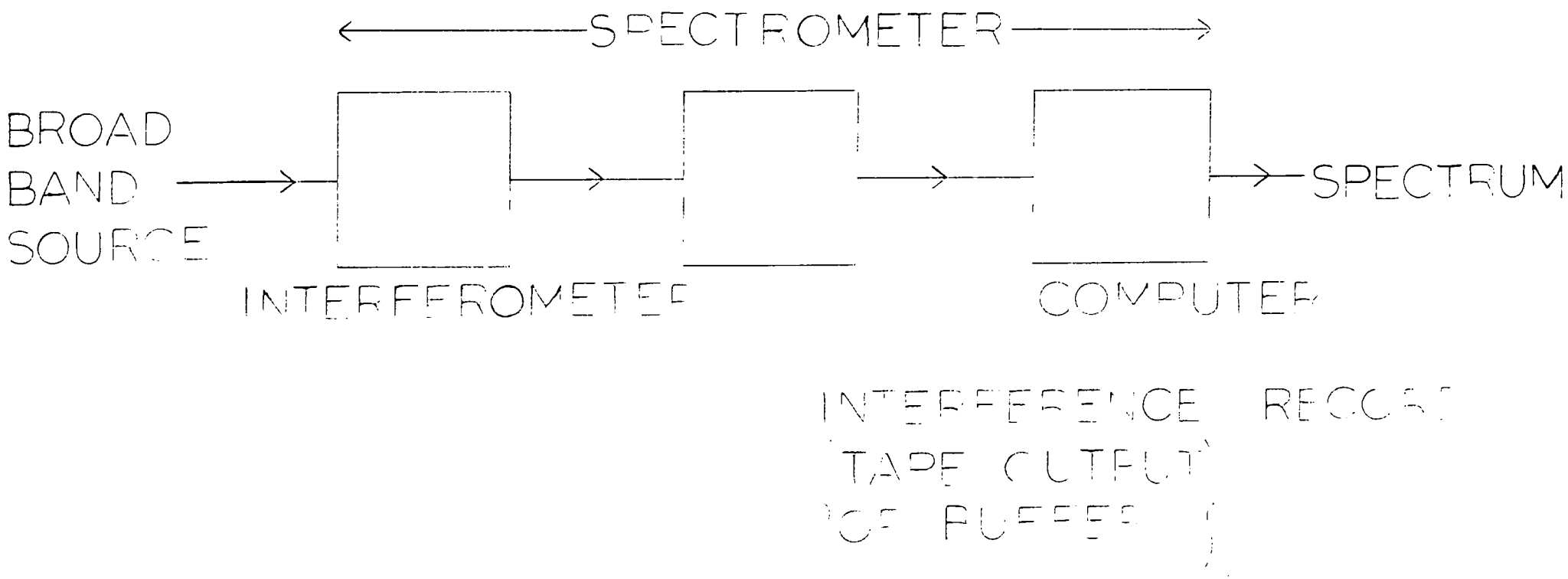

FIG. 3 SCHEMATIC REPRESENTATION OF A FOURIER SPECTROMETER

radiation emitted by a black-body source at 1000^{o}K lies within the frequency range 0-100 cm^{-1} (ref. 8, p. 13).

1.5 Beam-splitter operation

The most crucial part of the Michelson interferometer is the beam-splitter or beam-divider. The purpose of the beam-splitter is to firstly divide the wave-trains from the source into two separate beams, so that an optical path-difference can be introduced into one beam relative to the other, and secondly to collect the returning wave-trains so that interference can occur between the recombined beams. The beam-splitter is thus vital to the operation of the Michelson interferometer.

The beam-splitter is placed at 45^{o} to the incident beam from the source and the ideal beamsplitter would be an infinitely thin film having no absorption and giving 50% reflection and 50% transmission of the incoming beam. Even using this perfect beam-splitter it should be noted that 50% of the radiation from the source is returned to the source, rather than being sent to the detector. In the Michelson interferometer 50% of the radiation in each beam returning to the beam-splitter is once again reflected and 50% is transmitted. Thus only 50% of the source radiation reaches the detector, and hence even with a perfect beam-splitter the Michelson interferometer is only 50% efficient in using the radiation available from the source.

In the far-infrared, thin dielectric film beam-splitters are used since they have approximately equal transmissivities and reflectivities. Multiple beam interference occurs in the beam-splitter itself (this should not be confused with the interference occuring between the recombined beams which only occurs when the beams are focused on the detector window using a lens) and the resulting white light interference pattern can be used to align the interferometer, to ensure that the mirrors are normal to the beams. The fringes are observable, when the interferometer is in the balanced position, by placing a white card in the recombined beam. The fringe contrast

is increased by altering mirror tilts to give the best possible alignment.

The intensity at a given point in the image plane in the recombined beam will vary depending upon the degree of constructive interference. Thus a bright fringe will be observed when (ref. 14, p. 710)

$$2nt.\cos\Theta = (m+\tfrac{1}{2})\lambda \qquad m = 0,1,2..... \qquad 1.34$$

where n is the refractive index of the film,

t is the thickness of the film

Θ is the angle at which the refracted rays pass through the film

λ is the wavelength of the radiation

Letting $\bar{\nu}_{max}$ be the frequency for maximum transmission, i.e. the frequency for the centre of the bright fringe:

$$\bar{\nu}_{max} = (2m+1)_{/4nt.\cos\Theta} \qquad m = 0,1,2..... \qquad 1.35$$

Using n = 1.85, t = 12.5 μm and an angle of incidence to the film of 45^{o}, giving an angle of refraction of 22.5^{o} (by Snell's Law $\sin i_{/\sin r} = n$) gives $\bar{\nu}_{max}$ = 117, 351, and 585 cm^{-1} for m = 0,1 and 2 respectively. Table 1.1 gives the first frequencies of maximum transmission for given thicknesses of beam-splitter. The frequencies were calculated using eqn. 1.35 with a refractive index of 1.85 and an angle of incidence of 45^{o}.

The multiple interference in the beam-splitter thus shows 'hooping' as a function of frequency and this limits the useful range of the interferometer to regions away from the centres of the dark fringes. Very little energy reaches the detector for frequencies near $\bar{\nu}_{min}$. Fig. 1.4 shows a theoretical transmission spectrum for a beam-splitter of 12.5 μm thickness. The experimentally observed characteristics of various beam-splitters will be dealt with in chapter 2, but it can already be seen that severe difficulties will arise if spectra are required over a few octaves of frequency. This will be especially troublesome in the low-frequency region. To scan any reasonable range in the submillimetre region several different beamsplitters have to be used. It is pertinent to note here that

Table 1.1 Theoretical frequencies of first maximum transmission for various thicknesses of beamsplitter

Gauge	Thickness /μm	Max. Trans. /cm^{-1}
400	100	15
200	50	29
100	25	59
50	12.5	117
25	6	234
15	3.5	468

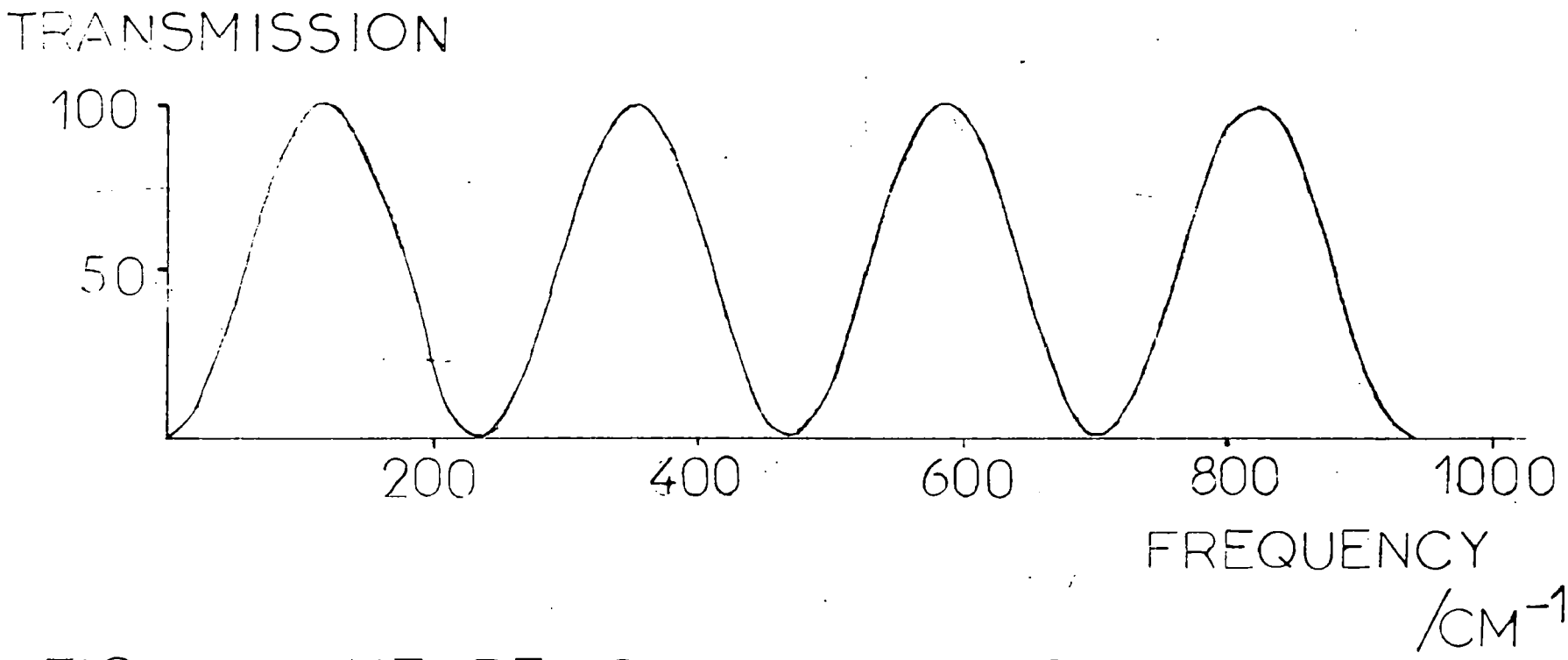

FIG 1.4 THEORETICAL TRANSMISSION FOR A 12.5 μm BEAMSPLITTER

polarising wire grids have been used as beam-splitters in the low-frequency region (15). There is no internal interference with these wire grids and hence no 'hooping' occurs.

1.6 Advantages and disadvantages of Fourier Transform Spectroscopy.

The principle advantage of Fourier Transform Spectroscopy over convential spectroscopy is its higher signal-to-noise ratio. This is a consequence of the interferogram containing information about all the spectral elements within the spectral range being studied. This advantage is known as the Multiplex advantage, and was first pointed out by Fellget (16,17). Using interferometric techniques each spectral element, N or spectral interval equal to the resolution, is observed for the total time taken to record the interferogram T. In a grating spectrometer each spectral element is studied only during the time interval $T_{/N}$ before the dispersive system moves to the next element. In the submillimetre region the principle source of noise is the detector, and hence the interferometer system is said to be detector-noise limited. In such a system the signal-to-noise ratio will be directly proportional to the incident power, and since the incident power is proportional to the square-root of the observation time, then the signal-to-noise ratio is also proportional to the square-root of the observation time. Thus for an interferometer the signal-to-noise ratio will be proportional to $T^{\frac{1}{2}}$, and for a dispersive instrument it will be proportional to $T^{\frac{1}{2}}/N^{\frac{1}{2}}$. Thus the interferometer is superior to the dispersive system in signal-to-noise ratio by a factor $N^{\frac{1}{2}}$. Fellget emphasized that the Multiplex advantage is a property of the system as a whole. It occurs when all the spectral elements or channels are observed simultaneously. Thus a photographic instrument fitted with a photographic plate is a multiplex system (18).

It is important to note here that the interferometer only gains its full advantage if the system is detector-noise limited. If, in fact, this is not the case and the system is source-noise limited, then variations in the source affect the whole spectrum, since the whole mean level is

affected in a non-dispersive instrument. A dispersive system would suit the source-limited situation more, since only the particular frequency being scanned at the time of the fluctuation will be affected by the source variations.

A second important advantage of interferometers over grating instruments was described by Jacquinot (19) as the 'throughput' or 'entendu' advantage. Put simply this states that the effective source area in a dispersive instrument is the slit area, and so the light flux within the instrument is limited by the area of the slits. This slit area cannot be large because the slits need to relatively narrow to give reasonable spectral resolution. The slits also have a maximum length which is determined by the size of the prisms which are used to create the dispersion in the instrument. The light flux in a dispersive instrument is thus small with respect to the total available from the source. With the interferometer the light flux is limited only by the size of the mirrors, which are usually over 7 cm in diameter, giving a light flux in the interferometer several orders of magnitude greater than that in a dispersive instrument.

Fourier Transform Spectroscopy has the major disadvantage that a computer is necessary to produce the spectrum, and although high speed digital computers make the computation of the spectrum straight-forward, the lack of immediate intelligibility of the interferogram is still a drawback. When an on-line computer is not available significant delays can occur between running an interferogram and obtaining the spectrum. These disadvantages are slightly offset by the fact that the resulting spectrum can be easily obtained in digital form, which lends itself to further mathematical processing of the spectrum e.g. averaging of spectra, intensity calculations and band-shape or relaxation rate studies.

1.7 Fourier Transform Spectroscopy bibliography

The literature of Fourier Transform Spectroscopy is now extensive and books by Möller and Rothschild (20), Chantry (8) and Bell (12) review

the subject completely. An extensive Fourier Transform Spectroscopy bibliography is given by Bell (ref. 12, pps. 321-364).

CHAPTER 2

DESCRIPTION OF INSTRUMENT AND PERIPHERALS

2.1 The basic interferometer

The interferometer used was of the Michelson type marketed by Beckman-RIIC Ltd. as the FS-720 Fourier Spectrometer. The instrument was of modular construction, and is shown schematically in fig. 2.1.

The source module, A contains the mercury vapour lamp source with collimating optics, a chopper for beam modulation and a magnetic reed switch to provide the reference signal for the demodulator circuit. The beam-splitter module contained the beam-splitter mounting optics and the fixed mirror, where alignment adjustments could be made. The moving mirror drive was contained in the module C and the condensing optics in module D. A sample chamber, E and detector module, F complete the interferometer. The fixed and moving mirrors together with the collimating and condensing mirrors were all front surface aluminised to give maximum reflectivity.

The electrical supplies to the interferometer, and the output of the interferogram were made using beckman-RIIC FS-720 electronics. The interferometer included a continuous driving motor for path-difference changes and a Moire grating system (activated by movement of the drive) to control the sampling of the interferogram. The drive system had a maximum travel of 5 cm from the Grand Maximum, giving a maximum path-difference of 10 cm, which corresponded to a maximum resolution of 0.1 cm^{-1}. (See chapter 3).

The mains supply to the electronics and source was made through two voltage stabilisers. The mains supply was firstly passed through an Ether transistor a.c. voltage regulator model T1000-2S, and then through a Beckman-RIIC power supply IR-720. These stabilisers helped to decrease the number of noise spikes (mostly caused by the switching on and off of apparatus on the same electrical phase network) being picked up from the mains and being recorded on the interferogram. Very rapid spikes were not eliminated completely and caused many problems. Long-term voltage drifts

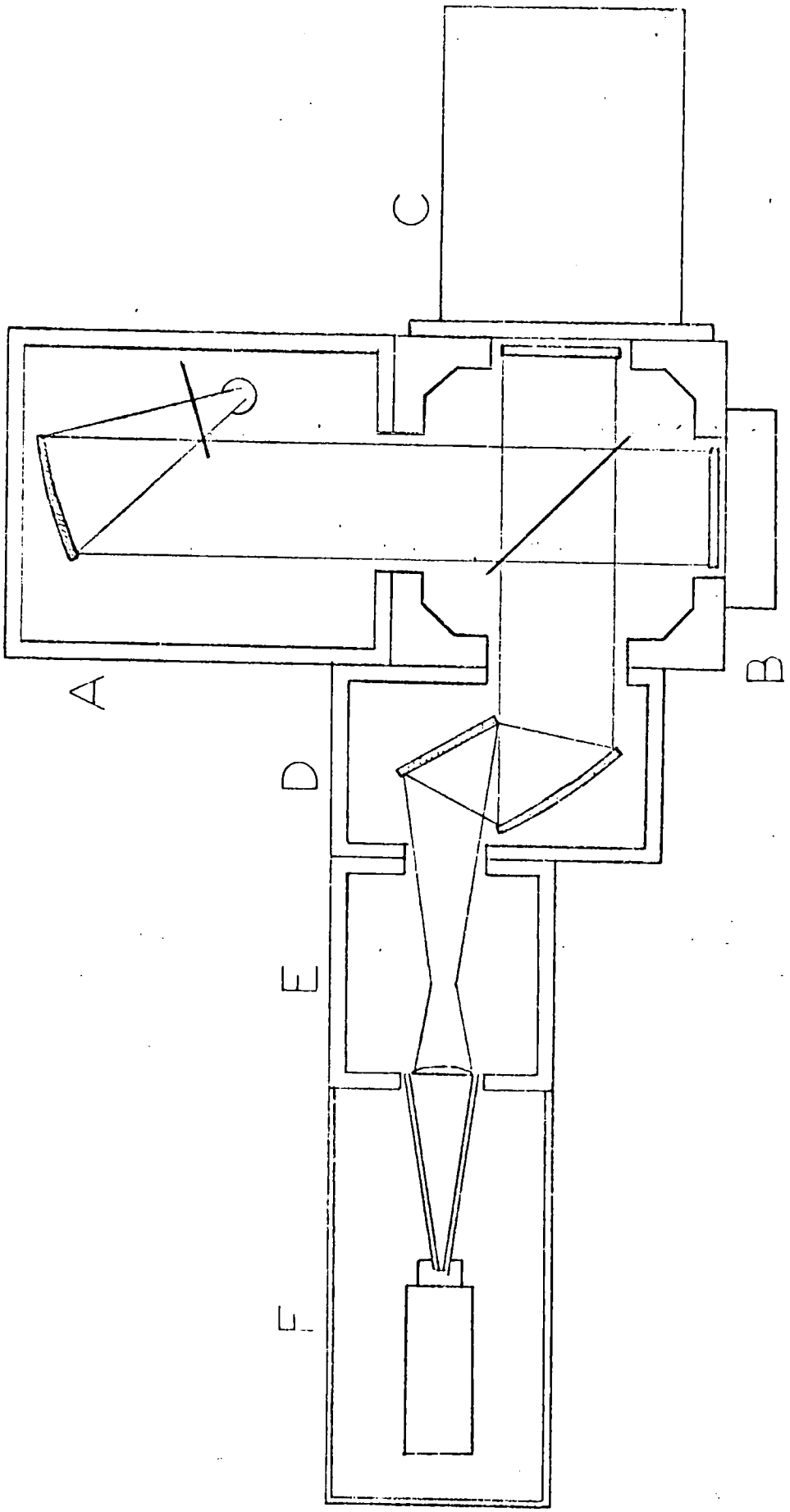

FIG 2.1 SCHEMATIC OF FS-720

and irregularities were also partially eliminated by the voltage stabilisers.

2.2 Sources

The source used was a 315 volts a.c. 90 watt stabilised mercury arc discharge lamp (Original Hanau ST75). The mercury lamp emits broad-band submillimetre radiation by thermal emission from its quartz envelope down to approximately 100 cm^{-1}. Below 100 cm^{-1} radiation is emitted from the hot plasma within the envelope. Such emission occurs down to approximately 2 cm^{-1}. The mercury vapour lamp is thus a good source for far-infrared studies, since broad-band radiation is emitted between 2 and 1000 cm^{-1}. The source had a water-cooled jacket to maintain the metallic source mounting at 323 to 333K. This prevented damage to the electrodes. A flow of about 2 litres per minute from the water mains was found sufficient to maintain the source at the correct temperature. The source mounting was fitted with a bimetallic strip to act as a circuit breaker in order to extinguish the lamp, should its temperature increase due to mains failure or decrease in pressure.

Some of the early work was conducted using Philips 125 watt high-pressure mercury vapour lamps, which find more common usage as street lamps. These lamps were much less stable than the 90 watt lamps, both in terms of short-term noise and long-term drift. The quartz envelope of these 125 watt lamps was dimpled to prevent channel spectra effects. The 90 watt lamps were not dimpled, but did not produce any observable interference effects.

2.3 Golay detector

The detector used for the majority of the work was a Unicam SP50 Golay infrared radiation detector with a 3mm diamond window. The details of the Golay cell are described here for comparison with the low-temperature Indium-Antimonide detector, which has been used to obtain some of the spectra below 50 cm^{-1}. (See section 2.14)

The Golay pneumatic-cell detector (21,22) is a thermal detector in that the radiation is detected by its heating effect. A chamber containing gas of low thermal conductivity is sealed at one end with a radiation window A (see fig. 2.2) through which radiation reaches a thin absorbing film B. The other end is sealed with a mirror membrane C. The gas is usually xenon, and, for the far-infrared spectral region, diamond is used as the window material. The absorbing film B has low thermal capacity and warms the gas with which it is in contact. This rise in temperature of the gas produces a corresponding rise in pressure, which in turn causes the mirror membrane C to be distorted. The absorption film B is a 0.01 μm thick film of colloidon, onto which a thin layer of aluminium has been deposited. The reflection film is similar but has a thicker aluminium layer. Movements of the reflection film are sensed by an optical relay, where light from an exciter source E, which is a stabilised 4 volt, 3 watt lamp (which is underrun to ensure long life) is focused with two condenser lenses F through a line grid G onto the mirror membrane C with a meniscus lens H. From the mirror membrane the light is reflected through the lower half of the grid and then onto the photocell K, by reflection at the mirror L. In the null position of the flexible mirror the lines of the lower half of the grid are imaged between the lines of the upper part, and no light passes from bulb to phototube. When radiation falls on the detector head the resulting movement of the flexible mirror causes a displacement of images of the lower part of the grid on the upper part, and light from the bulb then reaches the phototube, where the signal is recorded electrically. The small amount of heat developed by the incoming radiation is soon dissipated, and the cell returns to its equilibrium position. The time constant for these changes is about 10^{-2} seconds.

To prevent changes in room temperature from affecting the detector a fine leak D connects the detector to a large ballasting reservoir of gas, on the other side of the mirror membrane, which is insensitive to rapid

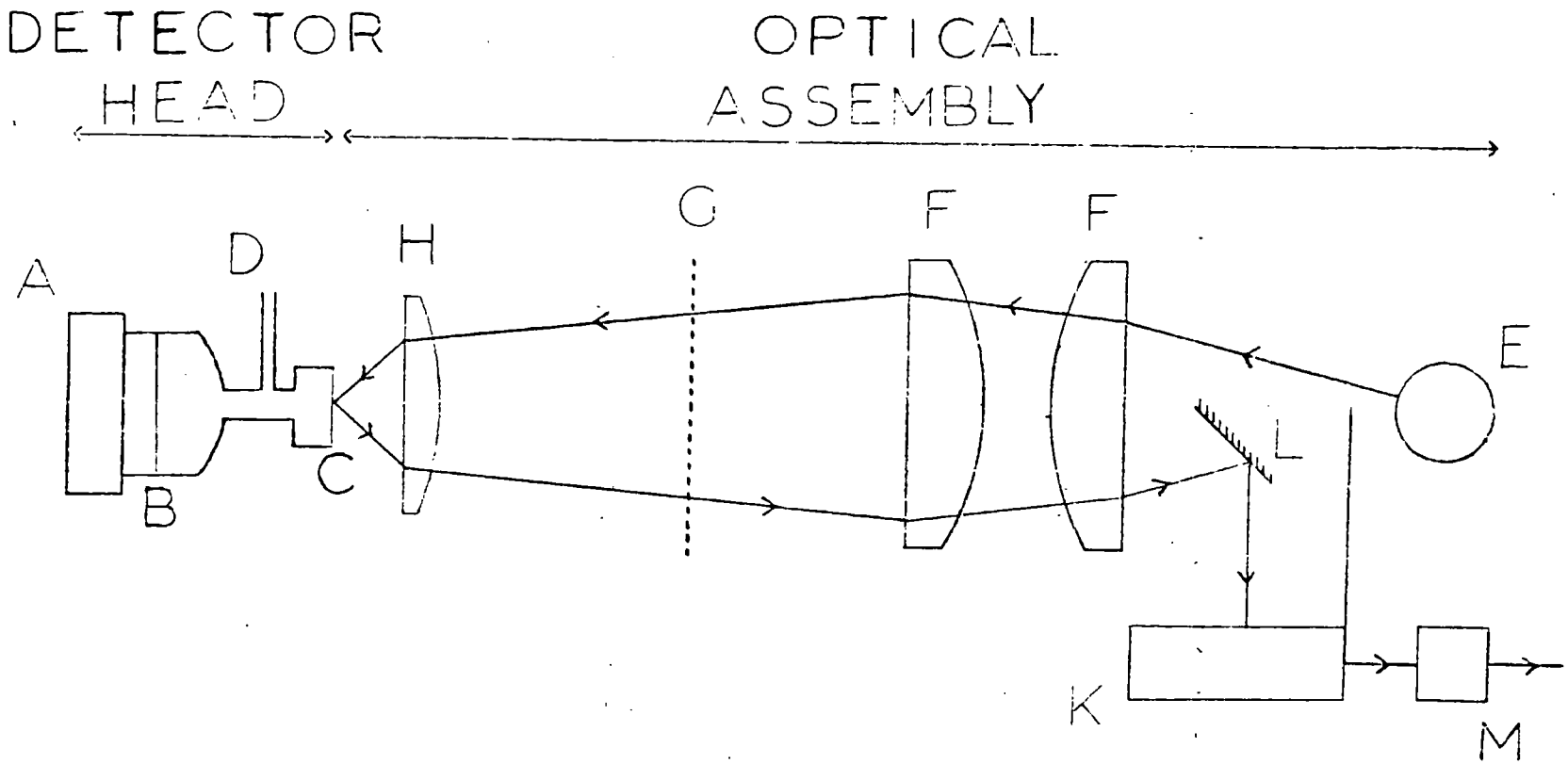

FIG. 2.2 SCHEMATIC OF GOLAY CELL

pressure variations. In the absence of a changing radiation signal the pressures on both sides of the mirror membrane are equal. The detector is thus an a.c. device, and the incident radiation must, therefore, be modulated. The modulation frequency with the FS-720 was 12.5 Hz. This was provided by chopping the beam with a rotating sectored wheel in the source module. The Golay detector is a frequency-independent far-infrared detector, with the frequency response being only dependent on the window material. By using a diamond window, radiation from the visible through the submillimetre-wave region can be detected, since the diamond has no infrared active lattice modes. The output from the phototube is amplified by use of a simple thermionic valve amplifier M, and is then passed to the Golay amplifier in the FS-720 electronics.

2.4 Moiré system

A Moiré grating system (attached to the moving mirror drive) provides the signal for the sampling of the interferogram. The Moiré system consists of two parallel gratings, one of which is mounted on the moving mirror drive, whilst the other is mounted on the base of the drive unit. Light from a small lamp (positioned on the moving mirror drive to one side of the moving grating) was collimated and shadows of the fringes fell on the fixed grating. Depending upon the relative position of the two gratings, light fell on the photocell positioned at the far side of the second grating. The Moiré gratings had a 4 μm ruling and hence the signal reaching the photocell passed from maximum to minimum after 2 μm of mirror movement, and back again after 4 μm of mirror movement. Since the path-difference between the two beams is twice the mirror movement, then for an 8 μm sampling interval the analogue to digital converter is triggered every time the Moiré signal passes through a maximum. For a 4 μm sampling interval the analogue to digital converter is triggered as the Moiré signal passes through both maxima and minima.

2.5 Golay amplifier and demodulator

The interferometer system gave a high signal-to-noise ratio by using tuned amplification and phase-sensitive detection techniques. The output signal from the Golay detector is small and this necessitates high amplification. The Golay amplifier used had a total gain of up to 90 dB. The signal from the Golay was capacitor-coupled to a pre-amplifier, which was a low-drift d.c. amplifier circuit tuned to the chopper frequency (12.5 Hz) by use of a frequency selective network in the feed-back loop. The pre-amplifier had a continuous gain control from 0 to 10 dB. The main amplifier was also a high-gain, low-drift d.c. amplifier with 0 to 80 dB gain in steps of 10 dB.

A magnetic reed switch, mounted on the source chopper, and activated by the passing chopper blades, controlled the demodulator circuit. The demodulator was necessary since the radiation was modulated so that it could be detected by the Golay. The demodulator was synchronised in both frequency and phase with the amplified Golay signal. A filter with 0.5 to 16 seconds time constant also acted as a chopper frequency rejector. A final d.c. amplifier compensated for the attenuation in the filter stage. This amplifier had two d.c. outputs. The 'low' (0 - 10 mV) output was used to drive the pen recorder, and the 'high' (0 - 10 V) output was used to drive the analogue to digital converter.

2.6 Analogue to digital converter

The analogue to digital converter was a 12-bit successive approximation type circuit. A trigger signal from the Moiré amplifier activates a circuit where the analogue input is compared with the voltage of a ladder circuit by the comparator. If the analogue input voltage is less than that on the ladder network, then the bistable remains at zero. If the input voltage is greater than the ladder voltage then the bistable flips over to register 1. The voltage of the ladder network successively halves as the comparator compares the remaining analogue voltage to that on

the ladder network corresponding to each bistable. This comparison and halving process continues through the 12 bistables corresponding to the 2^{11} to 2^{0} bits. On completion of the cycle the output from the ladder will be within one digit of the anologue input, thus giving a digitisation accuracy of 1 in 4096. The state of the 12 bistables is stored in buffer amplifiers and then passed to the paper tape punch to give a record of the sampled interferogram in pure binary notation.

2.7 Interferogram output

The interferogram signal, from the low terminal of the Golay amplifier, was recorded on a Smiths Industries Desk Type Servoscribe Potentiometric Recorder, on the 0 - 10 mV scale. The chart interferogram was always recorded as this visual observation of the interferogram helped in trouble-shooting (e.g. for interferogram mean level drift due to cell leakage). The output from the analogue to digital converter was recorded on 8-track paper tape using an Addo Ltd. Type 4 Tape Punch, which was capable of punching 18 characters per second. The tape code used was as shown in fig. 2.3. Channels 1 and 2 were not used and channel 3 was used as a index and was always punched. Channel 4 was used as an indicator for the first row of data. This was necessary since the 12 digits were recorded in 3 rows of 4 digits in data channels 5 to 8. The simple pure binary code assisted with manual reading of the tapes for checking purposes.

2.8 Experimental beam-splitter characteristics

The beam-splitters used were thin dielectric films of polyethylene terephthalate ('melinex' - registered trade name I.C.I Ltd.; 'mylar' - registered trade name E1 du Pont de Nemours Ltd.) as marketed by Beckman - RIIC Ltd. As discussed in chapter 1 the beam-splitter determines the useful frequency range of the interferometer and table 1.1 showed the theoretical frequencies at which maximum energy is transmitted for a given beam-splitter thickness. The transmission is not restricted to the first interference loop and fig. 2.4 shows the transmission of the first 4 loops of a 200

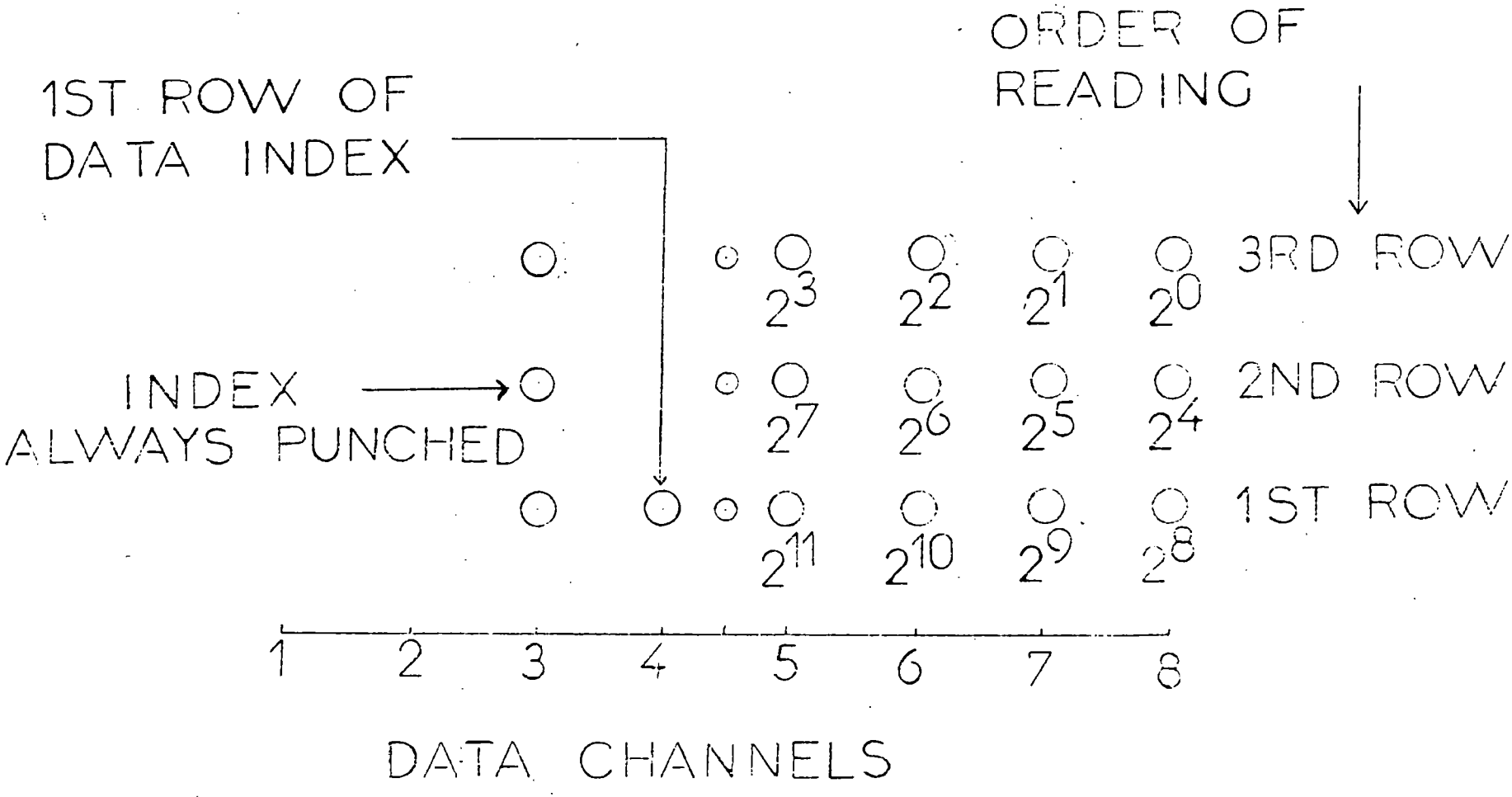

FIG 2.3 TAPE CODE

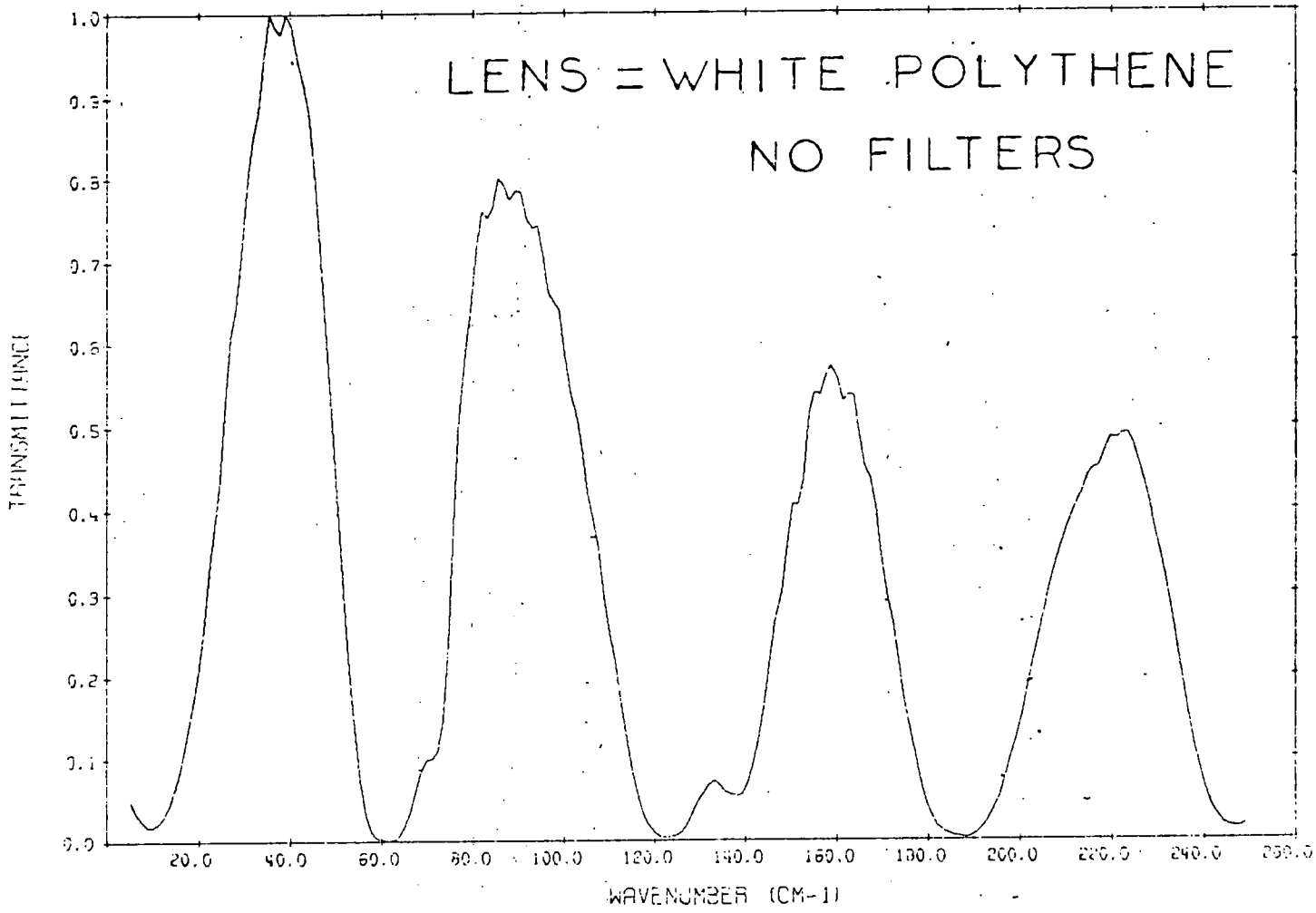

FIG. 2.4 TRANSMISSION OF 200 GUAGE BEAMSPLITTER

gauge (50 μm) beam-splitter in the frequency range 0 - 250 cm^{-1}. This non-ratioed spectrum was recorded using a white polythene field lens and no additional filtering. 1024 data points were sampled. The gradual decrease in transmission of the hoops to higher frequency is due to the increased absorption of the polythene lens optics (see fig. 2.10) and of the beam-splitter material itself.

Fig. 2.5 shows the normalised transmittance spectrum of the interferometer using a 25 gauge beam-splitter and a white polythene lens. 1024 points were computed. Absorption bands at 190 and 290 cm^{-1} are from the 'mylar' beam-splitter and bands at 380 and 435 cm^{-1} are due to absorptions in the polythene. A strong, fairly sharp absorption at 73 cm^{-1} can be seen when using a 50 gauge beam-splitter (see fig. 2.10). This band has been assigned to a polythene lattice mode (23). These absorptions usually ratioed out quite cleanly in a computed spectrum, but sometimes the 73 cm^{-1} band gave a small derivative feature. The 73 cm^{-1} band gave particular trouble because it was the narrowest and most intense of the bands present. The band has been seen to be temperature dependent (16), as would be expected for a lattice mode. The band moves to higher frequency as the temperature is decreased. The band occurs at 79 cm^{-1} at 90K.

The transmittance of the interferometer for a given beam-splitter is asymmetric about the frequency of maximum transmission for two reasons. Firstly, as mentioned previously, the lens and beam-splitter materials begin to absorb more strongly towards higher frequency. Secondly, the output from the source begins to increase rapidly above 100 cm^{-1}.

When running a spectrum it was necessary to carefully select the correct thickness of beam-splitter to give a maximum of energy in the region of interest. The energy in this frequency region was then optimised by the use of filters to remove the unwanted radiation. This is known as 'dynamic range' optimisation.

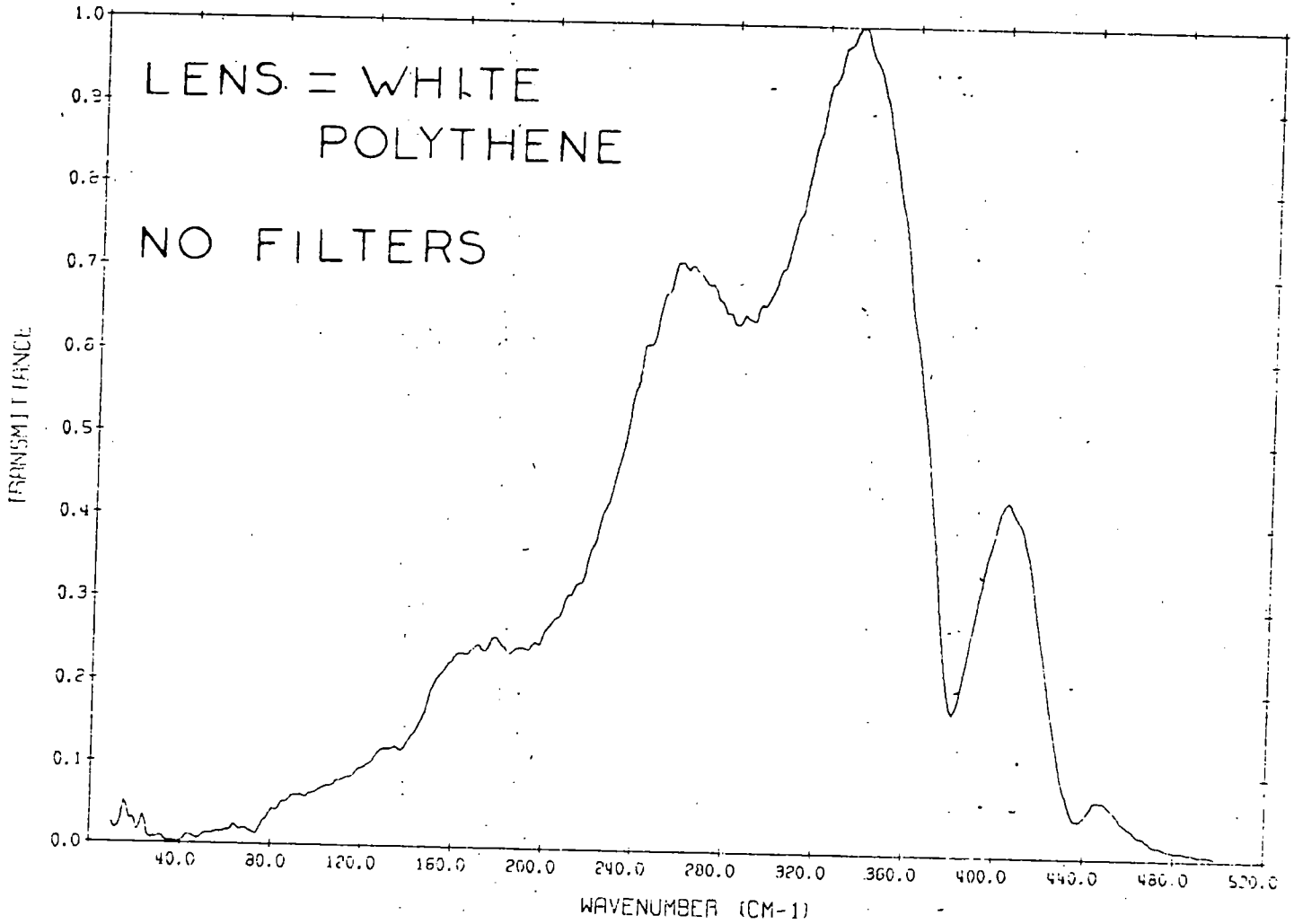

FIG. 2.5 BACKGROUND WITH 25 GUAGE BEAMSPLITTER

2.9 Filtering

To eliminate the high frequency radiation emitted by the source a black poythene filter is used. This filter was made by impregnating polythene with a small amount of carbon black. 50 μm thick filters were also cut from black polythene 'garden' bags and these were found to eliminate the majority of the radiation above 600 cm^{-1}. This high-frequency filtering was important for computational purposes because of the phenomenon of aliasing as discussed in chapter 3. Additional pieces of black polythene were found to shift the frequency of apparent maximum transmission to gradually lower frequencies.

A Yoshinaga filter (supplied by Beckman-RIIC Ltd.) was also used to eliminate high-frequency radiation. These filters utilise the strong absorptions of the alkali halides (due to lattice modes) and similar compounds to remove unwanted radiation. Yamada (24) developed a technique for suspending small amounts of crystalline powders in polythene to yield a filter with the desired transmission characteristics.

For low-frequency work crystalline quartz transmission filters were used to eliminate unwanted radiation. This low-frequency pass filter has a sharp absorption band at 126 cm^{-1}. A 3 mm thick crystalline quartz filter has a sharp high-frequency cut-off at 120 cm^{-1}. A 1 mm thick quartz filter has a cut-off at 200 to 220 cm^{-1}, but shows the sharp band at 126 cm^{-1}, and this sometimes causes ratioing problems.

For work below 100 cm^{-1} grooved polypropylene transmission filter gratings have also been used (25,26). The spacing of the grooves in the grating determines the high-frequency cut-off of the filters. Fig. 2.6 shows the performance of 3 such filters supplied by Beckman-RIIC Ltd. All 4 instrument backgrounds were recorded using a 100 gauge beam-splitter with a white polythene lens and black polythene filter. A summary of useful beam-splitter and filter combinations is given in table 2.2.

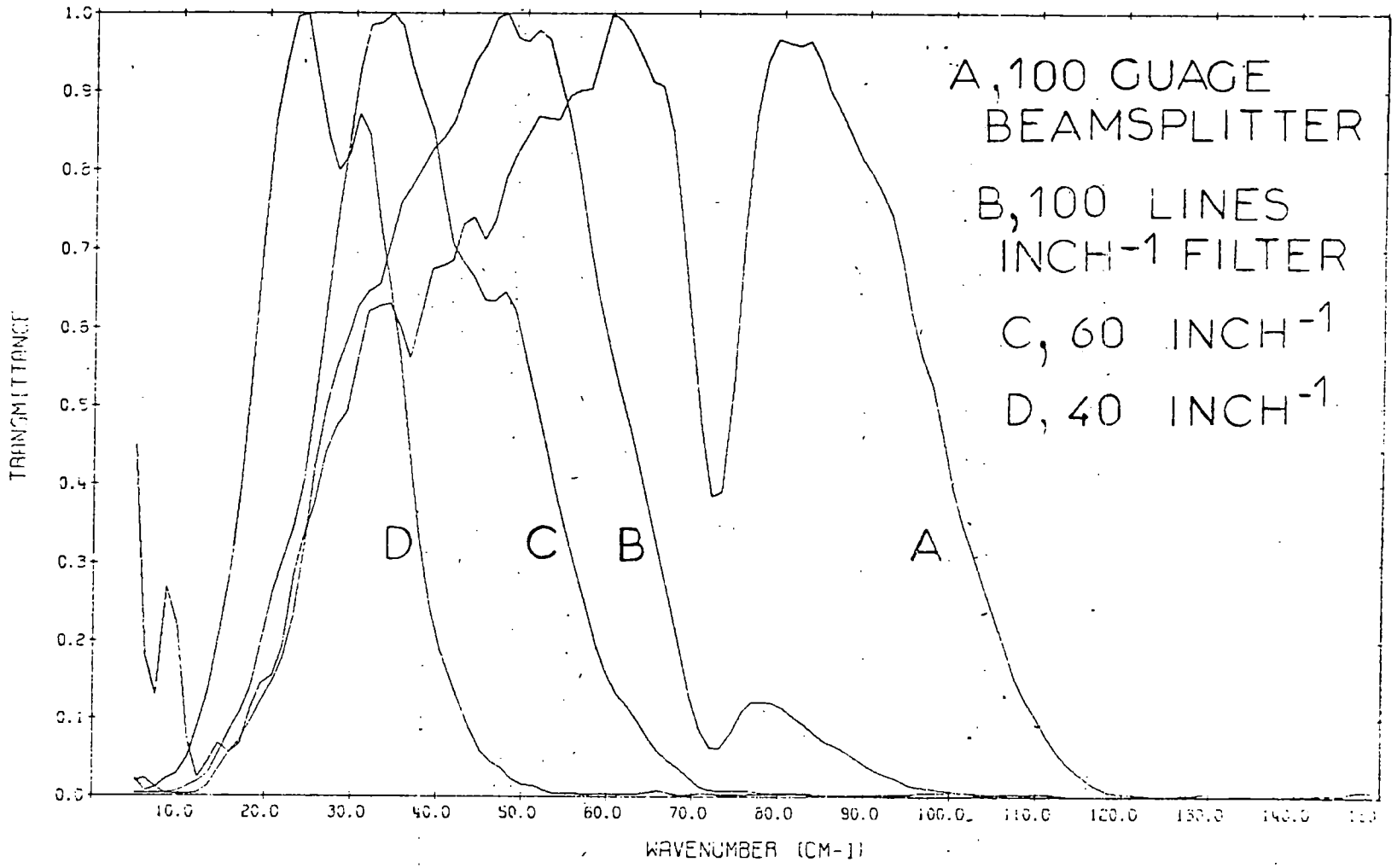

FIG. 2.6 GROOVED POLYPROPYLENE FILTERS

2.10 Reproducibility of the non-ratioed spectra

Fig. 2.7 exhibits the reproducibility of non-ratioed spectra which were recorded at intervals over a period of less than one day. The 3 instrument backgrounds shown were recorded within a 2 hour period using a 50 gauge beam-splitter with a white polythene lens and a black polythene filter. The fringe effect is due to interference in this black polythene filter. The precision is seen to be high as the maximum transmission difference was only approximately 3%, and all 3 curves can be seen to usually lie within 1% transmission. The differences between the backgrounds are exaggerated by the normalisation to peak noise rather than mean noise at maximum transmission. This is discussed in chapter 3. The normalisation constants employed to produce these transmission spectra show the high precision of the spectra. For the 3 backgrounds shown the normalisation constants were 0.332, 0.341 and 0.343. This gavea maximum difference of 0.01, which corresponds to a precision of 1%.

Fig. 2.8 shows the reproducibility of the single beam spectra over a much longer period. These 4 spectra were recorded at intervals over a period of 2 years. A 50 gauge beam-splitter and a black polythene filter were used. The maximum transmittance discrepance for these backgrounds was approximately 8%, and the backgrounds were seen to be usually within 2% transmission. The normalisation constants were 0.176, 0.183, 0.176 and 0.181 and showed the precision of the backgrounds to be about 1% transmission. The reproducibility of non-ratioed instrument backgrounds was thus seen to be very high, even over a considerable time period.

2.11 Vacuum system

Because the far-infrared absorption of atmospheric water vapour is very strong, the optical path of the radiation within the interferometer must be free from water vapour. Attempts to ratio out the water vapour absorptions were doomed to failure because of the sharpness of the vapour bands. The internal volume of the interferometer was found to be too large

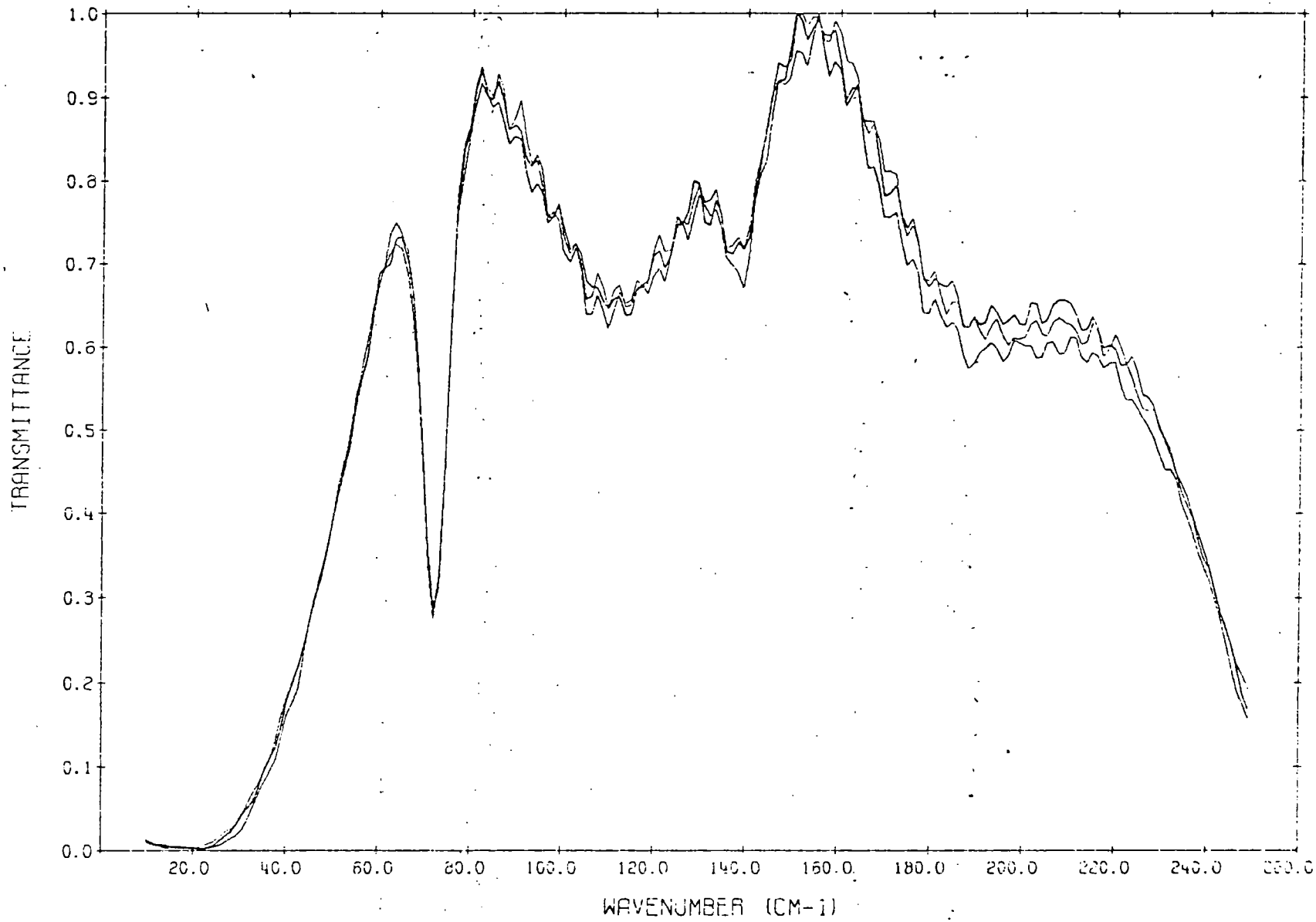

FIG. 2.7 SHORT-TERM REPRODUCIBILITY

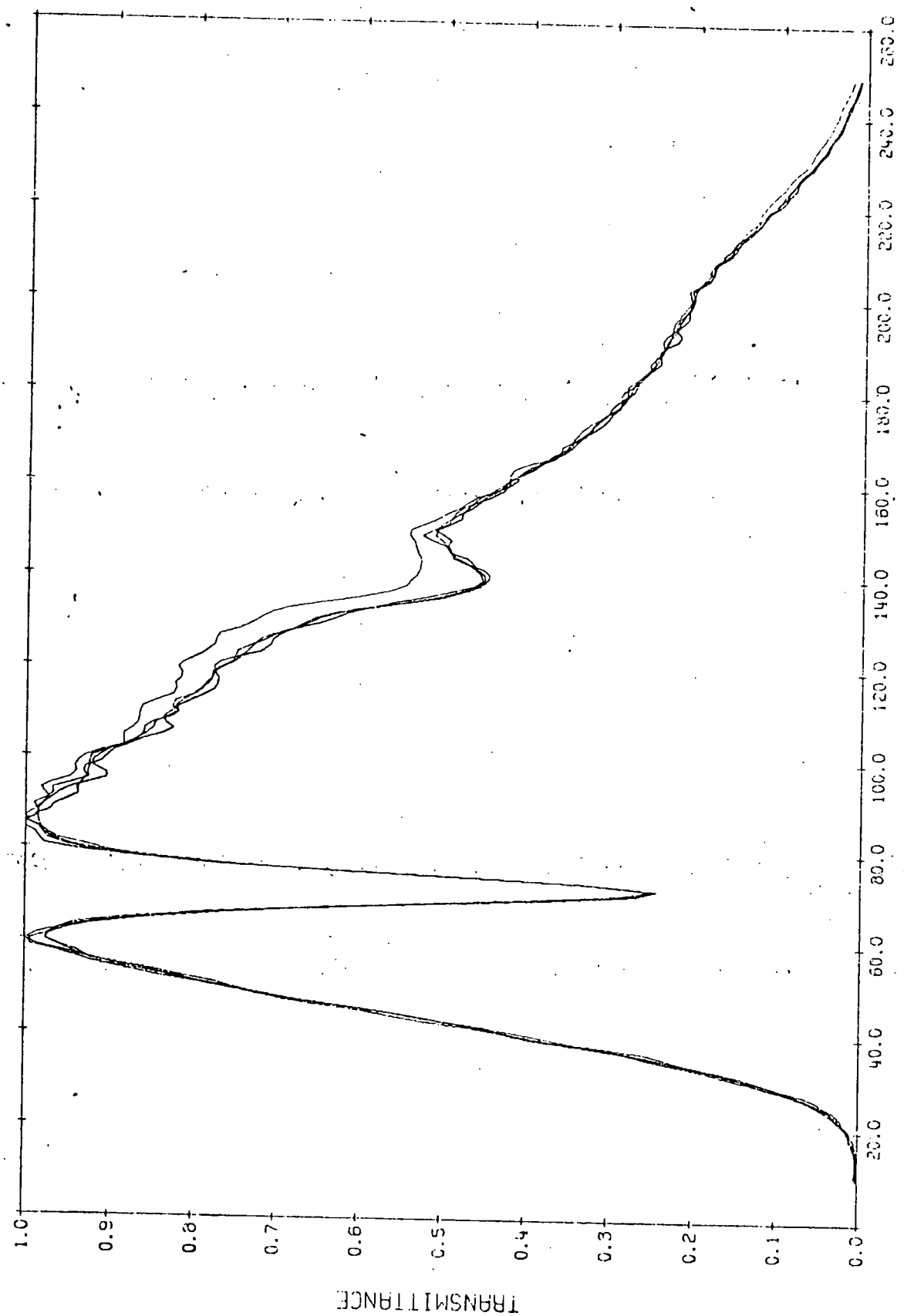

FIG. 2.8 LONG-TERM REPRODUCIBILITY

to allow successful purging of the whole instrument. It was thus evacuated to a pressure of between 0.02 and 0.05 torr, at which pressure no water vapour absorption was detectable at a resolution of 1 cm^{-1}. A Genevac Type GRD2 Double Stage Rotary Piston Pump with a displacement of 56 litres per minute was used to provide the vacuum. Typically a pumping time of 20 minutes was necessary to bring the interferometer down to 0.05 torr from atmospheric pressure.

2.12 Liquid cells

For standard transmission measurements, with the interferometer in the symmetric mode, the sample was placed before the detector in the recombined beam. Liquid samples were contained in semi-permanent cells, which were mounted in a suitable cell holder placed at the point where the converging recombined beam came to a focus. With these demountable cells the sample pathlength was created by sandwiching a spacer G, with a circular aperture, between two infrared transmitting windows E and F (see fig. 2.9). This assembly was then clamped between two stainless steel plates A and B. Two filling ports were mounted on the front plate A. These filling ports were sealed with polytetrafluoroethylene (teflon) washers and short steel screws. The screws used had conventional heads so that they could be tightened to give a very good vacuum seal. A teflon gasket D was placed between the front plate and the top window E to assist with the sealing around the entry ports. The upper window had two small holes drilled through it to enable filling of the sample area in the spacer. The filling ports C could be fitted with female Luer tapers. This enabled standard Luer syringes to be used for filling the cell. The two ports enabled easy cleaning of the assembled cell by flushing with solvent.

Both teflon and lead spacers were used in the demountable cells. The lead spacers gave a more effective seal at short pathlengths (below 0.01 cm), but were much less chemically inert than the teflon spacers. 3 mm polythene cell windows were used in all studies except where otherwise stated.

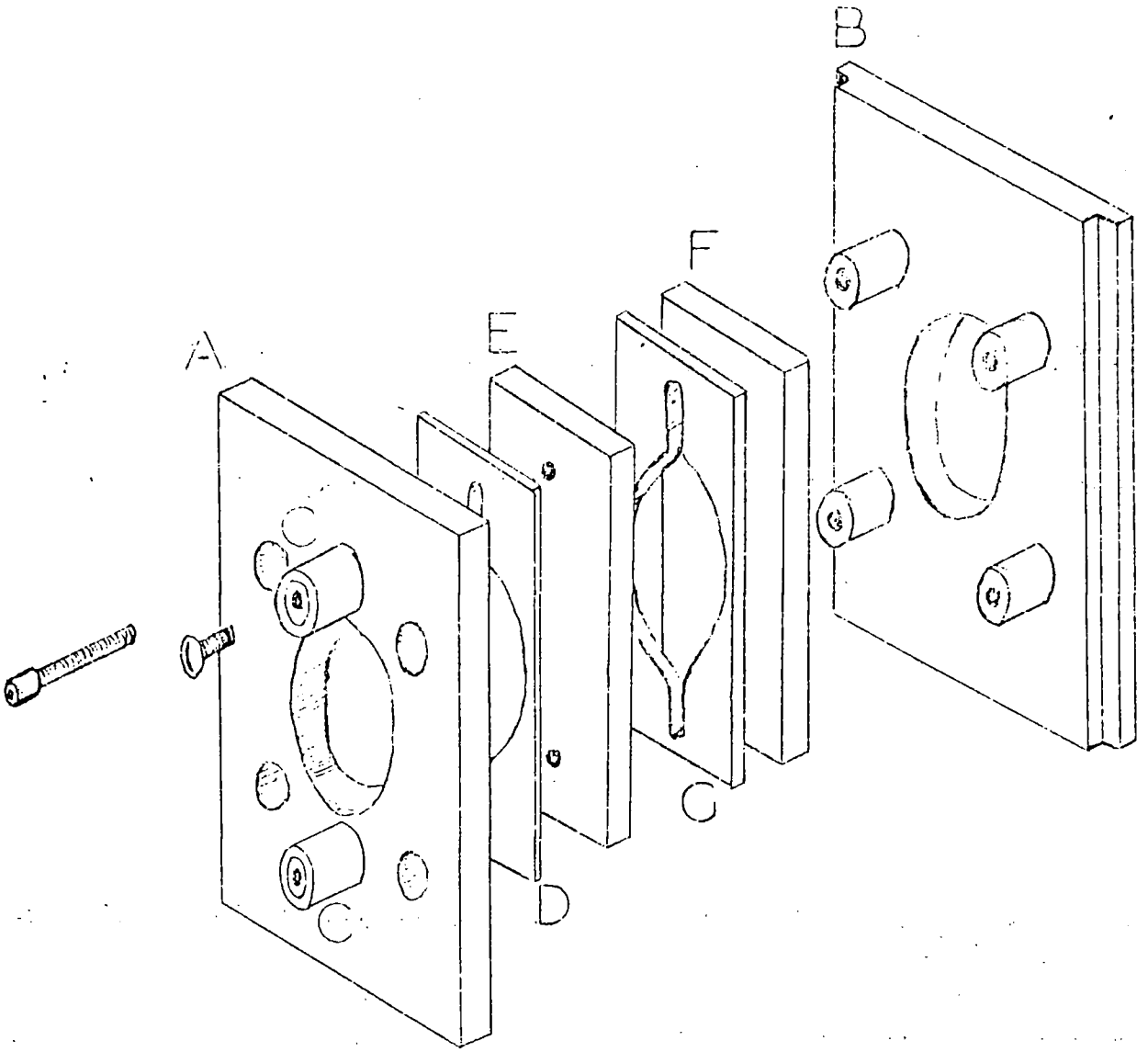

FIG 2.9 DEMOUNTABLE CELL

Thinner polythene windows were found to distort as a result of the high vacuum surrounding the cell in the instrument. Polythene windows were used in the frequency range 10 to 625 cm^{-1}, but were found to have several lattice absorptions in this region. The sharp band at 73 cm^{-1} (see fig. 2.10) was especially prominent. Polythene is inexpensive and, unlike most infrared transmitting materials, it is not brittle. Hence it could be clamped tightly to provide the necessary vacuum-tight seal.

Certain types of polythene were found to become contaminated by some of the organic solvents used. Benzene caused the surface of the polythene to swell and become spongy (presumably due to some form of occlusion of the solvent in the polythene lattice). High density polythene (HDPE) plates were more resistant to swelling and only became contaminated by the solvent after contact for a considerable time (contamination occurred if the plates were accidentally left in contact with the benzene overnight). The swelling was completely prevented by washing the cells with acetone after use each day. Polythene melts at about 383K and thus could not be used for high temperature studies.

Poly-4-methylpentene-1 (TPX) is similar to polythene in that it is a compressible plastic. It has the advantage that it is transparent in the visible region and this enabled observation as to whether or not a cell was completely full. The spectrum of TPX between 20 and 250 cm^{-1} is shown in fig. 2.11 and it can be seen that the material has a very low overall absorption, with no major bands occurring in this region. In respect of transmission properties TPX appeared to be superior to HDPE, but had the serious disadvantage that occlusion of organic solvents occurred much more rapidly than for HDPE. When using benzene as solvent the plates of TPX were found to become spongy after 1 hours contact. Hence these plates were of little use for such solvents. After contact with benzene the TPX plates took on the appearance of splintered glass, and never returned to their original transparency, the surface remaining opaque.

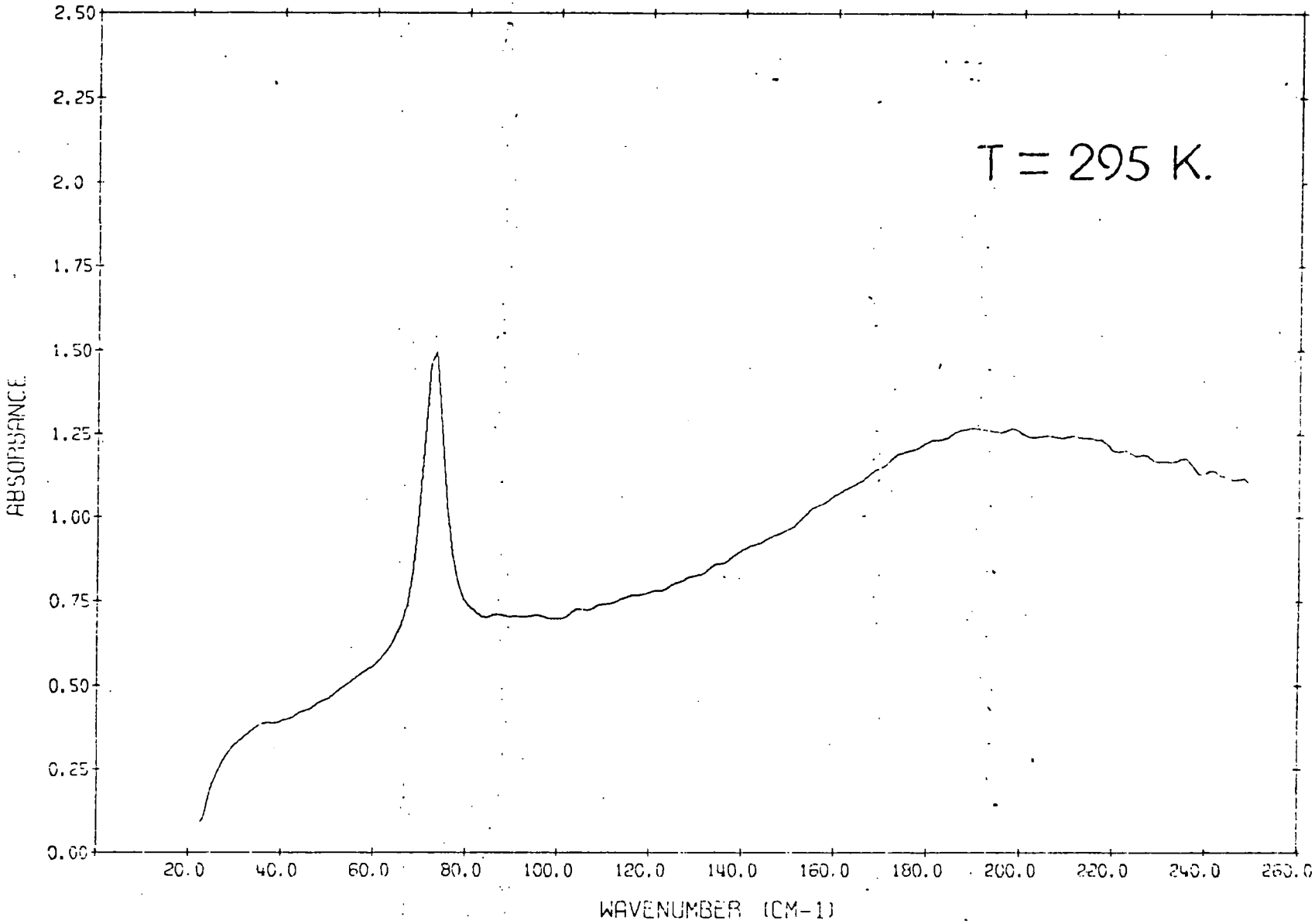

FIG. 2.10 6mm. HIGH DENSITY POLYTHENE

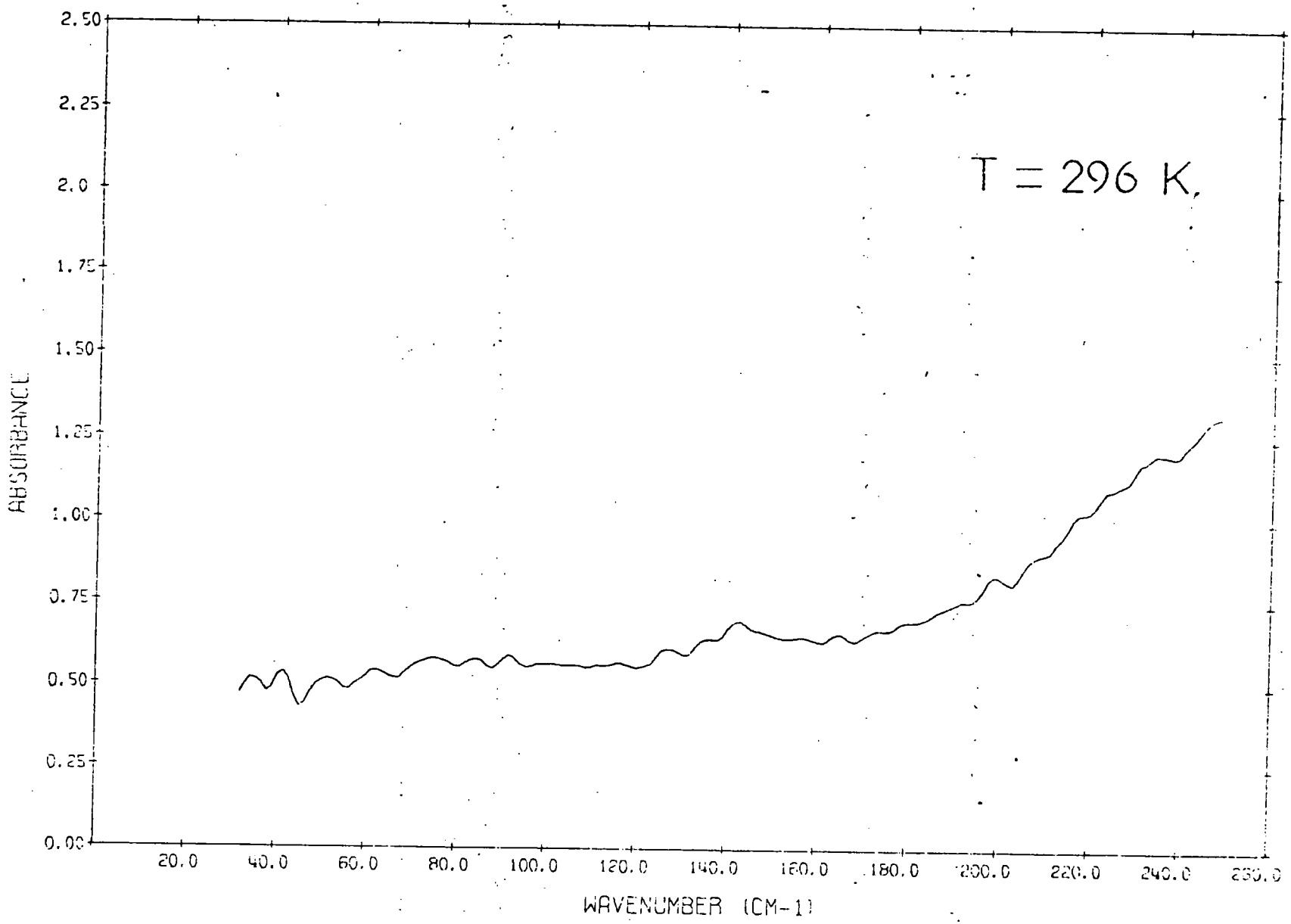

FIG. 2.11 5mm. POLY-4-METHYL-PENTENE-1

For very short pathlengths ($\sim$ 0.0012 cm) a pair of Beckman-RIIC wedged silicon metal windows were used. This was found to be necessary since the plates were not flat enough to give a good seal with such thin spacers. The silicon windows were very hard and inert, and were found to have no major absorptions between 40 and 250 cm^{-1} (see fig. 2.12). The transmission of these plates over this region was seen to be low (presumably mainly due to reflection losses) and spectra recorded using these plates had very high noise levels due to the high gains necessary. The silicon plates were wedged to minimise interference effects.

Such demountable cells using 12 μm spacers and silicon windows were not sealable at pressures below atmospheric. This being due to lack of the necessary cell compression due to fear of breaking the plates. This necessitated the use of an isolating window between the sample compartment and the collimating module. This window enabled the sample compartment and Golay chamber to be flushed with dry nitrogen, whilst the remainder of the instrument was evacuated. The most successful method of flushing was found to be using dry nitrogen gas from the line supply. The gas was passed through two traps surrounded by liquid nitrogen and then into the sample compartment through the pumping port in the side of the sample chamber. Inside the pumping port a 'T' piece was fitted. This had one large diameter tube which lead to a position above the sample holder, and a second small diameter tube which lead to a syringe needle inserted through the field lens. This flushed the light pipe between the Golay window and the field lens. The end of the syringe needle was bent through 90^{o}, so that the force of the nitrogen flow did not fall on the Golay window, but was rather directed against the walls of the light pipe. If the nitrogen flow was directed at the window then this caused the Golay window to vibrate and a noisy spectrum resulted. Typical flushing times for the isolated sample compartment were 50 minutes to 1 hour. Flushing was always continued until none of the typical water vapour modulation was noticeable on the

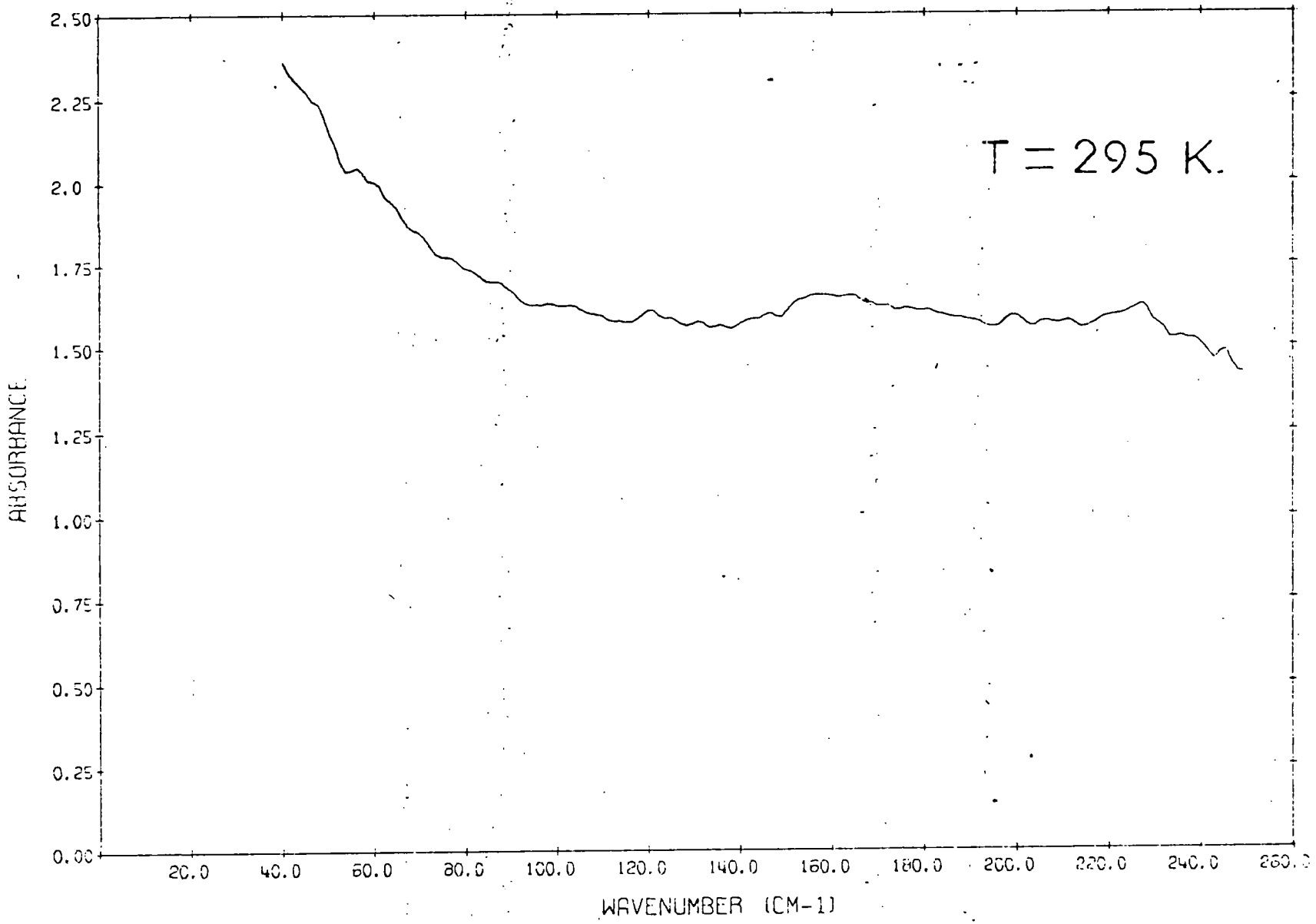

FIG. 2.12 TWO 3mm. WEDGED SILICON PLATES

interferogram.

2.13 Variable temperature control

Spectra of liquid samples at various temperatures were obtained by using the Beckman-RIIC variable temperature unit VLT-2, which incorporates a Eurotherm TEM-1C Automatic Temperature Controller with a range from 83 to 523K. The temperature was controlled by simply setting the required temperature on the dial. A coolant was used which boiled at a slightly lower temperature than that required. The cell was mounted in a cell holder block (see fig. 2.13), which was topped with a refrigerant reservoir. Heating to maintain the required temperature was provided by two electrical coils mounted on the sides of the cell block. A copper / constantan thermocouple was mounted in a hole in the cell block and this was connected to the temperature control unit. This thermocouple determined the amount of electrical heating necessary. A second thermocouple was mounted in a hole in the liquid cell top plate and was used to monitor the actual temperature of the cell itself. After placing the cell mounting block in the interferometer the instrument was always evacuated before any refrigerant was poured into the reservoir. If this was not done then condensation of water vapour occurred on the walls of the reservoir and also on the transmission windows of the cell itself.

For temperatures above ambient no refrigerant was necessary, and the temperature was maintained by the electrical heaters, which compensated for the normal heat losses from the cell to the atmosphere. When a temperature below ambient was required then a refrigerant was poured into the reservoir, and incremental heating from the heaters maintained the steady temperature as the refrigerant was boiled away. When a temperature was required which was not close to the boiling point of a suitable coolant, then some method of decreasing the thermal contact between the refrigerant and the cell holder became necessary. This prevented coolant from being boiled away at a very high rate, by allowing the cell holder to reach thermal

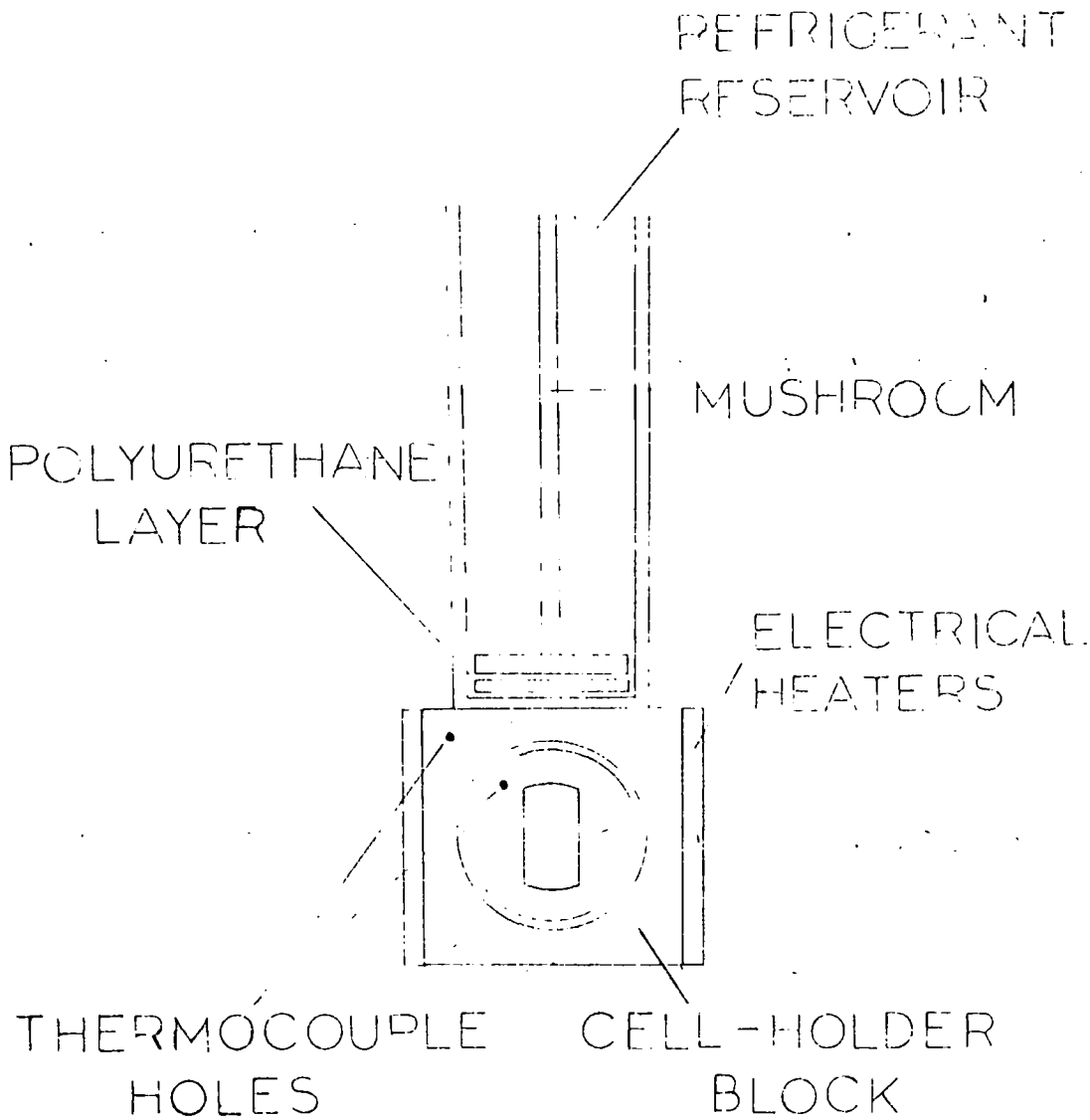

FIG 2.13 VARIABLE TEMPERATURE CELL MOUNTING BLOCK

equilibrium at a temperature considerably higher than that of the boiling point of the refrigerant. This partial thermal barrier was supplied by a thin layer of polyurethane foam supported on the end of a 'piston-like' device known as a mushroom (see fig. 2.13). The thickness of the polyurethane foam controlled the amount of thermal insulation. If too thick a layer of polyurethane was used there was no thermal contact between the cell block and the refrigerant, and thus thermal equilibrium was never reached at the temperatures below ambient.

Good thermal contact was necessary between the cell holder block and the cell itself. This was maintained by a thin layer of silicon grease smeared around the edges of the cell. The temperature of the cell itself was monitored by use of a thermocouple and recorder, and was often found to be different from that set on the dial by as much as 2K. Most of the temperature studies were conducted above ambient temperature, and hence no refrigerant was necessary. For temperatures between 233 and 303K solid carbon dioxide in acetone was found to be a very efficient coolant. For lower temperatures the following refrigerants were useful : liquid air boiling at 126K, liquid oxygen boiling at 90K and liquid nitrogen boiling at 77K.

The refrigerant reservoir was kept well topped-up for the whole time that the spectrum was being recorded. When using solid carbon dioxide in acetone it was important to ensure that there was always solid carbon dioxide present in the reservoir. The best results with this coolant mixture were achieved by filling the reservoir approximately one-fifth full with acetone, to obtain a good thermal contact, and by filling the rest of the reservoir with solid carbon dioxide broken into small pieces of 0.5 to 1 cm diameter. By ensuring that solid carbon dioxide was always present in the reservoir then the reservoir could be topped-up with more solid carbon dioxide during the running of an interferogram, without affecting the temperature of the cell. Using this technique it was found that the temp-

erature of the cell could be maintained to within ±0.5K for over 2 hours in the temperature range 243 to 313K.

2.14 Cooled Germanium bolometer

2.14.1 Apparatus description

In an attempt to obtain useful spectra below 50 cm^{-1} a Germanium bolometer with preamplifier, as supplied by Queen Mary College Industrial Research Ltd., has been used. The bolometer was designed to work at liquid Helium temperatures (4.2K at atmospheric pressure). The cryostatt used for maintaining the low temperature was the Oxford Instruments Co. Ltd. MD 800 detector cryostatt CA 5176, which was a compact custom built liquid Helium cryostatt designed principally for cooling infrared detectors. It was particularly useful for interferometric spectroscopy because of its long hold times (of the order of 24 hours with one liquid Helium filling). The bolometer is shown in fig. 2.14 and consisted of an inner Helium can A, to which the Germanium crystal B was attached. The Helium can was surrounded by a radiation shield maintained at 77.3K by a can of liquid nitrogen C which forms the upper part of the radiation shield. The two cans were surrounded by a vacuum case which supported the necks of the helium and nitrogen cans. The space between the cans was maintained at a high vacuum to ensure that there was no thermal contact between the helium can and the nitrogen can or the surroundings.

The cryostatt had optical access through 20 and 25 mm aperture windows of TPX in the radiation shield and vacuum case respectively. Electrical access from the germanium crystal to the amplifier box, which was mounted on the side of the vacuum case, was made through a BNC socket and a 4-pin plug. The preamplifier used was originally designed for use in conjunction with a search coil in a spacebourne magnetometer, and was a wide-band (1 Hz to 100 kHz) low noise field effect transistor input amplifier (30a). The output from this amplifier replaced the Golay signal in the instrumental set-up as described in section 2.5. The detector signal was

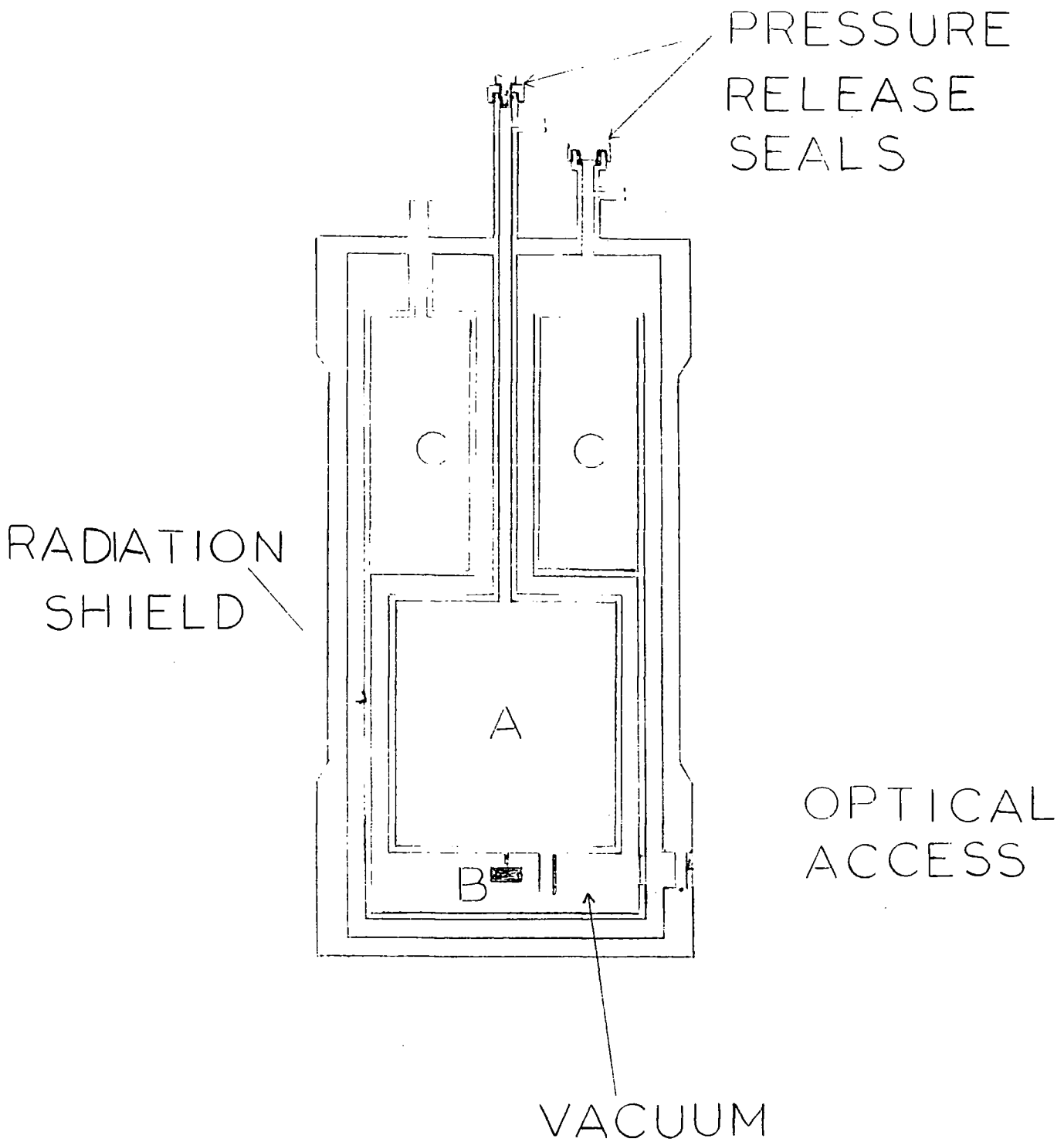

FIG 2.14 COOLED BOLOMETER CRYOSTAT

modulated at 12.5 Hz, as for the Golay detector, by use of the chopper in the source beam.

It was necessary to filter out much of the high frequency radiation to prevent 'swamping' of the bolometer by the high energy radiation. A sapphire quartz filter was used to filter out much of this radiation, since it had a cut-off at 250 cm^{-1}. The quartz cuts-on again at about 1000 cm^{-1}, and so an additional filter of black photographic paper was necessary. The filters were maintained at liquid helium temperature to prevent room temperature signals reaching the detector from these filters.

Many special precautions proved necessary when using the liquid helium. The extreme cold caused by the liquid could cause extensive tissue damage to any exposed skin, similar to that due to a severe burn. All contact with the liquid thus had to be avoided. The extreme cold could also cause condensation of atmosperic air onto exposed liquid helium, or gas cooled surfaces. The nitrogen present in this liquid air would then evaporate leaving behind an oxygen enriched liquid, which would be potentially explosive. To prevent ignition of grease, oil or other combustible materials in contact with air-condensing surfaces, then all exposed surfaces were kept absolutely clean at all times. As liquid helium has a very low heat of vapourisation of 20.9 $J.g^{-1}$ (compare liquid nitrogen 198 $J.g^{-1}$) it was kept in vacuum insulated containers to minimise evaporation. The storage vessels contained a radiation shield to intercept heat input due to thermal radiation from ambient temperature. This radiation shield was a concentric liquid nitrogen vessel. The storage vessels were not sealed, but were covered to prevent moisture condensing out of the air. The latter could cause the formation of a blockage known as an 'ice-bridge' in the neck of the vessel. Such a blockage would cause a serious pressure build-up since the gas to liquid volume ratio for helium is 700 to 1.

A simple bunsen valve was used to prevent entry of water vapour into the liquid helium. The bunsen valve acted as a simple one way valve,

and maintained a small pressure of helium vapour above the liquid and thus minimised evaporation. Bunsen valves (see fig. 2.15) were made from 4" lengths of 0.875" internal diameter thick-walled black neoprene tubing. A diagonal cut approximately 1" deep was made in the tubing wall, so that the wall was just cut through. This cut acted as the pressure release, because if the pressure inside the vessel increased, then the wall of the valve was pressed outwards, thus opening the cut and releasing the pressure. The top of the valve was sealed with a close-fitting rubber bung. The valve fitted closely over the neck of the storage vessel.

The liquid helium was transferred from the storage vessel to the cryostatt by means of a vacuum insulated transfer tube. This consisted of two concentric stainless steel tubes bent in the form of an inverted 'U'. The annular space between the tubes was evacuated on a diffusion pump to 10^{-3} torr. This vacuum would cryopump to about 10^{-6} torr as the liquid helium began to flow along the central tube, and thus provided adequate thermal insulation.

The liquid helium was driven over into the cryostatt by use of the pressure of gaseous helium in the storage vessel. A transfer 'T-piece' was machined as shown in fig.2.16. A football bladder was attached to position A on the 'T-piece' and the transfer tube B was clamped in position in the liquid helium storage dewar by the screw cap C. To achieve a liquid helium transfer the tap on the recovery branch was closed, and the pressure inside the dewar was built up by a few squeezes of the bladder. The helium gas forced into the dewar from the bladder was relatively warm compared to the liquid helium, and thus caused vapourisation of further helium, thus building up the pressure. This pressure gradually began to force liquid helium up the inner passage of the transfer tube. The first liquid helium was vapourised because the tube was relatively warm, but gradually the flow of cold gas cooled down the transfer tube, and eventually liquid helium began to pass along the tube. A blue 'plume' (presumably caused by liquid

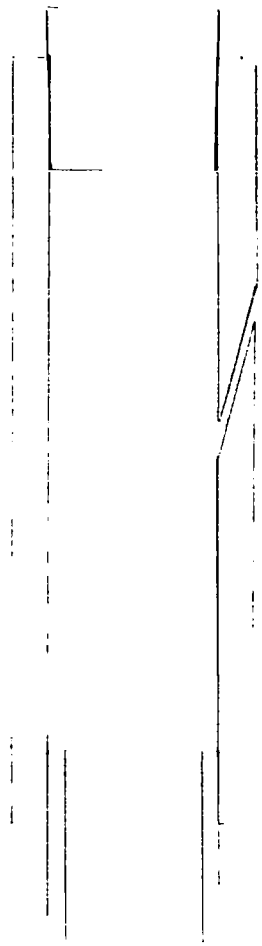

FIG 2.15 BUNSEN VALVE

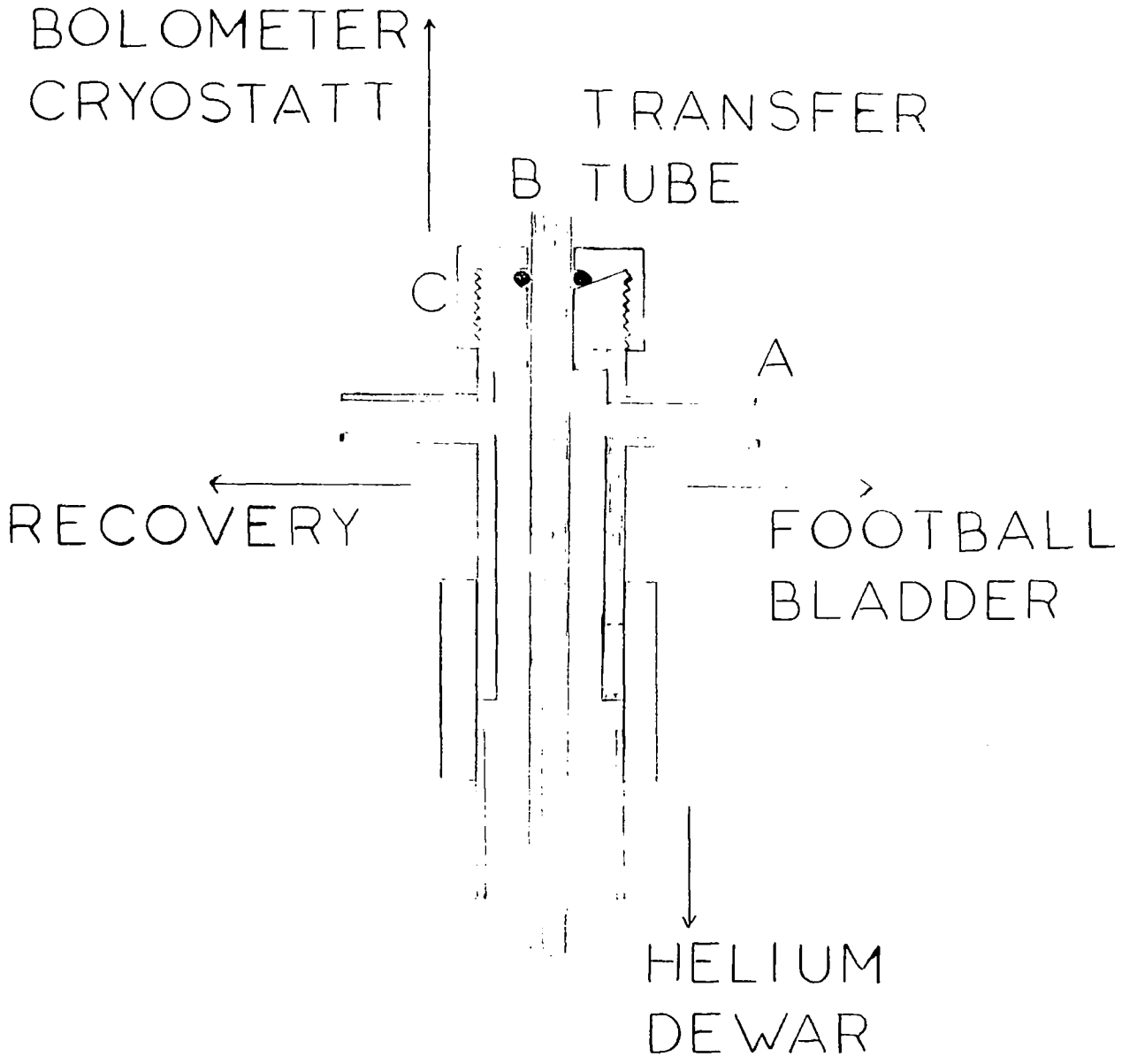

FIG 2.16 HELIUM TRANSFER T-PIECE

oxygen being frozen out of the air) was observed when liquid helium began to flow. The rate of flow of liquid helium was controlled by use of the tap in the recovery branch, which when opened decreased the pressure in the storage vessel and thus decreased the flow.

2.14.2 Operating procedure

The vacuum space of the cryostatt was firstly pumped down to below 10^{-1} torr using a two-stage rotary vacuum pump (but see end of this section). The cryostatt was then cooled down to liquid helium temperature. To minimise the amount of liquid helium used during the cooling, the cryostatt was firstly pre-cooled with liquid nitrogen. The procedure employed was to fill the central helium can with nitrogen, by use of a 5 mm diameter stainless steel tube and funnel. This was placed down the liquid helium transfer tube entry port. The upper nitrogen can was then filled with liquid nitrogen. The liquid nitrogen was left in the helium can for two hours whilst the cryostatt pre-cooled. The long pre-cooling time was due to the very high thermal capacity of the cryostatt, which was necessary to produce the long hold times required for interferometry. The liquid nitrogen was then removed from the helium can by a pressure of nitrogen gas from the line supply. To achieve this the stainless steel tube was sealed in the neck of the helium can by use of plasticine. The nitrogen gas was then blown in through the pumping side-arm on the neck of the helium can. The gas flow forced out the liquid nitrogen, which was collected by use of a length of neoprene tubing. For the longest hold times it was necessary to ensure that thenitrogen was completely removed from the helium can. Any nitrogen present when the liquid helium entered would be solidified, and would then cause the helium to boil away. The stainless steel tube was therefore carefully placed so as to just touch the bottom of the can. For minimum liquid helium loss the liquid nitrogen would be forced out by helium gas, but this was never attempted.

As soon as the liquid nitrogen had been removed the helium

transfer was begun. (see section 2.14.1) When the helium can was nearly full with liquid helium, then the flow of escaping gaseous helium from the pumping side-arm and around the transfer tube was seen to oscillate. This was subsequently taken as an indication that the helium can was nearly full. The blue 'plume' from the side-arm indicated that the helium can was full, and the helium transfer was then immediately discontinued.

At this time the signal level from the detector was monitored as a check that the cryostatt had taken the liquid helium. The noise level was recorded for a period of about 1 minute, with the bolometer crystal at 4.2K. To gain the maximum sensitivity from the bolometer the temperature was then decreased further by pumping on the liquid helium. Between its boiling point (4.2K) and what is known as the lambda point (2.17K), liquid helium exhibits the characteristics of normal liquids and is known as Helium-I. Below the lambda point liquid helium exhibits the phenomenon of superfluidity or zero viscosity, and has an anomalously high thermal conductivity for an inert gas. Below the lambda point it is known as Helium-II. When the output from the bolometer crystal was monitored whilst the pumping operation was in progress, then it was noticed that the signal became very noisy when the pressure was just above that required (35 torr) to produce the temperature of 2.17K. At the lambda point the bolometer signal suddenly disappeared, and this was assumed to be caused by the preamplifier being switched off, because of the very noisy nature of the signal. After about a minute the preamplifier switched on again and the signal was seen to be free from all observable noise.

A schematic representation of the pumping system employed in conjunction with the cryostatt is shown in fig. 2.17. A very large capacity vacuum pump was necessary to obtain the low temperatures between 1.4 and 1.5K, where the bolometer was reaching its maximum efficiency. An Edwards High Vacuum Single Stage Rotary Pump ES330 with a capacity of 330 litres per minute was used. 1" internal diameter neoprene tubing was used through-

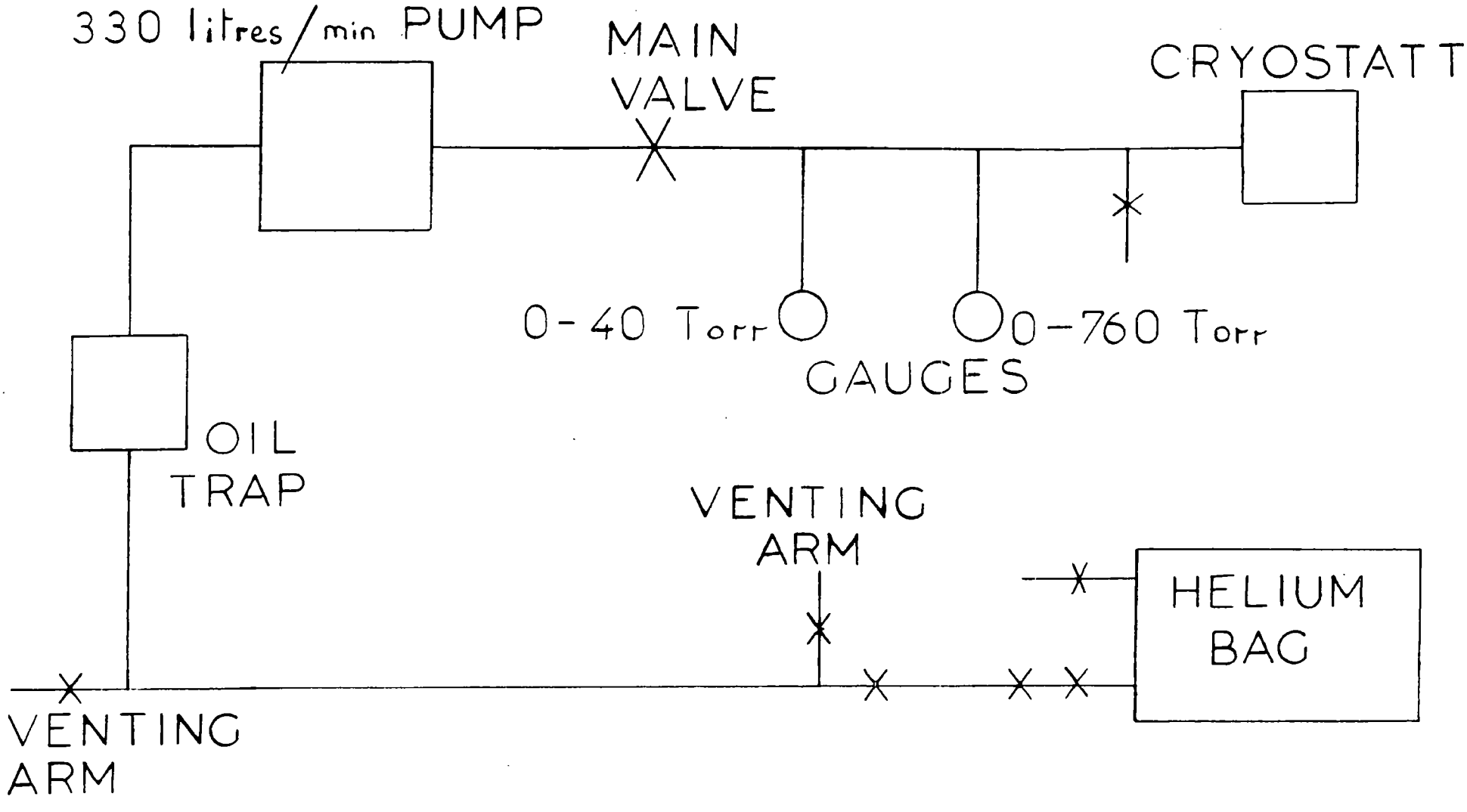

FIG. 2.17 SCHEMATIC OF PUMPING SYSTEM

out the main pumping line to ensure maximum possible pumping speed. The helium gas was recovered by passing the vacuum pump exhaust through an oil mist filter and then through $\frac{1}{2}$" diameter copper tubing to a 25 m^3 neoprene bag.

The pressure above the liquid helium was firstly decreased only very slowly by having the main pumping valve only partially open. The pumping operation from 760 torr down to 40 torr took about 1 hour typically. The pumping speed was then gradually increased, by slowly opening the main pumping valve, as the lambda point was reached. After the lambda point had been passed then the main pumping valve was then fully opened. The typical base pressure was 2 to 3 torr, which corresponded to a temperature of 1.4 to 1.5K.

After the bolometer had been used for a few weeks then considerable difficulty was experienced in filling the helium can with liquid helium. It was concluded that this was due to thermal contact between the helium can and either the nitrogen can or the outer casing. This could have been due to too high a pressure in the vacuum space. It was concluded that it would be necessary to use a diffusion pump backed by a rotary pump to obtain a vacuum below 10^{-3} torr in the vacuum space.

2.14.3 Typical results

It very soon became apparent that the cooled bolometer was producing vastly improved spectra in the 10 to 100 cm^{-1} region, relative to those obtained when using the Golay detector. Fig. 2.18 shows the instrument background obtained when using the pumped bolometer at 1.5K with a 100 gauge beamsplitter and no additional filtering. This spectrum was compared with fig. 2.6 (spectrum A), which was the instrument background obtained under identical conditions except that a Golay detector was used. The spectrum obtained when using the bolometer showed a very low noise level, which was negligible when compared with that observed in the Golay background. The spectrum obtained using the bolometer was further superior

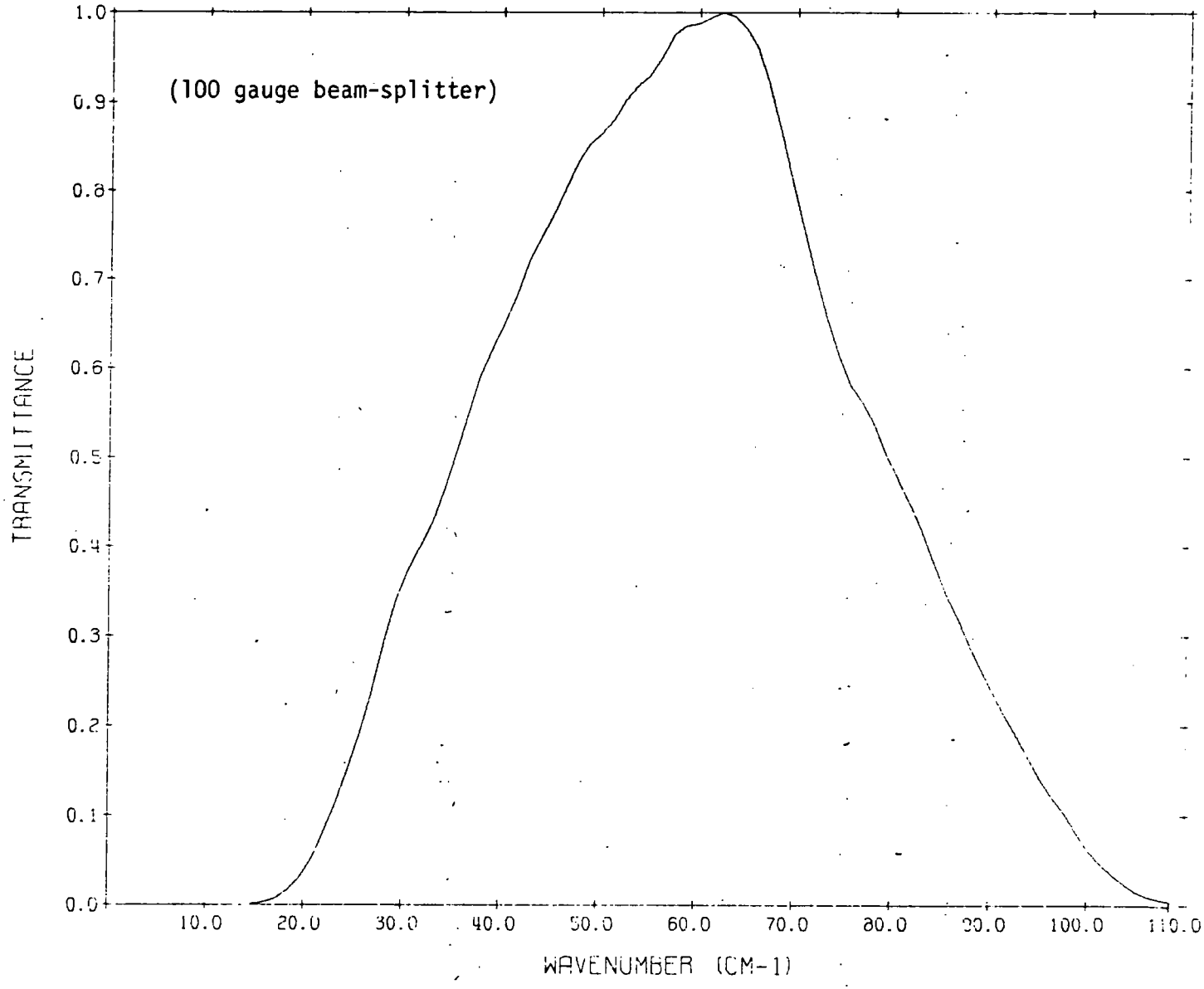

FIG 2.18

INSTRUMENT BACKGROUND USING PUMPED BOLOMETER (1.5 K)

in that it showed no polythene band. The bolometer utilises a light-pipe, rather than a lens, to focus the radiation on the detector window. Hence there is no polythene in the beam for an instrument background when the bolometer is used.

Fig. 2.19 shows the instrument background obtained using the pumped bolometer at 1.5K and a 200 gauge beam-splitter and a 3 mm black polythene filter. This spectrum had a high frequency cut-off at about 55 cm^{-1} which was due to the strong polythene absorption centred at 72 cm^{-1}. Fig. 2.20 shows the first two hoops of the instrument background obtained using a 400 gauge beam-splitter and the 3 mm black polythene filter, with the pumped bolometer at about 1.4K. This spectrum showed that good ratioed spectra should be obtainable down to 7 to 8 cm^{-1} and possibly even lower.

Fig. 2.21 shows the spectrum for a 0.021 cm pathlength of 0.54 mol. dm^{-3} tetra-n-butylammonium chloride in benzene ratioed against the same pathlength of pure benzene using the pumped bolometer at 1.5K. The spectrum was recorded using a polythene windowed demountable cell as described in section 2.12. The ratioing method used was as detailed in chapter 3. No additional filtering was used to obtain these spectra and the useful frequency range was seen to extend from 15 to 100 cm^{-1}. The small blip at 72 cm^{-1} was due to imperfect ratioing of the two single beam spectra, causing the polythene band from the polythene windows of the cell to be observed as a derivative feature.

Fig. 2.22 shows the spectrum obtained using a 0.01 cm crystalline quartz filter and the Golay detector. The crystalline quartz was used to limit energy to the 10 to 100 cm^{-1} region, so as to, hopefully, improve the spectrum in this region. The interferometer was run with a drive speed of 10 μm per second path-difference and time constant of 0.5 seconds. The spectrum should be compared with that of fig.2.21. The quality of this ratioed spectrum using the Golay was very low. This was due to the very small energy in absolute terms in the 10 to 100 cm^{-1} region. The 72 cm^{-1}

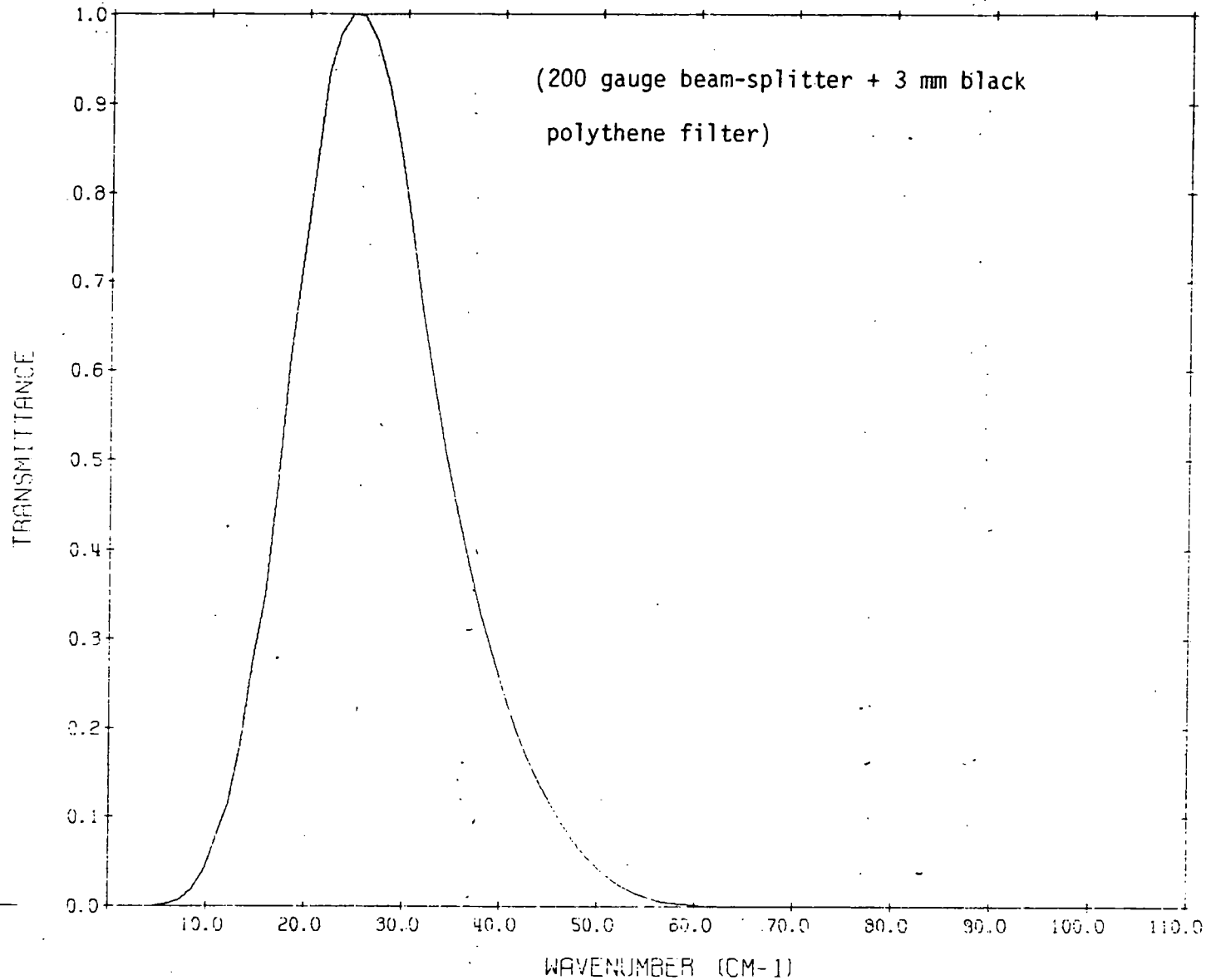

FIG 2.19

INSTRUMENT BACKGROUND USING PUMPED BOLOMETER (1.5 K)

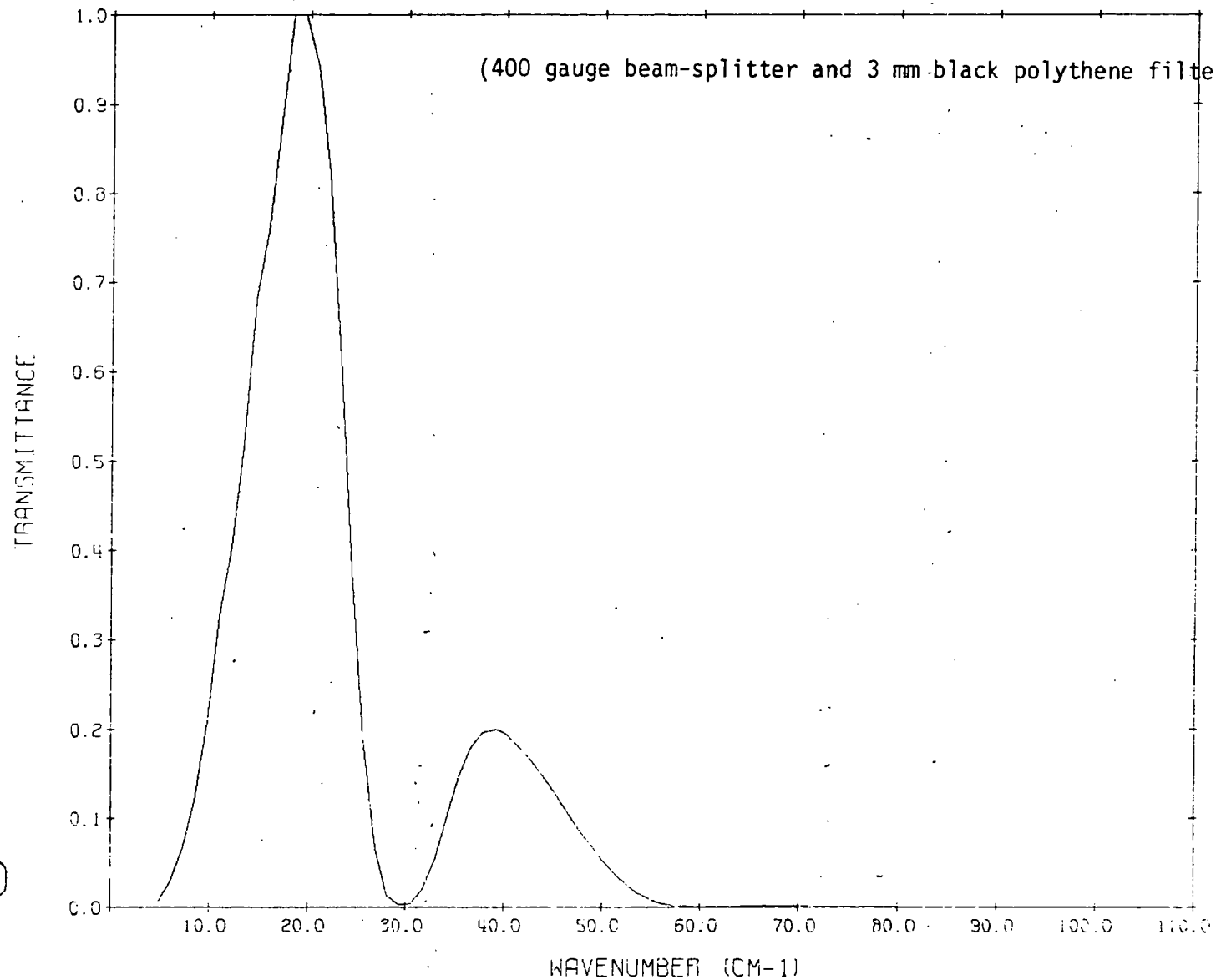

FIG 2.20

INSTRUMENT BACKGROUND USING PUMPED BOLOMETER (1.5 K)

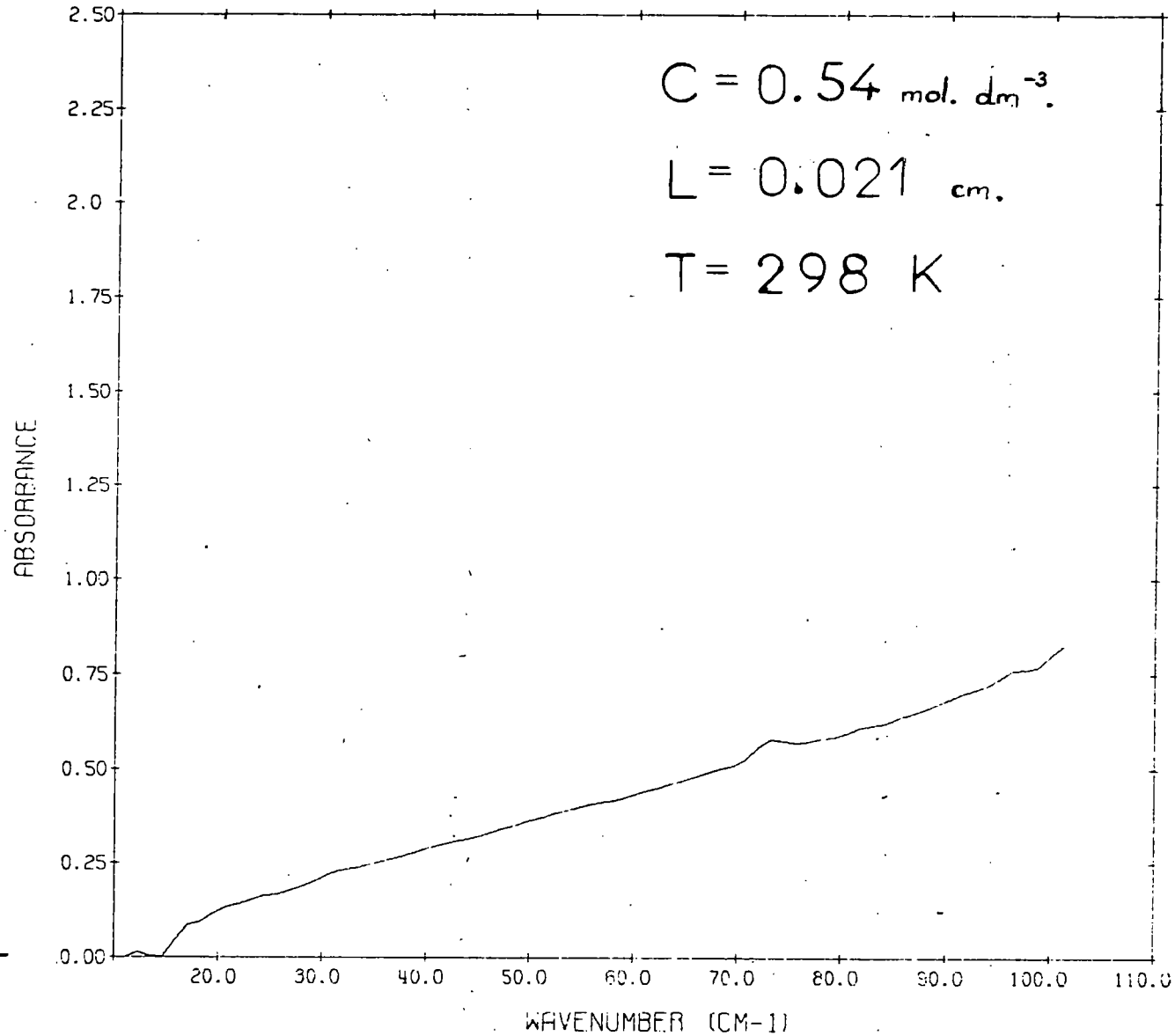

FIG 2.21

BU4N+CI- IN BENZENE USING PUMPED BOLOMETER (1.5 K)

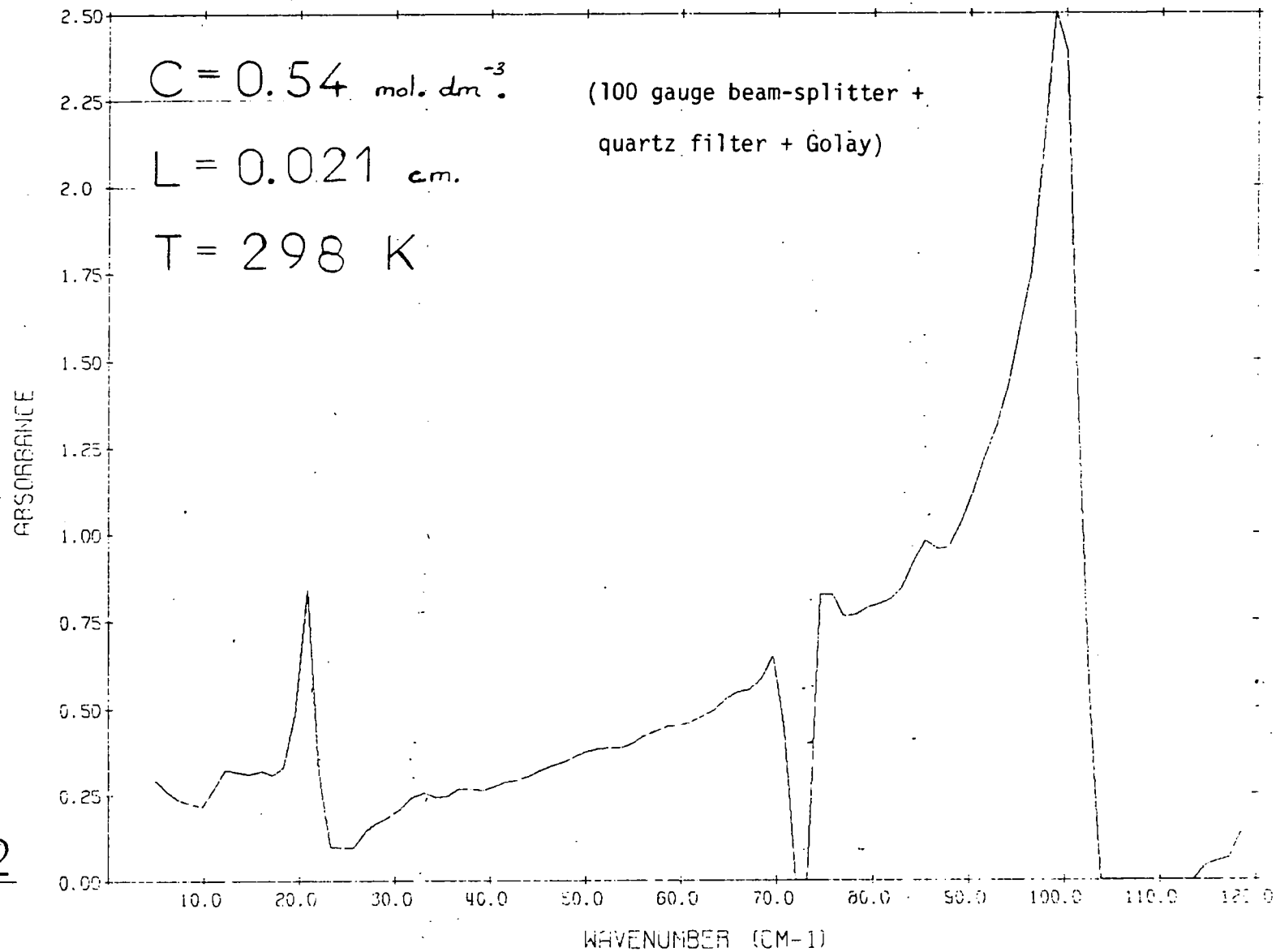

FIG 2.22

BU4N+CI- IN BENZENE USING GOLAY

band of the polythene window and lens causes the transmission to fall to zero. At high frequency the absorbance values show the derivative type spectrum characteristic of lack of energy in the wings of the band. Fig.2.23 shows the ratioed spectrum obtained using a time constant of 8 seconds for the Golay amplifier and a drive speed of 1 μm per second. This spectrum showed no improvement on the faster recorded spectrum. This was possibly due to drifting of the source over the four hours necessary to record a single background or sample spectrum. These spectra serve to emphasize the significant improvement in the performance of the interferometer in the 10 to 100 cm^{-1} region, when the Golay detector was replaced by the cooled bolometer.

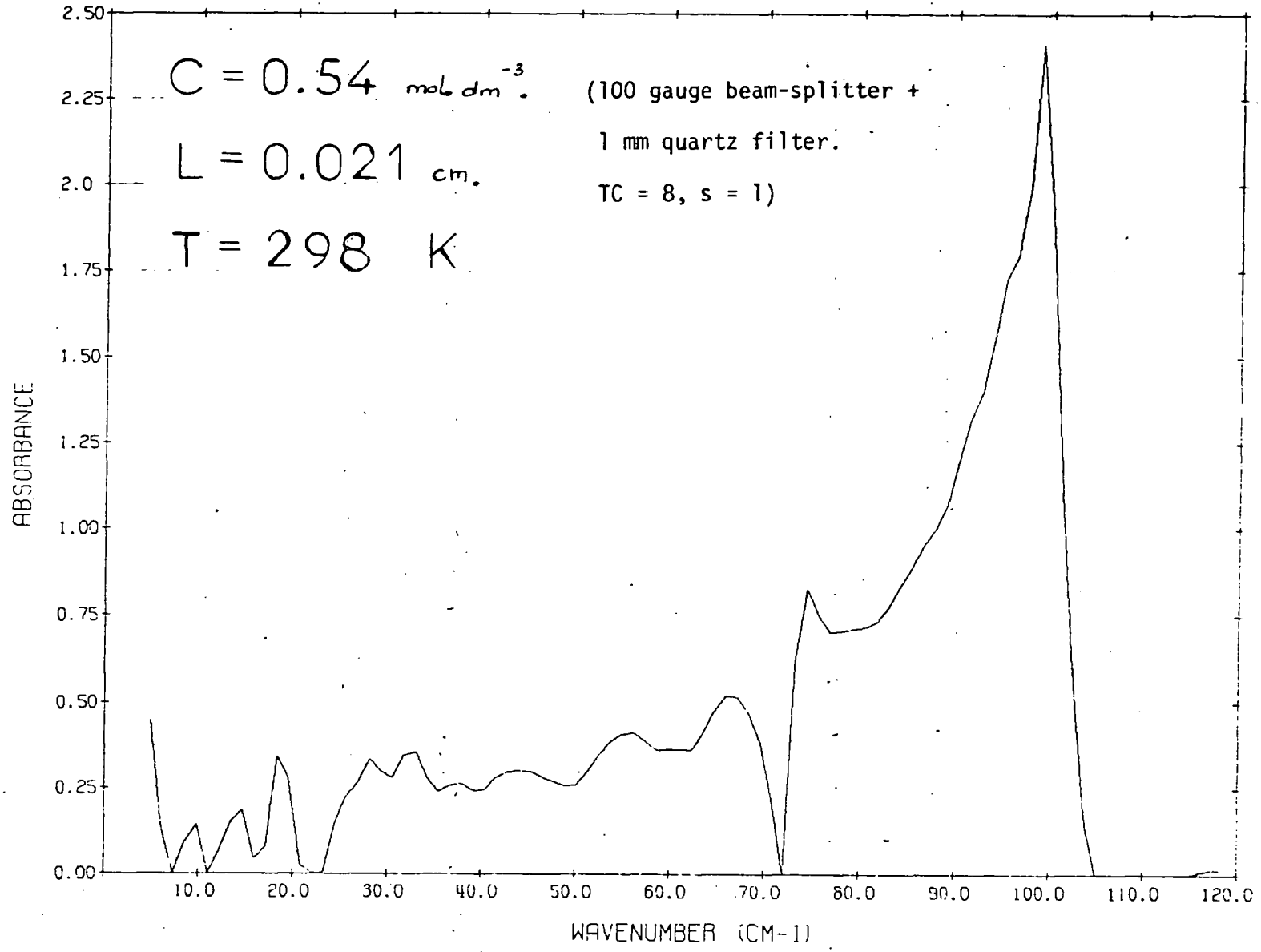

FIG 2.23 BU4N+Cl- IN BENZENE USING GOLAY

Table 2.1 Frequencies of 10% transmission for various ruled polypropylene filters

groove spacing lines / inch	frequency at 10% transmission /cm^{-1}
100	110
60	60
40	40
30	30
20	20

Table 2.2 Summary of useful beam-splitter and filter combinations

beam-splitter gauge	filters[a]	low limit (10% trans.) /cm^{-1}	max. trans. /cm^{-1}	high limit (10% trans.) /cm^{-1}
25	WL	140	320	460
25	WL + BF	120	330	430
50	WL + BF	40	150	240
50	BL	30	90	220
50	WL + QF	30	90	125
50	WL+QF+BF	30	80	125
50	WL+YOSH	35	130	250
100	WL + BF	20	60	110
100	WL+BF+100PF	20	50	70
100	WL+BF+60PF	17	35	63
100	WL+BF+40PF	13	25	44
200	WL + BF	16	36	55
200	WL+BF+QF	15	38	55
400	WL + BF	14	20	24
400	WL+QF+BF	12	20	26

[a] WL = Beckman-RIIC Ltd. white polythene field lens

BL = Beckman-RIIC Ltd. black polythene field lens

BF = 50 μm black polythene filter

QF = 1 mm crystalline quartz filter

YOSH = Beckman-RIIC Ltd. Yoshinaga filter

100PF = 100 lines/inch ruled polypropylene filter

60PF = 60 lines/inch ruled polypropylene filter

40PF = 40 lines/inch ruled polypropylene filter

CHAPTER 3

COMPUTATION OF THE SPECTRUM AND DATA HANDLING

3.1 Computation of the spectrum from the interferogram

In this section an attempt will be made to develop the theory of computation of the spectrum with particular reference to the programme used in Durham. All computer computations were carried out on the Northumbrian Universities Multiple Access Computer (NUMAC), which at the time of this work was an IBM 360/67 computer. Spectra were obtained from the interferograms by use of the Fourier transform programme FTRAN4 (Fourier TRANsform), which was written in Fortran IV language. This programme was a modified version of the programme DCH05277 as previously used in this laboratory (27,28). The modified programme involves a complete autocorrelation phase-correction with a Cooley-Tukey Fourier Transform routine (29).

The control parameters initially read in determine the type of computation employed, and the way in which the spectral output data is to be represented. A short description of the input parameters follows, but a more detailed explanation, including the necessary formats, is contained in the programme listings and programme input data listings in Appendix A1. The constants N and FSINT control the length of the interferogram to be transformed, and hence the resolution in the spectrum. N is the number of interferogram points and FSINT is the sampling interval in μm of total path-difference between the two beams (i.e. twice the actual mirror movement). If the interferogram is recorded from L cm of mirror displacement before the Grand Maximum to L cm beyond, the resolution R, obtained is given by (ref. 8, chap. 3):

$$R = \frac{1}{2L} \quad cm^{-1} \qquad 3.1$$

Thus the resolution obtainable from a Michelson interferometer is the reciprocal of twice the maximum mirror displacement from the zero-path-difference position. The maximum number of points that can be transformed using programme FTRAN4 is 2048 (1024 either side of zero-path-difference), which, with a sampling interval of 8 μm gives a maximum mirror displacement of 0.8192 cm and a corresponding resolution of 0.61 cm^{-1} in the

computed spectrum.

The digitised interferograms for both sample and background are read into the computer store, with the background first, by use of a tape read programme DCL99SPY, which employs the PL1 language library subroutine *PL1LIB. The digitised interferograms were stored as card images, usually in temporary files. A typical interferogram recorded from -0.1 to +0.1 cm path-difference is shown in fig. 3.1. The array index records the order of the elements of the sampled interferogram array as they are recorded from negative path-difference through the Grand Maximum to positive path-difference. The card data is read into the transform programme, FTRAN4, by a subroutine TPREAD, which returns to the main programme the total number of interferogram points as well as the interferogram array itself. The end of the interferogram is indicated by a negative number placed at the end of the card images by the tape read programme DCL99SPY. The subroutine SUBDH is next called, where the interferogram array is searched for its maximum value by a further subroutine AMX. This maximum value is then taken as the Grand Maximum position, and the required number of points (N/2) are then taken either side of this.If there are points short on either side of the Grand Maximum, then the data is padded out by repeating the first or last member of the interferogram array, to make up to the required number. A warning signal is printed on the printer output and the number of inserted points recorded.

The interferogram array (now from 1 to N exactly) is then summed and the average value computed. This average value is then subtracted from all the array elements, to remove the non-modulated part of the interferogram. This averaging process has the advantage over other techniques, where the last element of the interferogram array is subtracted from the whole array. In the latter method the noise in the wings of the interferogram can lead to serious uncertainties in any single element chosen, and hence to large errors in the computation of the modulated interferogram.

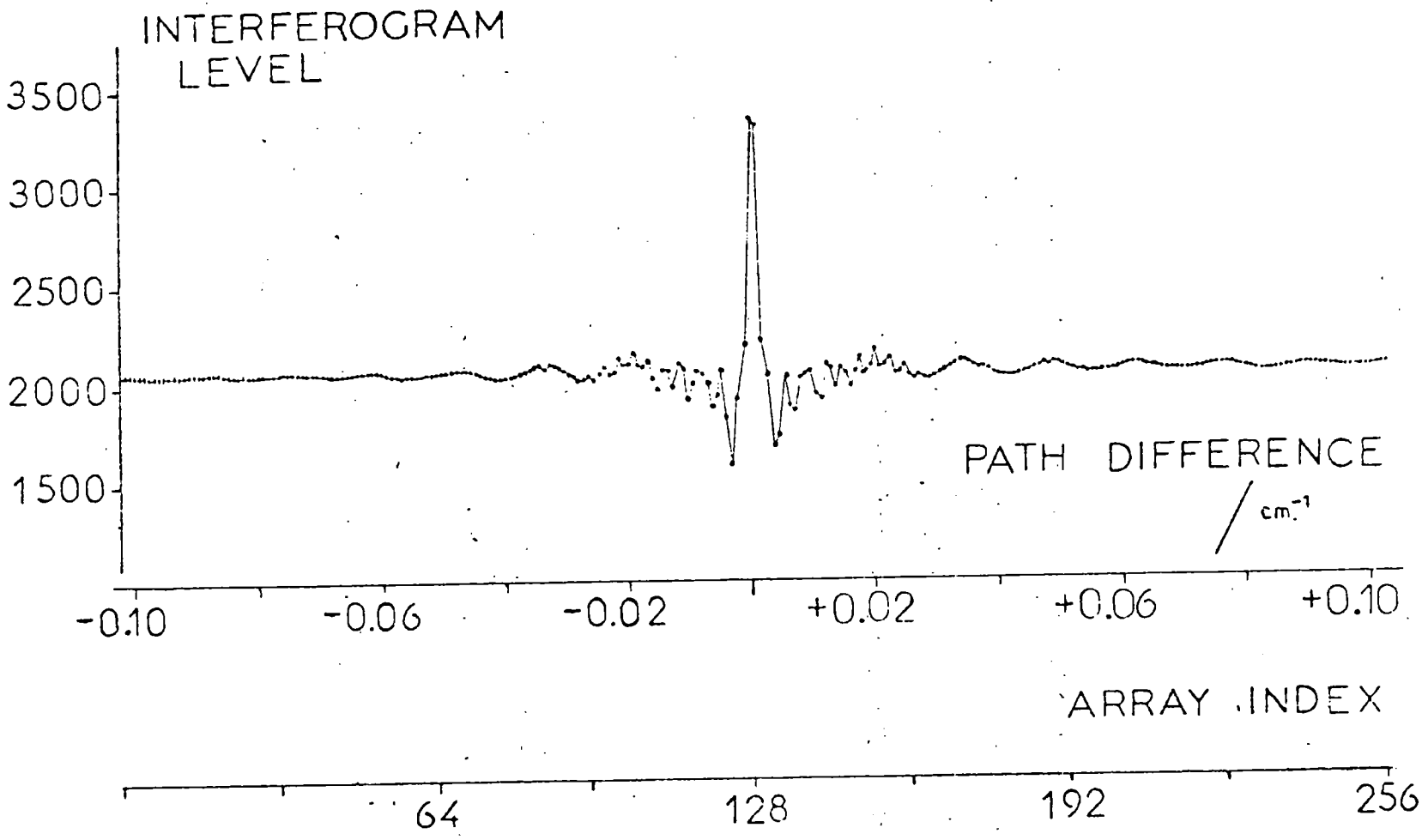

FIG. 3.1 DIGITISED INTERFEROGRAM

Richards (30) recommends taking the average of the interferogram array for points near the end of the array, and then to use this long path-difference level as the mean interferogram level. By averaging over the whole interferogram we are attempting to remove any effects which drifting of the source or detector may have on the mean interferogram level. This drifting could cause inaccuracies in computed intensities from the ratioed spectra. This procedure normally gave modulated interferograms which fell to within ±20 in the wings (on a scale -2048 to + 2048), showing 1% accuracy in determination of the mean interferogram level.

As already mentioned, the programme uses the Cooley-Tukey fast Fourier transform procedure, where the spectral distribution is obtained from a one-sided Fourier cosine transform. Since only one side of the interferogram is being transformed it is necessary to correct the interferogram function for any asymmetry introduced, either by instrument imperfections (31,32), or by the sampling process itself (33). Asymmetry in the interferogram due to sampling is caused by the finite size of the sampling steps, and hence the high probability that a sample will not be taken at exactly zero-path-difference. If the starting point of the interferogram is not at zero-path-difference, then a phase error $\phi(\bar{\nu})$ is introduced, which makes the interferogram asymmetric about the Grand Maximum, and produces artificial asymmetry in the computed absorption bands.

A symmetric interferogram function is obtained by an autocorrelation procedure, whereby the whole of the asymmetric interferogram is convoluted with a section of the same interferogram about zero-path-difference giving an essentially symmetric interferogram. The convolution process is defined by:

$$h(x) = f(x)*g(x) = \int_{-\infty}^{+\infty} f(u).g(x-u).\delta u \qquad 3.2$$

where the asterisk denotes convolution.

Programme FTRAN4 employs a routine which convolves the whole interferogram with itself to give a completely symmetric interferogram. Fig. 3.2 shows

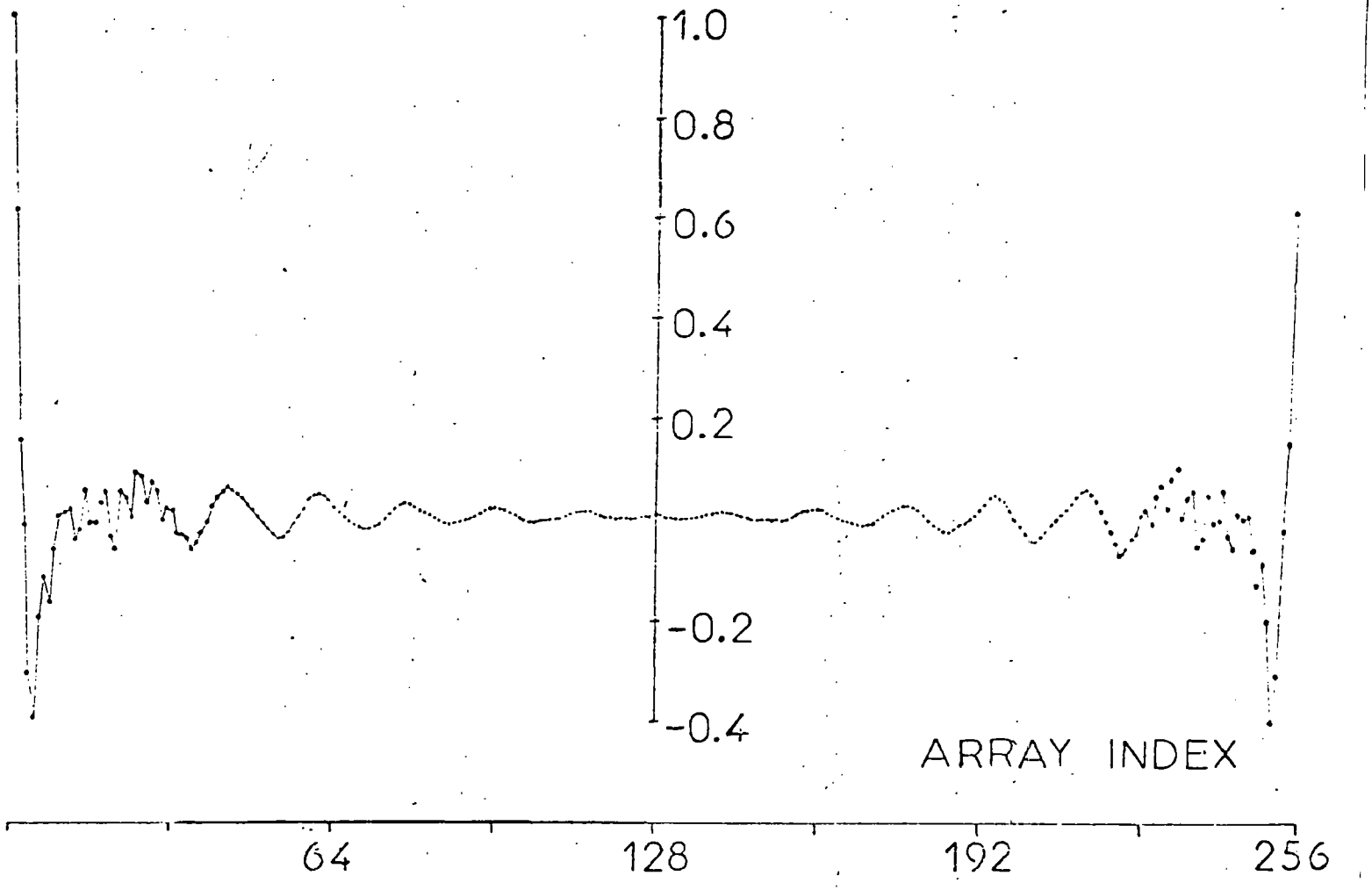

FIG. 3.2 AUTOCORRELATED INTERFEROGRAM

the normalised, autocorrelated interferogram derived from the interferogram of fig. 3.1. The array index now records the number of interferogram elements starting from zero-path-difference (array element 1) to the maximum path-difference (array element 128). The autocorrelated interferogram can be seen to be symmetric about the maximum path-difference position. It should be noted that by convolving the interferogram array with itself, the array elements are in fact being squared, and it is thus necessary to square-root each of the transformed array elements to give the correct spectral intensity distribution.

A second method for obtaining a symmetric interferogram function will be mentioned for completeness, since it is used to obtain refractive index data from asymmetric interferometry (see chapter 8). The method is due to Forman et al (34), and involves calculation of the phase error $\phi(\bar{\nu})$ introduced by the asymmetry in the interferogram. The phase function $\phi(\bar{\nu})$ is calculated from a small portion of the original interferogram, and a correction function is obtained as the Fourier transform of $\exp(j\phi(\bar{\nu}))$. This correction function is apodised (see later in this chapter) and then convoluted across the original interferogram to produce an essentially symmetric function about zero-path-difference. This method has the advantage that the phase errors can be recovered, and is particularly useful in dispersive interferometry, where the phase values can be used to obtain dispersion curves.

The alternative to obtaining a totally symmetric interferogram is to compute the spectrum using a full double-sided power transform (35), which handles the asymmetry and gives values for the phase errors. The disadvantage of the full double-sided power transform is that the signal-to-noise ratio is less than that for the single-sided transform, since the whole of the interferogram is transformed. The power transform produces a spectrum with a non-linear signal-to-noise ratio, where the ratio is poorer to low frequency. This made the power transform unsuitable

for our purposes, as the majority of our spectra in this study were recorded below 300 cm^{-1}.

The interferogram can only be recorded over a finite path-difference, whereas the modulation of the sinusoidal functions, which make up the interferogram is present to infinite path-difference. Hence the interferogram function is being truncated before the modulation in it has reached zero amplitude. This truncation is the equivalent of introducing a noise spike at the end of the interferogram array. Fourier transformation of these noise spikes gives a sinusoidal ripple throughout the spectrum, which appears as a very high noise level, and causes sharp lines in the computed spectrum to be accompanied by subsidiary maxima. The noise spike introduced by the necessary truncation is effectively removed by a mathematical process known as apodisation. It is arranged that the modulation of the interferogram is smoothly reduced to zero amplitude at maximum path-difference. Programme FTRAN4 employs the apodisation function:

$$APOD(k) = \cos^2(k\pi/N) \qquad 3.3$$

where k is an integer varying between 1 and the number of points to be apodised, and N is the total number of points to be transformed. This apodisation function is illustrated in fig. 3.3, with N = 256, where it can be seen that the function falls smoothly to zero at array index 128, which corresponds to the maximum path-difference recorded in the interferogram of fig. 3.1. The results of this mathematical smoothing can be seen by comparing fig. 3.4 (which shows the normalised apodised interferogram corresponding to the interferogram of fig. 3.1) with fig. 3.2, which shows the normalised, non-apodised autocorrelated interferogram. The apodisation can be seen to have reduced the amplitude of modulation towards the maximum path-difference, which occurs in the centre of the figure.

The actual Fourier Transformation of the apodised, autocorrelated interferogram, to give the spectral data is handled by subroutine SUBTM. Forman (31) pointed out the tremendous time savings, which could be achieved

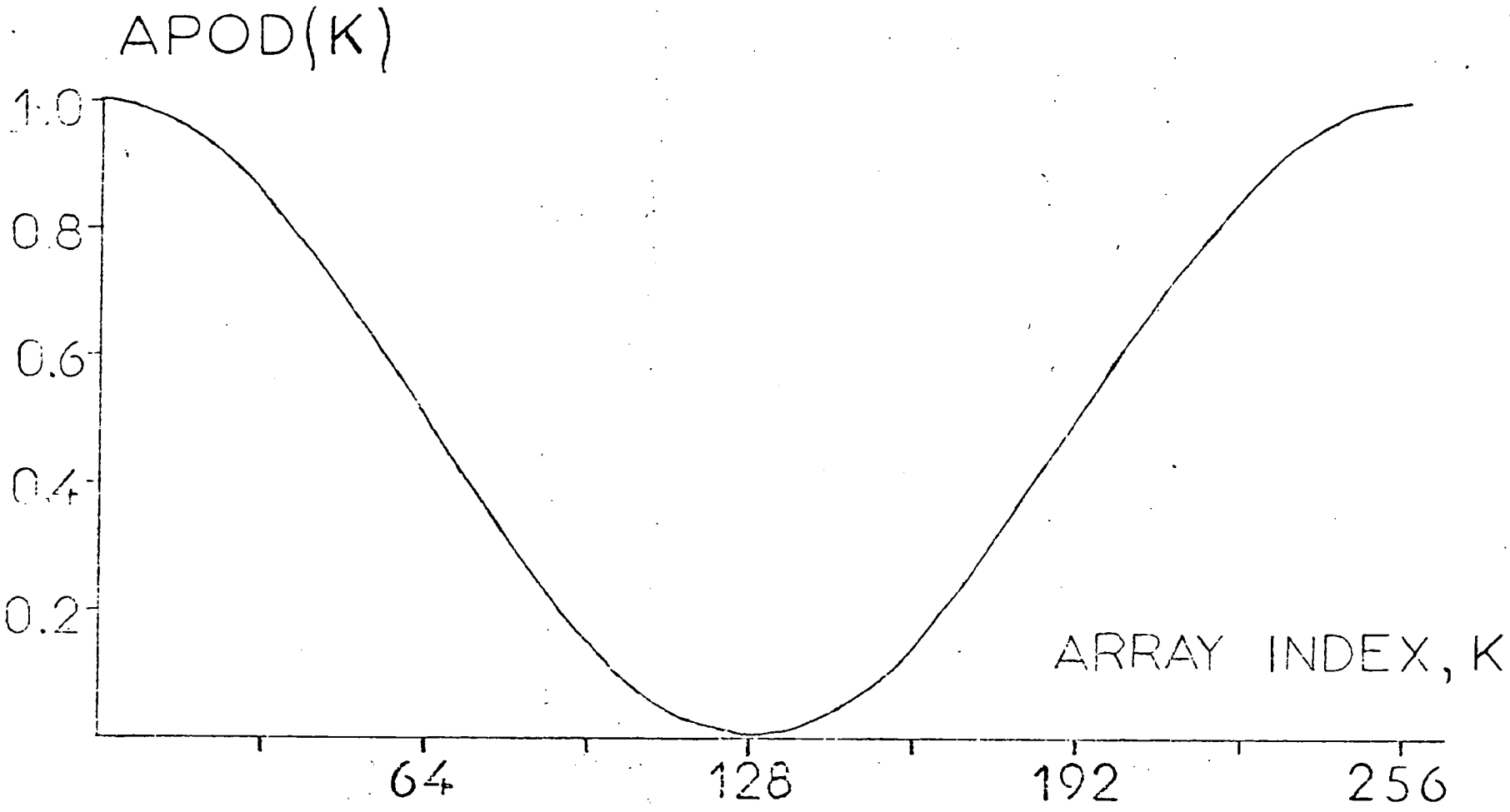

FIG. 3.3 APODISATION FUNCTION

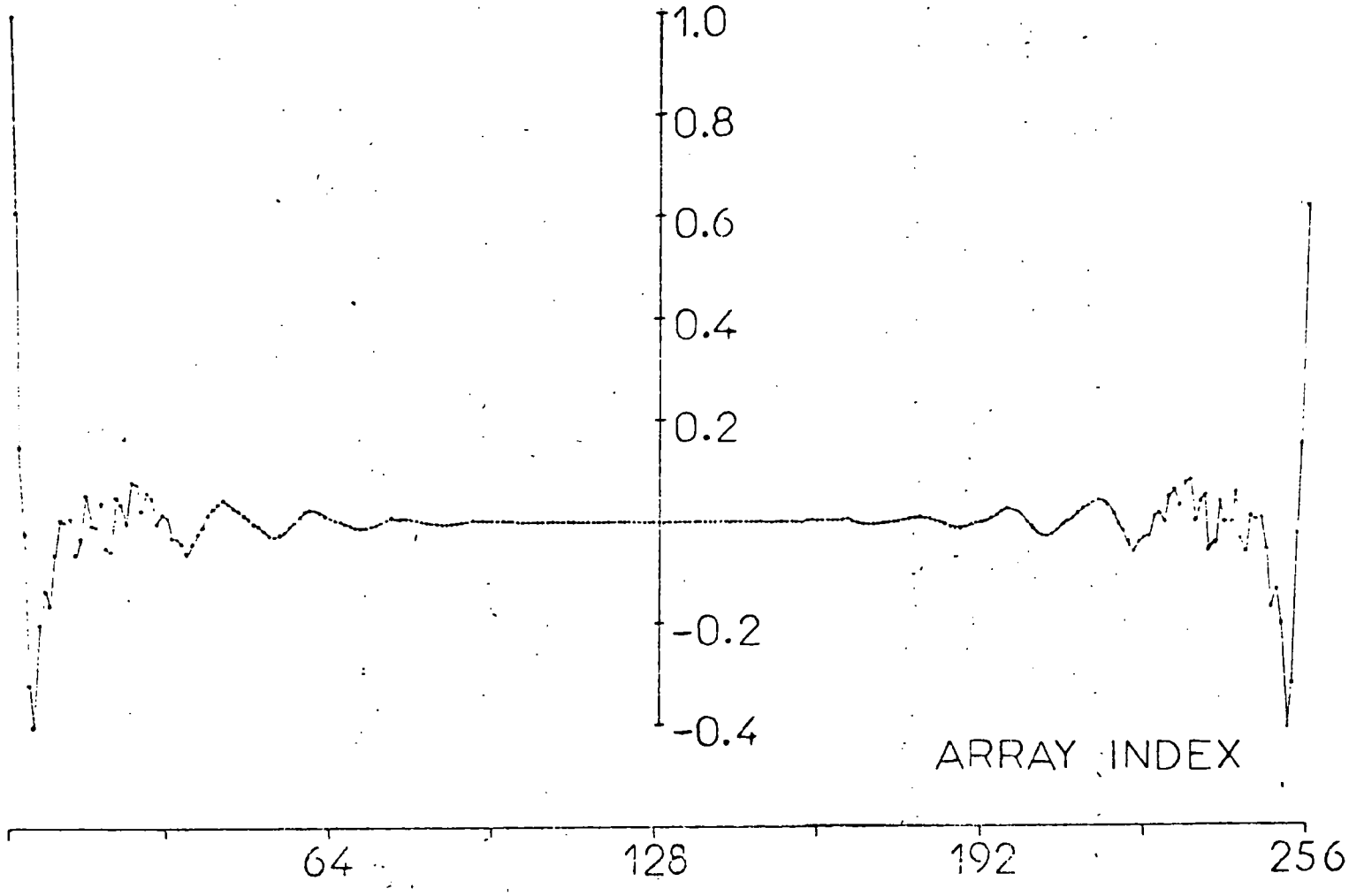

FIG. 3.4 APODISED INTERFEROGRAM

by using the fast Fourier transform algorithm (29). Bingham and Morrow (36) and Connes (ref. 37, p. 83) have given explanations of the algorithm, and it has recently been reviewed by Bell (ref. 12, p. 237). In the Cooley-Tukey algorithm only numbers of points which are powers of 2 can be transformed (i.e. 64, 128, 256, 512, 1024 or 2048 points). In the programme FTRAN4 the algorithm has been slightly modified so that the transformed elements come out in the correct order for spectrum plotting as a function of increasing frequency.

The programme stores the background transformed element array, and returns to read the sample interferogram, which is reduced, autocorrelated, apodised and Fourier transformed in a similar manner to the background interferogram. Before the spectrum is plotted, subroutine SUBPT calculates the wavenumber corresponding to each element in the transformed array. This brings us to a discussion of the theory of sampling, and the phenomenon of aliasing.

The interferogram function is an experimental quantity which cannot be represented analytically, and hence the integration has to be performed numerically. The interferogram is not recorded as a continuous function, since it must be digitised for computer input. The digitisation occurs when the mirror drive has changed the path-difference between the beams by some integral multiple of the sampling interval x_o. The interferogram (as recorded on paper tape) is thus a sampled version containing $2n+1$ observations of the intensity $I(mx_o)$, where $m = -n.....0.....+n$. The subroutine SUBTM actually carries out the Fourier summation:

$$S(\bar{\nu}) \quad \alpha \quad x_o . \Sigma_{m=-n}^{m=+n} I'(mx_o).\cos(2\pi\bar{\nu}mx_o) \qquad 3.4$$

whereas, as can be seen from eqn. 1.31, the desired spectral function is given by:

$$S(\bar{\nu}) \quad \alpha \int_{-\infty}^{+\infty} I'(x).\cos(2\pi\bar{\nu}x) \qquad 3.5$$

The change in limits for path-difference, from the whole range to infinity, to a limited range, results in the spectrum having only limited resolution

as discussed in chapter 1. The replacement of a continuous function by a sampled function, and the replacement of the integration by a summation leads to the phenomenon termed aliasing.

Eqn. 3.4 enables the determination of a number of cosine waves, whose sum passes through the observed points, and hence satisfies the equation. If a pure cosine wave of frequency $\bar{\nu}_0$ satisfies eqn. 3.4, then the spectral function $S(\bar{\nu})$ can be recovered. However since the cosine function repeats every 2π radians then:

$$\cos(2\pi\bar{\nu}_0 m x_0) = \cos(2\pi\bar{\nu}_0 m x_0 + n2\pi m)$$
$$= \cos(2\pi m x_0(\bar{\nu}_0 + n/x_0) \qquad 3.6$$

where n and m are both integers.

Therefore an infinite number of higher frequencies:

$$\bar{\nu}_n = \bar{\nu}_0 \pm n/x_0 \qquad n = 1,2,3..... \qquad 3.7$$

will also satisfy eqn. 3.4. This equation will only give a true spectrum for frequencies between 0 and n/x_0. Similarly, since the cosine function reflects about π radians then:

$$\cos(2\pi\bar{\nu}_0 m x_0) = \cos(\pi nm \pm 2\pi m x_0 \Delta\bar{\nu}_0)$$
$$= \cos(2\pi m x_0(n/2x_0 \pm \Delta\bar{\nu}_0)) \qquad 3.8$$

where $\Delta\bar{\nu}_0 = \pi nm \pm \bar{\nu}_0$

and n and m are once again both integers.

Thus the sum in eqn. 3.4 is the same for all values of:

$$\bar{\nu}_0 = n/2x_0 \pm \Delta\bar{\nu}_0 \qquad n = 1,2,3..... \qquad 3.9$$

and true spectral information is restricted to the range 0 to $1/2x_0$ radians. For an interferogram sampled every 8 μm of path-difference (x_0 = 8 μm), the aliasing or folding frequency is $10^4/16 = 625$ cm^{-1}. The interferogram must not contain spectral information for frequencies above the aliasing frequency, or these will be reflected about the aliasing frequency, and will appear in the spectrum of the region below the aliasing frequency. This high-frequency spectral information can be removed by using suitable filters.

The aliasing problem in interferometry is equivalent to that of stray light in grating spectroscopy.

The subroutine SUBPT calculates the aliasing frequency, and hence the frequency increment of the Fourier spectral elements, by dividing by the number of elements. Thus for an 8 μm sampling interval (4 μm of mirror movement) a 1024 point double-sided interferogram gives a frequency increment of 625/512 = 1.22 cm^{-1}. The transformed element data is then truncated to the required spectral region, by supplying lower and upper frequency limits. The background transformed element array is then normalised by dividing through by the largest element in the array, and the square-root of each element is taken to provide the spectral intensity. This is plotted as a function of frequency as the normalised background spectrum. Subroutine SUBLP sets up the transmission axes, and subroutine SUBGP conducts the plotting. The normalised sample spectrum is then plotted in a similar manner. Figs. 3.5 and 3.6 show background and sample transmittance spectra, the background spectrum being computed from the interferogram of fig. 3.1. (The resolution is 1/4 that normally achieved during standard runs, since a 256 point computation has been used rather than the typical 1024).

The subroutine SUBCOR is called to calculate the increase in gain from the instrument gain settings, used to record the background and sample interferograms. With the Beckman-RIIC Ltd. FS200/7 electronics the gain measurements are made in decibels (dB) as defined (38) by:

$$dB = 20 \log_{10}(V_1/V_2) \qquad 3.10$$

where V_1 and V_2 are the amplifier output and input voltages respectively. The ratio V_1/V_2 is the gain of the amplifier, which can be calculated by rearrangement of eqn. 3.10 as:

$$\text{gain} = V_1/V_2 = \exp(2.303.dB/20) \qquad 3.11$$

The FS200/7 electronics have both course and fine gain controls. The course gain determines the amplification produced in the main Golay amplifier, and is calibrated in decibels. The fine gain controls the Golay pre-

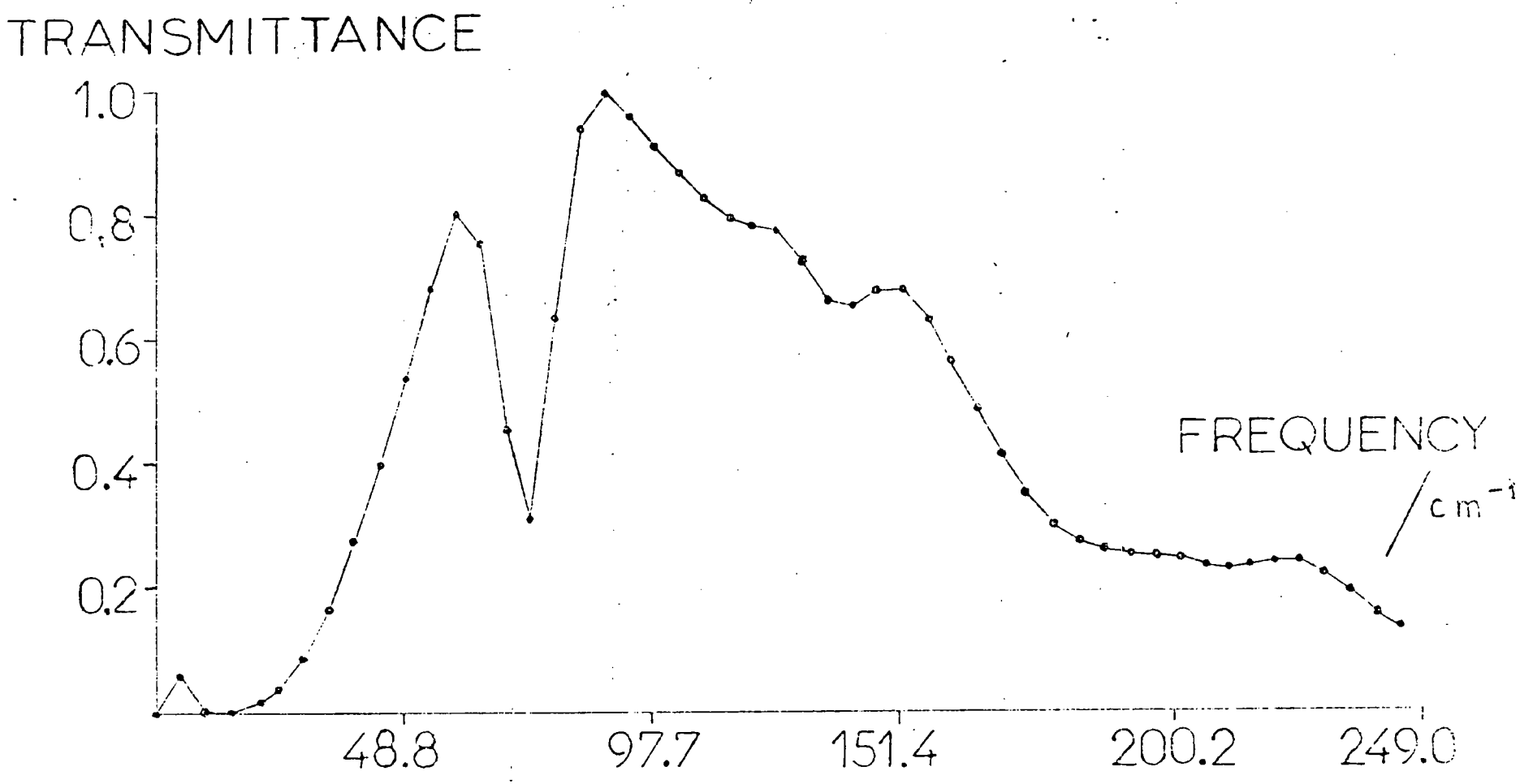

FIG. 3.5 BACKGROUND TRANSMITTANCE

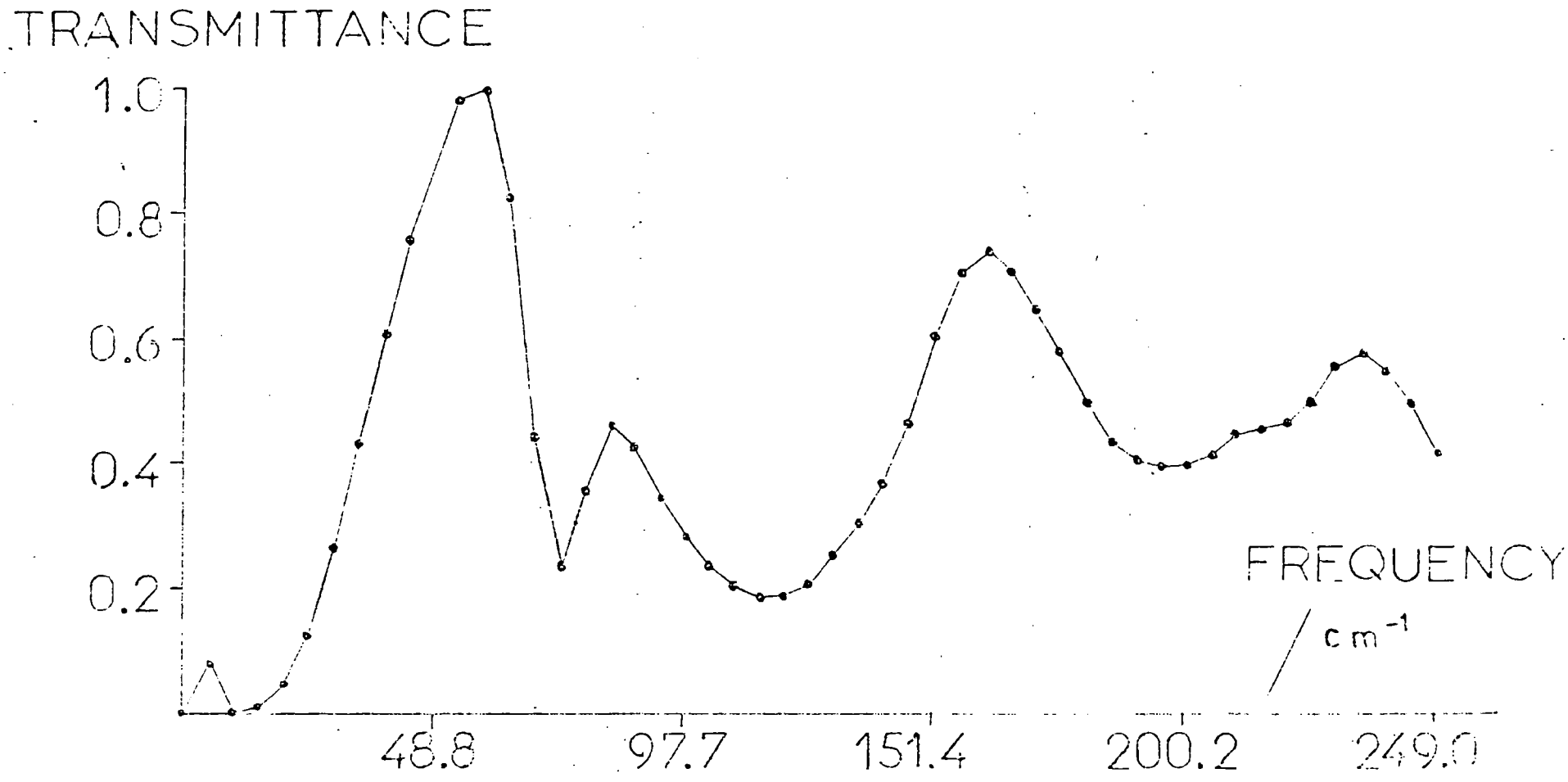

FIG. 3.6 SAMPLE TRANSMITTANCE

amplifier, by use of a helipot dial reading from 0 to 999 with a total gain of 10 dB. The gain produced by the preamplifier is not linear with respect to the reading of the helipot dial, and must be determined by use of a fine gain potentiometer calibration curve (39) as shown in fig. 3.7.

The course and fine gains are summed for both background and sample interferograms, and a gain correction factor calculated as the reciprocal of exp(2.303.dB/20). This correction factor is passed to the main programme, where the transformed elements, as stored before normalisation, for the sample are divided by those for the background. The square-root of the resulting elements is then taken to give the ratioed transmittance array. The elements of this array are then multiplied by the gain correction factor, to give the transmission spectrum corrected for the gain difference between the sample and backgound interferograms. Fig. 3.8 shows the ratioed transmittance spectrum for the background and sample transmittance spectra of figs. 3.6 and 3.7.

The ratioing of the original, non-normalised, transformed elements eliminates problems due to the normalisation to peak noise, encountered with programme DCH05277 (20, 21), in which the normalised transformed elements were ratioed. The ratioing procedure in the programme DCH05277 made necessary a correction for the different normalisation constants employed in producing the normalised background and sample transmittance spectra. If noise was predominant in the spectrum, the use of DCH05277 for computation led to serious errors in the values for the ratioed elements throughout the spectrum, due to inaccuracies in the normalisation constants. The improvements made to this routine in FTRAN4 are especially important when the resulting spectra are to be used for intensity measurements, since it is then important that the highest accuracy possible be achieved in the levels of the transmittance curves.

The final spectrum can be plotted on the line printer as the transmittance spectrum or as the absorbance spectrum where:

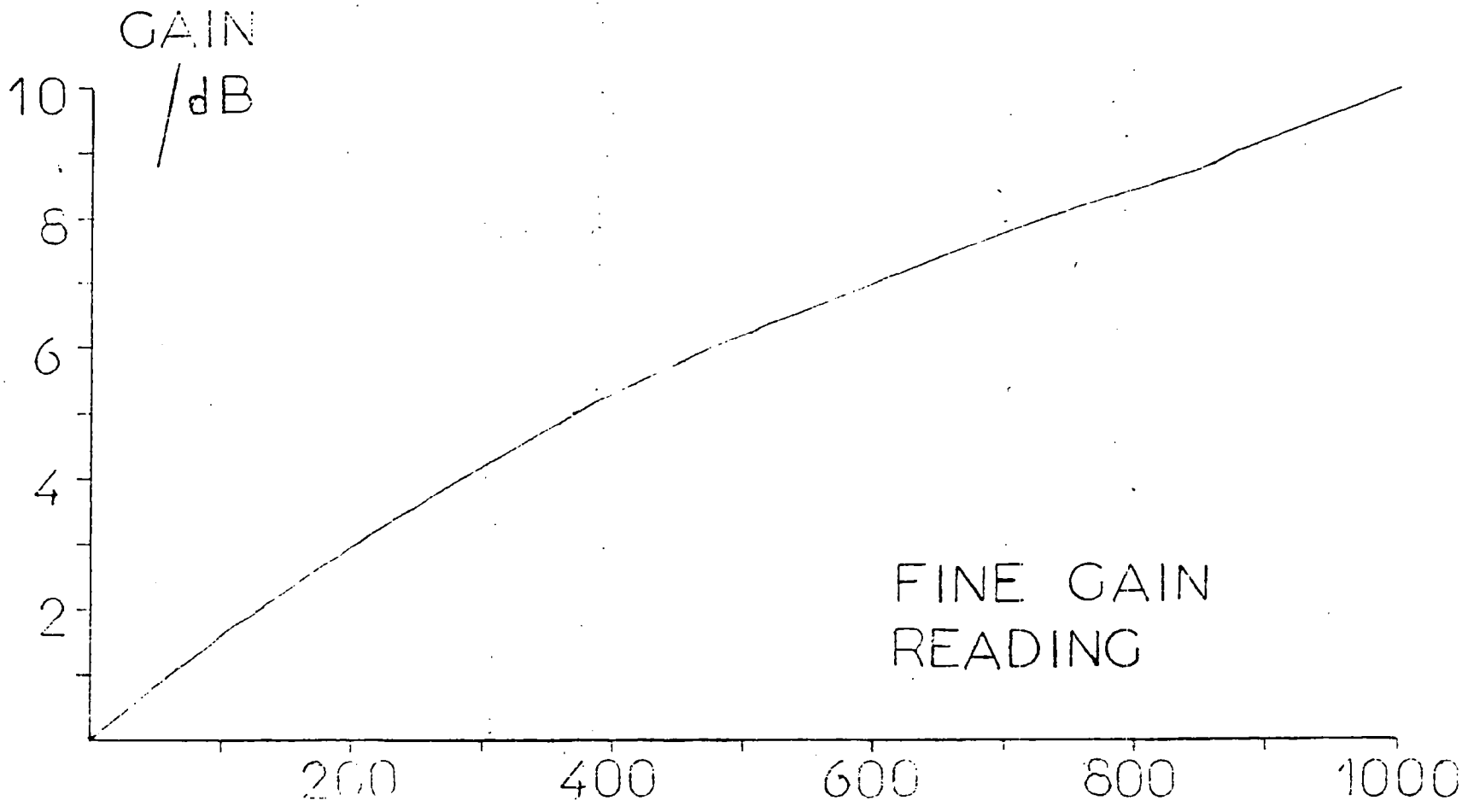

FIG. 3.7 FINE GAIN CALIBRATION CURVE

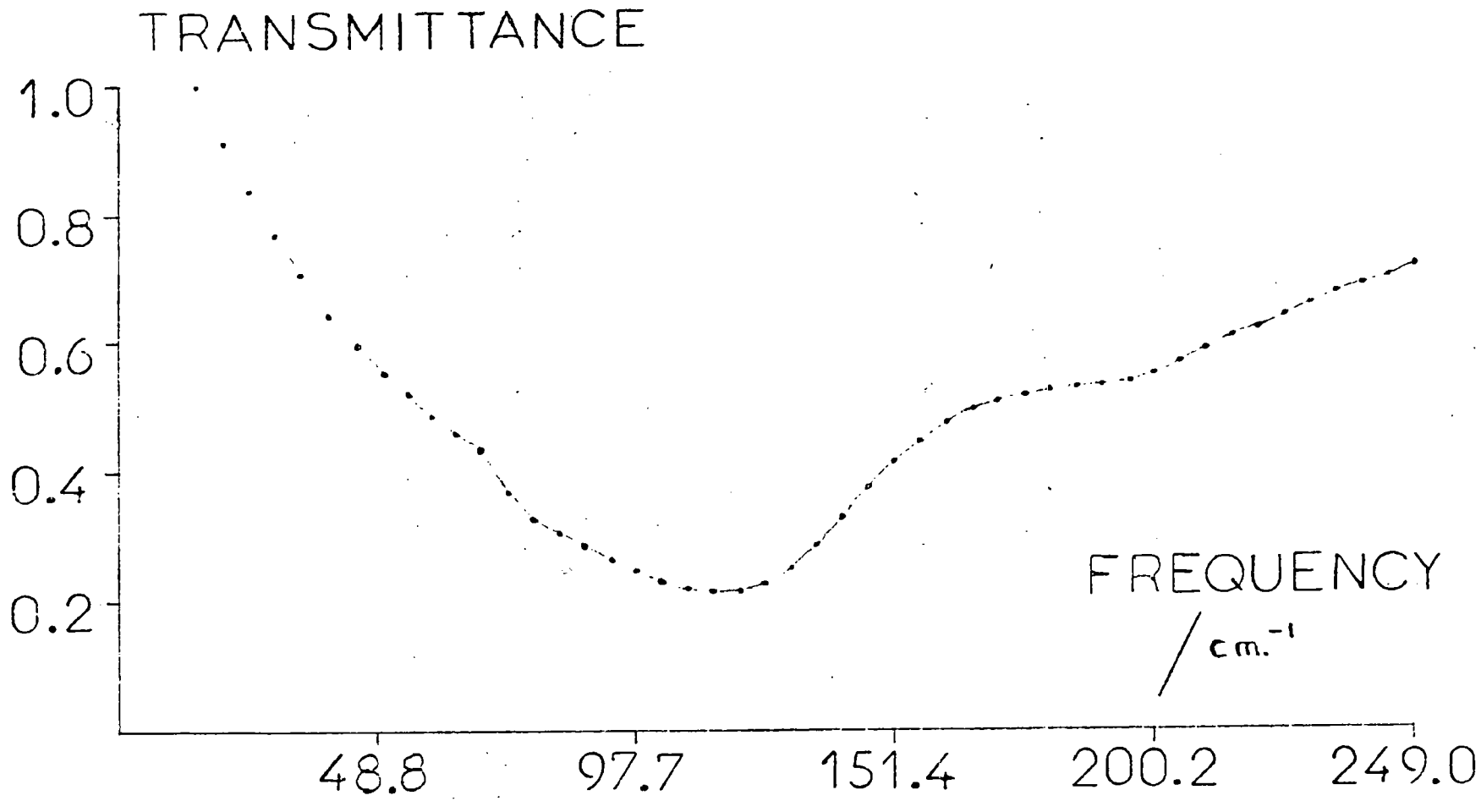

FIG. 3.8 RATIOED TRANSMITTANCE

$$\text{Absorbance} = \log_e(1/\text{transmittance})_{\bar{\nu}}$$

$$= \log_e(T_o/T)_{\bar{\nu}} \qquad 3.12$$

where T_o is the background transmittance

and T is the sample transmittance.

If the transmittance spectrum is required then the axes are set up by the subroutine SUBLP, and the spectrum plotted by the subroutine SUBGP. If the absorbance spectrum is required then the axes are set up by the subroutine SUBLPL, and the spectrum plotted by the subroutine SUBGPL. If required the ratioed transmittance spectrum can be outputted to a separate file or device, and can be copied to *PUNCH* to give a card deck copy of the frequency/transmittance data, which can be used for further computation.

A graph plotting programme GPLOT3 was used to obtain the spectra as continuous curves, rather than the dot spectra produced by the line printer with programme FTRAN4. The frequency/transmittance data produced by the programme FTRAN4 is read in and initially converted to natural logarithm absorbance by use of eqn. 3.12. The spectrum is usually plotted as $\log_e$ absorbance with an increasing wavenumber scale. Various abscissal frequency scales are available, and the absorbance scale can be plotted with either 2.5 or 1.0 absorbance units full-scale. The units for the absorbance scale are 'nepers', since absorbance is determined as the ratio of two powers as a natural logarithm. 1 neper equals 8.686 dB (39). Fig. 3.9 shows the ratioed absorbance spectrum obtained using programme GPLOT3 for the transmittance spectrum of fig. 3.8.

The absorbance data can also be plotted with a neper cm^{-1} (or neper m^{-1}) scale with programme GPLOT3, to take into account the effect of pathlength upon the strength of the absorption occurring.

$$\text{neper } cm^{-1} \ (m^{-1}) = \text{absorbance/pathlength} \qquad 3.13$$

where the pathlength is in cm (m).

Fig. 3.10 shows the absorbance spectrum of fig. 3.9 represented on such a neper m^{-1} scale.

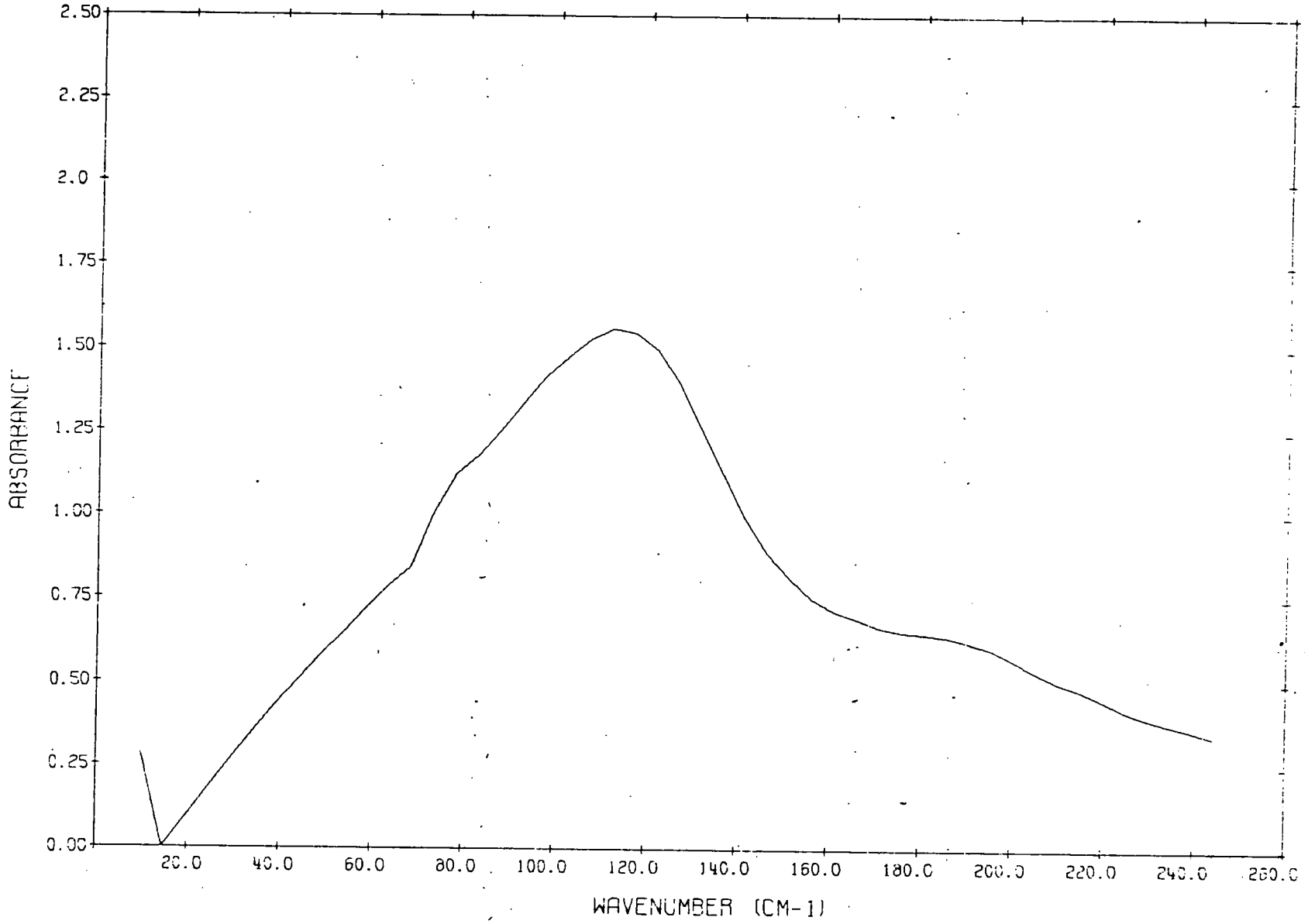

FIG. 3.9 ABSORBANCE (NEPER) SCALE

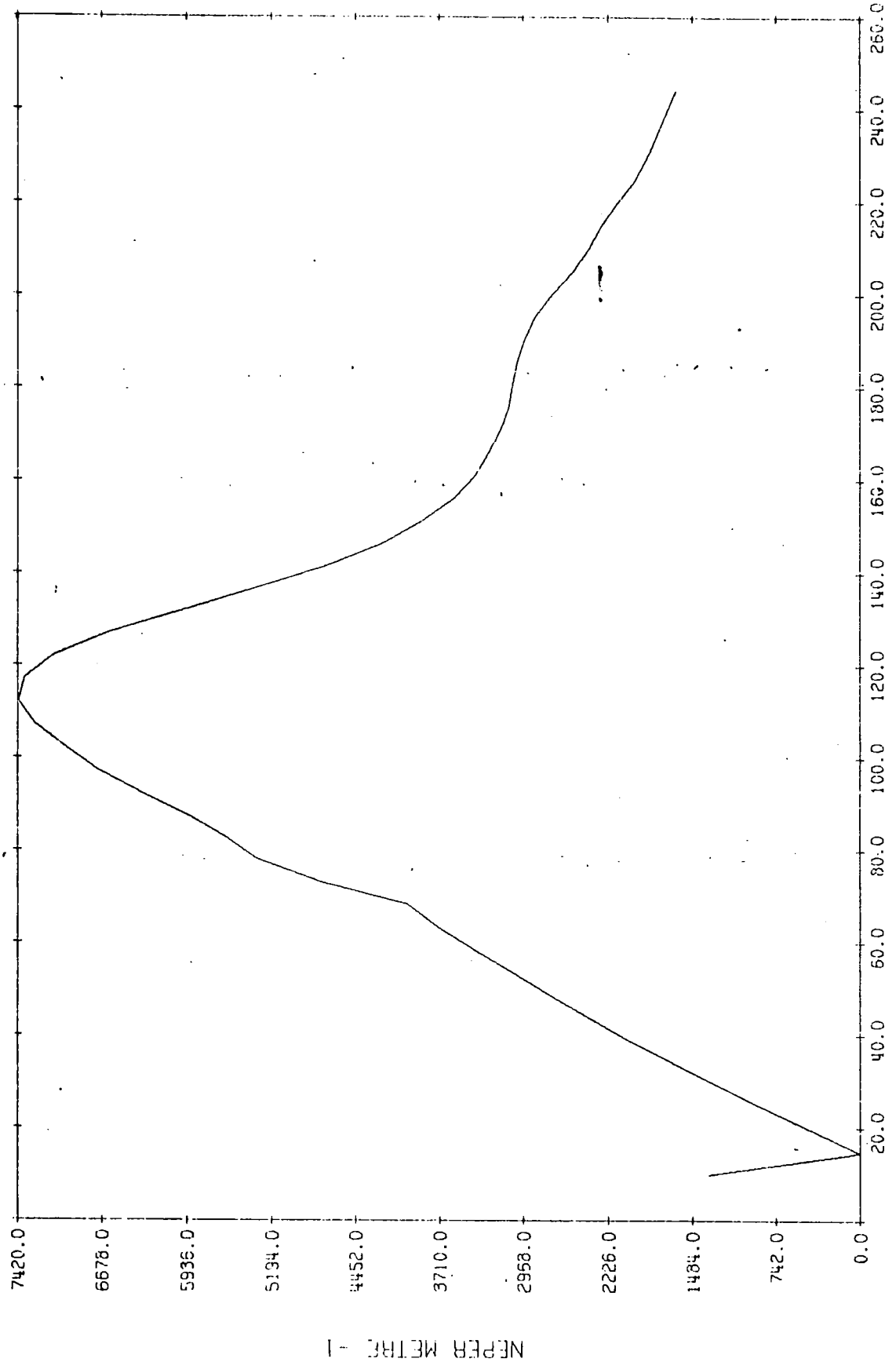

FIG. 3.10 NEPER METRE-1 SCALE

For solution work, where account needs to be taken of the effect of concentration on the strength of the absor ptions, the absorption data can be plotted on a neper m^2 $mol.^{-1}$ scale:

$$\text{neper } m^2 \text{ mol.}^{-1} = \text{absorbance/pathlength x concentration} \qquad 3.14$$

where the concentration has units mol. m^{-3}.

Fig. 3.11 shows the absorbance spectrum of fig. 3.9 represented on such a neper m^2 $mol.^{-1}$ scale.

3.2 Comparison of the theoretical and experimental resolution obtained using the FS-720 interferometer and the programme FTRAN4

In an effort to determine the experimental resolution achieved with the FS-720 a spectrum of water vapour was recorded. The sample chamber was partially filled with atmospheric water vapour by admittance of air. The sample chamber was sealed off from the remainder of the interferometer with a 3 mm white polythene window. 2048 point interferograms were recorded at 8 μm sampling interval for both the water vapour sample and the instrument background. The interferograms were recorded using a 25 gauge beam-splitter, with a white polythene lens and black polythene filter. Spectra were then computed over the region 35 to 500 cm^{-1}, using programme FTRAN4 with 512, 1024 and 2048 point portions of the tape. These water vapour spectra are shown in figs. 3.12 to 3.14. Figs. 3.12A, 3.13A and 3.14A show expanded plots of the relevent absorptions for clarity. The 512 point tape section represents a maximum mirror displacement of 0.1024 cm, and hence using eqn. 3.1 the theoretical resolution will be 4.88 cm^{-1}. The 1024 point tape section represents a maximum mirror displacement of 0.2048 cm and hence will have a theoretical, non-apodised resolution of 2.44 cm^{-1}. The 2048 point tape section represents a maximum mirror displacement of 0.4096 cm, and a theoretical, non-apodised resolution of 1.22 cm^{-1}.

To assist with the determination of the resolution achieved for the 3 computed spectra, each of the absorptions was indexed with the help

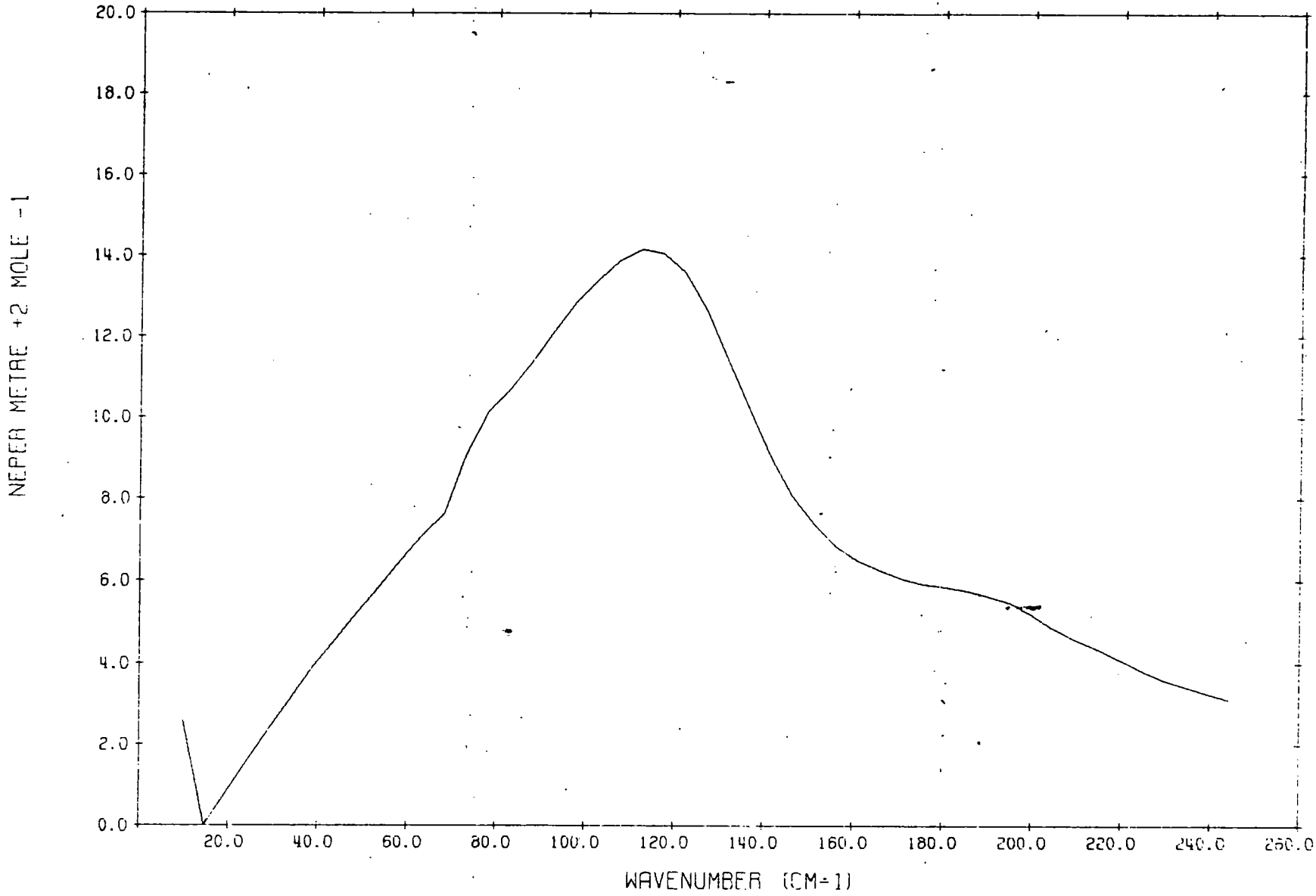

FIG. 3.11 NEPER METRE $^{+2}$ MOLE $^{-1}$ SCALE.

of a table of water vapour absorption frequencies published in the literature (ref. 20, p. 317). Table 3.1 shows the frequencies for the 59 water vapour bands within the spectral region 55 to 305 cm^{-1}, with greater than one-tenth the intensity of the 202 cm^{-1} band (which is the strongest in the region). All of the bands observed in the 3 computed spectra were assigned using these 59 absorptions. Tables 3.2 to 3.4 show the assignments for the bands observed in the spectra computed for the 512, 1024 and 2048 point interferograms respectively.

The tables and spectra were searched for pairs of bands which were just being resolved, and also for pairs of bands in which one of the bands appeared as a shoulder on the side of the other band. The latter indicating that the two bands were not quite being resolved. From table 3.2 and fig. 3.12 it can be seen that for the 512 point interferogram the bands indexed 15 and 16 were fully resolved. These bands corresponded to the 188.184 and 194.37 cm^{-1} bands in table 3.1, and so the resolution could be seen to be better than 6 cm^{-1}. The two resolved bands are denoted in figs. 3.12 and 3.12A by the letter A. It should be noted that the observed frequencies were taken from the line printer output, which had a 2.44 cm^{-1} interval for a 512 point interferogram. The magnitude of this interval causes the discrepance between observed and literature frequencies. Since it is the resolution being achieved that was of interest, then the more accurate literature values for the absorption frequencies were used for the calculation of the observed resolution. From figs. 3.12 and 3.12A it could also be seen that for a 512 point interferogram the band indexed 7 appeared as a definite shoulder on the side of the band 6. These bands correspond to the 104.57 and 100.55 cm^{-1} bands, and hence the resolution being achieved was not as good as 4 cm^{-1}. These two partially resolved bands are denoted by the letter B in figs. 3.12 and 3.12A.

For the 1024 point interferogram it could be seen from figs. 3.13 and 3.13A together with table 3.3 that the bands indexed 35 and 36 were

Table 3.1 Water vapour bands within the region 55 to 305 cm^{-1} with greater than one-tenth the intensity of the 202 cm^{-1} band.

(all cm^{-1})

55.705	121.90	177.534	253.98
57.269	126.997	181.380	254.01
64.029	132.666	188.184	266.24
68.060	138.990	194.37	278.27
73.259	139.76	202.47	278.49
75.523	140.708	202.69	280.35
79.776	149.056	202.909	282.25
82.153	150.519	208.49	289.43
88.079	151.30	213.908	302.93
92.540	153.45	221.72	302.99
99.024	157.63	223.69	303.14
99.14	157.87	226.64	
100.55	166.704	227.86	
104.570	170.358	231.21	
111.129	173.503	245.332	
120.084	176.02	253.82	

Table 3.2 Water vapour spectrum for 512 computed points

index	obs. freq. /cm^{-1}	assignment /cm^{-1}
1	56.15	55.705 + 57.269
2	63.48(w)	64.029
3	73.24	73.259
4	78.13(sh)	79.776 + 82.153
5	90.33	88.079 + 92.540
6	100.10	100.55 (99.024 & 99.14 as asymmetry)
7	104.98(sh)	104.570
8	122.07	120.084 + 121.90 (111.129 asy.)
9	131.84	132.66
10	139.16	138.99 + 139.76 + 140.708
11	151.37	149.056 + 150.519 + 151.30
12	156.23(sh)	153.45 + 157.63 + 157.87
13	170.90	170.358
14	175.78(sh)	176.02 + 177.534 + 181.38
15	187.99	188.184
16	195.31	194.37
17	202.64	202.69 + 202.47 + 202.909
18	209.96	208.49
19	227.05	227.86 (221.72 + 223.69 +226.64 asy.)
20	246.58	247.90

(continued)

Table 3.2 (continued)

index	obs. freq. /cm^{-1}	assignment /cm^{-1}
21	253.91	253.82 + 253.98 + 254.01
22	266.11(w)	266.24
23	278.32(sh)	278.27 + 278.49
24	280.76	280.35 + 282.25
25	290.53	289.43
26	302.73	302.93 +302.99 +303.14

Observed frequency taken from the line printer spectral output at a 2.44 cm^{-1} interval.

w = weak sh = shoulder

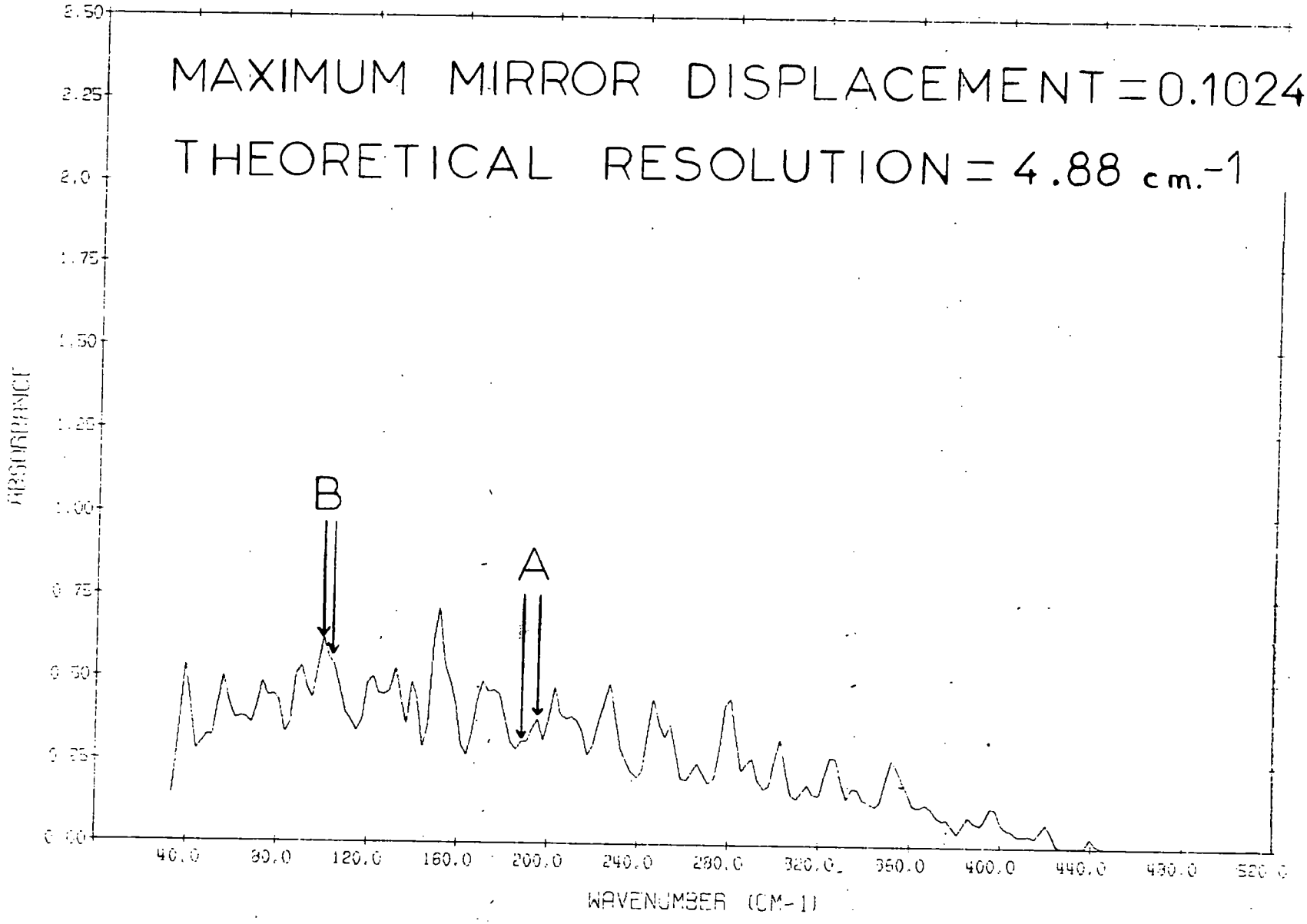

FIG. 3.12 WATER VAPOUR USING 512 POINTS

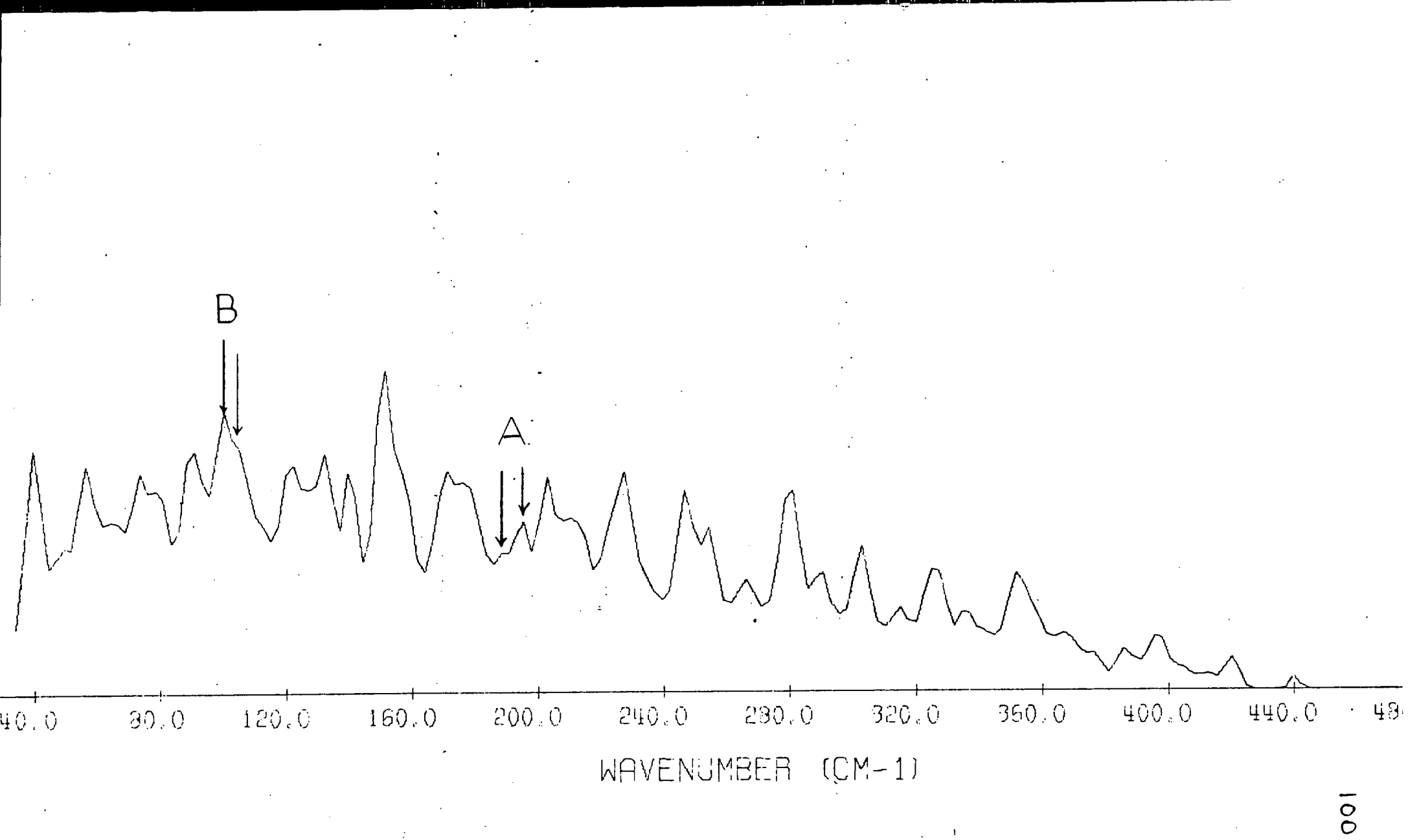

FIG. 3.12A 512 POINTS (EXPANDED)

Table 3.3 Water vapour spectrum for 1024 computed points

index	obs. freq. /cm^{-1}	assignment /cm^{-1}
1	56.15	55.705 + 57.269
2	63.48(w)	64.029
3	68.36(w)	68.060
4	73.24	73.259
5	79.35	79.776
6	81.79(sh)	82.153
7	87.89	88.079
8	92.77	92.540
9	100.10	100.55 (99.024 + 99.14 asy.)
10	104.98	104.570
11	111.08	111.129
12	122.07	120.084 + 121.90
13	126.95	126.997
14	131.84	132.666
15	140.38	138.99 + 139.76 + 140.708
16	150.15	149.056 + 150.519 + 151.30 (153.45 asy.)
17	157.47	157.63 + 157.87
18	166.02(w)	166.704
19	170.90	170.358
20	173.24(w)	173.503

(continued)

Table 3.3 (continued)

index	obs. freq. /cm^{-1}	assignment /cm^{-1}
21	177.00	176.02 + 177.534
22	181.88	181.38
23	187.99	188.184
24	194.09	194.37
25	202.64	202.47 + 202.69 + 202.909
26	208.74	208.49
27	213.62	213.908
28	222.17	221.72
29	227.05	226.264 + 227.86
30	231.93(w)	231.21
31	245.36(sh)	245.332
32	247.80	247.90
33	253.91	253.82 + 253.98 +254.01
34	266.11	266.24
35	278.32	278.49
36	281.98	280.35 + 282.35
37	288.09	289.43
38	302.73	302.93 + 302.99 + 303.14

Observed frequency taken from the line printer spectral output at a 1.22 cm^{-1} interval.

w = weak sh = shoulder

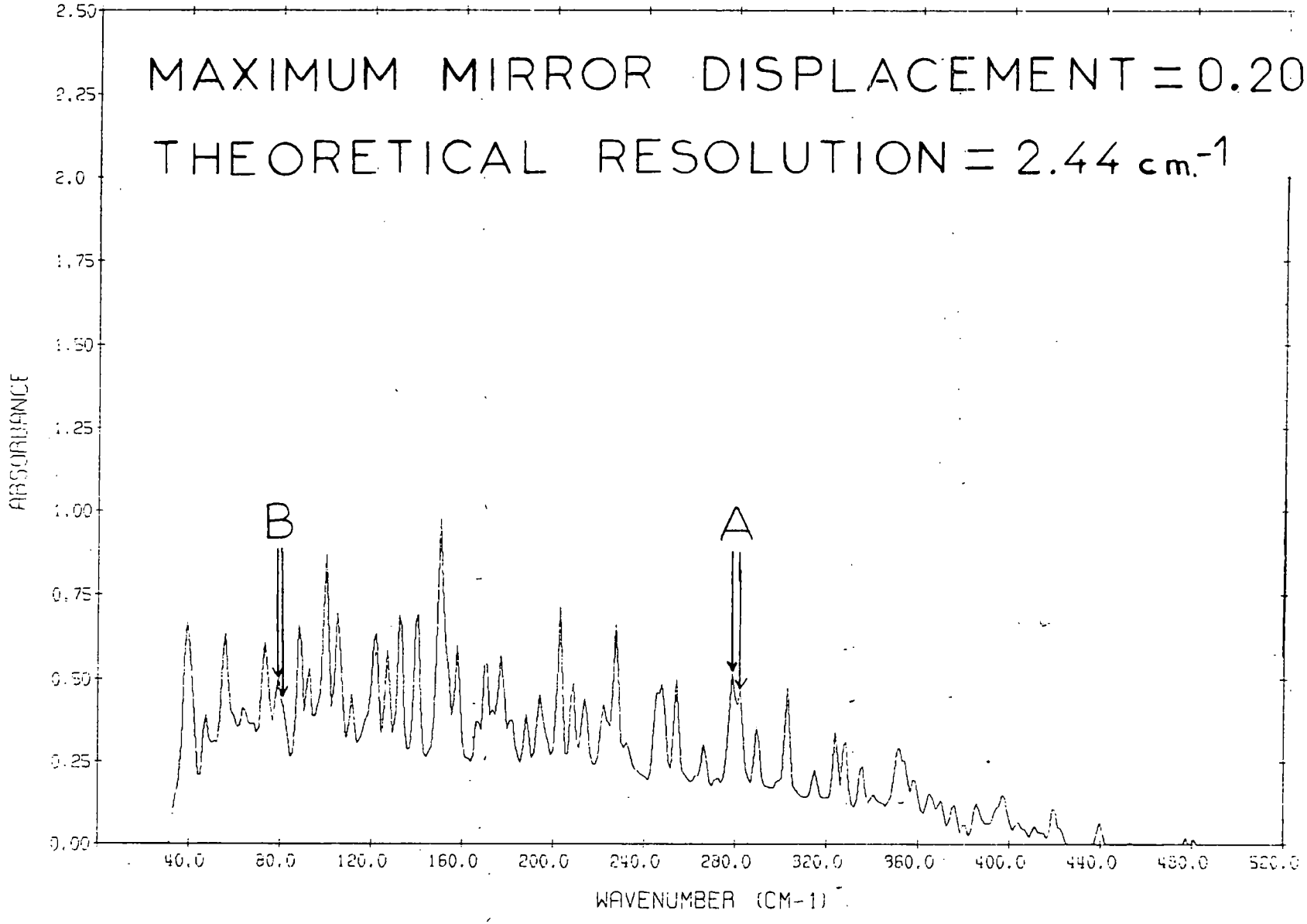

FIG. 3.13 WATER VAPOUR USING 1024 POINTS

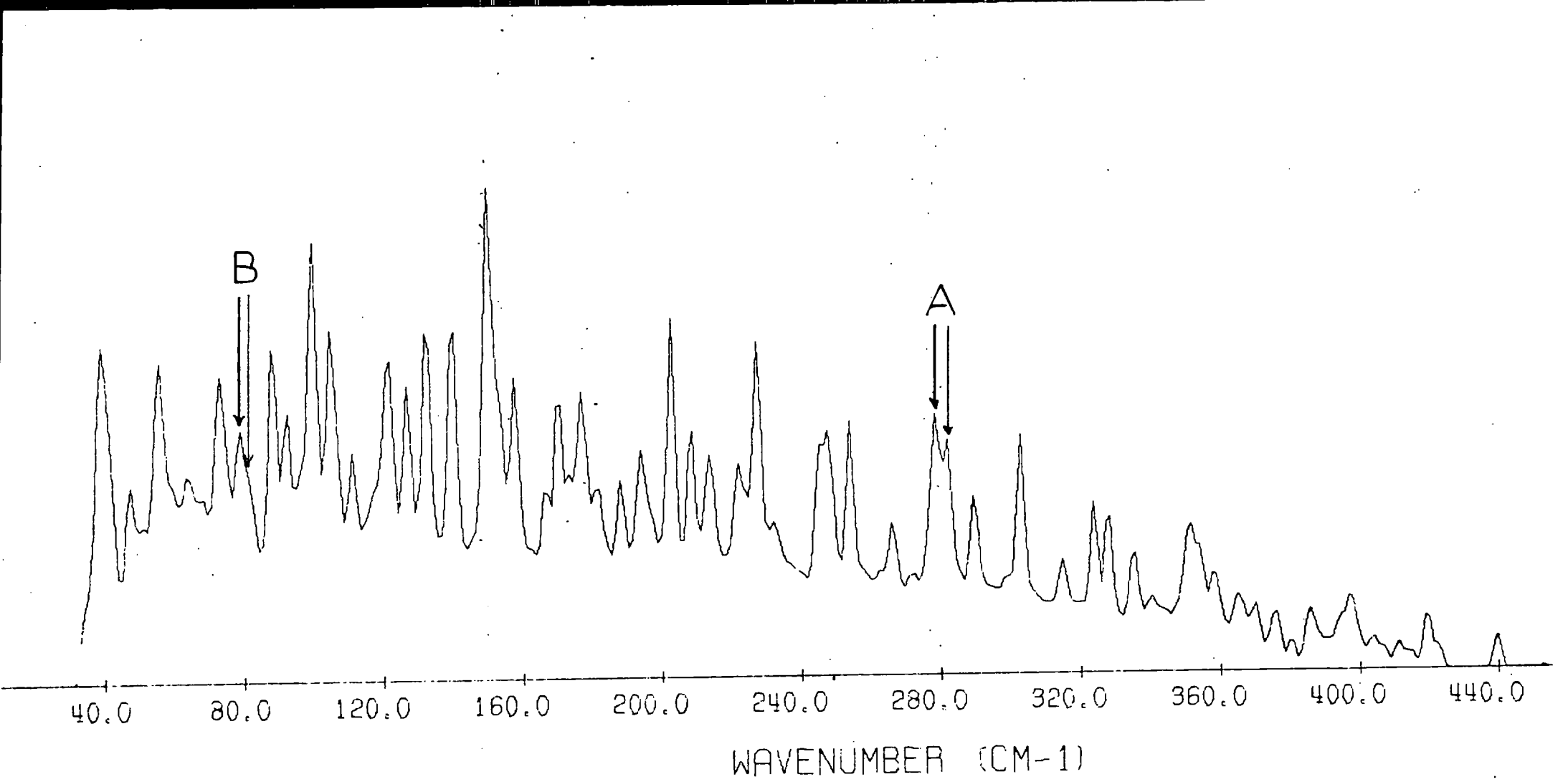

FIG. 3.13A 1024 POINTS (EXPANDED)

completely resolved, indicating that the resolution was better than 2.8 cm^{-1}. Band 6 appeared as a shoulder on the side of band 5, and so the resolution was poorer than 2.4 cm^{-1}. The resolved and unresolved band pairs are denoted by the letters A and B respectively on figs. 3.13 and 3.13A. The water vapour spectrum computed from the 2048 point interferogram is depicted in figs. 3.14 and 3.14A, and table 3.4. Bands 31 and 32 were seen to be fully resolved, and band 10 appeared as a shoulder on band 9, thus indicating that the resolution being achieved was better than 1.5 cm^{-1}, but not as good as 1.1 cm^{-1}. The resolved and unresolved bands are once again depicted by the letters A and B respectively on figs. 3.14 and 3.14A.

Taking the resolution as the mean of the values for the resolved pair of bands and the unresolved pair of bands, gave a resolution of 5 cm^{-1} for the 512 point interferogram, 2.6 cm^{-1} when using 1024 points and 1.3 cm^{-1} when using 2048 points. The linearity of the resolution with the reciprocal of interferogram length was as would be expected from eqn. 3.1, and indicated that the method used for calculating the resolution achieved was a viable one. This method of searching water vapour spectra between 50 and 300 cm^{-1}, for pairs of bands which just have, or have not, been resolved, depends critically upon the availability in the water vapour spectrum of a number of bands separated by frequencies comparable to the resolution. Water vapour was chosen because of its high number of far-infrared absorptions, which enable the resolution to be determined accurately.

The Rayleigh Criterion of resolution (ref. 40, p. 117) states that two lines of approximately the same intensities can be distinguished if the illumination between the lines decreases by 20 to 25% of their peak value. This somewhat arbitrary condition was developed for diffracted lines, where the condition holds when the maximum of one diffracted line falls over the minimum of the other line. The resolution as determined above may well be for a far less stringent condition than that for the Rayleigh criterion, because the minimum between the two bands did not occur at all for the

unresolved bands, and is only about 10% for the fully resolved bands. Pressure broadening may well be causing some increase in half-band width, and hence apparent decrease in resolution, but this is likely to be small for the low pressure of water vapour employed. However, the Rayleigh Criterion deals with bands of equal intensities. It will obviously require greater resolution to resolve a band of small intensity from the side of a more intense band, than to resolve two equally intense bands. Taking this point into account, the resolutions quoted may well be those for a condition equivalent to that cited by Rayleigh. All in all the values determined would seem to be reasonable indications of the resolution being achieved.

Tables 3.2 to 3.4 show that the wavenumber accuracy achieved in the computed spectrum was in all cases very high. It was always less than one-third of the resolution as determined above. Each table was searched for the maximum frequency discrepancy between the observed frequency and the literature frequency. The maximum discrepancy for singly assigned bands for the 512 point interferogram was seen to be 1.5 cm^{-1}, occurring for band 18. For the 1024 point interferogram the maximum discrepancy was 0.7 cm^{-1}, also occurring for band 18, and for the 2048 point interferogram the maximum discrepancy was 0.4 cm^{-1}, occurring for band 8. These figures show the extremely high wavenumber accuracy of the computed spectra.

The resolution obtained for the various tape lengths, all recorded with an 8 μm sampling interval, are contained in table 3.5.

Table 3.4 Water vapour spectrum for 2048 computed points

index	obs. freq. /cm^{-1}	assignment /cm^{-1}
1	53.71	53.444
2	55.54	55.705
3	57.37(sh)	57.269
4	59.81(w)	59.871
5	62.26(w)	62.30
6	64.09(w)	64.029
7	68.36(w)	68.06
8	72.63	72.186
9	73.24	73.259
10	75.07(sh)	75.523
11	79.35	79.776
12	81.79	82.153
13	87.89	88.079
14	92.16	92.540
15	95.83	96.187
16	100.71	100.55 (99.024 + 99.14 asy.)
17	104.98	104.570
18	111.08	111.129
19	117.80	117.97
20	120.24	120.084

(continued)

Table 3.4 (continued)

index	obs.freq. /cm^{-1}	assignment /cm^{-1}
21	122.07	121.90
22	126.95	126.997
23	132.45	132.666
24	139.16	138.99 + 139.76 + 140.708
25	150.76	150.519 + 151.30 (149.056 asy.)
26	153.20	153.45
27	158.08	157.63 + 157.87
28	166.63	166.704
29	170.29	170.354
30	173.34	173.503
31	176.39	176.02
32	177.61	177.534
33	181.27	181.38
34	187.99	188.14
35	194.09	194.37
36	202.64	202.69 + 202.47
37	208.13	208.49
38	214.23	213.908
39	221.56	221.72
40	224.00	223.69

(continued)

Table 3.4 (continued)

index	obs.freq. /cm^{-1}	assignment /cm^{-1}
41	226.44	226.264
42	227.66	227.86
43	245.36	245.332
44	247.80	247.90
45	253.91	253.82 + 253.98
46	266.11	266.24
47	278.32	278.27 + 278.49
48	280.15	280.35
49	281.98	282.25
50	289.31	289.43
51	302.73	302.93 + 302.99 + 303.14

Observed frequency taken from the line printer spectral output at a 0.61 cm^{-1} interval.

w = weak sh = shoulder

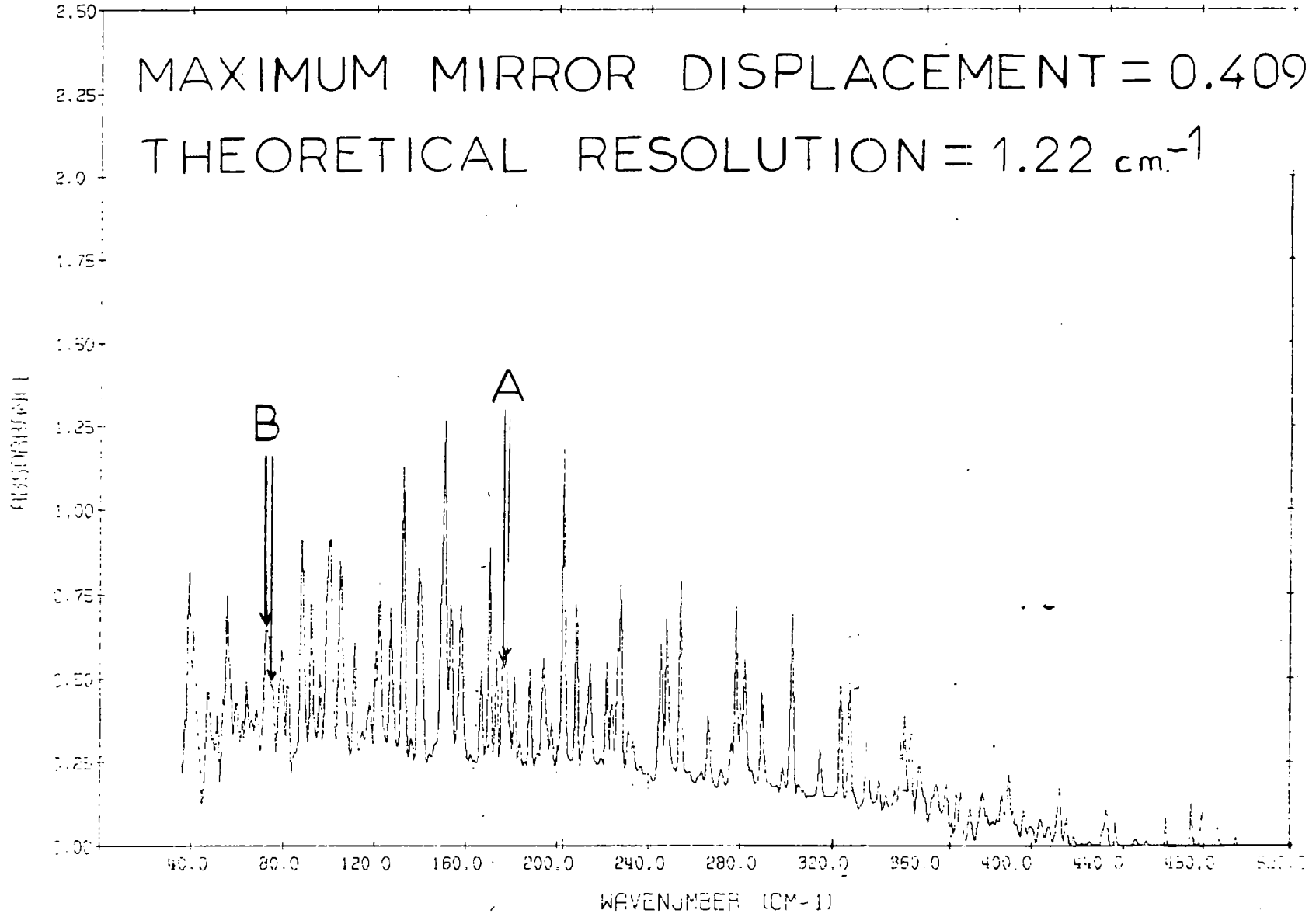

FIG. 3.14 WATER VAPOUR USING 2048 POINTS

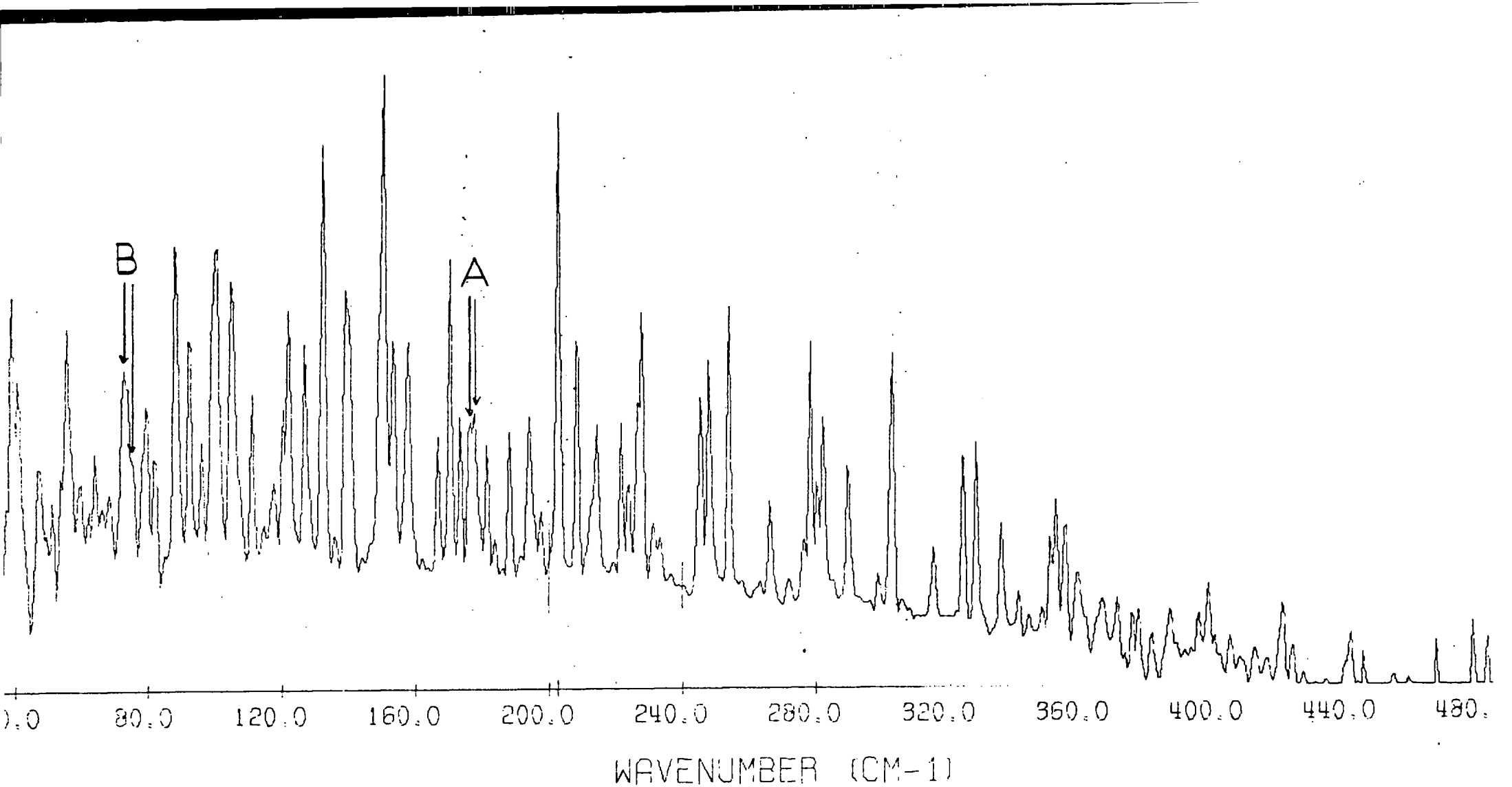

FIG. 3.14A 2048 POINTS (EXPANDED)

Table 3.5 Summary of resolution data for the water vapour sectra

(for 8 μm sampling interval in terms of path-difference)

number of points computed [a]	maximum mirror displacement [b] /cm	theoretical resolution [c] $/cm^{-1}$	experimental resolution [d] $/cm^{-1}$
512	0.1024	4.88	5.0
1024	0.2048	2.44	2.6
2048	0.4096	1.22	1.3

a double-sided interferogram.

b L of eqn. 3.1.

c from eqn. 3.1.

d average resolved and unresolved values for a pair of bands (see text).

PART B

IONIC SOLVATION STUDIES

CHAPTER 4

FAR-INFRARED STUDIES OF TETRA-N-ALKYLAMMONIUM SALTS IN VARIOUS SOLVENTS

4.1 Introduction to ionic solvation work

It has been recognised (41-47) for a considerable time that solvated ions are the predominant ionic species in solutions of ionic salts in solvents of relatively high permittivity. Ion pairs, triple ions and higher aggregates exist in solutions of ionic salts in solvents of low permittivity (48-52). Many of the physical properties determined for electrolyte solutions are bulk properties of the solution as a whole (viscosity, conductivity and freezing point depression), which gave no real indication of the microstructure at the ion itself. Far-infrared spectroscopy can yield information regarding the shortrange forces and solution structure at ion centres in ionic solutions, and so help in deducing the type of solvation occurring at the ion centres. Edgell and Watts (ref. 53, p. 85) first used far-infrared spectroscopy as a usefull means of elucidating ionic solution structure in 1965. They assigned a band at 190 cm^{-1} in solutions prepared by shaking sodium amalgam with dicobaloctacarbonyl ($Co_2(CO)_8$) in tetrahydrofuran (THF), to the motion of the Na^+ cation in the solvent (43). Similar bands, assigned to cation motions for Li^+ and K^+, occurring at 407 and 150 cm^{-1} respectively were discovered for $Li^+Co(CO)_4^-$ and $K^+Co(CO)_4^-$ in THF solutions (43).

Evans and Lo (48) observed the far-infrared spectra of some tetra-n-alkylammonium salts in benzene, and attributed the observed bands to the vibrations of ion pairs or quadrupoles, and possibly even higher aggregates. A band was observed at 120±3 cm^{-1} for tetra-n-butylammonium chloride, and one at 80±4 cm^{-1} for tetra-n-butylammonium bromide. For tetra-n-pentylammonium chloride a band was observed at 119±3 cm^{-1}, and for tetra-n-pentylammonium bromide at 80±4 cm^{-1}. The band thus showed strong anion dependence, and reduced mass calculations supported the assignments of the bands to the vibration of ion pairs.

The literature of far-infrared studies on electrolyte solutions soon expanded as work was conducted in a wide range of solvents of varying

permittivity, for a large number of electrolytes. Edgell has reviewed the work in the infrared and Raman studies of ions and ion pairs in organic solvents prior to 1972 (ref. 47, p. 153). Chapter 7 contains a summary of previous work in relation to the results obtained in this study.

The bands occurring for the cation 'rattling' in polar solvents, and for the vibration of ion pairs in relatively non-polar solvents, have very similar shapes. Both types of band have half-band widths of the order of 80 cm^{-1}. The similarities in the absorption profiles indicated that the processes giving rise to the absorptions in apparently widely different systems were in fact of similar origin. A study of the absorption bands of electrolytes dissolved in both polar and non-polar solvents was undertaken. It was hoped that this would throw additional light on the nature and origin of these far-infrared bands. In making more detailed studies than those previously undertaken for the bands of such systems, it was hoped that a dynamic model could be constructed from the results obtained, to satisfactorily explain the observed phenomena in terms of the cooperative motions of the ions and solvent molecules in the liquid phase.

The majority of the far-infrared electrolyte solution studies in the literature entailed only the measurement of frequencies of maximum absorption and studies of the effect of a change of cation, anion and solvent on the frequency of maximum absorption, to assist with the assignment of bands. Some work related the extinction coefficient at the band centre with the concentration of the salt species present. In this work the area under the absorption bands has been used to determine the intensity of the bands, and this area has been related to the concentration of salts present in the electrolyte solutions.

The effects on the absorption band of concentration of added electrolyte, solvent, temperature and phase have been studied. This chapter contains the results of an extensive study of the far-infrared absorptions of tetra-n-alkylammonium salts in the solvents benzene, carbon tetrachloride

and chloroform.

4.2 Tetra-n-butylammonium chloride in benzene

B.D.H. Analar benzene was used as solvent, and was used without further purification, except that it was stored over molecular sieves for at least two days prior to use. A Karl-Fischer titration showed less than 0.001% by weight of water in the benzene solvent. The tetra-n-butylammonium chloride ($Bu_4N^+Cl^-$) was purchased from Eastman-Kodak Ltd. and was stored over calcium chloride in a dessicator, and then used without further purification. The solutions of $Bu_4N^+Cl^-$ in benzene were made by weighing out the required amount of salt in a volumetric flask, and making up to the mark with dried benzene. (See section 4.2.2 for the effect of water on the spectra of the solutions.)

Spectra of $Bu_4N^+Cl^-$ in benzene were obtained in the conventional transmission mode over the range 20 to 250 cm^{-1}, using a 50 gauge beam-splitter with a white lens and 50 μm black polythene filter, as described in chapter 2. The 1024 point interferograms were computed giving a resolution of about 2.6 cm^{-1}, as described in chapter 3. The spectra illustrated are all ratioed absorbance spectra of solutions of the salt in benzene against a pure benzene solvent background. Fig. 4.1 shows the spectrum obtained for 0.70 mol dm^{-3} $Bu_4N^+Cl^-$ in benzene at 290K in a polythene windowed cell of 0.021 cm pathlength. The observed band can be seen to be very broad and to have a half-band width of about 80 cm^{-1}. Due to the extreme broadness of these far-infrared bands, it was very difficult to observe the wings of the bands, since, for frequencies above 220 cm^{-1} and below 30 cm^{-1}, the energy throughput of the interferometer is very low due to the beam-splitter minima, lack of source intensity and detector sensitivity. The absorption bands stretch over the whole useful range of the 50 gauge beam-splitter, the use of which is necessary to maximise the energy in the region of the band maximum around 120 cm^{-1}. The broadness of the band causes the discrepancy between the observed value of 115±5 cm^{-1}, for the frequency of maximum absorption,

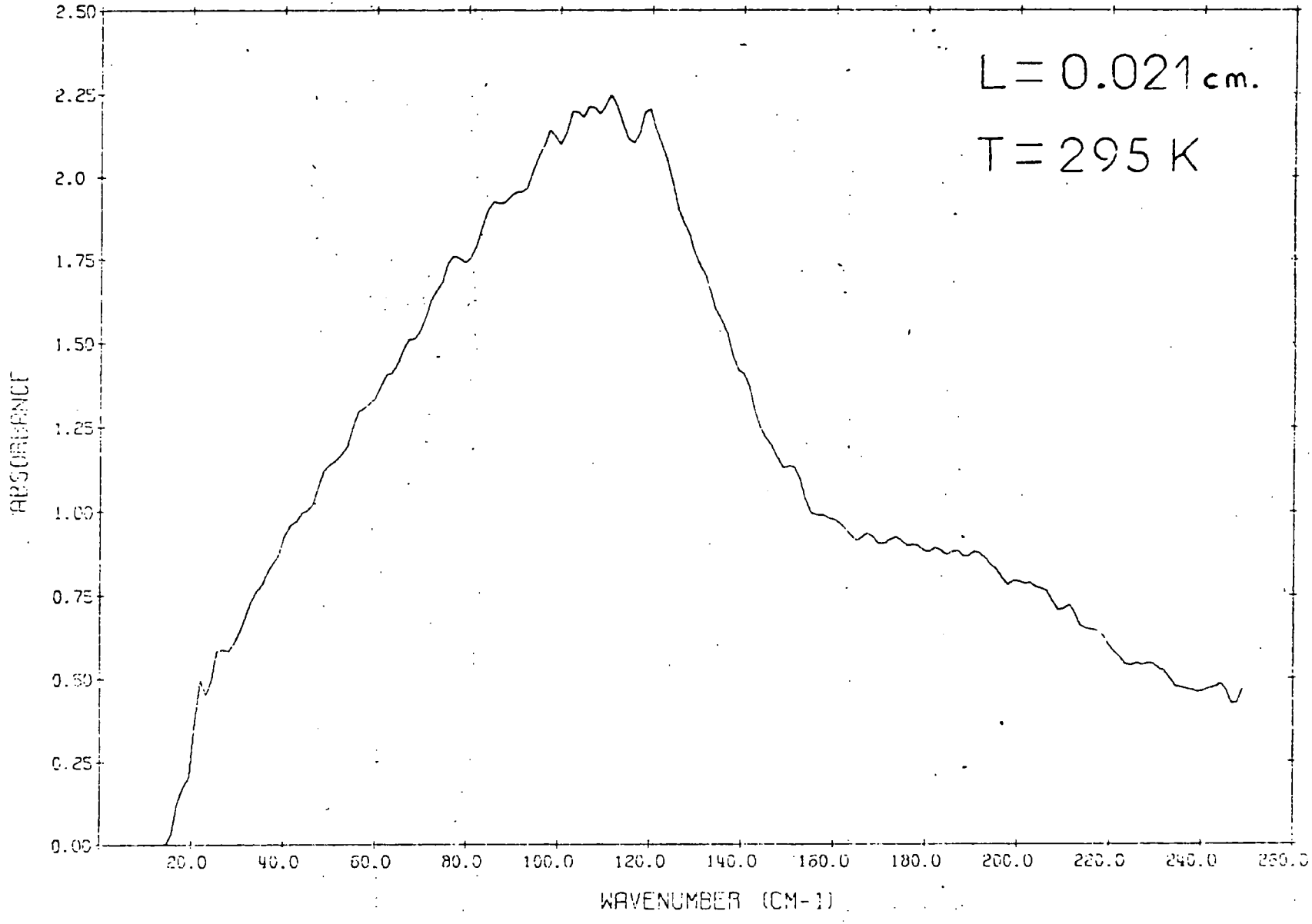

FIG. 4.1 0.7 mol. dm^{-3} BU4N+CI- IN BENZENE

and that of Evans and Lo (48), who measured the band centre as 120±3 cm^{-1}. The measurements of band profile, including computer resolution of overlapping bands, detailed in chapter 5, indicate that the band centre appears to be at 115 cm^{-1}.

Attempts were made to record the spectrum of $Bu_4N^+Cl^-$ in benzene, using various beam-splitter and filter combinations, to observe portions of the band under optimised conditions. The majority of the band, from 50 to 200 cm^{-1}, was observed easily by the use of a 50 gauge beam-splitter and a black polythene filter as described previously. The high frequency wing, between 150 and 350 cm^{-1}, was observed by using a 25 gauge beam-splitter. The low frequency wing, below 50 cm^{-1} and down to 30 cm^{-1}, was observed by using a 100 gauge beam-splitter and a crystalline quartz filter. The 100 gauge and 25 gauge spectra cover such a small proportion of the overall band, that they are of little use when obtained alone. Attempts to join up spectra recorded with various beam-splitters were unsuccessful, as the absorbance spectra often disagreed by between 5 and 10% at the overlap frequencies. These discrepancies suggested that the errors on the absorbance values may be as high as ±5%, whereas the precision of the transmission values for the backgrounds has already been shown to be ±1%. For preliminary results using a cooled detector see section 2.14.

The attempts to observe the whole band were thus unsuccessful, and the 50 gauge beam-splitter spectrum was taken as the best spectrum obtainable using dielectric beam-splitters. The use of a polarising grid beam-splitter would enable spectra to be recorded over a number of octaves of frequency in the region 2 to 250 cm^{-1}, since these beam-dividers do not rely upon thin film interference, with its consequent hooping, for their operation.

4.2.1 Effect of concentration on the spectra

An extensive concentration study of the broad band centred at 115 cm^{-1} was made for $Bu_4N^+Cl^-$ in benzene solutions. The primary interest

of this study was to determine the effect of concentration of the added salt on the intensity of the absorption. The area under the absorption spectrum as produced by programme GPLOT3 was measured by the use of a planimeter. The programme GPLOT3 produces a natural logarithm absorbance scale with a frequency scale linear in wavenumber, and hence the area under the absorption curve will be;

$$\text{Area} = \int_{\text{band}} \ln(T_o/T)_{\bar{\nu}} . \delta\bar{\nu}$$

$$A_i = \int_{\text{band}} \alpha(\bar{\nu}) . \delta\bar{\nu} \qquad 4.1$$

The constant intensity B_i, for the ith. band, can be calculated as (ref. 54, chap. 10);

$$B_i = 1/c\ell . \int_{\text{band}} \ln(T_o/T)_{\bar{\nu}} . \delta\bar{\nu}$$

$$B_i = \text{Area}/c\ell \qquad 4.2$$

where c_i is the concentration of the absorbing species in mol dm^{-3}, and ℓ is the pathlength in cm.

The units of the intensity B_i are thus $dm^3\ mol^{-1}\ cm^{-2}$. See chapter 7 for a discussion of the validity of intensity calculations in the far-infrared using eqns. 4.1 and 4.2.

The area under the absorption curve was also determined by the use of a simple integrator programme DCH0512. The programme utilises the digital transmittance/frequency output from programme FTRAN4, and computes the area by simple summing of the incremental areas beneath the absorption curve, bordered by the frequency interval of the input transmittance/frequency data. The two areas calculated for a given band are represented in the following tables as 'planimeter area' and 'computed area'. The two areas are averaged and the intensity calculated using eqn. 4.2.

As can be seen from fig. 4.1 the absorption curve does not drop to zero in the wings of the $Bu_4N^+Cl^-$ in benzene band. This is possibly due to the full wings of the band not being observed, due to the restrictions of the thin dielectric film beam-splitters as already described. There is also the further possibility that bands of half-band width even greater than

80 cm^{-1}, lie under the observed band. In order to make allowance for such bands, it was necessary to provide a baseline for the bands, so that the area could be restricted to that under the band in question. The fixing of a baseline for these bands was very difficult, due to their extreme broadness. There was the added complication that the wings of the band were possibly not being observed. This prevented an accurate baseline being interpolated between the wings. The situation was further complicated, since the presence of underlying bands will necessitate a curved baseline. The accurate fixing of the baseline was clearly impossible under the present circumstances, where the half-band width of the underlying band was as large as the useful frequency range of the beam-splitter.

Clearly, the situation had to be simplified before any useful work could be accomplished. This simplification was made by assuming that the baseline was linear. The programme DCH0512 constructs a straight line between the absorbance values for the lowest and highest frequency limits set by the control parameters. These limits were determined by inspection of the lineprinter output of the ratioed transmittance spectrum. Termination of the band was assumed to have occurred when a maximum occurred in the transmittance values, or when the noise in the wings was predominant, indicating that no useful areas would ensue. In the intensity work for $Bu_4N^+Cl^-$ in benzene, both the low frequency and high frequency limits were determined by the noise level in the wings. When using the planimeter for measurements of the area under the bands, the baselines were fitted by comparison between spectra at various concentrations, in an effort to gain some consistency. A great deal of care was taken in the fixing of the baseline, and those used were always the 'best' that could be achieved. Although the inavailability of the full wings of the bands precluded the calculation of accurate intensity values, the intensity values obtained should show consistency and reasonable precision, and should therefore indicate well the relative intensity changes occurring.

In an effort to test the validity of the baseline fitting method a precision check was conducted. Five separate solutions of 0.5 mol dm^{-3} $Bu_4N^+Cl^-$ in benzene were made up, and then four spectra recorded for each solution, the cell being refilled for each spectrum. A pure solvent background was recorded for each solution. The spectra were recorded using 0.021 cm pathlength, 3 mm polythene windowed, demountable cells, and a 50 gauge beam-splitter and 50 μm black polythene filter. 1024 point, double-sided interferograms were recorded with a path-difference sampling interval of 8 μm, giving an experimental resolution of about 2.6 cm^{-1}, as described in chapter 3. The 'computed' and 'planimeter' areas were measured, as detailed above, for each of the 20 spectra. These areas are shown in table 4.1, together with the average of the two areas. The average areas were then treated statistically to give a mean area, and a root mean square deviation. No weighting factors were employed in the calculation of the mean, which was found to be 132.8 cm^{-1}. The root mean square deviation σ was calculated by the formula (ref. 55, p. 40):

$$\sigma = \{1/(n-1)\Sigma_{s=1}^{n}(x_s-\bar{x})^2\}^{\frac{1}{2}} \qquad 4.3$$

where n is the number of observations x_s, and $\bar{x}$ is the mean value. Use of eqn. 4.3 gave a standard deviation of 22 cm^{-1}, which, when expressed as a percentage of the mean value, to give the coefficient of variation, was 17%. The large value for this coefficient of variation was considered to be a direct consequence of the difficulties experienced with the fitting of baselines as discussed previously. These precision values were only strictly true for 0.5 mol dm^{-3} $Bu_4N^+Cl^-$ in benzene solutions in 0.021 cm pathlength cells. However, since most of the inaccuracies were produced by the fitting of the baseline, which will presumably cause the same problems regardless of concentration, a precision of ±22 cm^{-1} was used as the possible error on all area measurements. The error bars on all the concentration/area graphs indicate the precision of ±22 cm^{-1} in the areas. The standard deviation was chosen as an indication of precision, rather than the coefficient

Table 4.1 Precision tests for 0.5 mol dm^{-3} $Bu_4N^+Cl^-$ in benzene

(L = 0.021 cm, T = 293K)

soln. no.	conc. /mol dm^{-3}	area 'computed' /cm^{-1}	'planimeter' /cm^{-1}	'average' /cm^{-1}
1	0.500	99.9	104.1	102.0
		116.2	121.4	118.8
		129.5	157.3	143.4
		101.1	130.5	115.8
2	0.498	118.1	117.3	117.7
		136.3	140.1	138.2
		164.9	170.9	167.9
		159.8	169.2	164.5
3	0.498	118.0	143.2	130.6
		164.4	140.7	152.6
		168.3	125.3	146.8
		167.0	142.9	154.9
4	0.498	137.0	150.0	143.5
		152.5	151.9	152.2
		136.5	138.2	137.4
		147.1	150.7	148.9
		153.6	141.6	147.6
5	0.506	101.1	95.5	98.3
		89.3	91.4	90.3
		97.6	118.1	107.9
		97.6	120.7	109.1

of variation, since it was considered that the lack of precision was due mainly to baseline fitting errors, which are not affected by concentration.

Table 4.2 shows the measured areas and calculated intensities for 20 solutions of $Bu_4N^+Cl^-$ in benzene for concentrations between 0.2 mol dm^{-3} and the solubility limit 1.4 mol dm^{-3}. The spectra were all recorded using a 0.3 cm polythene windowed demountable cell of 0.021 cm pathlength, with a 50 gauge beam-splitter and 50 μm black polythene filter. 1024 point, double-sided interferograms were recorded with an 8 μm path difference sampling interval, giving an experimental resolution of 2.6 cm^{-1}. The temperature was monitored and was found to be 290±2K for all runs. To obtain the best spectra possible in the minimum time the following procedure was adopted. Firstly the instrument was pumped down and a background of pure benzene solvent was recorded. The vacuum was then broken, and the cell refilled with the $Bu_4N^+Cl^-$ in benzene solution. Two runs were then performed on this solution, and then the cell was refilled with solvent and two more backgrounds recorded. The use of this technique halved the time spent evacuating the instrument, and yet gave a duplicate run for each concentration to act as a simple consistency check. Accurate intensities were calculated, since the sample and background interferograms were recorded one after the other. One of the spectra for each concentration had the background recorded first, and the other the sample first. This had no effect on the ratioed spectrum.

If a number of sample interferograms were recorded, and ratioed against a single background, then the noise in the computed spectrum tended to increase with the elapsed time between the recording of the sample and background interferograms. Thus, except where otherwise stated, for all the spectra shown the corresponding background and sample interferograms were recorded one after the other. However, the recording of a background interferogram for each sample introduces as much noise into the ratioed spectrum as does the sample interferogram itself. In fact the noise for the background

Table 4.2 Concentration dependence for the intensity of the 115 cm^{-1} band for $Bu_4N^+Cl^-$ in benzene

(L = 0.021 cm, T = 290K)

conc.	area				intensity
	'planimeter'	'computer'	'average'[a]	'average'[b]	B
/mol dm^{-3}	/cm^{-1}	/cm^{-1}	/cm^{-1}	/cm^{-1}	/dm^3 mol^{-1} cm^{-2}
0.21		13.4	13.4		
		20.2	20.2	16.8	3850±5040
0.25	53.1	50.0	51.5	51.5	9830±4230
0.30	54.1	65.5	59.8	59.8	9630±3540
0.34	74.9	90.1	82.5	82.5	11580±3110
0.35	46.5	46.1	46.3		
	49.6	41.4	45.5	45.9	6310±3020
0.40	108.0	101.8	104.9		
	66.7	93.7	80.2		
	76.6	102.2	89.4		
	75.2	104.9	90.1	91.2	11020±2640
0.42	62.3	61.9	62.1		
	55.7	61.7	58.7	60.4	6860±2520
0.46	160.6	148.5	154.4	154.4	16090±2300
0.51	166.9	165.9	166.4	166.4	15780±2070
0.52	154.2	146.4	150.3		
	153.6	146.1	149.8	150.0	13870±2030
0.55	191.6	193.6	192.6	192.6	16810±1920
0.60	220.4	211.5	215.9	215.9	17210±1760

(continued)

Table 4.2 (continued)

conc. /mol dm^{-3}	area 'planimeter' /cm^{-1}	'computer' /cm^{-1}	'average' /cm^{-1}	'average' /cm^{-1}	intensity /dm^3 mol^{-1} cm^{-2}
0.66	224.8	213.6	219.2		
	138.7	181.1	159.9		
	119.4	149.9	134.6		
	169.2	206.3	187.8	175.4	12760±1600
0.70	186.1	209.7	197.9		
	197.7	197.6	197.6	197.7	13580±1580
0.71	243.3	232.0	237.6	237.6	16110±1490
0.75	243.3	239.3	241.3	241.3	15430±1410
0.80	209.8	234.0	221.9	221.9	13300±1320
0.86	219.6	240.1	229.8	229.8	12910±1230
1.04		298.9	298.9		
		294.0	294.0	296.5	13710±1020
1.40		347.4	347.4		
		358.6	358.6	353.0	12120±760

[a] average area per spectrum.

[b] average area per concentration.

was sometimes greater than that for the sample, since the interferometer optics were optimised for the absorption of the sample, rather than that of the background. For the $Bu_4N^+Cl^-$ in benzene spectra the 50 gauge beam-splitter gave an energy maximum at 117 cm^{-1}, which was ideal for the band at 115 cm^{-1}. However, the energy available in the region of the 75 cm^{-1} band for the pure benzene (see chapter 5) solvent background was very low, and the spectrum in this region was noisy. The ratioed spectrum thus exhibited the noise from the background, especially at low frequencies.

The best ratioed spectra could presumably be obtained by recording a single background, using a very long Golay amplifier time constant to decrease the noise level. This could then be used as a background for all the sample tapes, which would be recorded with the usual time constant of 0.5 seconds. Spectra thus recorded would show the effects of drifting of the source, which is a problem in interferometry. The decrease in noise level of spectra recorded using the more stable German 'Original Hanau' source lamps, in preference to the Philips lamps, indicated that the system was in fact source noise limited (see chapter 1). This suggested that even the new sources were relatively unstable, and some experimental evidence supports this hypothesis. Although source drifting was not noticeable during the running of a single interferogram, over a full days runs the interferogram signal gradually decreased for a given sample. This indicated that there may well have been some long-term source drift, the source becoming less intense as it was run for long periods. Hence it was considered that the most accurate intensity values would be obtained by running a background and sample interferogram, one immediately after the other, with the same time constants. This procedure was employed throughout the concentration studies.

Returning to the $Bu_4N^+Cl^-$ in benzene studies, the solutions for concentrations near the solubility limit of 1.40 mol dm^{-3} were very viscous and difficulty was experienced in forcing the solutions through the narrow ports of the demountable cell. These concentrated $Bu_4N^+Cl^-$ in benzene solutions

tended to occlude significantly to the polythene windows, even over the 50 minute period necessary for the instrument to be pumped down and the interferogram recorded. The observed intensity values for the more concentrated solutions were therefore possibly less than the real values. No results suggested that there was significant occlusion below 1.0 mol dm^{-3} $Bu_4N^+Cl^-$ in benzene. No spectrum of the salt was observeable when the cell was emptied and the spectrum of the polythene plates recorded.

Fig. 4.2 shows a plot of the area of the 115 cm^{-1} band against the concentration of added salt for $Bu_4N^+Cl^-$ in benzene using the data of table 4.2. The average area was plotted with an error bar of ±22 cm^{-1}. The values of 'planimeter' and 'computer' areas were fed into the programme BEERSLAW to determine the 'best' straight line through all the data points. This programme involves a linear least squares analysis, to determine the slope of the 'best' straight line, and also computes the standard deviation of the points about this 'best' slope line and the intercept of the line with the origin. Using this programme, and taking the origin as a valid point, the data of table 4.2 gave a best straight line of slope = 272±7 dm^3 mol^{-1} cm^{-1}, which is represented in fig. 4.2 by the letter A. On dividing by the pathlength of 0.021 cm the intensity B_i was calculated as 13000±300 dm^3 mol^{-1} cm^{-2}. When the area data was employed without the restriction that the origin was a valid point, a slope of 310±16 dm^3 mol^{-1} cm^{-1} and an intensity of 14 900±800 was obtained. The intercept was calculated as -26±31 cm^{-1} which suggested that the best fit for the data would be through the origin. The higher intensity without the restriction that the origin was a valid point, suggested that Beers Law was not being obeyed for the system $Bu_4N^+Cl^-$ in benzene at concentrations between 0.2 and 1.4 mol dm^{-3}. All the area values were above the Beers Law linear plot through the origin, and this suggested that the linear relationship was not being obeyed. To verify this the intensity values have been calculated for each $Bu_4N^+Cl^-$ concentration, and are shown in table 4.2. Fig. 4.3 shows a plot of intensity B_i against

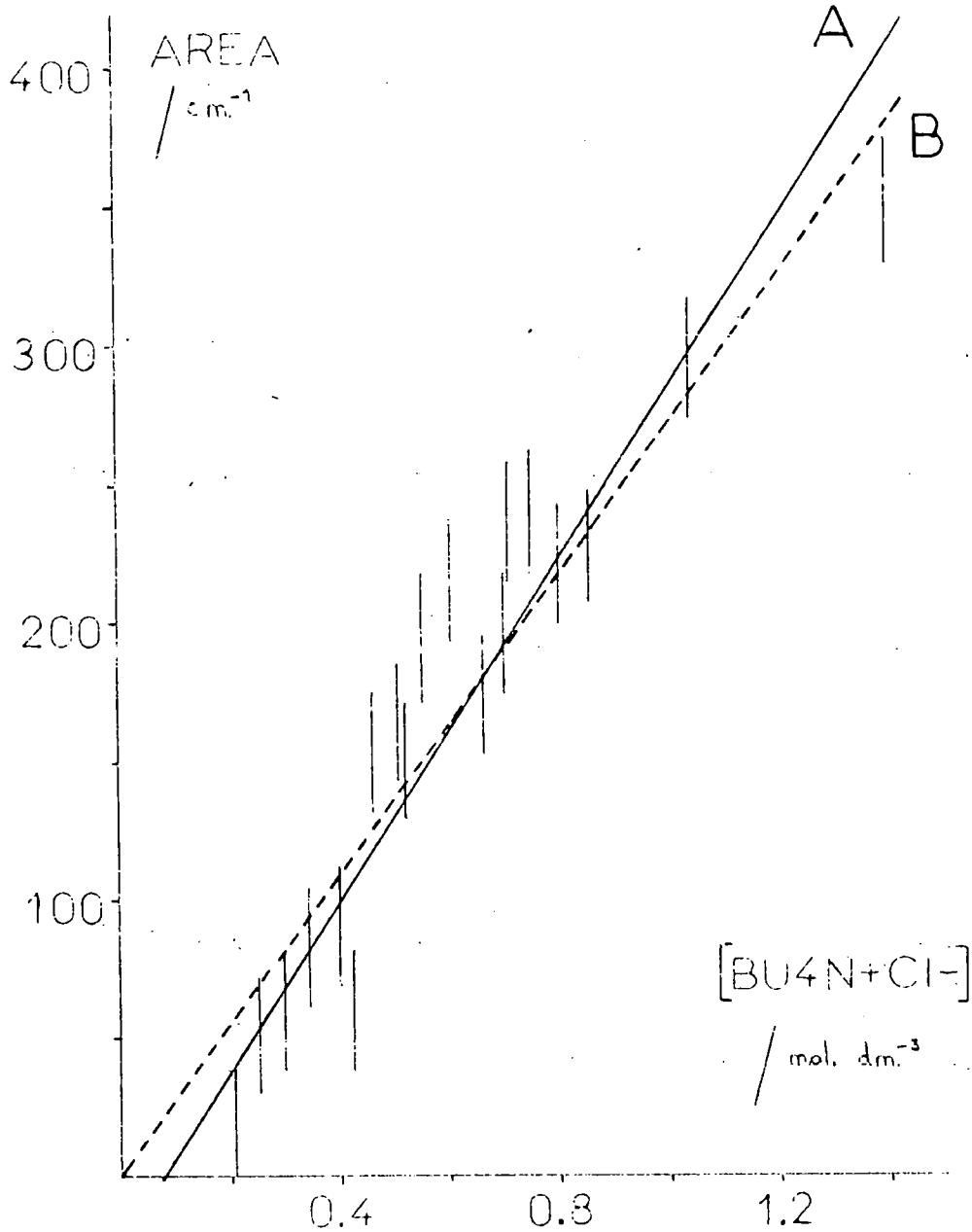

FIG 4.2 BU4N+Cl- IN BENZENE

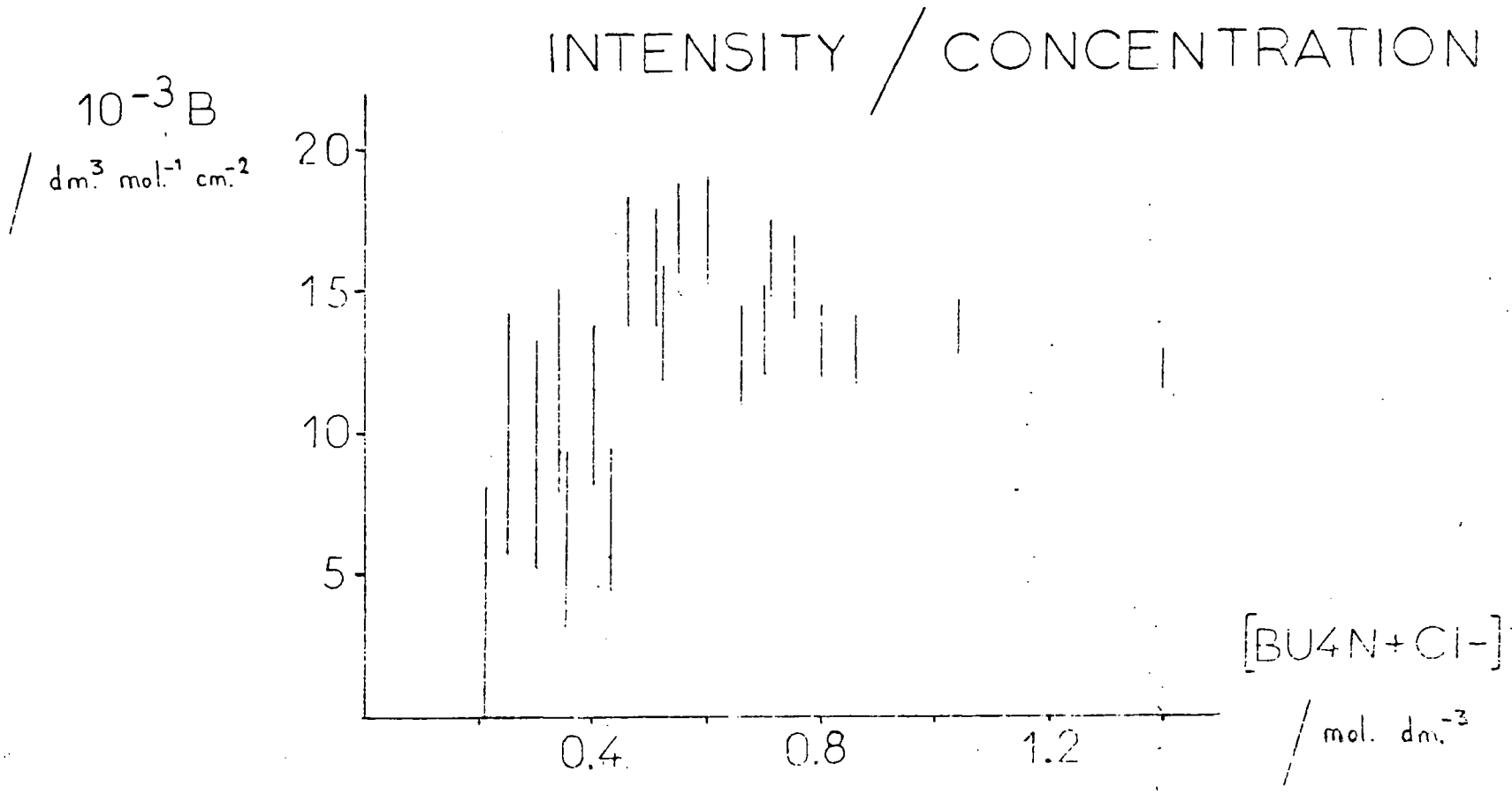

FIG 4.3 BU4N+Cl- IN BENZENE

concentration of $Bu_4N^+Cl^-$. Note that the intensity values for the 1.04 and 1.40 mol dm^{-3} concentrations were suspect because the area under the absorbance curve was too large for plotting using GPLOT3, and subsequent measurement with a planimeter. These intensities are labelled c in fig. 4.3 and table 4.2. Similarly the intensity of the 0.21 mol dm^{-3} concentration was suspect because the area was too small to be measured by the planimeter. This intensity is labelled b in fig. 4.3 and table 4.2.

Fig. 4.3 shows that the intensity gradually rises between 0.2 and 0.8 mol dm^{-3} and gives conclusive evidence that Beers Law does not hold over this concentration range for $Bu_4N^+Cl^-$ in benzene. The error bars were constructed assuming a constant precision for the measured area as discussed previously. The precision of the B_i values increased with concentration, since the B_i value was obtained by dividing the area by the concentration.

Spectra were also obtained for various concentrations of $Bu_4N^+Cl^-$ in benzene using 0.010, 0.0517, 0.1023 and 0.2053 cm pathlengths. The areas and intensities for the 115 cm^{-1} band were obtained as described previously, and are shown in table 4.3. The figures show a definite rise in the intensity with concentration, which is most marked in the low concentration range between 0.05 and 0.3 mol dm^{-3}. Fig. 4.4 shows the intensity values for all the $Bu_4N^+Cl^-$ concentrations run, at all pathlengths. The intensities for 0.21, 1.04 and 1.40 mol dm^{-3} concentrations have been omitted for the reasons previously given. Over the concentration range 0.05 to 1.20 mol dm^{-3} the 115 cm^{-1} band for $Bu_4N^+Cl^-$ in benzene was thus observed not to obey Beers Law. The intensity B_i changed from approximately 8 000 dm^3 mol^{-1} cm^{-2} at 0.05 mol dm^{-3} to approximately 20 000 dm^3 mol^{-1} cm^{-2} at 1.2 mol dm^{-3}.

The non-adherance to Beers Law, which would be expected to be valid if the absorbing species remained the same regardless of the concentration of the species in the solution, leads to some conclusions regarding the breaking-up of aggregates on dilution. In an ion aggregate each cation is presumably surrounded by a number of anions, and each anion by a number

Table 4.3 Intensity values for the 115 cm^{-1} band of $Bu_4N^+Cl^-$ in benzene using 0.01, 0.0517, 0.1023 and 0.2053 cm pathlengths

(T = 290K)

conc. /mol dm^{-3}	area /cm^{-1}	average area /cm^{-1}	intensity,B /dm^3 mol^{-1} cm^{-2}
0.010 cm pathlength			
1.02	256.6		
	234.6	245.6	24000±2150
1.20	260.8		
	227.6	244.2	20330±2150
0.0517 cm pathlength			
0.10	52.5	52.5	10310±4320
0.15	71.0	71.0	8970±2780
0.21	94.3	94.3	8880±2070
0.25	128.5	128.5	9870±1690
0.30	149.0	149.0	9610±1430
0.34	206.6	206.6	11617±1240
0.1023 cm pathlength			
0.05	31.8		
	31.3	31.5	6410±4480
0.09	55.9		
	58.2	57.1	6160±2380
0.10	73.5	73.5	7290±2180
0.20	154.6		
	153.1	153.8	7520±1080
0.2053 cm pathlength			
0.05	120.0		
	116.5	118.2	12000±2230
0.09	154.7		
	145.1	149.9	8070±1180

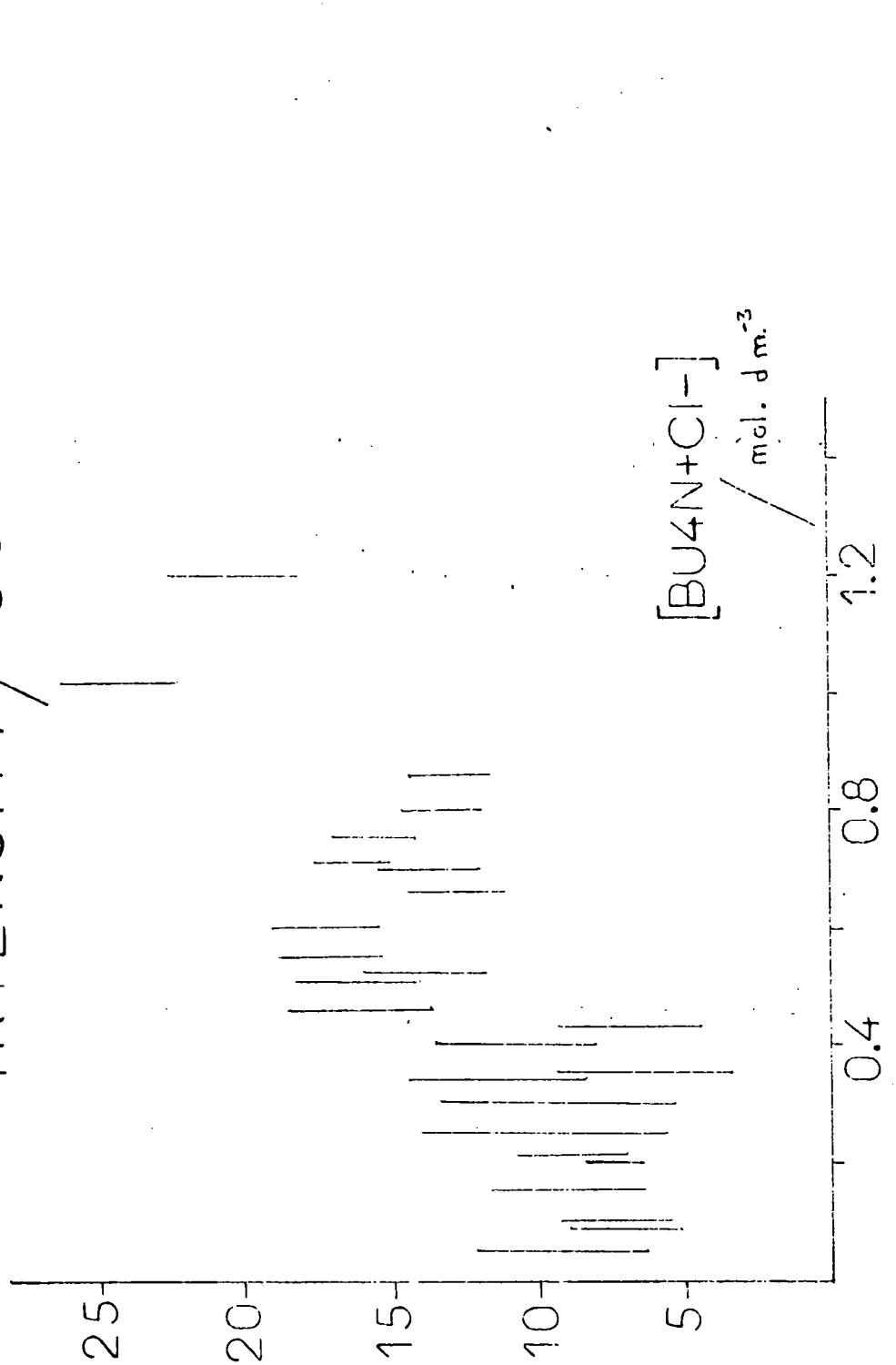

FIG. 4.4 BU4N+Cl- IN BENZENE

of cations. Thus if an absorption is due to vibration of ion pairs, then the total intensity for an aggregate will be the sum of the absolute intensities for all of the possible cation-anion vibrations. For a small aggregate there are fewer possible cation-anion vibrations, than for a large aggregate, and even though there are more such smaller aggregates present, the total intensity from all aggregates will be less than that from the original large aggregate. Consider 4 ion pairs in an aggregate arranged in the form of a cube (see fig.4.5). For the cube with an ion at every corner there are 12 cation-anion vibrations, represented by the edges of the cube. If this aggregate is then split into 2 then 2 ion quadrupoles exist arranged as squares. Each side of the squares represents a cation-anion vibration and so there are 4x2 = 8 such vibrations. If each of the ion quadrupoles then splits up, then 4 ion pairs are present, which have a total of only 4 cation-anion vibrations. Thus if an aggregate is breaking up on dilution, then the experimental intensity B_i would be expected to fall. This is exactly what was seen in practice for $Bu_4N^+Cl^-$ in benzene, and so it may be concluded that the size of the aggregate depends upon the concentration of the $Bu_4N^+Cl^-$ salt in the benzene solution.

If the dilution process is continued there will presumably come a time when only ion pairs are present in the solution, and when further dilution will have no effect on the intensity of the band, providing that the species giving rise to the absorption is a non-solvated ion pair. It is unfortunately impossible to study the 115 cm^{-1} band for $Bu_4N^+Cl^-$ in benzene at concentrations below 0.5 mol dm^{-3}, because of the long pathlengths which become necessary for the observation of the absorption. It should be noted here that the low-frequency 'collisional' absorption of the benzene solvent (see chapter 5) has been removed by ratioing against the same pathlength of pure benzene. The intensity for this 'collisional' band for pure benzene has been found to be approximately 43 dm^3 mol^{-1} cm^{-2} (see chapter 6), and hence for a pathlength of 0.2 cm the pure benzene absorption will have an

12 VIBRATIONS 8 VIBRATIONS 4 VIBRATIONS

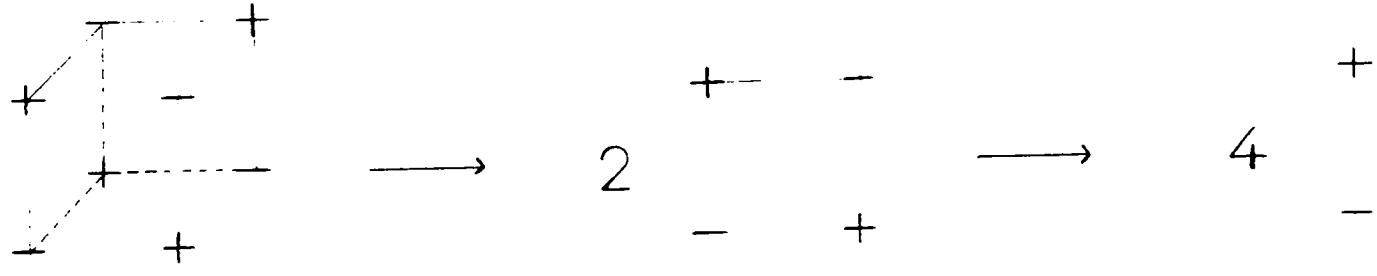

$1 \times 12 = 12$ $2 \times 4 = 8$ $4 \times 1 = 4$

FIG. 4.5 AGGREGATE SIZE AND NUMBER OF ION-PAIR VIBRATIONS

integrated area of 97 cm^{-1}, assuming the density of benzene to be 877 mol dm^{-3} (56). Taking an intensity B_i of 8 000 dm^3 mol^{-1} cm^{-2} for the aggregate band, which is reasonable according to fig. 4.4, an integrated area of 80 cm^{-1} was calculated for a 0.05 mol dm^{-3} solution of $Bu_4N^+Cl^-$ in benzene. Hence the band being ratioed out was more intense than the band under investigation, and very noisy spectra result. This was especially so to low frequency, where the interferometer optics were not optimised and there is subsequently very little energy, as discussed previously. Thus the lower concentration limit for investigation of the 115 cm^{-1} band for the system $Bu_4N^+Cl^-$ in benzene was 0.05 mol dm^{-3} when using the Golay cell for detection of the radiation. Use of a cooled germanium bolometer as a detector in conjunction with a polarising beam-divider should enable concentrations approaching those where only ion pairs exist to be examined. As an indication of the noise problem encountered for dilute solutions, when using a Golay detector, fig. 4.6 shows the spectrum of 0.048 mol dm^{-3} $Bu_4N^+Cl^-$ in benzene, obtained using a 0.3 cm polythene windowed demountable cell of 0.2053 cm pathlength and a 50 gauge beam-splitter. The resolution is again 2.6 cm^{-1}. The low frequency half of the spectrum was seen to be very noisy due to the ratioing out of the benzene collisional absorption.

4.2.2 Effect of water on the spectra

The large inaccuracies for the intensities of some of the $Bu_4N^+Cl^-$ in benzene solutions prompted a study of the effect of the presence of water in the solutions. Firstly a solution of 0.5 mol dm^{-3} $Bu_4N^+Cl^-$ in benzene was made up and immediately split into two portions. 4 spectra were recorded for one of the solutions, and the second solution was kept over molecular sieves for 2 days, before 4 spectra were likewise recorded. The average for 'computer' and 'planimeter' areas was determined for each spectrum, and then an average over the 4 spectra calculated. For the solution kept over molecular sieves the integrated area was 138.6 cm^{-1}, and for the solution recorded immediately this was 135.7 cm^{-1}. The areas were

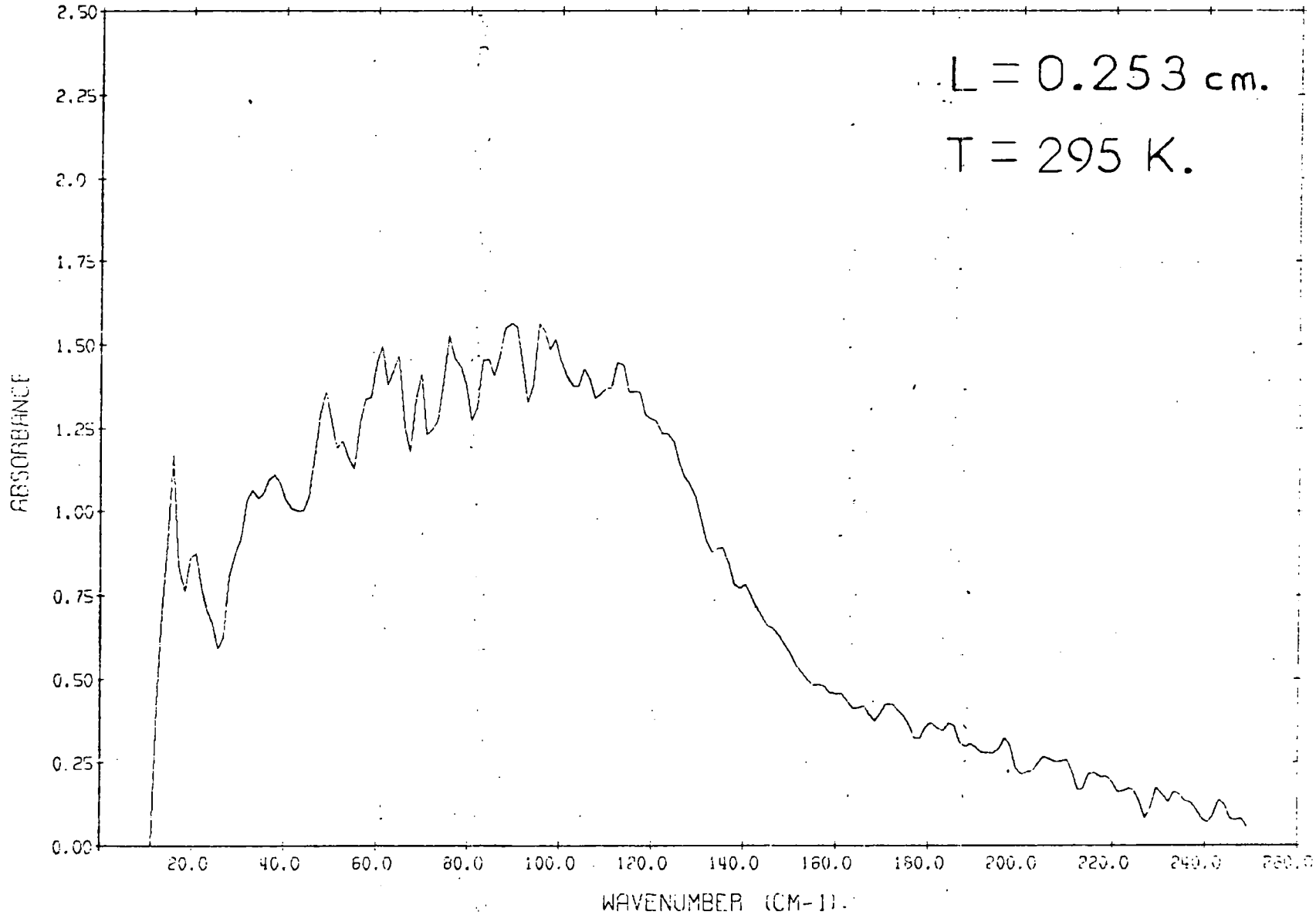

FIG. 4.6 0.048 mol. $dm.^{-3}$ BU4N+Cl- IN BENZENE

not significantly different, in the light of the precision of the measurements being ±22 cm^{-1}, and thus it was concluded that there was no water in the solutions, which could be removed by the use of molecular sieves. However, it is possible that the molecular sieves would not remove tightly bound water, which would still affect the absorption characteristics of the solution.

As the $Bu_4N^+Cl^-$ salt is deliquescent, and no special precautions were made to exclude water when the solutions were made up, apart from the making up of the solutions as quickly as possible, then it is probable that all the solutions contained a small amount of water. Karl-Fischer titrations were used to monitor water concentrations in the solutions, and the amount of water was found to be only 0.1 to 0.2% by weight. The Karl-Fischer titrations were extremely difficult to perform, presumably because the solutions were very viscous and had low conductivities, thus making the electrochemical end-point very difficult to detect.

Further tests were made to discover the effect on the 115 cm^{-1} band, by adding small quantities of water to a solution of 0.8 mol dm^{-3} $Bu_4N^+Cl^-$ in benzene, and then recording the spectra. Distilled water was added from a micro-syringe, and so the volume added was approximately known. The water content of these solutions was monitored by Karl-Fischer titrations, and the water content measured by this means was found to tie in well with the volume measured from the syringe. This tended to indicate that the Karl-Fischer method was giving fairly accurate values for the water content, and further suggested that very little water was so tightly bound that it was not detectable by a Karl-Fischer titration. Two spectra were recorded for each water concentration, using a 0.021 cm pathlength cell, and the resulting integrated areas for the 115 cm^{-1} band are shown in table 4.4. The area given is the average for 'computer' and 'planimeter' areas for the two spectra at the given concentration. These results are shown graphically in fig. 4.7, and illustrate that no significant intensity changes occurred

Table 4.4 Effect of water concentration on the area of the 115 cm^{-1} band for $Bu_4N^+Cl^-$ in benzene

(T = 290K, L = 0.021 cm)

volume added water /%	water content (Karl-Fischer) /%	band area /cm^{-1}
--	0.16	210
0.1	0.38	198
0.2	0.44	193
0.5	0.73	197
1.0	1.19	197

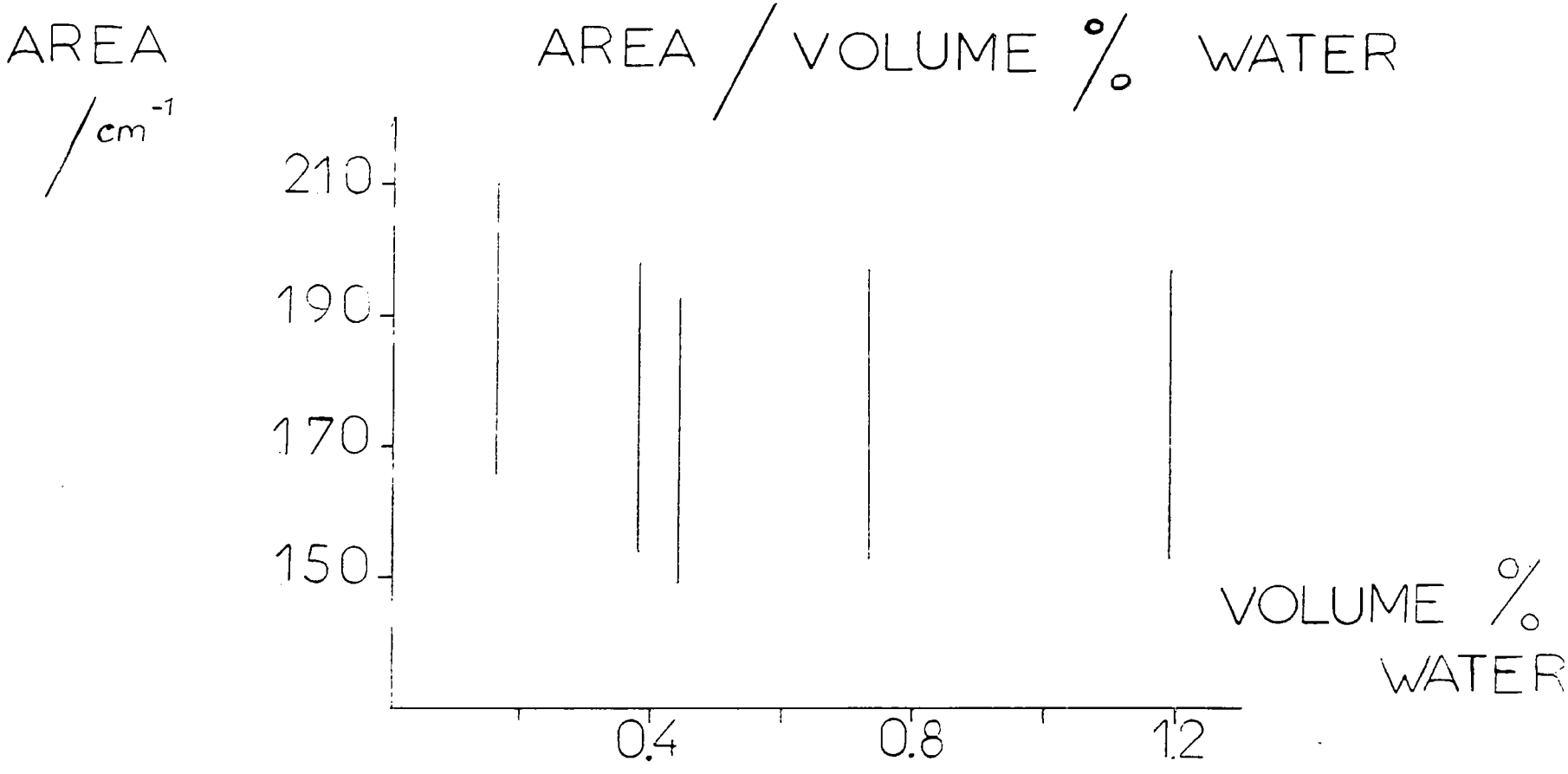

FIG. 4.7 BU4N+Cl− IN BENZENE / WATER

for the 115 cm^{-1} band, even when 1% of water was added. The only noticeable effect of the water on the spectrum in the 20 to 250 cm^{-1} region was the general increase in absorption over the whole frequency range, and the gradual rise in absorbance above 200 cm^{-1} as was observed for pure liquid water (see chapter 5). Addition of water to the solutions made little difference to the intensity of the 115 cm^{-1} band, and hence it was assumed that the small amounts of water absorbed in the salt as the solutions were made up had little effect on the spectra also.

As final proof some samples of the salt were dried by heating to about 353K, under vacuum to pump the water off. These attempts produced a fine white powder (similar in physical appearance to tetra-n-butylammonium perchlorate), which would not dissolve in benzene. It was thus concluded that the crystal structure or composition had been changed in the drying process. It is possible that small amounts of water have to be present in the salt before it will dissolve. However, the above studies have given an indication that small amounts of water contained in the salt have no effect on the intensity of the 115 cm^{-1} band.

4.2.3 Time dependence of the spectra

It was thought that some of the inaccuracies in the computed intensity values could have been due to the 115 cm^{-1} band showing a time dependence. A solution of 0.5 mol dm^{-3} $Bu_4N^+Cl^-$ in benzene was made up, and a sample quickly inserted into a 0.021 cm demountable cell with polythene windows. The instrument was quickly pumped down and interferograms were recorded continuously for a period of 5 hours. In this time 8 double-sided interferograms were recorded, each with 1024 points at an 8 μm path difference sampling interval. A pure benzene interferogram was then recorded, and used as a background for the computation of the 8 spectra. The resulting integrated areas for the 115 cm^{-1} band are shown in table 4.5, the time quoted being the mean time of recording for the corresponding interferogram. It can be easily seen that the absorption was constant from after 0.5 hours until 5

Table 4.5 Short-time dependence of the area of the 115 cm^{-1} band for $Bu_4N^+Cl^-$ in benzene

(T = 292K, L = 0.021)

time /hours	band area /cm^{-1}
0.66	152.6
1.33	147.6
1.99	146.8
2.66	148.9
3.33	154.9
3.99	138.2
4.66	143.5
5.33	152.2

hours after making up the solution.

The solution was then run once a day for 5 days, a benzene background being recorded for each spectrum, to determine if any changes in absorption occurred over a longer period. The areas obtained are shown in table 4.6, and since the precision of the measurements was only ±22 cm^{-1} then these areas indicate that the 115 cm^{-1} band shows no variation with time outside the precision of the measurements.

4.2.4 Effect of temperature on the spectra

The effect of temperature was studied using the Beckman-RIIC Ltd. variable temperature package as described in chapter 2. In this study the sample tapes were all recorded using one filling of the cell, and the temperature varied over the whole range of interest, starting at the lowest temperature and gradually increasing. The backgrounds were then recorded similarly. This procedure allowed matching of the sample and background temperatures to within approximately 1K, and since the changes in intensity produced by this temperature difference are smaller than those involved in measuring the integrated area, then this method of recording does not affect the results obtained.

A preliminary temperature study was made with 0.70 mol dm^{-3} $Bu_4N^+Cl^-$ in benzene at 293, 313 and 333K, using a 0.021 cm pathlength cell with polythene windows. The spectra showed very little change over this temperature range, as can be seen from table 4.7. The 0.70 mol dm^{-3} solution was also cooled to 253K and the spectrum of the frozen solution recorded. The intensity for the frozen solution band was slightly larger than that for the liquid solution, but the band was now much sharper. The half-band width for the liquid was 66 cm^{-1} and for the frozen solution was 32 cm^{-1} (see section 4.2.5 for a discussion of the solid solution spectra).

A more comprehensive study of the effect of temperature was undertaken using 0.252 mol dm^{-3} $Bu_4N^+Cl^-$ in benzene in a 0.021 cm pathlength cell. The study was conducted from just above the melting point of the

Table 4.6 Long-time dependence for the area of the 115 cm^{-1} band for $Bu_4N^+Cl^-$ in benzene

(T = 292K, L = 0.021 cm)

time /hours	band area /cm^{-1}
24	138.2
48	143.4
72	130.6
96	160.4
120	148.7

Table 4.7 Preliminary values for the effect of temperature on the intensity of the 115 cm^{-1} band for $Bu_4N^+Cl^-$ in benzene

(L = 0.021 cm, c = 0.252 mol dm^{-3})

temperature /K	band area / cm^{-1}	band intensity / $dm^3\ mol^{-1}\ cm^{-2}$	half-band width / cm^{-1}
293	100.1	7150	60
313	95.8	6850	64
333	97.2	6900	66
253	109.0	7800	32

solution at 279K to just below the boiling point at 349K. Fig. 4.8 shows typical spectra for 0.252 mol dm^{-3} $Bu_4N^+Cl^-$ in benzene at 294, 318, 334 and 349K, using a 0.021 cm pathlength. The resolution in these spectra was the usual 2.6 cm^{-1}. The results of this temperature study are shown in table 4.8 and graphically in fig. 4.9. These results showed that the intensity began to rise fairly steeply as the boiling point of the solution was approached.

If the absorbing species was beginning to break up with increasing temperature, as would be expected from the more rapid movements within the aggregate lattice, then the intensity would be expected to decrease in a similar fashion to that observed upon dilution. However this effect could possibly be masked by a second effect. When the temperature was increased the amplitude of vibration giving rise to the absorption would be expected to increase, and hence the change in dipole moment occurring during the vibration would increase. The intensity of an absorption is proportional to the square of the dipole moment change with respect to the normal coordinate for the associated vibration, and hence the intensity would be expected to increase with increasing temperature. The invariance of intensity with temperature between 279 and 328K could indicate that the dilution effect was decreasing the number of absorbing species, but that this decrease was being balanced by an increase in the vibrational amplitude for the vibrations within each absorbing species. Above 328K the increase in vibrational amplitude presumably became the dominant factor.

4.2.5 Solid solution spectra

It can be seen from fig. 4.1 that the 115 cm^{-1} band was asymmetric to low frequency. If the band was split into low- and high-frequency halves about the band centre, then the high frequency half had a semi-half-band width of about 30 cm^{-1}, and the low frequency half had a semi-half-band width of about 50 cm^{-1}. In order to investigate the possibility of there being two bands in this region it was decided to cool the solution, hoping

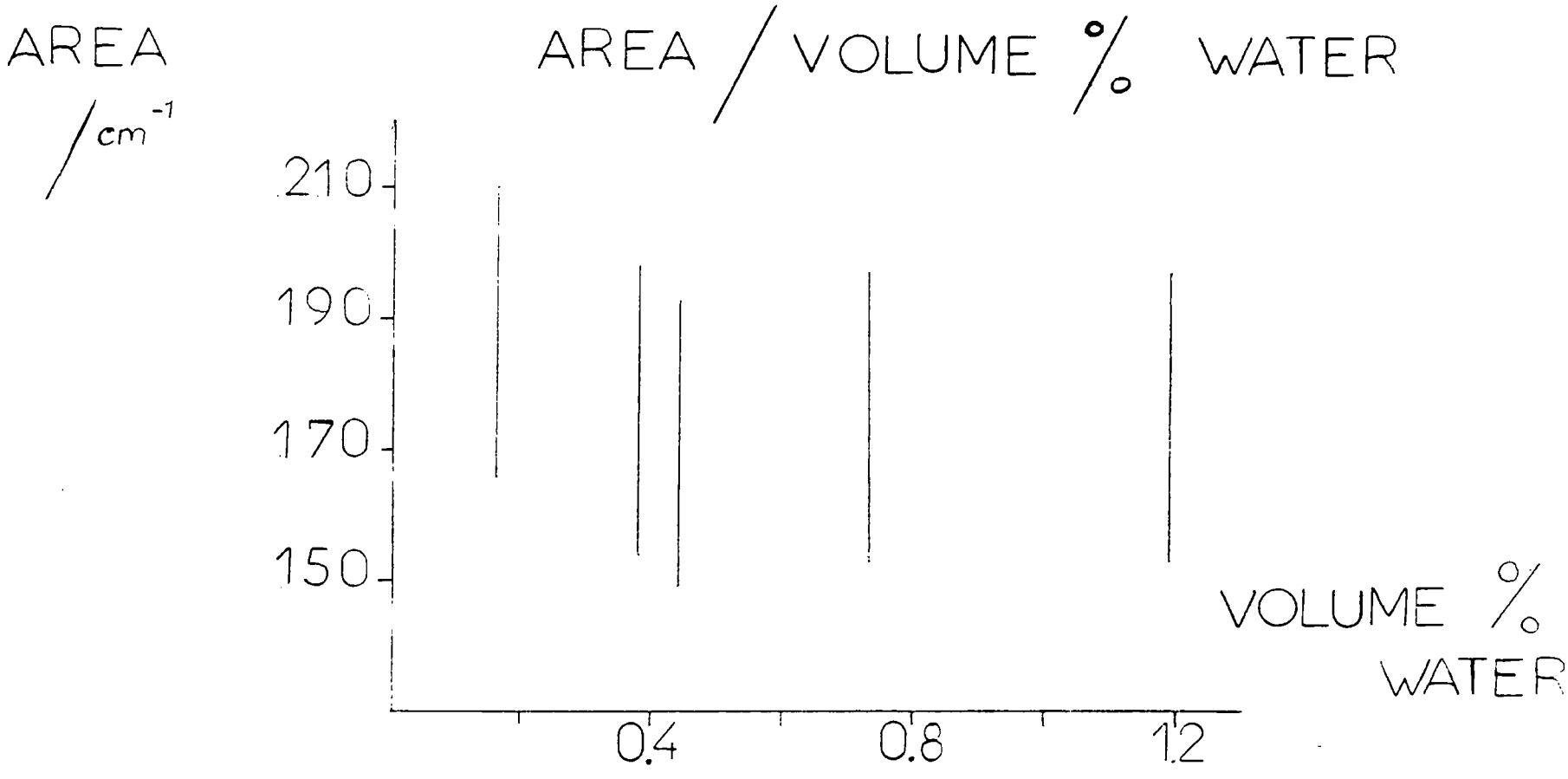

FIG. 4.7 BU4N+Cl− IN BENZENE / WATER

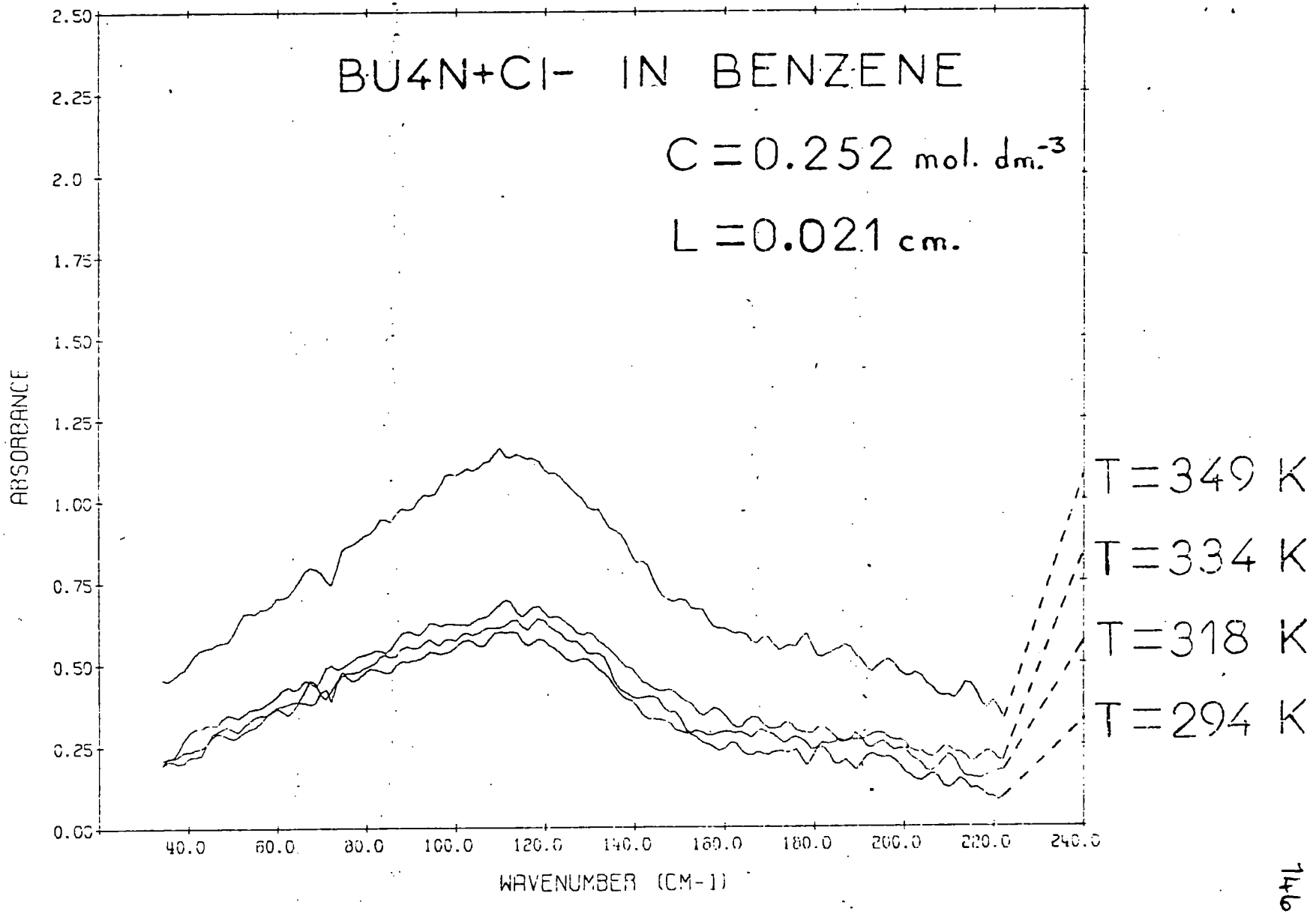

FIG. 4.8 EFFECT OF TEMPERATURE

Table 4.8 Effect of temperature on the intensity of the 115 cm^{-1} band for $Bu_4N^+Cl^-$ in benzene

(concentration = 0.252 mol dm^{-3}, L = 0.021 cm)

temperature /K	area[a] /cm^{-1}	intensity[b] /dm^3 mol^{-1} cm^{-2}
279	47.2	8 920
285	44.3	8 370
289	48.6	9 180
294	43.0	8 130
299	46.2	8 730
304	48.6	9 180
309	42.8	8 090
314	52.4	9 830
318	47.5	8 980
323	49.8	9 410
328	47.8	9 030
334	54.2	10 240
339	55.3	10 450
344	64.7	12 660
349	90.8	17 160

[a] ±22 cm^{-1}

[b] ±4 120 dm^3 mol^{-1} cm^{-2}

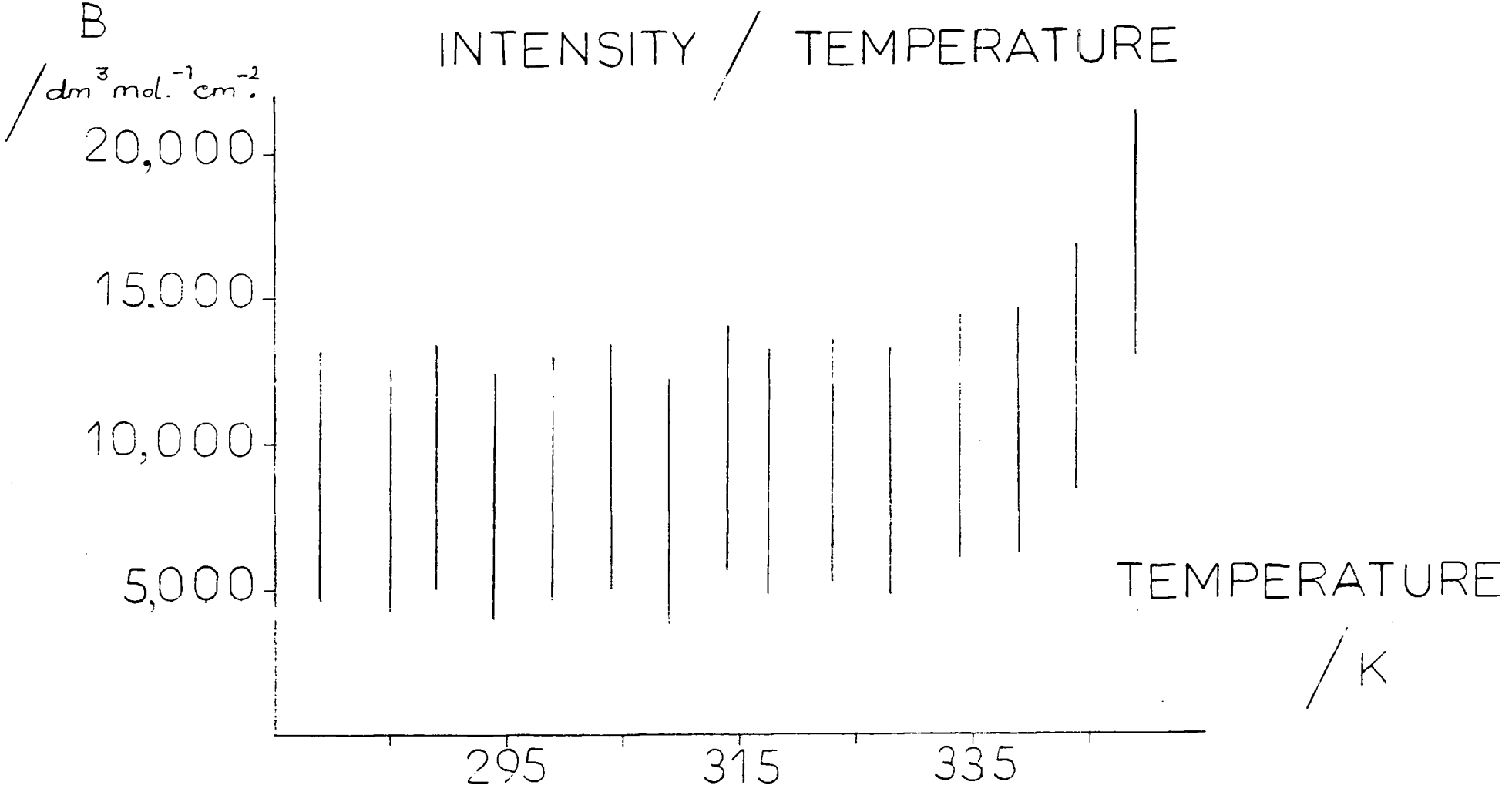

FIG. 4.9 BU4N+CI- IN BENZENE

that the half-band widths would be reduced, and possibly cause the absorptions to be resolved.

Fig. 4.10 shows the spectrum for the frozen solution of 0.70 mol dm^{-3} $Bu_4N^+Cl^-$ in benzene at 253K and 0.021 cm pathlength. The spectrum was obtained using the variable temperature cell as described in chapter 2, acetone and solid carbon dioxide being used as coolant. 2048 point, double-sided interferograms were recorded with an 8 μm path difference sampling interval, giving a resolution of approximately 1.3 cm^{-1}. The increased resolution was used in a further attempt to resolve out a second band. The band centre could be seen to be at 120 cm^{-1}, which indicated that a slight shift to higher frequency occurred upon freezing. The asymmetry to low frequency could now be positively identified as a second band, although the bands were still not fully resolved. The half-band width of the 115 cm^{-1} band had decreased to about 27 cm^{-1} in the solid, from about 60 cm^{-1} in the liquid solution. This indicated that the amplitude of vibration of the mode giving rise to the absorption had been decreased by the freezing process, and that the movements of the absorbing species had been localised in the solid solution with respect to the liquid solution.

Five spectra were recorded for the 0.70 mo dm^{-3} solution at 253K, and the integrated areas for the whole absorption in the region 20 to 250 cm^{-1} were measured and the average found to be 49 cm^{-1}. This area gave an intensity B_i = 3 400±1 500 dm^3 mol^{-1} cm^{-2} if a precision of ±22 cm^{-1} was once again assumed on the area, and if it was further assumed that the frozen solution had the same pathlength as the liquid solutions. This intensity was considerably lower than the 13 580±1 510 dm^3 mol^{-1} cm^{-2} obtained for the 0.70 mol dm^{-3} solution at 293K, and this once again reflected the localisation of the absorbing species upon cooling. (See chapter 5 for attempts to resolve the two component bands by computer fitting methods.)

On computation of these spectra it was further noticed that a

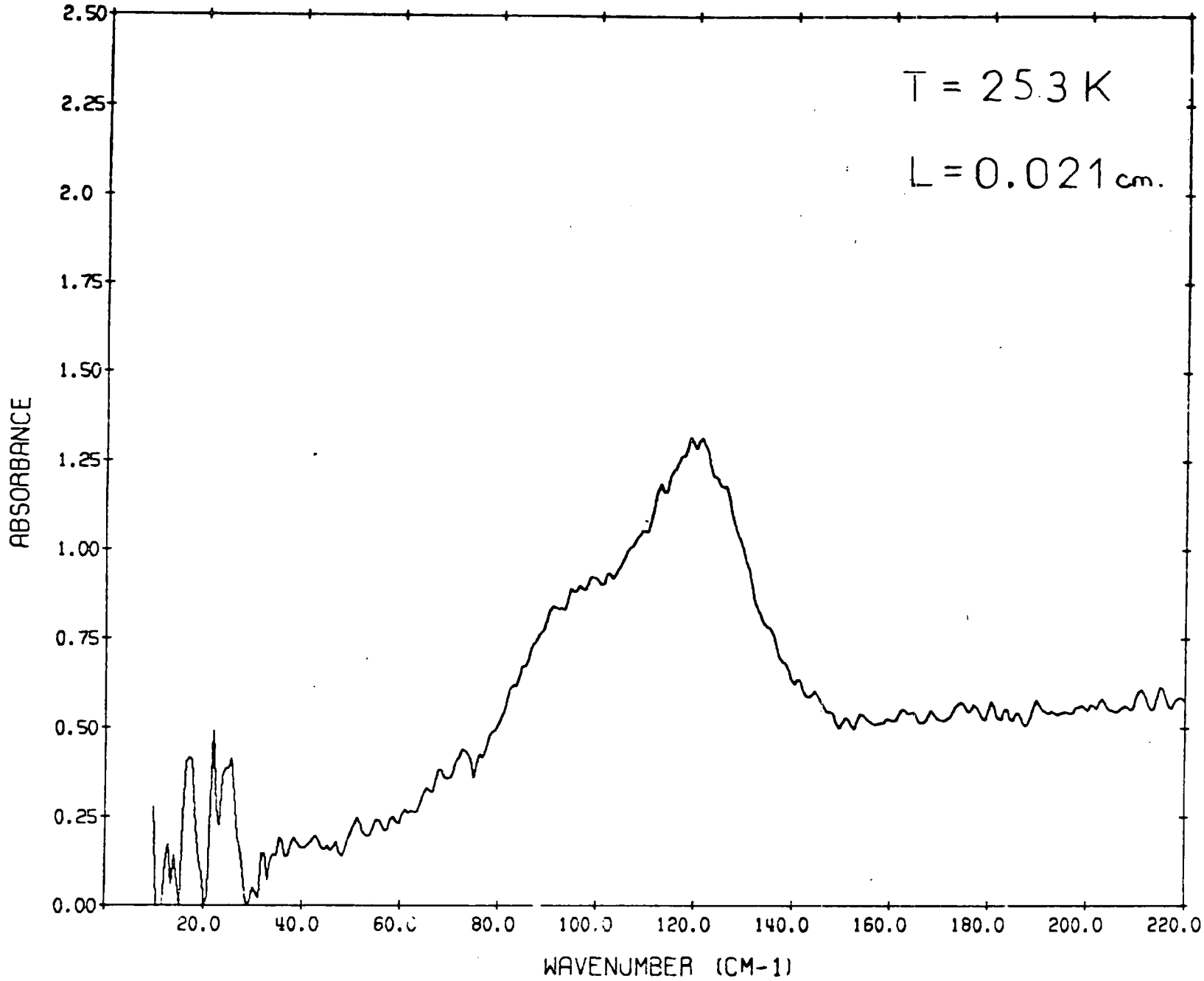

FIG. 4.10 0.70 mol. dm^{-3} $Bu_4N^+Cl^-$ IN BENZENE

doublet band arose at 403 and 416 cm^{-1} in the ratioed spectrum of the frozen solution. This doublet is shown in fig. 4.11 for 0.70 mol dm^{-3} $Bu_4N^+Cl^-$ in benzene at 253K, using a 0.021 cm pathlength cell. The resolution in the spectrum was 1.3 cm^{-1}. The spectrum was obtained by ratioing the solution spectrum against crystalline benzene contained in the same cell. The spectrum of crystalline pure benzene was also recorded at 253K and this showed the doublet at 402 and 413 cm^{-1}, the resolution being 1.3 cm^{-1}. (See fig. 4.12). The spectrum was obtained by ratioing 0.2 cm of crystalline benzene against 0.1 cm of crystalline benzene. The area under the doublet was found to be 13.8 cm^{-1} as an average of 4 spectra, which gave an intensity of 12.3 dm^3 mol^{-1} cm^{-2} for the doublet. The intensity was calculated with respect to the benzene concentration. The benzene concentration was taken as 11.27 mol dm^{-3} calculated on the assumption that the density of benzene remains at 877 g dm^{-3}, which is the density at 293K (56).

This doublet has been observed at 403 and 418 cm^{-1} in crystalline benzene by Hollenberg and Dows who assigned the doublet to the $\nu_{20}(e_{2u})$ benzene vibration, the splitting being due to the lifting of the degeneracy in the crystalline material (57,58). The numbering of the assignments for the D_{6h} benzene molecule follows that of Herzberg (ref. 59, pps. 118, 364 and 365). The ν_{20} band was only observed in crystalline benzene, and not in glassy benzene nor in the liquid, where it is apparently too weak to be observed. The band is formally forbidden in the infrared for the isolated molecule (ref. 59, p. 364), but is allowed by the site symmetry of the crystal.

The intensity of the doublet in the 0.70 mol dm^{-3} $Bu_4N^+Cl^-$ in benzene solution was calculated to be 8.9 dm^3 mol^{-1} cm^{-2} with respect to the benzene concentration, from an area of 2 cm^{-1}. (This assumed that the benzene concentration was the same in the solution as in pure benzene). The measured intensity of the doublet in the ratioed solution spectrum was the increase in intensity of this band relative to that in pure crystalline

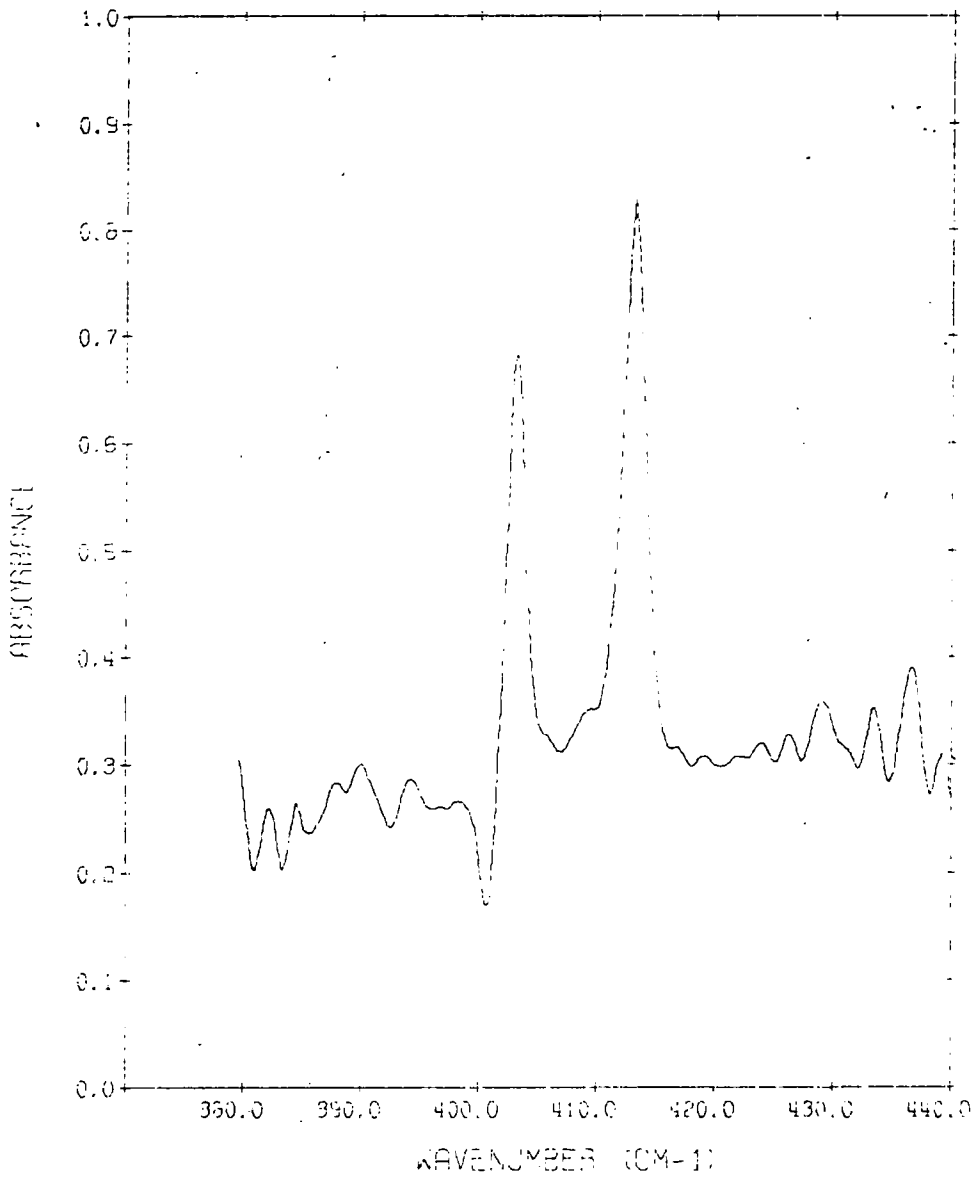

FIG. 4.11 0.75 mol. dm.$^{-3}$ BU4N+Cl- IN BENZENE

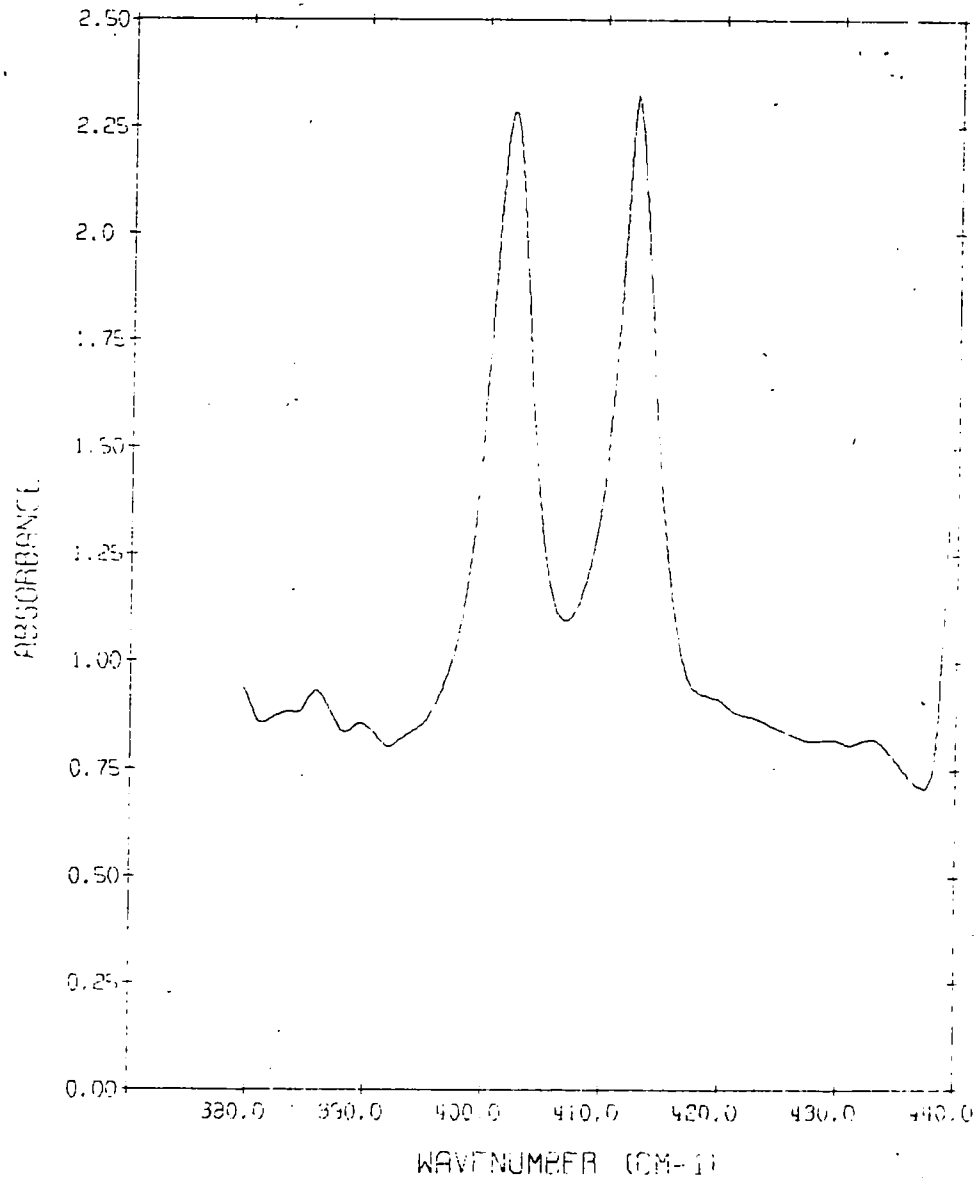

L = 0.100 cm

T = 253 K

FIG. 4.12 PURE CRYSTALLINE BENZENE

benzene. This increase in intensity was thus 73%, which indicated a severe perturbation of this benzene mode in the crystalline solution, due to the presence of the dissolved $Bu_4N^+Cl^-$. The position of the doublet was not significantly altered by the addition of the dissolved salt. The small derivative feature occurring to the low frequency side of the 402 cm^{-1} band in fig. 4.11 showed that the band may be shifted to slightly higher frequency in the crystalline solution, relative to the pure crystalline benzene, but the magnitude of the shift was very small. The splitting pattern of this band was not altered,and hence the nature and symmetry of the benzene crystal was not being drastically altered by the added salt in the crystalline solution. The intensity perturbation is an electronic effect caused by changes in the transition moment for the vibration (see chapter 7 for discussion).

The intensity of the doublet was found to be very sensitive as to the mode of preparation of the crystalline sample at the required temperature. The intensity of the doublet in the 'crash cooled' crystalline sample was much less than that for a crystalline sample, where the temperature had been decreased slowly. Consequently all the solid solutions were cooled slowly in an effort to ensure consistent sample crystallinity. The effects on the far-infrared lattice spectrum produced by differing methods of sample preparation have previously been observed by Harada and Shimanouchi for crystalline benzene (60). The slow cooling was achieved by careful use of the Beckman-RIIC Ltd. temperature controller unit. The cell was filled with solution at room temperature,and then placed in the mounting block, and the interferometer evacuated. The reservoir was then partially filled with acetone. Small pieces of solid carbon dioxide were then added to cool the cell down, the temperature being monitored continually, and the amount of solid carbon dioxide added being sufficient to decrease the temperature of the cell by about 1K per minute. The temperature control unit was set to 253K and the heating coils were switched on when the temperature reached

254K. Solid carbon dioxide was then added to bring the temperature down to 253K, the amount added being increased to ensure that solid carbon dioxide was present when the required temperature of 253K was reached. The whole cooling procedure took about 1 hour for each sample.

This difficulty with non-uniformity of the samples precluded the study of the effect of the $Bu_4N^+Cl^-$ salt concentration in the solid benzene solutions on the intensity of the ν_{20} doublet, since the doublet intensities were so small. Such a study could have helped in discovering the method by which the salt perturbs the intensity of the doublet, and could have indicated the mode of interaction of the salt with the benzene solvent in the crystalline sample.

4.2.6 Studies of benzene internal modes

The discovery of the perturbation of the ν_{20} internal benzene mode by the presence of dissolved $Bu_4N^+Cl^-$ in the crystalline solution prompted a study of the other internal modes, in both liquid and solid $Bu_4N^+Cl^-$ in benzene solutions. The spectra were recorded using a Grubb Parsons Ltd. GS2A infrared grating spectrometer. A spectrum for 51 μm of pure benzene at 293K was recorded over the 3 ranges of the instrument, which is calibrated in μm, 5 μm to 20 μm (2000 to 500 cm^{-1}), 3.5 to 5 μm (2856 to 2000 cm^{-1}) and 2.5 to 3.5 μm (4000 to 2856 cm^{-1}). Potassium bromide windows were used as they gave reasonable transmission over the whole frequency range. The spectrum for 0.70 mol dm^{-3} $Bu_4N^+Cl^-$ in benzene in the same 51 μm cell was also recorded on the same chart paper. The spectra were superimposable to within 1% transmission over the whole frequency range, and as the precision obtained for duplicate runs with the pure benzene background was also about 1%, then it was concluded that no significant perturbation of any benzene internal modes occurred for $Bu_4N^+Cl^-$ in benzene at a concentration of 0.70 mol dm^{-3}. The spectra for both solvent and solution were also recorded using 1.20 mol dm^{-3} $Bu_4N^+Cl^-$ in benzene in a 64 μm pathlength cell at 293K, in the hope that the increased concentration

would make any perturbation observeable. The spectra were once again superimposable, in this case to within 0.5% transmission.

Spectra of 64 μm of 0.86 mol dm^{-3} crystalline $Bu_4N^+Cl^-$ in benzene and the same pathlength of crystalline benzene were recorded at 253 and 223K to determine if any other benzene internal modes, apart from the 404 cm^{-1} ν_{20} band were perturbed in the crystalline solution. The cooling process was carried out very slowly in order to avoid non-uniformity of sample problems, as described in the work on the 404 cm^{-1} doublet. Slow cooling was especially important for this study, since the only useable transmitting windows in this region were brittle, and would not have withstood thermal shock easily. Silver chloride windows were used in preference to potassium bromide, since the former are more resistant to thermal shocks (61). These AgCl plates were also fairly malleable, and could be worked at low temperatures, which helped them withstand the mechanical shock of the samples freezing. The spectra for the crystalline benzene and the crystalline solution were traced from the chart paper and superimposed, and are shown in fig. 4.13, where the solution spectra are represented by the dotted lines and the solvent spectra by the solid lines. It can be seen that very little change in either frequency or intensity occurred in going to the solution. Hollenberg and Dows (58), Yamada and Person (62) and Szczepaniak and Person (63) have observed the infrared spectrum of crystalline benzene. Szczepaniak and Person also observed the spectrum of a crystalline benzene/HCl complex (63). Very little change was observed in the infrared spectrum even for a HCl:benzene ratio of 13:1, but the changes observed enabled deductions to be made regarding the interaction of the HCl with the benzene. It was hoped that this exercise could be repeated for the crystalline $Bu_4N^+Cl^-$ in benzene solution.

Table 4.9 shows the observed frequencies and approximate strengths for the infrared absorptions for the crystalline benzene, and the crystalline 0.86 mol dm^{-3} $Bu_4N^+Cl^-$ in benzene solution at 253K. The literature values

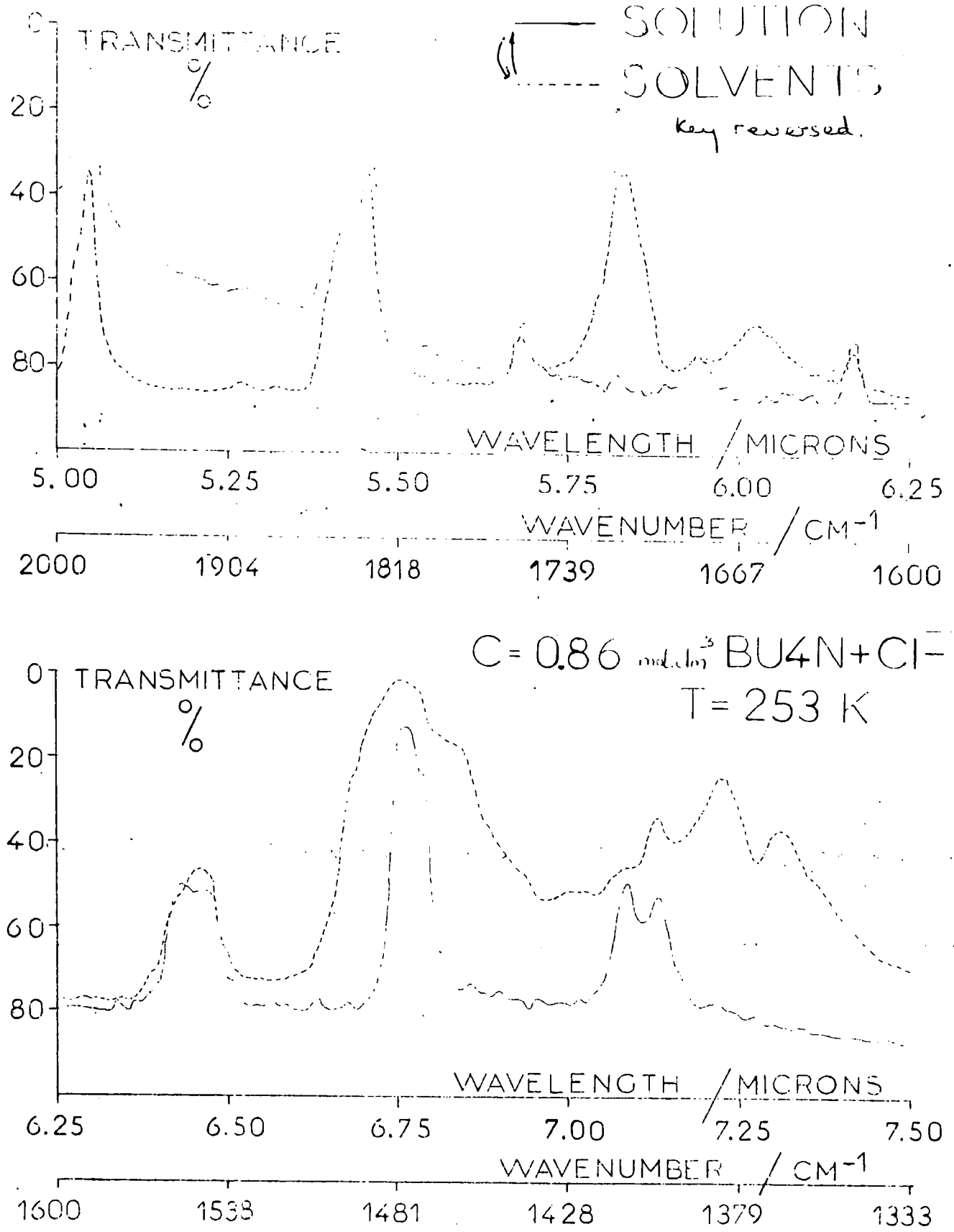

FIG.4.13a MID-INFRARED SPECTRA FOR CRYSTALLINE BENZENE/$BU_4N^+Cl^-$ IN BENZENE

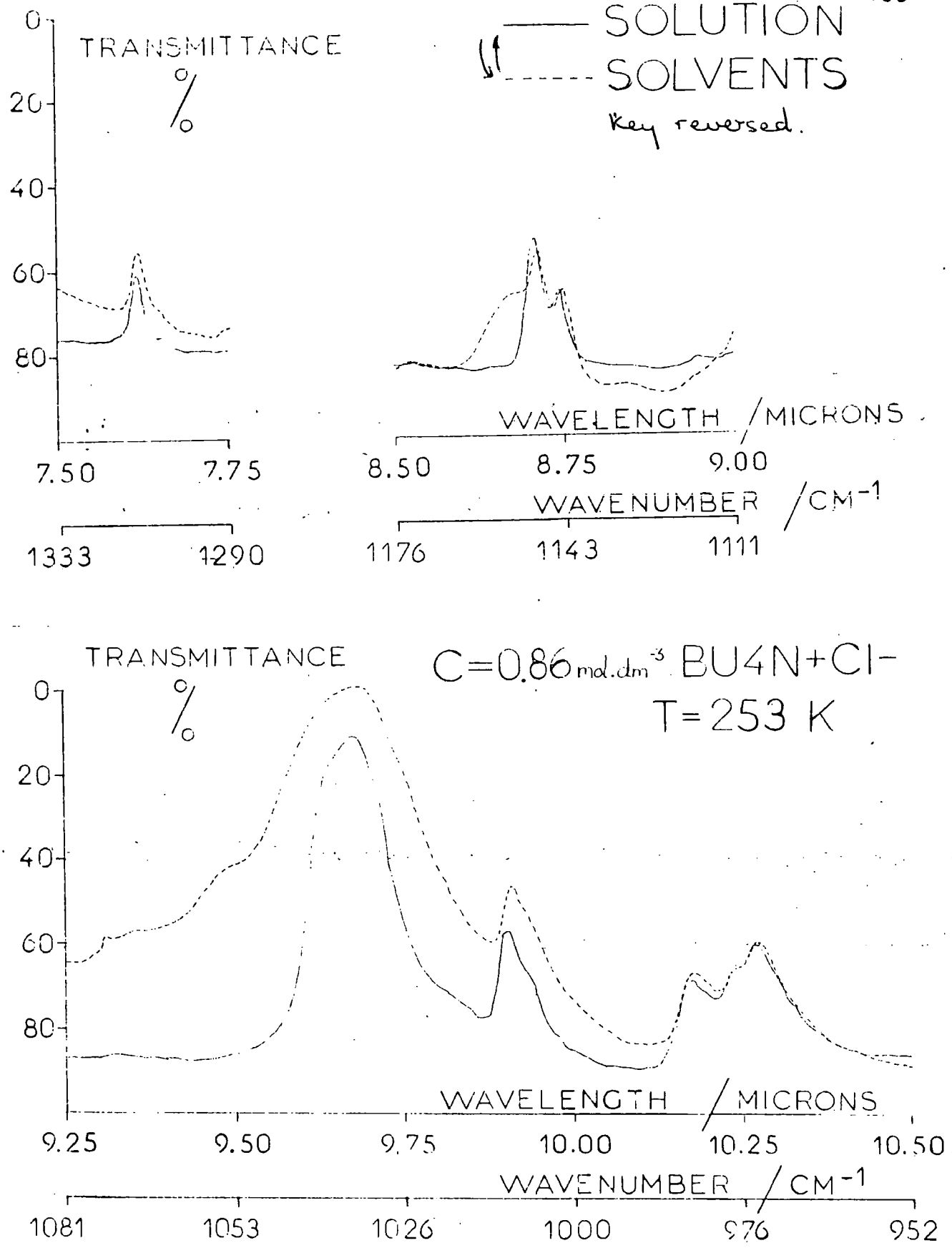

FIG. 4.13b MID-INFRARED SPECTRA FOR CRYSTALLINE BENZENE/ $BU_4N^+Cl^-$ IN BENZENE

Table 4.9 Infrared absorptions for a 0.86 mol dm^{-3} crystalline solution of $Bu_4N^+Cl^-$ in benzene at 253K

crystalline benzene		crys. soln.	assignment	assignment	symmetry	comments
this work /cm^{-1}	literature[a] /cm^{-1}	this work /cm^{-1}	Wilson[b]	Herzberg[c]		
1985(sh)		1988(sh)				
1980(s)	1979,1972	1983(s)	$\nu_{17}+\nu_5$	$\nu_{19}+\nu_7$	E_{1u}	no change
1852(sh)	1850(sh)	1850(sh)				
1838(s)	1835	1841(s)	$\nu_{10}+\nu_{17}$	$\nu_{19}+\nu_{11}$	E_{1u}	no change
1832(s)	1828	1831(s)				
1757(w)		1747(w)				
		1715(s)	$(n\text{-}Bu_4N^+)$			
1683(w)	1693	1683(w)		$2\nu_{11}$	A_{1g},E_{2g}	Raman active band
		1658(m)	$(n\text{-}Bu_4N^+)$			
1619(sh)	1615	1620(w)	$\nu_{12}+\nu_6$	$\nu_6+\nu_{18}$	E_{1u}	degeneracy removed
1615(w)	1613					
1558(m)	1555	1558(mw)				
1548(m)		1546(m)	$\nu_{11}+\nu_{10}$	$\nu_4+\nu_{15}$	E_{1u}	very little change
1542(sh)	1542					
1536(sh)	1538	1538(sh)				

Table 4.9 (continued)

crystalline benzene		cry.soln.	assignment	assignment	symmetry	comments
this work /cm^{-1}	literature[a] /cm^{-1}	this work /cm^{-1}	Wilson[b]	Herzberg[c]		
1479(s)	1477,1475	1481(s)	ν_{19}	ν_{13}	e_{1u}	very much broader
1472(sh)	1467	1472(sh)	ν_{19}	ν_{13}	e_{1u}	
		1462(sh)				
1410(m)	1412	1410(sh)	$\nu_{16}+\nu_5$	$\nu_{20}+\nu_7$	E_{1u}	1410 cm^{-1} band
1402(m)	1400	1402(m)				less intense
		1383(m)	$(n\text{-}Bu_4N^+)$			
		1372(m)				
1314(m)	1310	1314(m)	ν_{14}	ν_9	b_{2u}	
1306(sh)		1304(sh)				
1259(w)		1259(w)	$\nu_{16}+\nu_{10}$	$\nu_{20}+\nu_{15}$	E_{1u}	
1248(w)	1248	1249(w)				
		1155(sh)	ν_{15}	ν_{10}	b_{2u}	
1148	1146	1149(m)				
1144	1140	1144(m)				

Table 4.9 (continued)

crystalline benzene		crys. soln.	assignment	assignment	symmetry	comments
this work /cm^{-1}	literature[a] /cm^{-1}	this work /cm^{-1}	Wilson[b]	Herzberg[c]		
1038(sh)	1037					
1033(s)	1031	1033(s)	ν_{20}	ν_{14}	e_{1u}	broadened
1009(m)		1010(m)				
1006(sh)	1007	1008(sh)	ν_{12}	ν_{6}	b_{1u}	
983(m)	986	982(m)				
977(sh)	976	977(sh)	ν_{17}	ν_{19}	e_{1u}	
974(m)	973	974(m)				

[a] K. Szczepaniak and W.B. Person; Spectrochim Acta 28A, 15 (1972)

[b] E.B. Wilson, Jr.; Phys. Rev. 45, 706 (1934)

[c] G. Herzberg, ref. 43 p. 364

s - strong w - weak sh - shoulder m - medium vw - very weak

for crystalline benzene at liquid nitrogen temperature (77K) were taken from Szczepaniak and Person (63). The numbering of the assignments was according to Wilson (64), and the assignments according to Herzberg (59) are shown in parenthesis, and are used in the following discussion.

Of the 10 ungerade modes of benzene (ref. 59, p. 363) only the one a_{2u} and the three e_{1u} modes are allowed in the infrared spectrum of the gaseous phase. However in the crystal the selection rules are relaxed due to the C_i symmetry, and all the ungerade modes are allowed. The 10 gerade modes are not allowed in the infrared spectrum of the gas phase molecule, and were not observed in crystalline benzene. The appearance of these gerade modes for the Szczepaniak and Person HCl/benzene complex was attributed to a loss of order in the environment surrounding each benzene site, which caused a relaxation of the selection rules. The solid complex was, however, less perturbed from the crystalline benzene than was the liquid benzene where there were no selection rules for the free molecules. No such appearance of gerade bands was noticed on going from the crystalline benzene to crystalline $Bu_4N^+Cl^-$ solution, and so the environment of the benzene crystal was assumed to be changed very little with dissolution of the $Bu_4N^+Cl^-$ salt. This conclusion was hardly surprising in the light of the approximately 13-fold excess of benzene over dissolved salt in the 0.86 mol dm^{-3} solution.

The small changes in intensity and splitting of the bands has been used to determine the mode of interaction of the added salt with the benzene. The intensity of the 1410 cm^{-1} band of the $\nu_{20}+\nu_7$ doublet was decreased in the solid solution, indicating that the site symmetry was possibly decreased and the degeneracy of the mode once again being imposed. The 1410 cm^{-1} component was still present because there was a large excess of benzene, not all of which was influenced by the added salt. The 1558 cm^{-1} band was weaker in the solution than in the crystalline benzene, indicating that the splitting of the degenerate bands was being reduced because of the

changes in site symmetry at the benzene crystal.

The ν_{10} band was a doublet in both the crystalline solvent and solution, indicating that the interaction of the $Bu_4N^+Cl^-$ with the benzene was much less than that of the HCl with the benzene in the Szczepaniak and Person HCl/benzene matrix, where splitting of the ν_{10} benzene mode was not observed. The 1479 cm^{-1} ν_{13} mode was broadened in the solution, as was the 1033 cm^{-1} ν_{14} mode. The presence of the dissolved salt in the solid solution was seen to be making possible a more rapid vibrational relaxation of these modes, by some sort of specific interaction with the atoms.

The ν_{20}, ν_7, ν_4, ν_{13} and ν_{14} modes, which were perturbed in the crystalline solution, are shown in fig. 4.14. The ν_{20} mode is a C-C-C perpendicular bending mode and the ν_7 and ν_4 modes are C-H perpendicular bending modes. It thus appeared that the salt was interacting with the benzene in such a way that only the intensity and degeneracy of the 'out-of-plane' modes of the molecule are affected. The ν_{13} mode is a C-H parallel bending mode and the ν_{14} band is a C-C stretching mode, and it is these 'in-plane' modes that are broadened in the crystalline solutions. A discussion of the form of the interaction of the dissolved salt with the benzene solvent is given in chapter 7.

4.3 Tetra-n-butylammonium bromide in benzene

The effect of change of the anion on the low frequency absorption was determined by a study of tetra-n-butylammonium bromide ($Bu_4N^+Br^-$) in benzene. This salt was found to show a maximum at about 80 cm^{-1}, and hence a 100 gauge beam-splitter was used to obtain the spectra. No additional filtering was employed to optimise energy in the first beam-splitter hoop below 120 cm^{-1}. Use of a 0.1 cm crystalline quartz filter resulted in very high gains and subsequently noisy spectra. (See section 2.14). Fig. 4.15 shows the spectrum of 0.44 mol dm^{-3} $Bu_4N^+Br^-$ in benzene at 290K in a polythene windowed cell of 0.052 cm pathlength. It can be seen that use of the 100 gauge beam-splitter enabled good signal-to-noise ratios to be

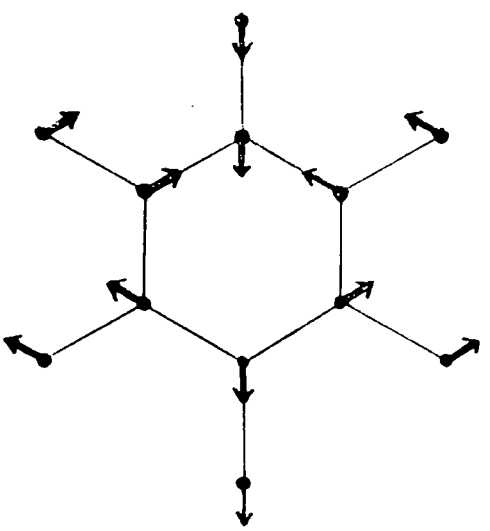

ν_{13}

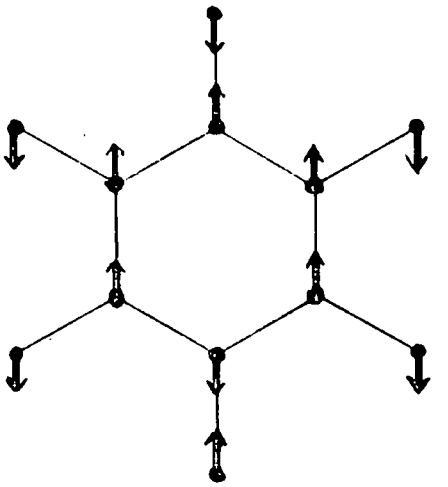

ν_{14}

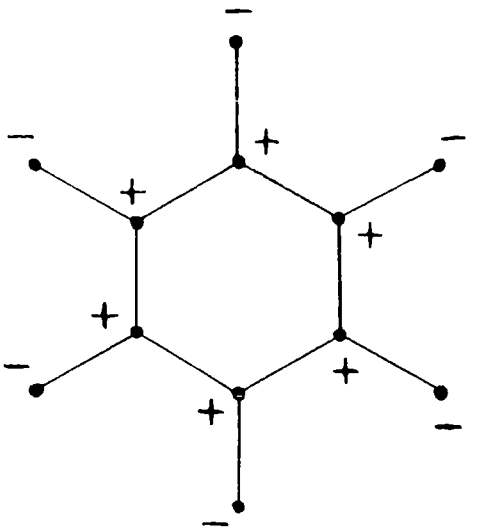

ν_4

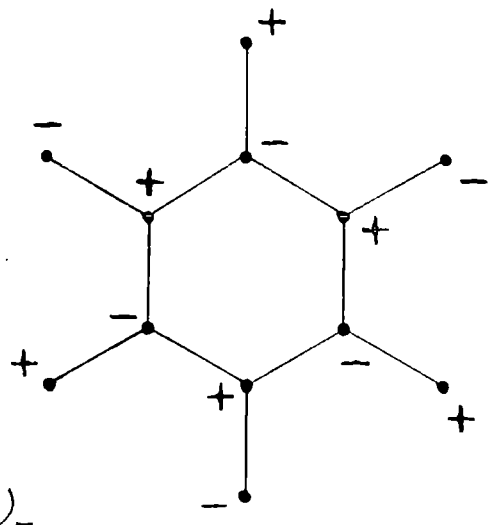

ν_7

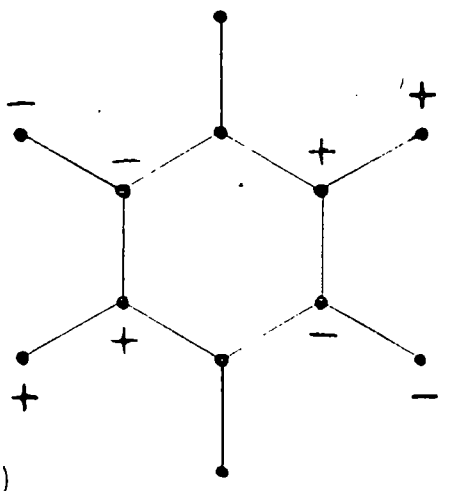

ν_{20}

FIG. 4.14 BENZENE MODES

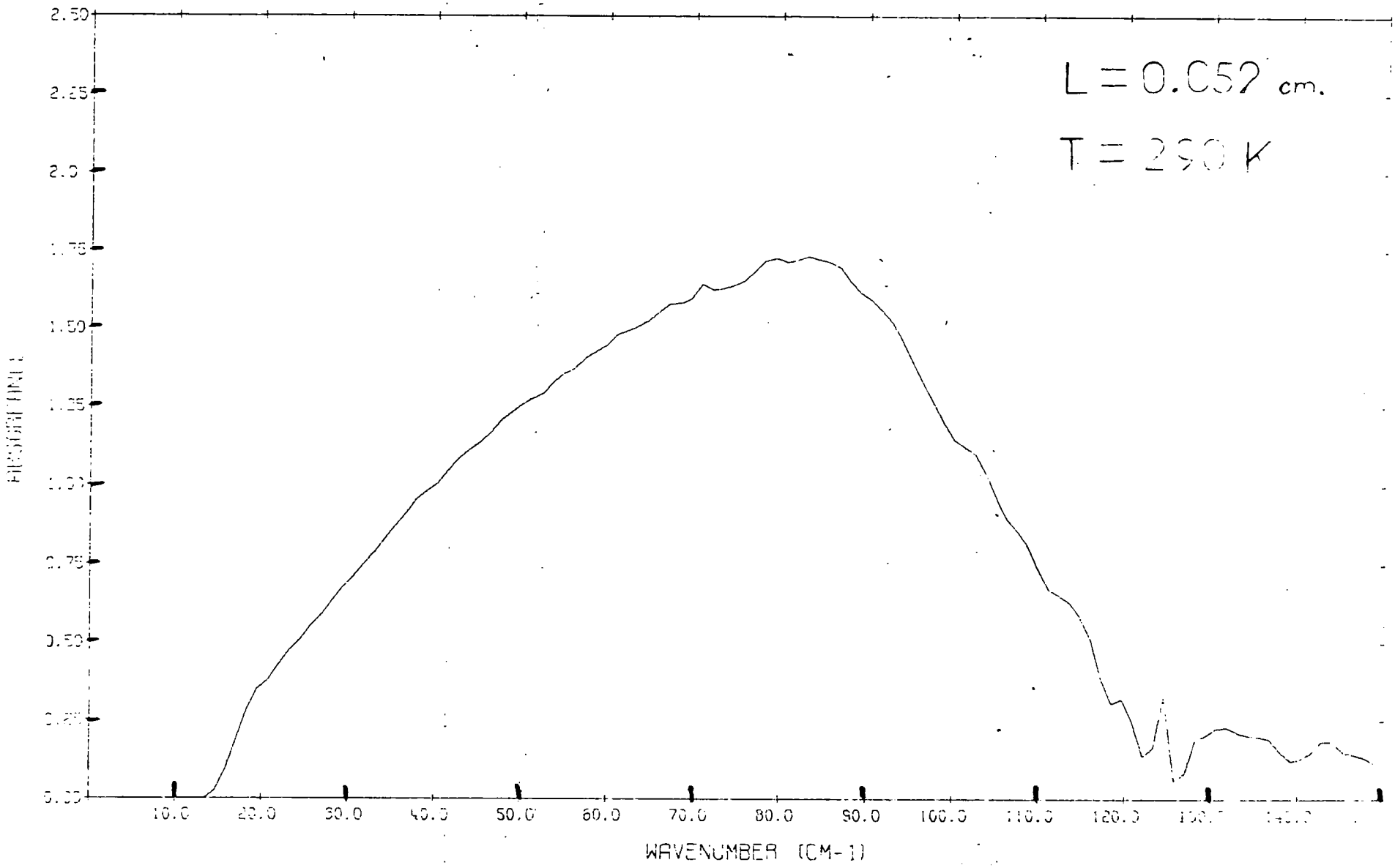

FIG. 4.15 : 0.44 mol. dm.$^{-3}$ BU+N+Br- IN BENZENE

achieved for the low frequency half of the band, but that the high frequency wing of the band was severely curtailed by the beam-splitter cut-off at approximately 120 cm^{-1}. The band centre for the $Bu_4N^+Br^-$ in benzene system was seen to be at about 85 cm^{-1}, and to have a half-band width of about 70 cm^{-1}.

4.3.1 Effect of concentration

The solubility of $Bu_4N^+Br^-$ in benzene was found to be about 0.45 mol dm^{-3}. The low frequency absorption was found to be less intense than that for the chloride, and made it necessary to run the spectra using a pathlength of 0.0517 cm. Spectra for 6 concentrations of $Bu_4N^+Br^-$ in benzene in the range 0.10 to 0.44 mol dm^{-3} were recorded, and the results are shown in table 4.10. Two spectra were recorded for each concentration, and the areas quoted were calculated from 'planimeter' and 'computed' areas as described for the chloride. Fig. 4.16 shows a plot of area under the 85 cm^{-1} absorption versus concentration for $Bu_4N^+Br^-$ in benzene. Beers Law was seen to be obeyed, within the limits of the experimental uncertainty, in the concentration range 0.1 to 0.4 mol dm^{-3}. The error bars were constructed by using the standard variation of the area as calculated for the chloride. The fitting of the baseline was still considered to be the major source of error in the intensity measurements. In the case of the bromide these errors were quite probably overestimates of the errors involved, since the frequency range over which the absorption occurred was less than that for the chloride. Thus it was relatively easier to fit the baseline. The BEERSLAW programme was used to calculate the slope of the best straight line for the 'computed' and 'planimeter' areas. A slope of 229±5 dm^3 mol^{-1} cm^{-1} was obtained when the origin was taken as a valid point. This is represented by line A in the figure. The intensity B_i, derived from this slope was 4 430±100 dm^3 mol^{-1} cm^{-2}. Line B represents the best fit to the data without the restriction of the origin as a valid point. The intercept for this line was -3.3±4.1 and hence could not be determined. The slope

Table 4.10 Intensities for the 80 cm^{-1} band for $Bu_4N^+Br^-$ in benzene

(L = 0.052 cm, T = 293K)

concentration /mol dm^{-3}	area /cm^{-1}	average area /cm^{-1}	intensity /dm^3 mol^{-1} cm^{-2}
0.10	22.2	21.3	4140±4260
	20.3		
0.16	32.8	33.1	3980±2660
	33.4		
0.30	71.1	69.1	4490±1420
	67.1		
0.36	83.6	83.0	4520±1180
	82.3		
0.40	83.9	93.0	4520±1060
	102.1		
0.44	103.3	98.5	4390±970
	93.7		

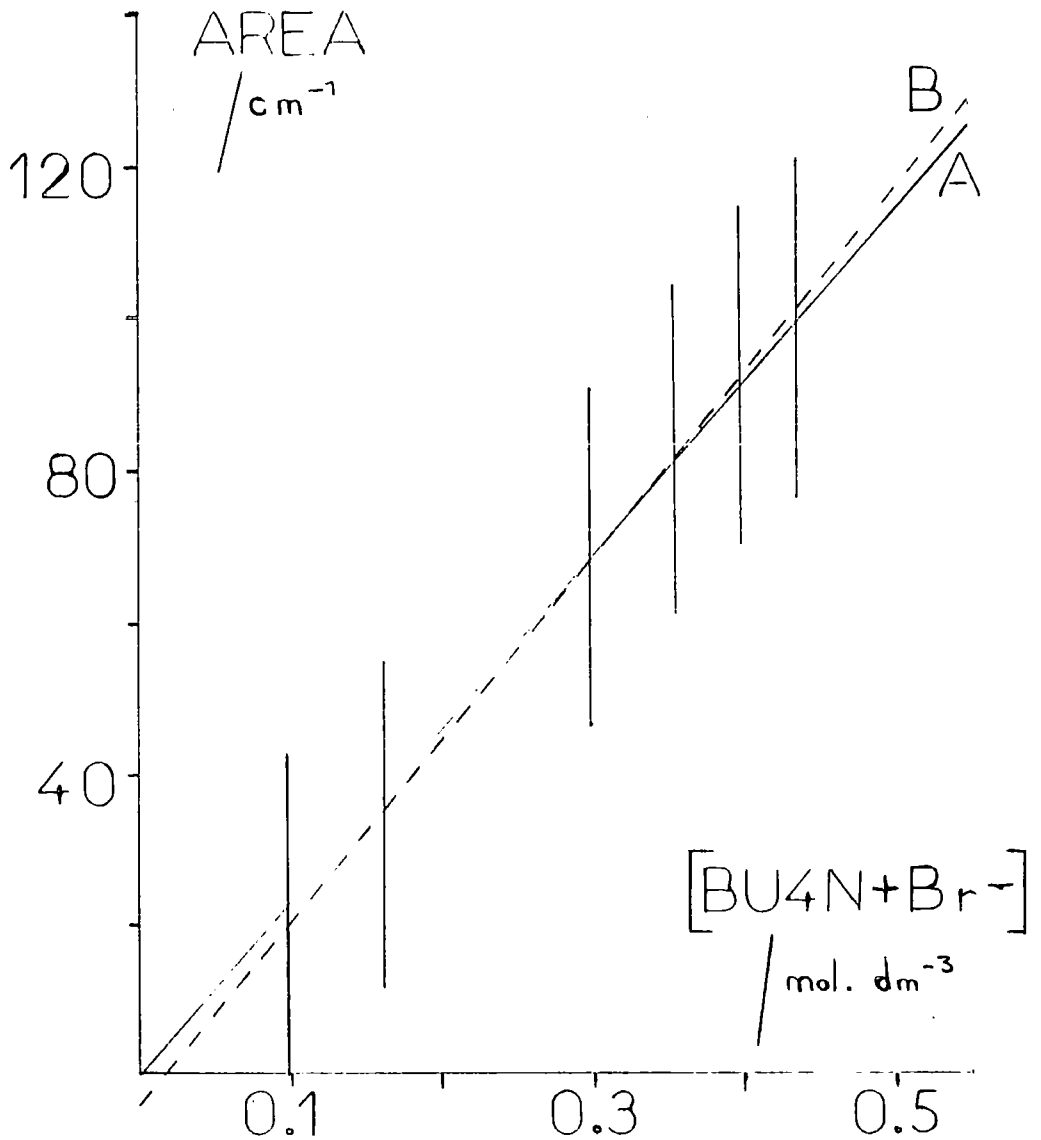

FIG. 4.16 BEER'S LAW PLOT FOR BU4N+Br⁻ IN BENZENE

L = 0.052 cm. T = 293 K

for this line was 240±13 $dm^3\ mol^{-1}\ cm^{-1}$, which gave an intensity B_1 of 4 640±250 $dm^3\ mol^{-1}\ cm^{-2}$. As the two intensity values thus calculated were not significantly different, and the standard deviations of the intensities were small, then Beers Law was assumed to hold for this concentration range, and the intensity of the 85 cm^{-1} absorption for $Bu_4N^+Br^-$ in benzene was taken as 4 430±100 $dm^3\ mol^{-1}\ cm^{-2}$.

On calculating the standard deviations for the intensities at each concentration it was noted that much care was needed in the interpretation of such integrated area/concentration data. Whilst the area values fitted very well to the straight line, it was noted from fig. 4.17 that the intensity values could in fact be increasing as was the case for the chloride. To determine whether or not the intensity was increasing with concentration it was necessary to cut down the error on the integrated band area measurement. This could be done by increasing the pathlength at which the spectra were run. However, this was not possible because of the background benzene absorption, from the collisional mode at 75 cm^{-1}, which lies under the absorption at 85 cm^{-1}. Increasing the pathlength resulted in very noisy spectra with the Golay detector, due to ratioing out problems. Use of a cooled detector would enable useable spectra to be obtained, and would allow a more accurate study of the intensity of the 85 cm^{-1} band with the concentration of the salt.

4.4 Tetra-n-pentylammonium chloride and tetra-n-heptylammonium chloride in benzene

The effect of change of cation on the far-infrared absorption was studied by recording the spectra of tetra-n-pentylammonium chloride ($Pe_4N^+Cl^-$) in benzene. The $Pe_4N^+Cl^-$ salt was purchased from Eastman Kodak Ltd. and was stored in a dessicator over calcium chloride, and was used without further purification. The spectra were recorded using a 50 gauge beam-splitter and a 0.0208 cm pathlength polythene windowed cell. The observed bands had a band centre at approximately 115±3 cm^{-1}, and a half-

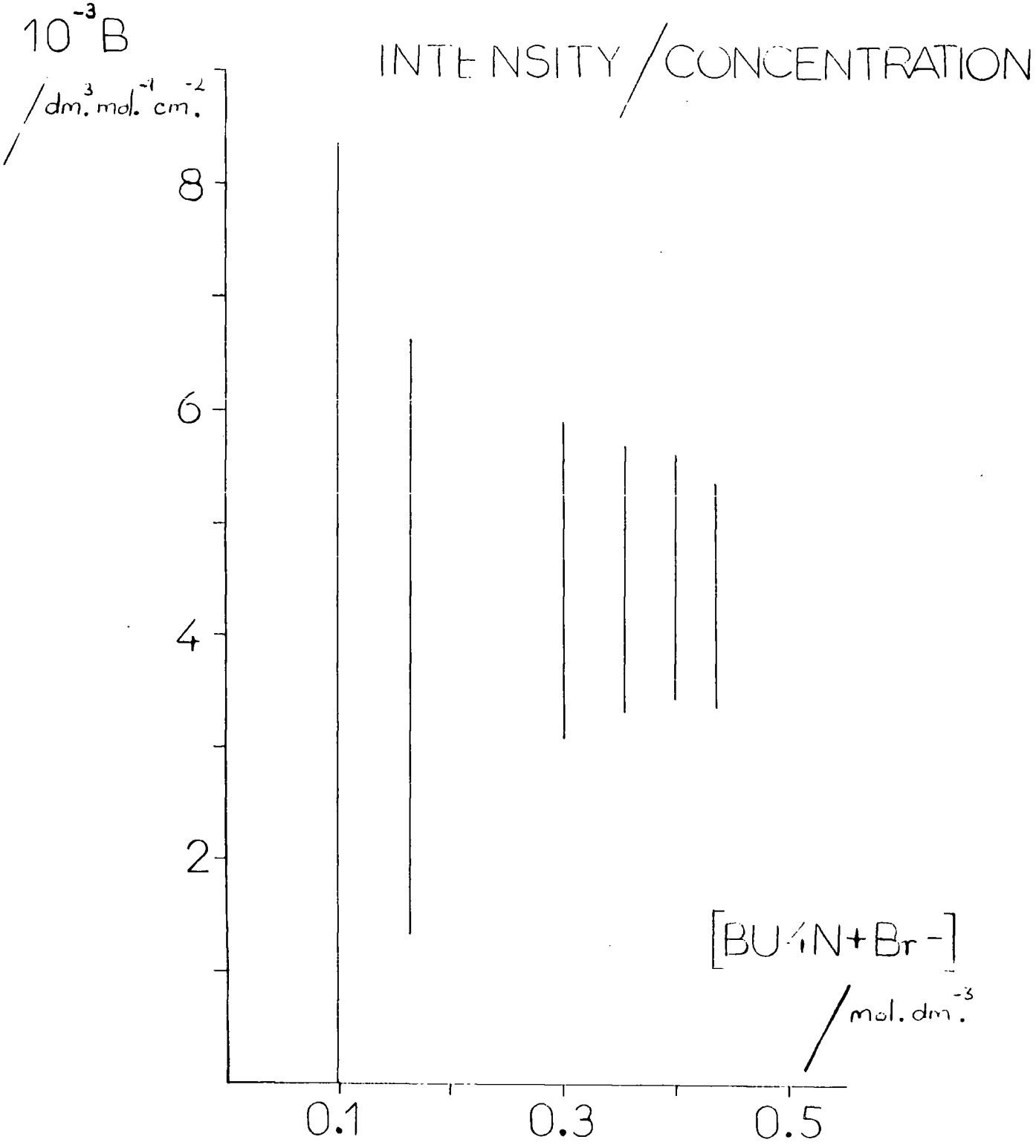

FIG. 4.17 BU4N+Br- IN BENZENE

band width of about 75±5 cm^{-1}. The spectrum for 0.7023 mol dm^{-3} $Pe_4N^+Cl^-$ in benzene can be seen in fig. 4.18. The band was very asymmetric to low frequency, the asymmetry being especially noticeable for the high concentrations of salt. The possibility of a low frequency component to the overall profile of the ion aggregate absorptions is investigated in chapter 5.

Two spectra were recorded for each of 6 concentrations of $Pe_4N^+Cl^-$ in benzene, and the integrated areas and hence the intensities for the overall absorption band were calculated as detailed previously. These areas and intensities are detailed in table 4.11. From these results it was difficult to determine whether or not the intensity was increasing with concentration, due to the small number of concentrations studied, and the apparent scatter of the intensities for the higher concentration solutions. However, the results did suggest that the intensity was rising with increasing concentration. This once again suggested that the $Pe_4N^+Cl^-$ ion aggregates were breaking up on dilution, as was seen to be the case for $Bu_4N^+Cl^-$. The intensity for the $Pe_4N^+Cl^-$ in benzene band was less than for $Bu_4N^+Cl^-$ in benzene. At about 0.3 mol dm^{-3} concentration the intensity for the $Pe_4N^+Cl^-$ salt was 3 500 dm^3 mol^{-1} cm^{-2}, whilst that for $Bu_4N^+Cl^-$ in benzene at the same concentration was 8 000 dm^3 mol^{-1} cm^{-2}.

The effect of change of cation was further studied by recording the spectra of 0.774 mol dm^{-3} tetra-n-heptylammonium chloride ($Hp_4N^+Cl^-$) in benzene. The salt was once again purchased from Eastman-Kodak Ltd., and was used without further purification. The same instrumental conditions were used in recording this spectrum as were used for the $Pe_4N^+Cl^-$ salt. The spectrum is shown in fig. 4.19. The band centre was measured as 112±3 cm^{-1}, and the half-band width as 80±5 cm^{-1}. The intensity was calculated from the two ratioed spectra of the 0.774 mol dm^{-3} $Hp_4N^+Cl^-$ as 8 400±1 400 dm^3 mol^{-1} cm^{-2}; the integrated areas being 130.3 and 140.3 cm^{-1}. It thus appeared that the intensity of the 112 cm^{-1} absorption for the $Hp_4N^+Cl^-$ salt was about the same as that for the $Pe_4N^+Cl^-$ salt in benzene. The asymmetry to low

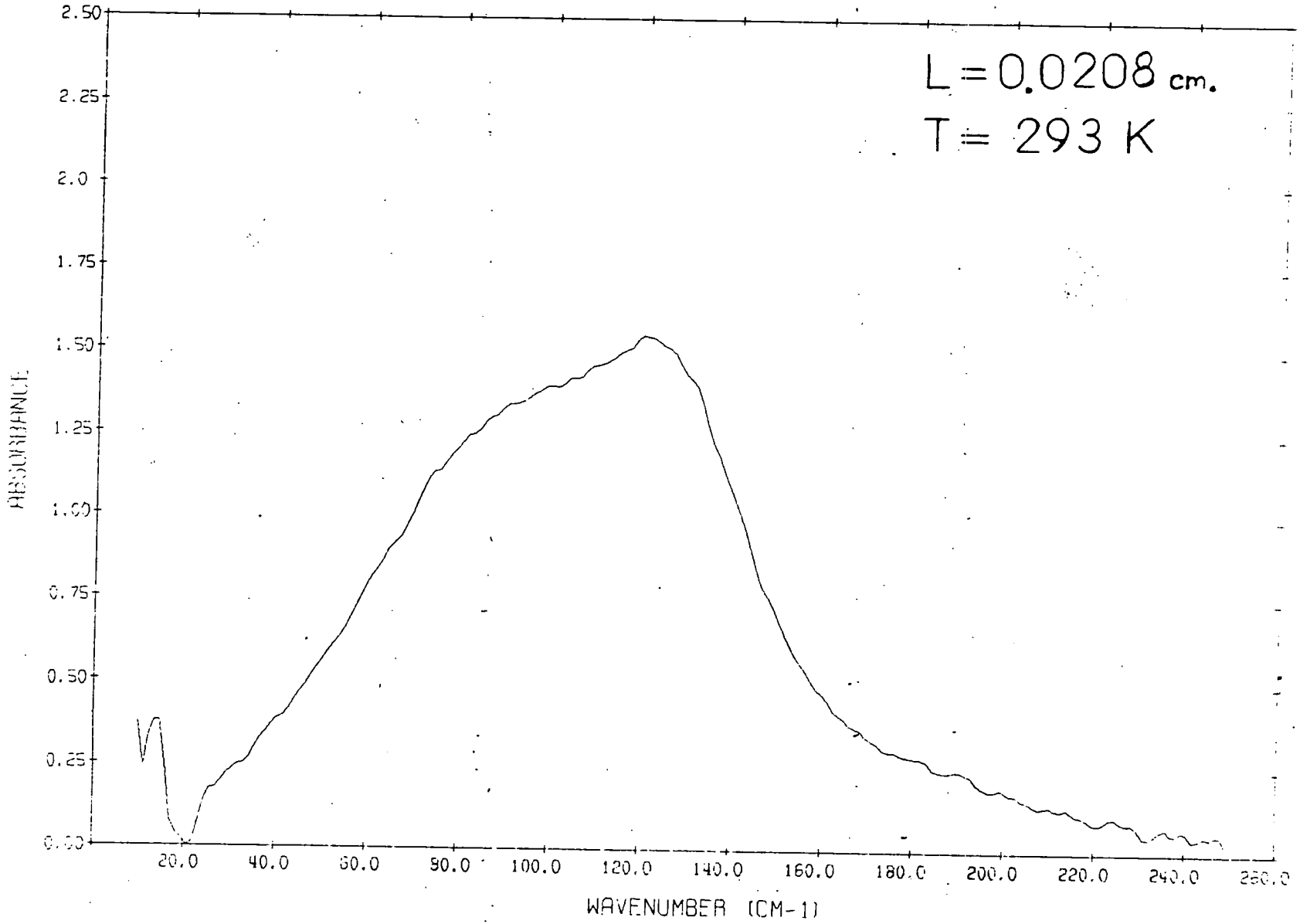

FIG. 4.18 0.7023 M PE4N+Cl- IN BENZENE

Table 4.11 Intensities for the 115 cm^{-1} band of $Pe_4N^+Cl^-$ and $Hp_4N^+Cl^-$ in benzene (L = 0.0208 cm, T = 297K)

concentration /mol dm^{-3}	area /cm^{-1}	average area /cm^{-1}	intensity /dm^3 mol^{-1} cm^{-2}
$Pe_4N^+Cl^-$			
0.132	11.28	10.71	3900±8000
	10.13		
0.264	18.34	18.60	3387±4000
	18.85		
0.528	39.10	40.68	3704±2000
	42.25		
0.702	128.13	123.29	8443±1500
	118.45		
1.055	137.84	131.74	6003±1000
	125.64		
$Hp_4N^+Cl^-$			
0.774	130.31	135.29	8403±1400
	140.27		

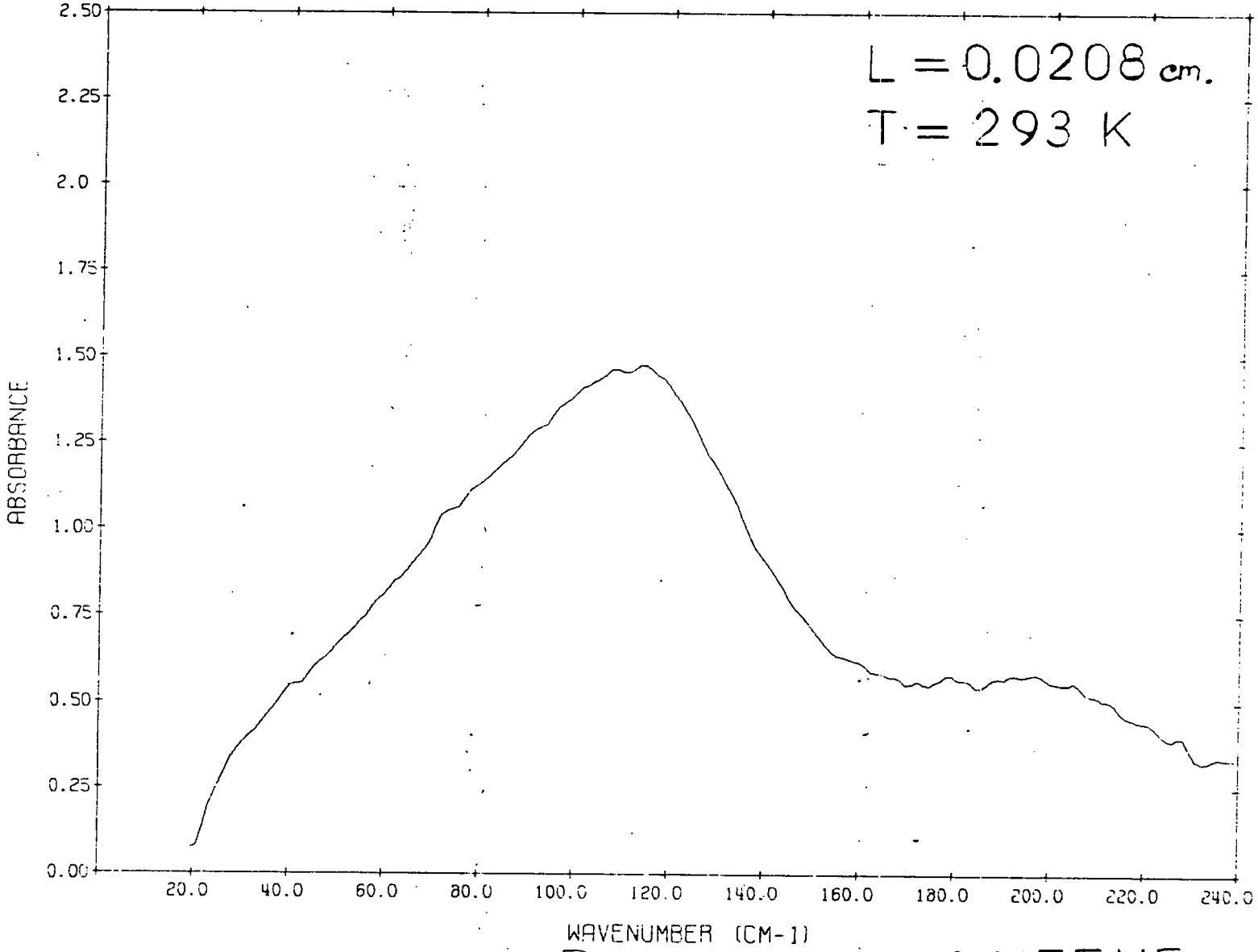

FIG. 4.19 0.77 M HP4N+Cl- IN BENZENE

frequency of the band centre was not nearly so pronounced in the $Hp_4N^+Cl^-$ as in the $Pe_4N^+Cl^-$ salt, when the spectra of the 0.7 mol dm^{-3} salts were compared. The low frequency component for the $Hp_4N^+Cl^-$ salt was thus less than that for the $Pe_4N^+Cl^-$ salt.

The 'sticking' of the salt solutions to the polythene cell windows was severe, especially for the $Hp_4N^+Cl^-$ in benzene solutions, and the cell was therefore rinsed with acetone immediately after each salt solution interferogram had been run. The cell plates were changed after one day of use with either the $Pe_4N^+Cl^-$ or $Hp_4N^+Cl^-$ solutions. This 'sticking' problem was thought to be a possible cause for the variations in the intensities for the higher $Pe_4N^+Cl^-$ concentrations.

4.5 Tetra-n-butylammonium chloride in carbon tetrachloride

The possible effect of solvent on the far-infrared absorption was investigated by using carbon tetrachloride (CCl_4) as a solvating medium for the tetra-alkylammonium salts. The CCl_4 was Hopkin and Williams 'Spectrosol' grade, and was dried over molecular sieves, but otherwise used without purification. Karl-Fischer titrations showed less than 0.01% water by weight in the pure solvent. $Bu_4N^+Cl^-$ was found to have a solubility of approximately 0.8 mol dm^{-3} in CCl_4, by making up a saturated solution by gradual addition of the salt. The solvent was then slowly pumped away from 25 cm^3 of this saturated solution under reduced pressure, and the resulting solid weighed. 5.563 g of salt was recovered, which was the equivalent of 0.803 mol dm^{-3} solution of the salt. This indicated that no stable solid solvate of the salt by the solvent was being formed.

Spectra of the $Bu_4N^+Cl^-$ salt in CCl_4 solution were recorded using a 50 gauge beam-splitter, and pathlengths of 0.0208 cm for concentrations between 0.1 and 0.8 mol dm^{-3}, and 0.152 cm for concentrations between 0.01 and 0.1 mol dm^{-3}, in polythene windowed cells. Fig. 4.20 shows the spectrum for an 0.0208 cm pathlength of 0.581 mol dm^{-3} $Bu_4N^+Cl^-$ in CCl_4. The measured band centre was found to be 114±2 cm^{-1}, and hence

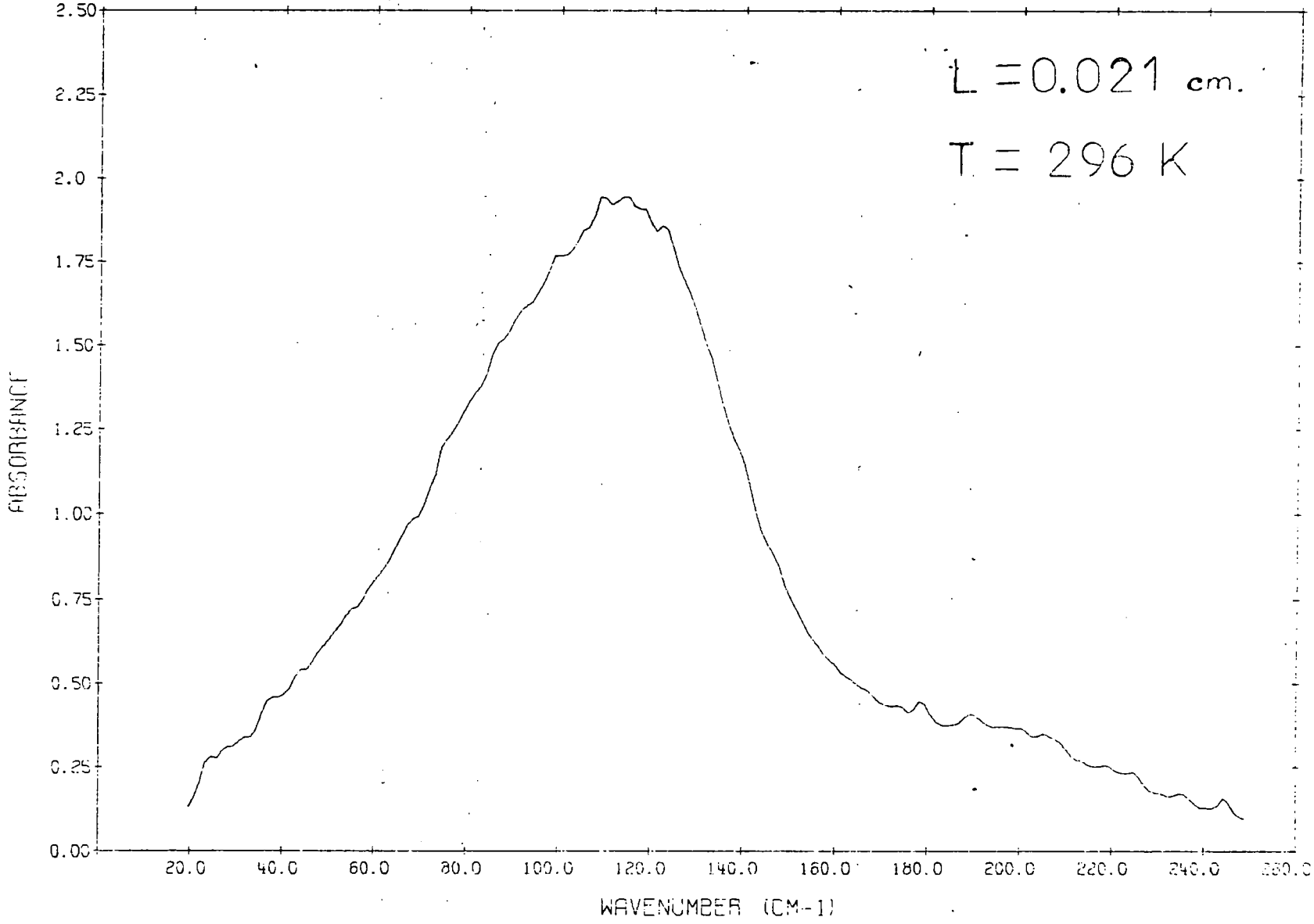

FIG. 4.20 0.581 mol. dm^{-3} BU4N+Cl- IN CARBON TETRACHLORIDE

no significant shift of band centre was seen to have occurred on changing the solvent from benzene to CCl_4. Table 4.12 shows the calculated integrated areas, and corresponding intensities for the far-infrared absorption. This table and fig. 4.21, which shows a Beers Law plot for the 0.021 cm pathlength spectra, indicated that the absorption obeyed Beers Law in this concentration range. The BEERSLAW best straight line programme was used to give the best values for the intensity of the absorption. Using the origin as a valid point, a slope of 264±5 $dm^3\ mol^{-1}\ cm^{-1}$ was obtained, which gave an intensity B_i of 12 700±230 $dm^3\ mol^{-1}\ cm^{-2}$. If the origin was not taken as a valid point a slope of 255±10 $dm^3\ mol^{-1}\ cm^{-2}$ was obtained with an intercept of 5.06±5.28 cm^{-1}. This data indicated that Beers Law was valid in this case. The latter slope gave an intensity B_i of 12 300±500 $dm^3\ mol^{-1}\ cm^{-2}$. The slopes of these best fits are represented in fig. 4.21, where line A is the fit through the origin and line B is that without restriction.

To determine whether the absorption species was changing at lower concentrations, spectra were also recorded for concentrations in the range 0.01 to 0.1 mol dm^{-3}, using a 0.152 cm pathlength cell. These spectra showed a considerably better signal-to-noise ratio than the spectra for the lower concentrations of $Bu_4N^+Cl^-$ in benzene. The low frequency collisional absorption of CCl_4 was much less than that for benzene, and so there were no serious 'ratioing out' problems for the CCl_4 solutions. Fig. 4.22 shows the spectrum of 0.152 cm of 0.079 mol dm^{-3} $Bu_4N^+Cl^-$ in CCl_4, and when compared with fig. 4.6 for 0.253 cm of 0.048 mol dm^{-3} $Bu_4N^+Cl^-$ in benzene, showed the significantly better signal-to-noise ratio below 100 cm^{-1}. The integrated areas and corresponding intensities for the far-infrared absorption are shown in table 4.12. The intensity showed no concentration dependence as shown in fig. 4.23, for the concentration range 0.01 to 0.10 mol dm^{-3}. It was therefore concluded that the absorbing species was not being affected by dilution, and hence that the aggregates were not breaking up. This can be seen from fig. 4.24, where the intensity for each concentration has been plotted against

Table 4.12 Intensities for the 115 cm^{-1} band for $Bu_4N^+Cl^-$ in CCl_4

(T = 294K, L = 0.021 and 0.152 cm)

concentration /mol dm^{-3}	area /cm^{-1}	average area /cm^{-1}	intensity /dm^3 mol^{-1} cm^{-2}
0.021 cm pathlength			
0.098	29.1	25.2	12 380±10790
	21.3		
0.196	60.4	56.5	13 860±5 400
	52.6		
0.291	76.2	77.3	12 790±3 640
	78.3		
0.392	133.3	123.9	15 190±2 700
	114.4		
0.524	136.4	127.3	11 680±2 020
	118.2		
0.581	150.2	155.5	12 860±1 820
	160.7		
0.688	170.2	166.0	11 610±1 540
	161.8		
0.783	219.4	215.3	13 220±1 350
	211.1		

(continued)

Table 4.12 (continued)

concentration /mol dm^{-3}	area /cm^{-1}	average area /cm^{-1}	intensity /dm^3 mol^{-1} cm^{-2}
0.152 cm pathlength			
0.0098	17.7	17.3	11 680±14 850
	16.9		
0.0185	33.8	31.8	11 340± 7 840
	29.8		
0.0399	68.8	71.3	11 770± 3 630
	73.8		
0.0790	121.3	119.1	9 930± 1 830
	116.9		
0.0980	137.2	140.0	9 410± 1480
	142.8		

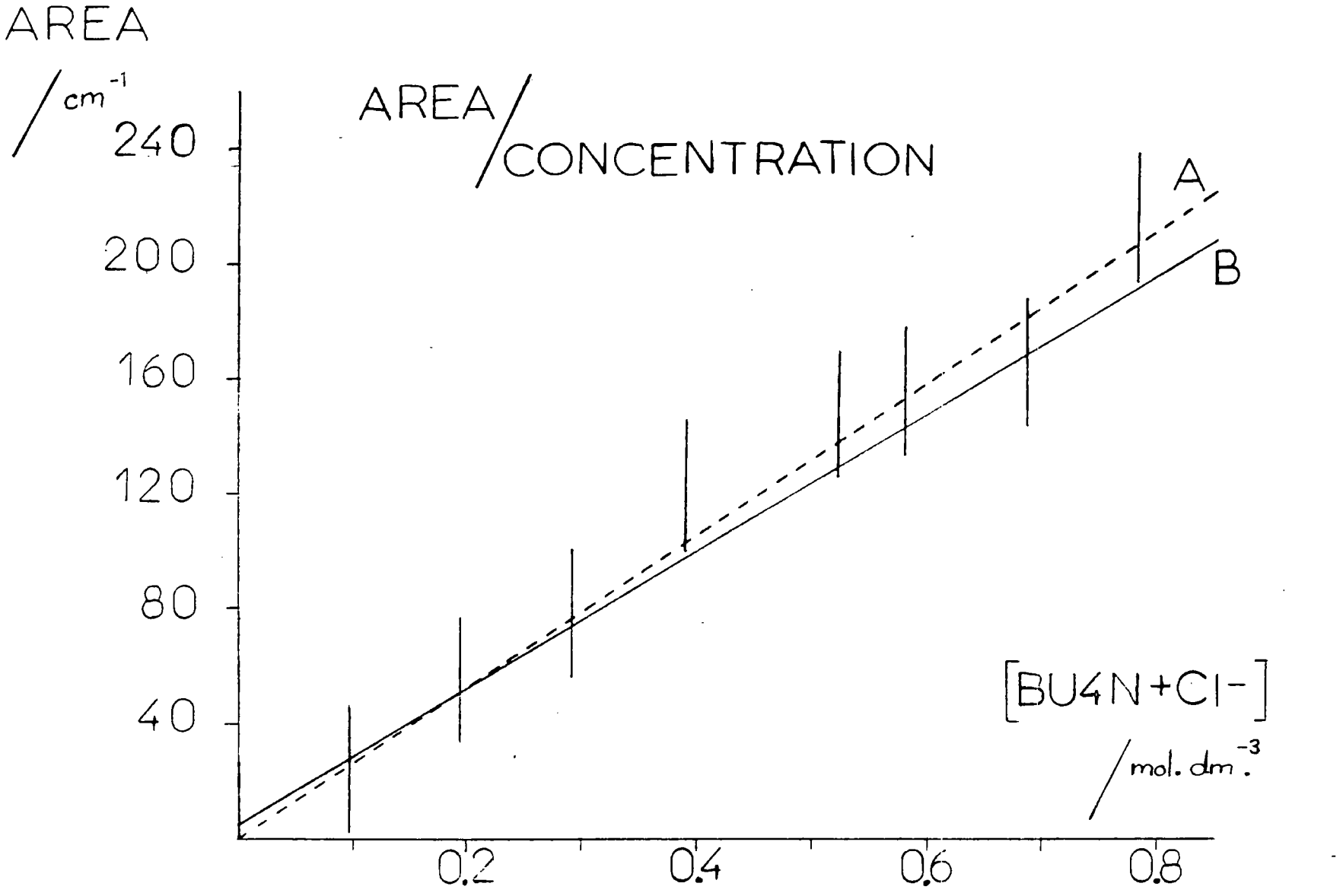

FIG. 4.21 BU4N+Cl- IN CARBON TETRACHLORIDE

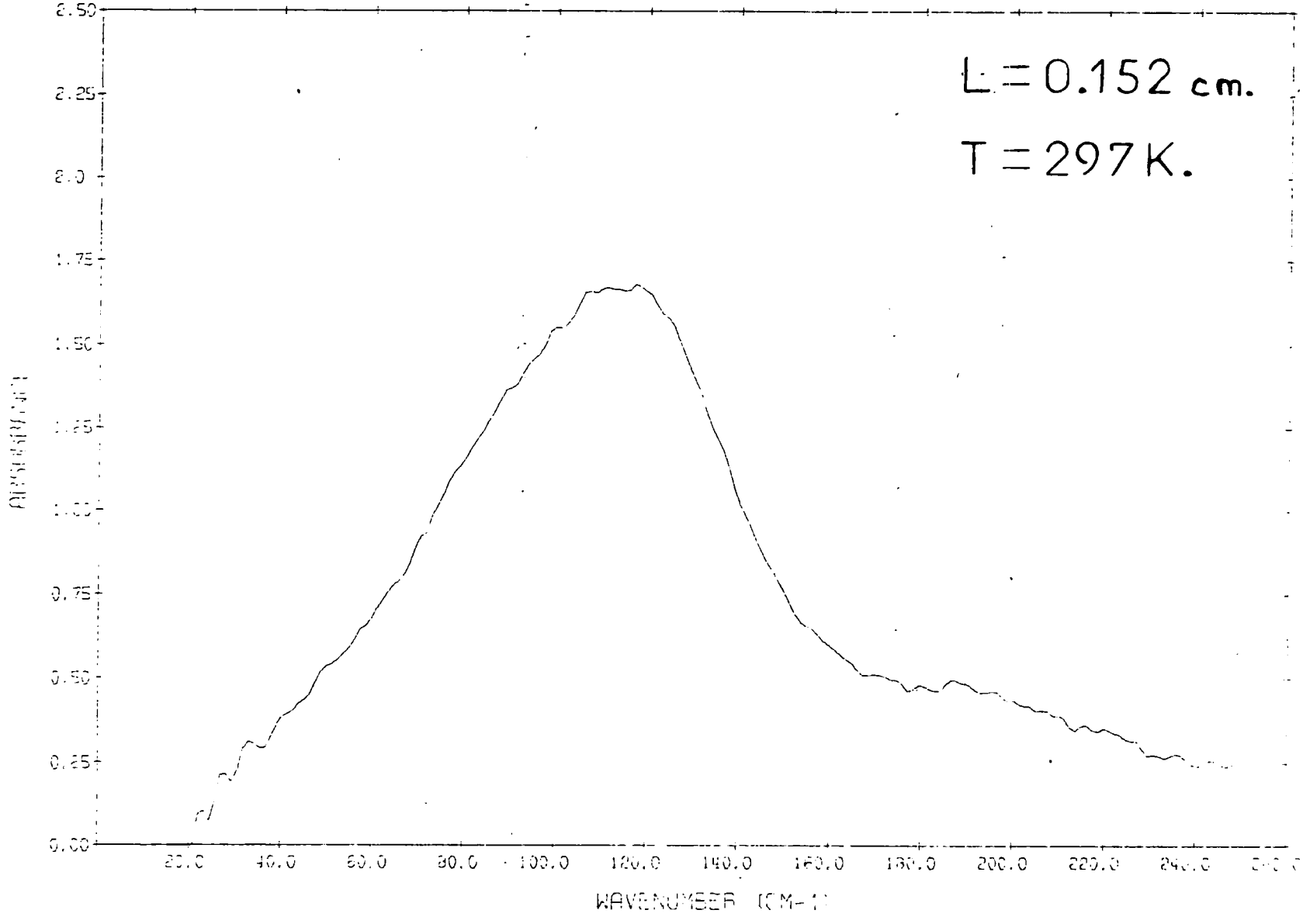

FIG. 4.22 0.079 mol. $dm.^{-3}$ BU4N+Cl- IN CCl4

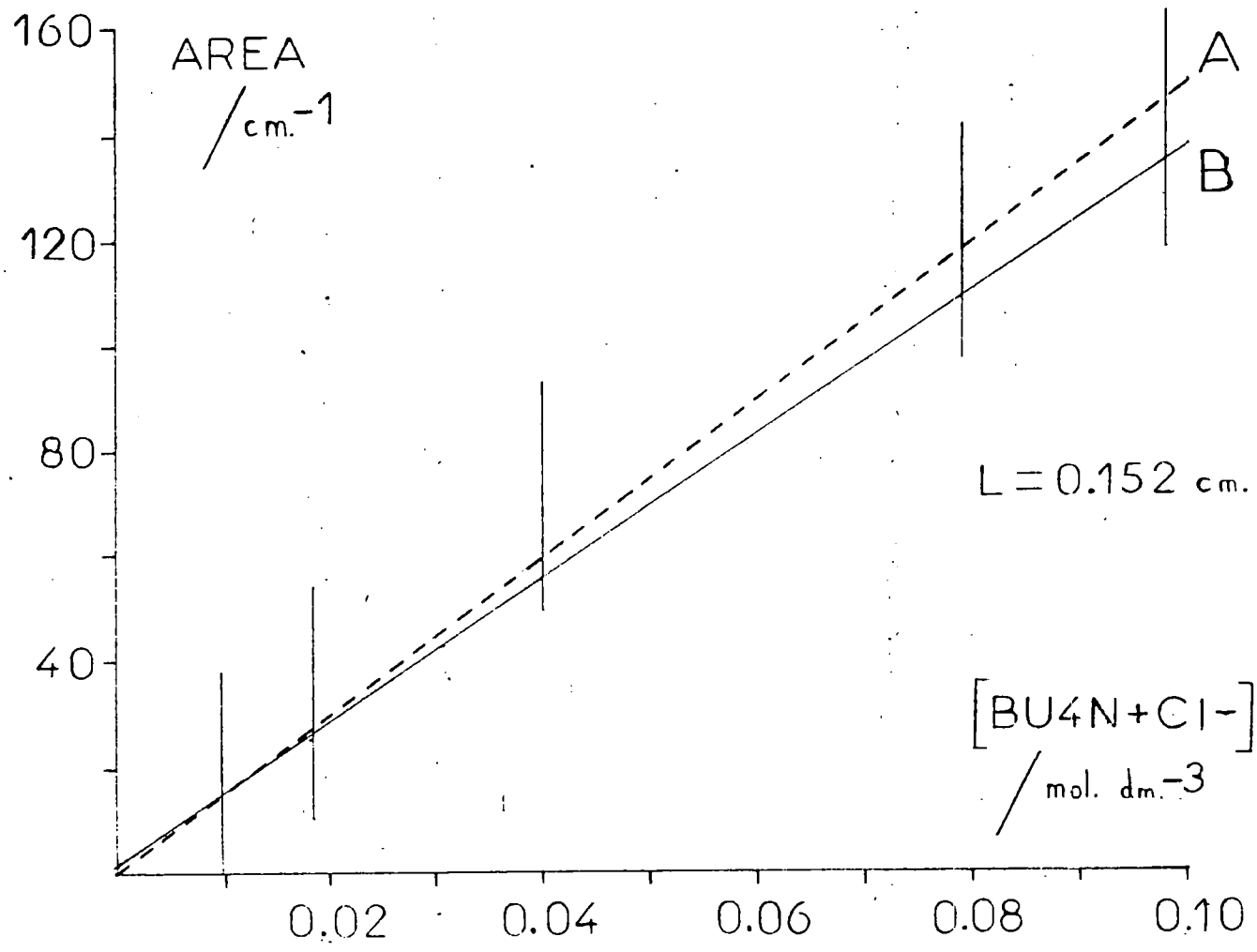

FIG.4.23 BU4N+Cl- IN CARBON TETRACHLORIDE

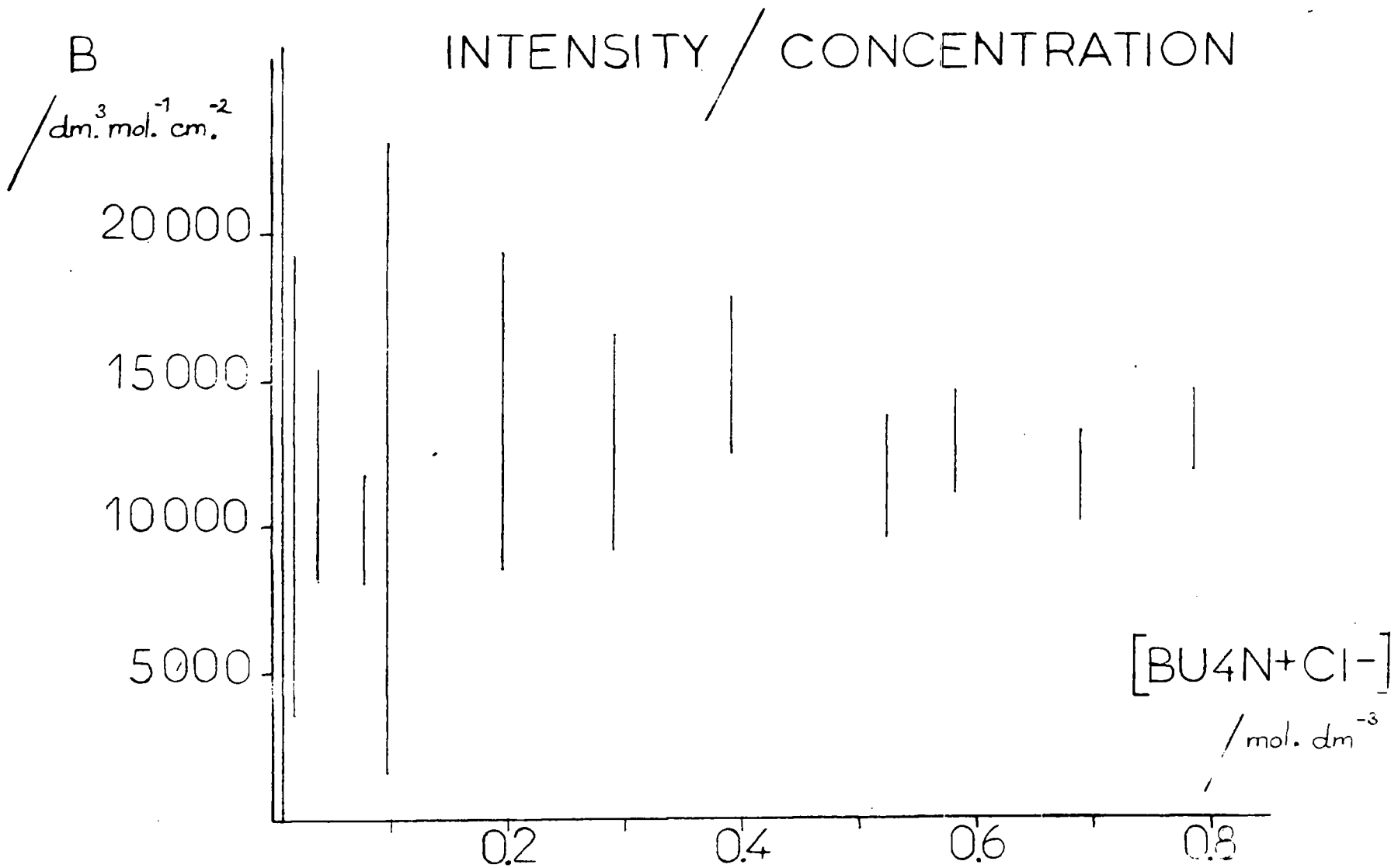

FIG. 4.24 BU4N+Cl- IN CARBON TETRACHLORIDE

the concentration. The error bars were once again calculated on the assumption that the precision on the area was ±22 cm^{-1}.

The intensity of the absorption band over the whole concentration range studied (0.01 to 0.8 mol dm^{-3}) was calculated by correcting all the areas to 0.021 cm pathlength, by assuming Beers Law to be valid as indicated above, and then using the programme BEERSLAW. For the 12 concentrations of $Bu_4N^+Cl^-$ in CCl_4 studied the 52 areas measured gave a slope of 264±4 dm^3 mol^{-1} cm^{-1} for the fit through the origin, with an intensity B_i of 12 700±200 dm^3 mol^{-1} cm^{-2}. If no restrictions were applied the least squares analysis gave a slope of 265±6 dm^3 mol^{-1} cm^{-1}, which gave an intensity B_i of 12 740±300 dm^3 mol^{-1} cm^{-2}. The intercept on the area axis for the latter fit was -0.4 ±2.3 cm^{-1}, which indicated that Beers Law was valid for this system.

Comparison of the ion aggregate band intensities for $Bu_4N^+Cl^-$ in benzene and CCl_4 solutions indicated that the solvent had very little effect on the intensity. The intensity for the benzene solutions was B_i = 13 000±300 dm^3 mol^{-1} cm^{-2} and that for CCl_4 solutions was B_i = 12 700 ±300 dm^3 mol^{-1} cm^{-2}. The intensity for the benzene solutions may well be an overestimate, because of the non-adherance to Beers Law, and the consequent shift of the best fit straight line to greater slope, because of the higher intensities for the higher concentration salt solutions. However the agreement for the two solutions indicated that the $Bu_4N^+Cl^-$ salt was present in the same state of aggregation for the CCl_4 solutions as for the higher concentration benzene solutions, which would dominate the Beers Law fit for the benzene solutions. From this invarience of the intensity with change of solvent it was concluded that, either the solvent took no part in the interactions that gave rise to the absorptions for the salt in the solution, or that the CCl_4 had exactly the same role in the $Bu_4N^+Cl^-$ in CCl_4 solutions as did the benzene in the concentrated $Bu_4N^+Cl^-$ in benzene solutions.

4.6 Tetra-n-butylammonium bromide in carbon tetrachloride

The spectra of the bromide salt were recorded by using a 100

gauge beam-splitter, which gave maximum energy at the maximum of the absorption in the salt, but precludes accurate measurements in the high frequency wing of the band. Only one concentration (0.274 mol dm^{-3}) was recorded, and spectra were recorded at 0.052 and 0.102 cm pathlengths. The spectrum for 0.052 cm of 0.274 mol dm^{-3} $Bu_4N^+Br^-$ in CCl_4 is shown in fig. 4.25. The band centre was measured as 73±3 cm^{-1}, and the half-band width as 50±5 cm^{-1}. The band centre had shifted from 80±3 cm^{-1} for the bromide salt in benzene. On a closer investigation of the spectrum it was noticed that the band was asymmetric to high frequency, rather than to low frequency as had been the case for the $Bu_4N^+Br^-$ in benzene. This indicated that for the bromide in CCl_4 the low frequency component of the absorption was now predominant. The 'computed' and planimeter areas were obtained as detailed previously, and the average areas calculated to give an intensity B_i of 6 000±1700 dm^3 mol^{-1} cm^{-2} for the two pathlengths. It appeared that the intensities for the $Bu_4N^+Br^-$ salt were higher in CCl_4 than in benzene, where the intensity was calculated as 4 430±100 dm^3 mol^{-1} cm^{-2}. However, the low precision for the intensity of the salt in CCl_4 allowed overlap with the intensity for the benzene solutions, and the intensity difference was thus not significant.

4.7 Tetra-n-butylammonium chloride in chloroform

To further study the possible effects of the solvent on the ion aggregate absorption the $Bu_4N^+Cl^-$ and $Bu_4N^+Br^-$ salts were also studied in chloroform. The solvent used was Hopkin and Williams 'spectrosol' chloroform, which was dried over molecular sieves, but then used without purification. Karl-Fischer titrations showed less than 0.01% water by weight in the dried chloroform solvent. The solubility of $Bu_4N^+Cl^-$ in $CHCl_3$ was found to be approximately 0.85 mol dm^{-3}, and so a series of spectra for concentrations between 0.1 and 0.8 mol dm^{-3} were recorded. Fig. 4.26 shows the spectrum obtained for 0.6 mol dm^{-3} $Bu_4N^+Cl^-$ in $CHCl_3$ at 0.0208 cm pathlength. The band centre was measured as 118±3 cm^{-1}, and the half-band width as 55±5 cm^{-1}, which was considerably narrower than the 80±5

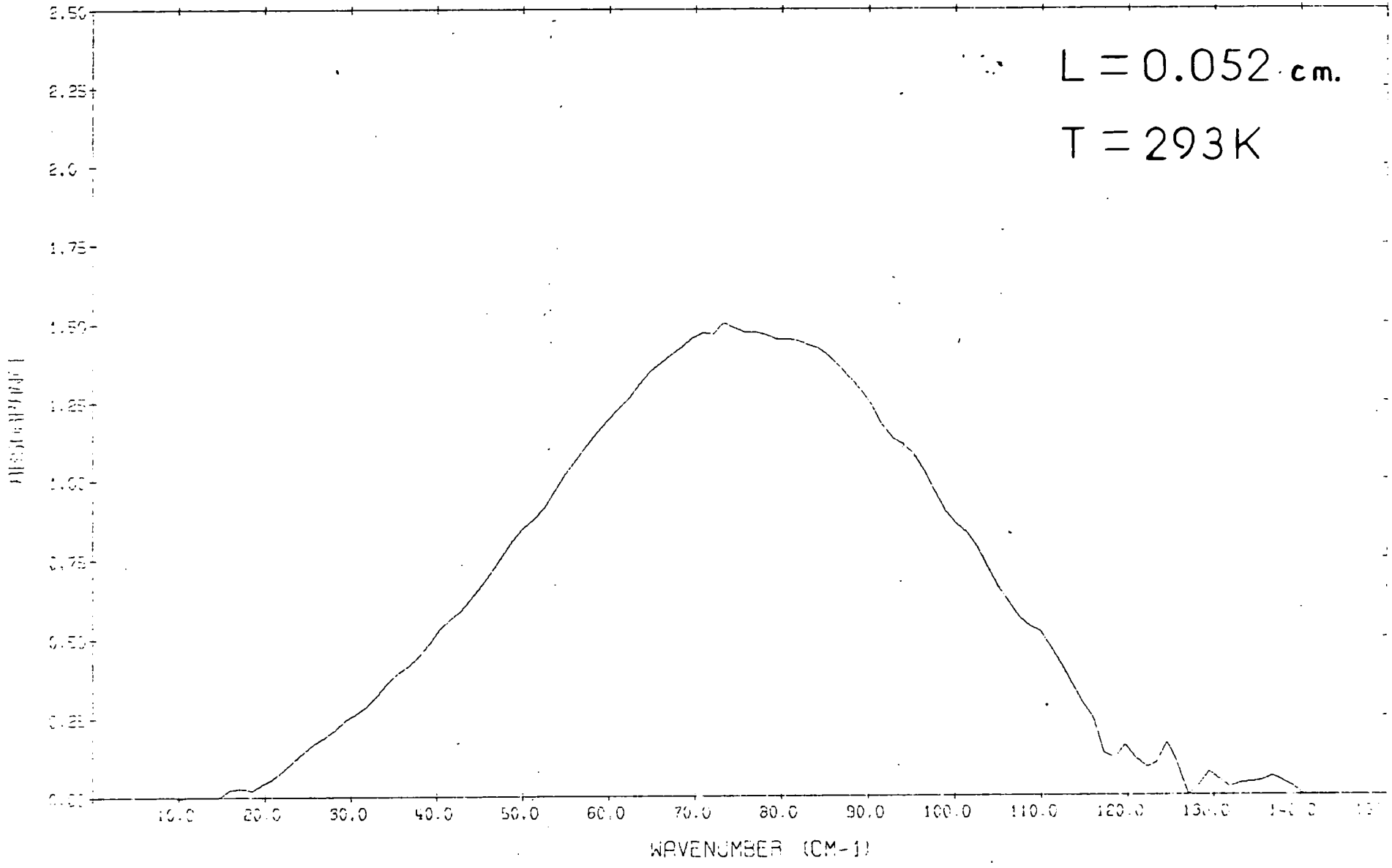

FIG. 4.25 0.274 mol. dm.$^{-3}$ BU4N+Br$^-$ IN CCl4

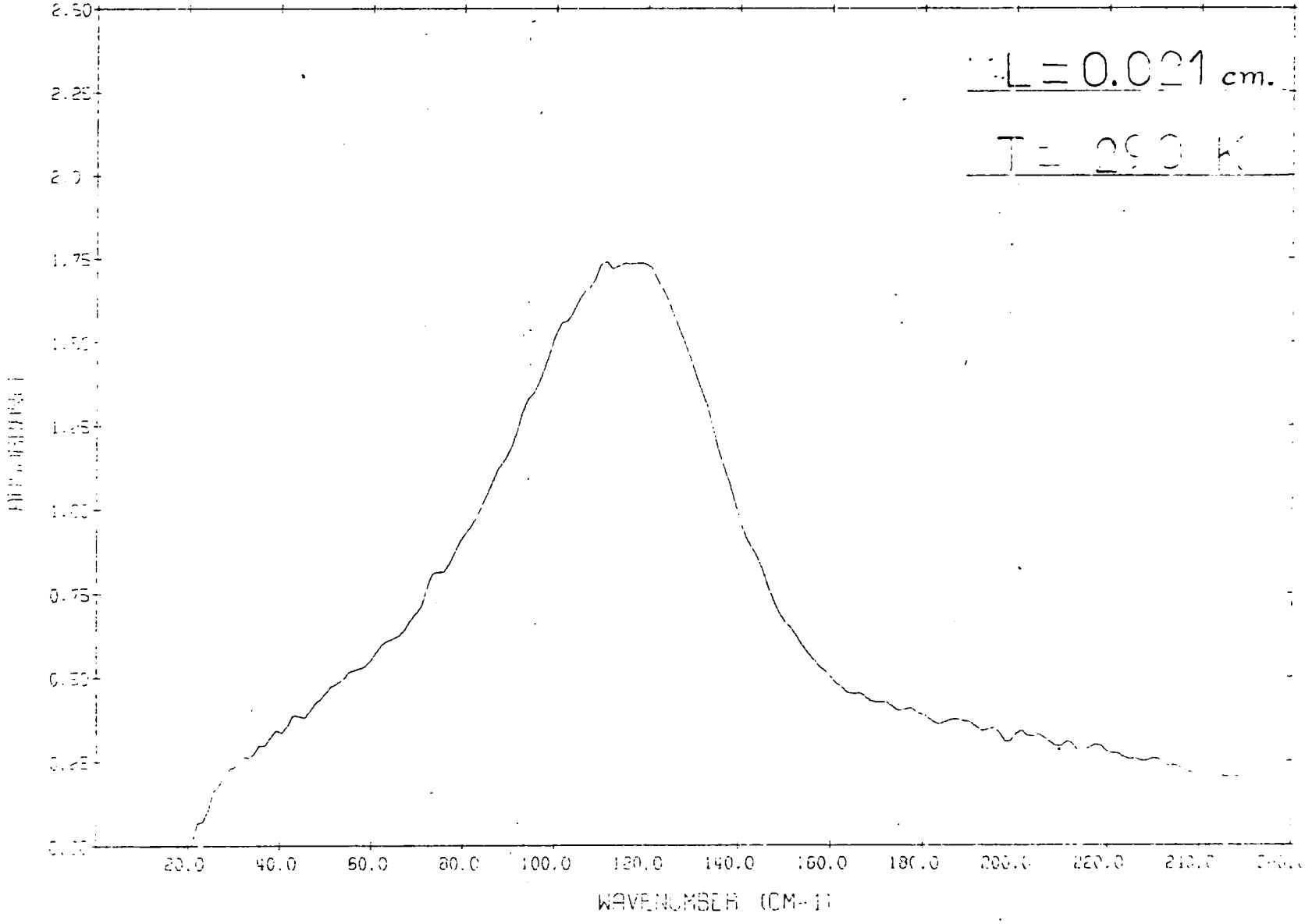

FIG. 4.26 0.6 mol. dm^{-3} $BU_4N^+Cl^-$ IN CHLOROFORM

cm^{-1} measured for $Bu_4N^+Cl^-$ in benzene and CCl_4. The band was almost symmetric about the band centre, and showed very little indication that a second component was present in the overall profile.

Table 4.13 shows the integrated areas and corresponding intensies observed for the band at 118 cm^{-1}, which were obtained as detailed for $Bu_4N^+Cl^-$ in benzene. The intensity values showed that there was possibly an increase in intensity with concentration, from 7 200±10 600 dm^3 mol^{-1} cm^{-2} at 0.1 mol dm^{-3} to 9 400±1 300 dm^3 mol^{-1} cm^{-2} at 1.2 mol dm^{-3}, but further showed that the increase was not statistically significant. This can be seen from fig. 4.27, which shows the plot of intensity against concentration for $Bu_4N^+Cl^-$ in $CHCl_3$. The 32 integrated areas for the 8 $Bu_4N^+Cl^-$ in $CHCl_3$ concentrations for which spectra were observed, were used with the BEERSLAW programme to give a slope of 193±2.6 dm^3 mol^{-1} cm^{-1}, and an intensity B_i of 9 300±100 dm^3 mol^{-1} cm^{-2}, with the origin taken as a valid point. Without this restriction the slope was determined as 201±6 dm^3 mol^{-1} cm^{-1}, which gave an intensity B_i of 9 700±300 dm^3 mol^{-1} cm^{-2}. The intercept on the area axis using the unrestricted fit was -4.2±2.8 cm^{-1}, and as this intercept was statistically significant from the origin, then this indicated that Beers Law did not hold over the concentration range 0.1 to 0.8 mol dm^{-3} for $Bu_4N^+Cl^-$ in $CHCl_3$. The unrestricted Beers Law fit to the area data is denoted by the letter B in fig. 4.28, and the fit through the origin is denoted by the letter A. The intensity values did not increase with concentration anywhere near as markedly for $Bu_4N^+Cl^-$ in $CHCl_3$ as for $Bu_4N^+Cl^-$ in benzene, where the intensity increased from 3 000 dm^3 mol^{-1} cm^{-2} at 0.1 mol dm^{-3} to approximately 20 000 dm^3 mol^{-1} cm^{-2} at 1.2 mol dm^{-3}. This indicated that the size of the aggregates was only changing marginally with concentration, and suggested that the chloroform in the chloroform solutions was not interacting with the $Bu_4N^+Cl^-$ aggregates as strongly as did the benzene in the benzene solutions. The intensity values themselves indicated that the $Bu_4N^+Cl^-$ in chloroform was in a similar state

Table 4.13 Intensities for the 115 cm^{-1} band of $Bu_4N^+Cl^-$ in $CHCl_3$

(L = 0.0208 cm, T = 293K)

concentration /mol dm^{-3}	area /cm^{-1}	average area /cm^{-1}	intensity /dm^3 mol^{-1} cm^{-2}
0.10	17.3 12.9	15.1	7 200±10 600
0.20	39.4 35.1	37.2	8 900± 5 300
0.30	50.6 56.6	53.6	8 600± 3 500
0.40	71.1 72.0	71.5	8 600± 2 600
0.52	107.9 104.2	106.0	9 900± 2 100
0.60	115.0 110.0	112.5	9 000± 1 800
0.69	126.4 146.0	136.2	9 400± 1 500
0.80	160.2 153.7	156.9	9 400± 1 300

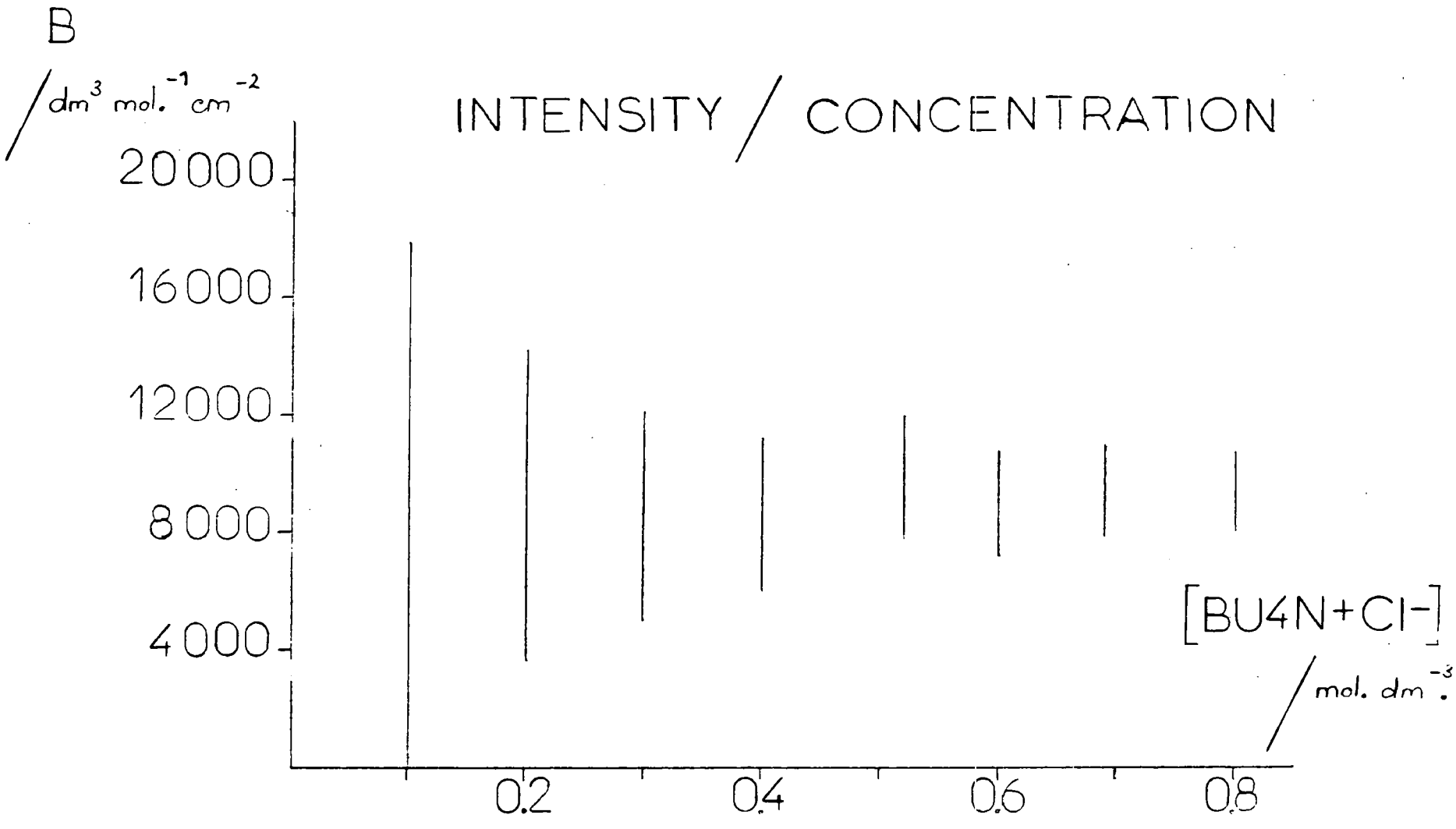

FIG. 4.27 BU4N+Cl- IN CHLOROFORM

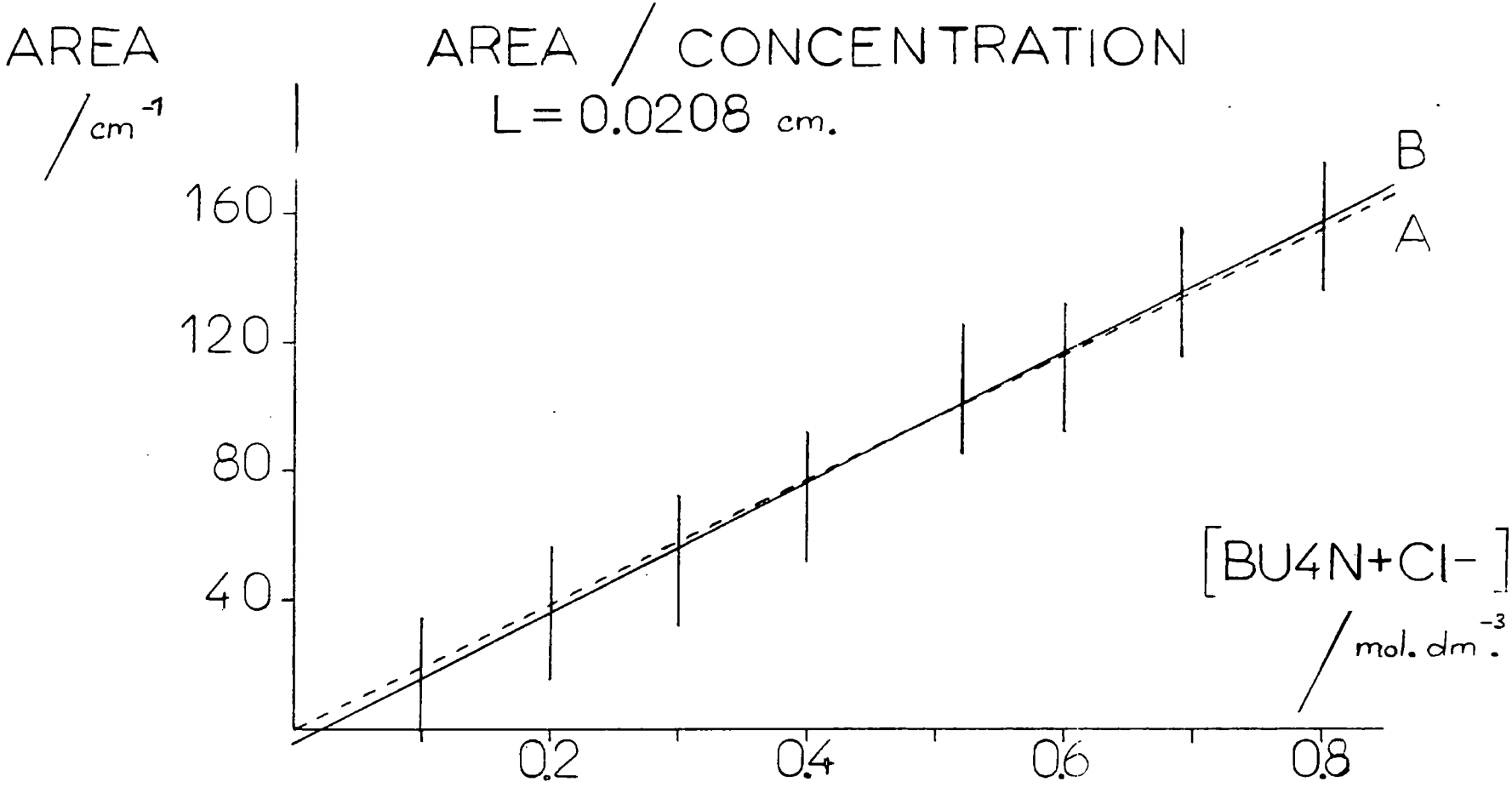

FIG. 4.28 BU4N+Cl− IN CHLOROFORM

of aggregation, throughout the concentration range 0.1 to 0.8 mol dm^{-3}, to the $Bu_4N^+Cl^-$ in benzene at approximately 0.4 mol dm^{-3}. The measured intensity further suggested that aggregation in the chloroform solvent was less extensive than in carbon tetrachloride, where the intensity was measured as 12 700±300 dm^3 mol^{-1} cm^{-2}.

4.8 Tetra-n-butylammonium bromide in chloroform

Spectra of $Bu_4N^+Br^-$ in $CHCl_3$ were recorded using a 100 gauge beam-splitter and a 0.0517 cm pathlength cell for concentrations between 0.21 and 0.64 mol dm^{-3}, and a pathlength of 0.0208 cm pathlength for a concentration of 0.69 mol dm^{-3}. Fig. 4.29 shows the spectrum observed for a 0.0517 cm pathlength of 0.345 mol dm^{-3} $Bu_4N^+Br^-$ in $CHCl_3$. The noise in the high frequency wing of the band was once again caused by the cut off of the 100 gauge beam-splitter, which was necessary to observe bands centred near 80 cm^{-1}. The band centre was measured as 79±3 cm^{-1}, and the half-band width as 50±5 cm^{-1}. The band appeared to be asymmetric to low frequency, and the overall profile suggested the possibility that a second component band was centred at 50±10 cm^{-1}. The integrated areas and calculated intensities for the far-infrared absorption of solutions of between 0.21 and 0.69 mol dm^{-3} $Bu_4N^+Br^-$ in $CHCl_3$ are shown in table 4.14. The weighted average of these intensities was taken as they showed such good agreement, and with a weighting factor of the reciprocal of the square of the standard deviation for the intensity at that particular concentration, the average intensity B_i was 3 900±500 dm^3 mol^{-1} cm^{-2}. Beers Law was thus seen to be adhered to very closely for the system $Bu_4N^+Br^-$ in $CHCl_3$ between 0.2 and 0.7 mol dm^{-3}. The intensity value fitted well with the 4 400 dm^3 mol^{-1} cm^{-2} measured for $Bu_4N^+Br^-$ in benzene.

4.9 Tetra-n-butylammonium iodide in chloroform

The effect of the anion on the far-infrared absorptions could be more extensively studied in chloroform than in either benzene or carbon tetrachloride, since the iodide, nitrate and perchlorate tetra-n-butyl-

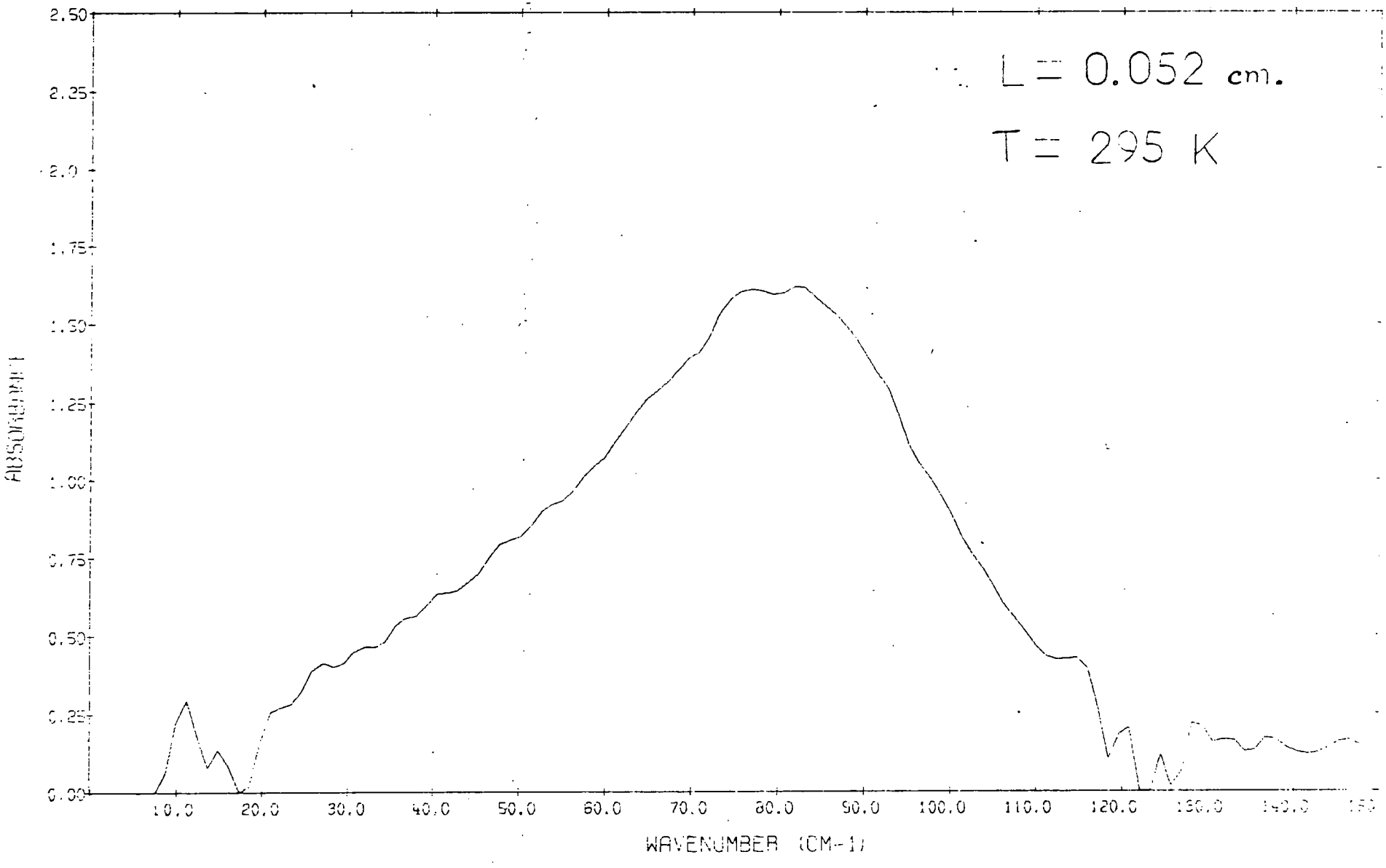

FIG. 4.29 0.345 mol. dm^{-3} $Bu_4N^+Br^-$ IN CHLOROFORM

Table 4.14 Intensities for the 80 cm^{-1} band for $Bu_4N^+Br^-$ in $CHCl_3$

(T = 290K, L = 0.0517 and 0.0208 cm)

concentration /mol dm^{-3}	area /cm^{-1}	average area /cm^{-1}	intensity /dm^3 mol^{-1} cm^{-2}
0.0517 cm pathlength			
0.21	41.3	39.3	3 600±2 000
	37.3		
0.25	53.0	57.3	4 400±1 700
	61.6		
0.35	74.2		
	70.1	70.9	3 900±1 200
	68.4		
0.47	91.3	92.3	3 800±1 000
	93.3		
0.56	117.4	112.3	3 900± 800
	107.2		
0.64	122.1	128.6	3 900± 700
	135.1		
0.0208 cm pathlength			
0.69	53.4	57.4	4 000±1 500
	61.4		

ammonium salts were all soluble in chloroform in sufficiently high concentrations for the absorptions to be observeable. The tetra-n-butylammonium iodide ($Bu_4N^+I^-$) was soluble to approximately 0.6 mol dm^{-3} in $CHCl_3$, whereas it was practically insoluble in benzene and CCl_4. (Less than 0.01 g of salt were soluble in 25 cm^3 of benzene, and hence the solubility was less than 0.0014 mol dm^{-3}.) The spectra for $Bu_4N^+I^-$ in $CHCl_3$ were recorded using a 100 gauge beam-splitter, and 0.0517 and 0.021 cm pathlength cells. The spectrum recorded for 0.0517 cm of 0.5112 mol dm^{-3} $Bu_4N^+I^-$ in $CHCl_3$ is shown in fig. 4.30. The band centre was measured as 61±3 cm^{-1}, and the half-band width as 50±5 cm^{-1}. The band appeared to be almost symmetrical about the band centre, and showed very little indication of the presence of a low frequency component. Table 4.15 shows the measured areas and corresponding intensities for the 3 concentrations of $Bu_4N^+I^-$ in $CHCl_3$ for which spectra were recorded. The weighted average intensity B_i was found to be 3 000±500 dm^3 mol^{-1} cm^{-2}.

4.10 Tetra-n-butylammonium nitrate in chloroform

Spectra of only one concentration of tetra-n-butylammonium nitrate ($Bu_4N^+NO_3^-$) in chloroform were recorded. The spectra were recorded for 0.0208 and 0.0517 cm pathlength by use of a 50 gauge beam-splitter. The spectrum observed for the 0.0517 cm pathlength of 0.324 mol dm^{-3} solution of $Bu_4N^+NO_3^-$ in $CHCl_3$ is shown in fig. 4.31. The band centre was measured as 100±3 cm^{-1}, and the half-band width as 65±5 cm^{-1}. The band appeared to be symmetric about the band centre. The integrated areas for the 0.324 mol dm^{-3} $Bu_4N^+NO_3^-$ in $CHCl_3$ solution were measured as 50.9±22 cm^{-1} for the 0.0208 cm pathlength, and 112.3±22 cm^{-1} for the 0.0517 cm pathlength, which gave intensities of 7 500±3 300 and 6 700±1 300 dm^3 mol^{-1} cm^{-2} respectively. The weighted average intensity B_i was found to be 6 800±1 800 dm^3 mol^{-1} cm^{-2}.

4.11 Tetra-n-butylammonium perchlorate in chloroform

A single spectrum for 0.618 mol dm^{-3} tetra-n-butylammonium

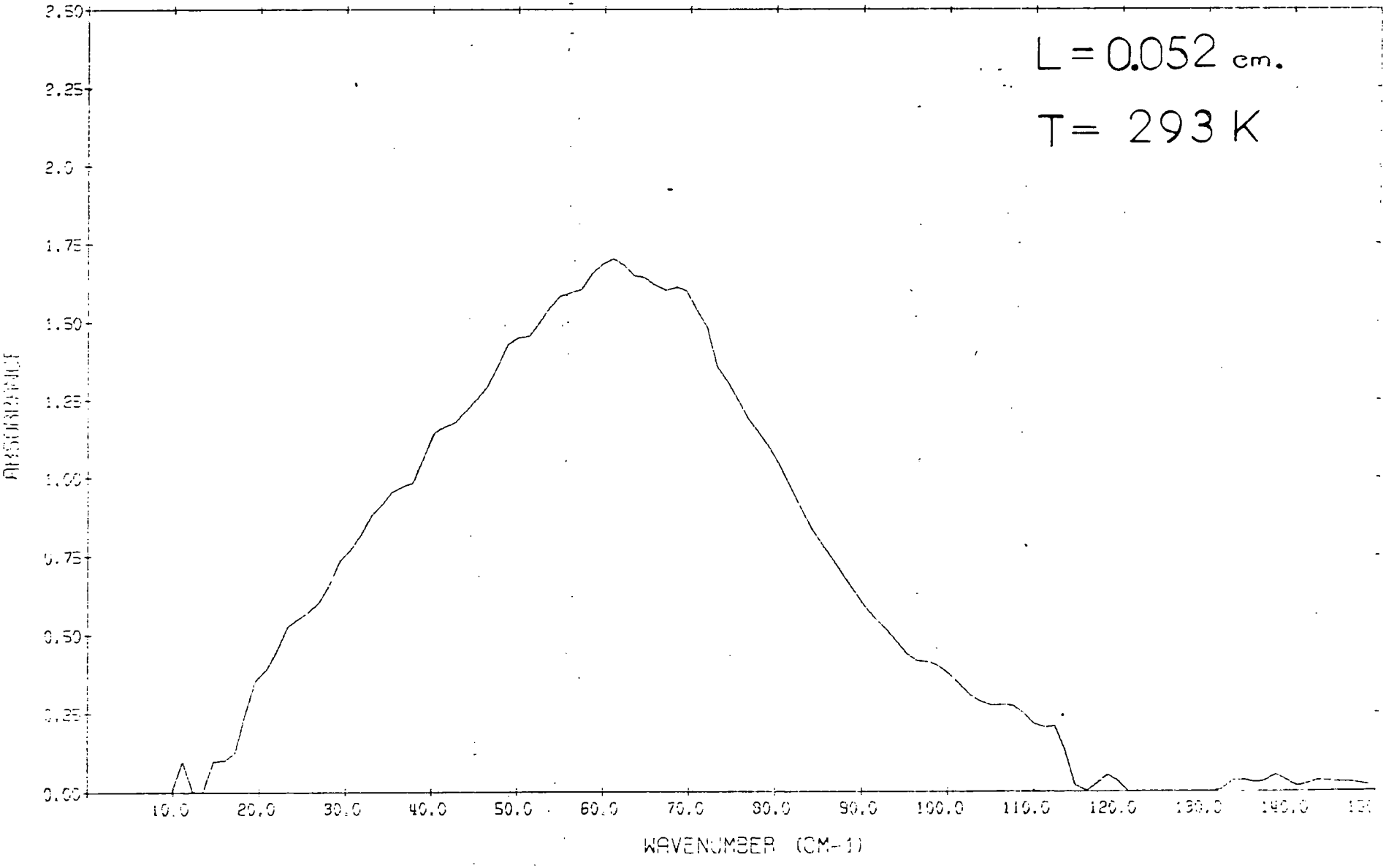

FIG. 4.30 0.542 M BU4N+I- IN CHLOROFORM

Table 4.15 Intensities for the 60 cm^{-1} band of $Bu_4N^+I^-$ in $CHCl_3$

(T = 293K, L = 0.052 cm)

concentration /mol dm^{-3}	area /cm^{-1}	average area /cm^{-1}	intensity /dm^3 mol^{-1} cm^{-2}
0.51	91.4	74.7	2 900±800
	57.9		
0.54	87.6	88.5	3 600±800
	89.3		
0.59	91.0	91.0	3 000±700

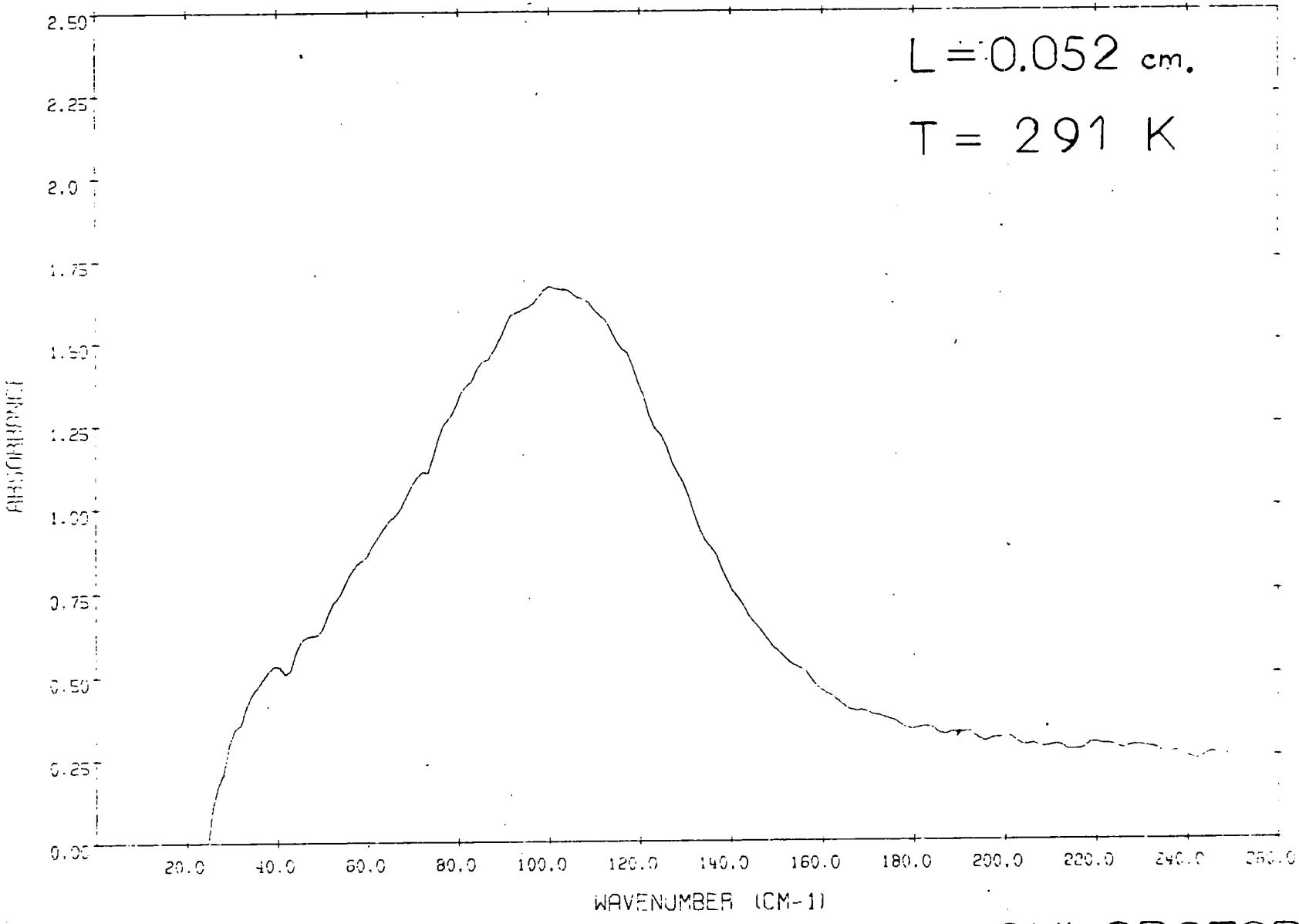

FIG.4.31 0.324 M BU4N+NO3- IN CHLOROFORM

perchlorate ($Bu_4N^+ClO_4^-$) in $CHCl_3$ was recorded using a 100 gauge beam-splitter, and a 0.0208 cm pathlength. The measured band centre was 85±3 cm^{-1}, and the half-band width was 65±5 cm^{-1}. The integrated area was measured as 95.5±22 cm^{-1}, which gave an intensity B_i of 7 400±1 700 dm^3 mol^{-1} cm^{-2}.

4.12 Tetra-n-butylammonium chloride in tetrahydrofuran

Attempts were made to observe the far-infrared absorptions of $Bu_4N^+Cl^-$ in more polar solvents, in the hope that these systems would throw more light on the nature of the interaction of the solvent with the dissolved salt. These studies were hampered by the increasing low frequency absorption of the solvent itself, as it became more polar. This 'Poley-Hill' absorption mechanism involves the 'libration' of the permanent dipole moment of the polar solvent molecule in the field of the polar solvent molecules surrounding it. This becomes very intense for highly polar molecules such as acetone, where the resulting broad absorption was centred at approximately 75 cm^{-1}. (See chapter 6.) These strong absorptions of the solvent caused severe 'ratioing out' problems, and made it impossible to record the far-infrared absorptions for the $Bu_4N^+Cl^-$ salt in either acetone or acetonitrile. The necessary pathlength to obtain approximately 50% transmission through the acetone was 0.005 cm, at which pathlength the 120 cm^{-1} absorption of the salt was not observable for a salt concentration of 4.0 mol dm^{-3} $Bu_4N^+Cl^-$ in acetone. Attempts were also made to dilute the acetone solvent in cyclohexane prior to dissolution of the salt. These attempts failed because the $Bu_4N^+Cl^-$ salt became almost insoluble in the acetone/cyclohexane mixture. The maximum concentration of $Bu_4N^+Cl^-$ which could be dissolved in 1.0 mol dm^{-3} acetone solution in cyclohexane was 0.03 mol dm^{-3} with respect to the acetone concentration in the sovent mixture. The 120 cm^{-1} absorption of the $Bu_4N^+Cl^-$ salt was not observable at this concentration at a pathlength of 0.02 cm, which was the maximum possible to obtain spectra with reasonable signal-to-noise ratios.

The lack of solubility of the $Bu_4N^+Cl^-$ in the acetone/cyclohexane and acetone/carbon disulphide mixtures indicated that the possible sites, in the acetone molecule for the solvation of the interacting species were being taken up by interactions with the inert solvent. This left few sites to act in the solvation of the $Bu_4N^+Cl^-$ salt and made the salt almost insoluble in the mixture.

The ratioed spectra of $Bu_4N^+Cl^-$ in acetone/cyclohexane against acetone/cyclohexane obtained in the above study, showed a broad residual absorption in the 75 cm^{-1} region. This suggested that the Poley-Hill absorption of the acetone was being intensified in the solution, and was thus not being completely ratioed out. The work performed in an investigation of the effect of dissolved salts on the acetone Poley-Hill absorption is contained in chapter 6. It was concluded that observations of the far-infared absorptions of the tetra-n-alkylammonium salts in highly polar solvents was impossible with the present experimental facilities.

Tetrahydrofuran (THF) was chosen as a solvent of medium polarity, and a spectrum of 1.28 mol dm^{-3} $Bu_4N^+Cl^-$ in THF was eventually obtained using a pathlength of 0.0205 cm. The spectrum is shown in fig. 4.32. This spectrum had a very low signal-to-noise ratio, because of the ratioing out of the Poley-Hill absorption, which was still much more intense than the 120 cm^{-1} band of the dissolved salt. The band centre was measured as 110±5 cm^{-1}, and the half-band width as 85±10 cm^{-1}. The integrated areas were measured by planimeter only, and the average area for the two spectra was calculated as 183 cm^{-1}, which gave an intensity B_i of 7 140±860 dm^3 mol^{-1} cm^{-2}, if the usual precision of ±22 cm^{-1} was assumed. This intensity was approximately the same as that obtained for 0.05 mol dm^{-3} $Bu_4N^+Cl^-$ in benzene, and this suggested that the aggregation of the $Bu_4N^+Cl^-$ in the THF solvent was low, as would be expected from the solvating nature of the THF. The band was once again clearly asymmetric to low frequency, and this suggested the presence of a low frequency component, possibly centred at

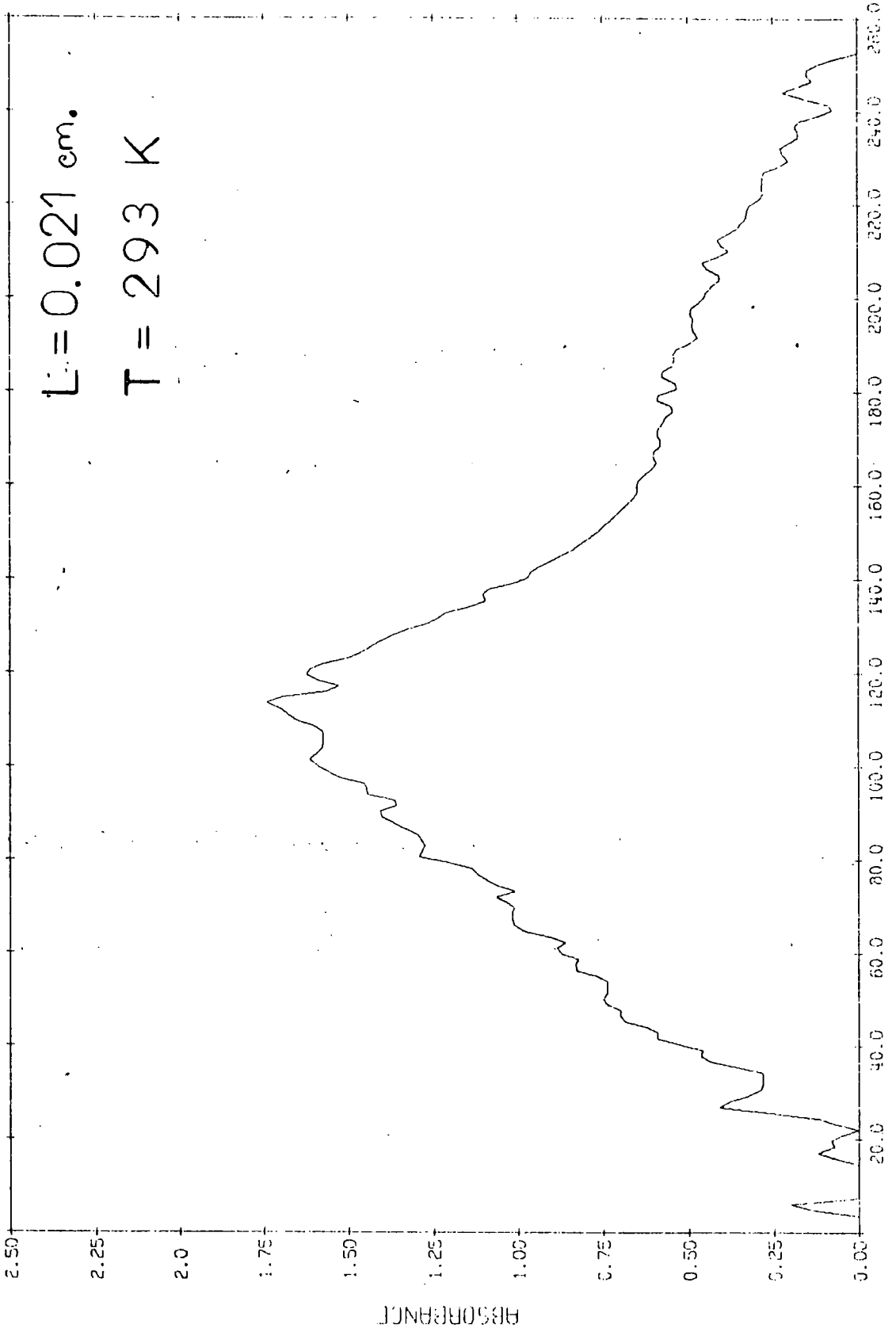

FIG. 4.32 1.28 M BU4N+Cl- IN TETRAHYDROFURAN

$60\pm10\ cm^{-1}$

4.13 Indications for the presence of a high frequency component in the overall absorption profiles

On careful comparison of the observed absorption spectra for the tetra-n-alkylammonium salts in various solvents it was noticed that, in addition to some of the spectra exhibiting low frequency components in the overall profile, some spectra also exhibited a high frequency component. $Bu_4N^+Cl^-$ showed such a component in all 4 solvents studied (benzene, CCl_4, $CHCl_3$ and THF). The band was clearly present in the spectrum of $Bu_4N^+Cl^-$ in benzene as can be seen from fig. 4.1. This spectrum indicated that the high frequency component would have a band maximum at about $180\pm10\ cm^{-1}$. This high frequency band was seen to be once again present for the CCl_4 solutions as can be seen from fig. 4.20, but the band appeared to be centred at a slightly higher frequency than for the benzene solution, the band centre now being at about $190\pm10\ cm^{-1}$. For $Bu_4N^+Cl^-$ in $CHCl_3$ the band was very weak, and there was some doubt as to its presence. However, careful comparison of the band profile on either side of the major band maximum at $120\ cm^{-1}$ showed that a weak broad band was present, centred at 180 to 190 cm^{-1}, as can be seen from fig. 4.26. The concentration of the salt was approximately the same for all the three spectra compared, and so it was concluded that it was not the salt concentration which was the deciding factor for the intensity of the high frequency component. A high frequency component centred at about $180\pm10\ cm^{-1}$ was clearly visible in the spectra of $Bu_4N^+Cl^-$ in THF solutions, as can be seen from fig. 4.32.

The spectra of $Hp_4N^+Cl^-$ in benzene indicated the presence of a fairly intense high frequency component in the overall absorption profile, as can be seen from fig. 4.19, where the frequency of the band centre was seen to occur at $180\pm5\ cm^{-1}$. In the spectra of $Pe_4N^+Cl^-$ in benzene the presence of the high frequency component was by no means obvious, as can be seen from fig. 4.18. Comparison of the profiles on either side of the

major band centre for this system was made more difficult, because of the presence of the strong low frequency component in the overall absorption profile.

The bromide salts showed no such high frequency component in any of the 3 solvents studied (benzene, CCl_4, and $CHCl_3$). It was necessary to record some spectra of the bromide salts with a 50 gauge beam-splitter, so that the high frequency tail of the major absorption at 80 cm^{-1} could be observed without degrading due to the 100 gauge beam-splitter cut-off, which would cause very poor signal-to-noise ratios in the region of the tail. The spectrum for 0.1023 cm pathlength of 0.637 mol dm^{-3} $Bu_4N^+Br^-$ in $CHCl_3$, recorded using a 50 gauge beam-splitter, is shown in fig. 4.33. This spectrum showed that even when the main absorption at 80 cm^{-1} was greater than 2.5 absorbance units, no higher frequency absorptions were detectable below 240 cm^{-1}. A similar spectrum, obtained with a 25 gauge beam-splitter showed a smooth baseline after the high frequency wing of the 80 cm^{-1} band until the 25 gauge beam-splitter cut-off at 440 cm^{-1}.

Fig. 4.34 shows the spectrum obtained for 0.0517 cm pathlength of 0.564 mol dm^{-3} $Bu_4N^+I^-$ in $CHCl_3$ recorded with a 50 gauge beamsplitter. This spectrum showed clearly that no high frequency component was making significant changes to the overall absorption profile for the spectrum of $Bu_4N^+I^-$ in $CHCl_3$. Similarly fig. 4.35 shows the spectrum obtained using a 50 gauge beam-splitter for a 0.01 cm pathlength of saturated $Bu_4N^+ClO_4^-$ in $CHCl_3$. This spectrum once again showed a 'clean' wing to the 85 cm^{-1} band, and a smoothly curving wing was likewise observed for $Bu_4N^+NO_3^-$ in $CHCl_3$, indicating that there was no high frequency component in the spectra for these two systems.

It was thus concluded that the high frequency component was present only in the tetra-n-alkylammonium chloride salt solutions. The solvent was seen not to be the deciding factor whether the high frequency band occurred or not. However, the solvent did have a marked effect on the

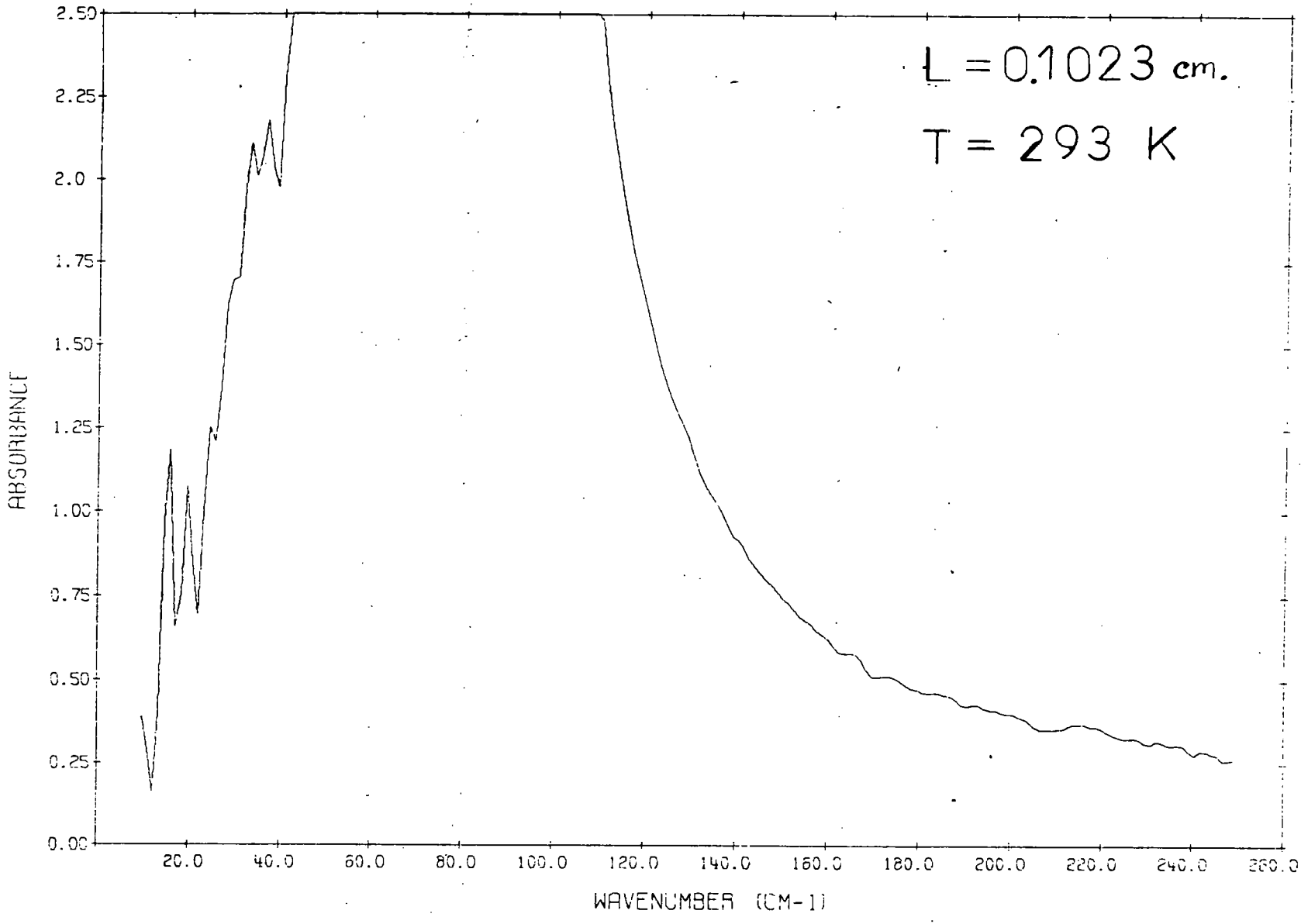

FIG.4.33 0.6365 M BU4N+Br- IN CHLOROFORM

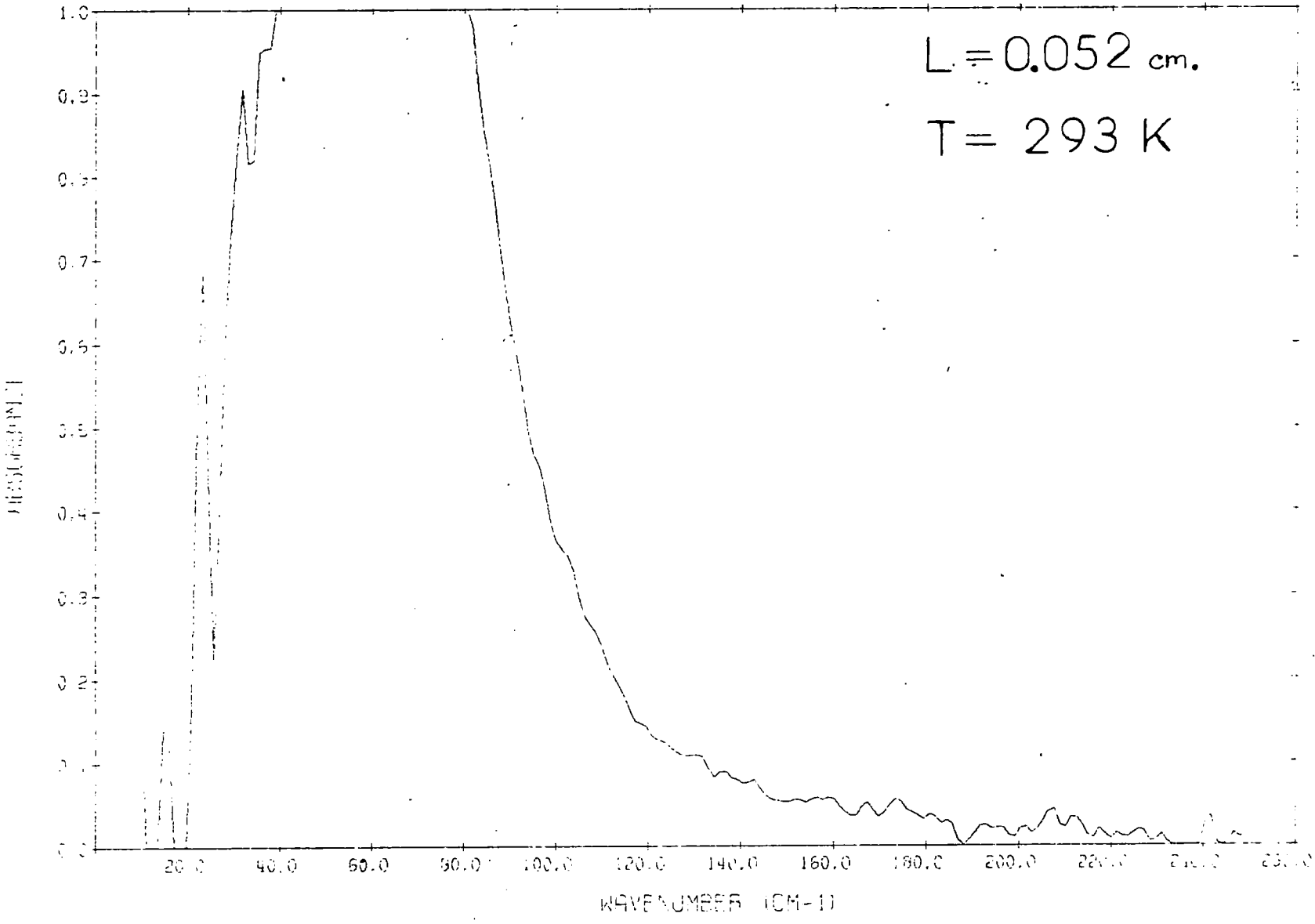

FIG.4.34 0.5462 M BU4N+I- IN CHLOROFORM

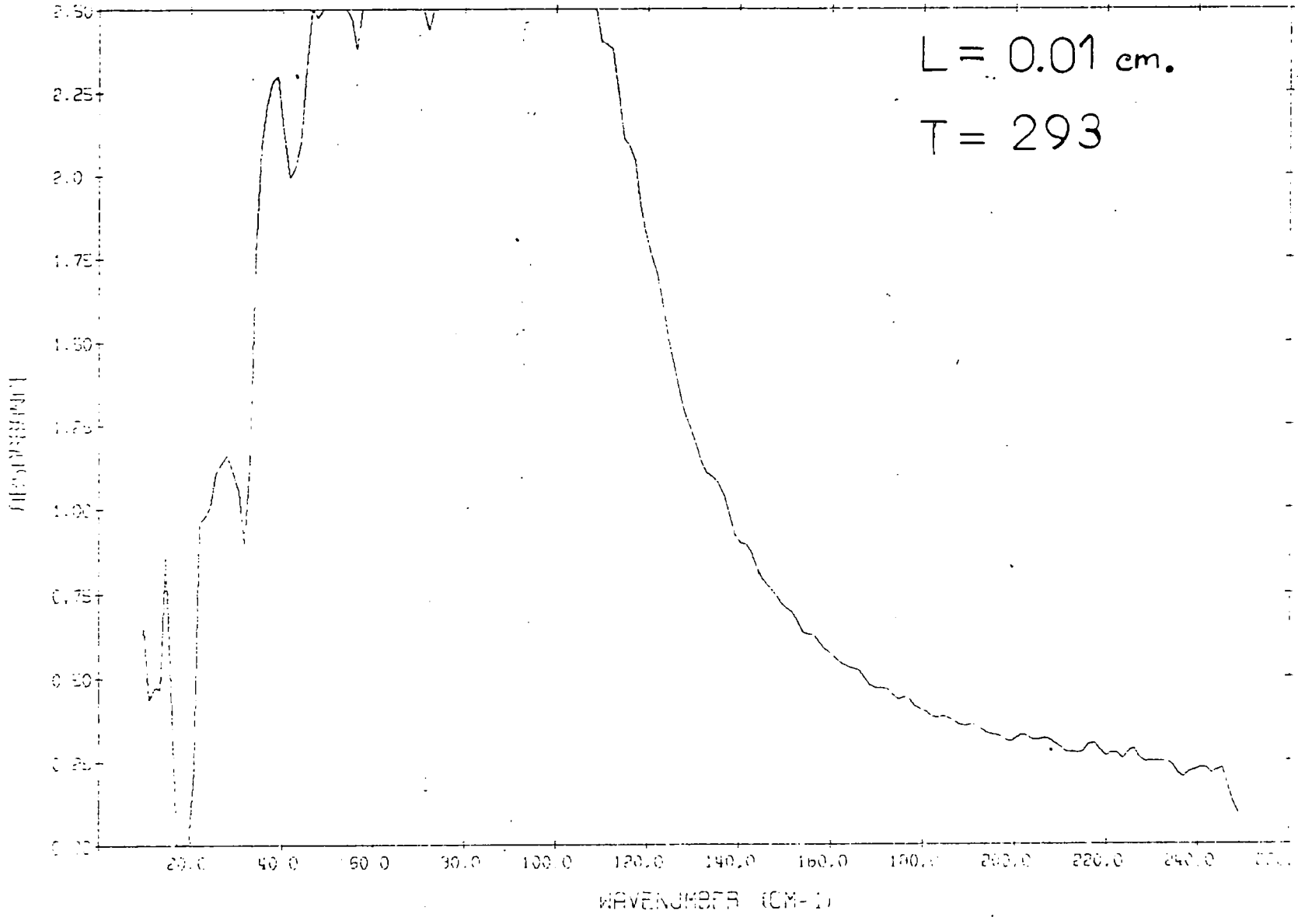

FIG.4.35 SATURATED BU4N+CIO4 IN CHLOROFORM

intensity of this high frequency component, since the $CHCl_3$ solvent reduced the band intensity greatly from that in the benzene solvent. The effect of cation on this band was seen to be small for the Bu_4N^+ and Hp_4N^+ salts, but the small intensity for the Pe_4N^+ salt (if a high frequency component appeared at all) indicated that the cation was possibly playing some role in the interactions giving rise to the high frequency absorption. Chapter 5 contains the results of computer fitting techniques to the overall absorption profile in attempts to resolve out component bands for these systems.

4.14 Summary

The intensity of the low frequency absorption was found to be concentration dependent for 3 salts ($Bu_4N^+Cl^-$, $Pe_4N^+Cl^-$ and $Hp_4N^+Cl^-$) in benzene but independent of concentration for the remaining tetra-n-alkylammonium salts in benzene, and for all the tetra-n-alkylammonium salts in the 3 other solvents studied (CCl_4, $CHCl_3$ and THF). For the $Bu_4N^+Cl^-$ salt in benzene the maximum intensity was seen to occur at about 0.8 mol dm^{-3} salt, indicating that at this concentration of the salt the size of the ion aggregates was at a maximum. Addition of water to the $Bu_4N^+Cl^-$ in benzene system decreased the overall intensity of the low frequency absorption, indicating that the salt aggregate was being broken down as interaction of the salt occurred preferentially with the water, rather than with the benzene. The intensity of the overall low frequency profile for $Bu_4N^+Cl^-$ in benzene was little affected by increasing temperature, except when the temperature approached the boiling point of the benzene solution, where a slight increase in absorption intensity occurred.

The values for band centre, half-band width and intensity for the overall profiles of the low frequency far-infrared profiles of the tetra-n-alkylammonium salts in the various solvents studied are summarised in tables 4.16 to 4.18. The suggested presence of low and high frequency components to the overall profiles is summarised in tables 4.19 and 4.20.

Table 4.16 Band centres for tetra-n-alkylammonium salt absorptions in various solvents

(all cm^{-1})

salt	C_6H_6	CCl_4	$CHCl_3$	THF
$Bu_4N^+Cl^-$	115±3	114±2	118±3	110±5
$Bu_4N^+Br^-$	80±3	73±3	79±3	------
$Bu_4N^+I^-$	insoluble	insoluble	61±3	------
$Bu_4N^+NO_3^-$	insoluble	insoluble	100±3	------
$Bu_4N^+ClO_4^-$	insoluble	insoluble	85±3	------
$Pe_4N^+Cl^-$	115±3	------	------	------
$Hp_4N^+Cl^-$	112±3	------	------	------

------ spectra not recorded

Table 4.17 Half-band widths for tetra-n-alkylammonium salt absorptions in various solvents

(all cm^{-1})

salt	C_6H_6	CCl_4	$CHCl_3$	THF
$Bu_4N^+Cl^-$	80±3	80±3	55±3	85±3
$Bu_4N^+Br^-$	70±3	50±5	50±5	------
$Bu_4N^+I^-$	insoluble	insoluble	50±5	------
$Bu_4N^+NO_3^-$	insoluble	insoluble	65±5	------
$Bu_4N^+ClO_4^-$	insoluble	insoluble	65±3	------
$Pe_4N^+Cl^-$	75±5	------	------	------
$Hp_4N^+Cl^-$	80±5	------	------	------

Table 4.18 Intensities for tetra-n-alkylammonium salt absorptions in various solvents

(all $dm^3\ mol^{-1}\ cm^{-2}$)

salt	C_6H_6	CCl_4	$CHCl_3$	THF
$Bu_4N^+Cl^-$	14 900±800[a]	12 300±500	9 700±300	7 140±860
$Bu_4N^+Br^-$	4 620±250	6 000±1 700	3 900±500	------
$Bu_4N^+I^-$	insoluble	insoluble	3 000±500	------
$Bu_4N^+NO_3^-$	insoluble	insoluble	6 800±1 800	------
$Bu_4N^+ClO_4^-$	insoluble	insoluble	7 400±1 700	------
$Pe_4N^+Cl^-$	6 000±1 000[a]	------	------	------
$Hp_4N^+Cl^-$	8 400±1 400[a]	------	------	------

------ spectra not recorded

[a] concentration dependent

Table 4.19 Low frequency component frequencies for tetra-n-alkylammonium salts in various solvents

(all cm^{-1})

salt	C_6H_6	CCl_4	$CHCl_3$	THF
$Bu_4N^+Cl^-$	70	70	? 40	60
$Bu_4N^+Br^-$	70	? 70	? 40	------
$Bu_4N^+I^-$	insoluble	insoluble	35	------
$Bu_4N^+NO_3^-$	insoluble	insoluble	< 40	------
$Bu_4N^+ClO_4^-$	insoluble	insoluble	< 40	------
$Pe_4N^+Cl^-$	70	------	------	------
$Hp_4N^+Cl^-$	70	------	------	------

------ spectra not recorded

Table 4.20 High frequency components for tetra-n-alkylammonium salts in various solvents

($\grave{a}b^{-1}\,cm^{-1}$)

salt	C_6H_6	CCl_4	$CHCl_3$	THF
$Bu_4N^+Cl^-$	180	180	180	180
$Bu_4N^+Br^-$	none	none	none	------
$Bu_4N^+I^-$	insoluble	insoluble	none	------
$Bu_4N^+NO_3^-$	insoluble	insoluble	none	------
$Bu_4N^+ClO_4^-$	insoluble	insoluble	none	------
$Pe_4N^+Cl^-$	180	------	------	------
$Hp_4N^+Cl^-$	185	------	------	------

------ spectra not recorded

none no high frequency component

CHAPTER 5

COMPUTER FITTING TO THE SPECTRAL PROFILES FOR TETRA-N-ALKYLAMMONIUM SALTS

5.1 Band fitting theory

In chapter 4 it was seen that the profiles of the absorption bands for tetra-n-alkylammonium salts in various solvents indicated the presence of more than one component. In order to study the interactions occurring for these systems the concentration dependence of the individual components has been determined. The resolution process was achieved by using computer band-fitting techniques, which are described in this chapter.

Two basic mathematical functions can be used to represent the profile of an absorption band. These are the Cauchy and Gaussian functions, which in their simplest forms are;

$$\text{Cauchy} \qquad y = a/(b^2+c^2) \qquad 5.1$$

$$\text{Gaussian} \qquad y = a.\exp(-b^2/c^2) \qquad 5.2$$

Strong (65) used both the Cauchy and Gaussian functions, and also a sum function containing both Cauchy and Gauss components, in his band fitting studies. These functions were given as (65);

$$\text{Cauchy} \qquad C(\bar{\nu}) = a/\{b^2+(\bar{\nu}-\bar{\nu}_o)^2\} \qquad 5.3$$

where $\bar{\nu}_o$ = wavenumber of band maximum

$2b = (\Delta\bar{\nu}_{\frac{1}{2}C})^{-1}$

$\Delta\bar{\nu}_{\frac{1}{2}C}$ = band width of Cauchy component at half peak height

a/b^2 = peak height

$$\text{Gauss} \qquad G(\bar{\nu}) = a/b^2.\exp\{-\ln 2(\bar{\nu}-\bar{\nu}_o/b)^2\} \qquad 5.4$$

where $b = 2(\ln 2)^{\frac{1}{2}}/\Delta\bar{\nu}_{\frac{1}{2}G}$

$\Delta\bar{\nu}_{\frac{1}{2}G}$ = band width of Gauss component at half peak height

$$\text{Sum function} \qquad S(\bar{\nu}) = f.G(\bar{\nu}) + (1-f).C(\bar{\nu}) \qquad 5.5$$

where f = fraction Gauss

Pitha and Jones (66) used a product function to represent the band profile, where;

$$P(\bar{\nu}) = h.\exp\{-X_2{}^2(\bar{\nu}-\bar{\nu}_o)^2\}/\{1+X_1{}^2(\bar{\nu}-\bar{\nu}_o)^2\} \qquad 5.6$$

where h = peak height

$X_1 = 1/\frac{1}{2}\Delta\bar{\nu}_{\frac{1}{2}C}$

$$X_2 = \ln 2/(\tfrac{1}{2}\Delta\bar{\nu}_{\frac{1}{2}G})^2$$

Seshadii and Jones (67) represented the Cauchy and Gauss functions by;

$$\text{Cauchy} \quad K_c(\bar{\nu}) = X_1/\{1+X_3^2(\bar{\nu}-X_2)^2\} \qquad 5.7$$

$$\text{Gauss} \quad K_g(\bar{\nu}) = X_1.\exp\{-X_4^2(\bar{\nu}-X_2)^2\} \qquad 5.8$$

where X_1 = peak height

X_2 = wavenumber of band maximum

$X_3 = (b_{Cauchy})^{-1}$ = 0 for pure Gauss

$X_4^2 = \ln 2/(b_{Gauss})^2$ = 0 for pure Cauchy

The Cauchy-Gauss product and sum functions were represented as;

$$\text{Product} \quad K_p(\bar{\nu}) = X_1/\{1+X_3^2(\bar{\nu}-X_2)^2.\exp\{-X_4^2(\bar{\nu}-X_2)^2\} \qquad 5.9$$

$$\text{Sum} \quad K_s(\bar{\nu}) = X_1/\{1+X_3^2(\bar{\nu}-X_2)^2\}+ X_5.\exp\{-X_4^2(\bar{\nu}-X_2)^2\} \qquad 5.10$$

For the sum function

X_1 = peak height of Cauchy component

X_5 = peak height of Gauss component

Now eqn. 5.3 can be rewritten as;

$$C(\bar{\nu}) = a/b^2\{1+b^2(\bar{\nu}-\bar{\nu}_o)^2\} \qquad 5.11$$

Eqns. 5.7 and 5.11 can now be compared;

$$X_1 = a/b^2 = \text{peak height} \qquad 5.12$$

$$X_3 = b = 2/\Delta\bar{\nu}_{\frac{1}{2}Cauchy} \qquad 5.13$$

Eqns. 5.4 and 5.8 can be compared;

$$X_1 = a/b^2 = \text{peak height} \qquad 5.14$$

$$X_4 = (\ln 2)^{\frac{1}{2}}/b = 2(\ln 2)^{\frac{1}{2}}/\Delta\bar{\nu}_{\frac{1}{2}Gauss} = 1.665/\Delta\bar{\nu}_{\frac{1}{2}G} \qquad 5.15$$

To demonstrate the difference between the Cauchy and Gauss profiles, these have been plotted as a function of wavenumber for a peak height of 0.1 units, band centre 100 cm^{-1} and half-band width 50 cm^{-1}. Eqn. 5.7 was used to obtain the Cauchy profile with parameters X_1 = 1.0, X_2 = 100.0 and X_3 = 0.04 ($X_3 = 2/\Delta\bar{\nu}_{\frac{1}{2}}$). The Gauss profile was obtained using eqn. 5.8 with parameters X_1 = 1.0, X_2 = 100.0 and X_4 0.0333 ($X_4 = 1.665/\Delta\bar{\nu}_{\frac{1}{2}}$). The profiles are given in table 5.1, and the data was plotted as a function of wavenumber in fig. 5.1. This figure shows clearly the difference between the profiles, and shows

Table 5.1 Cauchy and Gauss profiles ($X_1 = 1.0$, $X_2 = 100$, $X_3 = 0.04$, $X_4 = 0.0333$).

wavenumber	K_{Cauchy}	K_{Gauss}	wavenumber
0	0.0588	0.0000	200
5	0.0692	0.0001	195
10	0.0716	0.0001	190
15	0.0797	0.0003	185
20	0.0890	0.0008	180
25	0.1000	0.0020	175
30	0.1131	0.0044	170
35	0.1288	0.0093	165
40	0.1479	0.0183	160
45	0.1712	0.0347	155
50	0.1996	0.0626	150
55	0.2358	0.1059	145
60	0.2808	0.1697	140
65	0.3378	0.2572	135
70	0.4099	0.3690	130
75	0.5000	0.5000	125
80	0.6098	0.6421	120
85	0.7354	0.7788	115
90	0.8620	0.8949	110
95	0.9616	0.9724	105
100	1.0000	1.0000	

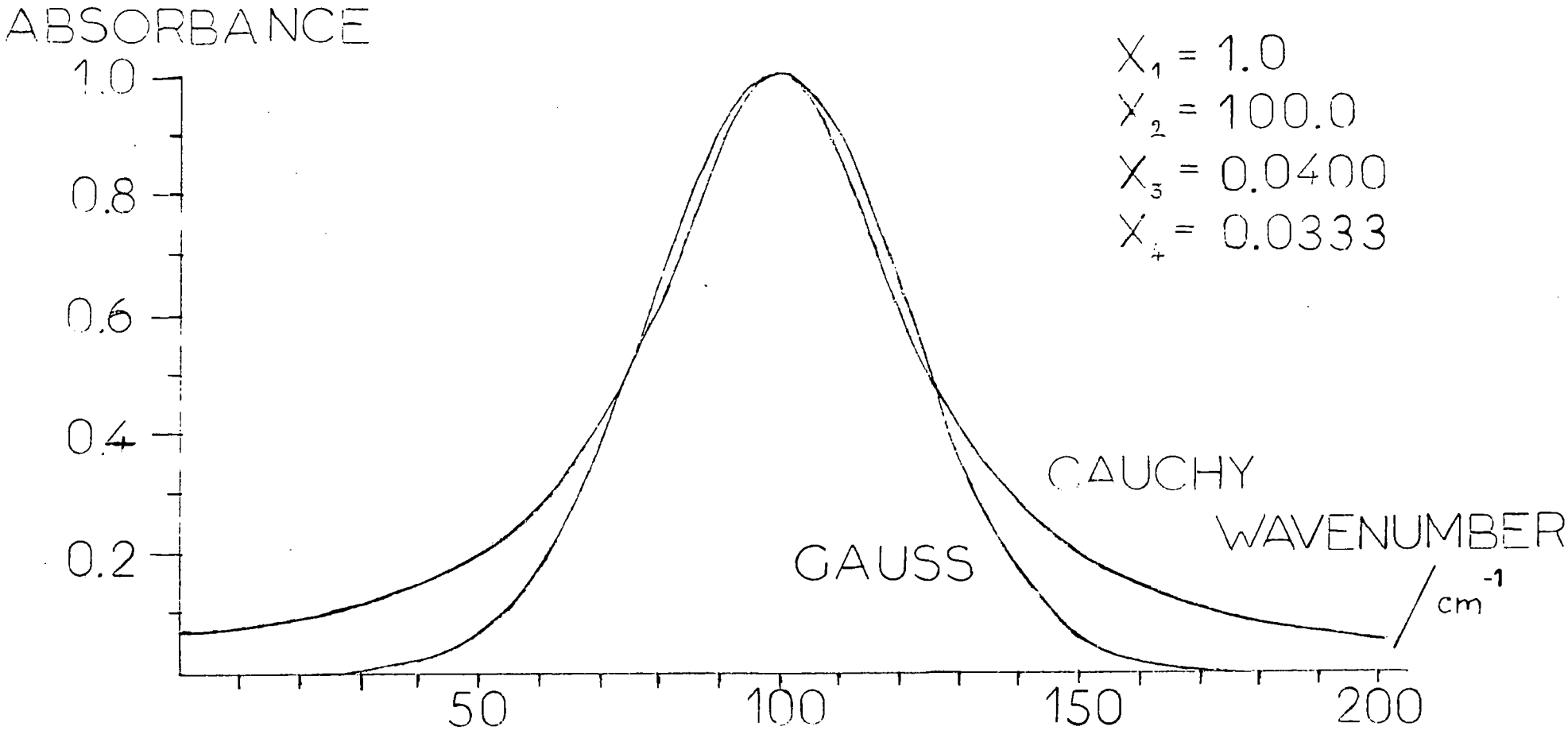

FIG. 5.1 PURE CAUCHY AND GAUSS BAND PROFILES

that a larger percentage of the area under the Gauss profile occurs within the half-band width, than for the Cauchy profile. The Cauchy profile is more intense in the wings than is the Gauss profile.

The intensity of a band can be calculated from the area under the absorption curve, and can be determined from the band profile by integrating the function representing the profile between the wavenumber limits of the band.

For the Cauchy profile;

$$\text{area} = \text{integral} = \int_{-\infty}^{+\infty} a/\{(\bar{\nu}-\bar{\nu}_0)^2 + b^2\}.d\bar{\nu} \qquad 5.16$$

This integration was performed by complex integration techniques (ref. 68, chapter 7 and ref. 69, chap. 17). The integral was first written as;

$$I = \int_{-\infty}^{+\infty} a/(\bar{\nu}-\bar{\nu}_0+bj)(\bar{\nu}-\bar{\nu}_0-bj) \qquad 5.17$$

where $j = (-1)^{\frac{1}{2}}$

The integral was then found as $I = 2\pi j\Sigma$residuals at the points of singularity. A point of singularity is obtained when the denominator of the function tends to zero.

when $\bar{\nu} = \bar{\nu}_0+bj$ then $a/(\bar{\nu}-\bar{\nu}_0+bj)(\bar{\nu}-\bar{\nu}_0-bj)$ tends to infinity

since $\bar{\nu}-\bar{\nu}_0-bj = 0$

Hence $\bar{\nu} = \bar{\nu}_0+bj$ was a point of singularity within the region, which in this case was a semi-circle in the upper half of the complex plane mounted on the real axis, and was the only point of singularity in this region for this function.

Therefore $I = 2\pi j$(residue for $\bar{\nu} = \bar{\nu}_0+bj$)

$$\text{Now residue} = \lim_{\bar{\nu}\mapsto\bar{\nu}_0+bj} a(\bar{\nu}-\bar{\nu}_0-bj)/(\bar{\nu}-\bar{\nu}_0-bj)(\bar{\nu}-\bar{\nu}_0+bj)$$

$$= \lim_{\bar{\nu}\mapsto\bar{\nu}_0+bj} a/(\bar{\nu}-\bar{\nu}_0+bj)$$

$$= a/(\bar{\nu}_0+bj-\bar{\nu}_0+bj)$$

Therefore residue $= a/2bj$

$$I = 2\pi ja/2bj = \pi a/b$$

$$\text{Area} = I = \pi a/b \qquad 5.18$$

In the Seshadii and Jones notation (67) this becomes;

$$\text{Cauchy area} = \pi X_1/X_3 \qquad 5.19$$

For the Gauss profile;

$$\text{Area} = I = \int_{-\infty}^{+\infty} a/b^2.\exp\{-\ln 2(\bar{\nu}-\bar{\nu}_0/b)^2\}.d\bar{\nu} \qquad 5.20$$

This can be integrated by substitution;

let $x = \bar{\nu}-\bar{\nu}_0$ then by differentiation $dx/d\bar{\nu} = 1$ i.e. $dx = d\bar{\nu}$

$$\text{Therefore } I = a/b^2 \int_{-\infty}^{+\infty} \exp\{-\ln 2.x^2/b^2\}.dx \qquad 5.21$$

making a further substitution $y = (\ln 2/b^2)^{\frac{1}{2}}.x$

therefore $y^2 = \ln 2.x^2/b^2$ $\quad dy/dx = (\ln 2/b^2)^{\frac{1}{2}}$

$$dx = dy.(b^2/\ln 2)^{\frac{1}{2}}$$

rewritting eqn. 5.21 gives;

$$I = a/b^2 \int_{-\infty}^{+\infty} \exp\{-y^2\}.(b^2/\ln 2)^{\frac{1}{2}}.dy \qquad 5.22$$

$$I = a/b(\ln 2)^{\frac{1}{2}} \int_{-\infty}^{+\infty} \exp\{-y^2\}.dy \qquad 5.23$$

This is now a standard integral (68,69);

$$\int_{-\infty}^{+\infty} e^{-u^2}.\,du = \pi^{\frac{1}{2}}$$

$$\text{Therefore } I = a\pi^{\frac{1}{2}}/b(\ln 2)^{\frac{1}{2}}$$

$$\text{Area} = I = a/b(\pi/\ln 2)^{\frac{1}{2}} \qquad 5.24$$

In the Seshadii and Jones notation (67) this becomes;

$$\text{Area} = \pi^{\frac{1}{2}}.X_1/X_4$$

$$\text{Area} = 1.772X_1/X_4 \qquad 5.25$$

5.2 Preliminary fits and precision tests

The absorbance as a function of wavenumber data obtained from the DCH0512 programme (27) was analysed using the Pitha and Jones PC118 Spectral Band Fit Optimisation Programme No. 3 (70). This programme matches the experimental band profile to the overall profile obtained from the sum of the component bands. Guessed values for X_1 (the peak height), X_2 (the band centre) and X_3 (controlling the Cauchy half-band width) or X_4 (controlling the Gauss half-band width) were fed to the programme after the experimental absorbance data. The programme generates the absorbance profile for the component bands and then sums these to give the total fitted

profile. This is then compared with the experimental profile, and the mean discrepance calculated. The mean discrepance is the sum of the differences between experimental and fitted profiles, and thus the 'dis' factor measures the precision of the fit. An iterative process changes the inputted variables, and 'dis' is minimised to give the 'best' fit. The iterative process is controlled by 3 parameters, UP, DOWN and CHANGE, which determine how the wavenumber, half-band width and peak height for the various components were varied in the search for the best fit. These parameters were fixed throughout our study as UP = 1000.0, DOWN = 0.01 and CHANGE = 0.5. The symmetrical triangular slit function was used throughout, and a spectral slit width of 2.5 cm^{-1} was used for the parameter SSW, for the absorption profiles obtained from interferograms with a total of 1024 points (see chapter 3).

The observed far-infrared bands for the tetra-n-alkylammonium salt systems were fitted to pure gauss components, since there appeared to be no appreciable absorption in the wings of the bands. The fitting of the absorption profiles to Gauss functions must be considered carefully. It was possible to obtain a close fit to Gauss functions for a Cauchy profile, where there had been considerable truncation of the wings of the band. Truncation of the wings almost certainly occurred for the tetra-n-alkylammonium salts spectra, due to baseline fitting errors for the very broad absorptions (see chapter 3). The fits could thus only be used as a means for gaining band parameters for comparison with those obtained using the same procedures for other systems. The fits could not be used to detect the percentage of a band which was of Cauchy or Gauss profile, and thus could not be used to assist in the determination of the mode of interactions in these systems. The fitting procedures were thus used only as a means of resolving the overlapping bands. The fits were then used to give band centres, half-band widths and areas, from which intensities were calculated for the components.

The sum function of eqn. 5.9 was used for a few preliminary

fits for the systems $Bu_4N^+Cl^-$ in benzene, $CHCl_3$ and CCl_4. All the fitted profiles had approximately 90% Gauss and 10% Cauchy components. The sum function was not further used be cause it involved fixing the ratio of Cauchy and Gauss component half-band widths, via the parameter CAY. This restriction seemed to us to be undesirable, and so the sum function was not used further. The product function proved far too complicated for the resolution of overlapping bands, and was not used after a few preliminary trials.

Firstly, the 21 spectra recorded for 0.5 mol dm^{-3} $Bu_4N^+Cl^-$ in benzene (see chapter 4) were fitted to a profile containing 3 pure Gauss bands. The band centres were inputted as 75, 115 and 180 cm^{-1}. Various sets of parameters were then fed in with the bands, and the lowest discrepance value taken as the best fit to the experimental data. The input data was varied widely for different runs, except that the band centres were fixed to within 5 cm^{-1} of the above values. The best fits were obtained from parameters showing a high degree of consistency for the 21 spectra.

Various tests were run to discover the effect of the input parameters chosen on the final fitted parameters. The following tests were conducted on a pure Gauss profile generated with band centre 70 cm^{-1}, half-band width 70 cm^{-1} and peak absorbance 1 unit, overlapped by a second band of pure Gauss profile with band centre 120 cm^{-1}, half-band width 70 cm^{-1} and peak absorbance 1.0 unit. The inputted band centre was found to determine the fit more than the half-band width or peak height. The band centre was found to be returned to the same output value only when the guessed value was within 15 cm^{-1} for the half-band width of 70 cm^{-1}. The values of guessed half-band widths could be varied between 20 and 200 cm^{-1} and yet still gave the same output value of 70 cm^{-1}. Likewise, the peak height could be varied between 0.1 and 5 absorbance units and still be returned to the correct output value of 1 absorbance unit. No further attempts were made to test how far the input values could deviate from their true value and yet give

true output values for a multiple band system, since this will vary with the overlap of the bands and the relative half-band widths and peak heights. Such tests would thus only be valid for a given concentration of absorbing species for a given system. Presumably the guessed half-band widths and peak heights will have to be much closer to their true values than those indicated in the test for the component bands of a multiple profile. The tests were conducted on a generated band, and not with an experimental band, which has associated with it an inherent noise level which will decrease the range over which the inputted guess will be returned to the true value.

It was decided that the component band centres must be chosen to within 5 cm^{-1} of their true values, and the half-band widths to within 20 cm^{-1} and the peak heights to within 0.2 absorbance units of their true values. These values being chosen for bands in the 50 to 200 cm^{-1} region, with half-band widths of 50 to 100 cm^{-1} and peak heights between 0.2 and 1.5 absorbance units. Thus, many different input values with band centres varying in 5 cm^{-1} steps were tried for each absorption profile, and the reproducibility of the output values was used as a test for their viability. The half-band widths were varied in 20 cm^{-1} steps.

The data obtained from the best fits for the 21 spectra of 0.5 mol dm^{-3} $Bu_4N^+Cl^-$ in benzene for the 75, 115 and 180 cm^{-1} components are shown in tables 5.2, 5.3 and 5.4 respectively. The centre of the component was obtained directly as X_2, and the half-band width was obtained by use of eqn. 5.15 from the outputted value of X_4. The area under the component band was calculated by use of eqn. 5.25. It should be noted that the programme DCH0512 used to obtain the absorbance as a function of wavenumber produces absorbance on a natural logarithmn scale, and hence the areas obtained were all multiplied by 2.303 to give the data for a common logarthmic scale. This enabled the areas obtained to be compared with those obtained in chapter 3.

Table 5.2 Band fitting precision tests

70 cm^{-1} component $Bu_4N^+Cl^-$ in benzene L = 0.021 cm

solution number	concentration /mol dm^{-3}	centre /cm^{-1}	$\Delta\bar{\nu}_{\frac{1}{2}}$ /cm^{-1}	area /cm^{-1}
1	0.500	73.4	73.1	54.2
		71.4	61.0	48.5
		62.1	62.1	58.6
		67.7	66.2	53.6
2	0.498	77.2	69.8	58.2
		73.2	65.3	59.1
		67.7	70.8	69.2
		69.9	74.6	100.8
3	0.498	73.8	75.9	56.4
		74.2	69.3	73.9
		69.8	61.1	61.9
		67.5	63.8	61.4
4	0.498	71.1	64.9	56.0
		68.6	67.7	63.8
		71.0	61.6	57.1
		67.3	67.6	67.9
		68.0	65.2	64.4
5	0.506	70.8	59.1	38.8
		70.0	60.9	37.0
		73.4	68.1	46.7
		71.7	61.9	44.5

Table 5.3 Precision tests

116 cm^{-1} component $Bu_4N^+Cl^-$ in benzene L = 0.021 cm

solution number	concentration /mol dm^{-3}	centre /cm^{-1}	$\Delta\bar{\nu}_{\frac{1}{2}}$ /cm^{-1}	area /cm^{-1}
1	0.500	117.9	53.5	45.9
		115.9	53.7	62.1
		114.5	58.1	87.2
		114.4	52.4	57.5
2	0.500	118.7	50.8	45.6
		117.2	52.5	54.8
		116.0	58.5	80.6
		117.2	54.9	74.2
3	0.498	114.8	55.3	56.5
		117.8	50.2	56.5
		116.8	51.8	70.2
		116.0	55.7	79.5
4	0.498	116.2	55.6	67.8
		116.3	58.0	73.7
		116.4	54.1	66.5
		115.8	53.9	66.6
		115.9	53.4	70.9
5	0.506	116.3	51.5	44.8
		115.1	50.8	38.5
		117.2	53.0	46.9
		115.7	51.9	48.7

Table 5.4 Band fitting precision tests

180 cm^{-1} component $Bu_4N^+Cl^-$ in benzene L = 0.021 cm

solution number	concentration /mol dm^{-3}	centre /cm^{-1}	$\Delta\bar{\nu}_{\frac{1}{2}}$ /cm^{-1}	area /cm^{-1}
1	0.500	183.7	81.6	36.2
		180.2	77.0	38.9
		182.3	74.9	43.4
		176.7	90.1	46.1
2	0.498	179.5	75.5	33.4
		176.3	80.5	40.7
		181.3	58.4	34.6
		181.5	68.5	41.4
3	0.498	181.5	73.6	35.6
		176.1	89.0	47.3
		179.1	80.3	41.1
		181.5	68.0	34.6
4	0.498	179.3	81.7	39.8
		179.8	78.1	41.7
		178.1	79.7	38.5
		175.8	94.0	56.9
		178.5	77.0	41.0
5	0.506	182.8	81.5	29.9
		175.9	105.0	36.3
		180.8	83.3	29.0
		181.0	88.0	37.4

The data for centre, half-band width and area all showed a high degree of reproducibility, which suggested that the fitting method was a viable one for the systems studied. The data was used to determine the precision of the band centre, half-band width and area as for the total band profile parameters, so that concentration and temperature studies could be attempted. These precisions are shown in table 5.5, where the mean area and root mean square deviations are also shown. The root mean square deviations were calculated by use of eqn. 4.3, for compatability with the data of chapter 4.

5.3 3 pure Gauss components fit for $Bu_4N^+Cl^-$ in benzene. Effect of concentration.

The absorption profiles, for the spectra of $Bu_4N^+Cl^-$ at various concentrations in benzene obtained with a pathlength of 0.021 cm, were fitted to a profile which was the sum of 3 pure Gauss components. The low frequency band was guessed as centre 70 and half-band width 66 cm^{-1}. The central component was positioned at 116 cm^{-1} with a half-band width of 54 cm^{-1}. The high frequency tail component was given centre 180 cm^{-1} and half-band width 80 cm^{-1}. Fig 5.2 shows a typical fit for 0.70 mol dm^{-3} $Bu_4N^+Cl^-$ in benzene for the 3 component bands. Tables 5.6 to 5.11 show the data obtained for the best fits for the 33 spectra representing the 20 concentrations of $Bu_4N^+Cl^-$ in benzene between 0.21 and 1.40 mol dm^{-3}. Table 5.6 shows the fitted centre for each spectrum, together with the average centre for each concentration. The half-band width and average half-band width are similarly detailed.

To determine the effect of concentration on the centre of the low frequency component, the fitted band centre was plotted as a function of concentration. This graph is shown in fig. 5.3. The error plotted was ± 3 cm^{-1}, as calculated in the precision tests and shown in table 5.5. The error was considered to be constant throughout the concentration range, and the treatment was thus compatable with that for the

Table 5.5 Results of precision tests for computer separated bands

0.5 mol dm^{-3} $Bu_4N^+Cl^-$ in C_6H_6 L = 0.021 cm T = 293K

centre	70±3	116±1	180±2
$\Delta\bar{\nu}_{\frac{1}{2}}$	66±5	54±2	80±10
area	59±13	62±13	39±16

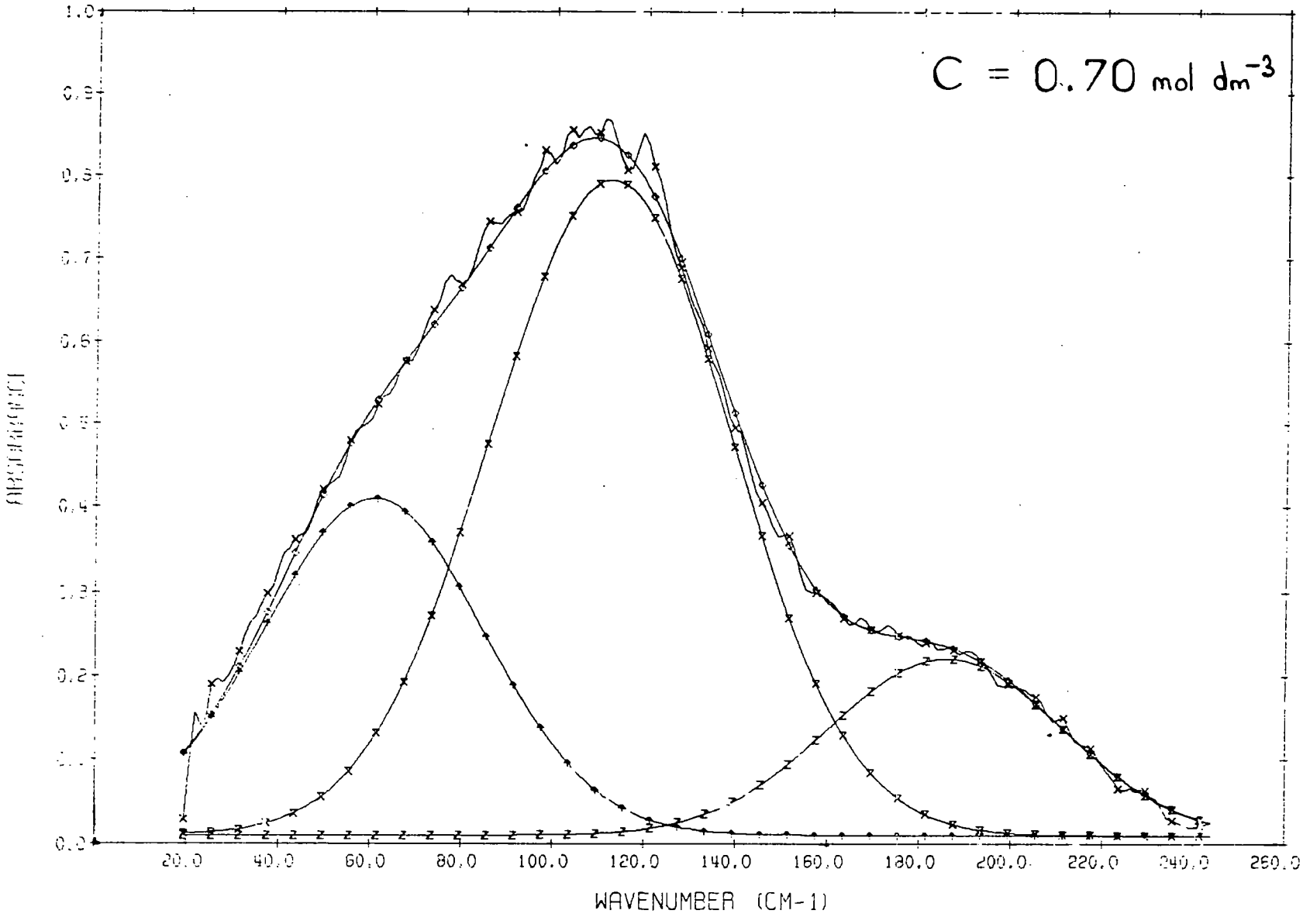

FIG. 5.2 3 PURE GAUSS FIT BU4N+CI- IN C6H6

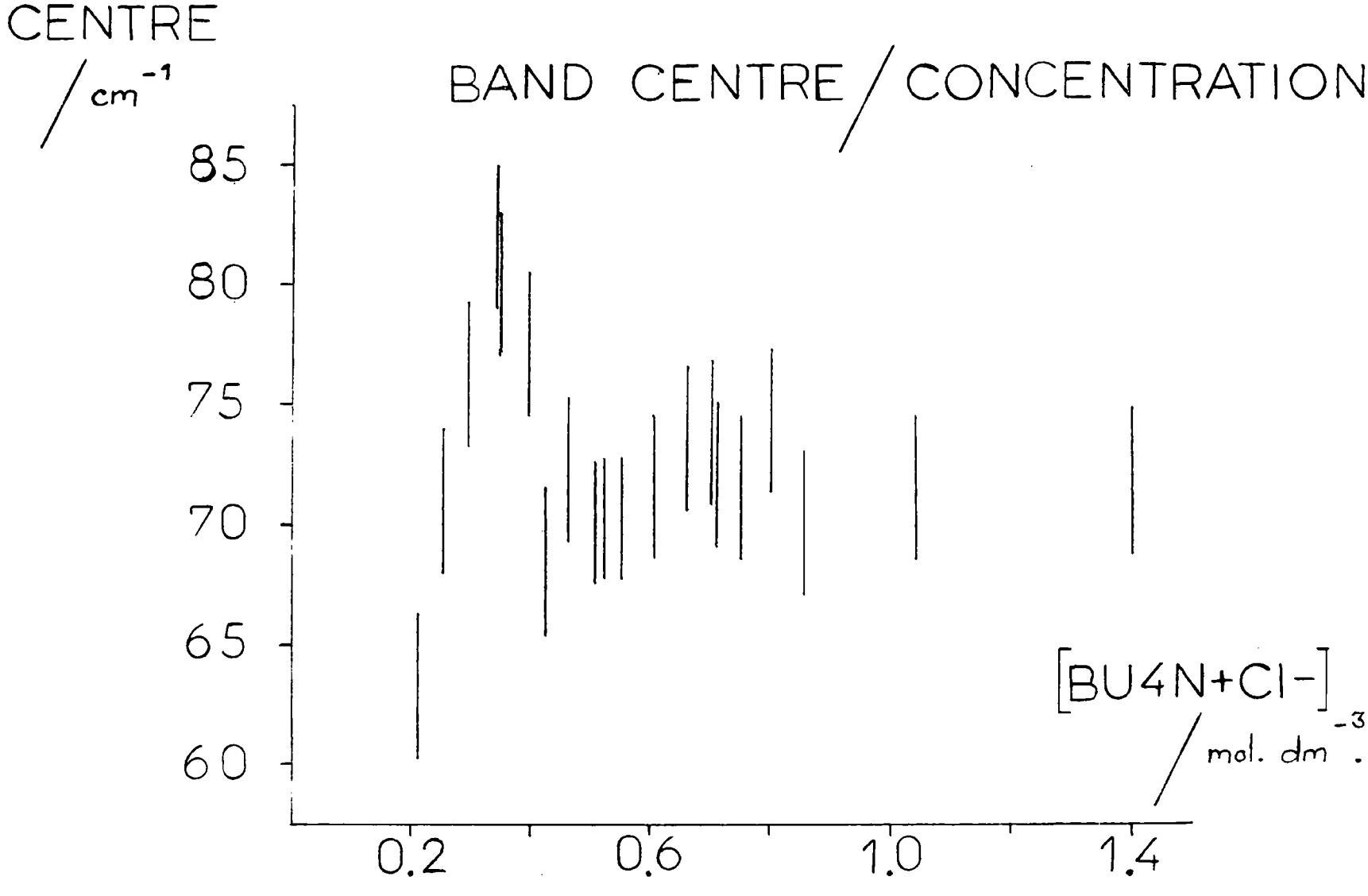

FIG. 5.3 73 cm^{-1} COMPONENT BU4N+Cl- IN BENZENE

Table 5.6 73 cm^{-1} component $Bu_4N^+Cl^-$ in benzene band centre $\bar{\nu}_o$ and half-band width $\Delta\bar{\nu}_{\frac{1}{2}}$

concn. /mol dm^{-3}	$\bar{\nu}_o$ /cm^{-1}	av. $\bar{\nu}_o$ /cm^{-1}	$\Delta\bar{\nu}_{\frac{1}{2}}$ /cm^{-1}	av. $\Delta\bar{\nu}_{\frac{1}{2}}$ /cm^{-1}	concn. /mol dm^{-3}	$\bar{\nu}_o$ /cm^{-1}	av. $\bar{\nu}_o$ /cm^{-1}	$\Delta\bar{\nu}_{\frac{1}{2}}$ /cm^{-1}	av. $\Delta\bar{\nu}_{\frac{1}{2}}$ /cm^{-1}
0.210	62.3	63.3	88.9	73.7	0.551	70.3	70.3	71.3	71.3
	64.2		58.4		0.603	71.5	71.5	73.2	73.2
0.252	70.9	70.9	69.0	69.0	0.661	71.5		74.1	
0.298	76.3	76.3	79.4	79.4		71.5	73.4	67.4	69.7
0.343	82.1	82.1	83.3	83.3		72.9		64.8	
0.350	78.5	80.0	64.3	57.0		77.8		72.6	
	81.6		49.3		0.700	73.8	73.7	75.0	74.6
0.398	78.8		76.2			73.5		74.2	
	80.4	77.6	67.9	70.1	0.709	72.1	72.1	74.3	74.3
	76.7		65.5		0.752	71.4	71.4	69.6	69.6
	74.7		70.7		0.802	74.2	74.2	67.4	67.4
0.423	66.0	68.6	89.3	82.7	0.855	70.1	70.1	75.1	75.1
	71.1		76.1		1.040	73.5	71.5	80.2	79.2
0.462	72.3	72.3	75.5	75.5		69.9		78.3	
0.507	70.0	70.0	75.0	75.0	1.400	69.5	71.8	60.9	62.0
0.520	72.9	70.2	71.4	69.2		74.1		63.1	
	67.4		67.0						

total profile detailed in chapter 4. The graph showed that the band centre was independent of concentration, throughout the range studied. The mean centre was 73 cm^{-1}, and the root mean square deviation ±1 cm^{-1}. The larger discrepancies in band centre occurred below 0.4 mol dm^{-3}, and were probably due to the low intensity of this component, which make the baseline errors more crucial. These values clearly supported the view that it was the actual error, and not the percentage error, that should be used in these studies, since the maximum discrepance occurred at low concentration.

Fig. 5.4 shows the graph for the half-band width data of the 73 cm^{-1} component. The band width was seen to remain approximately constant over the concentration range studied. Once again the greatest deviations from the mean value of 72±8 cm^{-1} were seen to occur at low concentrations.

Table 5.7 shows the area and intensity data for the low frequency component. Fig 5.5 shows the intensity plotted against concentration. This graph suggested that the intensity of the component increased with increasing concentration. The variation of intensity with concentration was seen to rely critically upon the low concentration data, and so the result had to be considered carefully. In an effort to clarify the situation the area under the component was plotted as a function of concentration. If the intensity was independent of concentration then such a plot would be linear. Fig. 5.6 shows this plot, which was still rather inconclusive, but once again indicated that the intensity increased with increasing concentration, although not markedly so. To obtain a value for the intensity of this component, for comparison with other systems, the BEERSLAW fitting programme was used to give the best linear least squares fit for the area/concentration data. The best straight line, using the origin as a valid point, is marked with an A in fig. 5.6. The slope was 124.9±6.3 dm^3 mol^{-1} cm^{-1}, which gave an intensity B_i of 5 220±30 dm^3 mol^{-1} cm^{-2}. The best straight line, using no restraints, is labelled B in the figure, and had a slope of 133.0±14.2 dm^3 mol^{-1} cm^{-1}, giving an intensity B_i of 6±390 690 dm^3

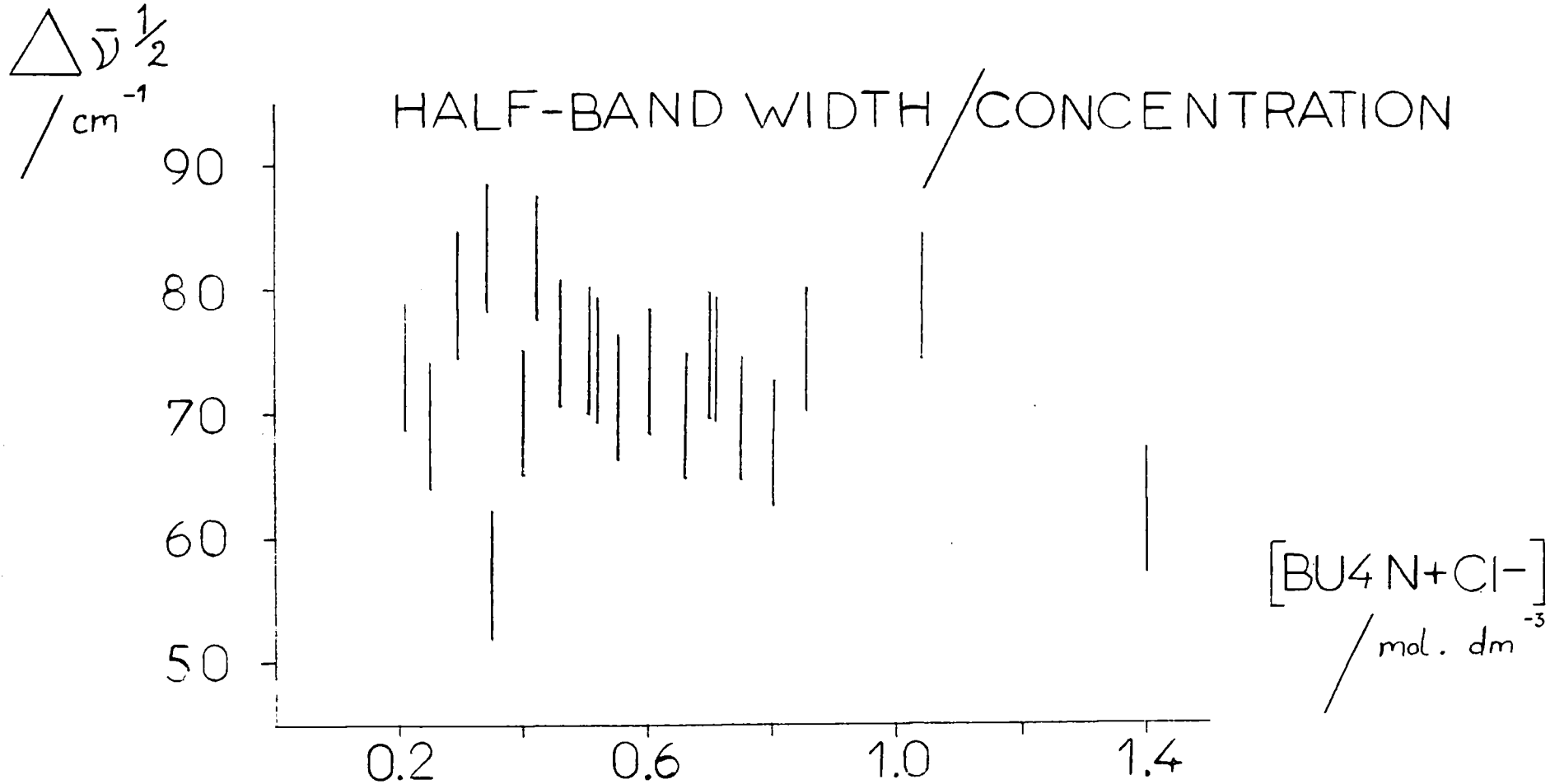

FIG. 5.4 73 cm^{-1} COMPONENT BU4N+Cl- IN BENZENE

Table 5.7 73 cm^{-1} component $Bu_4N^+Cl^-$ in benzene band area and intensity

concn. /mol dm^{-3}	area /cm^{-1}	av. area /cm^{-1}	intensity /dm^3 mol^{-1} cm^{-2}	concn. /mol dm^{-3}	area /cm^{-1}	av. area /cm^{-1}	intensity /dm^3 mol^{-1} cm^{-2}
0.210	7.6	6.3	1 400±2 900	0.551	85.5	85.5	7 400±1 100
	4.9			0.603	98.8	98.8	7 800±1 000
0.252	24.5	24.5	4 600±2 400	0.661	92.7		
0.298	30.3	30.3	4 800±2 000		84.1	85.0	6 100±900
0.343	50.1	50.1	6 900±1 800		66.1		
0.350	9.6	9.5	1 300±1 800		97.3		
	9.4			0.700	97.4	94.4	6 400±900
0.398	57.9				91.4		
	51.0	50.6	6 100±1 600	0.709	114.5	114.5	7 700±900
	42.2			0.752	99.8	99.8	6 300±800
	51.3			0.802	91.4	91.4	5 400±800
0.423	14.5	18.7	2 100±1 500	0.855	121.5	121.5	6 800±700
	22.8			1.040	178.4	183.3	8 400±600
0.462	69.9	69.9	7 200±1 300		188.1		
0.507	82.5	82.5	7 700±1 200	1.400	119.4	128.3	4 400±400
0.520	60.3	63.5	5 800±1 200		137.2		
	66.7						

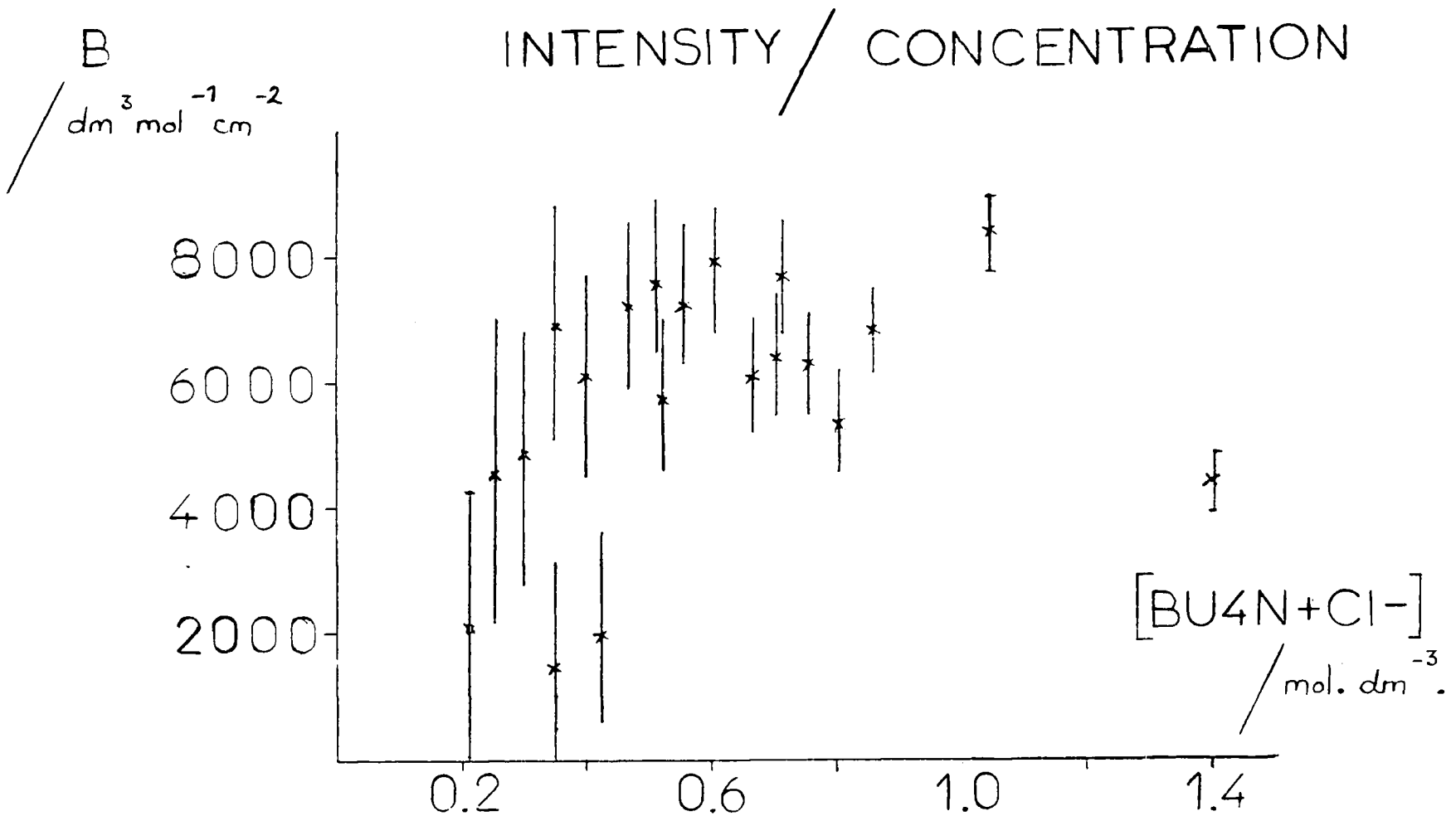

FIG. 5.5 73 cm^{-1} COMPONENT BU4N+Cl- IN BENZENE

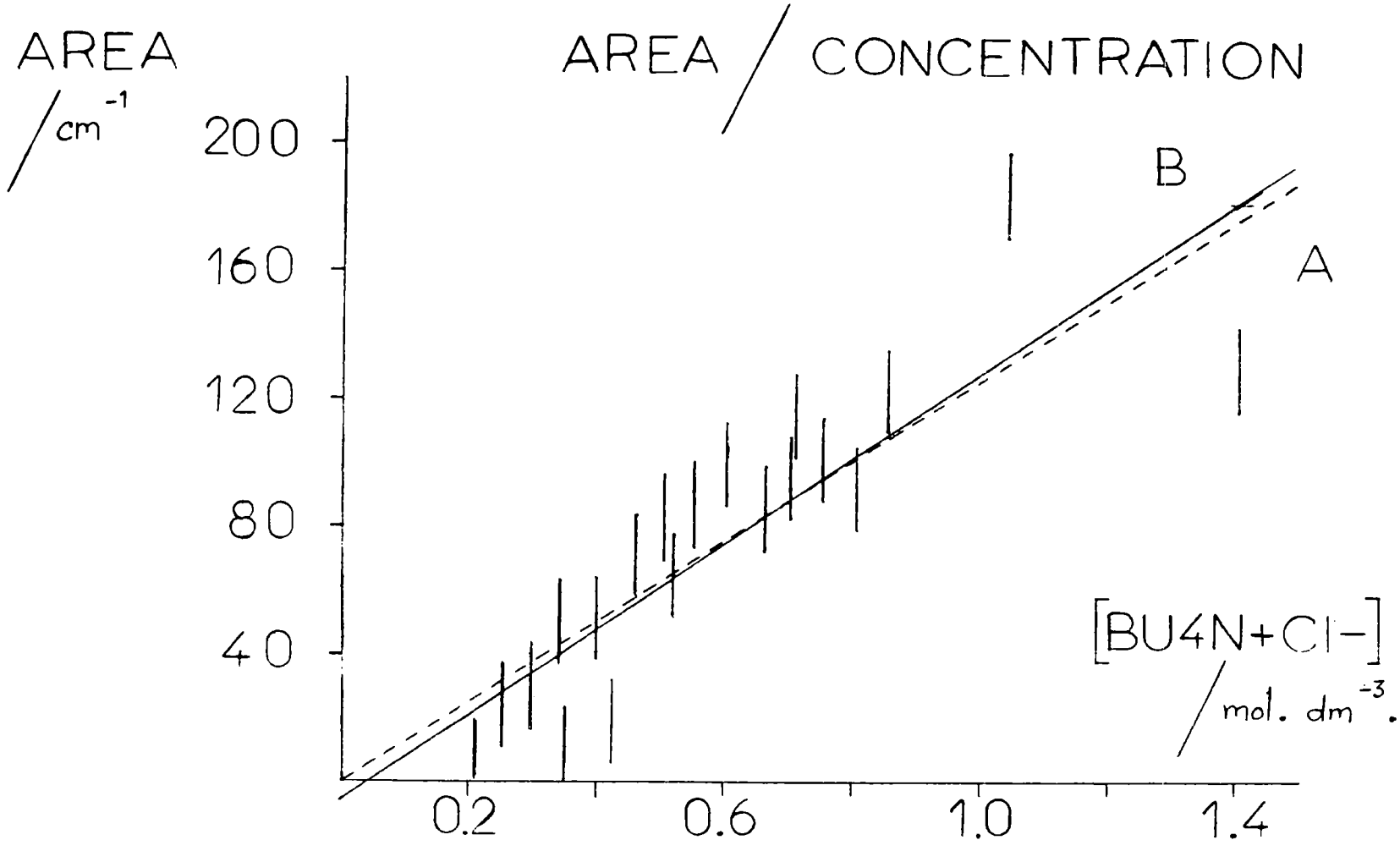

FIG 5.6 73 cm^{-1} COMPONENT BU4N+Cl- IN BENZENE

mol^{-1} cm^{-2}. This once again suggested that the intensity increased with concentration, since the unrestrained fit passed below the origin.

Table 5.8 shows the fitted band centre and half-band width of the central component, and fig. 5.7 shows the effect of concentration on the band centre. The band centre was seen to be invariant with concentration. The mean centre was calculated as 118±3 cm^{-1}. Fig. 5.8 shows the plot of half-band width against concentration for the central component. The graph showed that the half-band width appeared to increase to a maximum at 0.8 mol dm^{-3}. The average half-band width was found to be 53±4 cm^{-1}

Table 5.9 shows the area and intensity data for the 118 cm^{-1} component. Fig. 5.9 shows the intensity as a function of concentration, and shows clearly that the intensity of this band increases with increasing concentration. To obtain an average value for the intensity the area/concentration data was used with the BEERSLAW programme. Fig. 5.10 shows the fit through the origin with a slope of 113.5 dm^3 mol^{-1} cm^{-1}, which gave an intensity B_i of 4 740±250 dm^3 mol^{-1} cm^{-2}. This fit is labelled A. The unrestricted fit is denoted by the letter B, and had a slope of 119.7 ±12 dm^3 mol^{-1} cm^{-1}, and an intensity B_i of 5 760±580 dm^3 mol^{-1} cm^{-2}.

Table 5.10 shows the band centre and half-band width for the high frequency component. The band centre was plotted as a function of concentration, and the graph is shown in fig. 5.11. This graph showed that the frequency of this high frequency component did not depend upon the $Bu_4N^+Cl^-$ concentration. The mean band centre was found to be 181±6 cm^{-1}, the lower precision than for the other components being due to the low intensity of this component. Fig 5.12 shows the half-band width of the 181 cm^{-1} component plotted as a function of concentration. The half-band width was seen to be invariant with concentration, and the mean value was calculated as 72±19 cm^{-1}. Once again the low precision was due to the low intensity of the high frequency tail component.

Table 5.11 shows the area and intensity data for the high freq-

Table 5.8 118 cm^{-1} component $Bu_4N^+Cl^-$ in benzene band centre $\bar{\nu}_o$ and half-band width $\Delta\bar{\nu}_{\frac{1}{2}}$

concn. /mol dm^{-3}	$\bar{\nu}_o$ /cm^{-1}	av. $\bar{\nu}_o$ /cm^{-1}	$\Delta\bar{\nu}_{\frac{1}{2}}$ /cm^{-1}	av. $\Delta\bar{\nu}_{\frac{1}{2}}$ /cm^{-1}	concn. /mol dm^{-3}	$\bar{\nu}_o$ /cm^{-1}	av. $\bar{\nu}_o$ /cm^{-1}	$\Delta\bar{\nu}_{\frac{1}{2}}$ /cm^{-1}	av. $\Delta\bar{\nu}_{\frac{1}{2}}$ /cm^{-1}
0.210	112.4	112.0	50.5	50.1	0.551	120.2	120.2	56.4	56.4
	111.4		49.6		0.603	120.9	120.9	57.8	57.8
0.252	116.7	116.7	53.5	53.5	0.661	120.3		60.2	
0.298	118.2	118.2	53.8	53.8		117.7	118.7	54.5	55.8
0.343	121.2	121.2	48.3	48.3		118.3		55.2	
0.350	115.2	116.9	51.0	49.7		118.4		53.3	
	118.6		48.4		0.700	116.8	117.1	54.7	55.2
0.398	121.9		52.5			117.4		55.6	
	119.9	118.9	44.8	48.3	0.709	120.7	120.7	54.7	54.7
	116.6		46.7		0.752	120.2	120.2	56.9	56.9
	117.3		49.4		0.802	118.8	118.8	59.4	59.4
0.423	114.8	116.0	53.3	51.9	0.855	121.0	121.0	63.2	63.2
	117.2		50.5		1.040	115.2	116.8	52.4	53.2
0.462	121.5	121.5	59.5	59.5		118.4		54.0	
0.507	120.6	120.6	57.9	57.9	1.400	115.6	116.8	50.6	48.5
0.520	114.4	115.3	52.0	52.1		118.0		46.4	
	116.2		52.1						

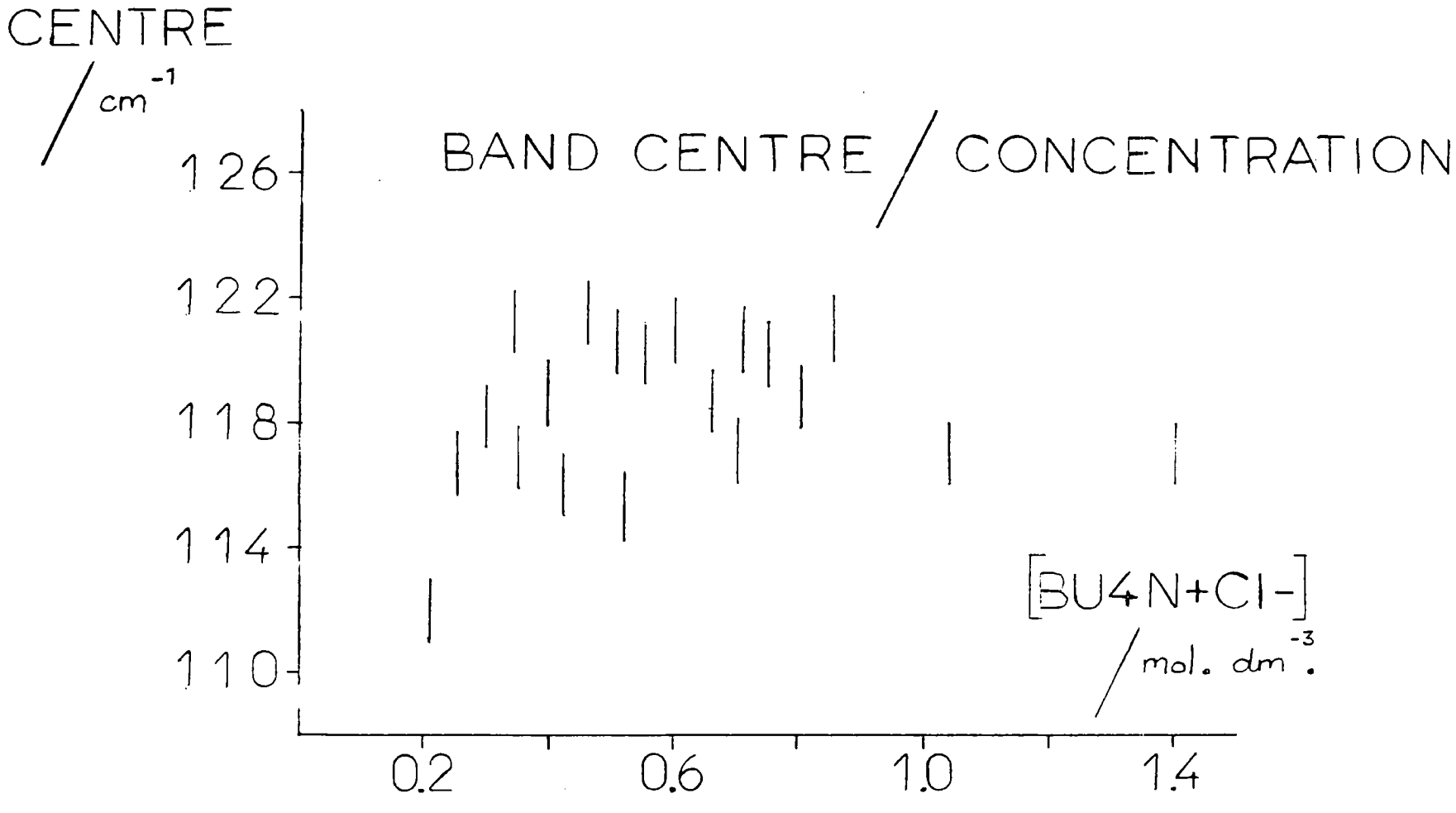

FIG. 5.7 118 cm^{-1} COMPONENT BU4N+Cl- IN BENZENE

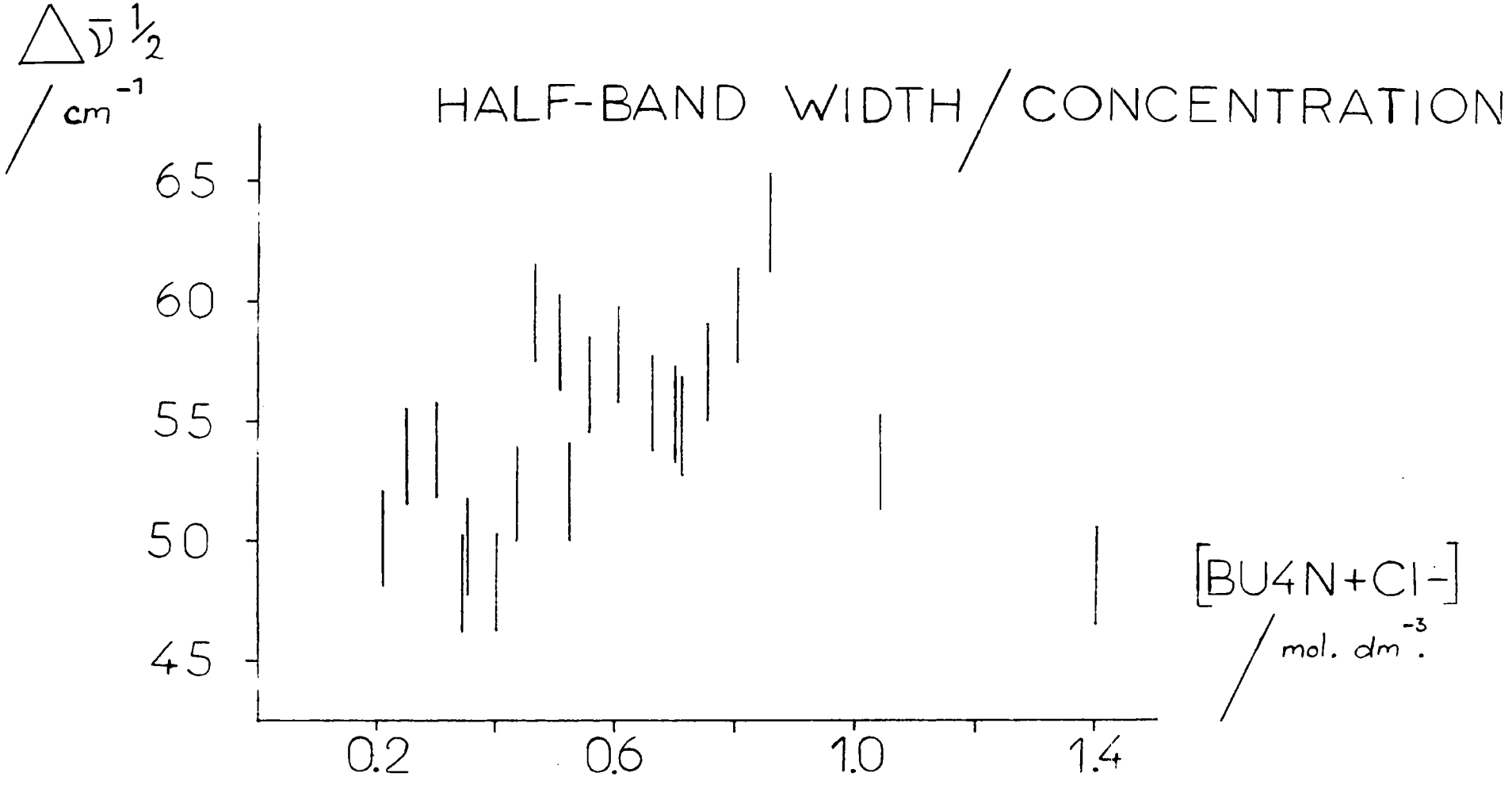

FIG 5.8 118 cm^{-1} COMPONENT BU4N+Cl- IN BENZENE

Table 5.9 118 cm^{-1} component $Bu_4N^+Cl^-$ in benzene area and intensity

concn. /mol dm^{-3}	area /cm^{-1}	av. area /cm^{-1}	intensity /dm^3 mol^{-1} cm^{-2}	concn. /mol dm^{-3}	area /cm^{-1}	av. area /cm^{-1}	intensity /dm^3 mol^{-1} cm^{-2}
0.210	4.5	3.4	770±2 900	0.551	85.6	85.6	7 400±1 100
	2.4			0.603	95.9	95.9	7 600±1 000
0.252	21.2	21.2	4 000±2 500	0.661	99.2		
0.298	23.0	23.0	3 700±2 100		85.9	87.2	6 300±900
0.343	22.2	22.2	3 100±1 800		77.8		
0.350	17.9	18.4	2 500±1 800		85.9		
	19.0			0.700	77.8	77.8	5 300±900
0.398	41.5	35.4	4 200±1 600		77.8		
	27.7			0.709	102.1	102.1	6 900±900
	36.2			0.752	112.4	112.4	7 100±800
	36.3			0.802	110.0	110.0	6 500±800
0.423	20.0	20.1	2 300±1 500	0.855	142.2	142.2	7 900±700
	20.1			1.040	107.1	114.4	5 200±600
0.462	70.3	70.3	7 200±1 300		121.7		
0.507	77.3	77.3	7 300±1 200	1.400	141.9	126.5	4 300±400
0.520	68.4	63.6	5 800±1 200		111.1		
	58.8						

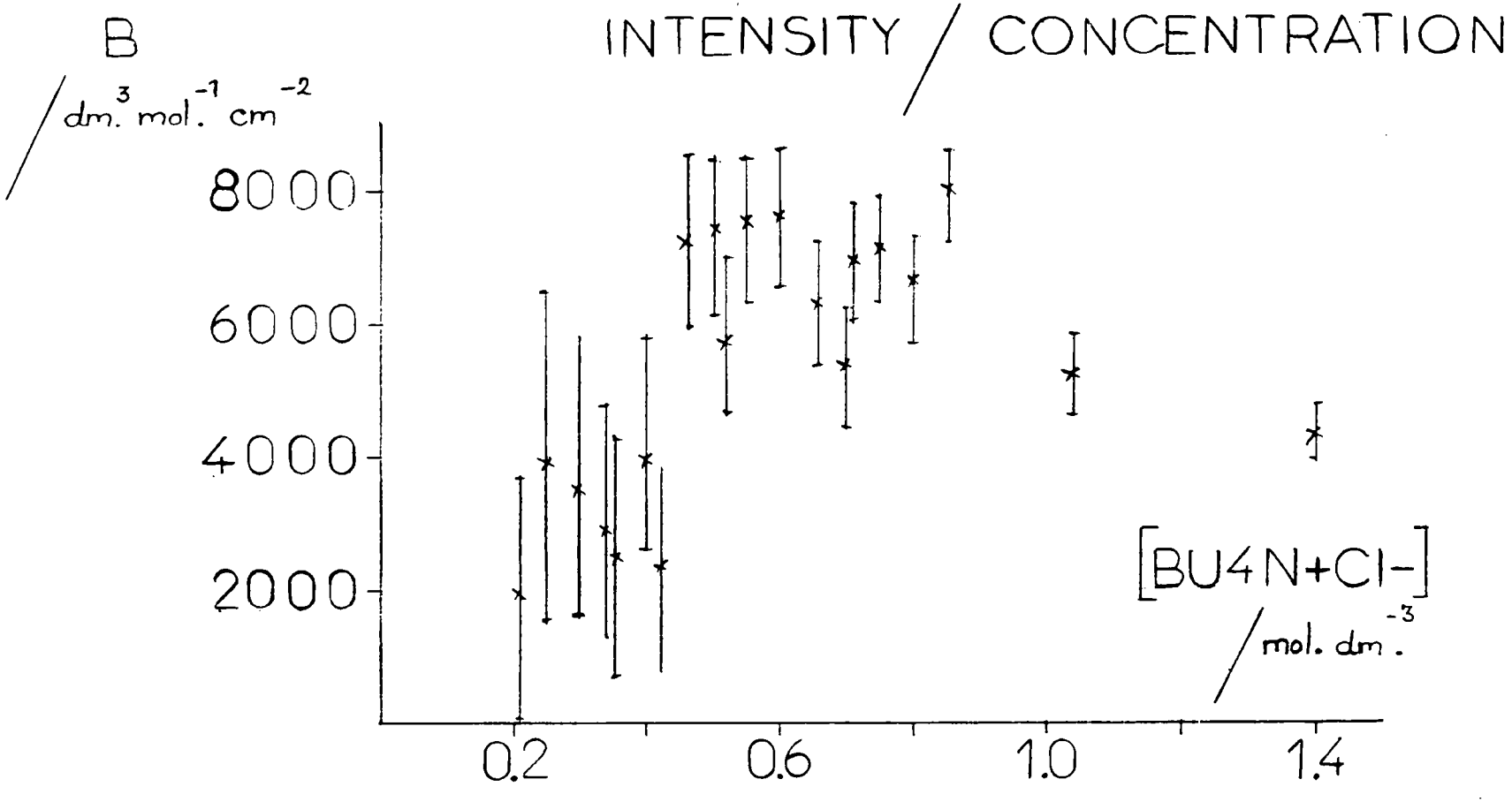

FIG. 5.9 118 cm^{-1} COMPONENT BU4N+CI- IN BENZENE

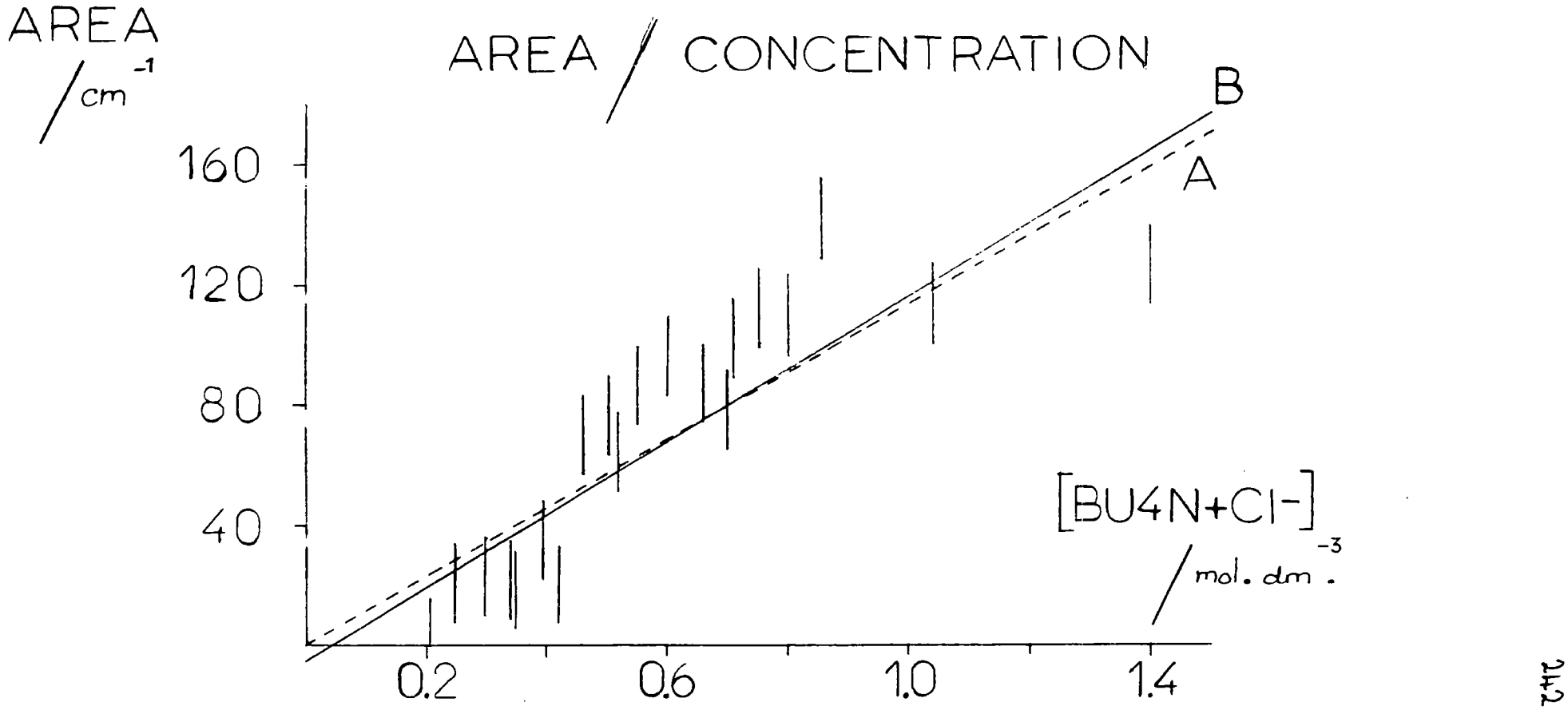

FIG. 5.10 118 cm^{-1} COMPONENT BU4N+Cl- IN BENZENE

Table 5.10 181 cm^{-1} component $Bu_4N^+Cl^-$ in benzene band centre $\bar{\nu}_o$ and half-band width $\Delta\bar{\nu}_{\frac{1}{2}}$

concn. /mol dm^{-3}	$\bar{\nu}_o$ /cm^{-1}	av. $\bar{\nu}_o$ /cm^{-1}	$\Delta\bar{\nu}_{\frac{1}{2}}$ /cm^{-1}	av. $\Delta\bar{\nu}_{\frac{1}{2}}$ /cm^{-1}	concn. /mol dm^{-3}	$\bar{\nu}_o$ /cm^{-1}	av. $\bar{\nu}_o$ /cm^{-1}	$\Delta\bar{\nu}_{\frac{1}{2}}$ /cm^{-1}	av. $\Delta\bar{\nu}_{\frac{1}{2}}$ /cm^{-1}
0.210	170.6	170.6	35.6	72.1	0.551	183.0	183.0	57.3	57.3
	170.6		108.7		0.603	184.4	184.4	52.8	52.8
0.252	181.1	181.1	101.6	101.6	0.661	184.9		53.2	
0.298	182.3	182.3	83.1	83.1		183.1	182.8	81.9	68.6
0.343	184.7	184.7	71.9	71.9		184.7		65.3	
0.350	183.4	183.8	67.7	64.2		178.6		74.0	
	184.3		60.7		0.700	182.2	182.5	67.7	67.8
0.398	183.3		54.8			182.9		67.8	
	160.9	173.1	110.9	89.0	0.709	182.2	182.2	56.3	56.3
	174.9		95.9		0.752	185.2	185.2	55.6	55.6
	173.5		94.6		0.802	184.8	184.8	55.5	55.5
0.423	182.5	182.0	72.1	75.8	0.855	188.6	188.6	53.0	53.0
	181.6		79.6		1.040	177.4	180.1	82.4	77.5
0.462	186.6	186.6	51.6	51.6		182.8		72.7	
0.507	183.1	183.1	55.0	55.0	1.400	181.9	179.8	84.6	91.7
0.520	183.3	184.1	82.3	82.7		177.6		98.8	
	184.9		83.1						

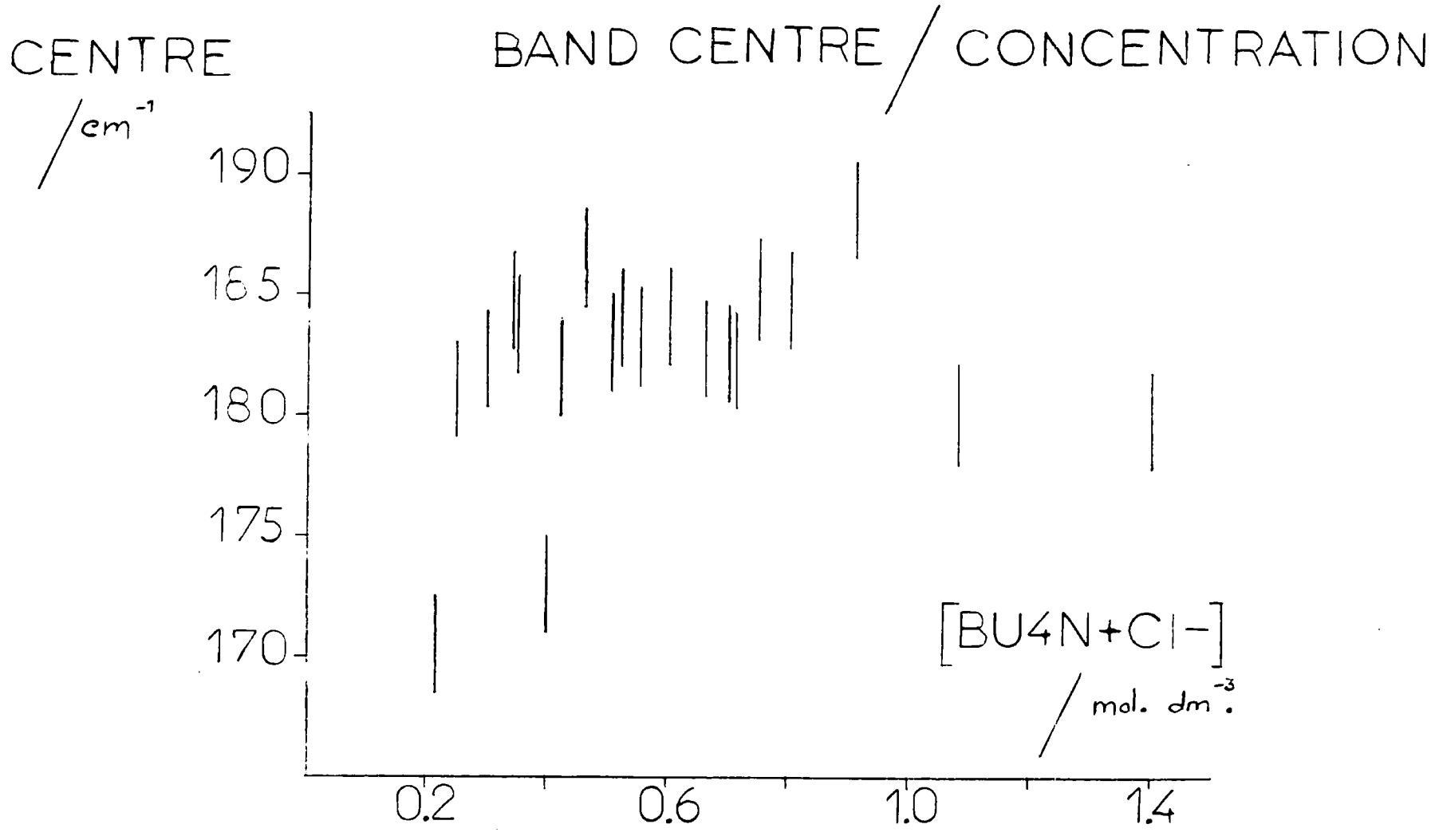

FIG. 5.11 181 cm^{-1} COMPONENT BU4N+Cl- IN BENZENE

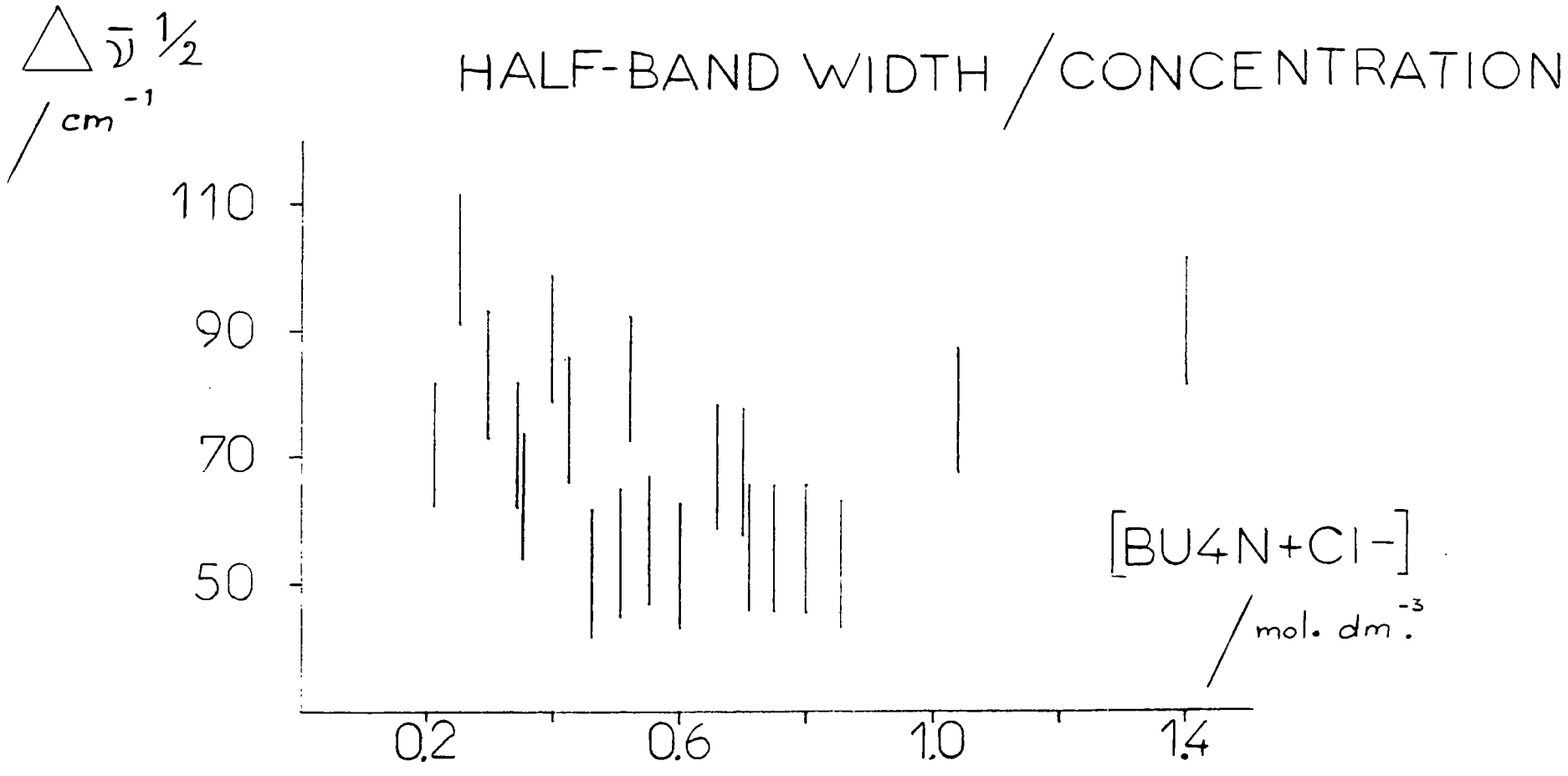

FIG. 5.12 181 cm^{-1} COMPONENT BU4N+Cl− IN BENZENE

Table 5.11 181 cm^{-1} component $Bu_4N^+Cl^-$ in benzene area and intensity

concn. /mol dm^{-3}	area /cm^{-1}	av. area /cm^{-1}	intensity /dm^3 mol^{-1} cm^{-2}	concn. /mol dm^{-3}	area /cm^{-1}	av. area /cm^{-1}	intensity /dm^3 mol^{-1} cm^{-2}
0.210	0.2	5.3	1 200±1 400	0.551	37.0	37.0	3 200±500
	10.5			0.603	40.7	40.7	3 200±500
0.252	20.2	20.2	3 800±1 000	0.661	37.3		
0.298	19.2	19.2	3 100±1 000		54.3	40.5	2 900±400
0.343	18.7	18.7	2 600±800		35.8		
0.350	11.3	10.3	1 400±800		34.7		
	9.4			0.700	38.5	36.9	2 500±400
0.398	22.1				35.3		
	31.8	31.2	3 700±700	0.709	48.6	48.6	3 300±400
	36.4			0.752	44.2	44.2	2 800±400
	34.6			0.802	38.1	38.1	2 300±400
0.423	15.6	18.5	2 100±700	0.855	56.8	56.8	3 200±300
	21.4			1.040	90.1	87.2	4 000±300
0.462	29.6	29.6	3 100±600		84.3		
0.507	32.7	32.7	3 100±600	1.400	81.1	89.9	3 100±200
0.520	41.3	40.8	3 700±500		98.6		
	40.3						

uency component. Fig. 5.13 shows the intensity as a function of concentration. The intensity of this component was seen to be constant over the concentration range studied. The least squares analysis programme gave a slope of 65.3±2.4 $dm^3\ mol^{-1}\ cm^{-1}$ for the fit, taking the origin as a valid point. This fit is denoted by the letter A in fig. 5.14, and corresponds to an intensity of 2 730±110 $dm^3\ mol^{-1}\ cm^{-2}$. A slope of 72.1±5.2 $dm^3\ mol^{-1}\ cm^{-1}$ was obtained for the unrestricted fit B, and this gave a value for the intensity of 3 470±250 $dm^3\ mol^{-1}\ cm^{-2}$.

The values for the band centres, half-band widths and intensities of the 3 components to the absorption profile for $Bu_4N^+Cl^-$ in benzene are summarised in table 5.29 at the end of this chapter.

5.4 3 pure Gauss component fit for $Bu_4N^+Cl^-$ in $CHCl_3$. Effect of concentration

The absorption profiles for the spectra of $Bu_4N^+Cl^-$ in $CHCl_3$ at various concentrations, obtained using a 0.021 cm pathlength, were fitted to a profile which was the sum of 3 pure Gauss components, in an exactly analogous manner to that for the salt in benzene. The initial input parameters for the fits were the same as those for the benzene solution spectra, i.e. bands centred at 70, 116 and 180 cm^{-1}, with half-band widths of 66, 54 and 80 cm^{-1} respectively. Fig. 5.15 shows a typical fit to the 3 components for the spectrum obtained for 0.70 mol dm^{-3} $Bu_4N^+Cl^-$ in $CHCl_3$. Tables 5.12 to 5.17 show the data obtained for the 3 components for the best fit for the 16 spectra at 8 concentrations of $Bu_4N^+Cl^-$ in $CHCl_3$ between 0.1 and 0.8 mol dm^{-3}.

Table 5.12 shows the fitted centre and half-band width for the low frequency component. The fitted centre is shown as a function of concentration in fig. 5.16. The errors shown are those calculated in the precision tests for $Bu_4N^+Cl^-$ in benzene. The fitted centre was seen to move to lower frequency with increasing concentration, the centre occurring at 83±3 cm^{-1} at 0.1 mol dm^{-3} $Bu_4N^+Cl^-$ and at 62±3 cm^{-1} at 0.8 mol dm^{-3}.

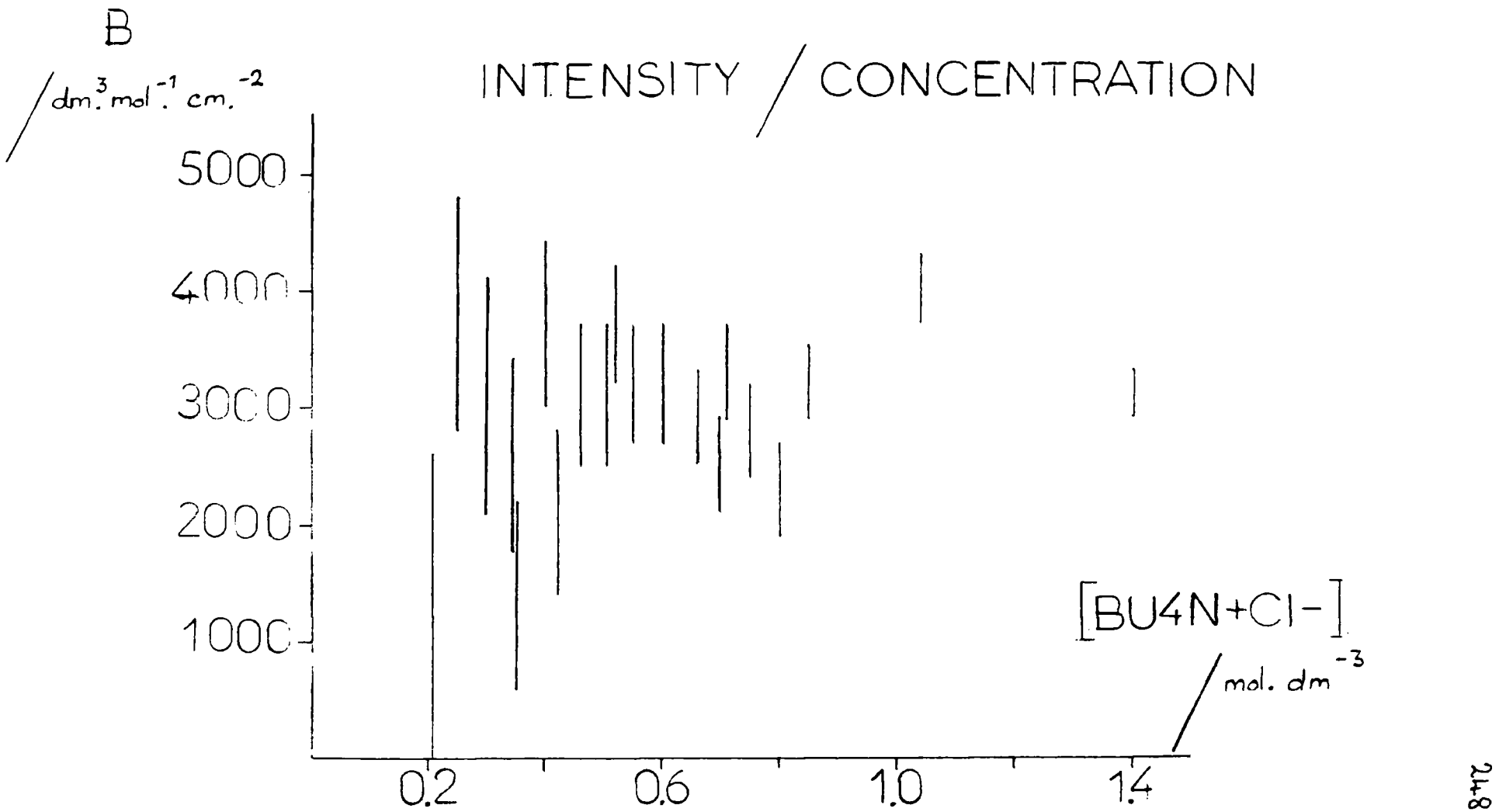

FIG. 5.13 181 cm^{-1} COMPONENT BU4N+Cl- IN BENZENE

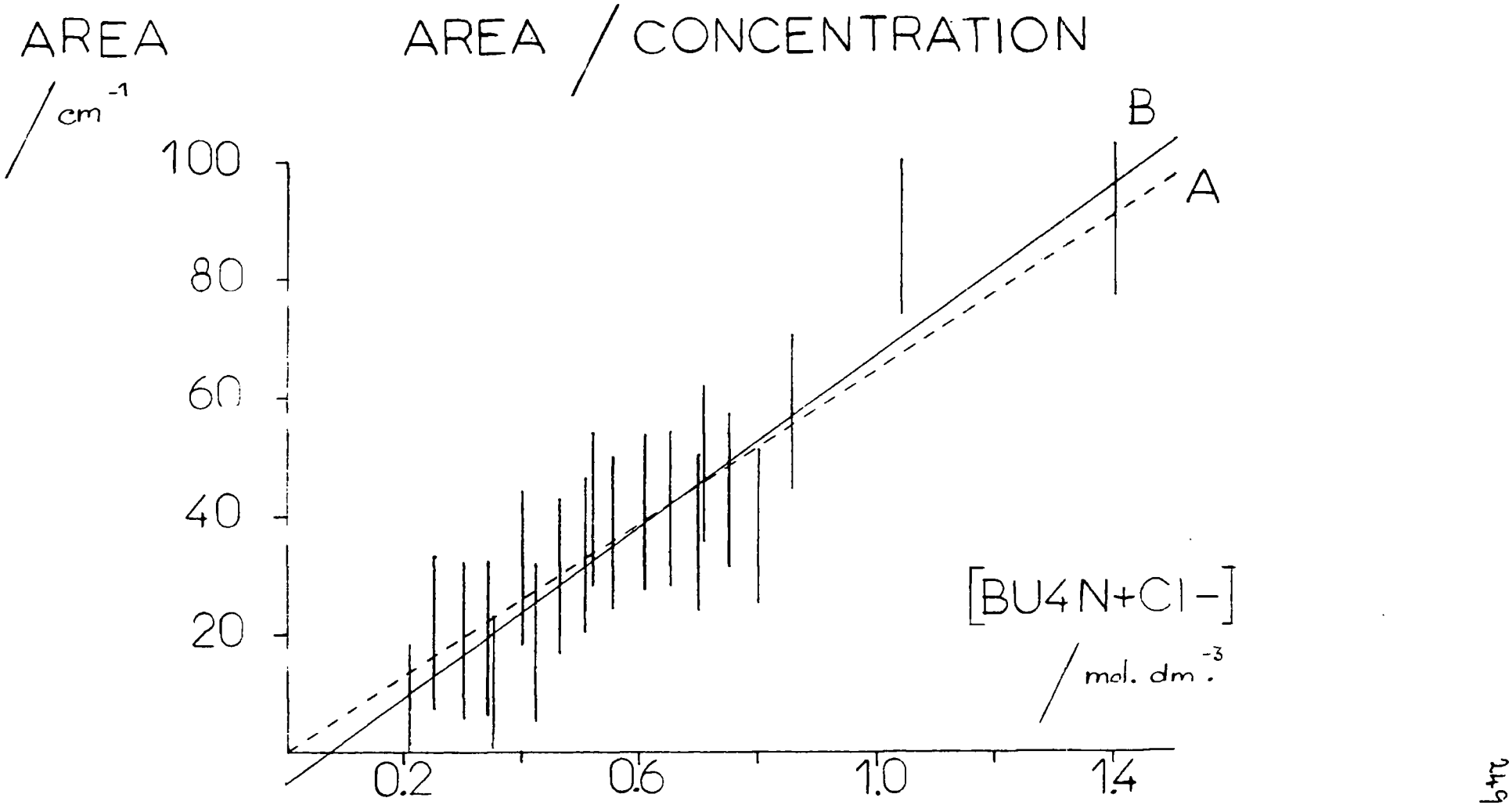

FIG. 5.14 181 cm^{-1} COMPONENT BU4N+Cl- IN BENZENE

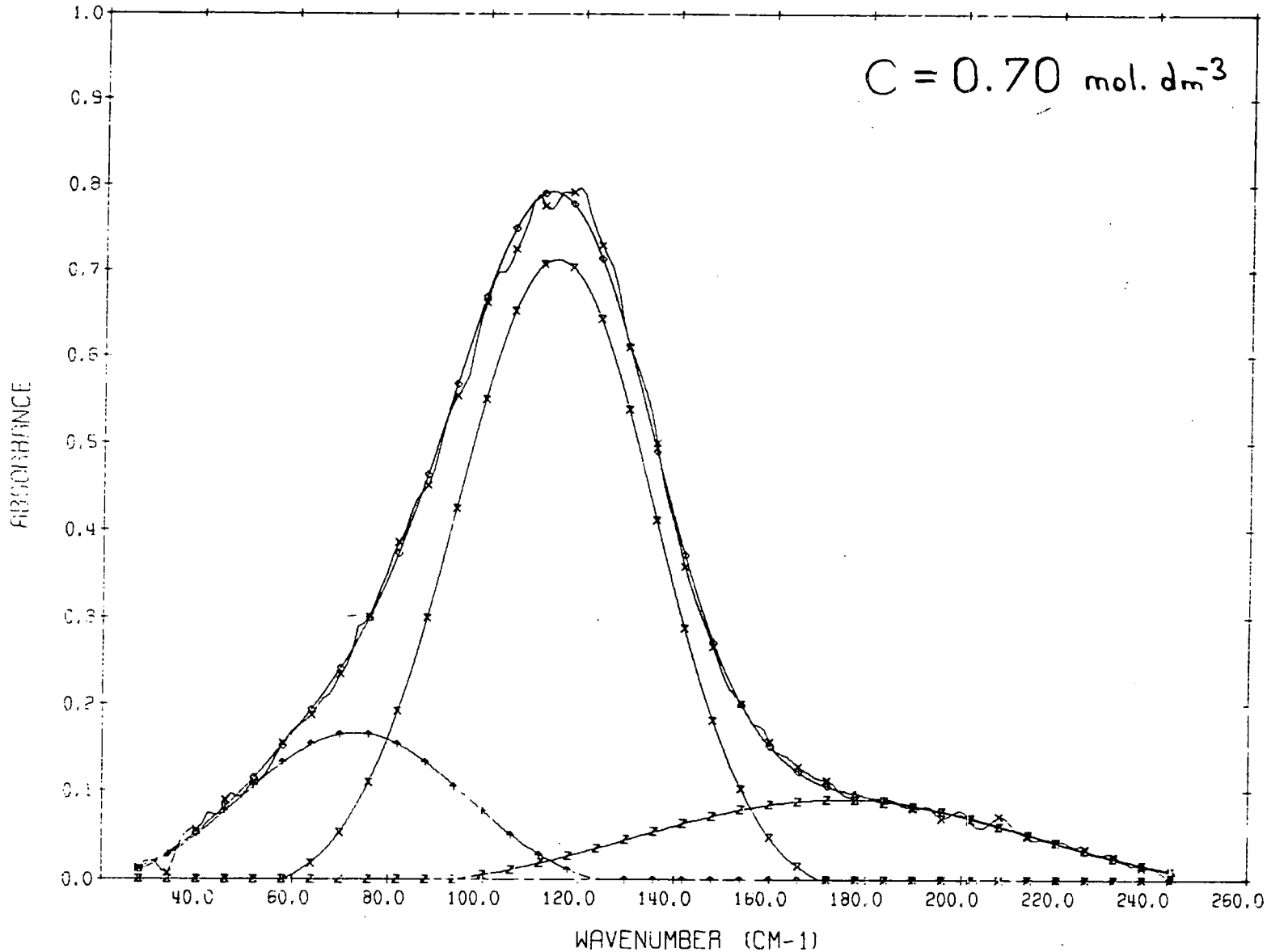

FIG. 5.15 3 PURE GAUSS FIT BU4N+CI- IN CHCI3

Table 5.12 70 cm^{-1} component $Bu_4N^+Cl^-$ in $CHCl_3$. $\bar{\nu}_0$ and $\Delta\bar{\nu}_{\frac{1}{2}}$

concn. /mol dm^{-3}	$\bar{\nu}_0$ /cm^{-1}	av. $\bar{\nu}_0$ /cm^{-1}	$\Delta\bar{\nu}_{\frac{1}{2}}$ /cm^{-1}	av. $\Delta\bar{\nu}_{\frac{1}{2}}$ /cm^{-1}
0.100	80.8	82.3	60.0	56.6
	83.9		52.6	
0.200	76.7	74.5	47.1	49.5
	72.2		52.0	
0.300	73.0	73.3	40.9	31.7
	73.5		22.6	
0.400	67.1	69.8	41.8	48.8
	72.5		55.9	
0.515	68.4	65.9	58.6	50.9
	63.4		43.1	
0.600	64.9	64.5	59.5	64.3
	64.1		69.3	
0.693	61.4	67.1	54.2	54.7
	72.8		55.2	
0.801	62.0	62.2	46.2	46.3
	62.5		46.4	

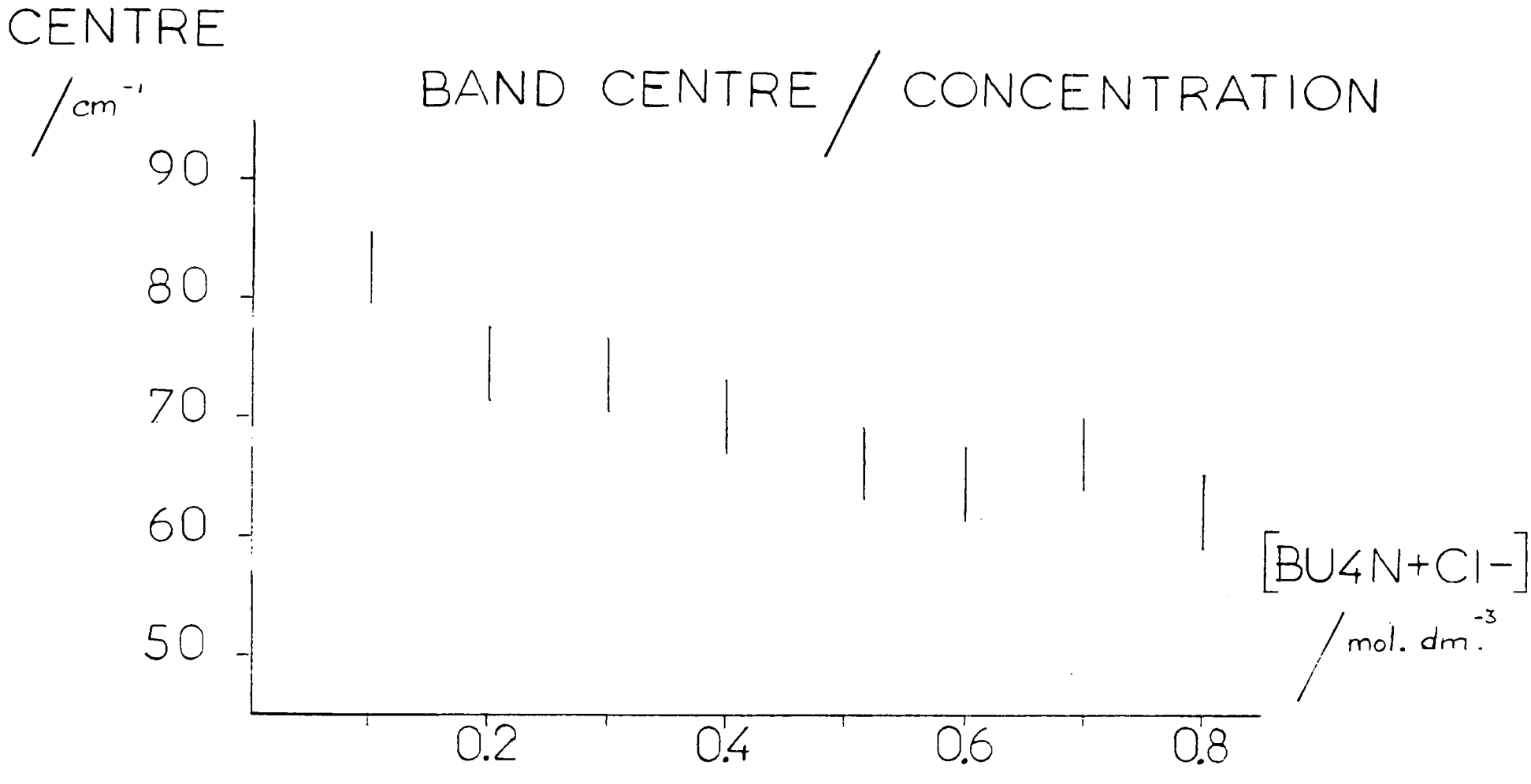

FIG 5.16 70 cm^{-1} COMPONENT BU4N+Cl- IN CHLOROFORM

The average band centre was calculated as 70±7 cm^{-1}, where the low precision was due to the dependence of band centre on salt concentration. Fig. 5.17 shows the plot of fitted band width against concentration, and showed that the half-band width was approximately constant, with a mean value of 50±11 cm^{-1}.

Table 5.13 shows the area and intensity data for the low frequency component, and fig. 5.18 shows the intensity as a function of concentration. The large uncertainty attached to each intensity value prevents any concrete conclusions, but it suggested that the intensity of this low frequency component may well have been invarient with concentration. The intensity was determined for comparison with other systems, and was found to be 1 590±110 dm^3 mol^{-1} cm^{-2} from a slope of 33.1±2.3 dm^3 mol^{-1} cm^{-1}, for the least squares fit with the origin taken as a valid point. This best fit is shown in fig. 5.19 where it is marked with the letter A. The unrestricted fit is denoted by the letter B, and had a slope of 37.5±4.8 dm^3 mol^{-1} cm^{-1}, which gave an intensity of 1 800±300 dm^3 mol^{-1} cm^{-2}.

Table 5.14 shows the centre and half-band width data for the central component for the spectra of $Bu_4N^+Cl^-$ in $CHCl_3$. Fig. 5.20 shows the band centres as a function of concentration, and indicated that the band centre shifted slightly to lower frequency with increasing concentration. The band centre occurred at 116±1 cm^{-1} for the 0.1 mol dm^{-3} solution, and at 113±1 cm^{-1} for 0.8 mol dm^{-3}, indicating that the frequency shift was small but significant. The mean band centre was calculated as 114±1 cm^{-1}. Fig. 5.21 shows the fitted half-band width as a function of concentration, and shows that the half-band width increased with increasing concentration. The half-band width was 47±2 cm^{-1} at 0.1 mol dm^{-3}, and increased to 53±2 cm^{-1} at 0.8 mol dm^{-3}. The mean half-band width was calculated as 50±2 cm^{-1}.

Table 5.15 shows the areas and intensities calculated for the central component. Fig. 5.22 shows these intensities as a function of concentration, and indicated that the intensity was not dependent upon the salt

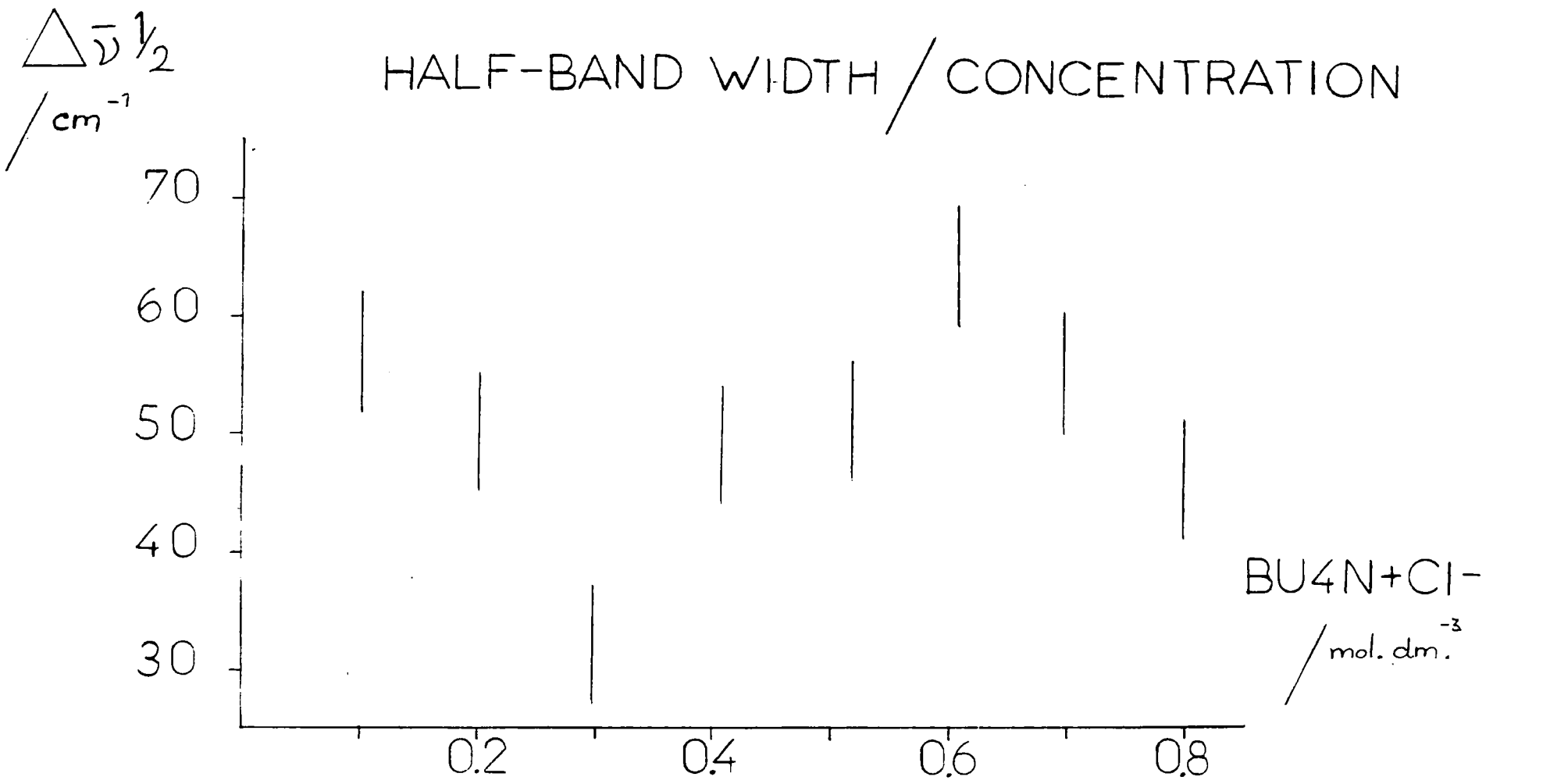

FIG. 5.17 70 cm^{-1} COMPONENT BU4N+CI- IN CHLOROFORM

Table 5.13 70 cm^{-1} component $Bu_4N^+Cl^-$ in $CHCl_3$. area and intensity

(L = 0.021 cm)

concn. /mol dm^{-3}	area /cm^{-1}	av. area /cm^{-1}	intensity /dm^3 mol^{-1} cm^{-2}
0.100	4.0 2.4	3.2	1 500±6 100
0.200	4.8 4.6	4.7	1 100±3 100
0.300	6.5 1.8	4.1	700±2 000
0.400	8.9 12.5	10.7	1 300±1 500
0.500	23.4 11.4	17.4	1 600±1 200
0.600	26.9 25.9	26.4	2 100±1 000
0.693	28.0 25.0	26.5	1 800±900
0.801	22.4 21.7	22.1	1 300±800

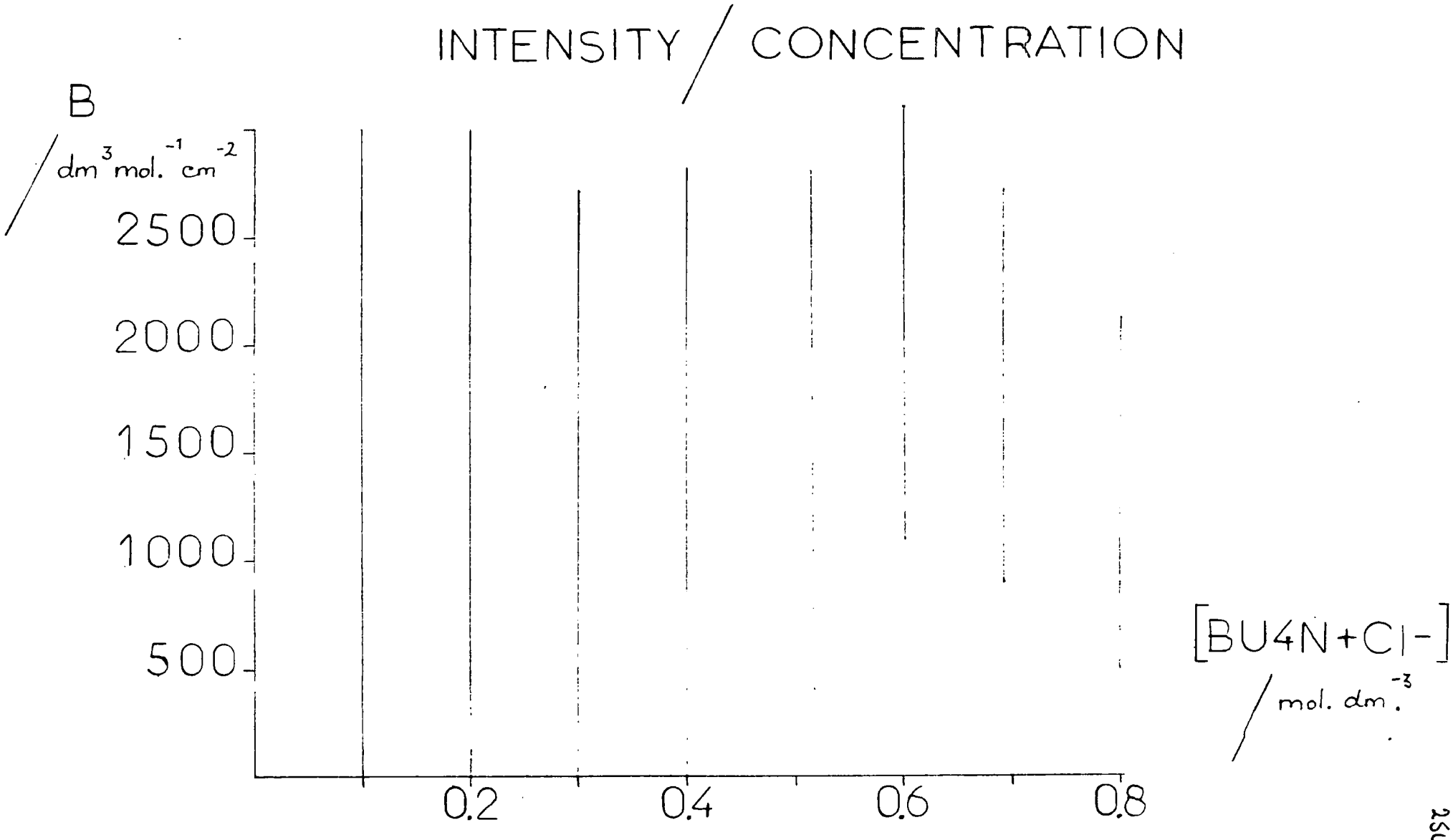

256

FIG 5.18 70 cm^{-1} COMPONENT BU4N+Cl- IN CHLOROFORM

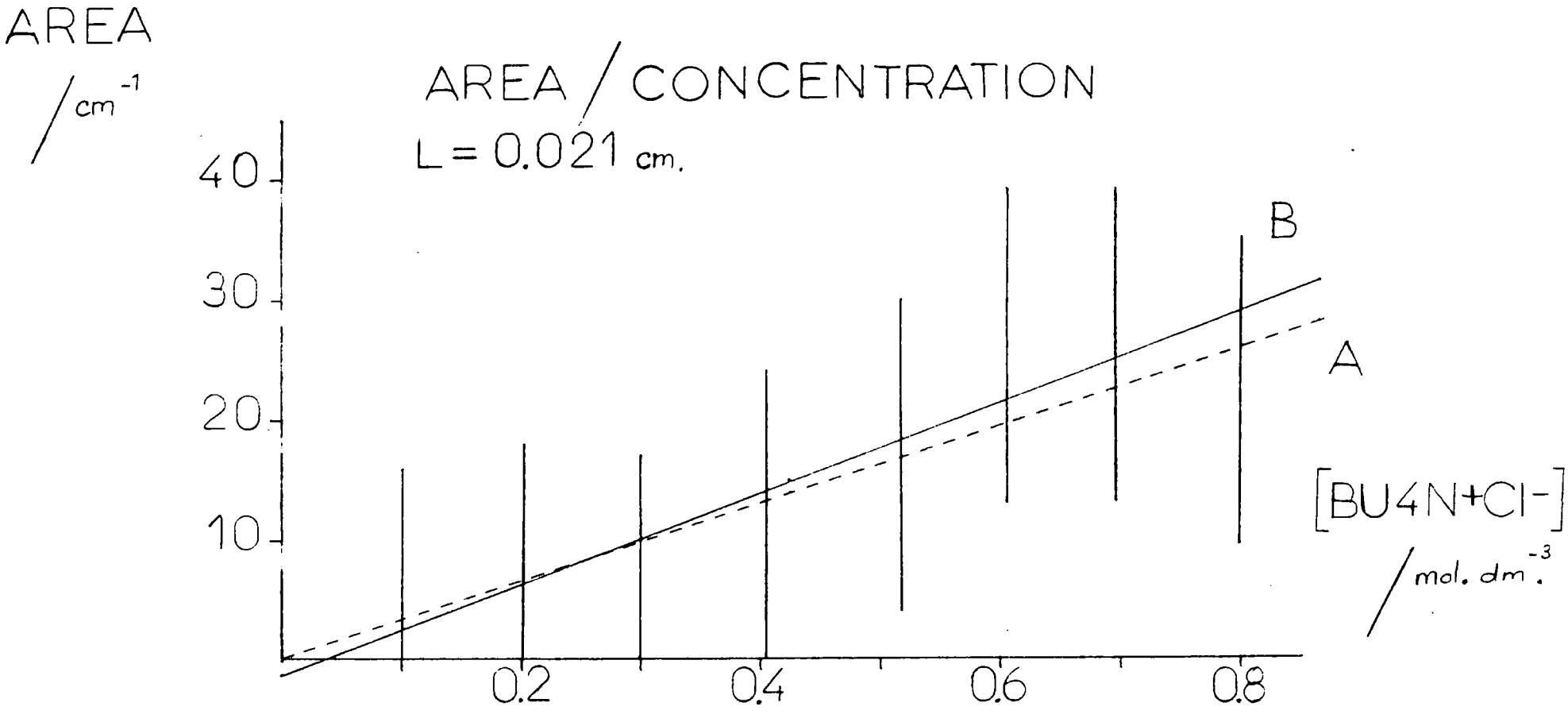

FIG.5.19 70 cm^{-1} COMPONENT $BU_4N^+Cl^-$ IN CHLOROFORM

Table 5.14 114 cm^{-1} component $Bu_4N^+Cl^-$ in $CHCl_3$. $\bar{\nu}_o$ and $\Delta\bar{\nu}_{\frac{1}{2}}$

concn. /mol dm^{-3}	$\bar{\nu}_o$ /cm^{-1}	av. $\bar{\nu}_o$ /cm^{-1}	$\Delta\bar{\nu}_{\frac{1}{2}}$ /cm^{-1}	av. $\Delta\bar{\nu}_{\frac{1}{2}}$ /cm^{-1}
0.100	115.4	115.6	46.9	47.1
	115.7		47.2	
0.200	115.5	115.0	48.7	48.2
	114.6		47.6	
0.300	114.2	114.1	47.4	48.3
	114.0		49.3	
0.400	113.1	114.0	50.2	49.7
	114.9		49.3	
0.515	114.2	113.4	49.1	50.9
	112.7		52.7	
0.600	113.8	114.3	50.8	51.2
	114.8		51.6	
0.693	112.8	113.6	53.6	51.1
	114.5		48.7	
0.801	112.5	112.7	52.9	52.7
	113.0		52.5	

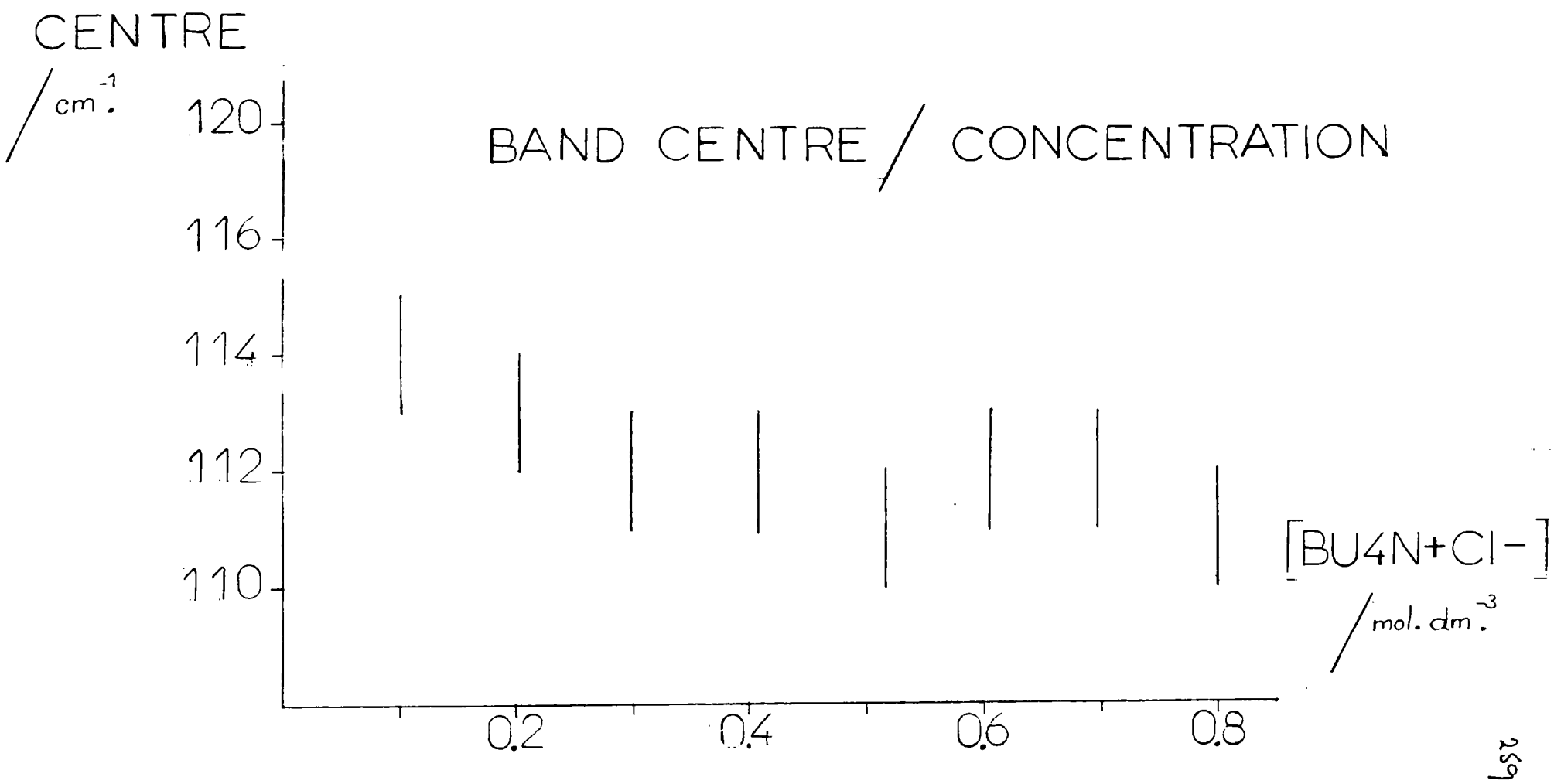

259

FIG. 5.20 114 cm^{-1} COMPONENT BU4N+Cl− IN CHLOROFORM

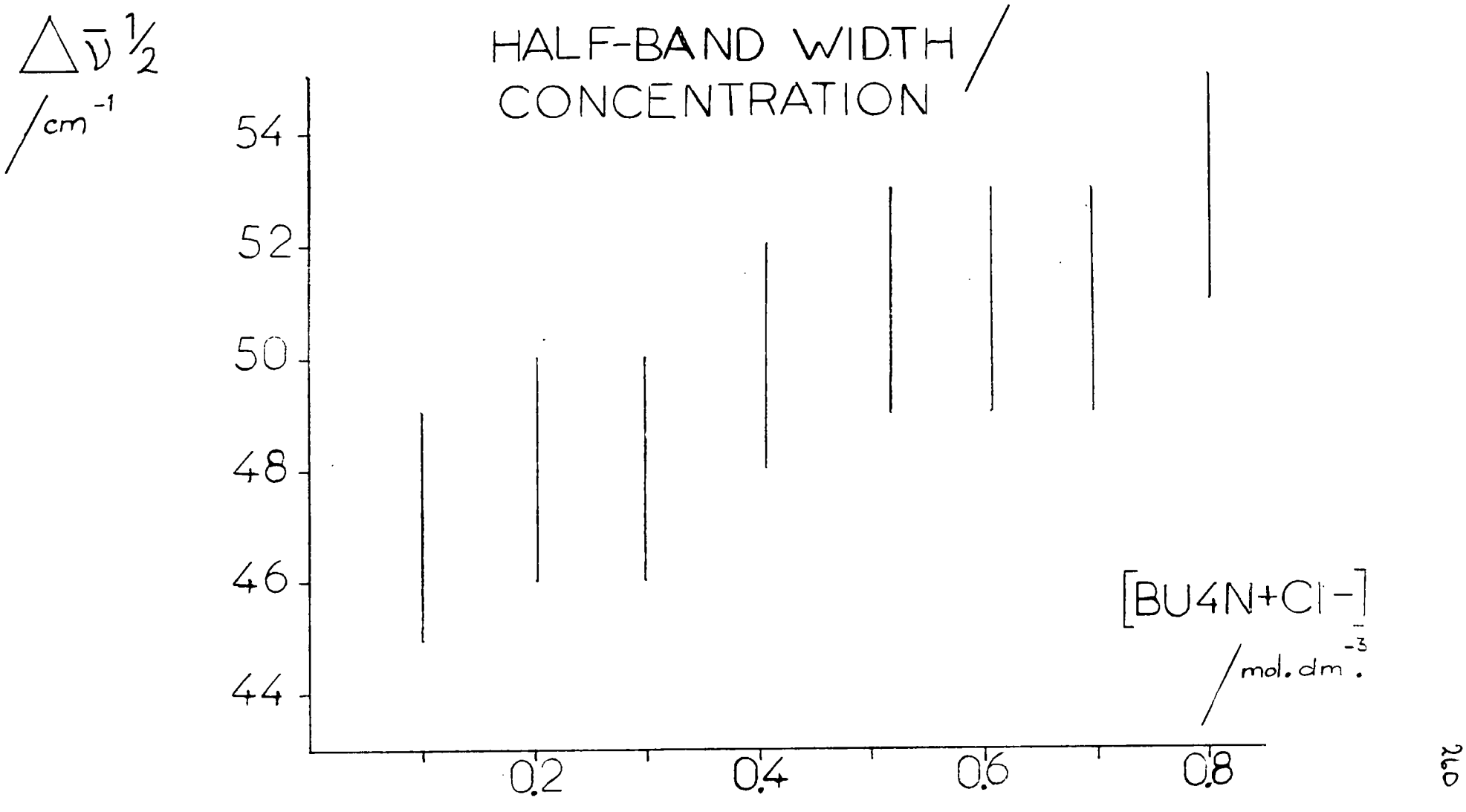

FIG. 5.21 114 cm^{-1} COMPONENT BU4N+Cl− IN CHLOROFORM

Table 5.15 114 cm^{-1} component $Bu_4N^+Cl^-$ in $CHCl_3$. Area and intensity

(L = 0.021 cm)

concn. /mol dm^{-3}	area /cm^{-1}	av. area /cm^{-1}	intensity /dm^3 mol^{-1} cm^{-2}
0.100	11.8 12.1	11.9	5 700±6 200
0.200	25.1 25.2	25.2	5 900±3 100
0.300	39.4 37.9	38.7	6 100±2 100
0.400	54.8 52.6	53.7	6 400±1 500
0.515	69.7 79.1	74.4	6 900±1 200
0.600	83.1 82.8	82.9	6 600±1 000
0.693	109.3 87.3	98.3	6 800±900
0.801	119.8 114.7	117.2	6 900±800

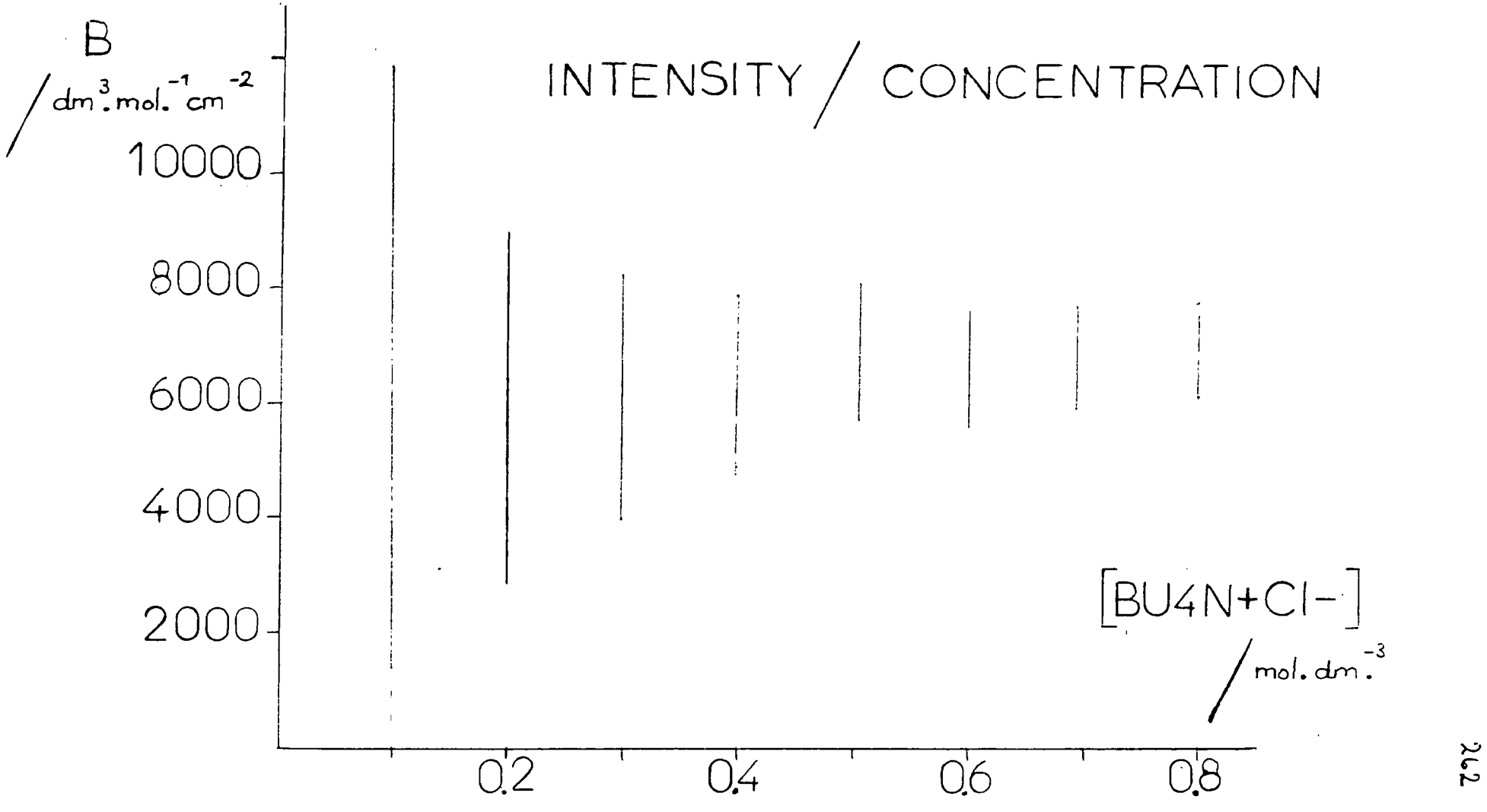

FIG.5.22 114 cm^{-1} COMPONENT BU4N+Cl− IN CHLOROFORM

concentration. Fig. 5.23 shows the area as a function of concentration, with the resricted fit labelled A and the unrestricted fit B. The slope of the fit through the origin was 141.4±2.5 $dm^3\ mol^{-1}\ cm^{-1}$, giving an intensity of 6 960±120 $dm^3\ mol^{-1}\ cm^{-2}$, and the unrestricted slope was 150 ±5.1 $dm^3\ mol^{-1}\ cm^{-1}$, giving an intensity of 7 210±240 $dm^3\ mol^{-1}\ cm^{-2}$.

Table 5.16 shows the centres and half-band widths for the best fits for the high frequency component of the absorption profile in the spectra of $Bu_4N^+Cl^-$ in chloroform. Fig. 5.24 shows the band centre as a function of concentration, from which it was deduced that the band centre was invarient with concentration. The mean band centre was calculated as 175±7 cm^{-1}, where the low precision was due to the low intensity of this component. Fig. 5.25 shows the half-band width of the 175 cm^{-1} component as a function of concentration, and suggested that the half-band width of this component was not affected by the concentration. The mean half-band width was 84±16 cm^{-1}.

Table 5.17 shows the areas and intensities calculated for the high frequency component for $Bu_4N^+Cl^-$ in $CHCl_3$. Fig. 5.26 shows the intensity as a function of concentration, and showed that the intensity was not dependent upon concentration. A good linear relation was obtained for area against concentration, as shown in fig. 5.27, and the slope of the restrained fit was 29.8±2.1 $dm^3\ mol^{-1}\ cm^{-1}$, giving an intensity of 1 430±100 $dm^3\ mol^{-1}\ cm^{-2}$. The unrestrained fit gave a slope of 31.7±4.6 $dm^3\ mol^{-1}\ cm^{-1}$, which gave an intensity of 1 520±220 $dm^3\ mol^{-1}\ cm^{-2}$.

The values for band centres, half-band widths and intensities of the 3 components of the absorption profile for the $Bu_4N^+Cl^-$ in $CHCl_3$ system are summarised in table 5.29 at the end of this chapter.

5.5 3 pure Gauss component fit for $Bu_4N^+Cl^-$ in CCl_4. Effect of concentration

The absorption profiles for the spectra of $Bu_4N^+Cl^-$ in CCl_4 at various concentrations, obtained using a 0.021 cm pathlength, were

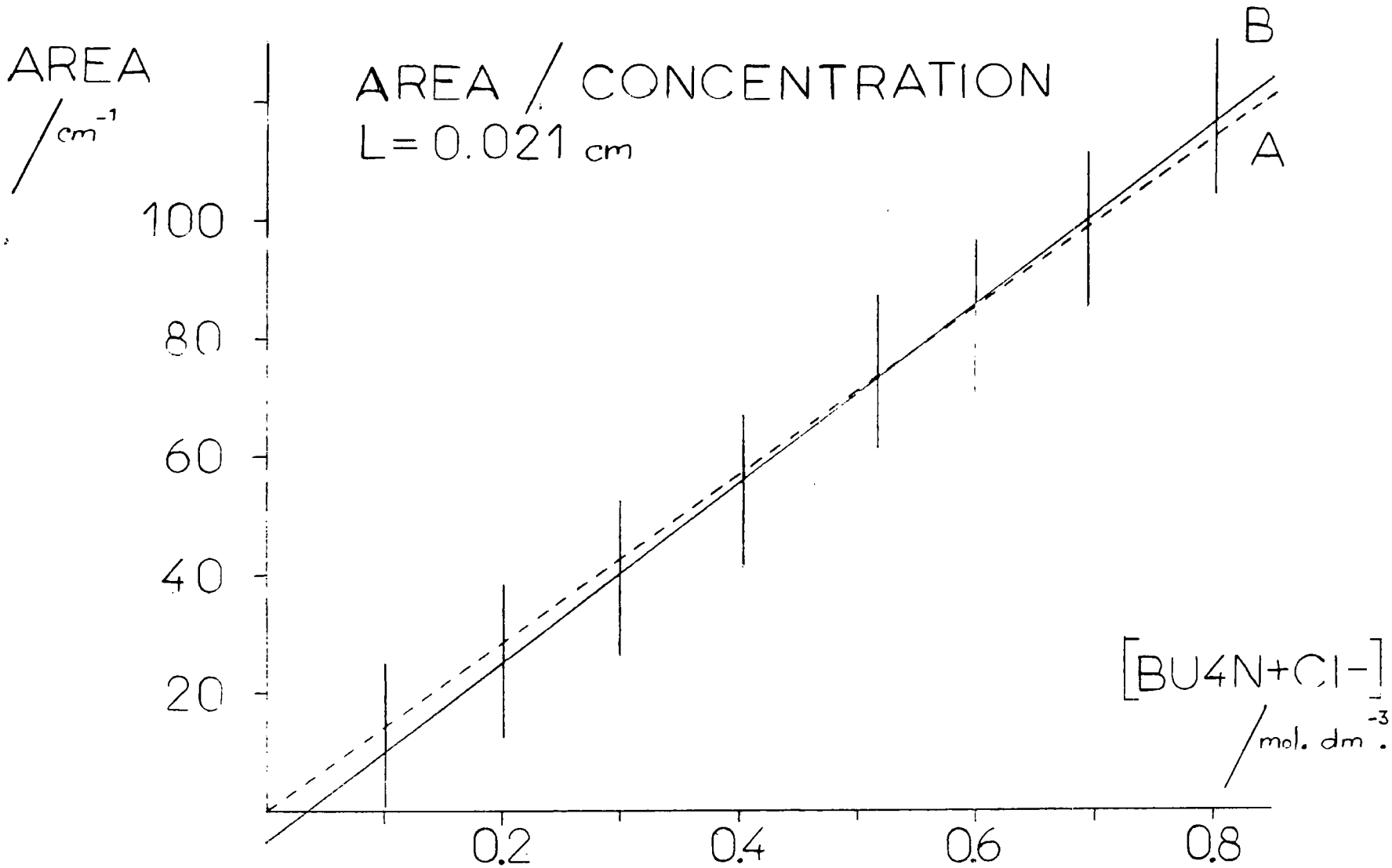

FIG. 5.23 114 cm^{-1} COMPONENT BU4N+Cl− IN CHLOROFORM

Table 5.16 175 cm^{-1} component $Bu_4N^+Cl^-$ in $CHCl_3$. $\bar{\nu}_o$ and $\Delta\bar{\nu}_{\frac{1}{2}}$

concn. /mol dm^{-3}	$\bar{\nu}_o$ /cm^{-1}	av. $\bar{\nu}_o$ /cm^{-1}	$\Delta\bar{\nu}_{\frac{1}{2}}$ /cm^{-1}	av. $\Delta\bar{\nu}_{\frac{1}{2}}$ /cm^{-1}
0.100	162.7	175.8	75.5	79.9
	188.9		84.2	
0.200	178.3	173.9	58.9	92.4
	169.4		126.0	
0.300	166.3	173.5	76.2	74.4
	180.6		72.5	
0.400	163.9	171.7	98.2	84.2
	179.6		70.2	
0.515	169.6	175.4	104.2	95.4
	181.2		86.5	
0.600	174.5	175.9	83.3	83.0
	177.3		82.6	
0.693	180.1	177.0	100.1	87.3
	173.8		74.4	
0.801	178.9	178.3	77.1	74.6
	177.8		72.1	

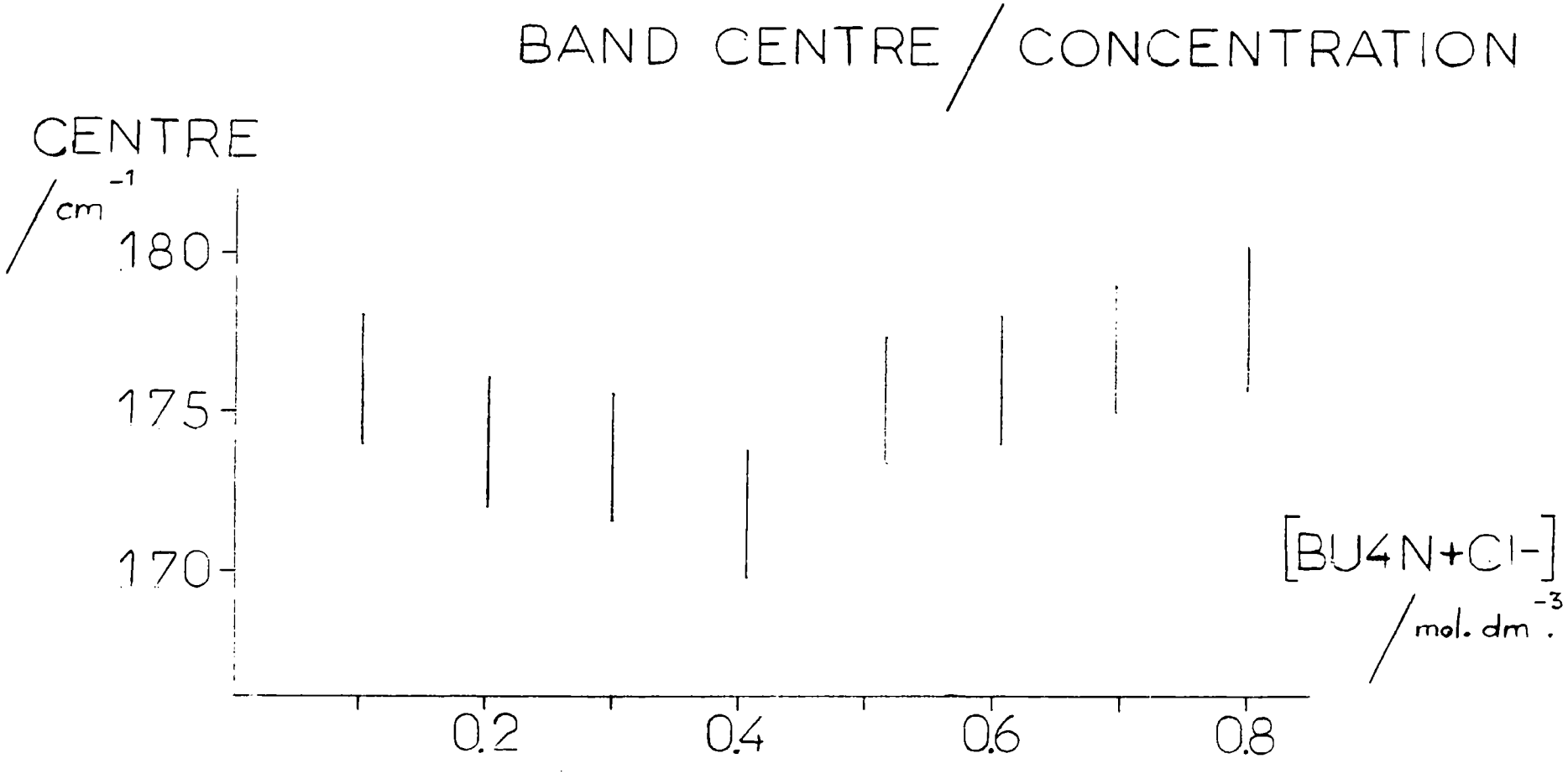

FIG. 5.24 175 cm^{-1} COMPONENT BU4N+Cl- IN CHLOROFORM

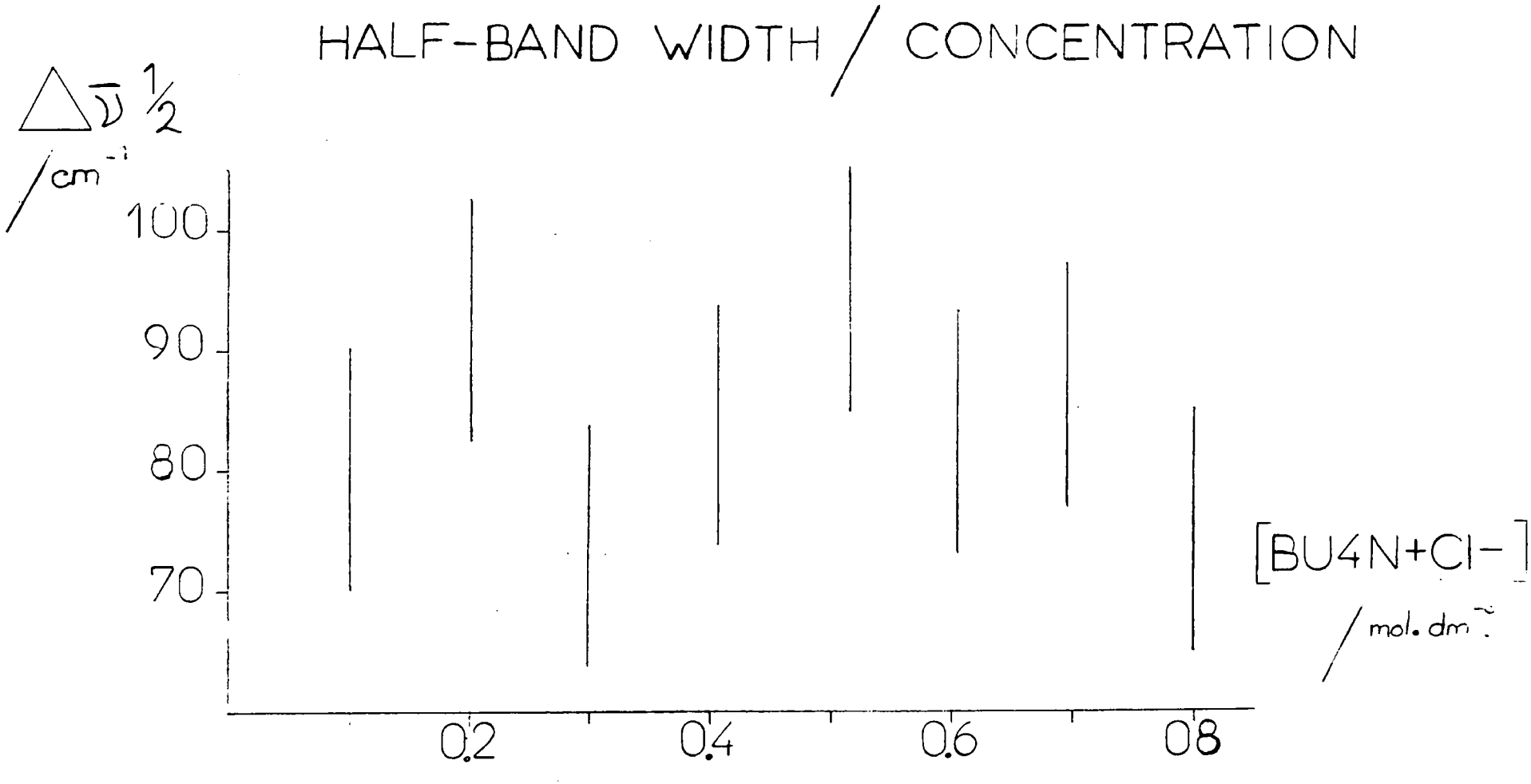

FIG.5.25 175 cm^{-1} COMPONENT BU4N+Cl− IN CHLOROFORM

Table 5.17 175 cm^{-1} component $Bu_4N^+Cl^-$ in $CHCl_3$. Area and intensity

(L = 0.021 cm)

concn. / mol dm^{-3}	area / cm^{-1}	av. area / cm^{-1}	intensity / dm^3 mol^{-1} cm^{-2}
0.100	2.9	3.0	1 400±3 000
	3.0		
0.200	3.5	4.7	1 100±1 400
	6.0		
0.300	4.8	4.6	800±1 000
	4.4		
0.400	10.7	9.0	1 100±700
	7.4		
0.515	25.9	22.7	2 100±600
	19.6		
0.600	19.5	19.2	1 500±500
	18.8		
0.693	20.6	23.6	1 600±400
	26.7		
0.801	19.8	19.0	1 100±400
	18.0		

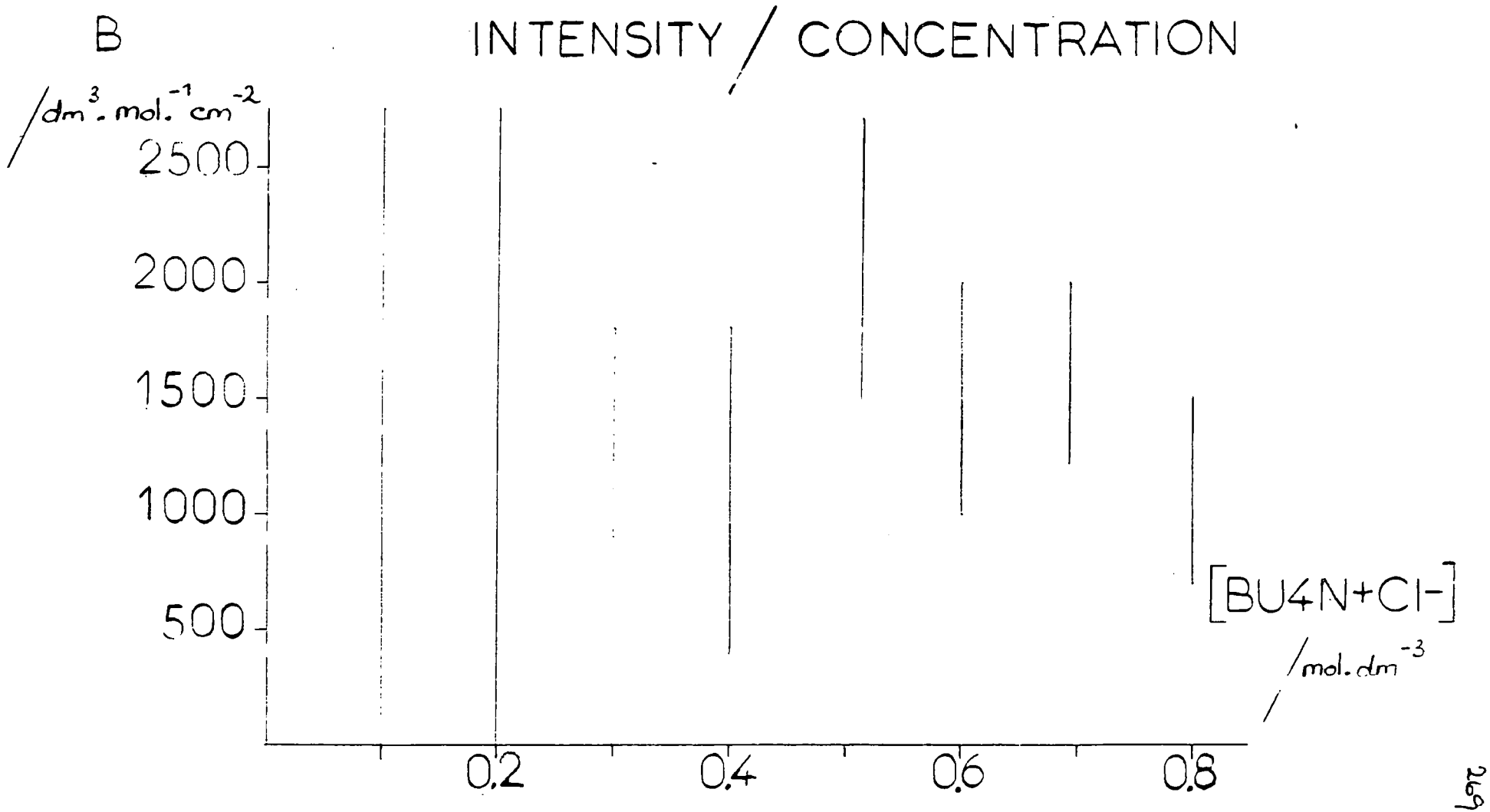

FIG. 5.26 175 cm^{-1} COMPONENT BU4N+CI- IN CHLOROFORM

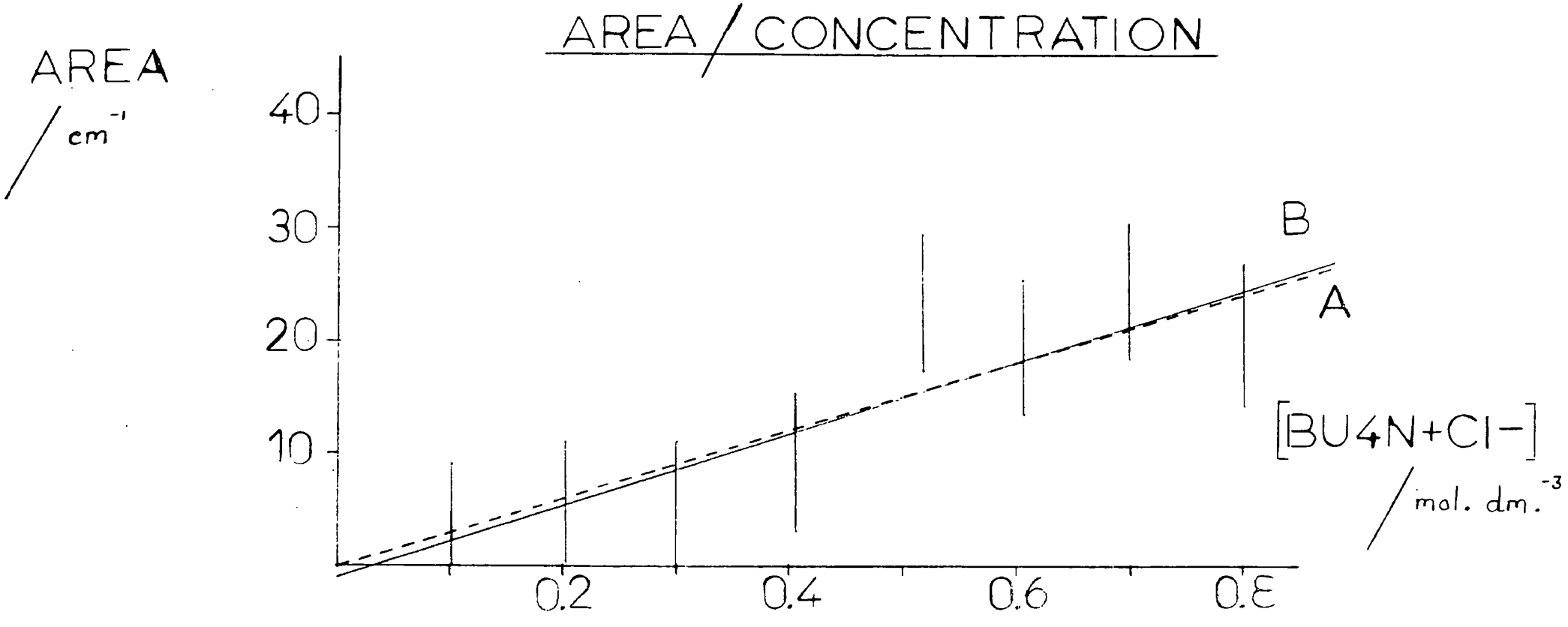

FIG 5.27 175 cm^{-1} COMPONENT BU4N+Cl⁻ IN CHLOROFORM

fitted to a profile, which was the sum of 3 pure Gauss components, in an exactly analogous manner to that used for the spectra in benzene solution. The initial input parameters for the fits were the same as those used for the fits to the benzene solution spectra, namely bands centred at 70, 116 and 180 cm^{-1}, with half-band widths of 66, 54 and 80 cm^{-1} respectively. Fig. 5.27A shows a typical fit for the 3 components for the spectrum obtained for 0.69 mol dm^{-3} $Bu_4N^+Cl^-$ in CCl_4. Tables 5.18 to 5.23 show the parameters obtained for the 3 components for the best fits to the 16 spectra at 8 concentrations of $Bu_4N^+Cl^-$ in CCl_4 between 0.10 and 0.78 mol dm^{-3}.

Table 5.18 shows the fitted band centre and half-band width for the low frequency component. The fitted centre was plotted as a function of $Bu_4N^+Cl^-$ salt concentration, and the resulting graph is shown as fig. 5.28. This graph suggested that there was a small decrease in wavenumber of the band centre with increasing concentration. The centre occurred at 84±3 cm^{-1} at 0.10 mol dm^{-3}, and fell to 73±3 cm^{-1} at 0.78 mol dm^{-3}. The average band centre was calculated as 75±6 cm^{-1} for comparison with other systems. Fig. 5.29 shows the half-band width as a function of salt concentration, and indicated that the half-band width was constant over the concentration range studied. The mean value of the half-band width was calculated as 64±6 cm^{-1}.

Table 5.19 shows the area and intensity data obtained from the parameters for the best fits. Fig. 5.30 shows the intensity as a function of concentration for the low frequency component, and indicated that the intensity was invarient with concentration. Fig. 5.31 shows the expected linear plot for area against concentration. The letter A indicates the best fit restrained to pass through the origin, which has a slope of 88.9±4.0 dm^3 mol^{-1} cm^{-1}, which gave an intensity of 4 270±190 dm^3 mol^{-1} cm^{-2}. The unrestricted fit had a slope of 76.0±7.9 dm^3 mol^{-1} cm^{-1}, which gave an intensity of 3 650±380 dm^3 mol^{-1} cm^{-2}.

Table 5.20 shows the centre and half-band widths for the central

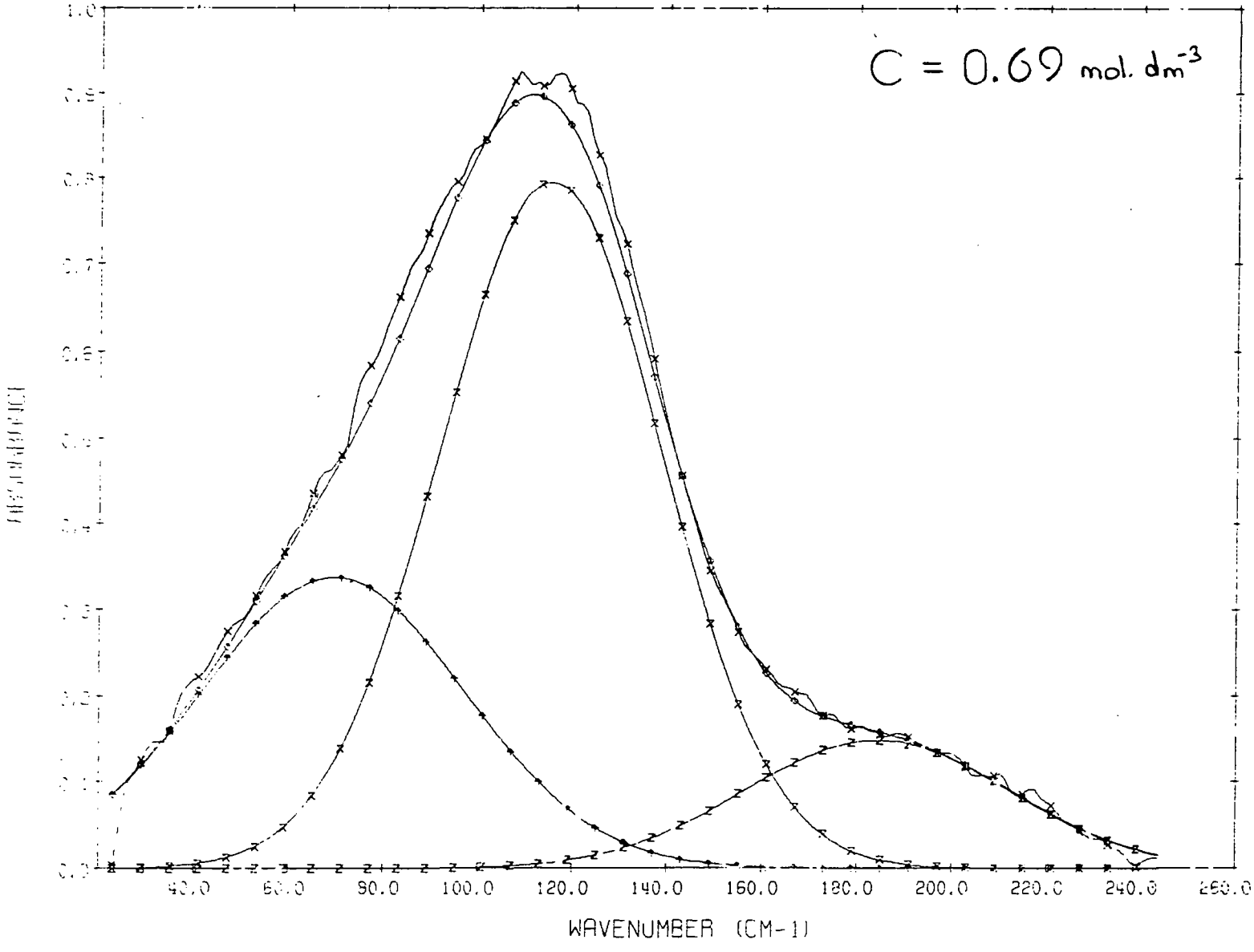

FIG. 5.27A 3 PURE GAUSS FIT BU4N+CI- IN CCI4

Table 5.18 75 cm^{-1} component $Bu_4N^+Cl^-$ in CCl_4. $\bar{\nu}_o$ and $\Delta\bar{\nu}_{\frac{1}{2}}$

concn. /mol cm^{-3}	$\bar{\nu}_o$ /cm^{-1}	av. $\bar{\nu}_o$ /cm^{-1}	$\Delta\bar{\nu}_{\frac{1}{2}}$ /cm^{-1}	av. $\Delta\bar{\nu}_{\frac{1}{2}}$ /cm^{-1}
0.098	84.1	83.7	71.3	67.5
	83.4		63.7	
0.196	83.2	78.4	49.7	58.8
	73.6		67.9	
0.291	75.5	78.1	59.0	63.4
	80.6		67.8	
0.392	69.4	72.0	59.9	63.7
	74.6		67.6	
0.524	67.9	71.3	62.7	63.4
	74.7		64.2	
0.581	76.1	74.3	64.4	66.8
	72.5		69.3	
0.688	69.3	69.7	65.8	63.2
	70.1		60.5	
0.783	78.5	72.8	68.0	61.4
	67.1		54.7	

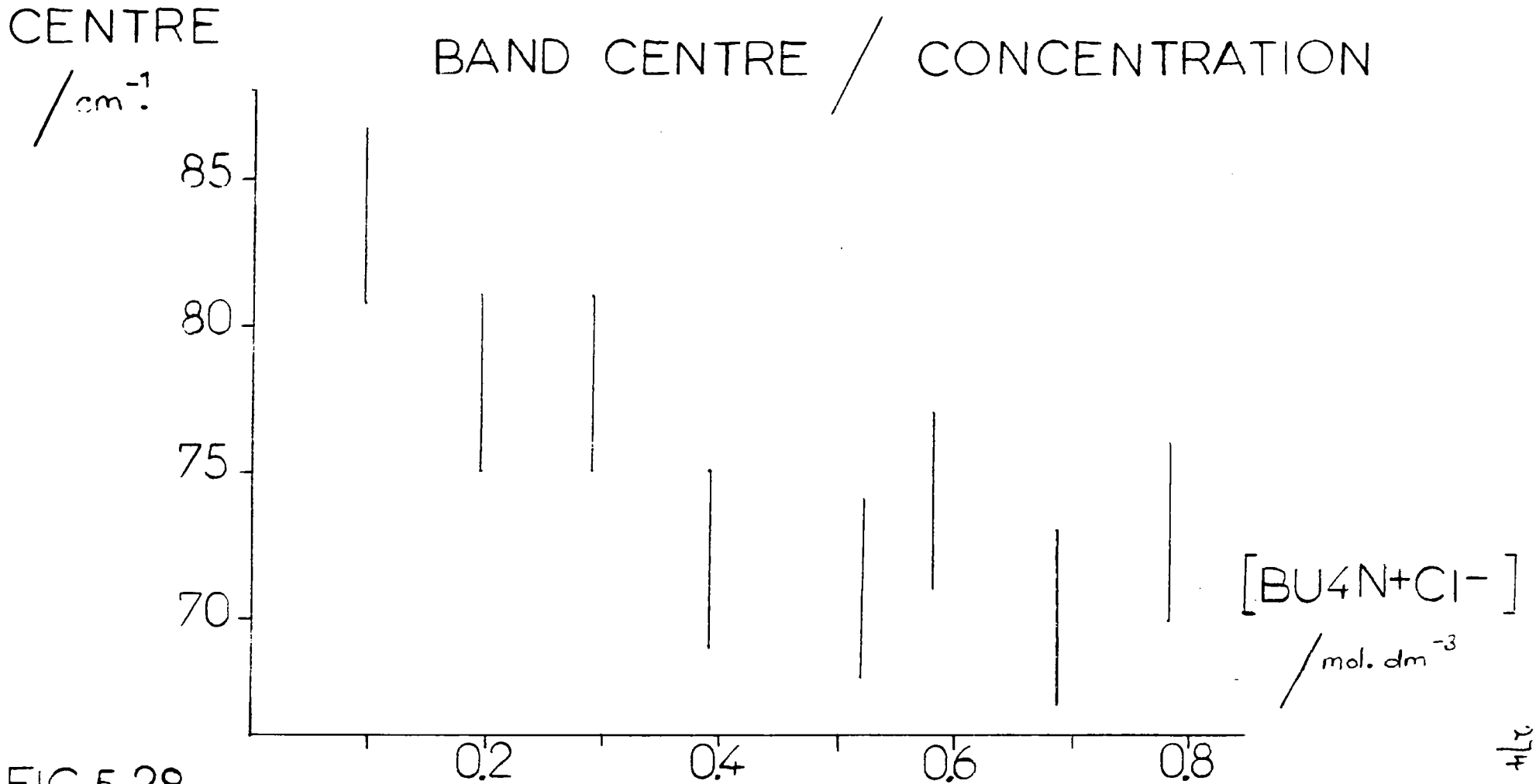

FIG.5.28

75 cm⁻¹ COMPONENT BU4N+Cl- IN CARBON TETRACHLORIDE

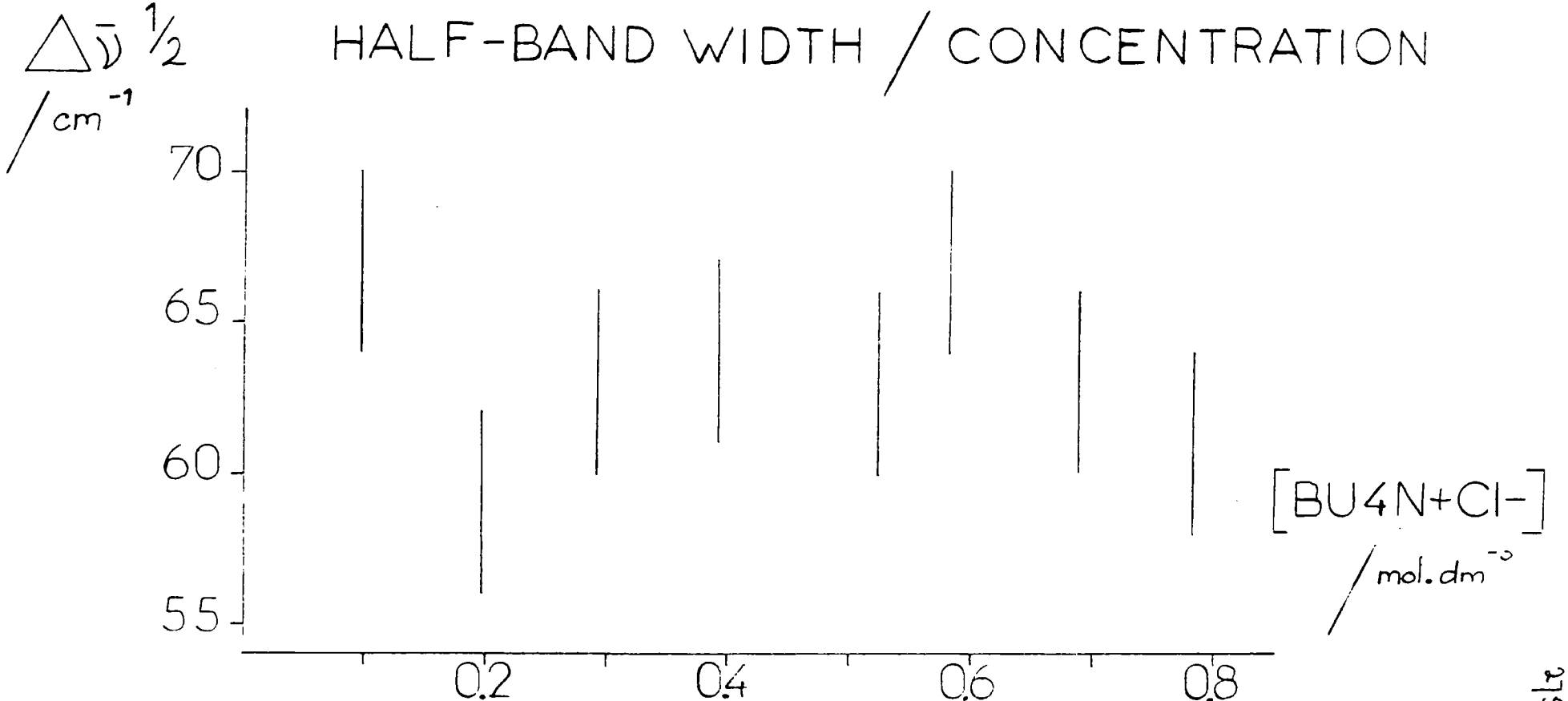

FIG. 5.29

75 cm^{-1} COMPONENT BU4N+Cl- IN CARBON TETRACHLORIDE

Table 5.19 75 cm^{-1} component $Bu_4N^+Cl^-$ in CCl_4. Areas and intensities

(L = 0.021 cm)

concn. /mol dm^{-3}	area /cm^{-1}	av. area /cm^{-1}	intensity /dm^3 mol^{-1} cm^{-2}
0.098	14.7 12.0	13.4	6 500±6 300
0.196	15.4 24.0	19.7	4 800±3 200
0.291	23.2 33.8	28.5	4 700±2 100
0.392	42.5 45.2	43.9	5 300±1 600
0.524	44.0 41.7	42.9	3 900±1 200
0.581	50.6 64.7	57.7	4 700±1 100
0.688	54.5 59.9	57.2	4 000±900
0.783	77.8 51.0	64.4	3 900±800

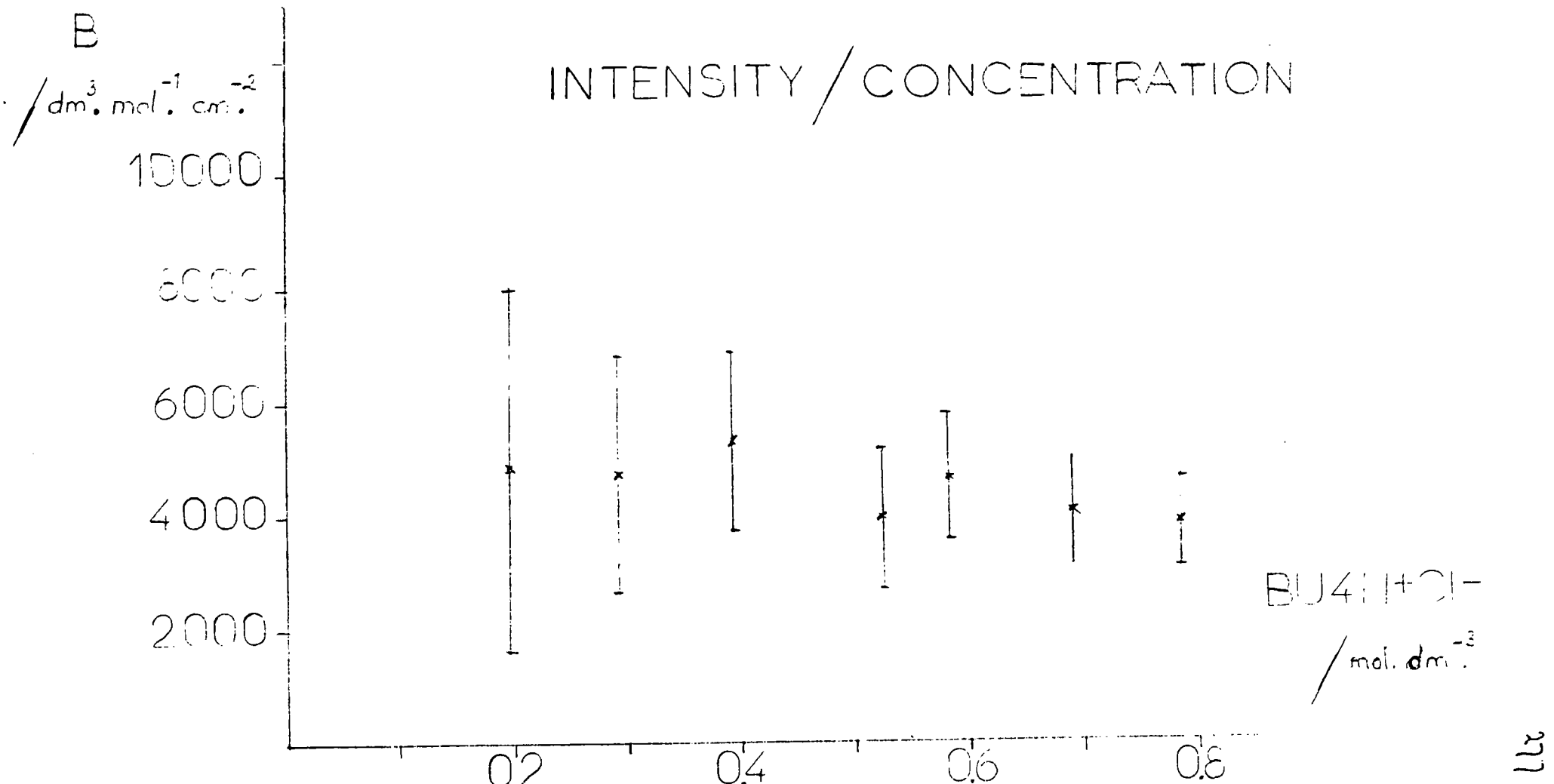

FIG.5.30

75 cm^{-1} COMPONENT BU4N+Cl− IN CARBON TETRACHLORIDE

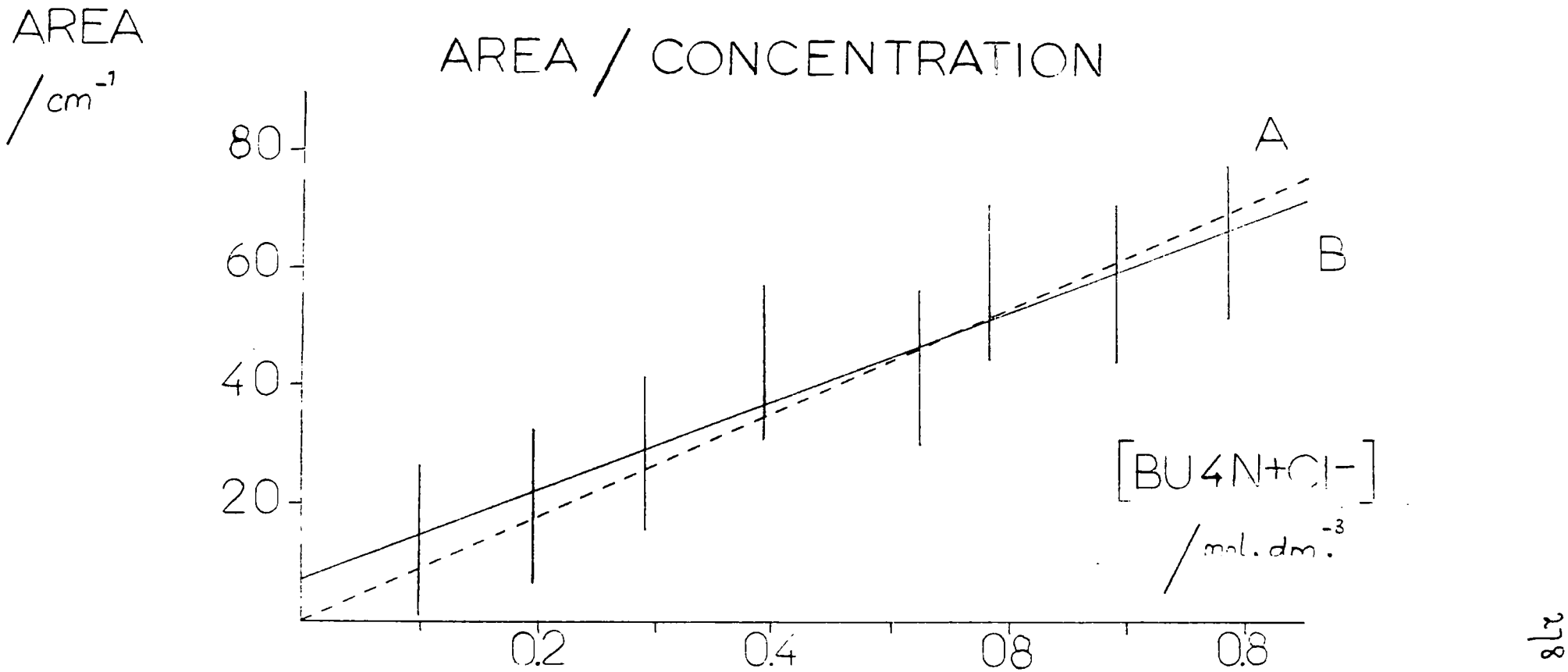

FIG.5.31

75 cm^{-1} COMPONENT BU4N+Cl- IN CARBON TETRACHLORIDE

Table 5.20 116 cm^{-1} component $Bu_4N^+Cl^-$ in CCl_4. $\bar{\nu}_o$ and $\bar{\nu}_{\frac{1}{2}}$

concn. /mol dm^{-3}	$\bar{\nu}_o$ /cm^{-1}	av. $\bar{\nu}_o$ /cm^{-1}	$\Delta\bar{\nu}_{\frac{1}{2}}$ /cm^{-1}	av. $\Delta\bar{\nu}_{\frac{1}{2}}$ /cm^{-1}
0.098	119.6	119.7	48.4	48.6
	119.8		48.8	
0.196	119.5	117.8	49.1	51.3
	116.1		53.4	
0.291	116.8	117.4	48.9	44.1
	118.0		39.3	
0.392	114.0	114.9	53.6	53.5
	115.8		53.4	
0.524	113.2	114.8	53.4	53.2
	116.3		53.0	
0.581	116.1	115.5	53.1	53.3
	115.0		53.5	
0.688	115.1	114.7	55.6	54.3
	114.2		53.0	
0.783	116.4	114.4	52.9	53.7
	112.4		54.6	

component from the overall profile for the spectra of $Bu_4N^+Cl^-$ in CCl_4. Fig. 5.32 shows the band centres as a function of concentration, and indicated that the band centre shifted slightly to lower frequency with increasing salt concentration. The band centre occurred at 120±1 cm^{-1} for 0.10 mol dm^{-3} solution, and decreased to 114±1 cm^{-1} for the 0.78 mol dm^{-3} solutions. The frequency shift was seen to be small, and to be equivalent to that occurring in the $Bu_4N^+Cl^-$ in $CHCl_3$ system. The mean band centre was calculated as 116±2 cm^{-1}. Fig. 5.33 shows the graph obtained when the fitted half-band widths were plotted as a function of concentration. The half-band width was seen to be approximately constant, with the possibility of a slight increase with increasing concentration. The band width was 49±2 cm^{-1} at 0.10 mol dm^{-3} and 54±2 cm^{-1} at 0.78 mol dm^{-3} solution, indicating that the increase was only just significant. The mean half-band width was calculated as 52±4 cm^{-1}.

Table 5.21 shows the areas and intensities calculated for the best fits to the central component for the $Bu_4N^+Cl^-$ in CCl_4 system. The intensities were plotted as a function of concentration, and the graph is shown in fig. 5.34, which indicated that the intensity was constant throughout the concentration range studied. An accurate determination of the intensity of this component was made by plotting the area against concentration as usual. The unrestricted fit had a slope of 156.7±11.2 dm^3 mol^{-1} cm^{-1}, which corresponded to an intensity of 7 540±540 dm^3 mol^{-1} cm^{-2}, and is denoted by the letter B in fig. 5.35. The restriction that the best line must pass through the origin made little difference to the slope, which was now 153.9±5.1 dm^3 mol^{-1} cm^{-2}, and gave an intensity of 7 400±250 dm^3 mol^{-1} cm^{-2}. The equal slopes of the restricted and unrestricted fits indicated further that the intensity was constant for this component.

Table 5.22 shows the band centres and half-band widths for the best fits for the high frequency component of the absorption profile in the spectra of $Bu_4N^+Cl^-$ in CCl_4. Fig. 5.36 shows the plot of the band centre

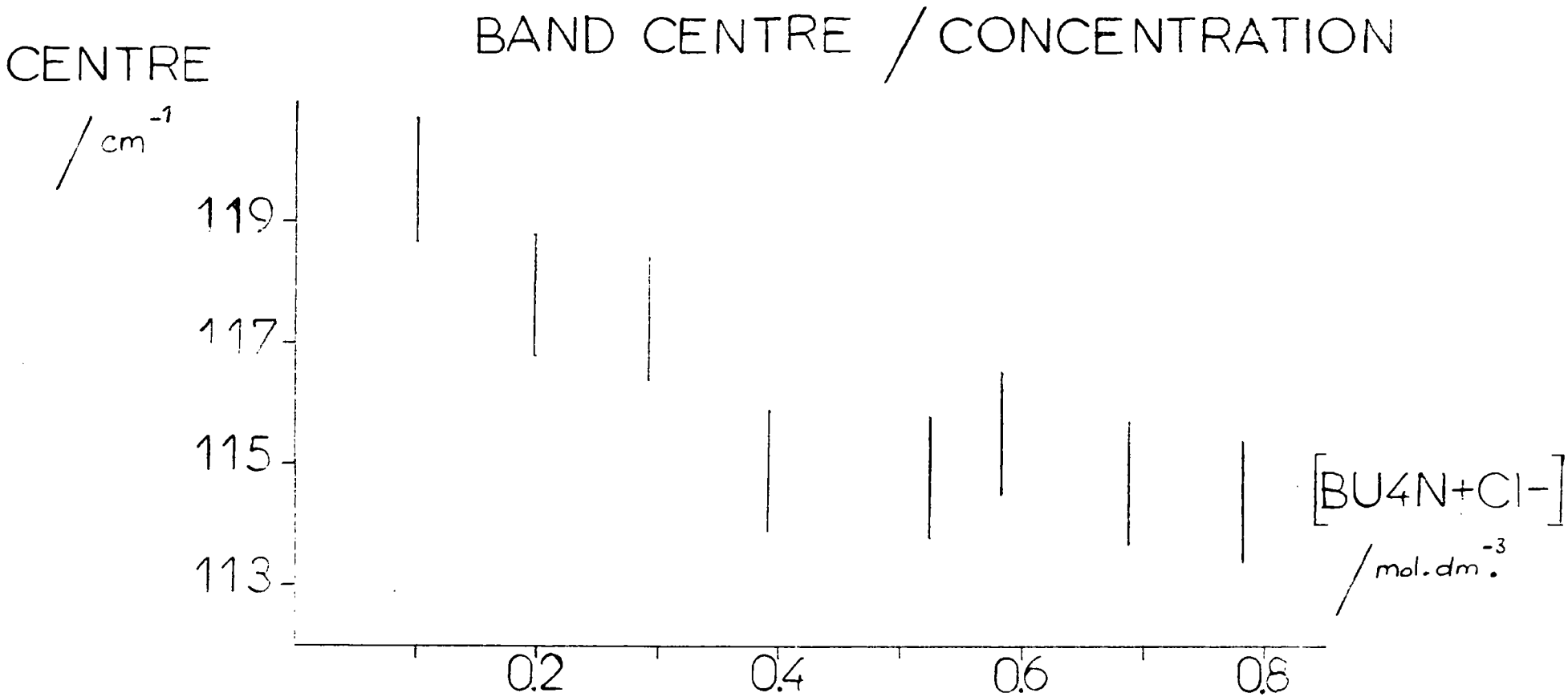

FIG. 5.32

116 cm.$^{-1}$ COMPONENT BU4N+Cl- IN CARBON TETRACHLORIDE

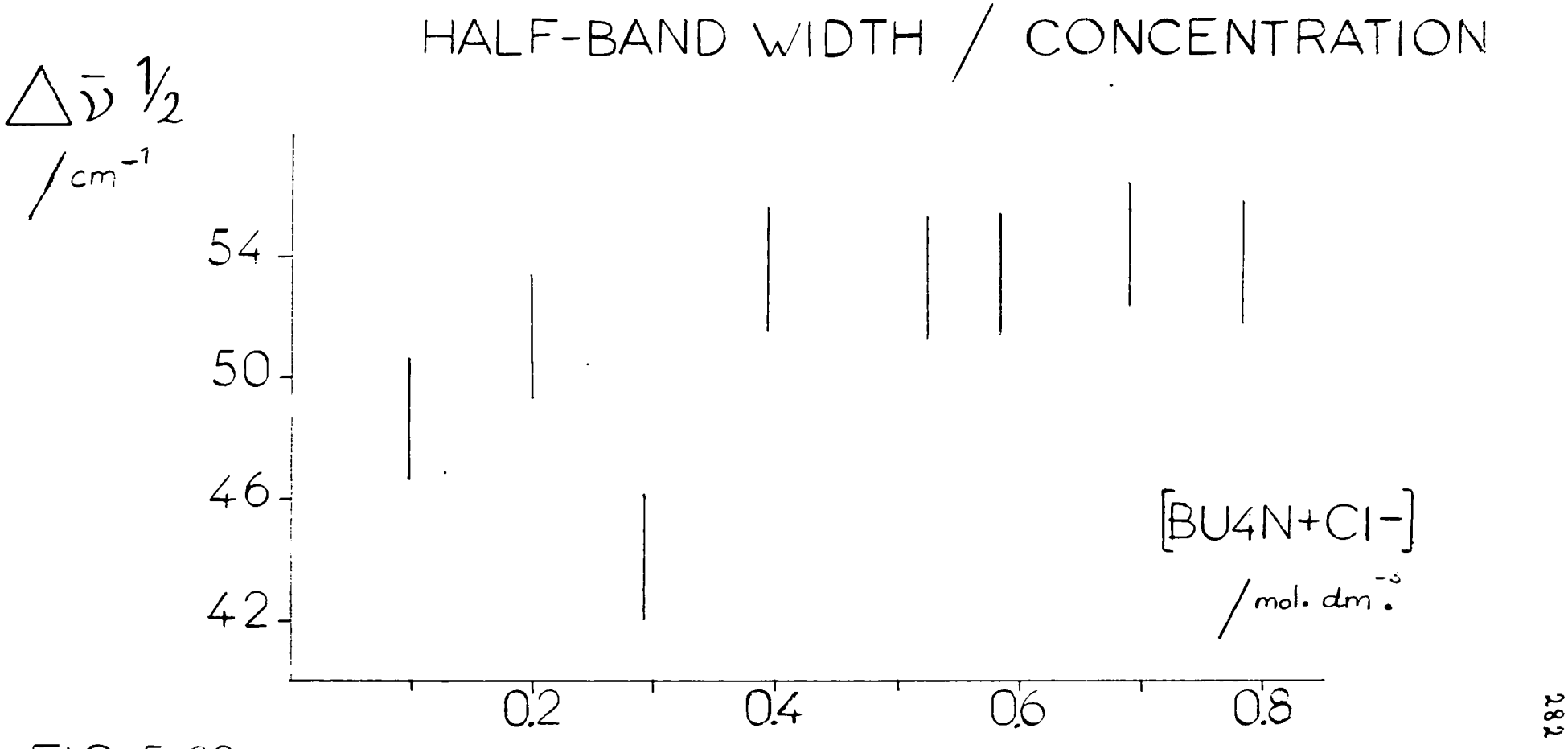

FIG. 5.33

116 cm^{-1} COMPONENT BU4N+CI- IN CARBON TETRACHLORIDE

Table 5.21 116 cm^{-1} component $Bu_4N^+Cl^-$ in CCl_4. Area and intensity

(L = 0.021 cm)

concn. /mol dm^{-3}	area /cm^{-1}	av. area /cm^{-1}	intensity /dm^3 mol^{-1} cm^{-2}
0.098	11.0 12.3	11.6	5 600±6 300
0.196	32.6 26.2	29.4	7 100±3 200
0.291	54.3 51.5	52.9	8 700±2 100
0.392	83.9 64.4	74.1	9 000±1 600
0.524	68.7 61.7	65.2	5 900±1 200
0.581	87.2 92.2	89.7	7 400±1 100
0.688	108.5 96.0	102.2	7 000±900
0.783	116.0 139.6	127.8	7 800±800

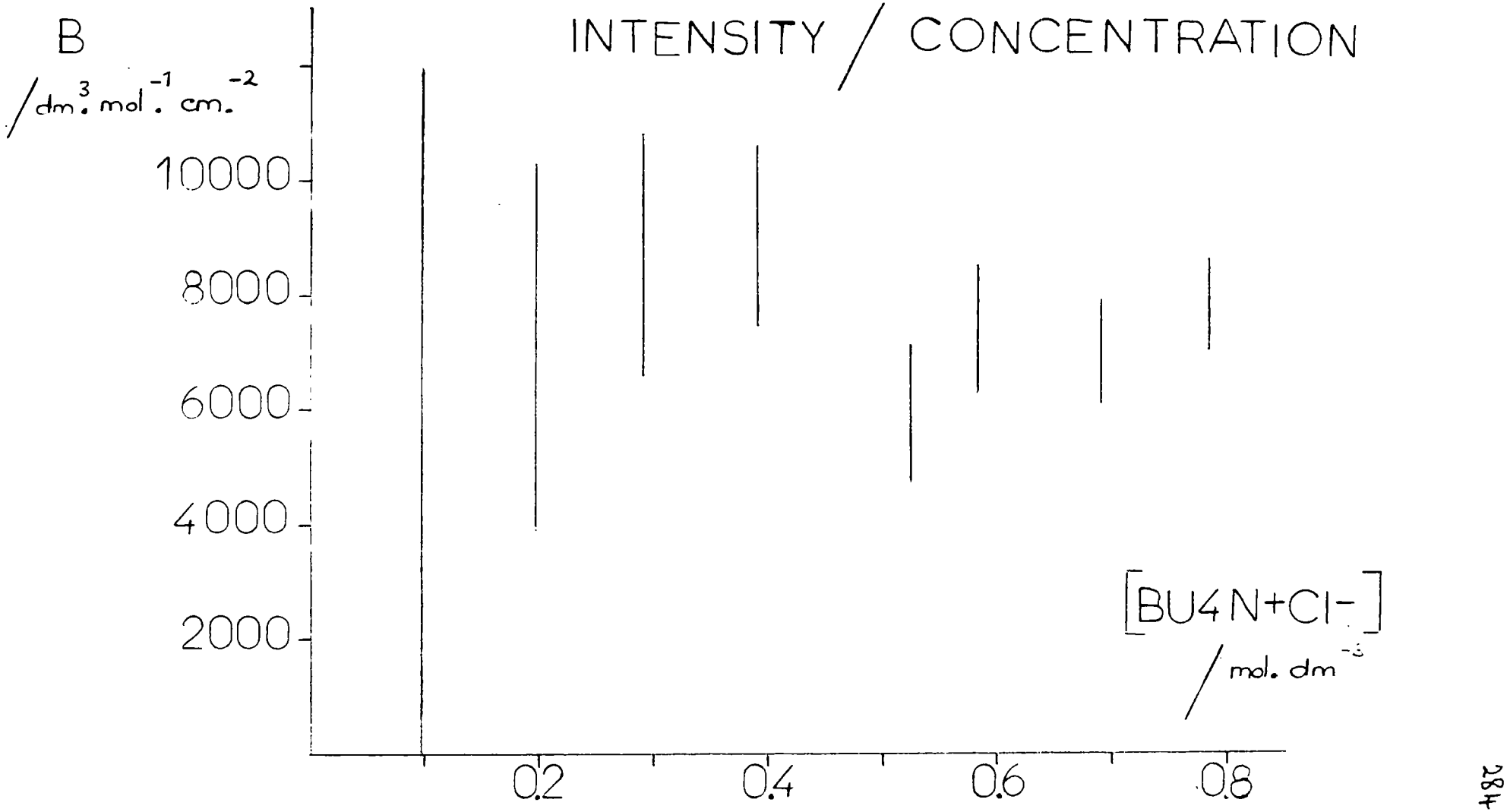

284

FIG. 5.34

116 cm^{-1} COMPONENT BU4N+Cl- IN CARBON TETRACHLORIDE

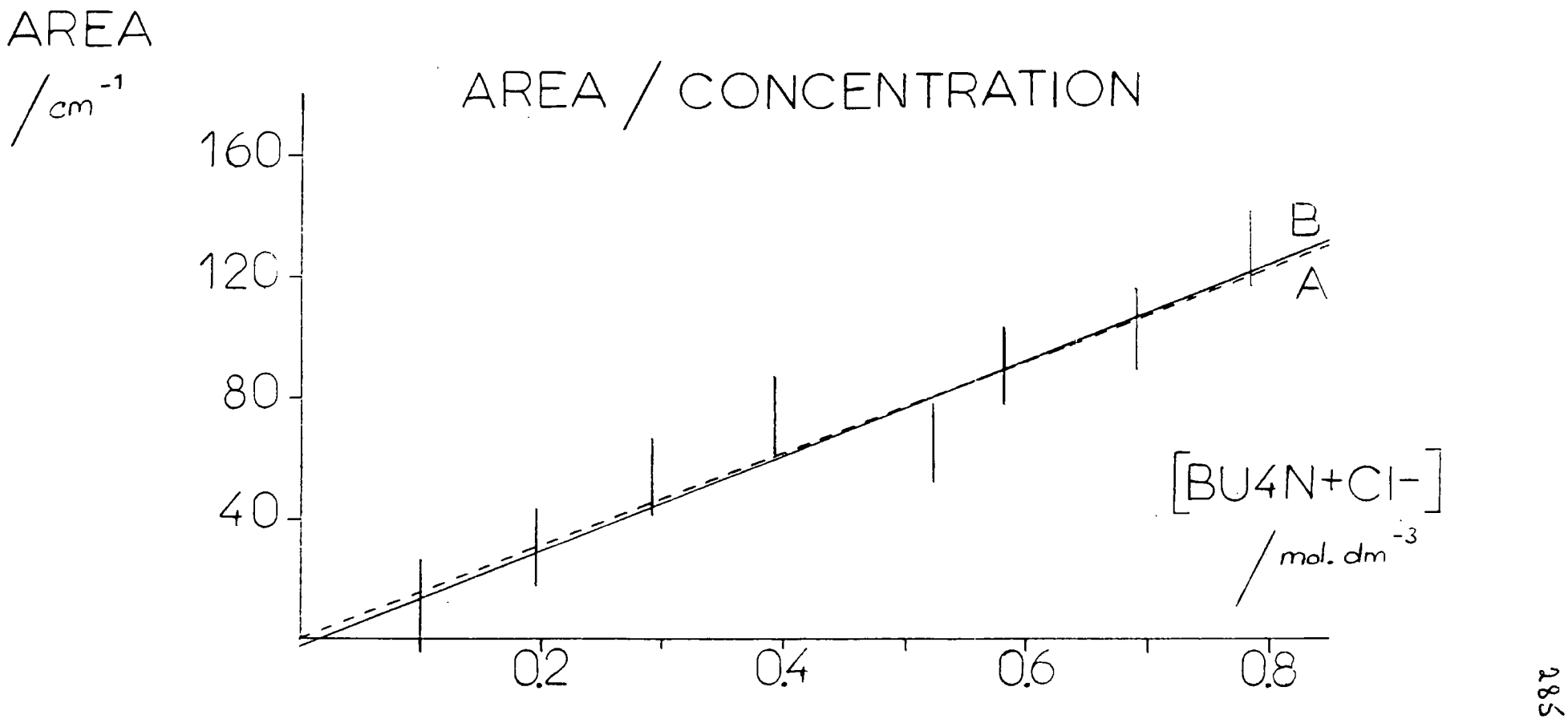

FIG. 5.35

116 cm^{-1} COMPONENT BU4N+Cl- IN CARBON TETRACHLORIDE

Table 5.22 184 cm^{-1} component $Bu_4N^+Cl^-$ in CCl_4 — $\bar{\nu}_o$ and $\Delta\bar{\nu}_{\frac{1}{2}}$

concn. /mol dm^{-3}	$\bar{\nu}_o$ /cm^{-1}	av. $\bar{\nu}_o$ /cm^{-1}	$\Delta\bar{\nu}_{\frac{1}{2}}$ /cm^{-1}	av. $\Delta\bar{\nu}_{\frac{1}{2}}$ /cm^{-1}
0.098	184.9	186.4	71.0	72.8
	188.0		74.6	
0.196	182.4	182.8	37.0	63.8
	183.1		90.6	
0.291	189.2	186.1	69.7	75.9
	183.0		82.0	
0.392	184.5	183.5	97.8	85.2
	182.4		72.7	
0.524	176.1	179.3	89.0	82.4
	182.5		75.9	
0.581	187.4	183.8	81.0	85.0
	180.2		89.0	
0.688	184.2	184.3	65.7	82.8
	184.3		99.8	
0.783	182.9	182.4	70.5	79.5
	181.8		86.5	

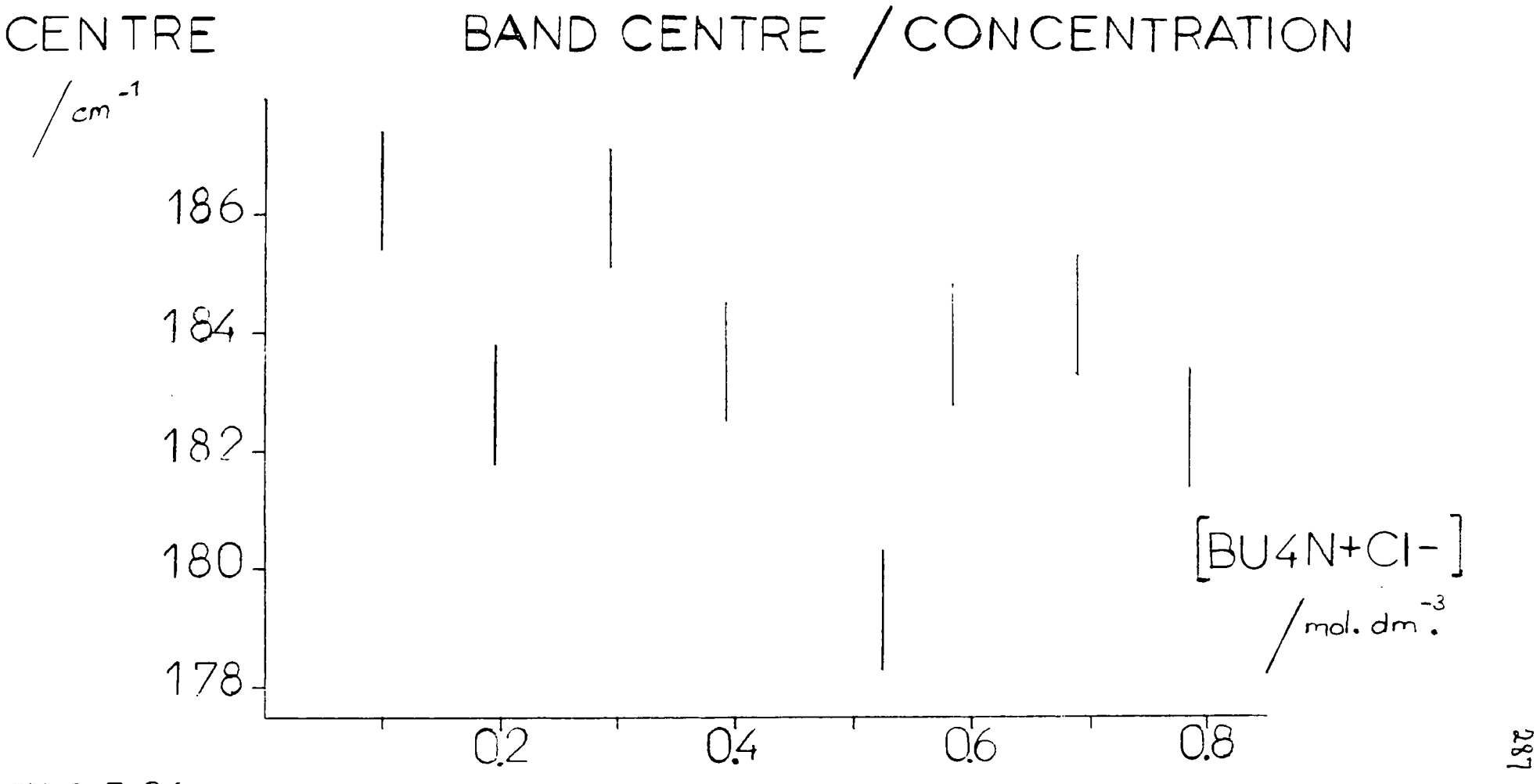

FIG.5.36

184 cm^{-1} COMPONENT BU4N+CI- IN CARBON TETRACHLORIDE

as a function of concentration, and this indicated that the band centre shifted slightly to lower frequency with increasing concentration. The band centre was 186±2 cm^{-1} at 0.10 mol dm^{-3} and fell to 182±2 cm^{-1} at 0.78 mol dm^{-3}, the decrease only just being significant. The mean band centre was calculated as 184±3 cm^{-1}. The half-band width of the 184 cm^{-1} component was plotted as a function of concentration, and the resulting graph is shown in fig. 5.37, which indicated that the half-band width was unaffected by concentration. The mean half-band width was calculated as 80±15 cm^{-1}, the low precision being due to the small intensity of the 184 cm^{-1} component.

Table 5.23 shows the areas and intensities determined for the high frequency component for the $Bu_4N^+Cl^-$ in CCl_4 system. The intensity data was plotted as a function of $Bu_4N^+Cl^-$ salt concentration, and the graph obtained is shown as fig. 5.38. The graph indicated that the intensity of the 184 cm^{-1} component was independent of concentration. To determine the intensity of this component accurately the area was plotted against concentration as shown in fig. 5.39. The letter A denotes the fit restricted to go through the origin, and the letter B the unrestricted fit. The slope of the restricted fit was 54.8±3.7 $dm^3\ mol^{-1}\ cm^{-1}$, which gave an intensity of 2 370±180 $dm^3\ mol^{-1}\ cm^{-2}$, and the slope of the unrestricted fit was 51.5 ±8.1 $dm^3\ mol^{-1}\ cm^{-1}$, which gave an intensity of 2470±390 $dm^3\ mol^{-1}\ cm^{-2}$.

The values for the band centres, half-band widths and intensities of the 3 components of the absorption profile for the $Bu_4N^+Cl^-$ in CCl_4 system are summarised in table 5.29 at the end of this chapter.

5.6 Effect of temperature on the 3 pure Gauss component fit for $Bu_4N^+Cl^-$ in benzene

To gain a further insight into the nature of the processes giving rise to the far-infrared absorption of the tetra-n-alkylammonium salts in benzene system the spectra obtained for $Bu_4N^+Cl^-$ in benzene at various temperatures (see section 4.2.4) were fitted to a sum profile of 3 pure

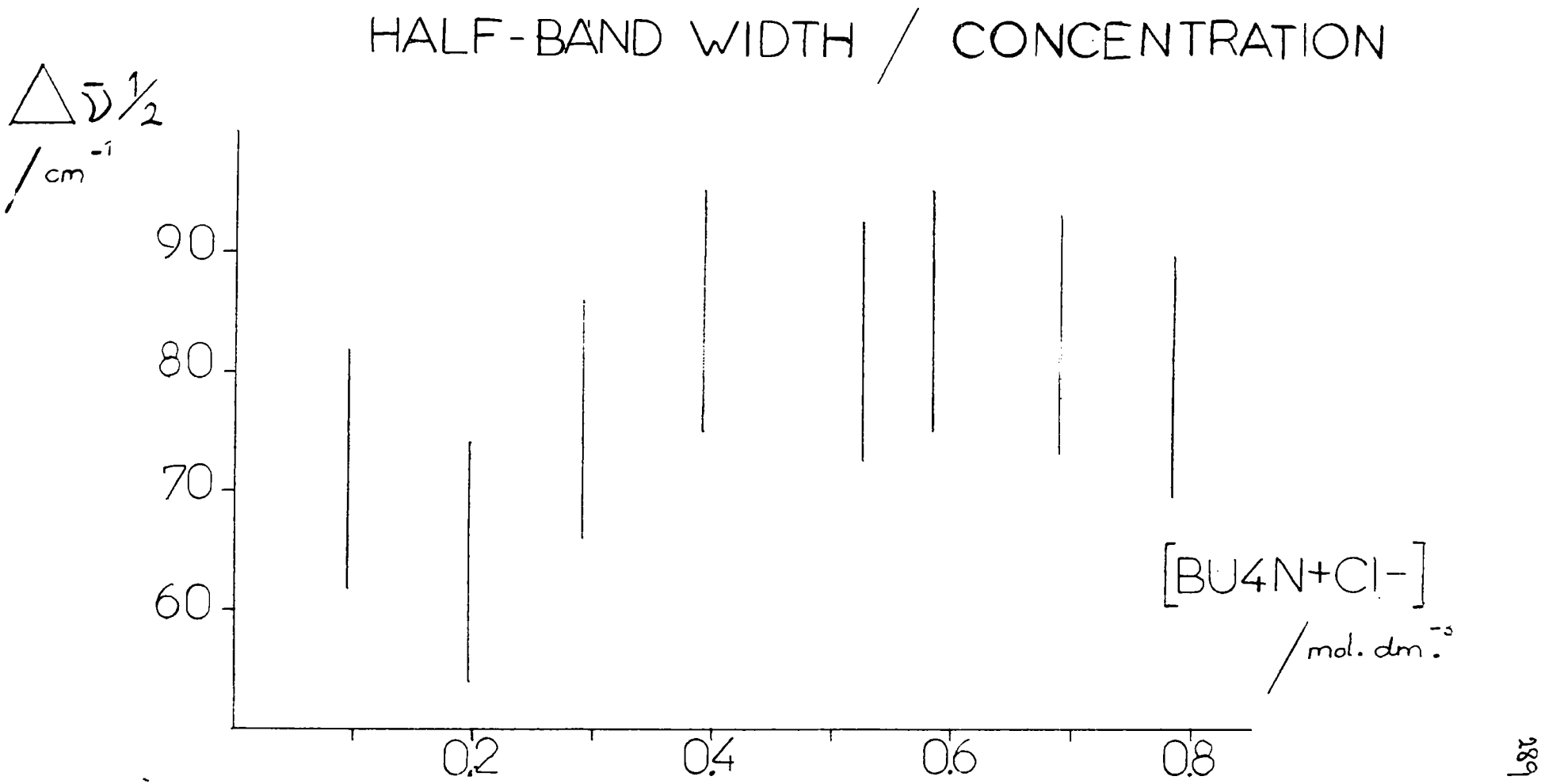

FIG. 5.37

184 cm^{-1} COMPONENT BU4N+Cl- IN CARBON TETRACHLORIDE

Table 5.23 184 cm^{-1} component $Bu_4N^+Cl^-$ in CCl_4. Areas and intensities

(L = 0.021 cm)

concn. /mol dm^{-3}	area /cm^{-1}	av. area /cm^{-1}	intensity /dm^3 mol^{-1} cm^{-2}
0.098	5.5	5.2	2 500±2 900
	4.8		
0.196	2.4	8.7	2 100±1 500
	15.0		
0.291	14.2	14.8	2 400±1 000
	15.3		
0.392	35.3	26.9	3 300±700
	18.4		
0.524	43.6	38.1	3 500±500
	32.6		
0.581	28.5	34.0	2 800±500
	39.6		
0.688	24.1	31.7	2 200±400
	39.3		
0.783	34.1	38.7	2 400±400
	43.2		

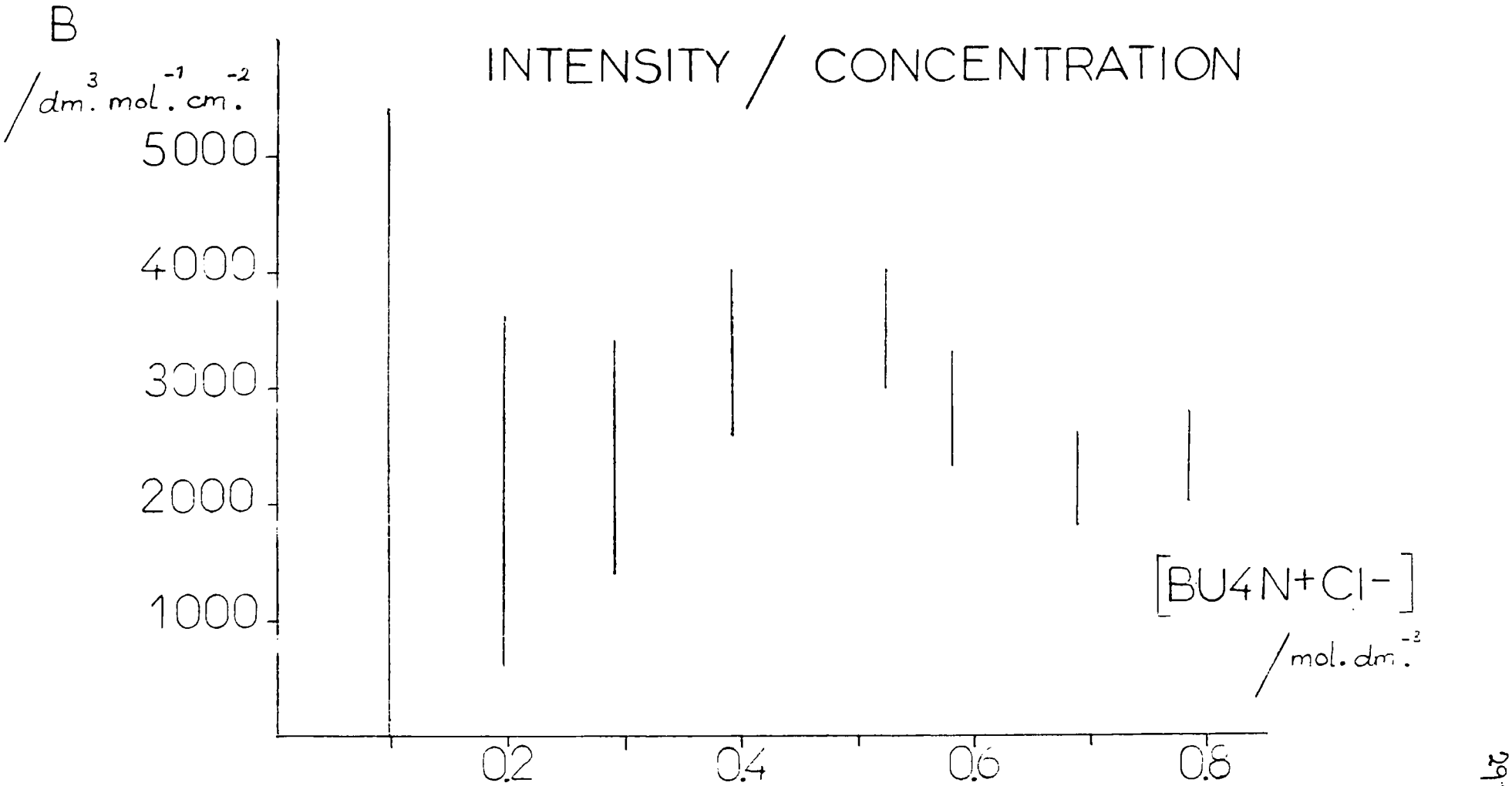

FIG. 5.38

184 cm^{-1} COMPONENT BU4N+Cl- IN CARBON TETRACHLORIDE

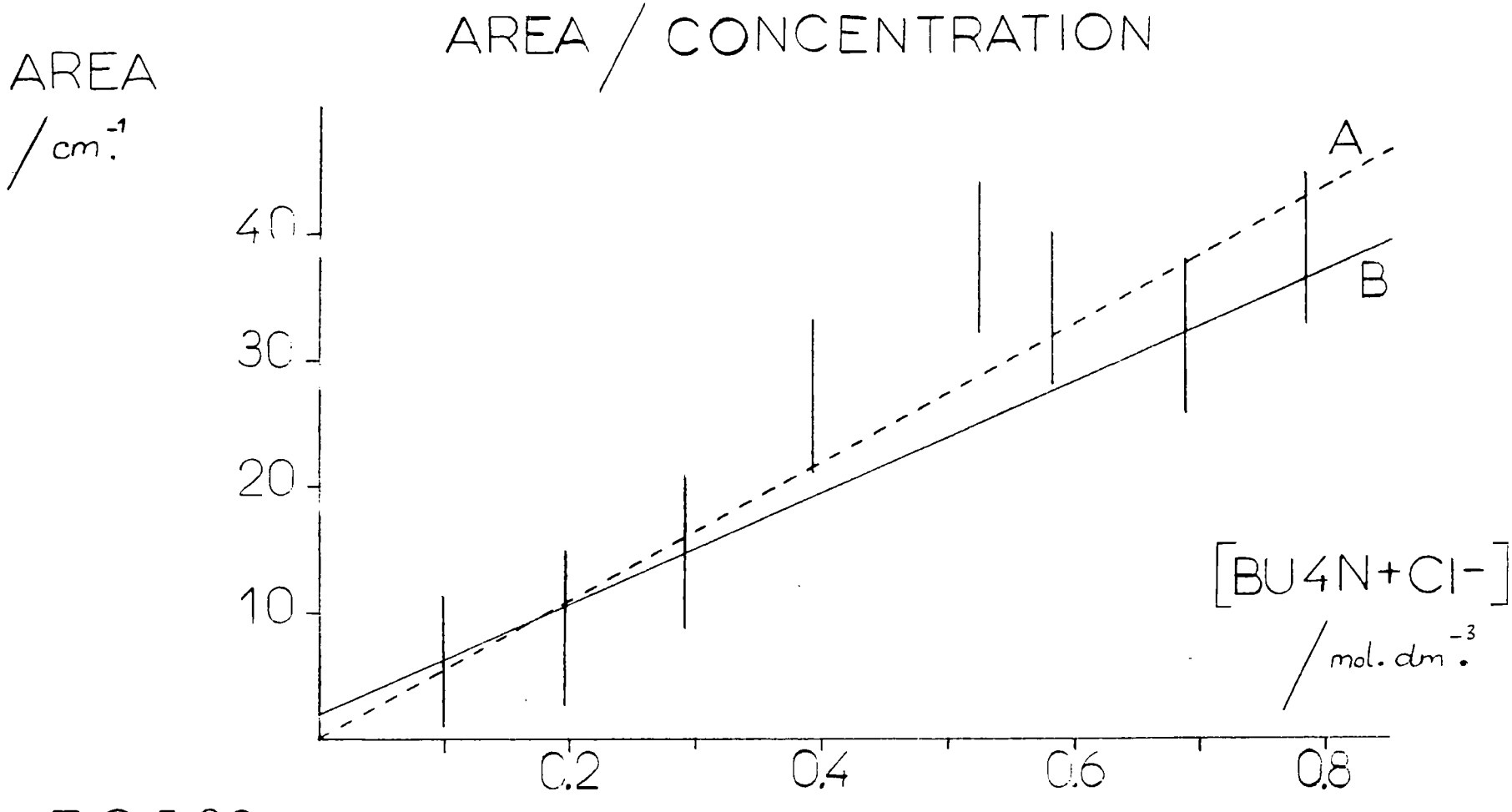

FIG. 5.39

184 cm^{-1} COMPONENT BU4N+Cl- IN CARBON TETRACHLORIDE

Gauss components. Studies were conducted to determine the effect of temperature on the band centre, half-band width and intensity for the 3 components. The initial input parameters for the fits were the same as those used for the initial fits to the benzene solution spectra, namely bands centred at 70, 116 and 180 cm^{-1}, with half-band widths of 66, 54 and 80 cm^{-1} respectively. Tables 5.24 to 5.26 show the parameters obtained for the 3 components for the best fits for the spectra of 0.252 mol dm^{-3} $Bu_4N^+Cl^-$ in benzene, obtained with a pathlength of 0.021 cm, for 14 temperatures between 285 and 349K. The temperature range being governed by the freezing and boiling points of the solution.

Table 5.24 shows the band centre, half band width, area and corresponding intensity for the low frequency component. Fig. 5.40 shows the band centre plotted as a function of temperature. The graph was inconclusive, but suggested that no significant change of band centre was occurring with increasing temperature. Fig. 5.41 shows the graph obtained when the half-band width was plotted as a function of temperature. This indicated that the half-band width increased slightly with increasing temperature. The half-band width increased from 59±5 cm^{-1} at 285K to 71±5 cm^{-1} at 349K. Fig 5.42 shows the component intensity as a function of temperature, and indicated that the intensity appeared to increase slightly with increasing temperature, although the increase was not significant. The intensity at 285K was 2 400±2 100 dm^3 mol^{-1} cm^{-2}, which rose to 4 100±2 100 dm^3 mol^{-1} cm^{-2} at 349K.

Table 5.25 shows the band centre, half-band width, area and corresponding intensity for the central component to the absorption profile. Fig. 5.43 shows the band centre as a function of temperature, and this indicated that the band centre was independent of temperature, the centre not deviating significantly from 116±3 cm^{-1}. The half-band width for the 116 cm^{-1} component was plotted as a function of temperature, and is shown in fig. 5.44. This was inconclusive, but suggested that the half-band width

Table 5.24 70 cm^{-1} component $Bu_4N^+Cl^-$ in benzene.

Effect of temperature. $\bar{\nu}_0$, $\Delta\bar{\nu}_{\frac{1}{2}}$, area and intensity.

(concn. = 0.252 mol dm^{-3}, L = 0.021 cm)

temp. /K	$\bar{\nu}_0$ /cm^{-1}	$\Delta\bar{\nu}_{\frac{1}{2}}$ /cm^{-1}	area /cm^{-1}	intensity /dm^3 mol^{-1} cm^{-2}
285	71.9	58.9	15.2	2 400
289	73.4	54.5	14.0	2 200
294	76.1	58.5	16.3	2 600
299	78.8	52.7	13.6	2 200
304	73.8	57.2	14.7	2 300
309	73.6	59.3	16.2	2 600
314	70.4	60.1	18.0	2 900
318	73.0	56.3	16.9	2 700
323	72.1	57.3	15.7	2 500
328	81.5	51.9	15.9	2 500
334	66.6	62.9	21.8	3 500
339	74.3	64.2	19.4	3 100
344	75.0	59.5	20.7	3 300
349	81.3	70.6	25.9	4 100

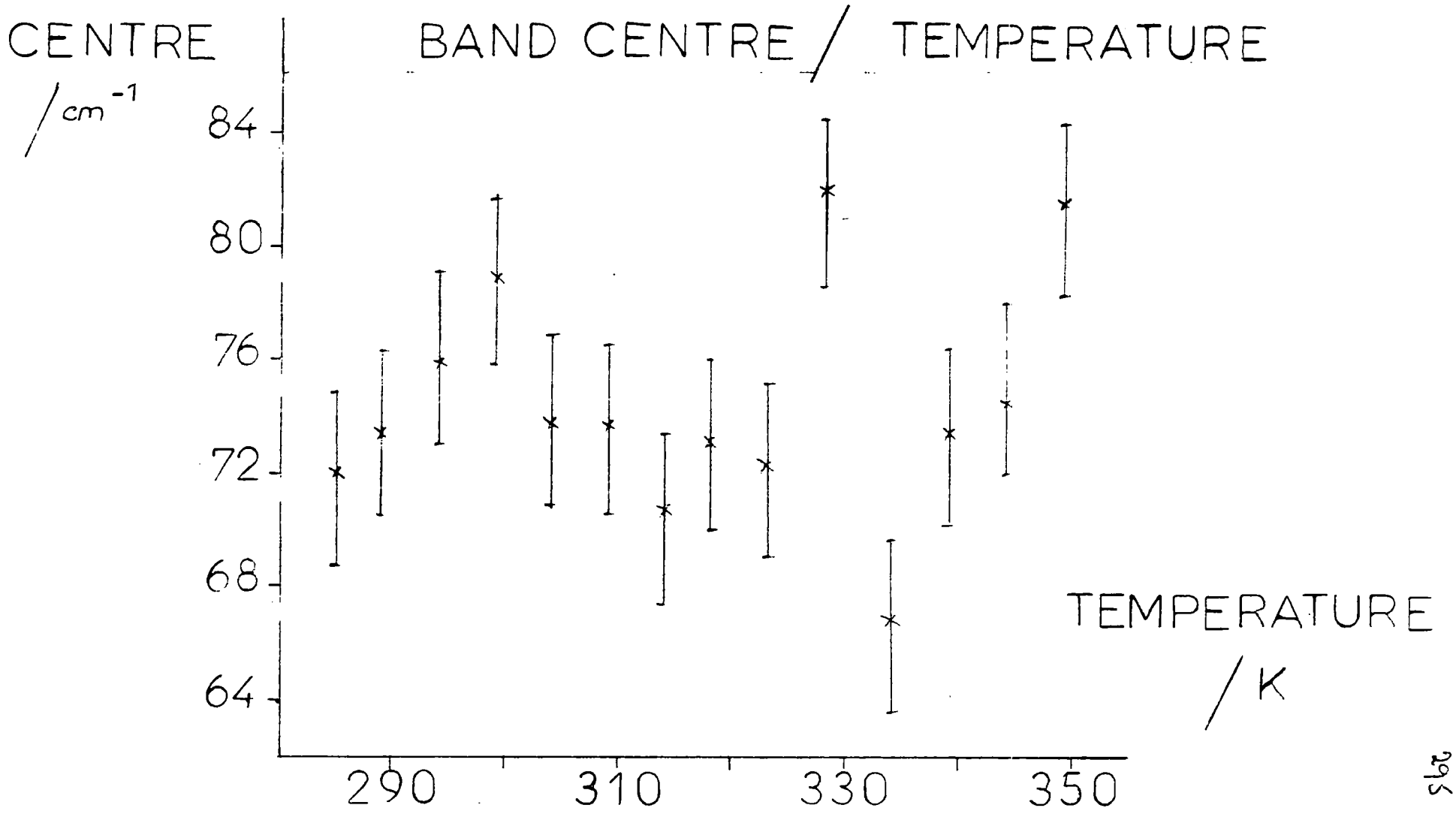

FIG 5.40 73 cm^{-1} COMPONENT BU4N+CI- IN BENZENE

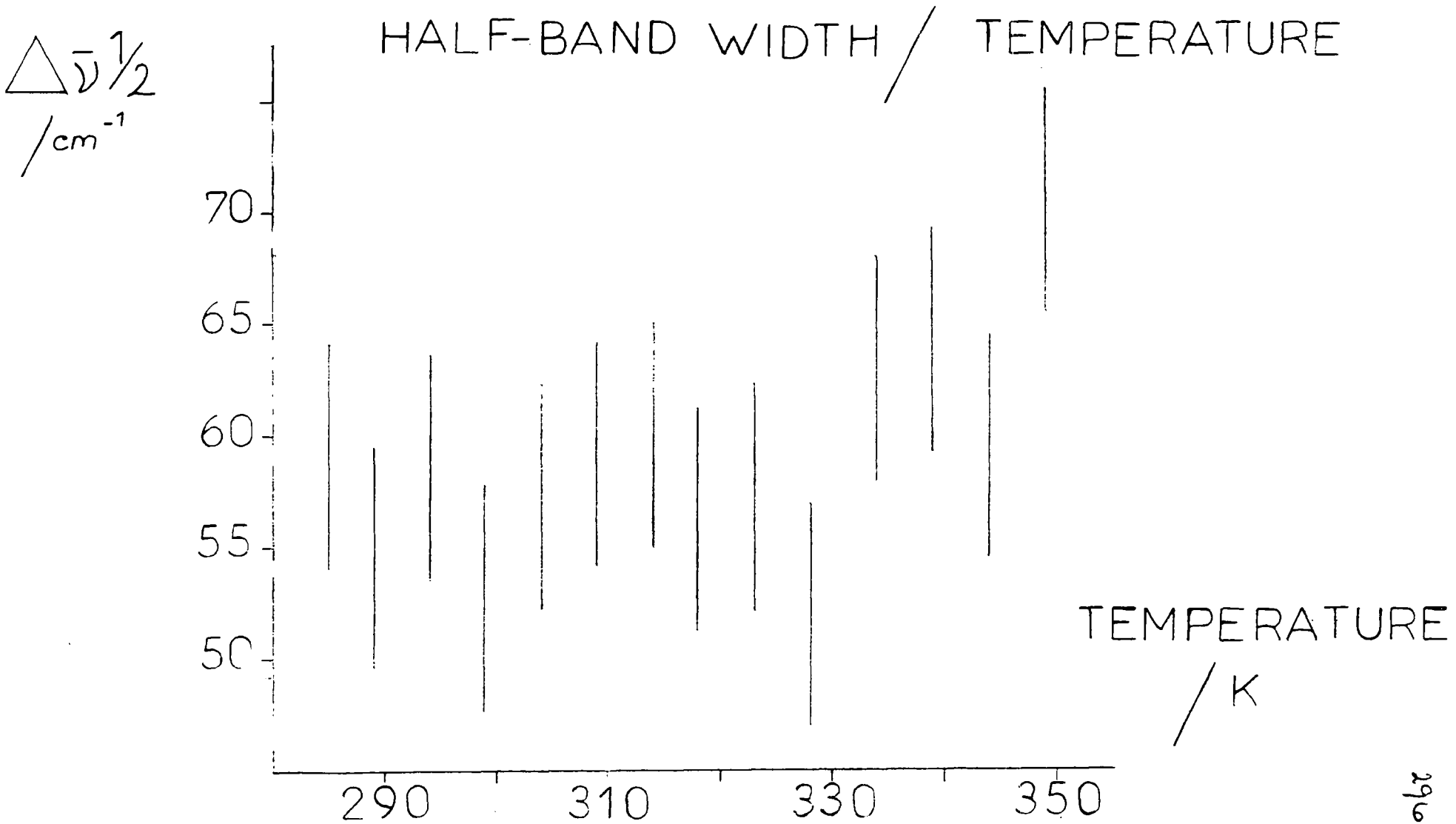

FIG. 5.41 73 cm^{-1} COMPONENT BU4N+CI- IN BENZENE

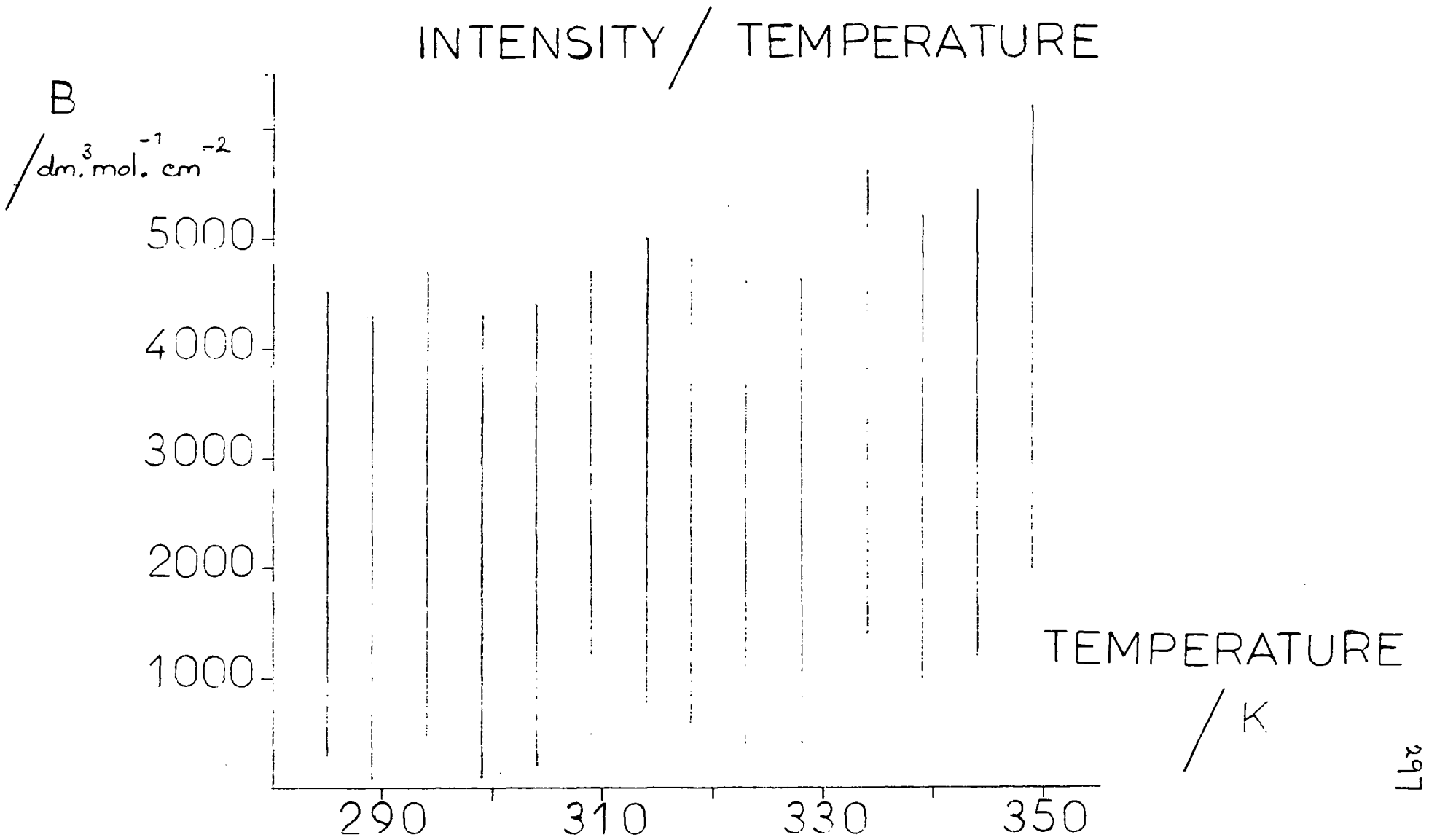

FIG.5.42 73 cm^{-1} COMPONENT BU4N+CI- IN BENZENE

Table 5.25 116 cm^{-1} component $Bu_4N^+Cl^-$ in benzene.
Effect of temperature. $\bar{\nu}_o$, $\Delta\bar{\nu}_{\frac{1}{2}}$, area and intensity

(concn. = 0.252 mol dm^{-3}, L = 0.021 cm)

temp. /K	$\bar{\nu}_o$ /cm^{-1}	$\Delta\bar{\nu}_{\frac{1}{2}}$ /cm^{-1}	area /cm^{-1}	intensity /dm^3 mol^{-1} cm^{-2}
285	116.3	55.5	30.5	4 900
289	117.0	51.9	23.3	3 700
294	118.5	52.9	22.0	3 500
299	118.9	47.9	18.8	3 000
304	116.6	54.7	23.6	3 800
309	117.5	50.7	22.0	3 500
314	116.7	55.8	26.3	4 200
318	117.8	51.9	24.6	3 900
323	117.0	53.6	25.1	4 000
328	119.1	41.8	16.6	2 600
334	114.3	55.0	26.6	4 200
339	117.3	58.6	28.3	4 500
344	119.0	53.6	25.4	4 000
349	117.7	59.9	36.7	5 900

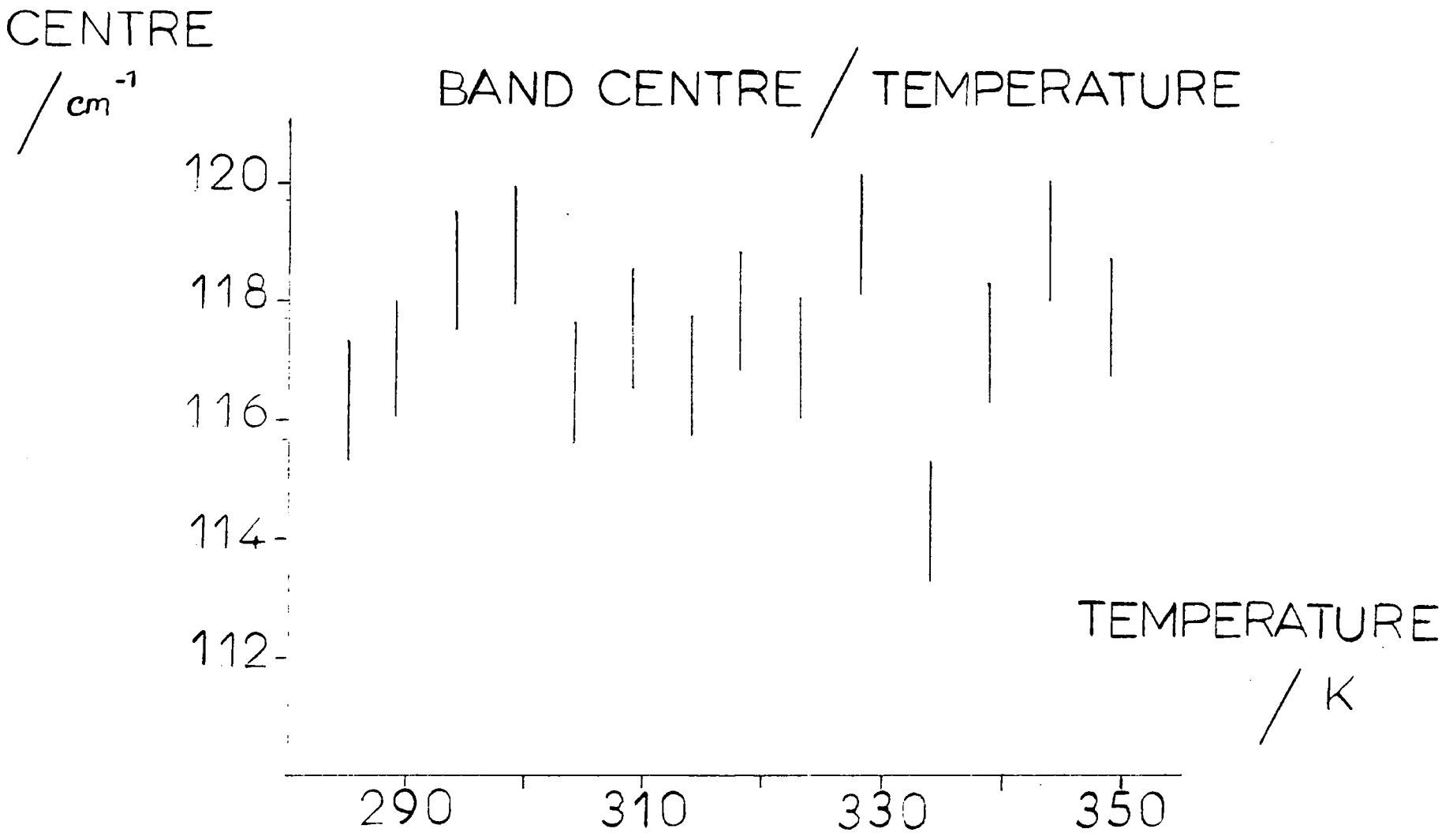

FIG.5.43 118 cm^{-1} COMPONENT BU4N+CI− IN BENZENE

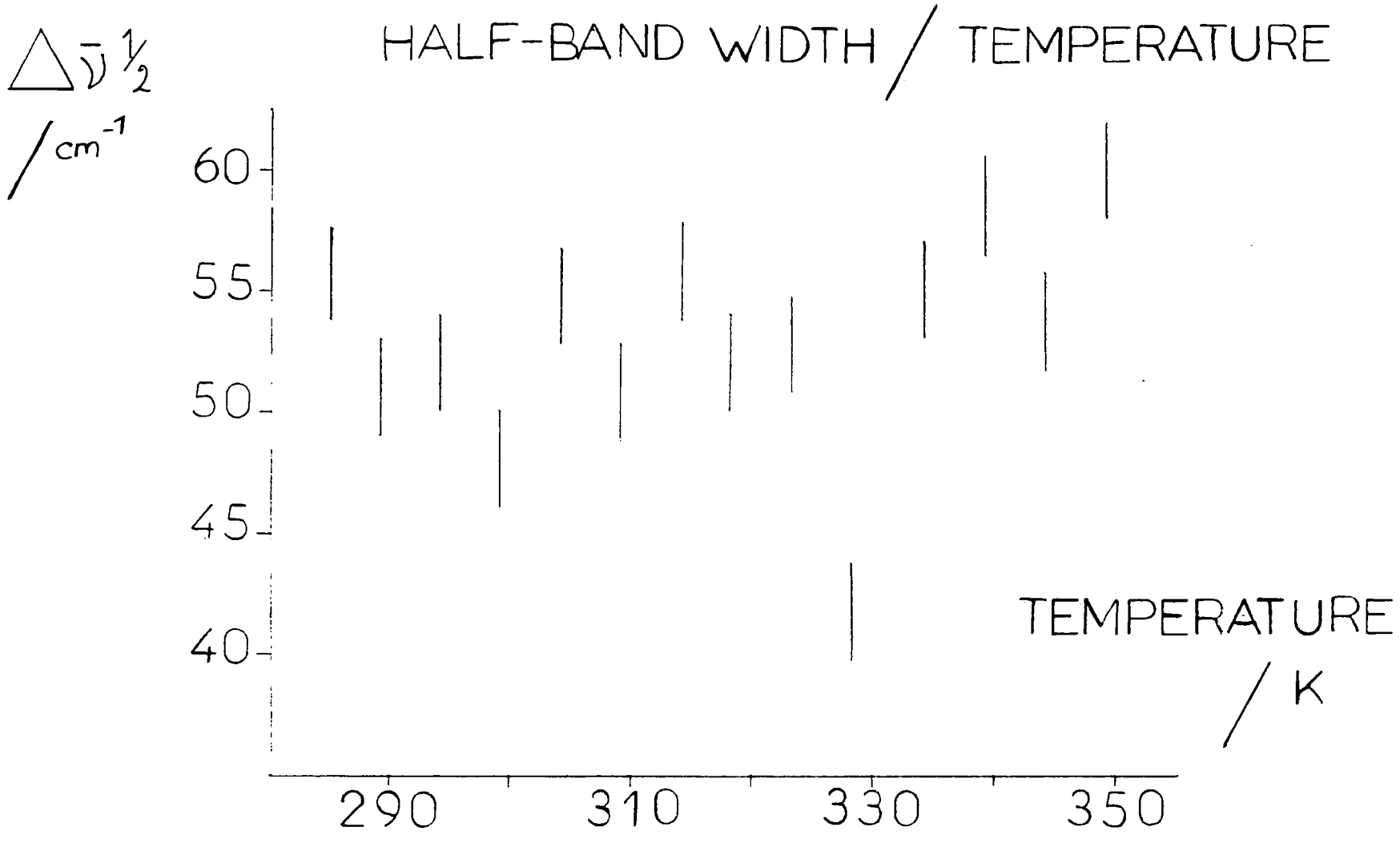

FIG. 5.44 118 cm^{-1} COMPONENT BU4N+CI- IN BENZENE

was increasing slightly with increasing temperature. The half-band width was 56±2 cm^{-1} at 285K and increased to 60±2 cm^{-1} at 349K. The value at 328K appeared to be suspect, here, and in fact throughout the temperature study. Fig. 5.45 shows the intensity of the central component as a function of temperature, and this graph indicated that the intensity was increasing with increasing temperature, rising from a value of 4 900±2 100 dm^3 mol^{-1} cm^{-2} at 285K to 5 900±2 100 dm^3 mol^{-1} cm^{-2} at 349K. A smooth curve could be drawn through the data if the 328K value was neglected, as for the other parameters.

Table 5.26 shows the band centre, half-band width,area and corresponding intensity for the high frequency component of the absorption profile. Fig. 5.46 shows the band centre as a function of temperature, which indicated that the band centre was independent of temperature, not deviating from 181±6 cm^{-1}. The half-band width of the high frequency component is shown as a function of temperature in fig. 5.47. The graph was inconclusive, but suggested that the half-band width of the high frequency component was decreasing slightly with increasing temperature. The half-band width at 285K was fitted at 75±10 cm^{-1} which decreased to 58±10 cm^{-1} at 349K. Fig. 5.48 shows the intensity of the 181 cm^{-1} band as a function of temperature, which indicated that the intensity showed no significant change as a result of changing temperature, lack of significance being due to the low precision of this data for the high frequency tail, due to its low absorbance.

5.7 2 pure Gauss fit for $Bu_4N^+Br^-$ in benzene

The absorption profiles for the spectra of $Bu_4N^+Br^-$ in benzene, at 3 concentrations obtained using a 0.052 cm pathlength, were fitted to a profile which was the sum of 2 pure Gauss components. The initial input parameters were centres of 60 and 75 cm^{-1}, with half-band widths of 80 and 60 cm^{-1} respectively. Fig. 5.49 shows the fit obtained for the spectrum of 0.398 mol dm^{-3} $Bu_4N^+Br^-$ in benzene. Tables 5.27 and 5.28 show the parameters obtained for the 2 components for the best fits for the 6 spectra at 3

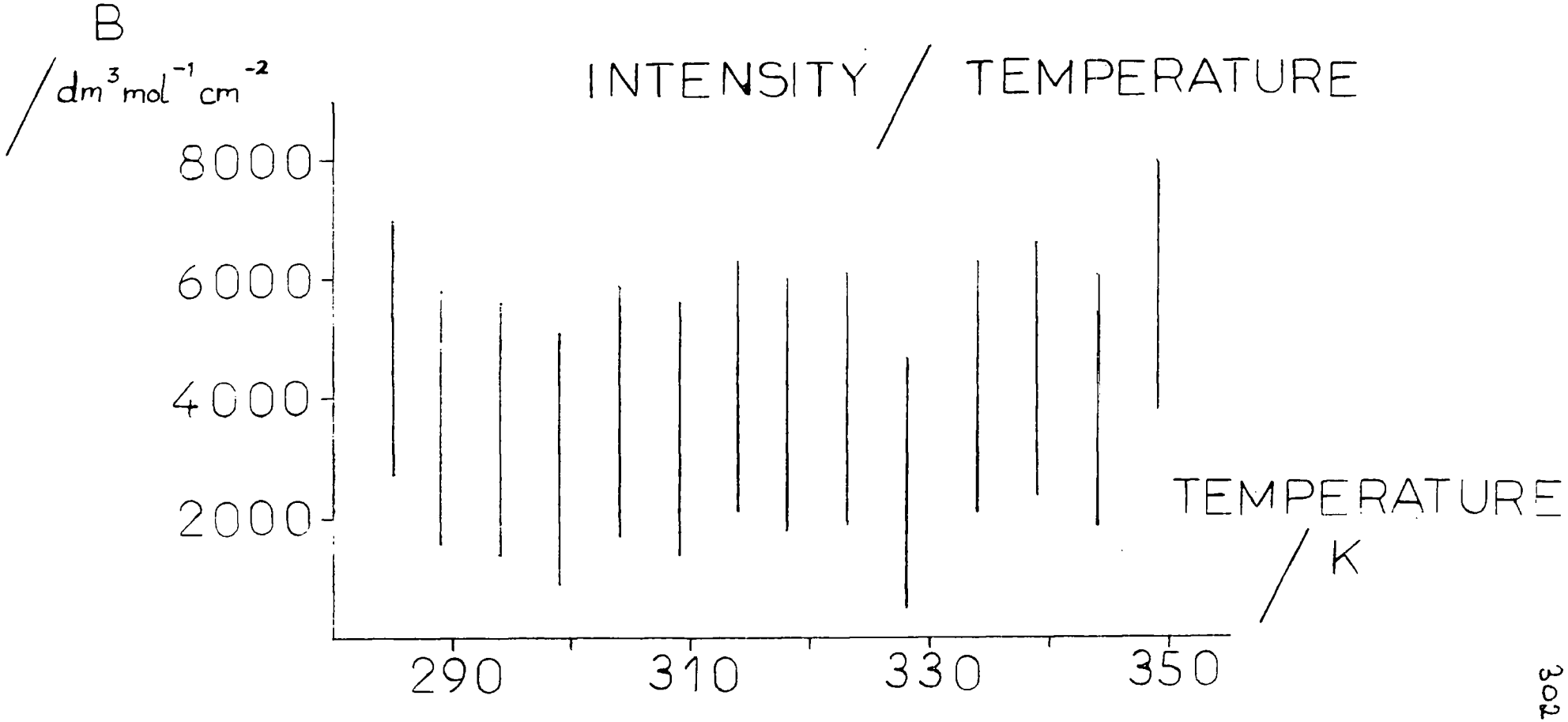

302

FIG 5.45 116 cm^{-1} COMPONENT BU4N+Cl- IN BENZENE

Table 5.26 181 cm^{-1} component $Bu_4N^+Cl^-$ in benzene.

Effect of temperature. $\bar{\nu}_0$, $\Delta\bar{\nu}_{\frac{1}{2}}$, area and intensity.

(concn. = 0.252 mol dm^{-3}, L = 0.021 cm)

temp. /K	$\bar{\nu}_0$ /cm^{-1}	$\Delta\bar{\nu}_{\frac{1}{2}}$ /cm^{-1}	area /cm^{-1}	intensity /dm^3 mol^{-1} cm^{-2}
285	186.3	74.8	8.7	1 400
289	180.7	65.8	8.8	1 400
294	182.2	51.2	6.3	1 000
299	181.0	49.5	4.5	700
304	182.2	54.9	6.5	1 000
309	180.0	52.6	5.3	800
314	182.7	59.2	6.9	1 100
318	180.8	52.8	7.8	1 200
323	179.5	52.0	5.8	900
328	170.4	66.6	8.2	1 300
334	175.6	107.9	24.8	4 000
339	181.6	52.9	5.8	900
344	180.6	57.7	8.0	1 300
349	182.6	57.3	10.7	1 700

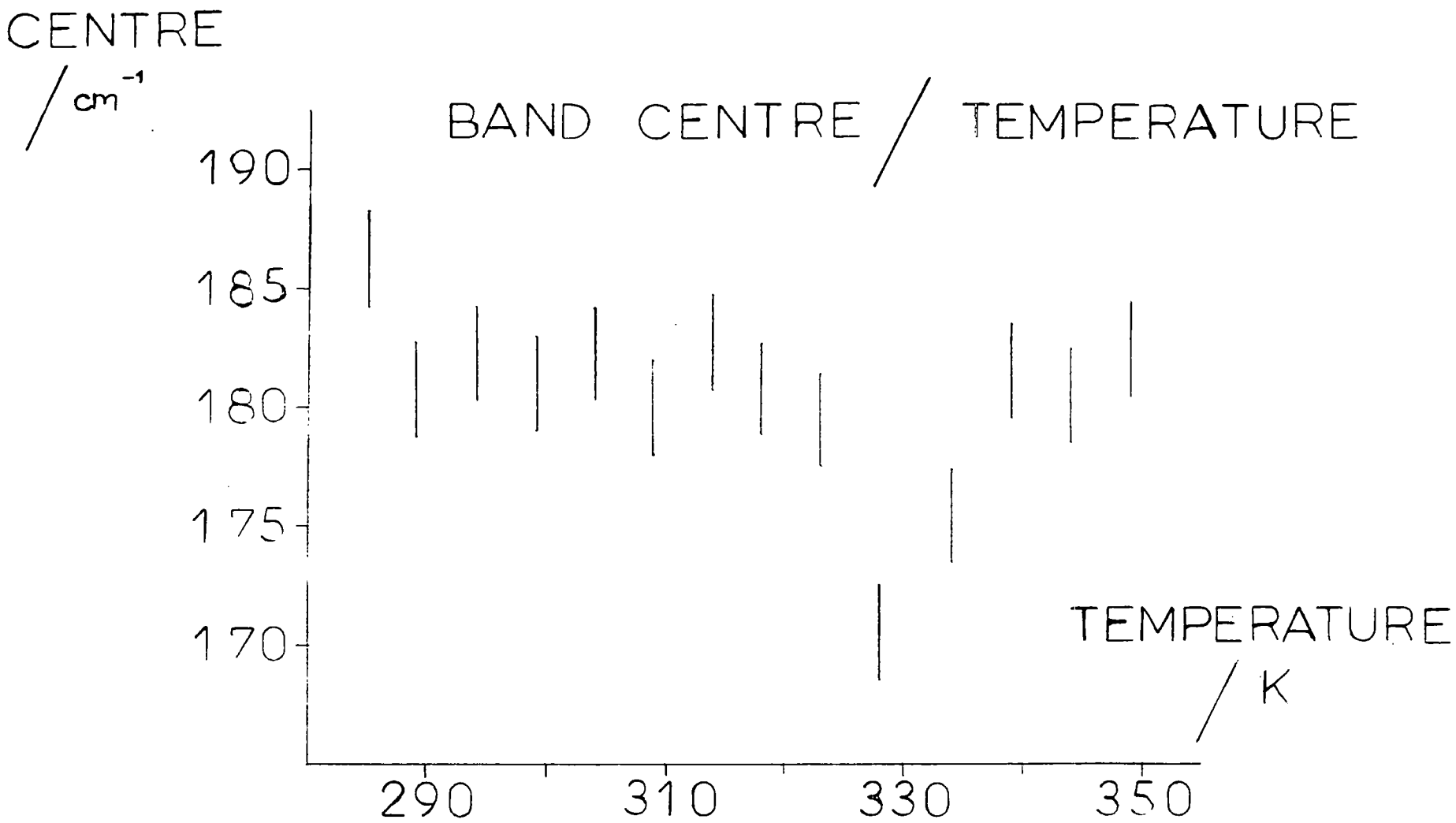

FIG 5.46 181 cm⁻¹ COMPONENT BU4N+Cl- IN BENZENE

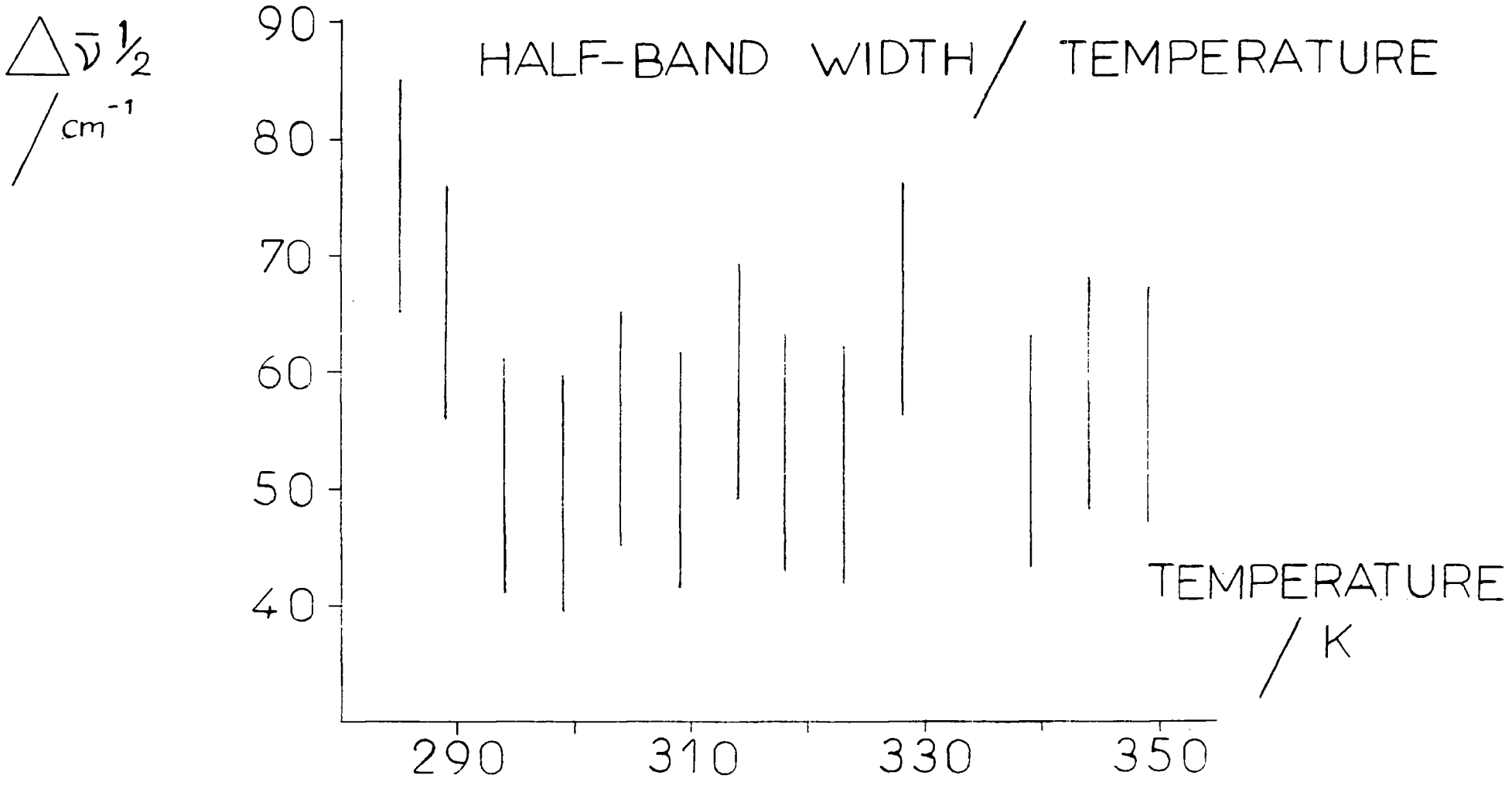

FIG. 5.47 181 cm^{-1} COMPONENT BU4N+CI- IN BENZENE

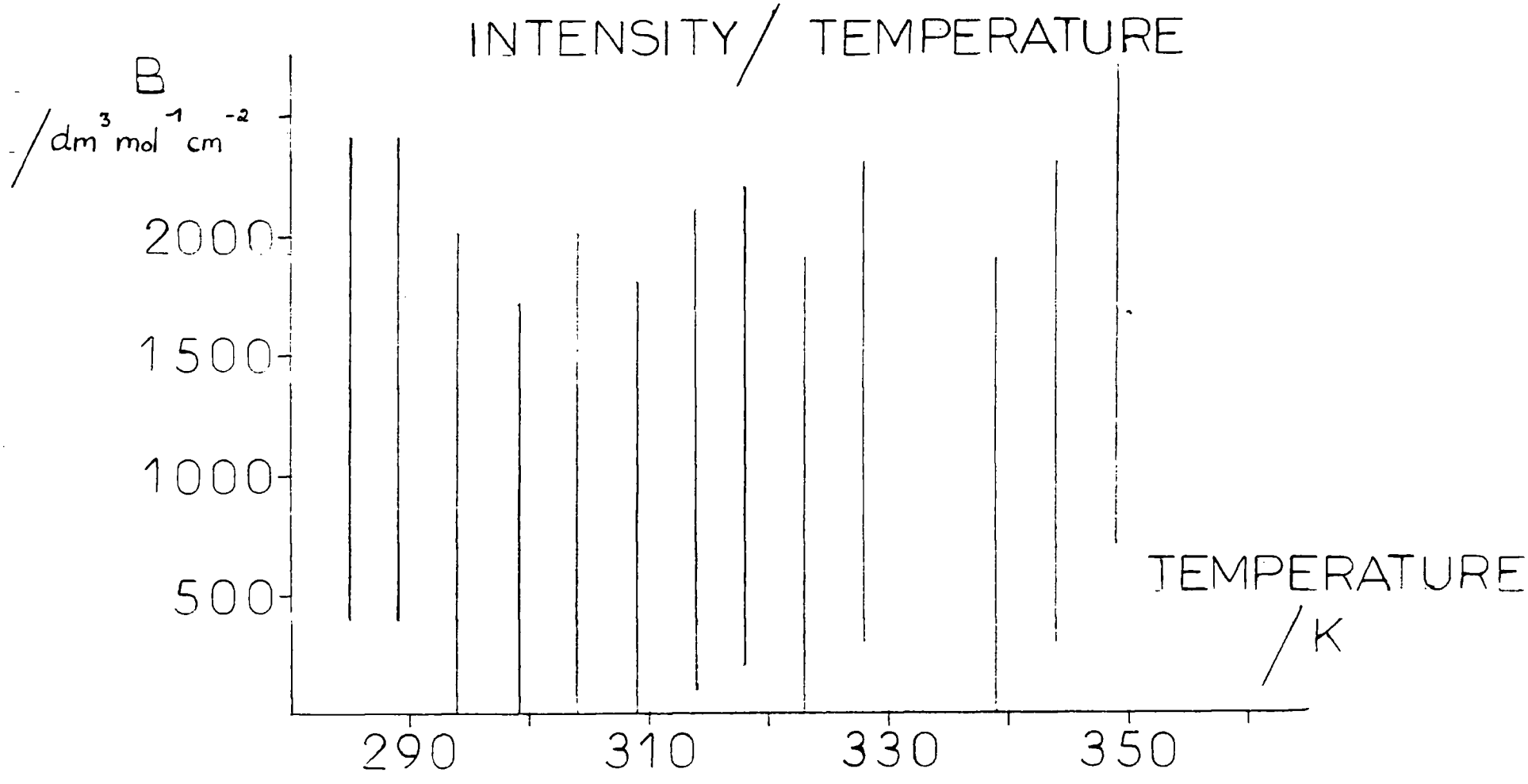

FIG. 5.48 181 cm^{-1} COMPONENT BU4N+Cl- IN BENZENE

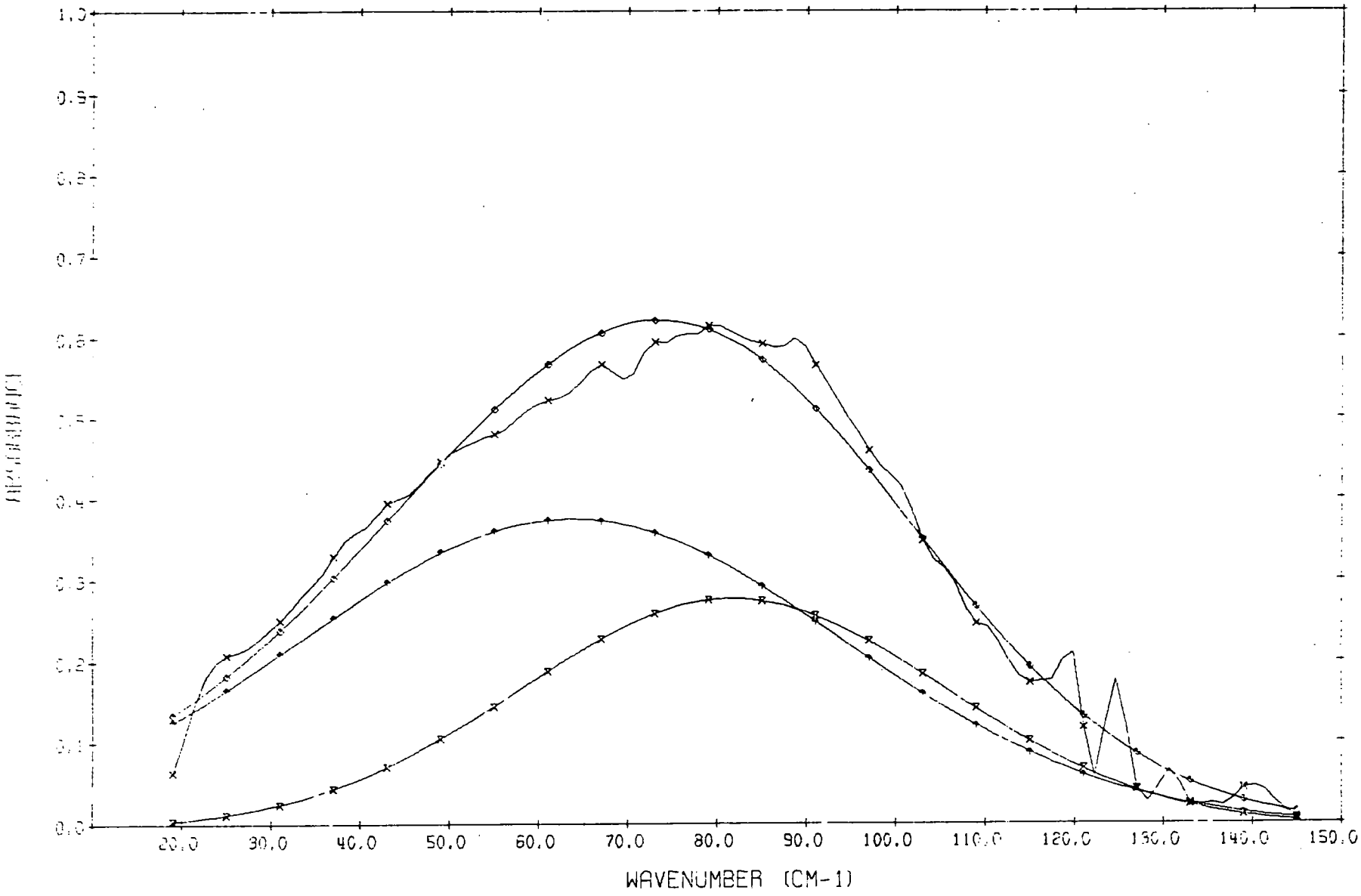

FIG. 5.49 3 PURE GAUSS FIT BU4N+Br- IN C6C6

Table 5.27 66 cm^{-1} component $Bu_4N^+Br^-$ in benzene

$\bar{\nu}_o$ and $\Delta\bar{\nu}_{\frac{1}{2}}$

concn. /mol dm^{-3}	$\bar{\nu}_o$ /cm^{-1}	av. $\bar{\nu}_o$ /cm^{-1}	$\Delta\bar{\nu}_{\frac{1}{2}}$ /cm^{-1}	av. $\Delta\bar{\nu}_{\frac{1}{2}}$ /cm^{-1}
0.298	71.7	69.3	83.8	80.8
	67.0		77.8	
0.355	66.8	67.9	70.6	72.7
	68.0		74.7	
0.398	60.7	61.6	75.3	73.1
	62.5		70.9	

Area and intensity (L = 0.052 cm)

concn. /mol dm^{-3}	area /cm^{-1}	av. area /cm^{-1}	intensity /dm^3 mol^{-1} cm^{-2}
0.298	54.9	53.8	3 473±839
	52.7		
0.355	62.3	63.6	3 443±704
	64.8		
0.398	63.6	62.3	3 009±628
	61.1		

Table 5.28 79 cm^{-1} component $Bu_4N^+Br^-$ in benzene.

$\bar{\nu}_0$ and $\bar{\nu}_{\frac{1}{2}}$

concn. /mol dm^{-3}	$\bar{\nu}_0$ /cm^{-1}	av. $\bar{\nu}_0$ /cm^{-1}	$\Delta\bar{\nu}_{\frac{1}{2}}$ /cm^{-1}	av. $\Delta\bar{\nu}_{\frac{1}{2}}$ /cm^{-1}
0.298	75.9	77.1	61.3	59.1
	78.2		56.8	
0.355	78.5	78.3	54.6	55.4
	78.0		56.2	
0.398	82.2	80.8	55.1	53.9
	79.3		52.7	

Area and intensity

concn. /mol dm^{-3}	area /cm^{-1}	av. area /cm^{-1}	intensity /dm^3 mol^{-1} cm^{-2}
0.298	28.1	29.8	1 922±839
	31.5		
0.355	30.6	31.0	1 682±704
	31.5		
0.398	43.9	43.2	2 084±628
	42.5		

concentrations from 0.298 to 0.398 mol dm^{-3}. No attempts were made to determine the variation of any of the parameters with concentration. The mean values for the band centres, half-band widths and intensities for the 2 components were calculated for comparison with other systems.

For the lower frequency component the mean band centre was determined as 66±3 cm^{-1}, the half-band width as 76±3 cm^{-1}, and the intensity as 3 300±500 dm^3 mol^{-1} cm^{-2}. For the higher frequency component the mean band centre was calculated as 79±1 cm^{-1}, the half-band width as 56±2 cm^{-1}, and the intensity as 1 900±500 dm^3 mol^{-1} cm^{-2}. As usual the intensities were calculated with respect to the $Bu_4N^+Br^-$ concentration. The viabilities of these fits was questionable, because of the proximity of the band centres of the two components, but the parameters were considered useful for comparison purposes.

5.8 Summary

The data in this chapter had to be carefully considered in the light of its statistical significance. This required careful graphical presentation of the results to determine if the changes obtained for the parameters as a function of concentration and temperature were in fact 'real'. The smoothness of the majority of the changes indicated that the methods of component resolution were in fact viable. It was carefully checked that changes in the centres and half-band widths were not merely due to changes in the intensity of other components. Table 5.29 shows the best fit parameters for the components to the 4 systems studied in this chapter. The band centres and half band widths are the mean values for each of the systems. The intensity values are those determined using the linear least squares analysis programme without restraint. The intensities were all calculated with respect to the tetra-n-alkylammonium salt concentrations.

The parameters for the central component for the $Bu_4N^+Cl^-$ salt system were seen to be remarkably similar in the 3 solvents used. This indicated that the absorption was due to the vibration of the ion aggregate

Table 5.29 Band parameters for best fit Gauss components for $Bu_4N^+Cl^-$ in benzene, CCl_4 and $CHCl_3$

	benzene	CCl_4	$CHCl_3$
$Bu_4N^+Cl^-$			
$\bar{\nu}_o$ /cm^{-1}	73±1	75±6	70±7
$\Delta\bar{\nu}_{\frac{1}{2}}$ /cm^{-1}	72±8	64±6	50±11
intensity /dm^3 mol^{-1} cm^{-2}	6 390±690	3 650±380	1 800±230
$\bar{\nu}_o$ /cm^{-1}	118±3	116±2	114±1
$\Delta\bar{\nu}_{\frac{1}{2}}$ /cm^{-1}	53±4	52±4	50±2
intensity /dm^3 mol^{-1} cm^{-2}	5 760±580	7 540±540	7 210±240
$\bar{\nu}_o$ /cm^{-1}	181±6	184±3	175±7
$\Delta\bar{\nu}_{\frac{1}{2}}$ /cm^{-1}	72±9	80±15	84±16
intensity /dm^3 mol^{-1} cm^{-2}	3 470±250	2 470±390	1 520±220
$Bu_4N^+Br^-$			
$\bar{\nu}_o$ /cm^{-1}	66±3		
$\Delta\bar{\nu}_{\frac{1}{2}}$ /cm^{-1}	76±3		
intensity /dm^3 mol^{-1} cm^{-2}	3 300±500		
$\bar{\nu}_o$ /cm^{-1}	79±1		
$\Delta\bar{\nu}_{\frac{1}{2}}$ /cm^{-1}	56±2		
intensity /dm^3 mol^{-1} cm^{-2}	1 900±500		

involving contact ion pair vibrations, since there was very little solvent dependence. The band centre and half-band width were seen to decrease slightly through the series of solvents benzene, CCl_4, $CHCl_3$, but the statistical significance of these shifts was seen to be questionable. The band centre of the low frequency component was seen to be fairly constant in the 73 cm^{-1} region, but the half-band width decreased from 72 cm^{-1} for benzene to 64 cm^{-1} for CCl_4 and 50 cm^{-1} for $CHCl_3$. The intensity for the low frequency component also decreased in the same order, from 6 400 dm^3 mol^{-1} cm^{-2} for benzene to 1 800 dm^3 mol^{-1} cm^{-2} for $CHCl_3$. The band centre of the high frequency component was seen to be constant at 180±5 cm^{-1}, and the half band width at 80±15 cm^{-1}. The intensity of this component was seen to decrease from benzene to CCl_4 to $CHCl_3$.

The variation of best fitted parameters with concentration and temperature for $Bu_4N^+Cl^-$ in benzene solutions is shown in table 5.30. The concentration studies indicated that for the low frequency component the band centre shifted to lower frequency, except in benzene where the centre was invariant. The half-band width was seen to be invariant in all 3 solvents. The intensity apparently increased with concentration in benzene, but was invariant in CCl_4 and $CHCl_3$. For the central component, in benzene the centre was invariant, but shifted to lower frequency for CCl_4 and $CHCl_3$. The half-band width reached a maximum at about 0.8 mol dm^{-3} salt concentration in benzene, and was seen to likewise increase up to 0.8 mol dm^{-3} concentration for the CCl_4 and $CHCl_3$ solutions. The intensity reached a maximum in all 3 systems; the maxima occurring at about 0.8 mol dm^{-3} in benzene, at about 0.4 mol dm^{-3} in CCl_4 and 0.5 mol dm^{-3} in $CHCl_3$. The maxima were not clearly defined in the latter two cases. For the high frequency band the band centre passed through a maximum at about 0.8 mol dm^{-3} in benzene, shifted steadily to lower frequency in CCl_4 and was invariant in $CHCl_3$. The half-band width increased in CCl_4, but was invariant with concentration in both $CHCl_3$ and benzene. The intensity reached a maximum value at about 0.5 mol dm^{-3} in

Table 5.30 Band parameters for best fit Gauss components for $Bu_4N^+Cl^-$ in benzene

Concn. /mol dm^{-3}	Temp. /K	$\bar{\nu}_o$ /cm^{-1}	$\Delta\bar{\nu}_{\frac{1}{2}}$ /cm^{-1}	B /dm^3 mol^{-1} cm^{-2}	$\bar{\nu}_o$ /cm^{-1}	$\Delta\bar{\nu}_{\frac{1}{2}}$ /cm^{-1}	B /dm^3 mol^{-1} cm^{-2}	$\bar{\nu}_o$ /cm^{-1}	$\Delta\bar{\nu}_{\frac{1}{2}}$ /cm^{-1}	B /dm^3 mol^{-1} cm^{-2}
0.252	285	71.9	58.9	2 400	116.3	55.5	4 900	186.3	74.8	1 400
	304	73.8	57.2	2 300	116.6	54.7	3 800	182.2	54.9	1 000
	314	70.4	60.1	2 900	116.7	55.8	4 200	182.7	59.3	1 100
	334	66.6	62.9	3 500	114.3	55.0	4 200	175.6	107.9	4 000
	344	75.0	59.5	3 300	119.0	53.6	4 000	180.6	57.7	1 300
0.350	293	80.0	57.0	1 300	116.9	49.7	2 500	183.8	64.2	1 400
0.462	293	72.3	75.5	7 200	121.5	59.5	7 200	186.6	51.6	3 100
0.551	293	70.3	71.3	7 400	120.2	56.4	7 400	183.0	57.3	3 200
0.661	293	73.4	69.7	6 100	118.7	55.8	6 300	182.8	68.6	2 900
0.752	293	71.4	69.6	6 300	120.2	56.9	7 100	185.2	55.6	2 800
0.855	293	70.1	75.1	6 800	121.0	63.2	7 900	188.6	53.0	3 200
1.040	293	71.5	79.2	8 400	116.8	53.2	5 200	180.1	77.5	4 000
1.400	293	71.8	62.0	4 400	116.8	48.5	4 300	179.8	91.7	3 100

CCl_4, but was invariant in both benzene and $CHCl_3$.

The temperature studies for $Bu_4N^+Cl^-$ in benzene showed that the band centre for all 3 components was invariant, but that the half-band width increased for the 73 and 118 cm^{-1} components, and remained constant for the 181 cm^{-1} component. The intensity was seen to increase with temperature for all 3 components.

The deductions made from these computer resolution techniques are contained in the discussion of the ion pair solvation work in chapter 7.

CHAPTER 6

FURTHER STUDIES OF IONIC SOLVATION

Chapter six is an amalgam of the remaining work attempted to study the interaction between solvent and dissolved electrolyte. The intention of the work was merely to compare the intensities, half-band widths and band centres for pure solvents, and solutions in more polar solvents, with those for the relatively non-polar systems discussed in chapter 4.

6.1.1 Pure benzene solvent spectra

The studies of the tetra-n-butylammonium salts in benzene systems suggested that the low frequency 'collisional' band of the benzene solvent was being intensified, and was giving rise to a low frequency component, which was observable in the ratioed spectrum. This was especially so for the $Bu_4N^+Cl^-$ in benzene system. To check this assignment for the 73 cm^{-1} component in the benzene solution spectra, far-infrared spectra of pure benzene solvent have been recorded. The band centre, half-band width and intensity have been measured.

The benzene used for these studies was the same as that for the solution work in benzene. Two pathlengths of benzene were recorded, and these two single beam spectra were ratioed to give the spectrum. This method was chosen as the most accurate, rather than the more usual ratioing against a 'non-absorbing' liquid. The latter method is inaccurate because of the appreciable absorption of these 'non-absorbing' liquids in the region below 100 cm^{-1}. The following procedure was employed to obtain the best possible benzene spectra from our recording system. The demountable cell with high density polythene windows (as detailed in chapter 2) was set up with the larger of the two pathlength spacers in place. The cell was then filled with dry benzene and the instrument evacuated. The spectrum for the longer pathlength was then recorded, using a 1024 point, double-sided interferogram, to give a 3 cm^{-1} resolution after computation. (See chapter 3). The interferometer was then let back up to atmospheric pressure, and the benzene withdrawn from the cell. The cell was then dismantled, and the shorter of the two pathlength spacers inserted, taking care to reproduce the earlier cell

geometry as closely as possible. Two interferograms were then recorded for this pathlength, and the cell was then once again dismantled, and the larger pathlength spacer inserted. This procedure of double runs was then repeated throughout a series of spectra. The time spent in recording the spectra was thus minimised. This technique gave significantly better ratioed spectra than others where several interferograms were recorded at one pathlength. This agreed with the results of chapter 4, where poor spectra were produced if there was a delay in recording background and sample spectra.

As expected, the band centre was found to occur at about 80 cm^{-1}. Various beam-splitters were tried, and it was found that the 50 gauge film gave the best compromise for observing the whole of the band. The band could be followed into the high frequency wing in the 200 cm^{-1} region, and a reasonable profile was obtained for the low frequency half of the band down to about 10 cm^{-1}. Fig. 6.1 shows the spectrum obtained by ratioing 0.2538 cm of benzene against 0.0517 cm of benzene at 293K. The interferograms were obtained using a 50 gauge beam-splitter, and the thin black polythene filter. The resolution obtained was approximately 3 cm^{-1}. The noise level present throughout the spectrum was due to the ratioing out of the benzene absorption from the background. This spectrum was seen to agree well with the spectrum obtained by Chantry et. al. (71), which has been assigned to 'liquid lattice' type motions (72).

Ten benzene absorption spectra were recorded at different pathlengths. The band centre was measured, and the average value was found to be 80±5 cm^{-1}, the large uncertainty being due to the broadness of the band. The baseline for this band for intensity calculations was drawn parallel to the wavenumber axis, since the low frequency wing could not be determined with any certainty. Thus the baseline level was determined by the high frequency wing only. The half-band widths for the 10 bands were measured from the spectra, and the average was found to be 80±10 cm^{-1}. (See later in this section for a more precise band centre and half-band width measurement using band fitting

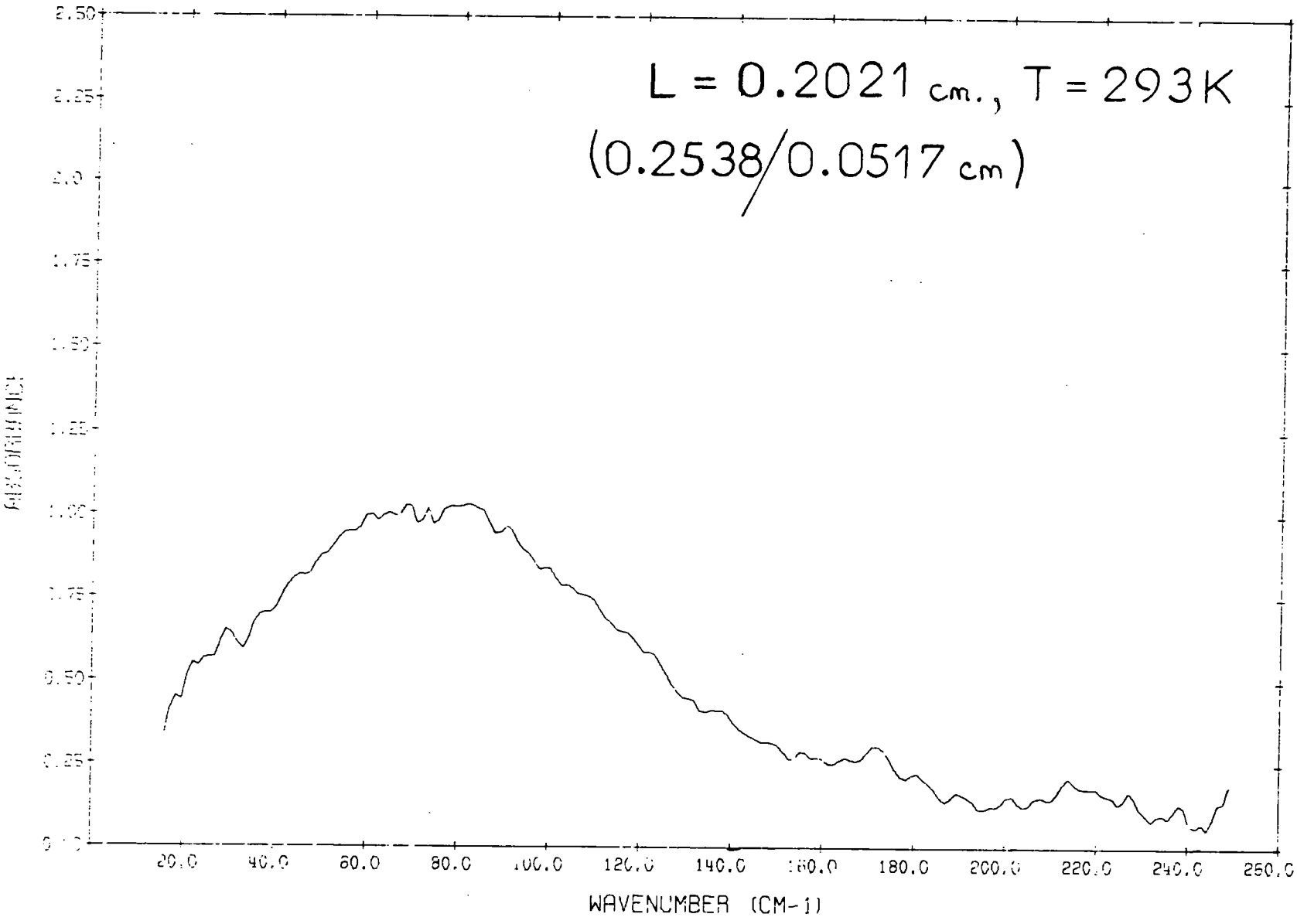

FIG. 6.1 0.2021 cm. PURE BENZENE

techniques). The areas under the absorption profile were measured for each of the 10 spectra, using a planimeter, and the results are recorded in table 6.1. The pathlengths quoted were determined by measuring the spacer thickness, by use of a micrometer screw gauge. The thickness was measured 10 times at various places around the spacer, and these values were then averaged to give the pathlengths of table 6.1. The areas quoted have associated with them an uncertainty of ± 20 cm^{-1}, which was calculated as the 'dead space' area below the fitted baseline. The error was thus the maximum discrepance on the area possible, and was thus different to previous error treatments. The area under the absorption band was plotted as a function of pathlength, and the graph is shown as fig. 6.2. The area/pathlength data was used with the programme BEERSLAW to give the best linear least squares fit to the data. This enabled a value for the band intensity to be calculated. The fit restricted to pass through the origin gave a slope of 494 ± 153 cm^{-2}, and is denoted by the letter A in the figure. This gave an intensity B_i of 43.9 ± 13.6 dm^3 mol^{-1} cm^{-2}, where the molarity of pure benzene was calculated as 11.26 mol dm^{-3} as in section 4.2.5. The unrestricted slope was found to be 521 ± 268 cm^{-2}, and is denoted by the letter B in fig. 6.2. This slope gave an intensity B_i of 46.3 ± 23.8 dm^3 mol^{-1} cm^{-2}. This intensity was seen to agree well with the provisional value of Chantry et. al. (71), where an integrated strength of 450 cm^{-1} was obtained for liquid benzene at 300K. This value would give an intensity B_i of 40 dm^3 mol^{-1} cm^{-2}. It should be noted here that the comparison of intensities between different systems is very difficult, because of the problems involved with the fixing of the baseline. Whilst intensity considerations are viable within a series of measurements for a given system, since a method of baseline fitting can be developed which suits that system, extreme care must be taken in comparing different systems.

To determine accurately the band centre and half-band width for the benzene low frequency absorption the spectra were fitted to a pure Gauss profile (see section 5.1 for details). The Gauss profile gave a better fit

Table 6.1 75 cm^{-1} band pure benzene. Area

sample pathlength /cm	background pathlength /cm	pathlength /cm	area /cm^{-1}
0.0208	0.0112	0.0096	12.51
0.0517	0.0208	0.0309	8.72
0.0517	0.0112	0.0405	20.30
0.1023	0.0517	0.0506	21.57
0.1023	0.0208	0.0815	25.42
0.1023	0.0112	0.0911	40.65
0.2538	0.1023	0.1515	80.39
0.2538	0.0517	0.2021	109.9
0.2538	0.0208	0.2330	113.6
0.2538	0.0112	0.2426	127.4

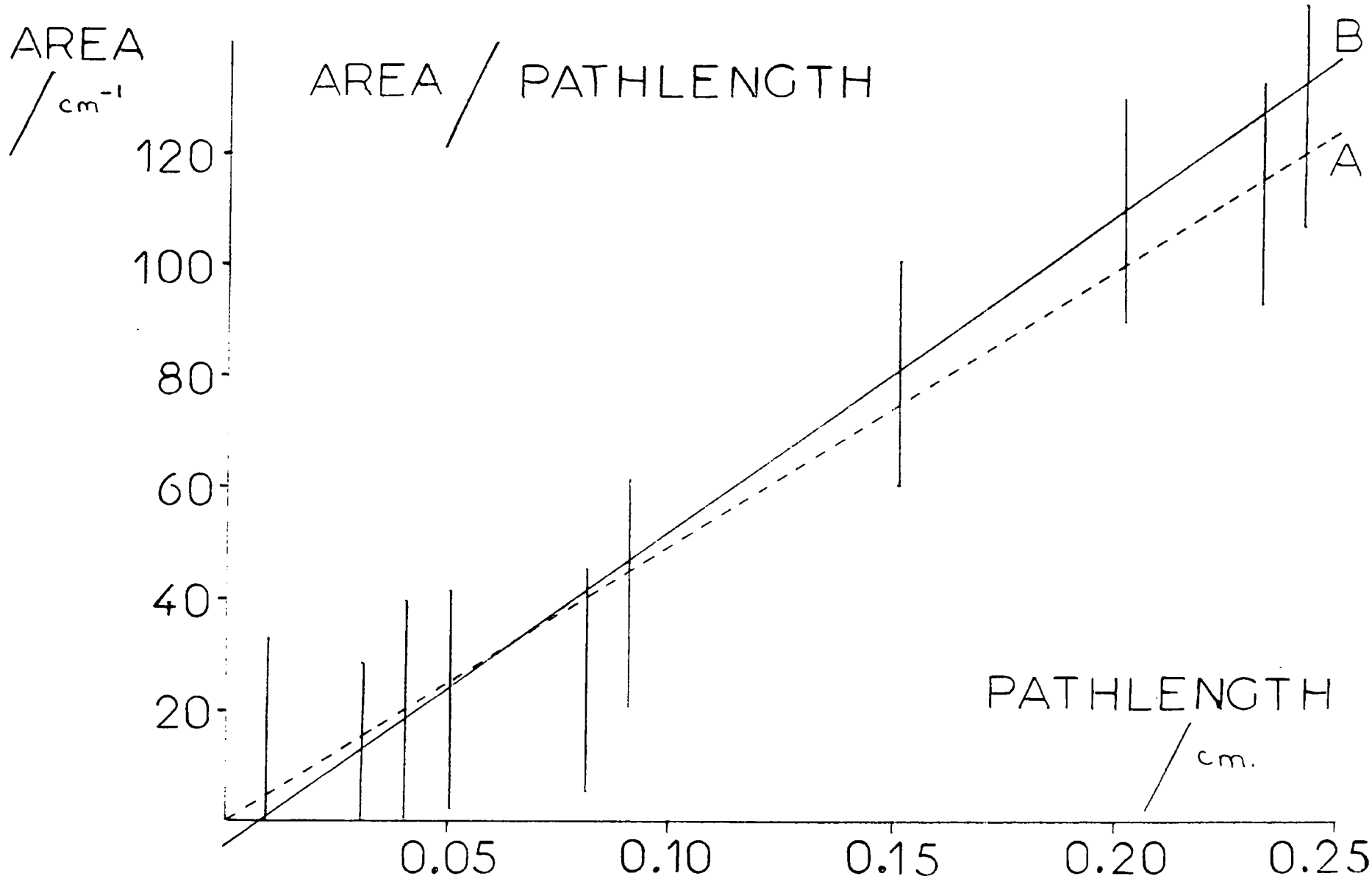

FIG. 6.2 80 cm^{-1} BAND PURE BENZENE

to the absorption profile than the Cauchy, as for the tetra-n-alkylammonium salts in non-polar solvent systems studied in chapter 5. This was possibly, once again, due to lack of data in the wings of the band, where the Cauchy profile dominates. The average band centre was found to be 75±1 cm^{-1}, and the average half-band width as 83±3 cm^{-1}. The errors were the root mean square deviation of the data set. A typical band fit is shown in fig. 6.3. This fit was for 0.2538 cm of benzene ratioed against 0.0112 cm of benzene. It was interesting to note that figs. 6.1 and 6.3 showed the possibility of a weak band occurring at about 180 cm^{-1}, the frequency at which the high frequency component of the $Bu_4N^+Cl^-$ in benzene system absorbed. This has not been further investigated here, but merits consideration in any further studies of these systems.

It has often been stated that fairly concentrated electrolytes have a pseudo-crystalline lattice (73), and so we decided to have a look at the spectra of crystalline solid benzene. Fig. 6.4 shows the spectrum obtained by ratioing 0.2538 cm of crystalline benzene at 253K against 0.1517 cm crystalline benzene at the same temperature. The spectra were recorded using the variable temperature cell, as detailed in chapter 2. The cooling agent used for the reservior was solid carbon dioxide in acetone. 2048 point interferograms were used to give a resolution of 1.5 cm^{-1}. A 50 gauge beam-splitter was used. This spectrum clearly showed that the band centre now occurred at 87±1 cm^{-1}. Bands of weaker intensity were seen to occur at 64±2 cm^{-1} and 76±2 cm^{-1}. The spectrum compared favourably with that obtained by Chantry et. al. (71), who observed the spectrum of crystalline solid benzene, and determined the main band centre as 97 cm^{-1}, with peaks of lower intensity at 53, 64 and 72 cm^{-1}. These authors, and others (60, 74-76) noted that the peak absorption values were dependent upon the temperature. Harada and Shimanouchi showed further (60) that the far-infrared spectra of benzene crystals grown under different conditions were quite different. In some cases the spectra were found to be sensitive to rotation in the beam of radiation

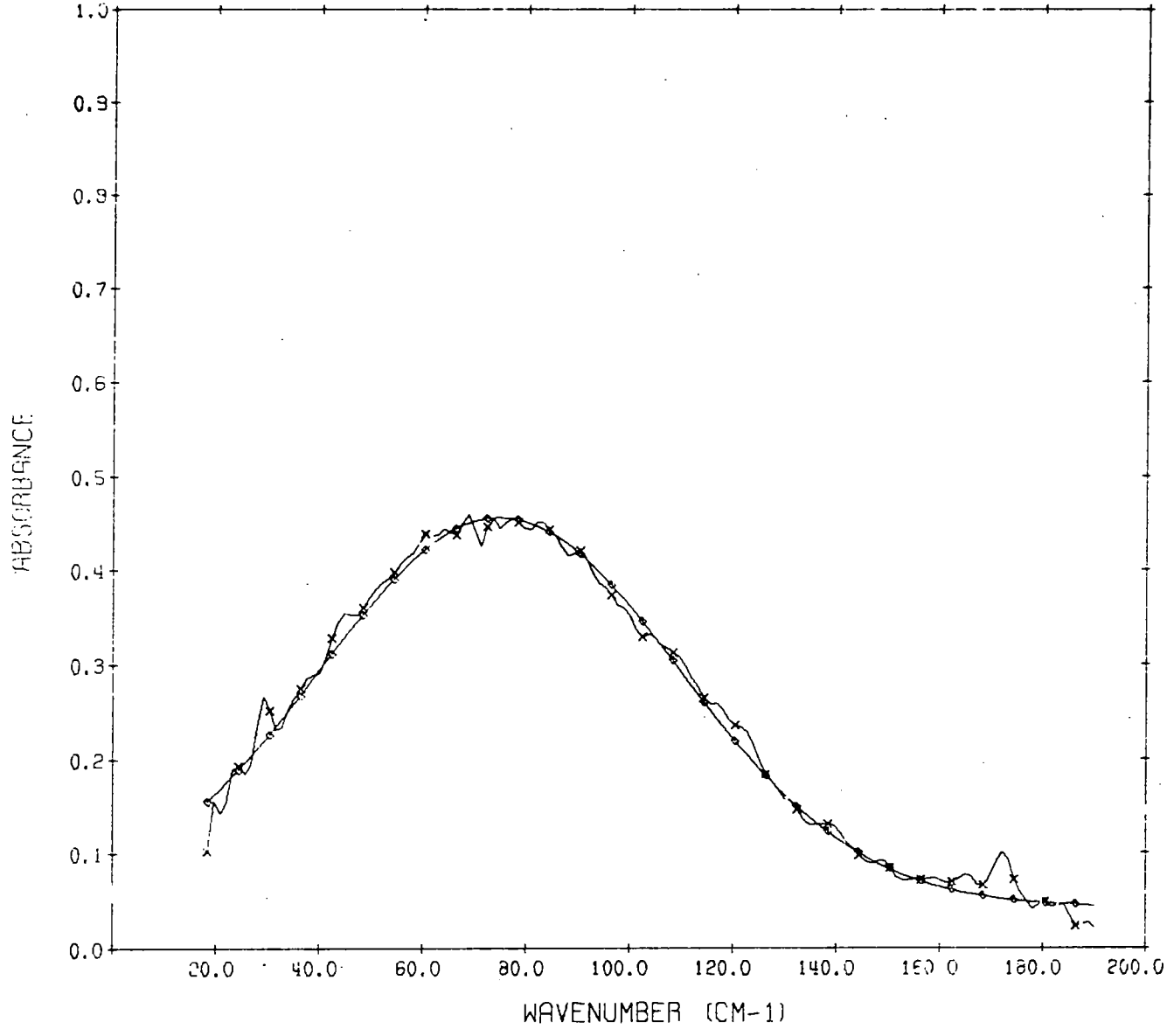

FIG. 6.3 0.2021 cm. PURE BENZENE BAND FIT

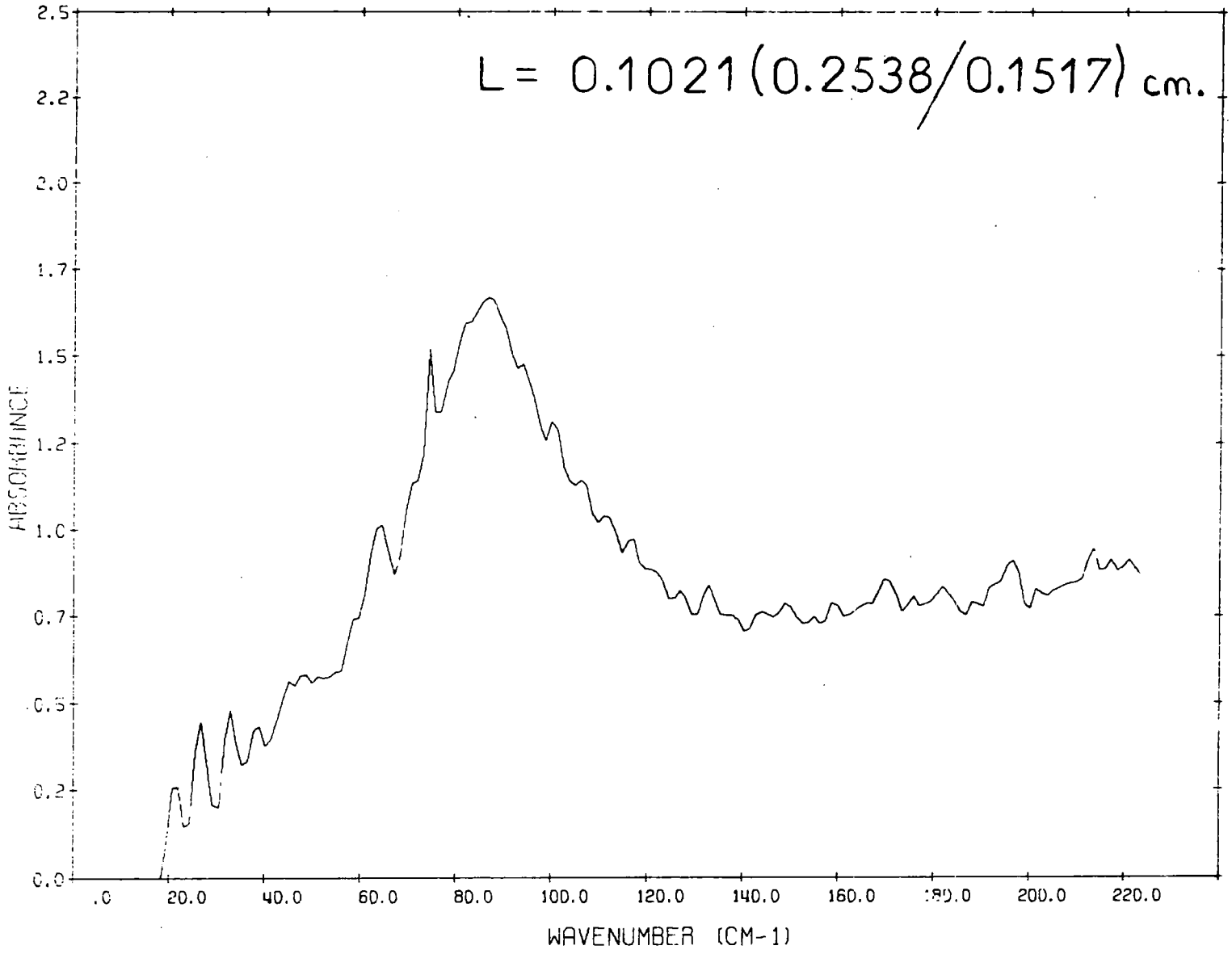

FIG. 6.4 0.1 cm. CRYSTALLINE BENZENE T = 253K

(60). Harada and Shimanouchi (75) showed that the major absorption peak occurred at 102 cm^{-1} at 80K, and 94 cm^{-1} at 140K, thus showing that the band centre moved to lower frequency with increasing temperature. 3 crystalline benzene spectra were recorded at 253K. The average band centre was measured as 88±2 cm^{-1}, and the average half-band width as 40±2 cm^{-1}. The areas under these absorption curves were measured as 63.6, 61.8 and 57.9 cm^{-1}, giving an average of 61.7±20 cm^{-1}, the uncertainty being determined from the dead space below the baseline as for the benzene liquid spectra. The intensity was then calculated assuming that the density of the solid benzene remained unchanged from that in the liquid as 879 g dm^{-3} (56). With the pathlength of 0.1023 cm and benzene concentration of 11.27 mol dm^{-3}, the intensity B_i was calculated as 54.8±18 dm^3 mol^{-1} cm^{-2}.

To determine accurately the band centre and half-band width for the crystalline benzene band the 3 spectra were fitted to a pure Gauss profile. A typical band fit is shown in fig. 6.5. The fitted band centres obtained were 87.2, 86.9 and 88.9 cm^{-1}, giving an average of 88±1 cm^{-1}. The fitted half-band widths were 41.8, 43.5 and 43.5 giving an average of 43±1 cm^{-1}.

Table 6.2 correlates the band parameters obtained for the low frequency absorptions for liquid benzene solvent at 293K, crystalline benzene solvent at 253K, and for 0.21 and 0.80 mol dm^{-3} solutions of $Bu_4N^+Cl^-$ in benzene both at 293K. The intensity of the low frequency component for the solutions was calculated with respect to the benzene concentration, and not the $Bu_4N^+Cl^-$ concentration as in chapter 5. The benzene concentration in these solutions was taken to be the same as that for pure benzene, being 11.26 mol dm^{-3}, calculated from the density and molecular weight. The intensity values thus calculated were seen to be minimum values, since the addition of the $Bu_4N^+Cl^-$ salt caused the concentration of the solution to be less than that for pure benzene. In fact this was seen to be unlikely to be the case since a significant increase in volume was noted for the more concentrated solutions was noticed when the salt was added.

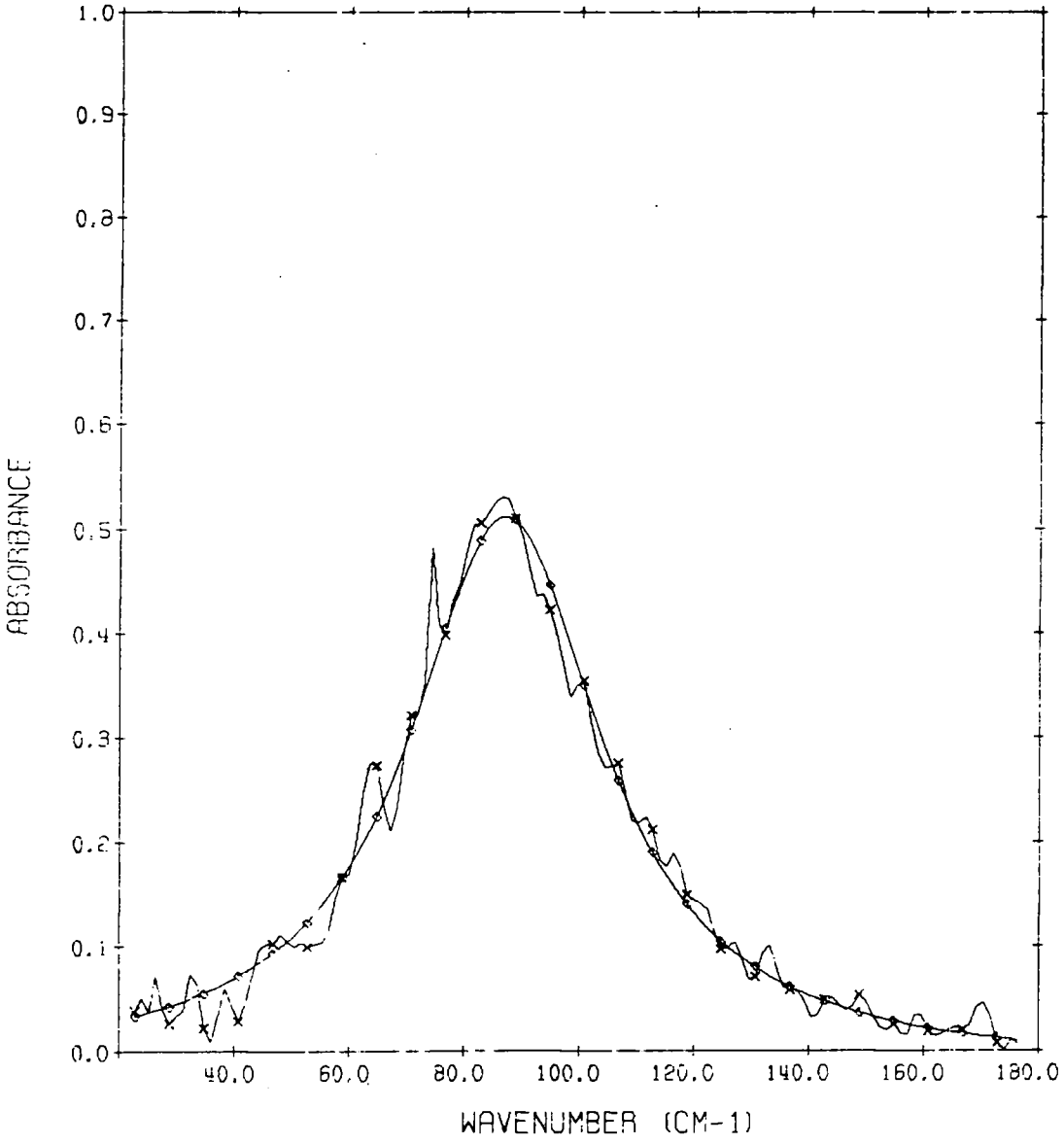

FIG. 6.5 0.1 cm. CRYSTALLINE BENZENE BAND FIT

Table 6.2 Band parameters for liquid, crystalline and solution low frequency bands for benzene.

	liquid[a]	crystalline[b]	solution[c]	solution[d]
band centre /cm^{-1}	75±1	88±1	63±3	74±3
half-band width /cm^{-1}	83±3	43±1	74±5	67±5
intensity /$dm^3\ mol^{-1}\ cm^{-2}$	46±24	55±18	27±50	387±50

a 293K

b 253K

c 0.21 mol dm^{-3} $Bu_4N^+Cl^-$ in benzene at 293K

d 0.80 mol dm^{-3} $Bu_4N^+Cl^-$ in benzene at 293K

The band centres and half-band widths were seen to be comparable in the 3 liquid systems. The average centre for the low frequency component for $Bu_4N^+Cl^-$ in benzene, from the band fits of table 5.6 was 73±1 cm^{-1}, which agreed well with the band centre of 75±1 for the pure benzene solvent absorption. The average half-band width for the $Bu_4N^+Cl^-$ in benzene low frequency component was 72±8 cm^{-1}, which was slightly lower than the 83±3 cm^{-1} for the pure benzene solvent.The intensity of the low frequency band, when calculated with respect to benzene concentration, was seen to be proportional to the concentration of the added $Bu_4N^+Cl^-$ salt, since the area of the band was seen to be linearly dependent upon the salt concentration from fig. 5.6. This proportionality was the case since the calculation of the intensity with respect to benzene involved division of the area by constant pathlength, and constant concentration.

The intensity values for the two solutions suggested that the benzene absorption was being severely intensified by the added electrolyte. The intensity of the benzene collisional band was doubled by the addition of about 0.4 mol dm^{-3} of added $Bu_4N^+Cl^-$. (It should be remembered here , that the low frequency component absorption was additional to the pure benzene solvent absorption, which had already been subtracted by ratioing against pure benzene.) At 0.8 mol dm^{-3} of added salt the benzene band was seen to be intensified by approximately 8 times its original value.

This section has indicated that the low frequency component for the $Bu_4N^+Cl^-$ salt in benzene was indeed a perturbed benzene collisional band.

6.1.2 Pure toluene solvent spectra

Spectra of pure toluene were recorded to determine if the band parameters were changed relative to those for benzene. This was done in the hope that toluene could be used as a further solvent for the tetra-n-alkyl-ammonium salts. Fig. 6.6 shows the spectrum obtained by ratioing 0.2538 cm of toluene against 0.0112 cm of toluene. The interferograms were recorded using a 50 gauge beam-splitter. 1024 point interferograms were recorded

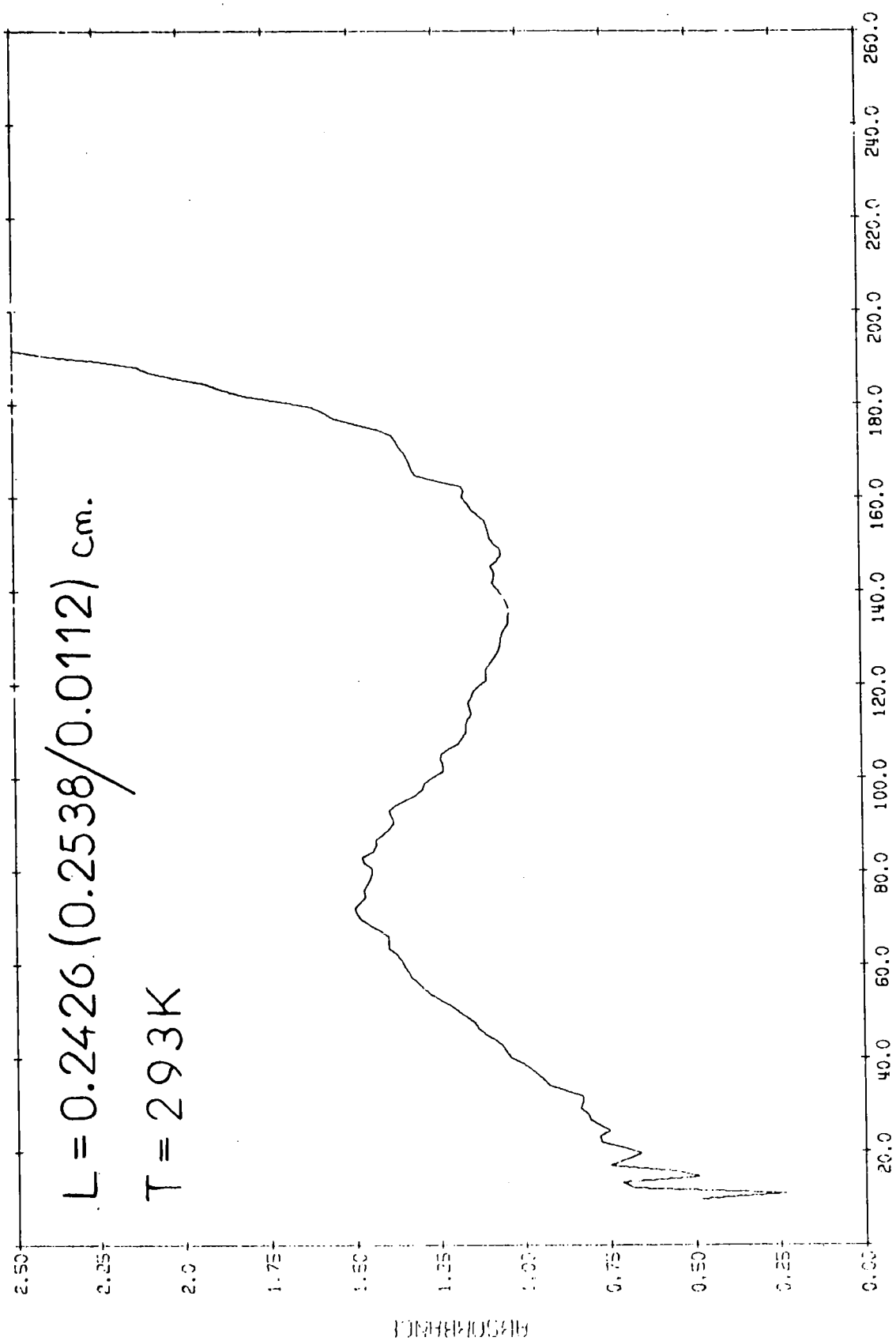

FIG. 6.6 0.24 cm. PURE TOLUENE

to give a resolution of 3 cm^{-1}. The low frequency band was seen to occur on the side of a strong absorption centred above 200 cm^{-1}, and this made measurements of the band parameters difficult. This strong band would also make studies of the spectra of tetra-n-alkylammonium salts in toluene almost impossible.

The band parameters were determined for use in conjunction with the spectra of $Ag^{+}ClO_4^{-}$ in toluene (see section 6.6). 4 toluene spectra were recorded, and the parameters determined are shown in table 6.3. The average band centre was 73±3 cm^{-1}, the average half-band width was 67±3 cm^{-1}, and the average integrated intensity A/L was 197 30±cm^{-2}. The density of toluene was taken as 866.5 g dm^{-3} at 293K (77), and the band intensity B_i was thus calculated as 21.3±3 dm^3 mol^{-1} cm^{-2}, since the molarity of pure toluene was calculated as 9.23 mol dm^{-3}.

6.2 Pure chloroform spectra

Spectra of pure chloroform were recorded for comparison with the spectra obtained for the solutions of tetra-n-alkylammonium salts dissolved in chloroform (see sections 4.7 to 4.11). Fig. 6.7 shows the spectrum obtained when 0.1023 cm of chloroform was ratioed against 0.0112 cm of chloroform. The spectra were obtained using a 50 gauge beam-splitter, and 1024 point interferograms were recorded to give a resolution of 3 cm^{-1}. The band centre was found to occur at approximately 36 cm^{-1},and, as can be seen from fig. 6.7, the low frequency half of the band was extremely difficult to observe. At the very low frequencies necessary the transmittance of the beam-splitter was rapidly decreasing, as was the efficiency of both the detector and source. Various beam-splitter and filter combinations were tried in order to obtain the best possible chloroform spectra in this region. Fig. 6.8 shows the spectrum obtained by ratioing 0.1023 cm of chloroform against 0.0112 cm of chloroform, where the interferograms were obtained using a 100 gauge beam-splitter and the black polythene lens. The resolution was once again 3 cm^{-1}. Fig. 6.8 showed that the profile could be obtained with reasonable accuracy down to

Table 6.3 Band parameters for pure toluene

sample pathlength /cm	background pathlength /cm	pathlength /cm	$\bar{\nu}_o$ /cm^{-1}	$\Delta\bar{\nu}_{\frac{1}{2}}$ /cm^{-1}	area /cm^{-1}	area/pathlength /cm^{-2}
0.2538	0.1023	0.1515	75	70	32	210
0.2538	0.0517	0.2031	76	66	33	165
0.2538	0.0208	0.2330	71	64	47	207
0.2538	0.0112	0.2426	72	68	50	205

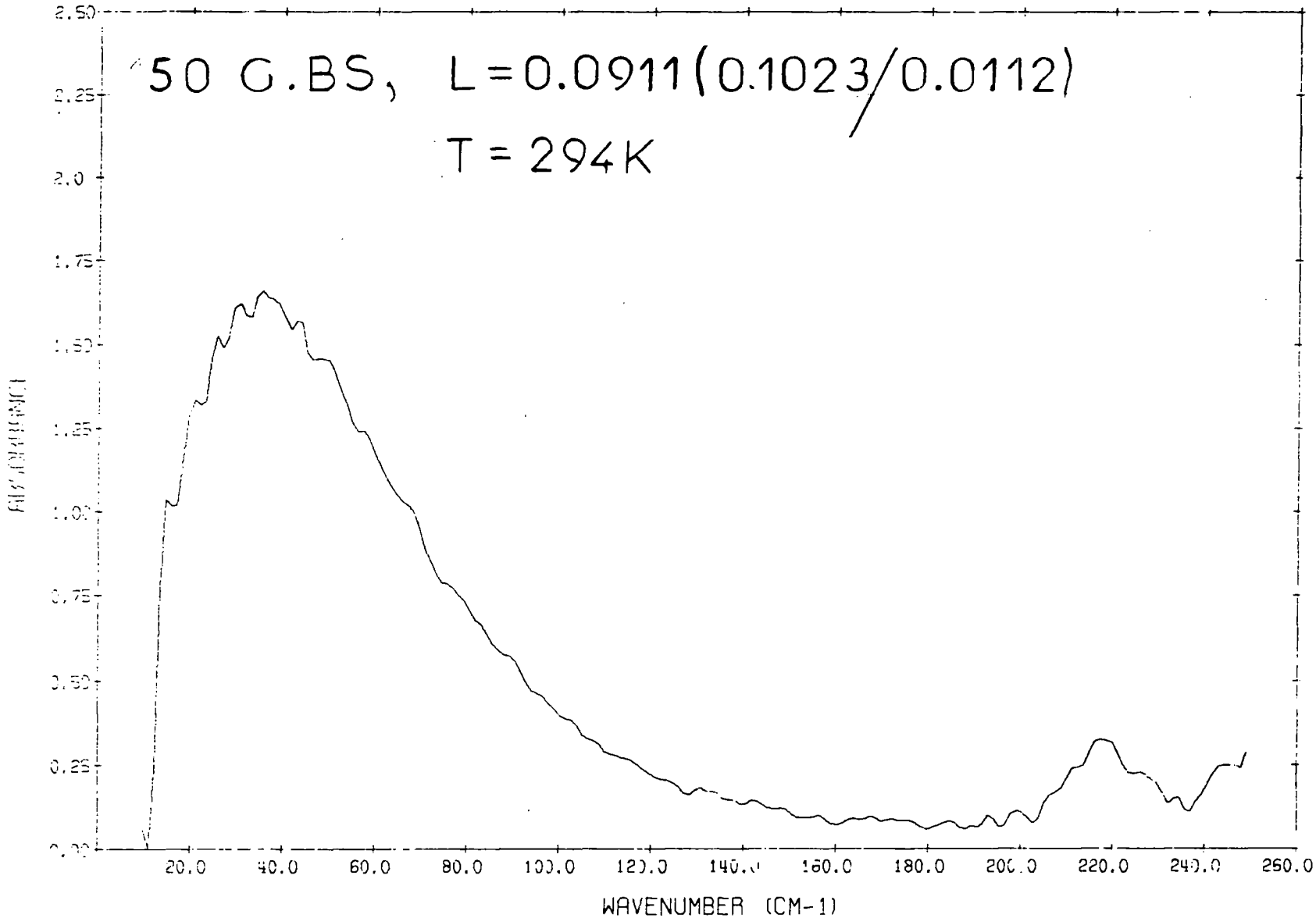

FIG. 6.7 0.091 cm. PURE CHLOROFORM

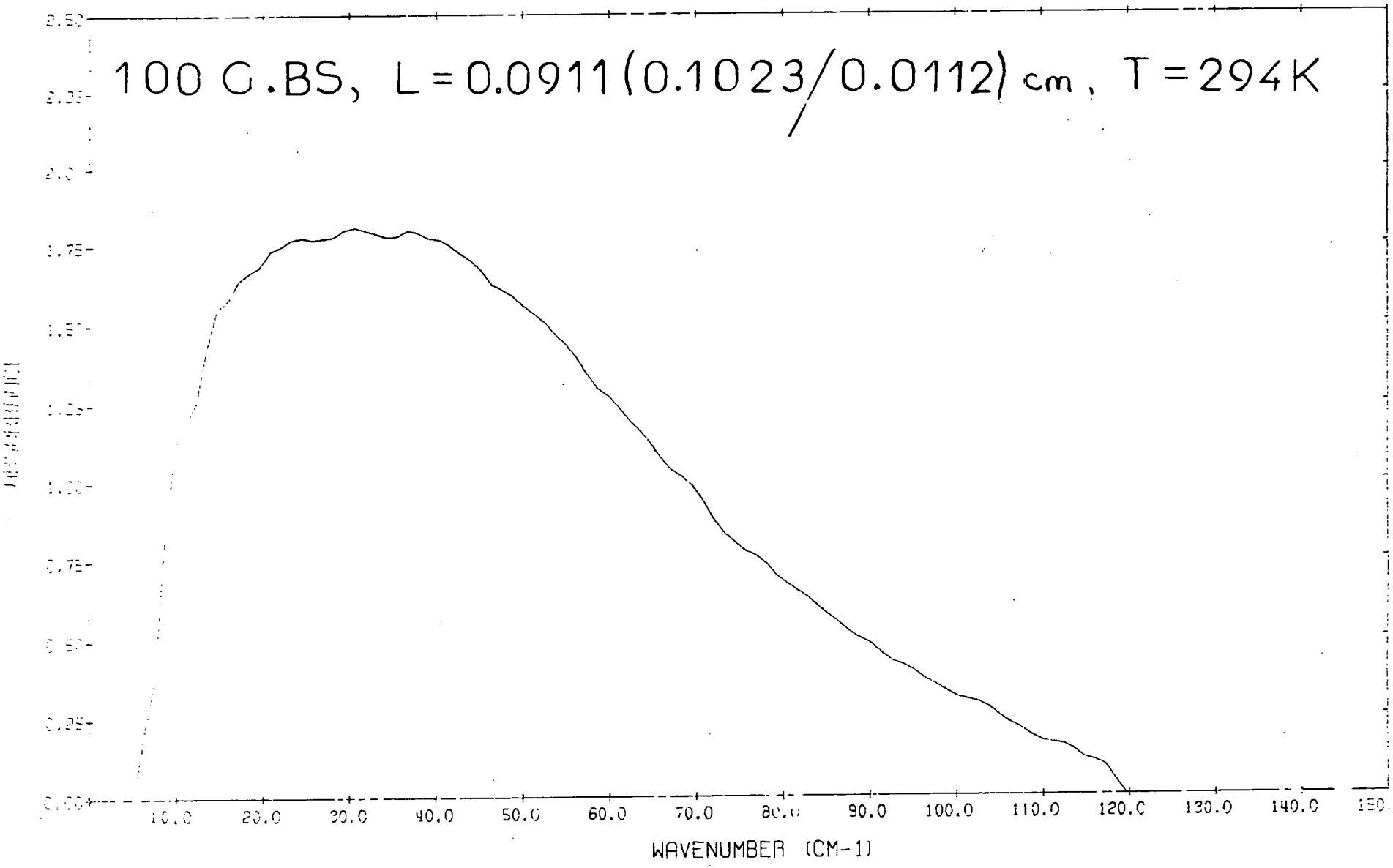

FIG. 6.8 0.091 cm. PURE CHLOROFORM

15 cm^{-1}. The low frequency wing was still not visible, and indeed the high frequency wing around 200 cm^{-1} was now marked by the first beam-splitter cut-off of the 100 gauge film. Fig. 6.9 shows the chloroform spectrum obtained for a ratio of 0.1023 and 0.0112 cm pathlengths, using a 400 gauge beam-splitter and a 0.1 cm crystalline quartz filter. This spectrum showed that the profile could be obtained accurately down to 10 cm^{-1}, but the spectrum so obtained had the disadvantage that the beam-splitter minima occurred every 30 cm^{-1}. Hence there were 3 regions of noise in the spectrum, due to the low transmitted intensity through these minima. However the spectrum obtained in this way was far better than might be thought possible, and could be easily corrected, as shown by the dotted lines in fig. 6.9, to obtain the accurate profile between 10 and 100 cm^{-1}. This spectrum was not satisfactory for observation of the whole low frequency band, because the high frequency wing had been truncated by the crystalline quartz filter, which cuts-in again at 110cm^{-1}. The filter was necessary with the 400 gauge beam-splitter to maximise the energy in the region below 100 cm^{-1}, in order that good spectra could be obtained at this low frequency. The filtering could be seen to be affecting the band profile, and the intensity of the band using the 400 gauge beam-splitter was seen to be considerably less than that using the 100 gauge beam-splitter.

The spectra gained using the 50 gauge beam-splitter were considered to be the best for obtaining the band parameters for the low frequency chloroform absorption. With this spectrum the baseline could be fitted by reference to the high frequency wing. 3 good spectra were analysed, and the band parameters are detailed in table 6.4. The band centre was found to be 36±1 cm^{-1}, and the half-band width 52±2cm^{-1}. The area under the absorption bands was measured using a planimeter. The integrated strength A/L was determined by dividing the area by the pathlength, and the average area was found to be 906 cm^{-2}. The errors on the area values were determined as the area of the dead space between the fitted baseline and the wavenumber axis.

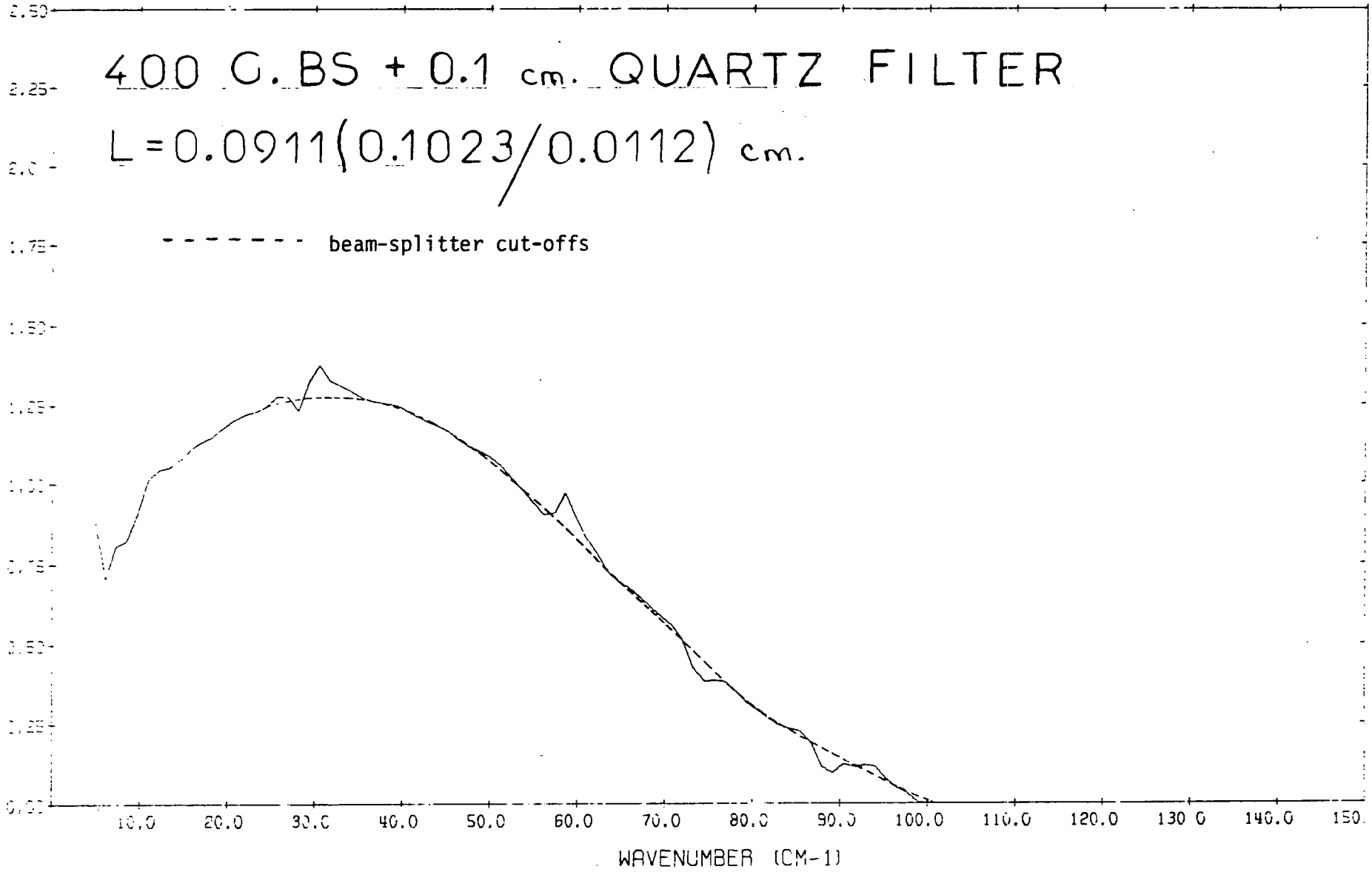

FIG. 6.9 0.091 cm. PURE CHLOROFORM

Table 6.4 Band parameters for pure chloroform

sample pathlength /cm	background pathlength /cm	pathlength /cm	$\bar{\nu}_o$ /cm^{-1}	$\Delta\bar{\nu}_{\frac{1}{2}}$ /cm^{-1}	area /cm^{-1}	area/pathlength /cm^{-2}
0.1023	0.0517	0.0506	36	54	42	830
0.1023	0.0208	0.0815	36	53	69	847
0.1023	0.0112	0.0913	36	50	95	1041

This was found to be approximately 10 cm^{-1}, as the typical baseline was fitted at 0.1 Neper. With a molecular weight of 119 g mol^{-1} for chloroform, and a density of 1500 g dm^{-3} (56), which gave a molarity of 12.56 mol dm^{-3} for the pure solvent, the intensity B_i was calculated as 72±10 dm^3 mol^{-1} cm^{-2}. Attempts were made to fit the chloroform spectra to pure Gauss profiles, to obtain more accurate band parameters. These were unsuccessful, presumably due to the poor quality of the spectra below the band centre, and the large asymmetry of the band. Approximately 36 cm^{-1} of the half-band width occurred for frequencies higher than the band centre, and only 18 cm^{-1} below the band centre. (See chapter 7 for a discussion of the validity of absorbance/wavenumber plots at low wavenumber.)

Table 6.5 correlates the band parameters obtained for the low frequency absorptions for pure chloroform solvent, and for 0.10 and 0.80 mol dm^{-3} solutions of $Bu_4N^+Cl^-$ in chloroform, all at 293K. The intensities were calculated with respect to the chloroform concentration, which was calculated as 12.56 mol dm^{-3} for pure chloroform. The half-band widths for the absorptions in the two systems, being 52±2 cm^{-1} for the pure solvent and 50±11 cm^{-1} as an average for the solutions were seen to be comparable. The band centre in the solutions was seen to be higher than that for the pure solvent. In the solutions the average band centre was 70±7 cm^{-1}, and the pure solvent 36±1 cm^{-1}. The intensities for the low frequency component for the solution were seen to be of the same order of magnitude as the chloroform absorption. The addition of the $Bu_4N^+Cl^-$ salt appeared to have less of an effect on the intensity than in the benzene solution. For the 0.8 mol dm^{-3} solution the intensity of the 70 cm^{-1} component was only just equivalent to that of pure chloroform, whereas for benzene at the same concentration the intensification was 8-fold.

It appeared that the chloroform solutions gave spectra that produced slightly different absorptions to those in benzene solution. The Poley-Hill absorption of the polar chloroform molecules appeared to be unaffected by

Table 6.5 Band parameters for pure liquid and solution low frequency bands for chloroform

	liquid	solution[a]	solution[b]
band centre /cm^{-1}	36±1	82±3	62±3
half-band width /cm^{-1}	52±2	57±5	46±5
intensity /$dm^3\ mol^{-1}\ cm^{-2}$	72±10	12±50	84±50

a 0.10 mol dm^{-3} $Bu_4N^+Cl^-$ in chloroform

b 0.80 mol dm^{-3} $Bu_4N^+Cl^-$ in chloroform

the addition of the $Bu_4N^+Cl^-$ salt. We propose that the new band occurring in the solutions of $Bu_4N^+Cl^-$ in chloroform was due to a collision-induced absorption caused by collisions of ions and ion pairs with the polarisable chloroform molecules (see chapter 7).

6.3 Carbon tetrachloride spectra

Spectra of pure carbon tetrachloride were recorded for comparison with the spectra obtained for the solutions of tetra-n-alkylammonium salts dissolved in carbon tetrachloride (see sections 4.5 and 4.6). Fig. 6.10 shows the spectrum obtained by ratioing 0.5116 cm against 0.2504 cm of carbon tetrachloride using a 100 gauge beam-splitter. 1024 point interferograms were recorded, which gave a resolution of 3 cm^{-1}. The band parameters obtained for spectra at 8 pathlengths are shown in table 6.6. The average band centre was found to be 43±2 cm^{-1}, and the average half-band width as 58±3 cm^{-1}. The error on the area was found to be ±20 cm^{-1}, from the dead space measurements, as for the chloroform spectra. The integrated strength (area/pathlength) was calculated and the average value computed as 84±40 cm^{-2}. The density of carbon tetrachloride was found to be 1 595 g dm^{-3} at 293K (78), and with a molecular weight of 154 the molarity of pure carbon tetrachloride was calculated as 10.4 mol dm^{-3}. Thus the intensity of the low frequency absorption centred at 43 cm^{-1} was found to be 8.1±4 dm^3 mol^{-1} cm^{-2}. No band fits were attempted for the pure carbon tetrachloride.

Table 6.7 correlates the band parameters for the low frequency band for pure carbon terachloride, and the low frequency component to the overall profile for the spectrum of the solutions of $Bu_4N^+Cl^-$ in chloroform. The figures showed that there was no comparison between the two sets of data, and thus indicated that the low frequency component for the solution spectra in carbon tetrachloride was unlikely to be a perturbed solvent lattice band.

6.4 Lithium perchlorate in tetrahydrofuran

The studies of ionic solvation were enlarged to include solvents of high polarity. These solvents had a large 'Poley-Hill' (2,4, 79-81)

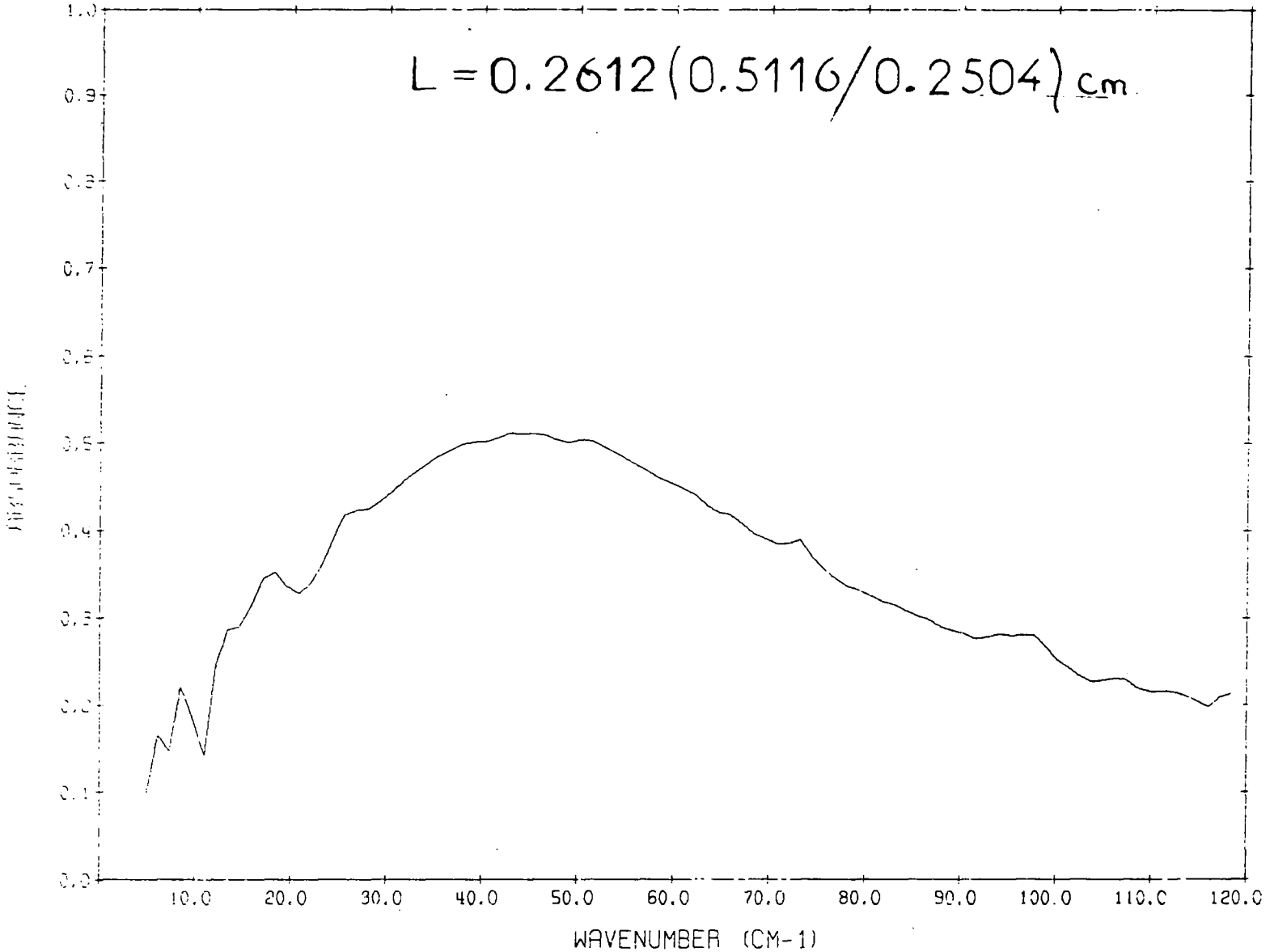

FIG. 6.10 0.261 cm. PURE CARBON TETRACHLORIDE

Table 6.6 Band parameters for pure carbon tetrachloride

sample pathlength /cm	background pathlength /cm	pathlength /cm	$\bar{\nu}_o$ /cm^{-1}	$\Delta\bar{\nu}_{\frac{1}{2}}$ /cm^{-1}	area /cm^{-1}	area/pathlength /cm^{-2}
0.1986	0.0517	0.1369	43	58	12.1	88.1
0.2504	0.0517	0.1987	42	60	19.0	95.4
0.2504	0.0208	0.2296	40	57	19.3	84.0
0.5116	0.2504	0.2612	43	55	18.4	70.5
0.5116	0.1986	0.3130	45	56	23.5	75.1
0.5116	0.0985	0.4131	46	60	37.5	90.7
0.5116	0.0517	0.4599	46	59	39.3	85.2
0.5116	0.0208	0.4908	41	60	41.8	85.1

Table 6.7 Band parameters for pure liquid and solution low frequency bands for carbon tetrachloride

	liquid	solution[a]	solution[b]
band centre /cm^{-1}	43±2	84±3	73±3
half-band width /cm^{-1}	58±3	68±5	61±5
intensity /$dm^3\ mol^{-1}\ cm^{-2}$	81±4	61±60	295±60

a 0.098 mol dm^{-3} $Bu_4N^+Cl^-$ in carbon tetrachloride

b 0.783 mol dm^{-3} $Bu_4N^+Cl^-$ in carbon tetrachloride

absorption, and thus made impossible studies of the tetra-n-alkylammonium salts in this solvent, because of the overlapping of the low frequency bands. Thus a solvent had to be found which had its characteristic absorptions at frequencies greater than 200 cm^{-1}. The absorption of $Li^+ClO_4^-$ in acetone was noted to occur at 420±5 cm^{-1}, which agreed well with the value of 425±3 cm^{-1} obtained by Popov et. al. (44). However the spectra in this region were seen to be much confused by overlap of the acetone 390 cm^{-1} absorption. Thus we decided to look at the spectra of $Li^+ClO_4^-$ in tetrahydrofuran, which was seen to have no absorption bands in the 400 cm^{-1} region.

Fig. 6.11 shows the spectrum obtained for a 0.250 mol dm^{-3} solution of $Li^+ClO_4^-$ in THF, obtained using a 0.0208 cm pathlength cell by ratioing against the same pathlength of pure THF. The interferograms were recorded over 1024 points to give a resolution of about 3 cm^{-1}. The 15 gauge beam-splitter was used. The band centre was observed at 400±5 cm^{-1}, and a high frequency component was clearly visible centred at 475±5 cm^{-1}. As far as can be determined the spectra of $Li^+ClO_4^-$ in THF have not been recorded previously, but the salt has been studied in several other solvents. In dimethylsulphoxide the band centre was 429 cm^{-1} (45,82); in dipropylsulphoxide 421 cm^{-1} (45); in dibutylsulphoxide 426 cm^{-1} (45); in pyridine 419 cm^{-1} (83); in 2-pyrrolidone 400 cm^{-1} (84); in 1-Me-2-pyrrolidone 398 cm^{-1} (84). Spectra of many other lithium salts in THF have been recorded mostly by Edgell et.al.. They showed that the band centres for the various salts in THF were 413 cm^{-1} for $Li^+Co(CO)_4^-$ (42); 387 cm^{-1} for Li^+Cl^- (42); 378 cm^{-1} for Li^+Br^- (42); 373 for Li^+I^- (42); 407 cm^{-1} for $Li^+NO_3^-$ (42) and 412 (42) and 410 cm^{-1} (41) for $Li^+BPh_4^-$. Thus the value obtained for $Li^+ClO_4^-$ of 400±5 cm^{-1} fits well into the series of salt absorptions in THF. Our results were thus in agreement with the suggestion that in lower dielectric constant solvents (THF ε_r = 7.58) the far-infrared vibrational frequency for the ion cage vibration is anion dependent. This implied that the anion was a member of the solvent cage, and thus gained intimate contact with the cation. This cation-anion contact

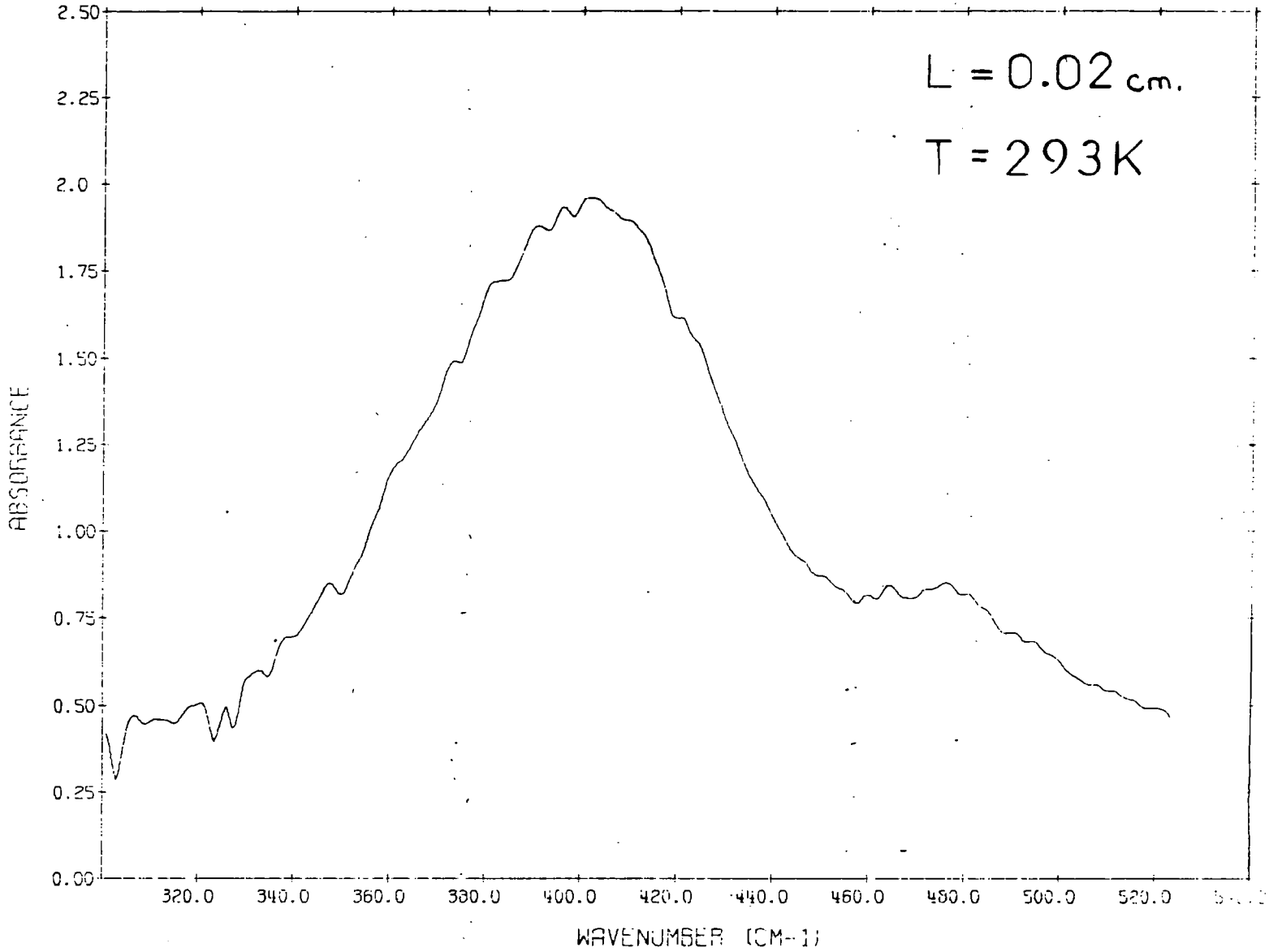

FIG. 6.11 0.25 mol. dm^{-3} $Li^{+}ClO_4^{-}$ IN THF

could be the cause of the high frequency component present in this system. However, no mention of such a high frequency component to any of the spectra for the salt/solvent systems listed above, where such cation-anion contact was thought to occur, was made in the literature. Further studies are required before any conclusions can be drawn.

The band parameters for 0.100 and 0.250 mol dm^{-3} $Li^+ClO_4^-$ in THF solutions are shown in table 6.8, where the area measured was that for the total profile. The band centre was seen to occur at 400±5 cm^{-1}, and had a half-band width of 68±5 cm^{-1}. The intensity appeared to be concentration dependent (although spectra for more concentrations were necessary to be sure of this). The average intensity was calculated as 22 000±4 000 dm^3 mol^{-1} cm^{-2}. The half-band widths and intensities were seen to be of the same order of magnitude as for the absorptions of the tetra-n-alkylammonium salts in less polar solvents. There thus appeared to be no apparent overriding difference between the far-infrared absorptions of polar and non-polar systems.

Band fits were made to the spectra of the 2 concentrations of $Li^+ClO_4^-$ in THF. The bands were once again found to give the best fit to the Gauss profile. The sum function gave a 5% Cauchy contribution to the overall profile. The band fit to the sum of two Gauss components centred at 398 and 477 cm^{-1} for the 0.25 mol dm^{-3} solution of $Li^+ClO_4^-$ in THF is shown in fig. 6.12. The band parameters obtained for the best fits are shown in table 6.9. These fits indicated that the intensity of the main band was concentration dependent, but that the intensity of the high frequency component was invariant with concentration. This had been found for the tetra-n-alkylammonium salts in the non-polar solvents. The intensity of the high frequency component was fixed as 1 300±100 dm^3 mol^{-1} cm^{-2}, with a band centre of 477±1 cm^{-1} and a half-band width of 53±3 cm^{-1}.

6.5.1 Sodium iodide in acetone spectra

To continue the studies of electrolytes dissolved in polar solvents, and to compare the absorption bands arising with those obtained from non-

Table 6.8 Band parameters for the 400 cm^{-1} total absorption profile for $Li^{+}ClO_4^{-}$ in THF.

concentration /mol dm^{-3}	$\bar{\nu}_o$ /cm^{-1}	$\Delta\bar{\nu}_{\frac{1}{2}}$ /cm^{-1}	area /cm^{-1}	intensity /dm^3 mol^{-1} cm^{-2}
0.100	400	65	31	
	395	66	34	18 100
	396	65	42	
	400	70	37	
0.250	402	70	134	
	403	73	136	26 000
	401	72	125	
	403	70	125	

Table 6.9 Band fit parameters for $Li^+ClO_4^-$ in THF

concentration /mol dm^{-3}	$\bar{\nu}_o$ /cm^{-1}	$\Delta\bar{\nu}_{\frac{1}{2}}$ /cm^{-1}	area /cm^{-1}	intensity /dm^3 mol^{-1} cm^{-2}
0.100	398	61	23	11 400
	478	55	3	1 400
0.250	399	66	103	20 600
	477	50	6	1 200

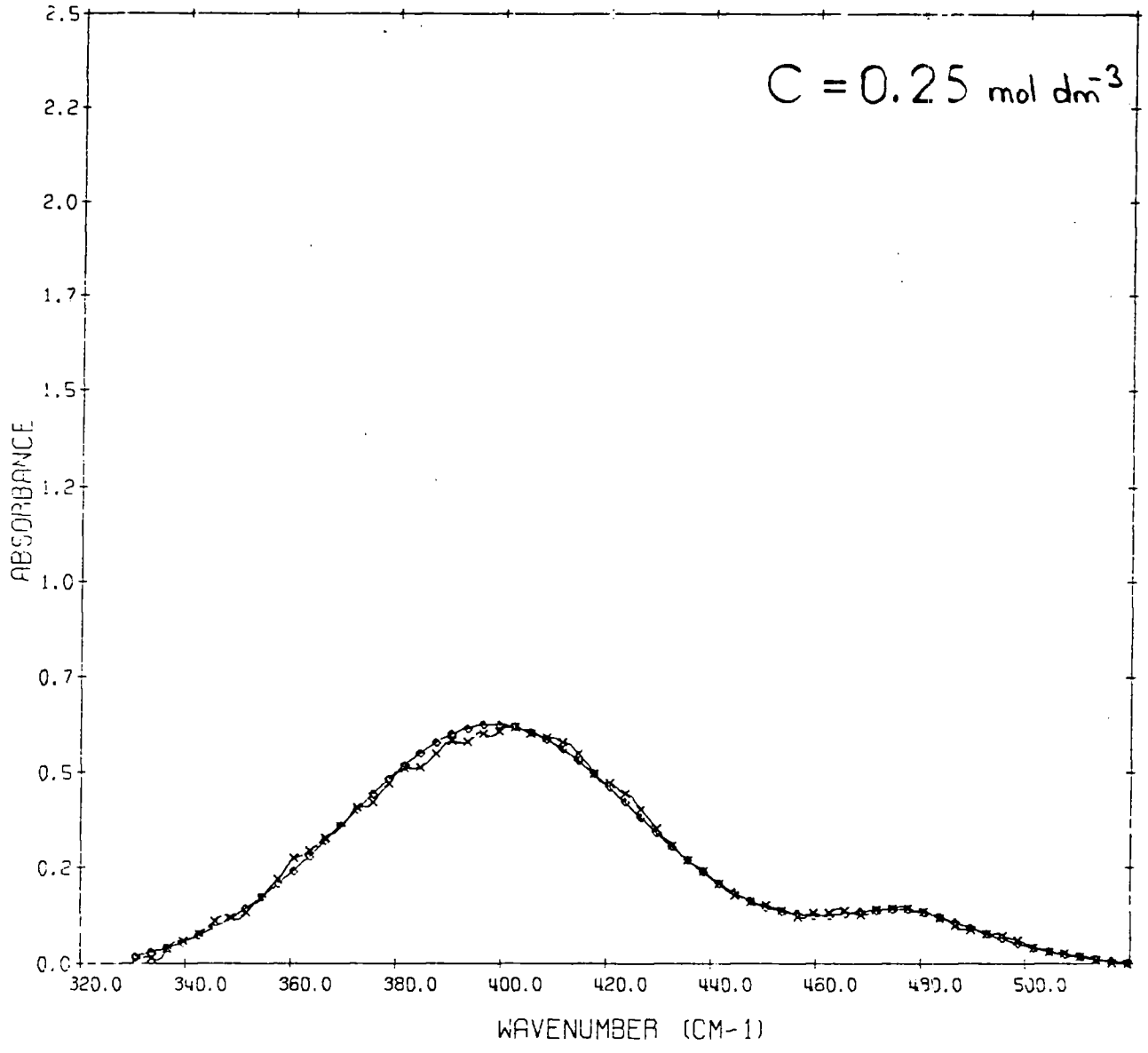

FIG. 6.12 BAND FIT FOR $Li^+ClO_4^-$ IN THF

polar systems, we decided to look at the spectra of sodium iodide in acetone. The sodium salt was chosen so that the electrolyte absorption at 192 cm^{-1} (44) was not masked by the 390 cm^{-1} acetone absorption. Fig. 6.13 shows the spectrum obtained for a 0.0119 cm pathlength of 0.842 mol dm^{-3} Na^+I^- in acetone ratioed against pure acetone. The band centre was seen to occur at about 188 cm^{-1}, and it could be clearly seen that the low frequency wing of the band was being severely curtailed by the ratioing out of the acetone Poley-Hill absorption. The intensity of the low frequency Poley-Hill absorption appeared to be diminished by the addition of electrolyte, and hence the absorption from the acetone in solution was less than that from the pure solvent background. This decrease in intensity would be expected if some of the dissolved ions took the places of solvent molecules in the cage of solvent molecules surrounding the librating molecule.

In an attempt to gain the band intensity for the Na^+I^- in acetone, absorption spectra were recorded and ratioed against a cyclohexane background. Fig. 6.14 shows the spectrum obtained for a 0.0119 cm pathlength of 1.0 mol dm^{-3} Na^+I^- in acetone ratioed against cyclohexane. Attempts were then made to determine the intensity of the Na^+I^- band, which now occurred as a shoulder on the side of the very strong acetone Poley-Hill absorption. A curving baseline was used to represent the high frequency profile for the acetone absorption, and the area was then measured by planimeter. The band parameters for the 180 cm^{-1} band are shown in table 6.10. The two spectra recorded against acetone showed a higher intensity than those recorded against cyclohexane. This could have been due to the baseline for the cyclohexane ratioed spectra being fixed too high. This was probably caused by the low frequency wing of the band being enveloped in the high frequency wing of the acetone absorption. The acetone absorption was too strong to allow calculation of the intensity of an overlapping band of much lower intensity. It thus appeared that the best value for the band intensity from the higher concentration solutions was 12 00$\pm$1 000 dm^3 mol^{-1} cm^{-2}, obtained from the

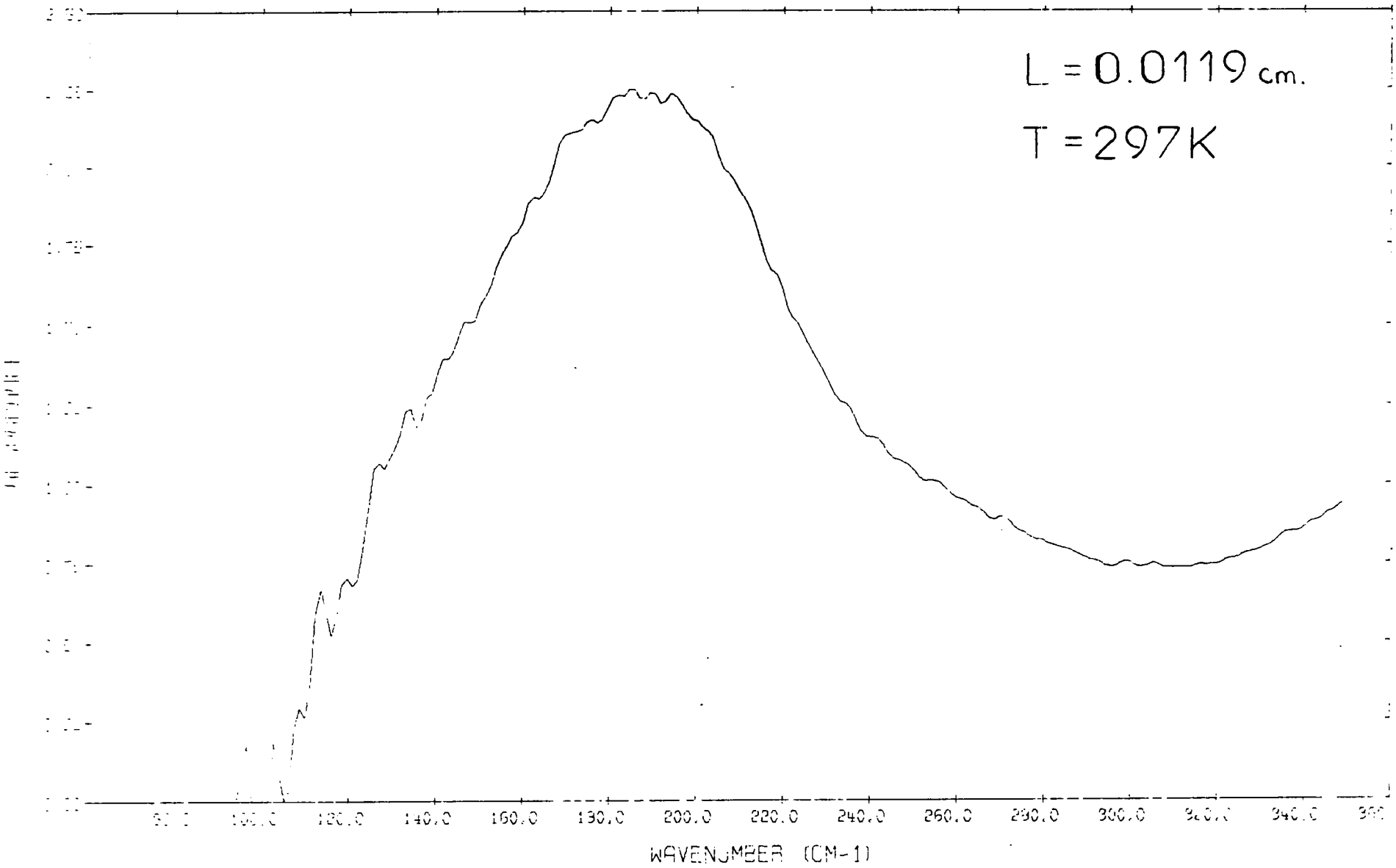

FIG. 6.13 0.842 mol. dm^{-3} Na^+I^- IN ACETONE

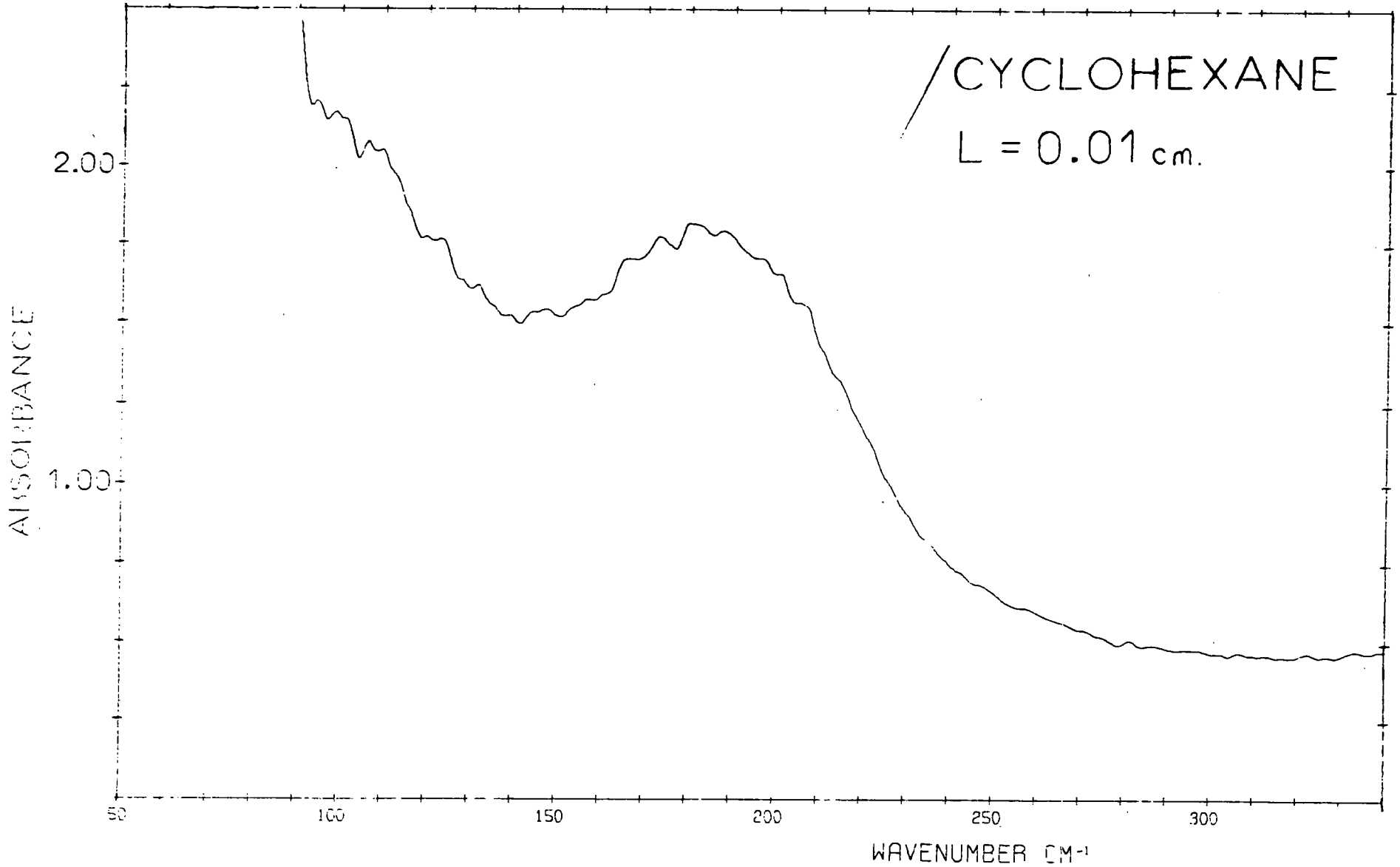

FIG. 6.14 1.0 mol. dm^{-3} $Na^{+}I^{-}$ IN ACETONE

Table 6.10 Band parameters for the 190 cm^{-1} band for $Na^{+}I^{-}$ in acetone

concn. /mol dm^{-3}	$\bar{\nu}_o$ /cm^{-1}	$\Delta\bar{\nu}_{\frac{1}{2}}$ /cm^{-1}	area /cm^{-1}	intensity /dm^3 mol^{-1} cm^{-2}
0.052[a]	190	44	6.69	
	191	42	6.86	6 820
	190	45	7.75	
0.104[b]	190	44	10.69	5 140
0.521[a]	190	46	27.85	5 400
0.824[a]	190	80	90.6	10 900
0.842[a]	188	67	129.2	12 920
1.000[b]	194	72	78.1	
	190	72	70.8	7 040
	196	68	62.5	

a ratioed against acetone

b ratioed against cyclohexane

acetone ratios.

The intensity for the lower concentrations up to about 0.5 mol dm^{-3} was seen to be approximately constant with a value of 6 000±1 000 dm^3 mol^{-1} cm^{-2}, and it thus appeared that the intensity of this band was concentration dependent over the whole range of concentration studied. This observation agreed with that of Popov et. al. (44), where they attributed a clean break in their peak absorbance/concentration plot to represent the replacement of one or more acetone molecules in the solvation shell of the Li^+ cation by the ClO_4^- anion. We would expect the intensity change to be more gradual as the concentration of the second type of environment gradually increased. Our studies have indicated that the break in the Popov plot was due to the solubility limit of the $Li^+ClO_4^-$ in acetone being reached. The salt would then presumably dissolve in the nitromethane, which was used as a dilutant for the acetone solvent, and this would then give a different slope for the peak absorbance/concentration plot. Table 6.10 showed, however, that some changes occurred in the environment of the Na^+ cation, as the half-band width for the absorption increased from 44±3 cm^{-1} to 70±3 cm^{-1} at the higher concentrations. No significant shift of band centre was observed. Presumably the absorptions from the two environments overlap, and the increased uncertainty of the band centre determination may well have been due to the presence of the additional component to the overall profile.

6.5.2 Sodium iodide in acetone in the mid-infrared

The shifting of the band centre and intensification of the 390 cm^{-1} internal acetone mode in solutions with dissolved electrolytes prompted a short study of further acetone internal modes in the mid-infrared region. The spectra were recorded using a Grubb-Parsons GS-2A Grating Spectrophotometer, coupled to a Solaratron Data Transfer Unit and Solaratron Digital Voltmeter and Westrex Teletype for digital recording of the transmission data.

Fig. 6.15 shows the spectrum for the 1095 cm^{-1} ν_{22} band for pure acetone, represented by the solid line, and for a 0.69 mol dm^{-3} solution of

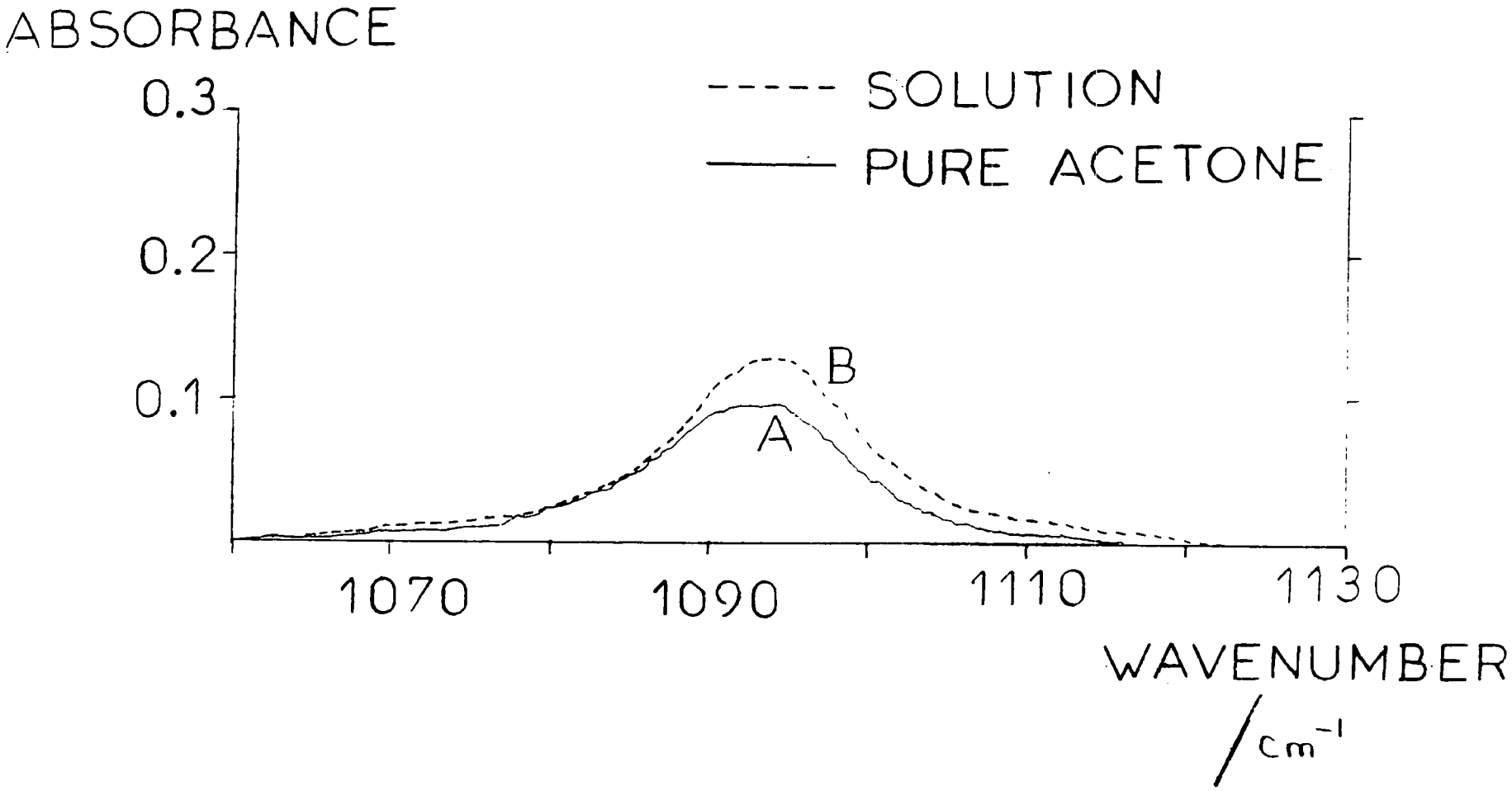

FIG. 6.15 1095 cm^{-1}, CH_3-ROCKING FOR ACETONE

Na^+I^- in acetone, represented by the dotted line. The spectra were recorded using a 0.0025 cm pathlength cell with sodium chloride windows. Table 6.11 shows theband parameters obtained for this CH_3-rocking mode (85), and it was seen both from the figure and the table, that there was very little difference in the absorption in this region in the pure solvent or in the solution. The autocorrelation curves for the two bands shown as fig. 6.16 once again indicated no significant differences between the CH_3-rocking mode in the pure solvent or in solution.

Fig. 6.17 shows the absorption for the 1216 cm^{-1} ν_{17} C-C-C stretching mode obtained for pure acetone, represented by the solid line, and for 0.69 mol dm^{-3} solution of Na^+I^- in acetone. represented by the dotted line. Once again the spectra were recorded using a 0.0025 cm pathlength cell. The manual slits of the spectrometer were set at 33.5 divisions which gave a resolution of about 1 cm^{-1}. Very little change was observable in band centre, intensity or half-band width. It was interesting to note that a high frequency component was observable at 1235 cm^{-1} in the spectrum for the Na^+I^- in acetone solution. The autocorrelation function could not be used for comparison of the 1235 cm^{-1} band in pure acetone, and in the Na^+I^- in acetone solution, since in the latter case the autocorrelation programme AUTO detected the second peak in the overall absorption profile and the programme thus failed. The band fitting routines could not be used to resolve these two components, to enable AUTO to be used on the single components, since the former required the band shape to be fixed. Further studies on the system were abandoned, since no significant changes were being achieved.

6.6 Silver perchlorate in benzene and toluene

Preliminary spectra of silver perchlorate in benzene solution were recorded to determine whether similar absorptions to those occurring in tetra-n-alkylammonium salts in benzene were observed. The silver cation is large, but has no internal vibration modes since only one atom is concerned.

Table 6.11 Band parameters for the 1095 and 1215 cm^{-1} bands for pure acetone and Na^+I^- in acetone solution

	$\bar{\nu}_0$ /cm^{-1}	$\Delta\bar{\nu}_{\frac{1}{2}}$ /cm^{-1}	area /cm^{-1}	
pure acetone	1093	15.0	11.3	11.9
	1094	14.0	12.4	
0.69 mol dm^{-3}	1093	14.0	12.0	12.3
Na^+I^- in acetone	1094	14.0	12.6	
pure acetone	1223	12.5	104.6	105.3
	1224	12.5	106.0	
0.69 mol dm^{-3}	1224	14.5	106.5	105.3
Na^+I^- in acetone	1224	14.0	104.0	

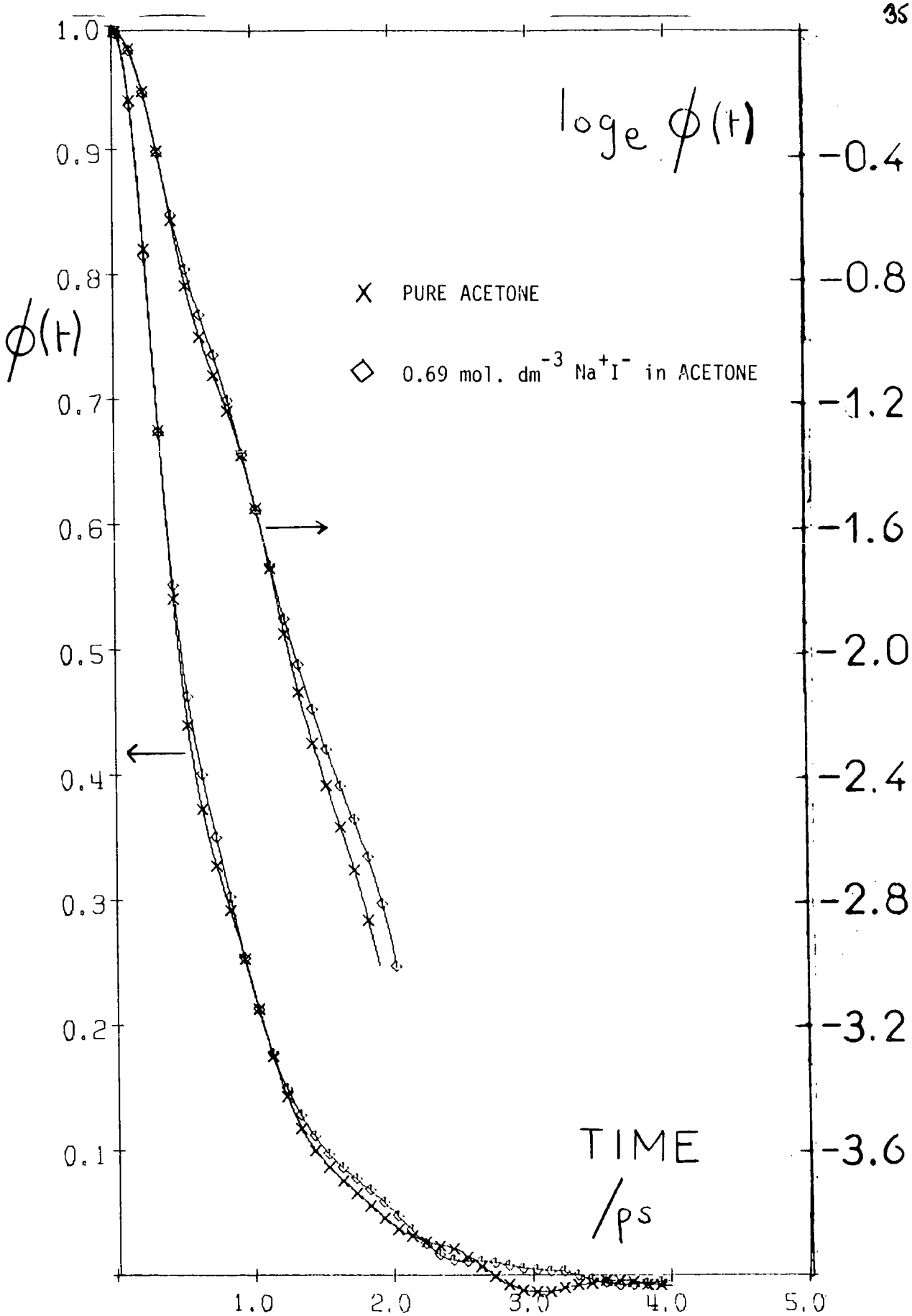

FIG. 6.16 AUTOCORRELATION FUNCTIONS

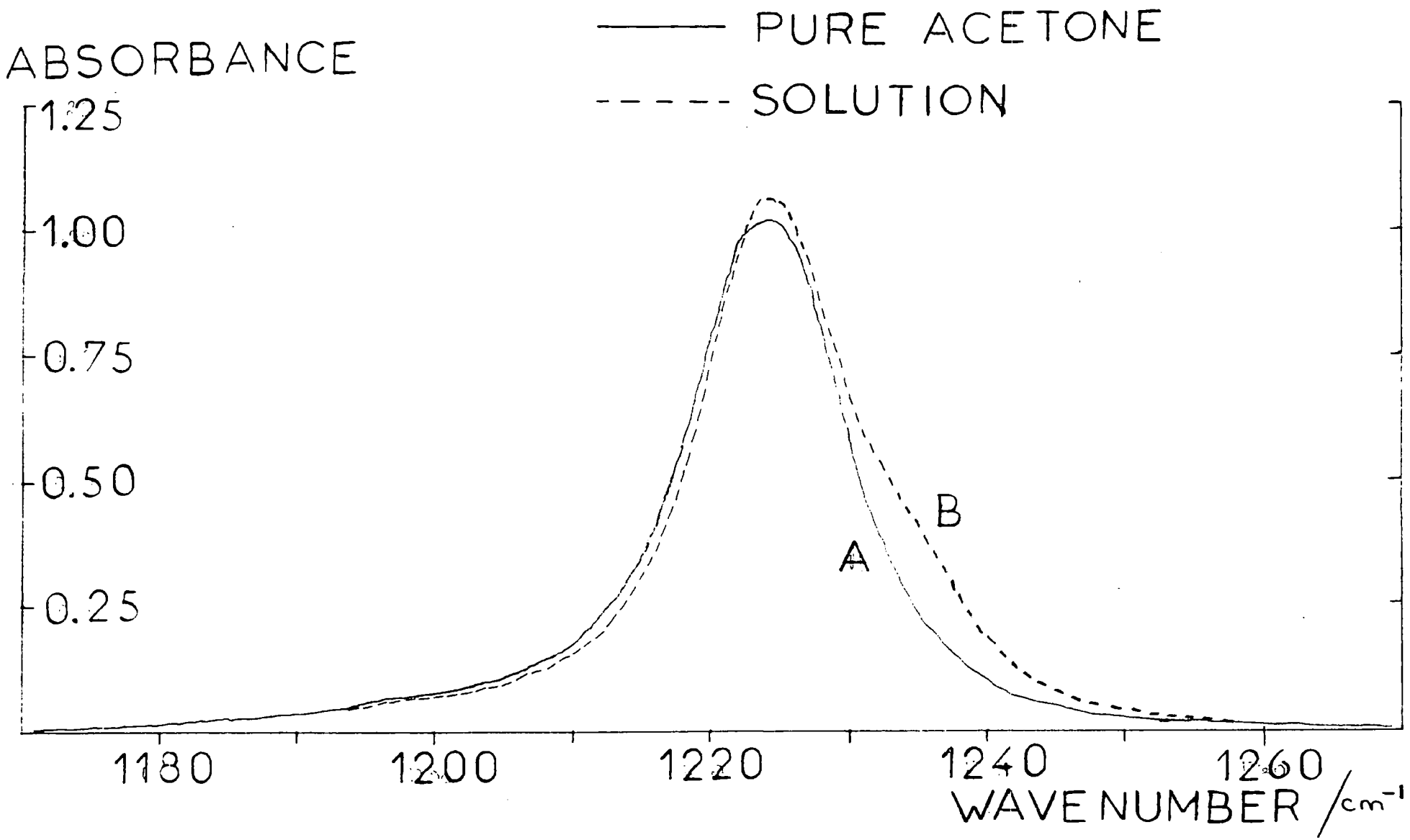

FIG. 6.17 1217 cm^{-1}, C-C-C STRETCHING FOR ACETONE

The silver cation was known to have a strong interaction with the benzene solvent (86-88), and we wondered what effects this might have on the far-infrared spectra of these systems.

Fig. 6.18 shows the spectrum obtained for a 0.1023 cm pathlength of 0.116 mol dm^{-3} $Ag^+ClO_4^-$ in benzene, ratioed against the same pathlength of pure benzene solvent. The resolution in this spectrum was about 3 cm^{-1}, obtained by recording 1024 point interferograms. The 50 gauge beam-splitter was used to obtain these spectra. Two band centres were clearly observable, although the bands overlapped considerably. The band centres were measured as 70±5 cm^{-1} and 140±5 cm^{-1}. The area underneath the total absorption profile was measured by planimeter for 2 spectra of the 0.116 mol dm^{-3} $Ag^+ClO_4^-$ in benzene recorded at 0.1023 and 0.0517 cm pathlengths. These areas were found to be 80 and 39 cm^{-1} respectively, and gave total band intensities of 6 700 and 6 600 dm^3 mol^{-1} cm^{-2}. The dead space below the baseline was calculated as ±20 cm^{-1}, which gave an uncertainty of 1 500 dm^3 mol^{-1} cm^{-2} on the intensity. The total band intensity was thus calculated as 6±650 1 500 dm^3 mol^{-1} cm^{-2} for the $Ag^+ClO_4^-$ in benzene system. This intensity was seen to be of the same order of magnitude as that obtained for the total absorption band for the tetra-n-alkylammonium salts in benzene. The intensity for the latter systems was 6 000 to 15 000 dm^3 mol^{-1} cm^{-2} (see section 4.2)

A spectrum of 0.78 mol dm^{-3} $Ag^+ClO_4^-$ in toluene was also recorded, and is shown as fig. 6.19. The spectrum was ratioed against pure toluene. A 50 gauge beam-splitter was used, and the resolution was about 3 cm^{-1}. Two bands were clearly observable, and the band centres were measured as 70±5 cm^{-1} and 135±5 cm^{-1}. The area underneath the total absorption profile was measured as 150 cm^{-1}, which gave an intensity B_i of 9 158±3 000 dm^3 mol^{-1} cm^{-2}. The uncertainty was calculated assuming an uncertainty in area of ±50 cm^{-1}, due to baseline fitting. No attempts were made to fit components to the overall profile for the single spectrum obtained for this system.

Using only the measured band centres for the component bands it

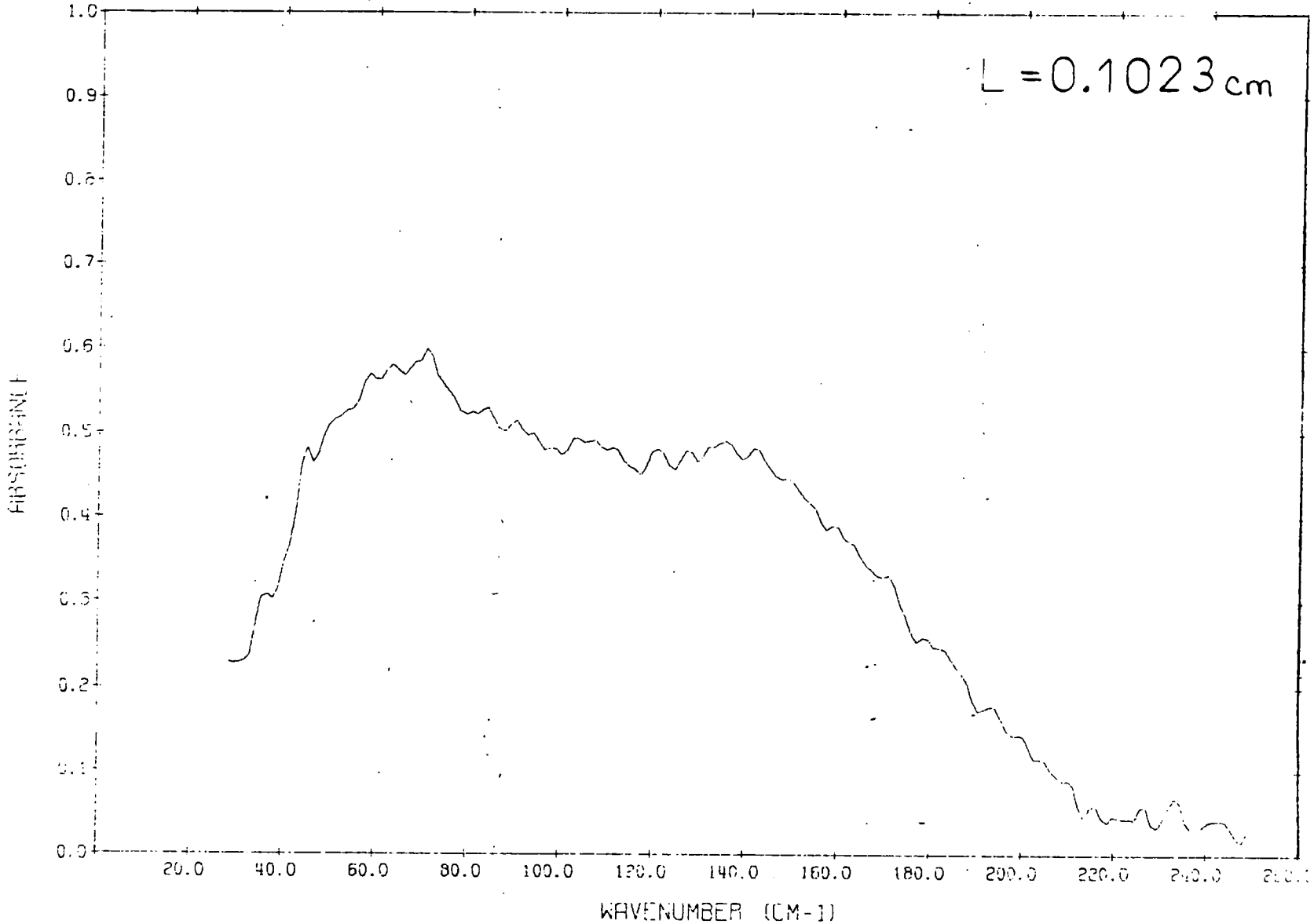

FIG. 6.18 0.116 mol. dm^{-3} $Ag^{+}ClO_4^{-}$ IN BENZENE

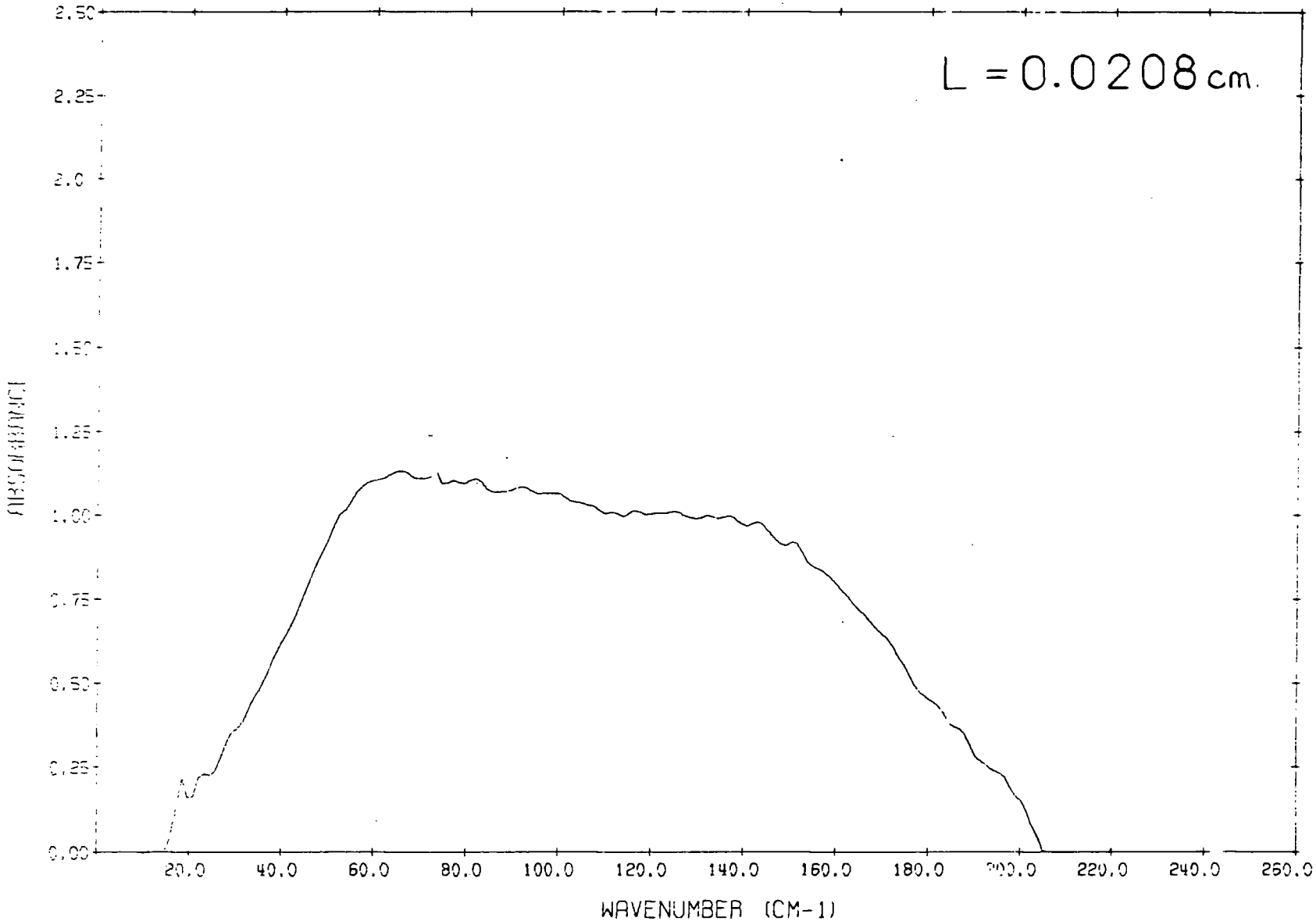

FIG. 6.19 0.78 mol. dm^{-3} $Ag^{+}ClO_4^{-}$ IN TOLUENE

was seen that the data for $Ag^+ClO_4^-$ in both benzene and toluene was consistent with the view that the overall absorption profile contained at least 2 components. The low frequency component once again seemed to be a perturbed benzene and toluene solvent collisional band. The band centres in benzene were 75±5 and 140±5 cm^{-1}, whilst that of pure benzene was 75±1 cm^{-1}. In toluene the band centres were 70±5 and 135±5 cm^{-1}, whilst that of pure toluene was 73±3 cm^{-1}. These frequencies further suggested that the 'ion aggregate' absorption of the $Ag^+ClO_4^-$ was occurring at 138±5 cm^{-1}. This preliminary study has shown that the $Ag^+ClO_4^-$ in benzene and toluene forms systems comparable with those of the tetra-n-alkylammonium salts in benzene.

6.7 Summary.

The work described in this chapter has shown that the far-infrared absorptions for electrolytes dissolved in various solvents of varying relative permittivities and polarisabilities were in fact very similar. The band parameters showed surprisingly good agreement for solutions in both polar and non-polar media. This must cast some doubt upon the widely differing mechanisms which have been proposed to account for absorption in these systems. It is possible that some of the absorptions studied here arise from non-predominant species in the solutions, and since most solutions will contain a spectrum of environments, then the spectra may well be expected to be very similar in this case.

The possibility of a high frequency wing to some of these absorptions in more polar solvents, notably for the Na^+I^- in acetone and $Li^+ClO_4^-$ in THF systems, suggested that similar environments exist in these solutions as do for $Bu_4N^+Cl^-$ in benzene system.

Much more work is necessary on these systems before any concrete conclusions can be made, but it has been shown that the work so far was consistent with one component to the overall absorption being due to a perturbed solvent collisional mode. (See discussion in chapter 7).

CHAPTER 7

DISCUSSION OF THE IONIC SOLVATION STUDIES

7.1 Historical introduction to the theory of solvation

A dictionary definition (89) for solvation is 'the association or combination of molecules of solvent with solute ions or molecules'. A solute dissolves in a given solvent because interactions occur between the solvent and the solute. Statements such as 'Nitrates of highly polarising cations dissolve in carbon tetrachloride without interaction with the solvent' (90) would appear to be incorrect, because the solute would presumably be insoluble if there were no interaction. It would have been more correct, in this case, to have said that the infrared spectrum of the nitrates was not changed upon dissolution in carbon terachloride. Many such instances occur in the literature, and these may well be due to a general lack of understanding of the solvation process.

In the dissolution of a salt the crystal lattice is broken down into smaller units, so that microscopic solvation by the solvent molecules can occur. Ion pairs and single ions will be the basic units into which the salt lattice will be broken down, and it is these entities that interact with solvent molecules, and make the solute soluble. The energy released when a solute particle interacts with solvent molecules, to form a semi-stable entity, is known as the solvation energy of the solute particle. It is this energy gain that overcomes the solute crystal lattice energy, and enables the lattice to be broken down. Thus a salt will dissolve if the ion pair solvation (or the total of anion solvation, cation solvation and the 'ionising power' of the solvent) exceeds the crystal lattice energy of the salt. The 'dissociating or ionising power' of the solvent is the ability of the solvent to support ionisation, and is usually reflected by the relative permittivity.

Ionic salts are usually found to be soluble in dipolar aprotic solvents. The salts are dissociated in solution, even for poorly solvating media such as acetonitrile, where there is apparently little solvation of either anion or cations (91). Anions were also shown to be poorly solvated in dipolar aprotic solvents (92). Anions were seen to be less solvated than

cations in such solvents (93-95), which contrasted with the studies in aqueous solution, where anions had much greater solvation energies than cations of comparable size. (96).

Solvation ranges from one extreme, in which donor and acceptor properties result in definite stable compounds, through intermediate aggregates and unstable coordination compounds, to very weak van der Waals interactions. The more definite interactions were the first to be studied. Specific donor-acceptor interactions were observed for solutions of silver salts in acetonitrile (97). The silver salt was seen to be more soluble in acetone than in water. Such specific interactions were used to explain why copper(II) iodide was more soluble in acetonitrile than in water (97,98). We have attempted to study solvation in less-solvating solvents such as benzene, carbon tetrachloride, chloroform and acetone. Chloroform is a weak protic solvent (proton donor), which presumably solvates by a weak hydrogen-bonding interaction. Acetone is a dipolar aprotic solvent (relative permittivity greater than 15, and hydrogen atoms present not able to form hydrogen bonds), for which anions are thought to be solvated by ion-dipole interactions. The solvation is further enhanced by interaction due to the mutual polarisability of the anion and the solvent molecule. The latter process becoming increasingly important as the size of the anion increases.

Benzene and carbon tetrachloride are non-polar solvents (relative permittivity less than 15). In such solvents there is usually extensive ion aggregation (99). This was thought to be due to the high forces occurring between the ions. These forces are much higher than the ion-ion forces occurring in polar solvents, where the major interaction has been seen to be between solvent and solute. Geddes and Kraus (100) showed that, in non-polar solvents such as benzene, electrolytes exist as ionic dipoles only at concentrations below about 10^{-5} mol dm^{-3}. The presence of multipoles at higher concentrations was deduced from the non-linearity of plots of relative permittivity increase, and dielectric polarisation decrease, against concentration

(101). The authors found that multipole formation was minimised for ions with high electrical asymmetry. Electrolytes having large symmetrical ions, such as Bu_4N^+, showed a very marked tendency to build up highly complex neutral structures or aggregates. The association of ion dipoles was also governed by the dipole moment of the ion pair (102). Freezing point depression work (103) indicated that for 0.01 mol dm^{-3} solutions of tetraisoamylammonium nitrate in dioxane the apparent molecular weight was 4-times the formula weight. This indicated that there was association of 4 ion pairs, even at this relatively low concentration. Only at a concentration of about $2x10^{-4}$ mol dm^{-3} was the apparent molecular weight close to the formula weight. For the silver perchlorate in benzene system apparent molecular weight determinations (104) have shown that 2 ion pairs predominate at $2x10^{-4}$ mol dm^{-3}. For tetra-n-butylammonium thiocyanate in benzene (102) freezing point depression has shown that for 0.1 mol dm^{-3} solution the association number (the ratio of apparent molecular weight to the formula weight) was about 20. The association number was 30 for 0.2 mol dm^{-3}, with a maximum of 32 for 0.3 mol dm^{-3}, decreasing to about 20 for 0.8 mol dm^{-3} salt. Conductivity measurements also indicated that considerable increase in the number of ions present was occurring with increasing concentration. The conductivity passed through a minimum with increasing concentration. No attempt was made in any of these studies to discuss the nature of the ions produced by such concentration changes. Strong and Kraus (73) suggested that concentrated benzene solutions should be considered as solutions of benzene in the fused salt. For solvents of low relative permittivity, the dissociation constant was found to increase with temperature (105). This indicated that the association decreased with increasing temperature.

Szwarc, in his extensive study of ionic solvation (106), suggested that ion pairs could exist in two distinct forms as loose and tight ion pairs. He reasoned that an ion surrounded by a tight solvation shell could approach a counterion without hindrance until its solvation shell contacted the

partner. Thereafter, the associate either maintained the structure of a solvent separated, loose ion pair, or the solvent molecules separating the partners were squeezed out and a tight contact ion pair formed. For solutions of tetra-n-alkylammonium salts in low relative permittivity solvents, the permittivity was seen to have very little effect on the calculated dipole moment of the ion pair (107). Szwarc (106) used this to establish that the cation and anion in the ion pair polarised each other at intimate contact, as envisaged by the model of the contact ion pair. Molecular models for the tetra-n-alkylammonium ions have been constructed in this laboratory. They were seen to have an open structure, consisting of a central core and four alkyl limbs projecting at tetrahedral directions into the solvent. The ion pair is thought to have the anion sitting on the threefold axis (i.e. in the cavity formed by the three alkyl limbs), so that the centres of charge were at the distance of closest approach.

Thus the data obtained from conductivity studies and colligative properties suggested that a complete spectrum of environments exist in solution. These range from the completely separate solvent surrounded ions in polar systems, through systems where the counterion enters the solvation shell of the first ion, to ion pairs and higher aggregates where the solvent molecule has been expelled from the close proximity of the ions. This leads to difficulties in understanding the role of the solvent in these systems. A vast literature of electrochemical studies of ionic solvation has been built up, both for polar and non-polar solvents (73,100-104,108-133), and the ideas concerning solvation in very dilute solution are fairly well understood.

7.2 Previous infrared studies and interpretations

The early work using infrared spectroscopy did not easily lead to such simple conclusions as the electrochemical studies. In fact much confusion was generated by the early spectroscopic studies. There was a general lack of convincing nature of interpretation. The following summary

abstracts the work which produced conclusions in accord with the bulk of the infrared work. Many contributions have not been considered. Edgell (106) summarised the spectroscopic work admirably. The low wavenumber spectra of alkali metal salts in polar solvents, such as acetone (44) and dialkylsulphates (45,82,134,135) were seen to be anion independent, and were explained by assuming that the alkali ion vibrated in solution relative to its cage of neighbouring molecules. This vibration affected the vibrations and hence the absorptions of surrounding solvent molecules. In less polar solvents (e.g. THF (43,136)) the low wavenumber infrared absorptions were found to be anion dependent, and this was explained by assuming that the near-neighbour solution species (either solvent molecules or anions) may have small displacements in the vibration, in addition to the displacement of the alkali ion. Thus in THF solutions the anion was placed in the near-neighbour environment of the cation. Solvent molecules must also be near neighbours of the alkali ion on physical grounds, and must make a significant contribution to the force causing the alkali ion vibration in THF solutions. This suggested a model for this vibration in THF, in which the alkali ion vibrated in a cage formed by solvent molecules and anions. The cage elements, as well as the alkali ion, move in the vibration as was suggested by the frequency variation with both cation change and cation isotope substitution. For solutions in D.M.S.O. for instance, which showed no such anion dependence, it appeared that all cation near neighbours were solvent molecules. Two types of solvent structure were seen to be capable of giving rise to such a cage. (i) The cation and anion together with solvent molecules were coupled in a single structural unit of some stability, with one or more molecules between the two ions. This was known as a solvent-separated ion pair. (ii) The anion occupied a less stable structural position in the solvent, which would be at relatively larger distances from the cation and its solvent near neighbours. The ions were then free ions. Another type of solution entity predominating in low relative permittivity solvents were cluster ions as already discussed.

Popov, by vapour phase osometric measurements (137), showed that for lithium chloride solutions in acetone it was reasonable to assume that in addition to contact ion pairs, there existed in solution higher ionic or molecular aggregates. This result agreed with spectroscopic (44), conductivity (138) and kinetic isotope exchange measurements (139) on the bromide and chloride salts.

^{23}Na and ^{7}Li N.M.R. measurements have been used for elucidation of immediate chemical environment of the ions in different solvents (140-152). N.M.R. probes have also been used to determine preferential solvation in mixed solvents (144).

Very low frequency (0.01 to 0.3 cm^{-1}) relative permittivity studies by Lestrade et. al. and others (49-52,153-160) have been used to study the relatively long time behaviour of dissolved electrolyte solutions. The complex permittivity studies showed the behaviour of systems in the time scale 3 000 to 100 ps, whereas the far-infrared region shows the behaviour in the time scale 3 to 0.1 ps. A large variety of salts, over wide concentration ranges, have been studied in both polar and non-polar solvents. Studies include $Li^+ ClO_4^-$, $Mg^{2+}(ClO_4^-)_2$, Li^+Cl^-, Li^+I^- and $Bu_4N^+I^-$ in ethanol (153), and $Li^+ClO_4^-$ in ethyl acetate (155) and in tetrahydrofuran and benzene mixtures (49). In the latter study a model was proposed, which involved the Brownian linear motion of the ions between collisions. Tri-butylammonium picrate in benzene (156), and tetra-n-butylammonium bromide and thiocyanate in benzene (154) have also been studied, and it was shown that the observed relaxation processes were more complex in this non-polar solvent, than in more polar solvents. Lithium chloride has also been studied in ethyl acetate and tetrahydrofuran (52). These studies showed that the complex permittivity functions for electrolyte systems were seen to be very similar in both polar and non-polar solvents.

Many different techniques have been employed in the presentation of far-infrared spectroscopic data. We have used a transmittance/linear

wavenumber plot in all our experimental work. We thus decided to study the applicability of linear wavenumber plots and intensity calculations for very low frequency bands.

Infrared spectra have conventionally been represented by plotting transmittance or absorbance as a linear function of wavenumber. The linear wavenumber function was applicable in the normal infrared region, where the absorptions were due to the vibrations of molecules, since the absorption energy was equal to the band vibration energy, which approximated to that of an harmonic oscillator (161). Thus the spectrum is a function of absorption against energy, which has been conventionally represented on a wavenumber scale. The absorption bands in the infrared were often seen to be symmetrical when represented as a linear function of wavenumber, and hence the spectra were represented thus. The bands were symmetrical since the harmonic vibration potential wells were symmetrical as a function of internuclear distance, the variation of this causing the dipole moment changes which give rise to the absorption.

The low frequency bands that we have observed were often far from symmetrical. Indeed for bands occurring at a frequency of about 30 cm^{-1}, with a half-band width measured as 80 cm^{-1} it is impossible for the bands to be symmetrical on a linear wavenumber scale. (since negative frequencies are impossible) The study of the theory of lineshapes of absorption bands is still very much in its infancy, even for simple systems, and little work has been accomplished for the condensed phase. The broad absorptions of compressed carbon dioxide gas in the far-infrared have led to a theory of lineshape for the collisional process (162,163), which led the infrared spectroscopists to plot absorption bands as linear wavenumber functions. However similar studies have also produced results represented as a logarithmn wavenumber plot (164), and so studies of lineshape have not really assisted in the problems of representation of spectra.

To determine the effects of different plotting procedures on our

observed spectra, and indeed to determine if there was any noticeable effect on the presence of the three proposed components to the overall profile, one of the recorded spectra has been plotted under the various functions possible. Table 7.1 shows the absorbance data as a function of wavenumber for a spectrum obtained for a 0.70 mol dm^{-3} solution of $Bu_4N^+Cl^-$ in benzene, which was considered typical for the systems in this work. Logarithmn wavenumber, the wavenumberxabsorbance product, absorbance/wavenumber and logarithmn absorbance are also tabulated. Figs. 7.1 to 7.6 show the various 'spectra' obtained by different plotting of this data. Fig. 7.1 shows the absorbance/wavenumber plot as used for representation of spectra in this work. The component band centres appeared at 68, 108 and 190 cm^{-1} as indicated by the arrows. The low frequency wing of these low frequency absorptions can be minimised by plotting the spectrum as the product wavenumber x absorbance as a function of wavenumber. The spectrum was plotted in this manner in fig. 7.2, which now clearly showed the presence of the high frequency component. The component centres were seen to be at 68, 116 and 200 cm^{-1}, the lowest frequency component being only detectable as a small shoulder. The slight shift to higher frequency for the components in this representation was due to the multiplication by wavenumber, which emphasised any band towards high frequency. The low frequency wing of the band was emphasised by plotting absorbance/wavenumber as a function of wavenumber as shown in fig. 7.3. As was expected the high frequency component was only visible at 190 cm^{-1} as a shoulder, and the two other components were shifted to lower frequency than that seen in the normal absorbance plot. The lower frequency components were measured as having band centres at 49 and 88 cm^{-1}. Amplifying the low frequency wing was seen to emphasise the poor signal-to-noise ratio at low frequency. The common logarithmn absorbance as a function of wavenumber plot of fig. 7.4 was seen to compress the high frequency absorbance values, and thus would be beneficial for strongly absorbing systems. This plot showed no benefit for our systems, but did confirm component bands at 68, 108 and 190

Table 7.1 Absorbance/Wavenumber data for figs. 7.1 to 7.6

$\bar{\nu}$ /cm^{-1}	log $\bar{\nu}$ /cm^{-1}	α /neper	$\alpha\bar{\nu}$ /neper cm^{-1}	$\alpha/\bar{\nu}$ /neper cm	log α /neper
9.8	0.990	0.000	0.00	0.0000	$-\infty$
14.7	1.166	0.110	1.61	0.0075	-0.959
19.5	1.291	0.103	2.01	0.0053	-1.000
24.4	1.388	0.505	12.33	0.0207	-0.692
29.3	1.467	0.624	18.29	0.0213	-0.205
34.2	1.534	0.805	27.50	0.0235	-0.094
39.1	1.592	0.874	34.15	0.0224	-0.059
44.0	1.643	0.968	42.56	0.0220	-0.014
48.9	1.689	1.117	54.52	0.0229	0.048
53.7	1.730	1.206	64.76	0.0225	0.081
58.6	1.768	1.312	76.89	0.0224	0.118
63.5	1.803	1.378	87.50	0.0217	0.139
68.4	1.835	1.487	101.67	0.0218	0.172
73.2	1.865	1.501	109.90	0.0205	0.176
78.1	1.893	1.678	131.12	0.0215	0.225
83.0	1.919	1.780	147.73	0.0214	0.250
87.9	1.944	1.929	169.53	0.0220	0.285
92.8	1.967	2.029	188.21	0.0219	0.307
97.7	1.990	2.106	205.69	0.0216	0.323
102.5	2.011	2.146	220.01	0.0209	0.332
107.4	2.031	2.119	227.58	0.0197	0.326
112.3	2.050	2.157	242.21	0.0192	0.334
117.2	2.069	2.130	249.65	0.0182	0.328
122.1	2.087	2.013	245.71	0.0165	0.304
127.0	2.120	1.730	228.07	0.0131	0.238

Table 7.1 (continued)

$\bar{\nu}$ /cm^{-1}	log $\bar{\nu}$ /cm^{-1}	α /neper	$\alpha\bar{\nu}$ /neper cm^{-1}	$\alpha/\bar{\nu}$ /neper cm	log α /neper
131.8	2.120	1.730	228.07	0.0131	0.238
136.7	2.136	1.508	206.15	0.0110	0.178
141.6	2.151	1.360	192.60	0.0096	0.134
146.5	2.166	1.170	171.43	0.0080	0.068
151.4	2.180	1.047	158.53	0.0069	0.020
156.3	2.194	0.984	153.73	0.0063	-0.007
161.1	2.207	0.948	152.78	0.0059	-0.023
166.0	2.220	0.920	152.66	0.0055	-0.036
170.9	2.233	0.888	151.74	0.0052	-0.052
175.8	2.245	0.877	154.11	0.0050	-0.057
180.7	2.257	0.858	154.92	0.0047	-0.067
185.6	2.269	0.838	155.51	0.0045	-0.077
190.4	2.280	0.857	163.20	0.0045	-0.067
195.3	2.291	0.832	162.50	0.0043	-0.080
200.2	2.301	0.822	164.46	0.0041	-0.085
205.1	2.312	0.745	152.74	0.0036	-0.128
210.0	2.322	0.709	148.86	0.0034	-0.149
214.8	2.332	0.687	147.51	0.0032	-0.163
219.7	2.342	0.599	131.57	0.0027	-0.223
224.6	2.351	0.573	128.63	0.0026	-0.242
229.5	2.361	0.523	120.00	0.0023	-0.282
234.4	2.370	0.452	105.89	0.0019	-0.345
239.3	2.379	0.492	117.62	0.0021	-0.308
244.1	2.388	0.464	113.21	0.0019	-0.334
249.0	2.396	0.471	117.44	0.0025	-0.327

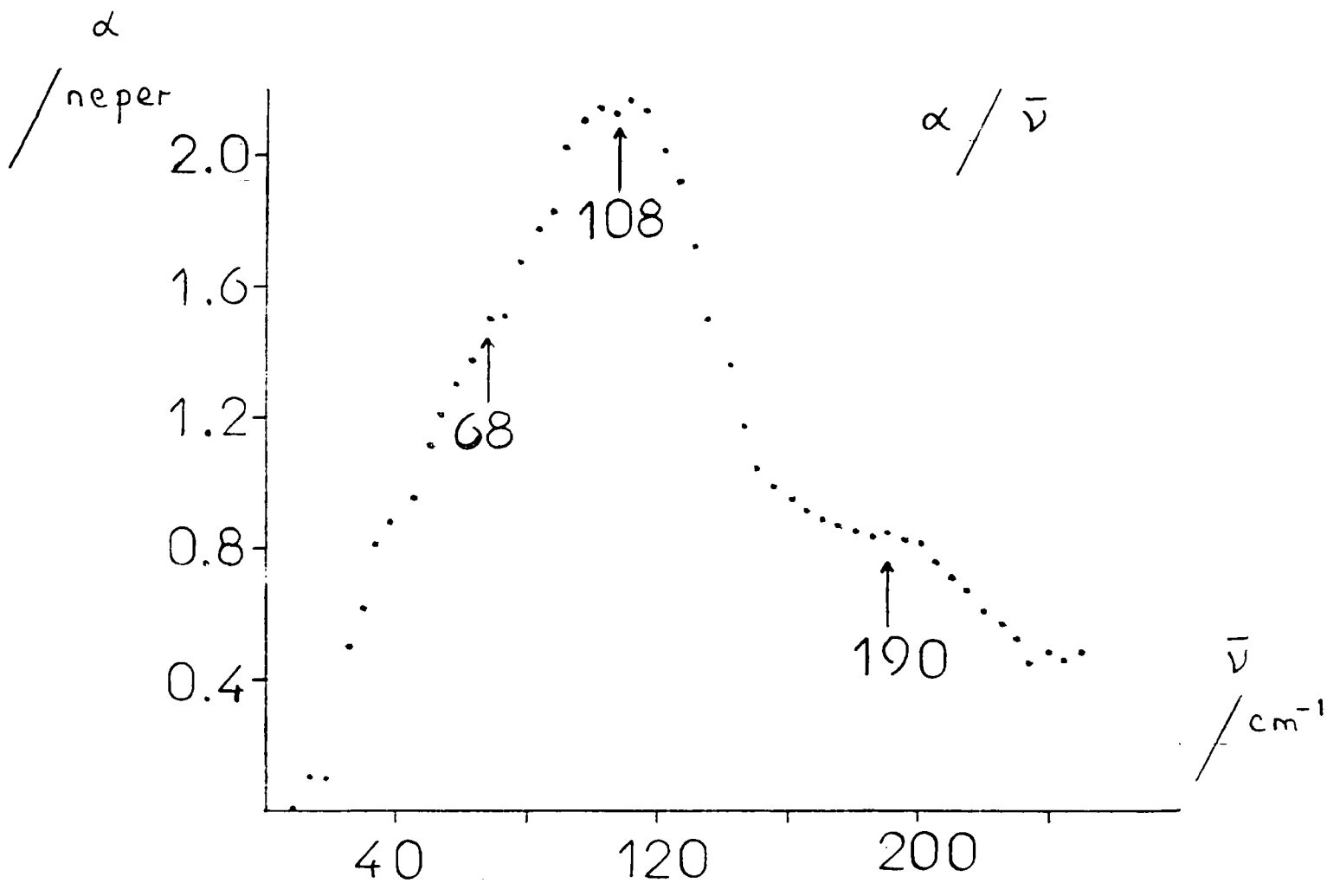

FIG. 7.1 ABSORBANCE / WAVENUMBER

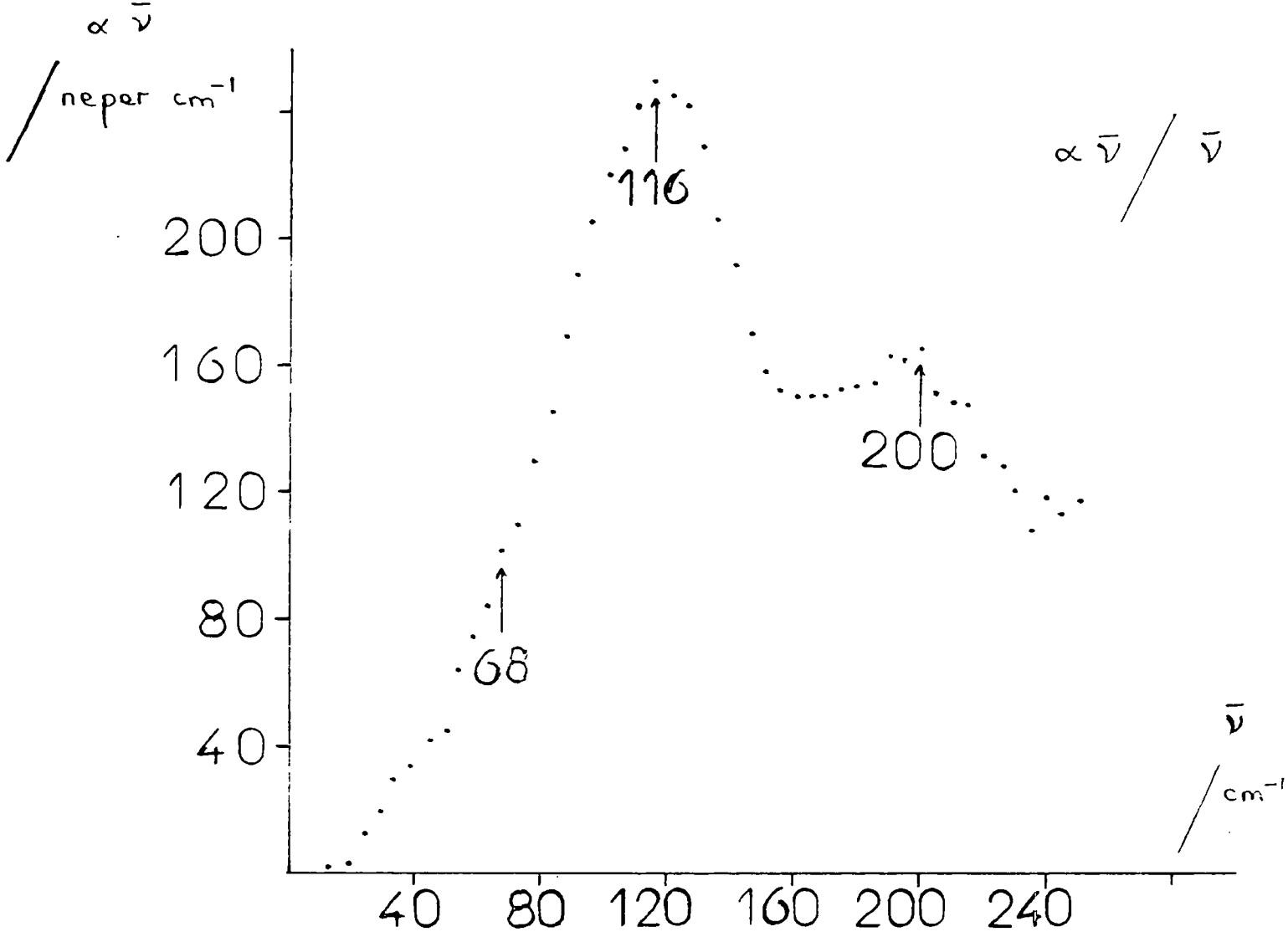

FIG. 7.2 ABSORBANCE X WAVENUMBER / WAVENUMBER

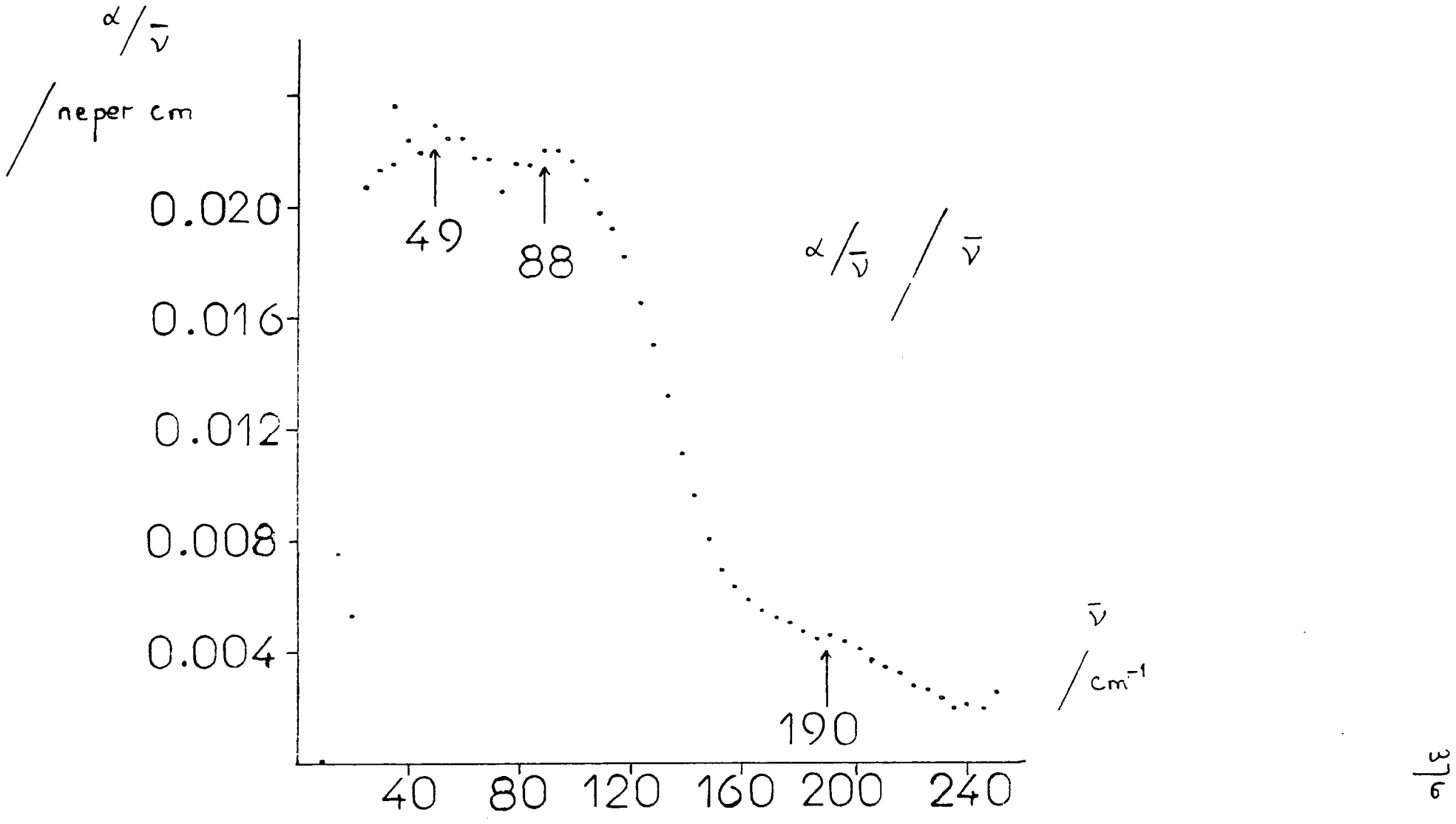

FIG. 7.3 ABSORBANCE ÷ WAVENUMBER / WAVENUMBER

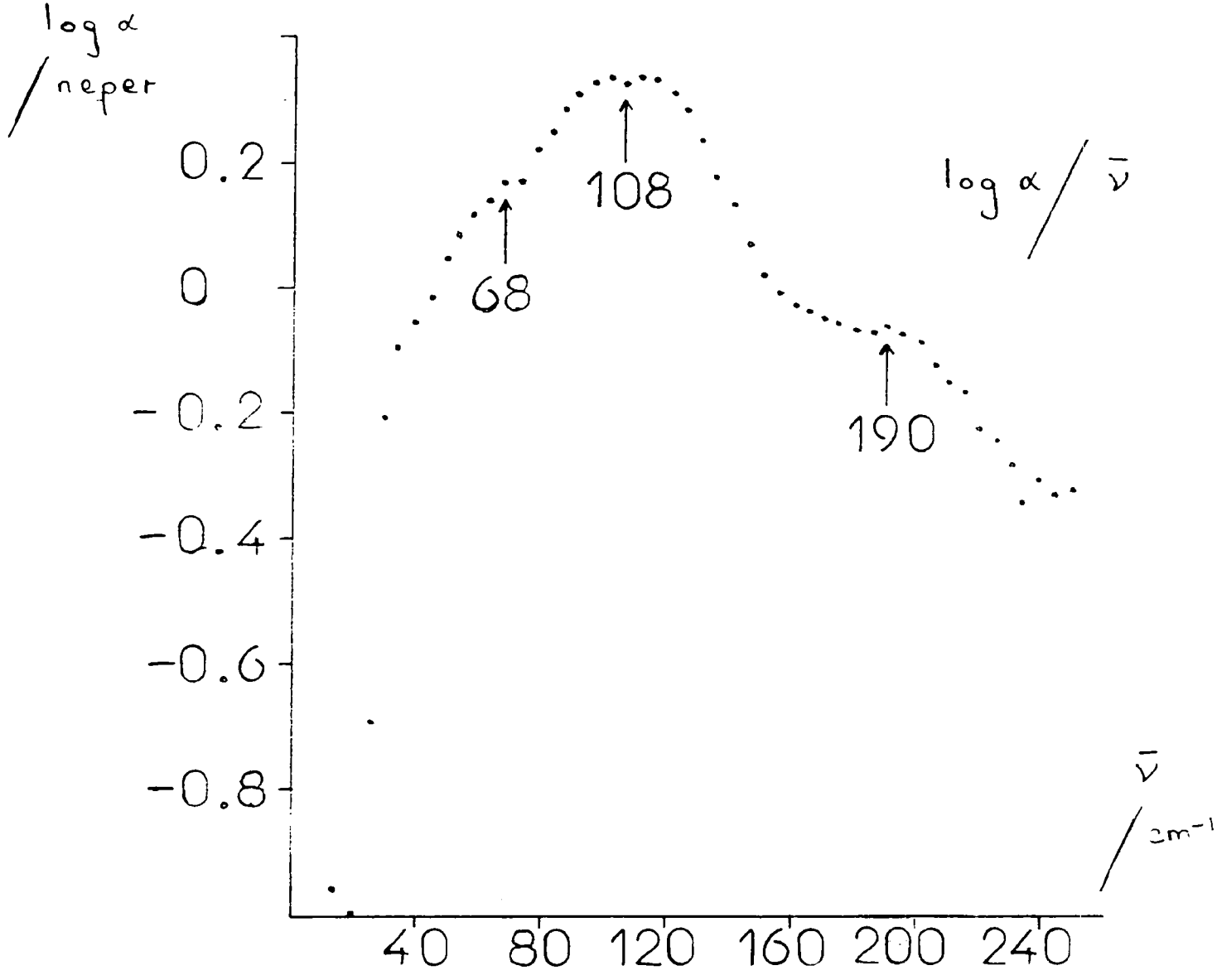

FIG. 7.4 LOG. ABSORBANCE / WAVENUMBER

cm^{-1}. Fig. 7.5 shows the plot obtained when absorbance was taken as a function of logarithmn of wavenumber. The low wavenumber region was expanded and this was seen to be a useful method for far-infrared spectra representation below about 100 cm^{-1}. Components were seen at 69, 110 and 190 cm^{-1}, showing no significant shift from those obtained for the normal absorbance against wavenumber plot. Finally fig. 7.6 shows the spectrum as a logarithmn absorbance against logarithmn wavenumber plot. This plot expanded both the low frequency and low absorbance regions as expected, and once again showed component centres at 69, 110 and 190 cm^{-1}.

It thus appeared that all the spectra were useful in qualification of the suspected presence of component bands to an overall profile, with the possible exceptions of the $\alpha\bar{\nu}$ and $\alpha/\bar{\nu}$ plots, which were seen to distort the spectrum and to increase asymmetry. In this work linear absorbance/linear wavenumber plots have been used throughout for representation of spectra, and the data was thus presented in the form most common in spectroscopy.

We now turn to the more complicated problem of the applicability of intensity calculations from these very broad, very low frequency bands. The intensity has been calculated from eqn. 4.2, which is repeated here for clarity;

$$B = \int_{\text{band}} \varepsilon(\bar{\nu}).d\bar{\nu} \qquad 7.1$$

where $\varepsilon(\bar{\nu})$ is the extinction coefficient calculated as;

$$\varepsilon(\bar{\nu}) = \alpha(\bar{\nu})/c\ell \qquad 7.2$$

Eqn. 7.1 is valid only when the range of integration is minimal with respect to the frequency of maximal absorption. This is seen to be the case for bands in the 3 000 cm^{-1} region with half-band widths of the order of 10 cm^{-1}, where the range of integration is likely to be only 50 cm^{-1}. To discover the reasons behind the limitation of the viability of the intensity calculation via eqn. 7.1 we need to consider the quantum mechanical approach to the theory of radiation absorption.

Einstein developed a theory for absorption of radiation, and

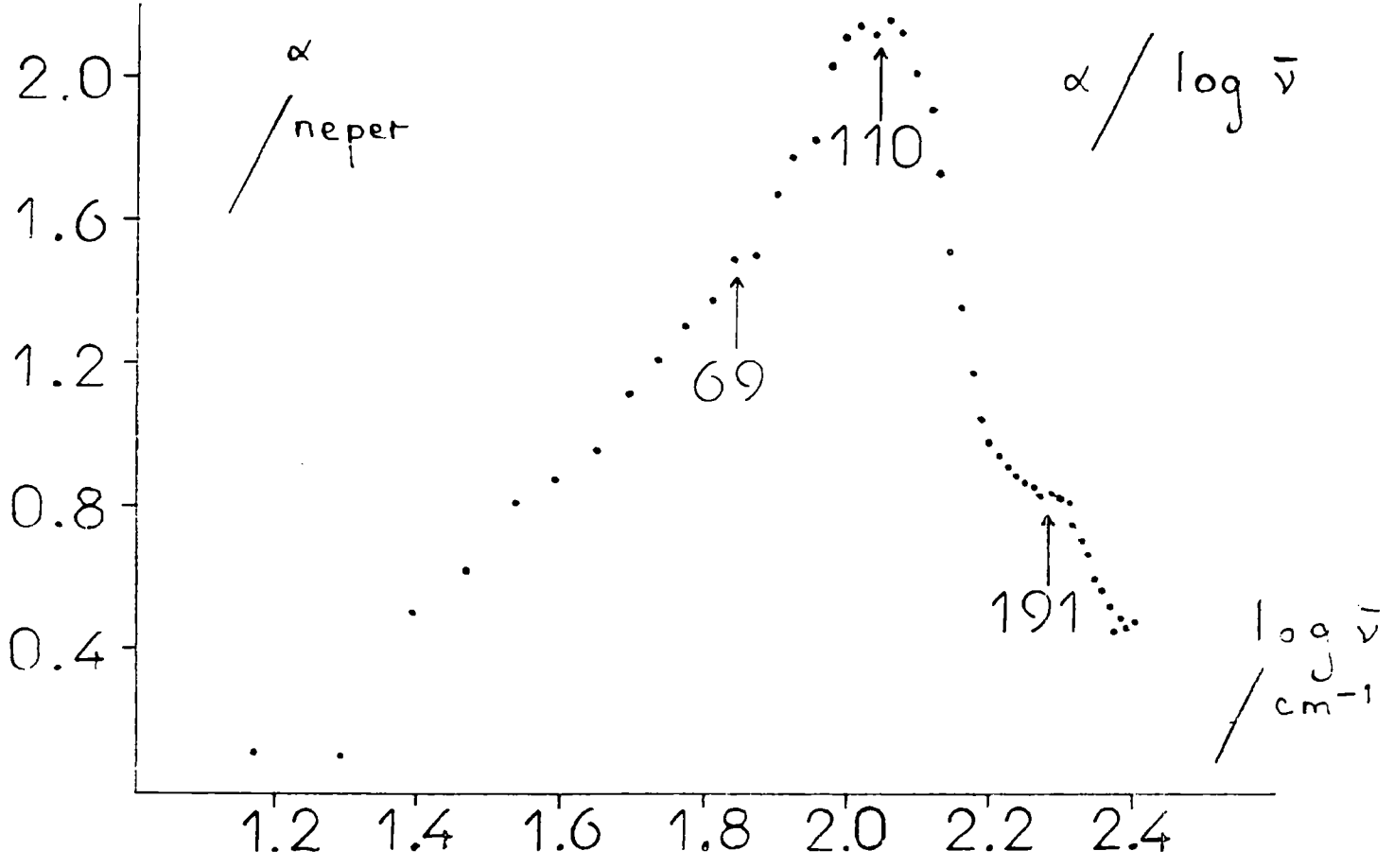

FIG. 7.5 ABSORBANCE / LOG. WAVENUMBER

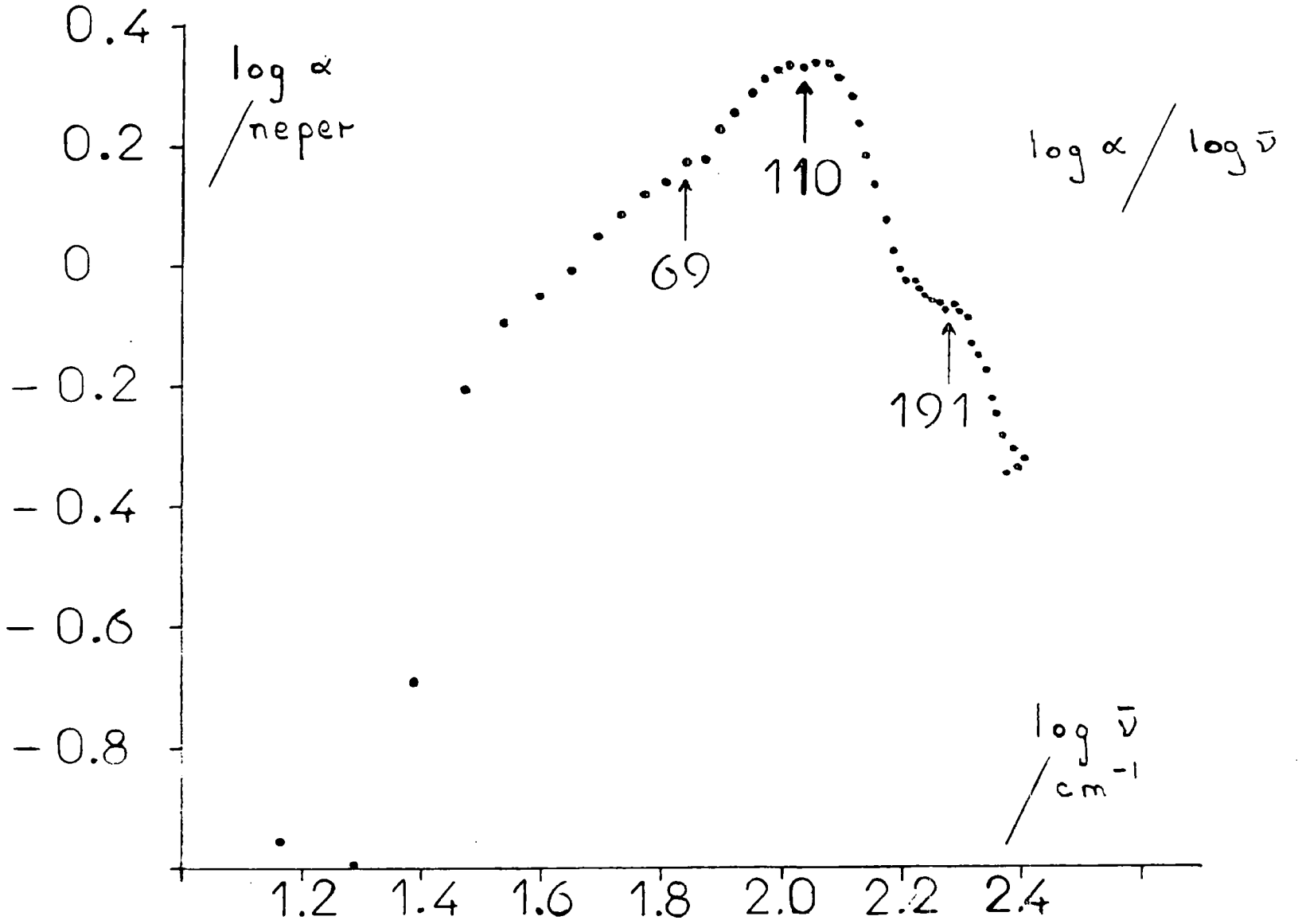

FIG. 7.6 LOG. ABSORBANCE / LOG. WAVENUMBER

introduced a coefficient B_{fi}, known as Einstein's coefficient of stimulated absorption (165). Transitions from the initial to final states were seen to occur with a probability which was proportional to the square of the transition dipole moment between initial and final states (166);

$$B_{fi} \propto |d_{fi}|^2 \qquad 7.3$$

The extinction coefficient obtained by calculation from the transition probability has been related to the extinction coefficient obtained experimentally (166);

$$\varepsilon(\bar{\nu}) = (10^3/\ln 10).Lh\bar{\nu}B_{fi}(\bar{\nu}) \qquad 7.4$$

where L is Avogadro's number

and h is Planck's constant

Thus the integral over the absorption band, as measured experimentally by the area under the absorption profile, is given by;

$$\int_{\text{band}} \varepsilon(\bar{\nu}).d\bar{\nu} = (10^3/\ln 10).Lh\int_{\text{band}} \bar{\nu}B_{fi}(\bar{\nu}).d\bar{\nu} \qquad 7.5$$

The integral of the right hand side of eqn. 7.5 cannot be determined, since Einstein's coefficient is not known as a function of wavenumber. To enable the relationship between microscopic and macroscopic parameters to be developed it has been assumed that both the wavenumber $\bar{\nu}$, and the Einstein coefficient $B_{fi}(\bar{\nu})$ are constant over the region of integration of the band, i.e. over the total band-width. Clearly this approximation will only be valid when the band is very narrow or, more precisely, when the total band width over which the integration takes place is negligible with respect to the wavenumber of maximum absorption. Thus for very narrow bands at high frequency the approximation in eqn. 7.6 is valid;

$$\int_{\text{band}} \varepsilon(\bar{\nu}).d\bar{\nu} \sim (10^3/\ln 10).Lh\bar{\nu}_{fi}B_{fi}(\bar{\nu}_{fi}) \qquad 7.6$$

where $\bar{\nu}_{fi}$ is the wavenumber of maximum absorption, corresponding to the energy difference between initial and final states.

and $B_{fi}(\bar{\nu}_{fi})$ is the Einstein coefficient at the frequency of maximum absorption.

Thus the absorption bands for our systems will give integrated intensities which are unlikely to correspond to intensities calculated from microscopic properties, since the band width was by no means negligible with respect to the frequency of maximum absorption. It is interesting to note with regard to intensity calculations, that satisfaction of eqn. 7.6 relies on the minimum integration range. This is opposite to the usual requirement that integration must be carried out over the whole band. According to theory for Gauss and especially Cauchy profiles this necessitates integration from $+\infty$ to $-\infty$ (167). Clearly the relating of intensity data to microscopic properties is bound to be fraught with difficulty.

Intensity calculations have also been made (164,168) using a natural logarithmn wavenumber energy axis, the intensity then being given by (ref. 169, chap. 10);

$$\Gamma = \int_{\text{band}} \varepsilon(\ln\bar{\nu}).d(\ln\bar{\nu}) \qquad 7.7$$

The relation to the Einstein coefficient now being;

$$\int_{\text{band}} \varepsilon(\ln\bar{\nu}).d(\ln\bar{\nu}) \sim (10^3/\ln 10).Lh\ln(\bar{\nu}_{fi})B_{fi}(\ln\bar{\nu}_{fi}) \qquad 7.8$$

Where the conditions for close approximation are now that the logarithmn of the band width in wavenumbers is negligible with respect to the logarithmn of the wavenumber of the band centre. This condition is more easily satisfied for low frequency bands, due to the logarithmic scale and the compression of the higher wavenumber data where the absorption will occur (see fig. 7.5). This method was not chosen because of the expansion of the low frequency data, which was of relatively low quality, due to our experimental arrangement (see chapter 3).

7.3 The aims of this work in terms of interpretation

Three questions arise during the interpretation of the far-infrared spectra for the solutions of salts in relatively non-polar media. The first aim of this work was the assignment of the bands in the observed spectra. This involved the assignment of these bands to the various dynamic phenomena which can occur in this region of the spectrum. This assignment was then tested

by the study of spectral variations with parameters such as concentration and temperature. The solvent and ion dependence of the spectra were also studied to assist in the verification of the assignments.

Secondly various models were to be used for the description of the interactive and dynamical processes contributing to the far-infrared spectra. Simple electrostatic (anion-cation vibration) and polarisation (induced dipole-ion interactions) models have been considered, and are discussed later in this chapter. A more complicated orientation/translation model, based on the stochastically modulated oscillator theory of Kubo has also been considered. This latter model considers the vibrational mode to be a solvent surrounded ion pair (which is unrealistic for anything but a very dilute solution, but which may be applicable since the spectra vary little with concentration). The ion pairs are then considered to be in pseudo-isolation and are treated as though they are quasi-stationary. This is possible since the far-infrared studies between 33 cm^{-1} and 330 cm^{-1} correspond to relaxation times of 1.0 and 0.1 psec. respectively, whereas Lestrade has shown, by dipolar relaxation measurements, that the elapsed time between collisions for such systems is of the order 100 to 300 psec. (49-51,157). The model thus considered involves a stable vibrating ion pair, in which the lifetime is long compared with the vibrational period, whose solvation shell of surrounding solvent molecules is considerably perturbed by interactions with the charged species. This model will be considered elsewhere (170).

The third aim was to correlate the spectral properties with other data. Electrochemical data such as conductivity measurements, and colligative properties such as freezing point depressions and osmotic pressure measurements were considered to be especially important.

7.4 Assignment of bands

7.4.1 Introduction

It is appropriate here to consider the nature of the possible

processes leading to absorption in the far-infrared for the systems under consideration. These are as follows;

1. Low frequency internal modes or difference bands. In the case of the tetra-n-butylammonium salts these may arise in either the cation, or in the case of the perchlorate salt in the anion as well, since the latter is a polyatomic species.

2. Low frequency stretching modes of ion pairs and clusters. There will be a large number of possibilities for such stretching modes as discussed in chapter 4.

3. The high frequency wing or plateau of the Debye relaxational absorption.

4. The Poley-Hill (2,4,79-81) absorption, which is the short time part of the Debye process. This involves the libration (torsional oscillation) of a dipole within a cage of solvent molecules. The surrounding molecules provide a potential well in which the dipole librates. The Debye absorption (171) is due to reorientation of a permanent dipole, particularly by rotational and diffusional processes. Debye absorption is observed principally in the microwave region, but a plateau extends into the far-infrared region up to about 100 cm^{-1} (172,173).

5. Collision induced absorption (174-181). The motion of ions and ion pairs within the solution causes variations in electrical fields. This leads to production of a transient dipole, which causes absorption of radiation. The absorption will have frequencies corresponding to the collision rates in the liquids (i.e. in the 30 to 300 cm^{-1} region.). Such absorptions are known for simple non-polar liquids (182-186). In our system the interactions will be expected to be of the dipole-induced dipole type. There will be many different effects due to the many possible multipoles, and the complexity of the system will be further increased by the possibility of 'self' and 'cross' polarisation terms between the ions and the solvent.

The low frequency internal modes can be dismissed from our spectra since they would involve sharp absorptions. The Debye plateau can be ignored

when the spectra are plotted on an absorbance scale, since the numerical values would be negligible. Thus there are likely to be three contributions to our far-infrared spectra, namely the ion cluster stretching modes, the Poley-Hill absorption and the collision induced absorption.

It has been shown in chapter 5 that the overall profile to the low frequency absorptions for tetra-n-butylammonium salts in relatively non-polar solvents is composed of at least three bands. There could, of course, be more than three bands, but three gives a good fit to the observed spectra, and thus presents the simplest system for interpretation. Table 7.2 shows the fitting parameters for a typical spectrum (0.55 mol dm^{-3} $Bu_4N^+Cl^-$ in benzene). The DIS factor quoted in the table is a measure of the 'goodness' of the fit. It is outputted by the fitting programme, and is calculated by taking the difference in transmission values between the fitted and original curves at each frequency interval. This is known as the transmittance residual. The residuals are then squared and the mean value taken over the frequency range of the inputted data. The DIS parameter is then calculated as the square root of this mean value. It is thus the root mean square of the transmittance residuals. Table 7.2 showed that the best fit was obtained with 3 pure Gauss components. No attempts were made to fit the absorption profile to more than 3 components. For comparison a DIS parameter of 0.0003 was obtained when a pure Cauchy band was fitted. The sum function gave 99% Cauchy with a DIS parameter of 0.0003 for the same band, during tests to optimise the fits to the observed spectra. A better fit was obtained with pure Gauss components than for pure Cauchy, but this should be treated with caution, since the baseline problem (discussed in chapter 6) may well be changing the shape of the absorption profile.

7.4.2 The 120 cm^{-1} band

The central component to the overall profile at 120 cm^{-1} has been shown to be both cation and anion dependent, and hence it has been assumed that the band arises from ion cluster vibrations involving both the

Table 7.2 DIS parameters for various fits

(0.55 mol dm^{-3} $Bu_4N^+Cl^-$ in benzene)

type of fit	DIS[b]
single pure Gauss component	0.174
single pure Cauchy component	0.320
single component with sum function	0.196[a]
two pure Gauss components	0.019
two pure Cauchy components	0.033
three pure Gauss components	0.013
three pure Cauchy components	0.047

[a] 90% Gauss fit produced

[b] DIS = root mean of the sum of the squares of the residuals for fitted and experimental absorbance data

anion and the cation. The vibration of the ion cluster would be expected to be the sum of the ion pair type vibrations.

It has been shown from the extensive fitting data that the band shape is essentially unchanged with changes of temperature. The band centre and half-band width remain constant within the experimental error over a temperature range of 70K. There is very little change in either band centre or half-band width over the concentration range 1.4 to 0.05 mol dm^{-3}. Likewise there is little change in the band parameters when the solvent is changed from benzene to carbon tetrachloride and chloroform. The intensity of the band was seen to be concentration dependent. The intensity reaches a maximum at about 0.5 mol dm^{-3}. This has been accounted for by the building up of the number of ion pairs in the ion clusters as the concentration increases up to 0.5 mol dm^{-3}, and then the slow breaking down of the clusters at even higher concentration. This has been discussed in chapter 4, and is entirely in line with the conclusions previously drawn from permittivity (101), conductivity (102), and freezing point measurements (103,104).

Supporting evidence for the assignment of the 120 cm^{-1} band as an internal mode (or modes) of the ion aggregate is forthcoming through simple force constant calculations. If the assumption is made that the ion pair vibrates along a line joining the ion centres, then the diatomic approximation may be used for this normal mode. This harmonic approximation gives (ref. 187, p. 160);

$$\bar{\nu}_{obs} = 1/2\pi c(K_{obs}/\mu')^{\frac{1}{2}} \qquad 7.9$$

where K_{obs} is the force constant of the ionic bond

and μ' is the reduced mass of the ion pair

For the simple ion pair the reduced mass is given by (ref. 187, p. 37);

$$\mu' = m_A m_C/m_A+m_C \qquad 7.10$$

where m_A and m_C are the masses of anion and cation.

Eqn. 7.9 shows that the observed band centre is proportional to $\mu^{-\frac{1}{2}}$, providing that the force constant is in fact invariant for the systems being

studied. If the restoring force between the ions is purely coulombic, then the force constant will be the same for all the salts studied. Table 7.3 shows the observed band centres for the seven tetra-n-alkylammonium salts studied, together mith the reduced masses for the salts. The solvent change for the iodide, nitrate and perchlorate was unavoidable, since these salts were not sufficiently soluble in benzene to allow observation of the low frequency absorptions. Fig. 7.7 shows that the observed band centre $\bar{\nu}_{obs}$ is indeed proportional to $\mu'^{-\frac{1}{2}}$, within the experimental uncertainty. To obtain some measure of the closeness of the model approximation, the calculated frequencies for the various salts were determined on the assumption that eqn. 7.9 was valid. The force constant used for the calculation was that determined for $Bu_4N^+Cl^-$ in benzene (K_{obs} = 26.7±0.4 Nm^{-1}), which was determined from the observed band centre of 115±3 cm^{-1} by use of eqn. 7.9. The differences between observed and calculated frequencies for the band centre ($\bar{\nu}_{obs}-\bar{\nu}_{calc}$) were seen to be small, especially for the $Bu_4N^+Br^-$, $Pe_4N^+Cl^-$ and $Hp_4N^+Cl^-$. The $Bu_4N^+I^-$, $Bu_4N^+NO_3^-$ and $Bu_4N^+ClO_4^-$ salts had larger differences indicating that the model does not fit so well for these salts. For the $Bu_4N^+I^-$ salt the calculated band centre was seen to be greater than the observed band centre, indicating that the bonding in this salt is stronger than would be expected from the purely electrostatic model. For the $Bu_4N^+NO_3^-$ and $Bu_4N^+ClO_4^-$ salts the calculated band centres were seen to be less than the observed band cenres, indicating that the bonding is weaker for these salts than that expected from the coulombic point charge model. This suggested that the ionic charge may well be delocalised over the polyatomic ion, rather than being restricted to the central atom.

The model is now further tested by comparing the observed force constants with that calculated from the purely electrostatic model. The force between two point charges is given by (ref. 188, p. 10);

$$F = Q_1Q_2/4\pi\varepsilon r^2 \qquad 7.11$$

where Q_1 and Q_2 are the two charges

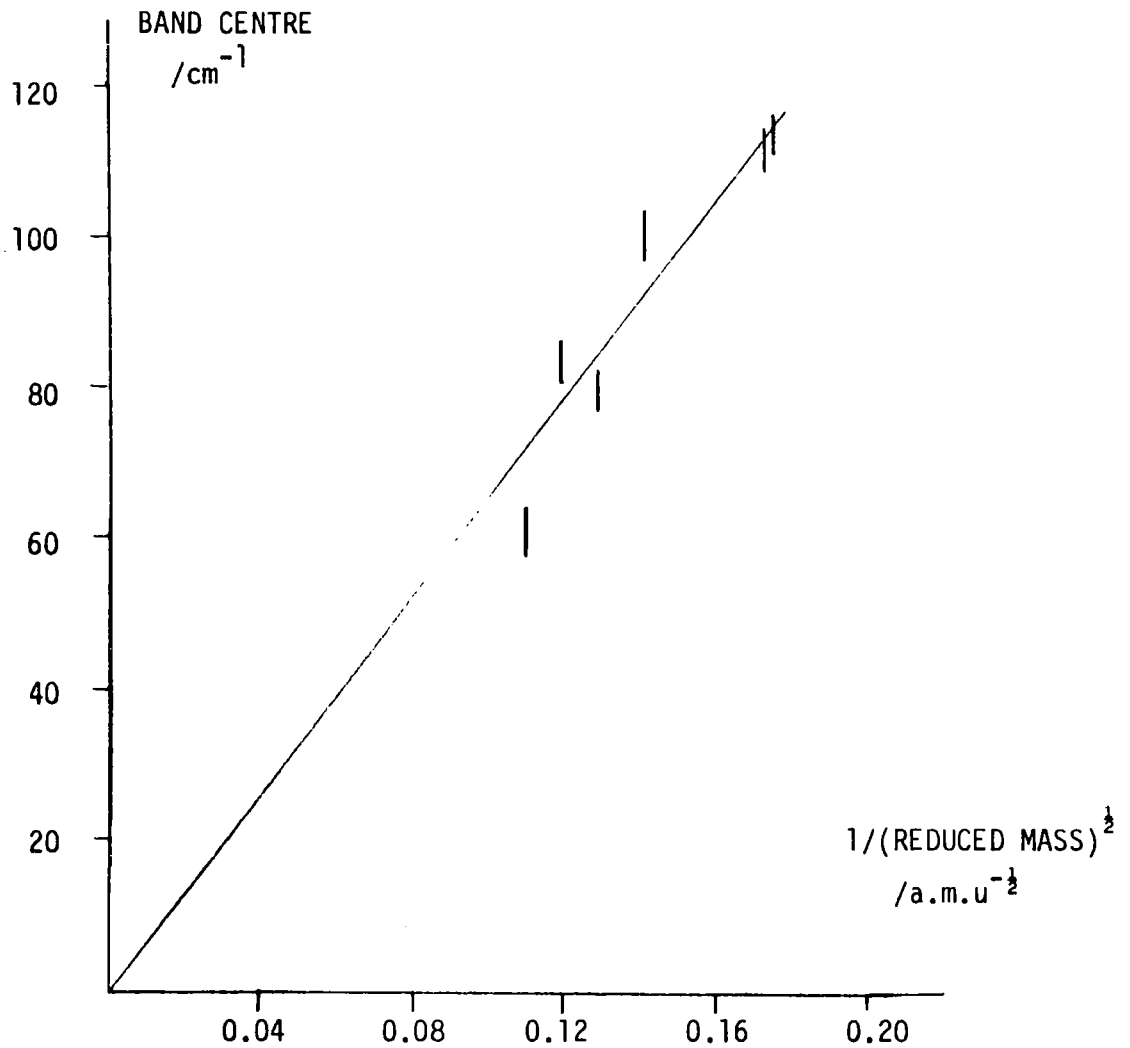

Fig. 7.7 Observed band centres as a function of reciprocal root reduced mass

Table 7.3 Observed and calculated band centres for the ion pair model

salt	obs. $\bar{\nu}_o$ /cm^{-1}	μ' /a.m.u.	$\mu'^{-\frac{1}{2}}$ /a.m.u.$^{-\frac{1}{2}}$	calc. $\bar{\nu}_o$ [c] /cm^{-1}
$Bu_4N^+Cl^-$	115±3[a]	30.93	0.176	-------
$Bu_4N^+Br^-$	80±3[a]	60.11	0.129	82.5±2.2
$Bu_4N^+I^-$	61±3[b]	83.31	0.110	70.1±1.8
$Bu_4N^+NO_3^-$	100±3[b]	49.38	0.142	91.0±2.4
$Bu_4N^+ClO_4^-$	85±3[b]	70.50	0.119	76.2±2.0
$Pe_4N^+Cl^-$	115±3[a]	31.69	0.178	113.6±3.0
$Hp_4N^+Cl^-$	112±3[a]	32.64	0.175	111.9±2.9

a benzene solution

b chloroform solution

c calculated assuming $\bar{\nu}_o$ $Bu_4N^+Cl^-$ = 115±3 cm^{-1}, giving K_{obs} = 26.7±0.4 N m^{-1}.

ε is the permittivity of the medium

r is the separation between the charges

Thus for two univalent ionic charges;

$$F = e^2/4\pi\varepsilon_o\varepsilon_r r_{AC}^2 \qquad 7.12$$

where e is the electronic charge (1.6×10^{-19} C)

ε_o is the permittivity of free space (8.854×10^{-12} C V^{-1} m^{-2})

ε_r is the relative permittivity of the medium

The force constant is the restoring force per unit displacement, and can thus be calculated as the derivative of the force with respect to distance;

$$K_{calc} = dF/dr = -2e^2/4\pi\varepsilon_o\varepsilon_r r_{AC}^3 \qquad 7.13$$

The negative sign indicates that the restoring force acts in opposition to the movement of the bond from the equilibrium position. Thus the observed force constant can be compared with a calculated force constant if a value for the inter ion separation is known. The sum of the ionic radii for the chloride anion and the tetra-n-butylammonium cation were found to be 0.49 nm (189,ref 190, chap. 2). Thus taking ε_r = 2.28 for benzene, K_{calc} was determined as 1.7 N m^{-1}, which is an order of magnitude smaller than the observed force constant K_{obs} of 26.7 N m^{-1} for 0.5 mol dm^{-3} $Bu_4N^+Cl^-$ in benzene. This suggested that the ions in solution must be closer than would be expected from their individual ionic radii. The ionic separation necessary to produce the observed force constant was also calculated using eqn. 7.13. The required inter-ion separation was calculated as 0.17 nm, which is clearly far smaller than would be expected, but is of the correct order of magnitude.

The values of the calculated inter-ion separations (calculated from eqn. 7.13 using the observed force constant K_{obs}), for various concentrations of the salts, are shown in tables 7.4 and 7.5. Table 7.4 shows the effect of concentration on the force constant and inter-ion separation for $Bu_4N^+Cl^-$ in benzene, chloroform and carbon tetrachloride. Table 7.5 compares the values of force constants and inter-ion separation for the various salts studied in benzene, chloroform, carbon tetrachloride and tetrahydrofuran.

Table 7.4 Calculated force constants and inter-ionic sparation for the ion pair model

concn. /mol dm^{-3}	$\bar{\nu}_o$ /cm^{-1}	K_{obs} /N m^{-1}	$r_{AC\ obs}$ /nm
$Bu_4N^+Cl^-$ in benzene			
0.21	112±1	22.9±0.4	0.206±0.001
0.50	121±1	26.7±0.4	0.196±0.001
0.80	119±1	25.8±0.4	0.198±0.001
1.40	117±1	25.0±0.4	0.200±0.001
$Bu_4N^+Cl^-$ in chloroform			
0.10	116±1	24.6±0.4	0.156±0.001
0.50	114±1	23.7±0.4	0.158±0.001
0.80	113±1	23.3±0.4	0.159±0.001
$Bu_4N^+Cl^-$ in carbon tetrachloride			
0.10	120±1	26.3±0.4	0.199±0.001
0.50	115±1	24.1±0.4	0.204±0.001
0.80	114±1	23.7±0.4	0.205±0.001

Table 7.5 Calculated force constants and inter-ionic separation for the ion pair model

solvent	$\bar{\nu}_o$ /cm^{-1}	ε_r	K /N m^{-1}	r_{AC} /nm
$Bu_4N^+Cl^-$				
C_6H_6	121±1[a]	2.28	26.7±0.4[c]	0.196±0.001[c]
CCl_4	115±1[a]	2.24	24.1±0.4[c]	0.204±0.001[c]
$CHCl_3$	114±1[a]	4.95	23.7±0.4[c]	0.158±0.001[c]
THF	110±5[b]	7.39	22.1±2.0	0.141±0.002
$Bu_4N^+Br^-$				
C_6H_6	79±1[a]	2.28	22.1±0.6	0.209±0.002
$CHCl_3$	79±3[b]	4.95	22.1±1.7	0.161±0.004
$Bu_4N^+I^-$				
$CHCl_3$	61±3[b]	4.95	18.3±1.8	0.172±0.017
$Bu_4N^+NO_3^-$				
$CHCl_3$	100±3[b]	4.95	29.1±1.7	0.147±0.003
$Bu_4N^+ClO_4^-$				
$CHCl_3$	85±3[b]	4.95	30.1±2.1	0.146±0.004
$Pe_4N^+Cl^-$				
C_6H_6	115±3[b]	2.28	24.7±1.3	0.201±0.004
$Hp_4N^+Cl^-$				
C_6H_6	112±3[b]	2.28	24.2±1.3	0.203±0.003

[a] from computer best fits

[b] eye-fitted centres

[c] 0.5 mol dm^{-3} salt

The calculated values for r_{AC} were all seen to be smaller than those estimated for the charge separation from the measured dipole moments (160,189,ref. 191, chap. 2), where the separation was measured as 0.4 to 0.5 nm for a series of tetra-n-butylammonium salts. It should be noted here that the latter studies were carried out in dilute solution where the predominant species is likely to be the ion pair, rather than the more complex aggregate of our studies. The small separations calculated from our studies agree, however, with those determined from dielectric studies (156,157,192-195) on similar complexes. It has been suggested (195) that formation of the large aggregates leads to a reduction in the 'effective' charge separation.

As the degree of aggregation changed with concentration, then this would be expected to be reflected in the observed force constants and inter-ion separations. Table 7.4 shows that small, but significant, changes occur in both K_{obs} and r_{AC} as the concentration changes. The observed force constant reaches a maximum at about 0.5 mol dm^{-3} and then decreases again at higher concentration. This ties in with our own intensity measurements and also with the permittivity (101), conductivity (102) and freezing point depression work (103,104).

Table 7.4 showed that the force constants for tetra-n-butylammonium salts in chloroform were seen to decrease in the order chloride, bromide, iodide. This was presumably due to the increase in the anion-cation separation, due to the increase in size of the anion.

The inter-ion separation was seen to be smaller in chloroform than in either benzene or carbon tetrachloride. This seems rather strange, and can only be explained by assuming that the weakly polar solvent somehow stabilises the aggregates. This latter conclusion, of course, assumes that no drastic changes in the system have been caused by the change to the more polar solvent. The spectra suggest that this is not the case.

It thus seems likely that the ion pair model is a good one for this system, despite the evidence (101-104) that the average size of the

ion aggregate is of the order 20-30 ion pairs for solutions of the concentration used in this study.

Having been successful with force constant calculations using the ion pair model, we decided to make some intensity calculations using the same model. It has already been shown in chapter 5 that the 120 cm^{-1} band intensity depends upon the concentration of the dissolved salts. The simplest approximation for the intensity calculation involves the use of non-polarisable point charges. The intensity can be calculated from (ref. 169, chap. 10);

$$B = N\pi/3c^2(\delta\vec{\mu}/\delta Q)^2 \qquad 7.14$$

where N is the Avagadro constant (6.023×10^{23} mol^{-1})

c is the velocity of light (3×10^8 m s^{-1})

$\delta\vec{\mu}/\delta Q$ is the vibrational coordinate

For the simple ion pair;

$$\vec{\mu} = r_{AC}e \qquad 7.15$$

where r_{AC} is the inter-ion separation

e is the electronic charge (1.6×10^{-19} C)

Now $$\delta\vec{\mu}/\delta r = e \qquad 7.16$$

Introducing the normal coordinate;

$$\delta\vec{\mu}/\delta Q = e/m^{\frac{1}{2}} \qquad 7.17$$

where m is the reduced mass of the ion pair

Thus from eqn. 7.14

$$B = N\pi e^2/3c^2m \qquad 7.18$$

This gives a value of B = 3 140 dm^3 mol^{-1} cm^{-2} for the intensity, which shows reasonable agreement with the experimental intensity of 5 760 dm^3 mol^{-1} cm^{-2}, obtained as the average over the concentration range studied.

It has been pointed out that the dipole moment for polarisable ions will be significantly lower than that calculated using eqn. 7.15 (ref. 196, chap. 5). The effects of mutual polarisation of the ions must be taken into account. Williams (160) used the following expressions for the dipole

moment of a pair of polarisable ions;

$$\vec{\mu}_{eff} = er_{AC}(1-\alpha_{eff}/4\pi\varepsilon_o\varepsilon_r r_{AC}^3) \qquad 7.19$$

where α_{eff} is the effective ion polarisability.

Thus $$\delta\vec{\mu}/\delta Q = (e + 2e\alpha_{eff}/4\pi\varepsilon_o\varepsilon_r r_{AC}^2)m^{-\frac{1}{2}} \qquad 7.20$$

The tetra-n-butylammonium cation polarisability (196) was used as α_{eff}, since this is much higher than the polarisability of the halide ion. The calculated effective dipole moment and resulting intensity for various inter-ion separations are shown in table 7.6. The value for r_{AC} necessary to give agreement with the observed intensity (5 760 $dm^3\ mol^{-1}\ cm^{-2}$) was seen to be about 0.32 nm. This is once again lower than that for the sum of the ionic radii, which is 0.49 nm (189), but is greater than the 0.17 nm necessary to produce the observed force constant from eqn. 7.9.

It can thus be seen that the calculated intensity data for a polarisable ion pair or cluster are semi-quantitatively correct.

7.4.3 The 80 cm^{-1} band

The band centred at 80 cm^{-1} showed very little variation in band position or half-band width on changing either the salt or the solvent. It has been noted previously (ref. 190, chap. 2,197) that bands occurring in this low frequency region for solutions containing polar complexes were often of hybrid character. The two mechanisms likely to produce absorption in this region are the Poley-Hill (2,4,79-81) and collision induced absorptions (179-181), which were discussed briefly in section 7.4.1. The Poley-Hill absorption is assumed to be due to the libration of the ion pair dipole within a cage of solvent molecules. The collision induced absorption is considered to be due to induced dipoles in solvent molecules due to collisions with the 'trapped' ion pair dipole.

It has been shown (ref. 198, p. 71,6) that the Poley-Hill mechanism will lead to a rapid decrease in band frequency with increasing temperature, whereas any absorption arising from modulation of electric fields by collisions would lead to an increase in band frequency with increasing temperature. It

Table 7.6 Calculated intensities for the 120 cm^{-1} band for the polarisable ion pair model

r_{AC} /nm	$10^{30}\vec{\mu}$ ($=er_{AC}$) /Cm	$10^{30}\vec{\mu}_{eff}$ eqn. 7.19 /Cm	$B_{calc.}$ /dm^3 mol^{-1} cm^{-2}
0.20	32	4.13	33 100
0.25	40	8.40	12 760
0.30	48	10.70	6 760
0.35	56	12.13	4 430
0.40	64	13.04	3 340
0.45	80	14.11	2 410

was shown in chapters 4 and 5 that our low frequency studies indicated that the band showed no obvious change in frequency with temperature. It seems possible that both mechanisms contribute to the absorption at 80 cm^{-1}, and that they both contribute approximately 50% of the band intensity.

The intensity of the Poley-Hill absorption will be proportional to the number of dipoles in unit volume of the solution, N', whereas the collisional absorption will have N'^2 dependence if a binary collision is assumed. Thus;

$$B_{total} = \int \alpha(\bar{\nu})d\bar{\nu}$$
$$= N'A_{Poley} + N'^2(A' + A'' + ...)_{Collision} \qquad 7.21$$

where A' and A" etc. are the terms for the various possible collisions.

A' is the term for the binary collisions between ions and solvent molecules

A" is the term for the binary collisions between ion dipoles and solvent molecules

The Poley-Hill intensity can be calculated, since the Gordon intensity Sum rule (199) has been used (198,200-203) to calculate the intensity arising from the rotation of the rigid dipole. The intensity per molecule can be calculated from;

$$\int_0^\infty \alpha_p(\bar{\nu}).d\bar{\nu} = \{(n_\infty^2+2)^2/9n_\infty\}\pi\vec{\mu}_{AC}^2/3c^2(1/I_x + 1/I_y) \qquad 7.22$$

where $\alpha_p(\bar{\nu})$ is the absorption coefficient as a function of wavenumber

I_x and I_y are the moments of inertia perpendicular to the direction of the dipole moment $\vec{\mu}_{AC}$

n_∞ is the infrared refractive index.

The internal field correction $(n_\infty^2+2)^2/9n_\infty$ is difficult to apply, because the refractive index is not known. This correction was ignored, and the intensity per mole was calculated by use of;

$$B_{Poley} = N\pi\vec{\mu}_{AC}^2/3c^2(1/I_x + 1/I_y) \qquad 7.23$$

Table 7.7 shows the calculated contribution of the Poley-Hill absorption, using eqn. 7.23, for cation-anion separations of 0.2, 0.3 and 0.4 nm, and for effective ion pair dipoles of 10, 20 and 30 x 10^{-30} Cm. The values being chosen so as to span the possible values for the system. The observed intensity for this band was seen to be about 6 390 dm^3 mol^{-1} cm^{-2}, and thus the Poley-Hill absorption can account for a maximum of approximately 50% of the total intensity of the 80 cm^{-1} band. This intensity assumes an effective dipole moment of 33 x 10^{-30} Cm, and an average cation-anion separation r_{AC} of 0.3 nm. This is a very large effective dipole moment, compared with the dipole moment of 10 x 10^{-30} Cm, necessary to give the correct intensity for the 120 cm^{-1} absorption, with the polarisable ion pair model, and suggested that the Poley-Hill absorption may be providing less than 50% of the total intensity of the 80 cm^{-1} band.

The contribution to the 80 cm^{-1} band by collision induced processes can be estimated by use of a simple dipole-induced dipole expression (relating to the term A" in eqn. 7.21). If the dipole-solvent distance R is assumed to be large compared with the inter ion separation r_{AC}, then the potential at the solvent molecule can be represented as (204,ref. 205, p.303);

$$V = \vec{\mu}_{AC}\cos\theta/4\pi\varepsilon_o\varepsilon_r R^2 \qquad 7.24$$

where θ is the angle the solvent molecule makes with the axis of the dipole

The electric field dipole can be found as the first derivative of the electrical potential with respect to distance;

$$E = 2\vec{\mu}_{AC}\cos\theta/4\pi\varepsilon_o\varepsilon_r R^3 \qquad 7.25$$

For maximum interaction ($\cos\theta = 1$, $\theta = 0$) the dipole induced in the solvent is given by;

$$\vec{\mu}_{ind} = \alpha_s E = 2\vec{\mu}_{AC}\alpha_s/4\pi\varepsilon_o\varepsilon_r R^3 \qquad 7.26$$

where α_s is the polarisability of the solvent

The intensity can then be calculated by use of eqn. 7.14 since;

Table 7.7 Calculated Poley-Hill intensity contribution for the 80 cm^{-1} band

r_{AC} /nm	$10^{47} I$ /kg m^2	$10^{30} \vec{\mu}_{AC}$ /Cm	B_{Poley} /dm^3 mol^{-1} cm^{-2}
0.3	462.6	33.0	3 036
0.3	462.6	20.0	1 093
0.3	462.6	10.0	273
0.4	822.4	33.0	1 704
0.4	822.4	20.0	615
0.4	822.4	10.0	154
0.5	1285.1	33.0	1 093
0.5	1285.1	20.0	393
0.5	1285.1	10.0	98

$$\delta\vec{\mu}/\delta Q = -6\vec{\mu}_{AC}\alpha_s/4\pi\varepsilon_o\varepsilon_r R^4 m^{\frac{1}{2}} \qquad 7.27$$

$$B_{collisional} = N\pi/3c^2 m(-6\vec{\mu}_{AC}\alpha_s/4\pi\varepsilon_o\varepsilon_r R^4)^2 \qquad 7.28$$

Eqn. 7.28 has been used to calculate the collisional intensity contribution by using the value for $\vec{\mu}_{AC}$ from eqn. 7.19. Table 7.8 shows the calculated intensity values for a range of effective dipole moments and dipole-solvent distances. The polarisability of benzene was taken as 11.48×10^{-40} C m^2 V^{-1}. The permittivity used was that of pure benzene ($\varepsilon_r = 2.28$) to parallel the previous model calculations. The reduced mass m was taken as that of an ion pair/solvent molecule. The required intensity of about 3 000 dm^3 mol^{-1} cm^{-2} is obtained for a value of the ionic dipole-solvent distance of about 0.25 nm for an effective dipole moment $\vec{\mu}_{AC}$ of 33×10^{-30} Cm. The latter value being chosen to tie in with the Poley-Hill calculation. Once again the value for the dipole-solvent distance R appears to be very small, especially when one considers that the free ion pair dipole moment has been used, rather than the necessarily lower value for a cluster of dipoles.

A further intensity calculation for possible collisional interaction (relating to A' in eqn. 7.21) between an ion and a solvent molecule. The field due to a univalent ion at a distance D from the charge is given by;

$$E = e/4\pi^2\varepsilon_o\varepsilon_r D^2 \qquad 7.29$$

The induced dipole at this point is given by;

$$\vec{\mu}' = \alpha_s E \qquad 7.30$$

$$\vec{\mu}' = \alpha_s e/4\pi^2\varepsilon_o\varepsilon_r D^2 \qquad 7.31$$

Calculating the intensity via eqn. 7.14 gives;

$$\delta\vec{\mu}'/\delta Q = -2\alpha_s e/4\pi^2\varepsilon_o\varepsilon_r D^3 m^{\frac{1}{2}} \qquad 7.32$$

where m is the reduced mass for the ion-solvent molecule system.

$$B = N\pi/3c^2(2\alpha_s e/4\pi^2\varepsilon_o\varepsilon_r D^3 m^{\frac{1}{2}})^2 \qquad 7.33$$

The values of calculated intensity for both chloride ion-solvent and tetra-

Table 7.8 Calculated intensity contribution for the collision induced absorption through dipole-induced dipole interactions

effective dipole-solvent distance R /nm	effective dipole moment μ_{CA} /Cm	intensity B /$dm^3\ mol^{-1}\ cm^{-2}$
0.20	33.0	19 000
	20.0	7 170
	10.0	1 800
0.25	33.0	3 340
	20.0	1 210
	10.0	300
0.30	33.0	780
	20.0	280
	10.0	70
0.35	33.0	227
	20.0	81
	10.0	20
0.40	33.0	78
	20.0	28
	10.0	7

n-butylammonium ion-solvent collisional interaction are shown in table 7.9. The values taken for the parameters were as for the other model calculations. Values for the ion-solvent distance have been chosen between 0.10 and 0.25 nm, for comparison with the dipole-solvent interaction calculation. The required intensity of about 3 000 $dm^3\ mol^{-1}\ cm^{-2}$ is obtained with an ion-solvent distance of about 0.27 nm. It thus appeared that both anion-solvent and cation-solvent interactions would be contributing to the intensity of the collisional portion of the low frequency band. Presumably higher multipoles would have to be considered in a full intensity calculation, but these calculations would become very difficult, because of the complexity of the system and the lack of knowledge as to the concentration of the different multipoles. If both cation- and anion-solvent collisional interactions are considered to produce equal intensity, then the anion-solvent distance required is about 0.23 nm, and the cation-solvent distance is about 0.27 nm, to give the required intensity of 1 500 $dm^3\ mol^{-1}\ cm^{-2}$ for each portion.

These small inter-species distances agree well with the measurement of average distance between solution particles made by Lestrade (157, 193,194), with the complex permittivity measurements on tetra-n-butylammonium salts. Lestrade has interpreted these results to indicate that the ions are restricted to move within the region of space in the interior of the aggregates. It is thus possible that the relatively small number of benzene molecules involved in interactions with the ionic dipole are compressed by the cluster formation. Further, some of the benzene molecules may well be trapped within the cages formed by the open structure of the alkyl chains. This is consistent with the assertion of some authors (73), that concentrated benzene solutions should be regarded as solutions of benzene in the fused salt.

7.4.4 The 180 cm^{-1} band

In the studies of the tetra-n-alkylammonium salts this band was only seen to be present for the chlorides. The frequency of the band was seen

Table 7.9 Calculated intensity contribution for collision induced absorption through ion induced dipole interactions

ion-solvent distance D /nm	intensity $B_{ion\text{-}solvent}$ Bu_4N^+/C_6H_6 /$dm^3\ mol^{-1}\ cm^{-2}$	Cl^-/C_6H_6 /$dm^3\ mol^{-1}\ cm^{-2}$
0.10	134 400	321 400
0.15	11 900	28 200
0.20	2 100	5 000
0.25	551	1 300
0.30	184	442

to be independent of solvent, but the intensity of the band was seen to depend upon the solvent. The frequency of the band was not dependent upon the cation, but the intensity appeared to be cation dependent (see chapter 5). This suggested that solvation of the chloride ion may be occurring in the solution. Such a band due to anion-solvent vibration has in fact been observed for the spectra of rubidium, caesium, potassium and tetramethylammonium fluorides in acetic acid (206). The band assigned to the anion-solvent interaction was seen to occur at about 280 cm^{-1} for the fluoride ion in the acetic acid solvent. The absorption bands were seen to be very broad even when compared to those due to the cation-solvent interaction, and thus seem to be similar to the bands observed for the chloride ion benzene system. The acetic acid solvent is strongly hydrogen-bonding, and hence a hydrogen-bonding interaction would be expected for the fluoride anion, which being very small is very susceptible to hydrogen-bond formation. Such an interaction seems less likely in benzene and carbon tetrachloride solvents, although it would be more likely in chloroform and tetrahydrofuran. Studies in more polar solvents have shown that Li^+I^- in acetone and $Li^+ClO_4^-$ in THF have the possibility of a high frequency component. It thus seems likely that no simple explanation in terms of anion solvation can be given for this high frequency component to the overall band profile.

Another possibility was that the high frequency band was a combination band. The frequency of about 180 cm^{-1} is approximately the sum of the frequencies of the two other bands observed for this system. The ion vibration band occurs at 120 cm^{-1} and the librational/collisional band occurs at 80 cm^{-1}, giving a sum of 200 cm^{-1}. The occurrence of a high frequency component for the Li^+I^- in acetone and $Li^+ClO_4^-$ in THF systems suggested that the latter explanation of the high frequency component band was perhaps a viable one. For the $Li^+ClO_4^-$ in THF the ion librational interaction produces a band at approximately 425 cm^{-1}, and the Poley-Hill absorption for THF has been measured to have a band centre of about 55 cm^{-1}. The high frequency

component at 477 cm^{-1} thus seems likely to be a combination band (55+425=480). The $Na^{+}I^{-}$ in acetone system is slightly different, since here it is the 1215 cm^{-1} internal acetone mode that has a high frequency component, rather than the inter-species mode as for the other systems. The high frequency component occurred at 1235 cm^{-1}, which is a little low since we have measured the Poley-Hill frequency to be about 40 cm^{-1}. (1215+40=1255).

It thus seems possible that the high frequency component is a combination band, but a much more detailed study in a wider range of systems is required before any concrete conclusions can be drawn. Our stochastically modulated oscillator model gives added evidence that the high frequency component is a combination band as a result of the theory for this model (170).

7.5 Indications as to the structure of the near ion environment

Sections 4.2.5 and 4.2.6 have shown that only the benzene out-of-plane modes were affected by the addition of the tetra-n-butylammonium salts to the benzene solvent. The ν_{16} C-C-C out-of-plane rocking mode was seen to be severely pertubed, and this implied that interaction with the benzene ring occurred in such a way as to affect only the out-of-plane modes. This would not appear to be the expected behaviour for a donor-acceptor interaction of the tetra-n-butylammonium cation-solvent system (207,208). For the latter type complex perturbation of the totally symmetric benzene modes would be expected. The perturbation of the out-of-plane modes might be the expected behaviour for a strong electrostatic interaction by the ions with the $p\pi$-bonding orbitals of the benzene molecule, and one can envisage a model for the system with the tetra-n-butylammonium ion 'sitting' on the ring of electron charge of the benzene $p\pi$-system.

The perturbation of the benzene internal modes implies a very strong interaction between the ions and the solvent. This is entirely in accord with deductions from our intensity measurements and also those from complex permittivity measurements and freezing point determinations, which have

already been discussed.

PART C

DISPERSIVE FAR-INFRARED STUDIES

CHAPTER 8

SOLID PHASE REFRACTIVE INDEX MEASUREMENTS

8.1 Theory for refractive index measurements

Experimental work between 1963 and 1969, by Chamberlain and Gebbie (209-216) at the National Physics Laboratory, and independently by Bell and Russell (217-223) at Ohio State University, showed how a Michelson interferometer could be applied to the determination of refractive index spectra. The mathematical theory for the ref ractive index work has been developed by two approaches. A method using impulse response functions (ref. 224, p. 261) was used by Bell, who published the theory of Dispersive Fourier Transform Spectroscopy in these terms (219,223). Chamberlain (225) presented the theory by assuming the broad band radiation to be composed of monochromatic components of varying amplitudes. The properties of the broad band were then considered as the sum of the properties of the superimposed monochromatic elements. This approach is parallel to that applied to Non-Dispersive Fourier Transform Spectroscopy in chapter 1, and will be used in this section to develop the necessary theory for Dispersive Fourier Transform Spectroscopy.

In Non-Dispersive Fourier Spectrometry the sample is normally placed before the detector as shown at A in fig. 8.1. For broad band spectral radiation the intensity reaching the detector, (as a function of the path-difference, x, between the two beams) shows a pronounced maximum at zero-path difference, where all wavelengths are in phase. The transmitted power spectrum is related to the modulating part of the interferogram by a cosine Fourier integral as shown in chapter 1.

In Dispersive Fourier Transform Spectroscopy an optically thin specimen of an isotropic dispersive medium is introduced into only one beam of the interferometer, as shown in position B in fig. 8.1. The symmetry of the arrangement is now upset, and although there is still a prominent Grand Maximum, this is now displaced from the zero path-difference position, by an amount dependent upon the optical thickness of the specimen. The interferogram is now no longer symmetrical about the brightest fringe. The distortion of the symmetrical interferogram usually only occurs in the region of the bright-

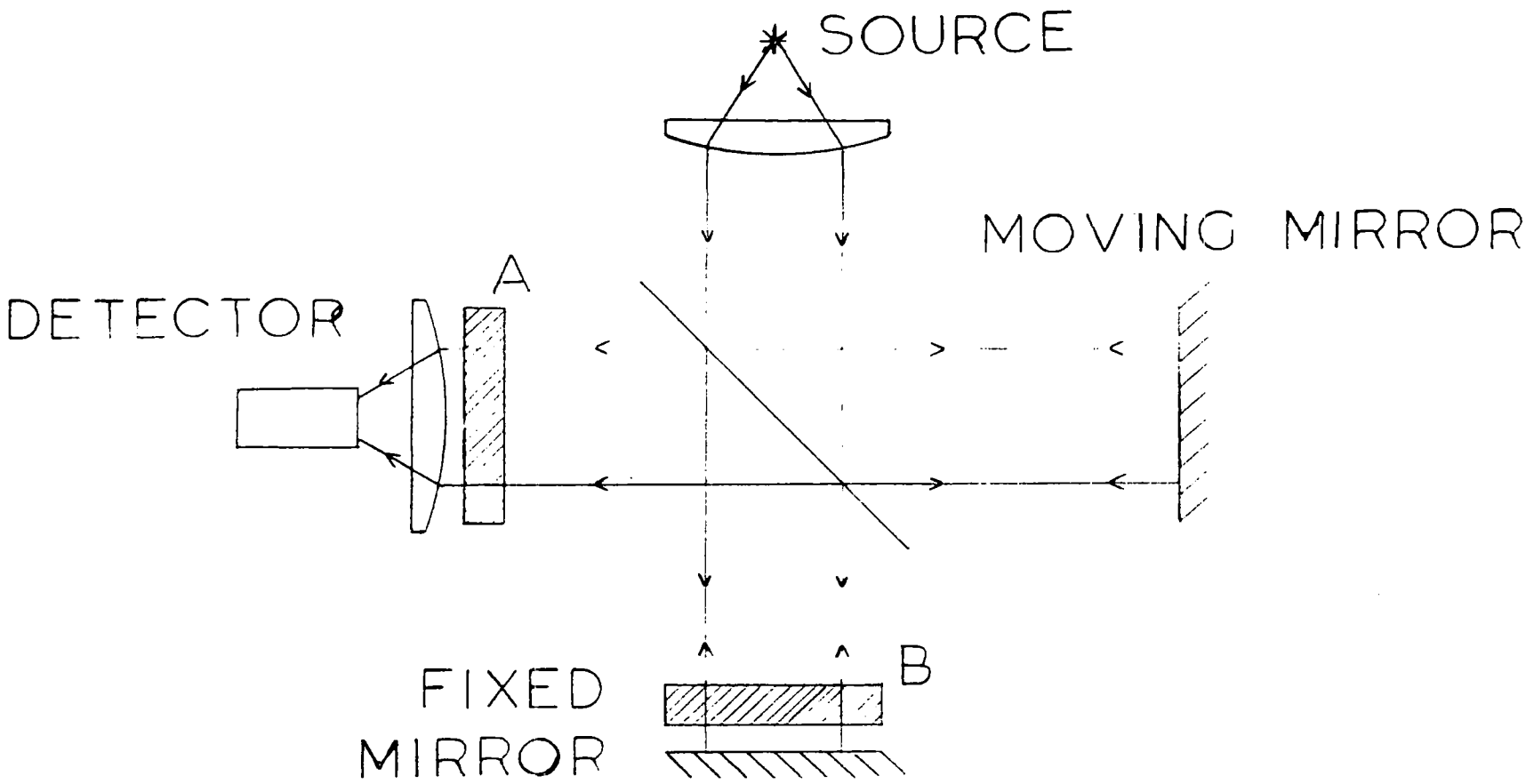

FIG. 8.1 SAMPLE POSITIONS FOR DISPERSIVE (B) AND NON-DISPERSIVE SPECTROSCOPY

test fringe. The distortion only occurs to the positive side of zero path-difference. Fig. 8.2 shows a symmetrical background interferogram obtained with no dispersive specimen in the interferometer. An unsymmetrical interferogram due to the dispersion of 0.0105 cm thickness of teflon (placed at position B in fig. 8.1) is shown in fig. 8.2b. The displacement of the brightest fringe from zero path-difference increases with the thickness of the dispersive sample.

Chamberlain (225) related the displacement of the brightest fringe from the zero path-difference position $\bar{x}$ (measured in path difference units), to the mean refractive index of the dispersive sample $\bar{n}$, by the definition;

$$\bar{x} = 2(\bar{n}-1)d \qquad 8.1$$

where d is the thickness of the dispersive sample

The path difference $\Delta(\bar{\nu})$ introduced by the sample at frequency $\bar{\nu}$ cm^{-1} is;

$$\Delta(\bar{\nu}) = 2\{n(\bar{\nu})-1\}d \qquad 8.2$$

from eqn. 8.1, where $n(\bar{\nu})$ is the refractive index of the sample at frequency $\bar{\nu}$ cm^{-1}. Imperfect adjustment of the interferometer, or omission of compensating windows causes a path-difference error $\delta_o(\bar{\nu})$, which is denoted by a small residual phase difference $\Phi_o(\bar{\nu})$, where;

$$\Phi_o(\bar{\nu}) = 2\pi\bar{\nu}\delta_o(\bar{\nu}) \qquad 8.3$$

The electric vector in the recombined beam can be obtained in a similar manner to that used in chapter 1, and can be written as the Fourier integral;

$$\Phi(\bar{\nu}) = 2\pi\bar{\nu}\{\Delta(\bar{\nu}) + \delta_o(\bar{\nu})\} \qquad 8.4$$

Combining equations 8.2 to 8.4 gives;

$$n(\bar{\nu}) = 1 + 1/4\pi\bar{\nu}d\{\phi(\bar{\nu}) - \phi_o(\bar{\nu}) + 2m\pi\} \qquad 8.5$$

where $\phi(\bar{\nu})$ is the principle value of the true phase difference $\Phi(\bar{\nu})$ given by eqn. 8.4, where $-\pi < \phi(\bar{\nu}) < \pi$.

Calculation of $n(\bar{\nu})$ is difficult unless m = 0 in eqn. 8.5, and this necessitates the restriction that the path difference introduced by the specimen

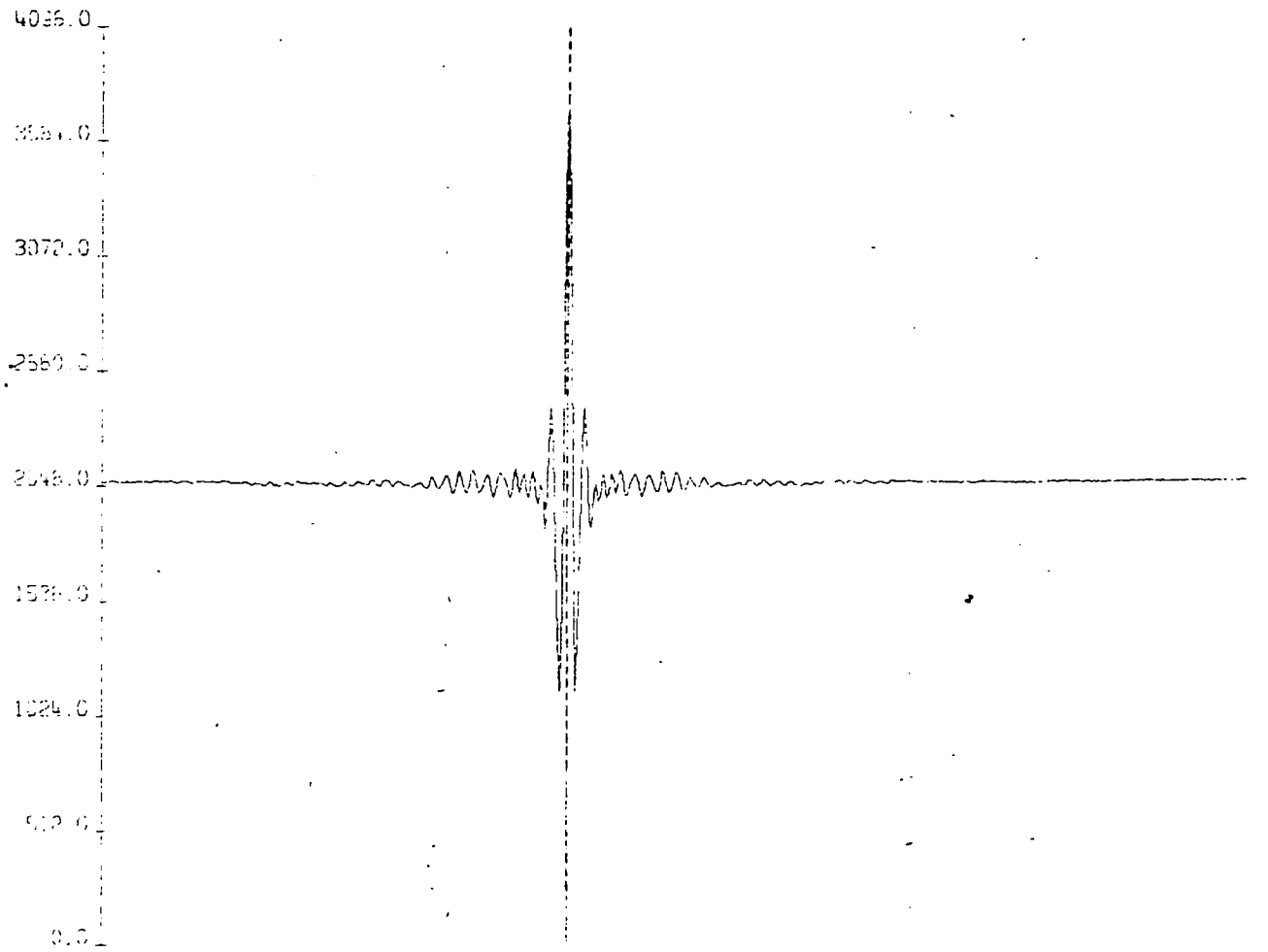

FIG. 8.2a SYMMETRIC BACKGROUND INTERFEROGRA

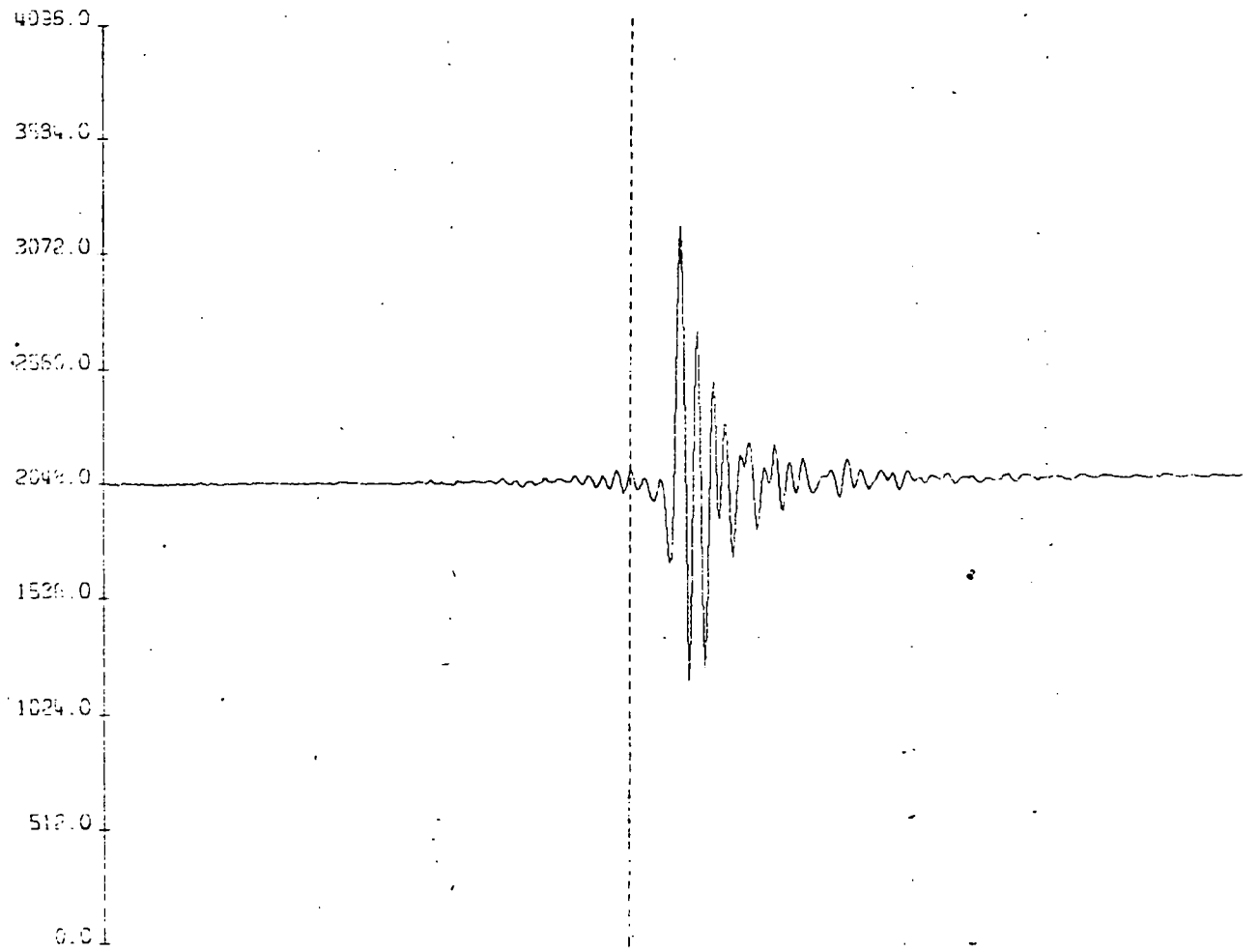

FIG. 8.2b 0.0105 cm TEFLON INTERFEROGRAM

satisfies the relationship;

$$|\Delta(\bar{\nu})| < 1/2\bar{\nu}$$

or $$|2\{n(\bar{\nu}) - 1\}d| < 1/2\bar{\nu} \qquad 8.6$$

for all wavenumbers $\bar{\nu}$ in the spectral band studied. Equation 8.5 has been developed by using the position of zero path-difference as the centre for Fourier Transformation of the interferogram. If the origin of the interferogram is now shifted to the displaced Grand Maximum then eqn. 8.4 becomes;

$$\Psi(\bar{\nu}) = \phi(\bar{\nu}) - 2\pi\bar{x}\bar{\nu} \qquad 8.7$$

and eqn. 8.5 becomes;

$$n(\bar{\nu}) = 1 + \bar{x}/2d + 1/4\pi\bar{\nu}d\{\psi(\bar{\nu})-\phi_0(\bar{\nu})+2m\pi\} \qquad 8.8$$

where $\psi(\bar{\nu})$ is the principal value of the phase-difference $\Psi(\bar{\nu})$, such that $-\pi < \psi(\bar{\nu}) < \pi$. Restrictions to the possible path-differences, such that $m = 0$, require satisfaction of the relationships;

$$|\Delta(\bar{\nu})-\bar{x}| < 1/2\bar{\nu}$$

or $$|2\{n(\bar{\nu})- \bar{n}\}d| < 1/2\bar{\nu} \qquad 8.9$$

Eqn. 8.9 indicates that the optical thickness $n(\bar{\nu})d$ must not depart from the mean optical thickness $\bar{n}d$ by more than $1/4\bar{\nu}$ at any wavenumber $\bar{\nu}$.

The interferogram is expressed as;

$$G(y) = \int_{-\infty}^{+\infty} \rho(\sigma).\cos(\Psi(\bar{\nu})-2\pi y\bar{\nu}).d\bar{\nu} \qquad 8.10$$

where $\rho(\bar{\nu})$ is the transmitted power spectrum

The cosine and sine transforms with respect to the coordinate y having an origin at $x = \bar{x}$ are respectively;

$$P(\bar{\nu}) = \int_{-\infty}^{+\infty} G(y).\cos 2\pi\bar{\nu}y.dy$$

$$\doteq \rho(\bar{\nu}).\cos\psi(\bar{\nu}) \qquad 8.11$$

and $$Q(\bar{\nu}) = \int_{-\infty}^{+\infty} G(y).\sin 2\pi\bar{\nu}y.dy$$

$$= \rho(\bar{\nu}).\sin\psi(\bar{\nu}) \qquad 8.12$$

The refractive index is given by;

$$n(\bar{\nu}) = 1 + \bar{x}/2d - 1/4\pi\bar{\nu}d\{\arctan(Q(\bar{\nu})/P(\bar{\nu})) + m_1\} \qquad 8.13$$

assuming $\phi_0 = 0$

Hence $n(\bar{\nu})$, the refractive index at frequency $\bar{\nu}$, can be recovered from

knowledge of $\bar{x}$, the displacement of the brightest fringe from zero path-difference, d the thickness of the dispersing sample and $P(\bar{\nu})$ and $Q(\bar{\nu})$, the cosine and sine Fourier transforms of the interferogram function.

8.2 Programming to obtain phase and refractive index values

The phase values, as a function of frequency, $\psi(\bar{\nu})$ were obtained by use of the programme DCH0690, which utilises a procedure due to Forman et. al. (31), whereby the phase error introduced by the asymmetry in the interferogram was calculated. A listing of programme DCH0690, together with an input data listing, is contained in Appendix A1.2. The procedure was used to correct for asymmetry in the interferogram due to inadvertant misalignment of the interferometer, when used in the non-dispersive mode. Only a few correction points were taken around the zero path position, and these were then used to develop a correction function, which was used to make the interferogram totally symmetric (see chapter 3). We have used the programme DCH0690 to give phase values for asymmetric interferograms obtained with the interferometer in the dispersive mode. For a 1024 point interferogram the Forman correction function was determined for the whole 1024 points. This gives 1024 phase values for the asymmetry in the interferogram. Thus when a 1024 point double-sided interferogram was computed, the 1024 phase values had a frequency increment equal to one half of the resolution calculated assuming that no apodisation was employed. The phase data was thus usually represented with a frequency interval which gave two points per resolution, and thus paralleled the transmission data.

To determine the validity of the use of the Forman correction function under these circumstances, a number of dispersive interferograms were recorded for thin samples of polytetrafluoroethylene (teflon). The refractive index spectrum for teflon had previously been obtained by Chamberlain and Gebbie (212), who used the full cosine and sine Fourier Transform technique and eqn. 8.13. Thin samples of teflon of between 0.0105 and 0.0229 cm thickness were placed in a holder to stretch the films slightly and

remove any creases. The film holder was then placed in position in the fixed mirror arm of the interferometer. The film holder had a diameter of only 3 cm, and so a diaphragm was constructed to cut down the diameter of the interferometer beams, so that all the fixed mirror beam passed through the sample. The diaphragm was placed at the source port entrance to the beam-splitter module, and had an internal diameter of 1.9 cm. The light beams of the interferometer were seen to be divergent, which necessiated the smaller diameter of the diaphragm relative to the sample holder (for effects of beam divergence see section 8.3).

The anomolous dispersion of teflon was observed by Chamberlain (212), and found to be centred at 202 cm^{-1}. A 25 gauge beam-splitter was thus used to give a maximum energy in this region. 1024 point interferograms were recorded with a 4μm sampling interval. The instrument was carefully optically aligned prior to insertion of the sample, for normality of the fixed and moving mirrors, by adjusting the tilt of the fixed mirror via the caliper adjustments. The mirrors were aligned whilst in a position of zero path-difference, by observing the maximum constructive interference from the two interferometer beams. The symmetry of the interferogram about zero path-difference was then observed over the normal mirror movement (0.2048 cm either side of zero path-difference). The mirrors were considered normal when the difference between the fringes, for positions of the moving mirror equidistant from zero path-difference, was less than 1% of the depth of modulation for the brightest fringe. This result indicated that the fixed and moving mirror were normal to each other throughout the path of the moving mirror. The instrument was aligned at atmospheric pressure, and hence the many signatures due to the sharp water vapour absorptions were used for detecting any asymmetry throughout the moving mirror travel.

The instrument was then evacuated and a series of background interferograms recorded. The phase values for the backgrounds were almost constant, since no dispersive sample was present. Table 8.1 and fig. 8.3

Table 8.1 Phase values for symmetric background interferogram

frequency /cm^{-1}	phase /radians		frequency /cm^{-1}	phase /radians
95.21	-0.13		146.48	-0.18
97.66	-0.12		148.93	-0.19
100.10	-0.11		151.37	-0.20
102.54	-0.12		153.81	-0.16
104.98	-0.12		156.25	-0.19
107.42	-0.09		158.69	-0.20
109.86	-0.14		161.13	-0.19
112.30	-0.14		163.57	-0.20
114.75	-0.12		166.02	-0.23
117.19	-0.14		168.46	-0.21
119.63	-0.13		170.90	-0.23
122.07	-0.17		173.34	-0.21
124.51	-0.15		175.78	-0.24
126.95	-0.12		178.22	-0.22
129.39	-0.19		180.66	-0.24
131.84	-0.12		183.11	-0.21
134.28	-0.19		185.55	-0.23
136.72	-0.15		187.99	-0.23
139.16	-0.16		190.43	-0.21
141.60	-0.17		192.87	-0.26
144.04	-0.20		195.31	-0.25

(continued)

Table 8.1 (continued)

frequency /cm^{-1}	phase /radians		frequency /cm^{-1}	phase /radians
197.75	-0.25		249.02	-0.33
200.20	-0.27		251.46	-0.33
202.64	-0.23		253.91	-0.33
205.08	-0.27		256.35	-0.33
207.52	-0.28		258.79	-0.34
209.96	-0.28		261.23	-0.34
212.40	-0.27		263.67	-0.33
214.84	-0.25		266.11	-0.35
217.29	-0.27		268.55	-0.33
219.73	-0.29		271.00	-0.34
222.17	-0.26		273.44	-0.36
224.61	-0.28		275.88	-0.36
227.05	-0.29		278.32	-0.34
229.49	-0.30		280.76	-0.36
231.93	-0.30		283.20	-0.36
234.38	-0.29		285.64	-0.35
236.82	-0.32		288.09	-0.37
239.26	-0.29		290.53	-0.37
241.70	-0.32		292.97	-0.38
244.14	-0.32		295.41	-0.37
246.58	-0.33			

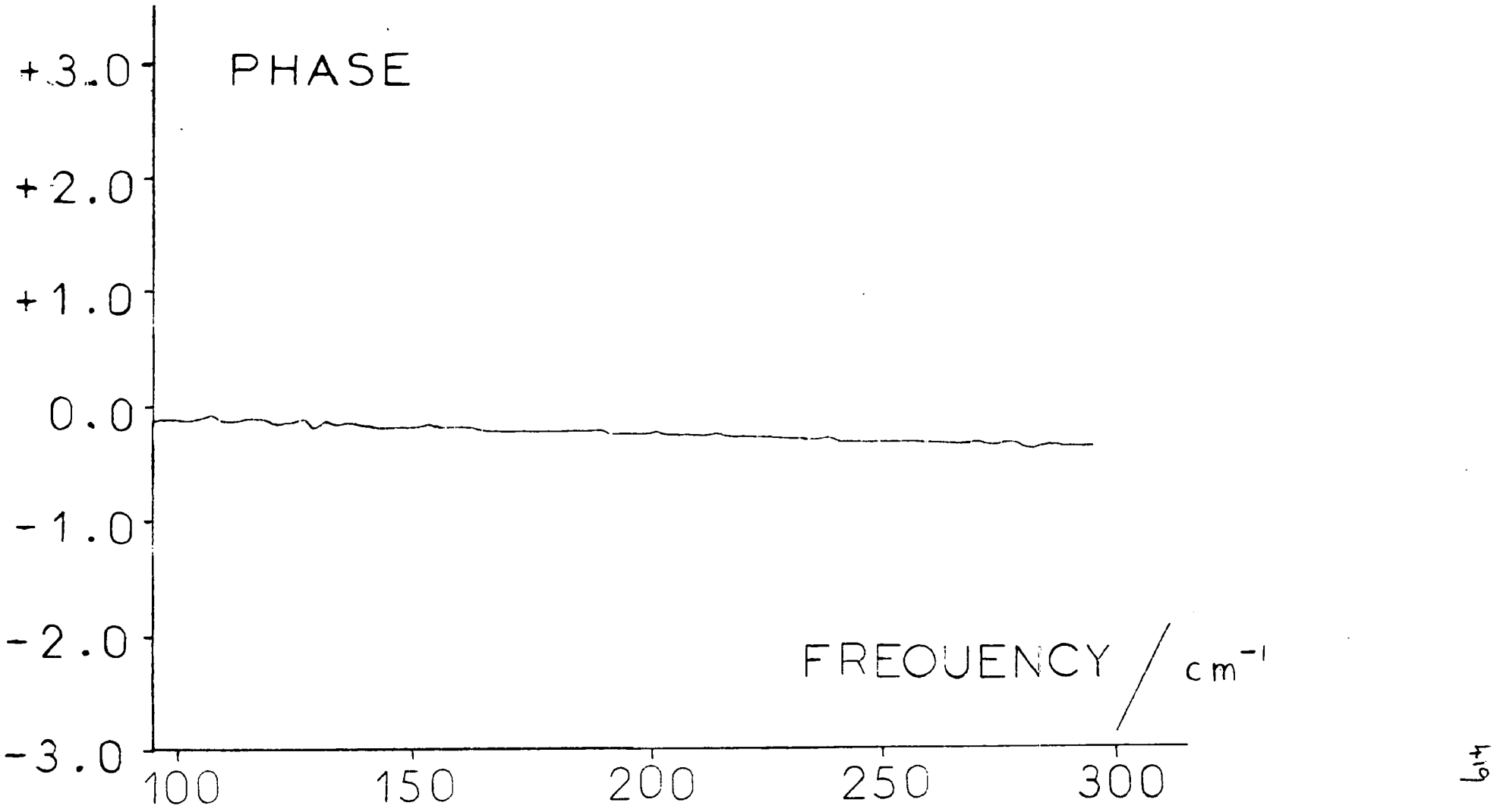

FIG. 8.3 PHASE FOR A SYMMETRIC INTERFEROGRAM

show the phase values obtained in the frequency range 100 to 300 cm^{-1}, using the symmetrical background interferogram recorded from -0.2048 to +0.2048 cm of path-difference with a 4μm sampling interval. The recorded interferogram was shown in fig. 8.2a. The full 1024 point interferogram points were used to develop the correction routine, with programme DCH0690, to give 1024 output phase values. The slight decrease in the phase values with increasing frequency was considered to be indicative of a small degree of misalignment still present in the interferometer.

The teflon sample interferograms were recorded without further alignment of the fixed mirror. This constant optical set-up ensured that the background phase values could be subtracted from the sample phase values, to take into account the maladjustment of the interferometer, and any phase changes occurring due to the refractive indeces of the background components such as the beam-splitter. The phase values between 100 and 300 cm^{-1}, for a 1024 point interferogram, as shown in fig. 8.2b, with a 4 μm sampling interval and 0.2048 cm maximum path-difference, for a 0.0105 cm teflon sample were computed using programme DCH0690, and are shown in table 8.2 and fig. 8.4. 1024 correction points were used to give 1024 phase values at an interval of 1.22 cm^{-1}. These phase values clearly indicated the presence of an anomolous dispersion centred at 203±5 cm^{-1} in the teflon sample. The close agreement between our phase curves, and those published by Chamberlain (212) indicated that our method of phase calculation was a valid one.

A simple programme, known as DCH0623, was developed to compute the refractive index as a function of frequency from the knowledge of the phase values for sample and background as a function of frequency. A listing of programme DCH0623 is contained in Appendix A1.3. The programme read in the phase values for the background and then the sample. The frequency interval of the phase data was calculated from the inputted number of points and the sampling interval. The phase values for background and sample were outputted in spectral form as a function of frequency. Averaging of up to 5 sample

Table 8.2 Phase values for 0.0105 cm teflon

frequency /cm^{-1}	phase /radians		frequency /cm^{-1}	phase /radians
95.21	-0.21		146.48	-0.07
97.66	-0.20		148.93	-0.08
100.10	-0.16		151.37	-0.14
102.54	-0.13		153.81	-0.14
104.98	-0.10		156.25	-0.11
107.42	-0.13		158.69	-0.09
109.86	-0.12		161.13	-0.08
112.30	-0.13		163.57	-0.06
114.75	-0.13		166.02	0.01
117.19	-0.21		168.46	0.03
119.63	-0.18		170.90	0.12
122.07	-0.21		173.34	0.14
124.51	-0.24		175.78	0.18
126.95	-0.22		178.22	0.21
129.39	-0.24		180.66	0.23
131.81	-0.22		183.11	0.27
134.28	-0.15		185.55	0.30
136.72	-0.13		187.99	0.42
139.16	-0.10		190.43	0.56
141.60	-0.11		192.87	0.78
144.04	-0.08		195.31	1.01

(continued)

Table 8.2 (continued)

frequency /cm^{-1}	phase /radians		frequency /cm^{-1}	phase /radians
197.75	1.43		249.02	-0.62
200.20	1.85		251.46	-0.60
202.64	-1.54		253.91	-0.59
205.08	-2.16		256.31	-0.56
207.52	-1.84		258.79	-0.55
209.96	-1.68		261.23	-0.54
212.40	-1.49		263.67	-0.49
214.84	-1.34		266.11	-0.46
217.29	-1.15		268.55	-0.41
219.73	-1.10		271.00	-0.37
222.17	-1.04		273.44	-0.38
224.61	-1.00		275.88	-0.51
227.05	-0.95		278.32	-0.63
229.49	-0.91		280.76	-0.67
231.93	-0.86		283.20	-0.67
234.38	-0.78		285.64	-0.65
236.82	-0.73		288.09	-0.62
239.26	-0.72		290.53	-0.57
241.70	-0.69		292.97	-0.61
244.14	-0.69		295.41	-0.61
246.58	-0.63			

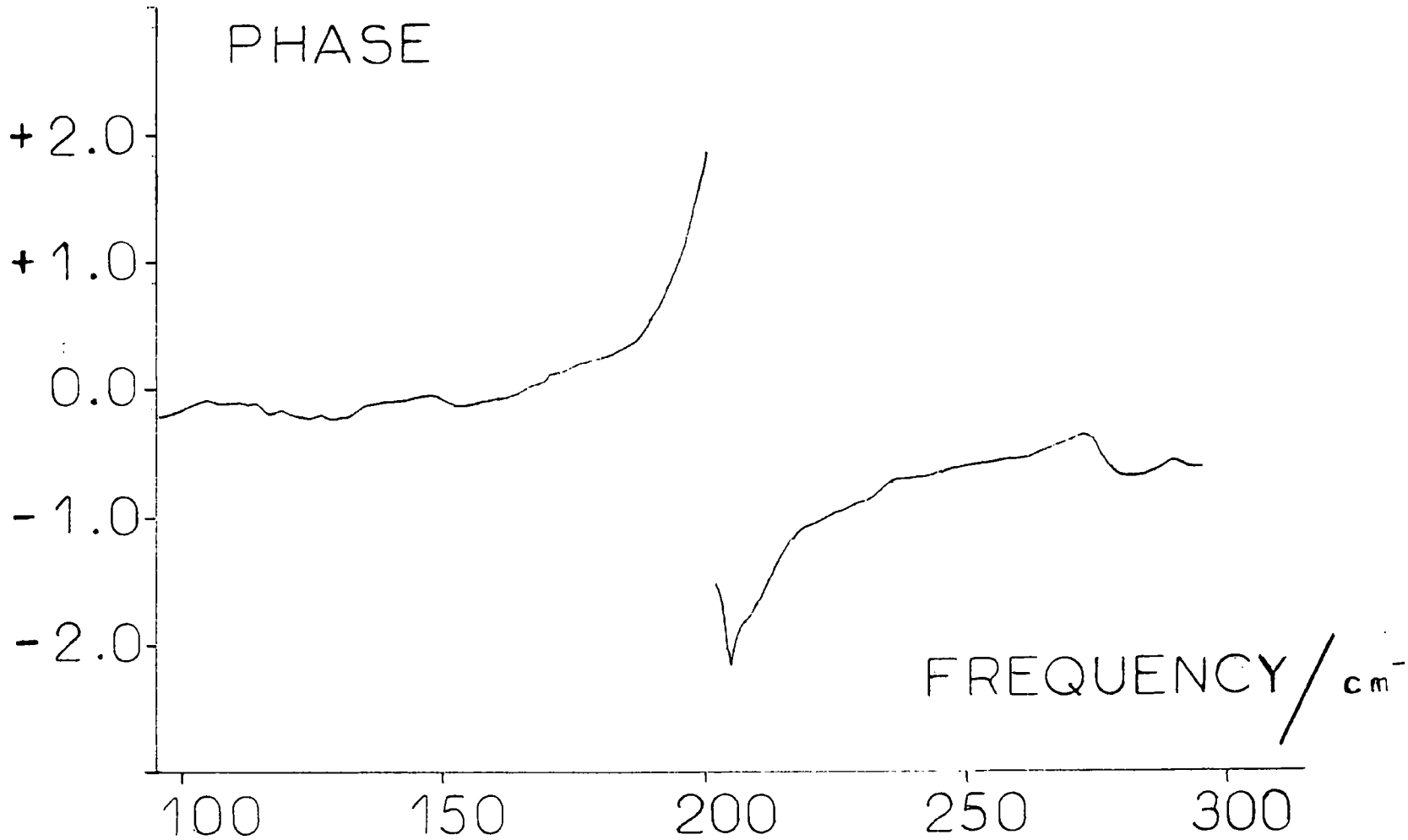

FIG. 8.4 0.0105 cm TEFLON PHASE VALUES

and 5 background phases was possible. The phase difference between sample and background was then calculated as a function of frequency, and the refractive index then computed using eqn. 8.8.

$$n(\bar{\nu}) = 1 + \bar{x}/2d + 1/4\pi\bar{\nu}d\{\psi(\bar{\nu})-\phi_0(\bar{\nu})+2m\pi\}$$

where $\psi(\bar{\nu})$ is the principal value of the sample phase at frequency $\bar{\nu}$, and $\phi_0(\bar{\nu})$ is the principal value of the background phase at frequency $\bar{\nu}$. To complete the computation it was necessary to know the displacement of the brightest fringe from zero path-difference $\bar{x}$, and the thickness of the sample d accurately.

The sample thickness was measured by careful use of a micrometer screw gauge. Twenty measurements of thickness were made on all the teflon samples. The medium thickness sample had an average thickness of 0.0134±0.0002 cm, where the quoted error was the standard deviation obtained for the 20 measurements using eqn. 4.3. The recorded thicknesses were 0.0134, 0.0137, 0.0136, 0.0137, 0.0137, 0.0136, 0.0135, 0.0134, 0.0133, 0.0132, 0.0132, 0.0133, 0.0132, 0.0132, 0.0132, 0.0131, 0.0135, 0.0134 0.0135 and 0.0132 cm. These measurements were taken around the circumference of the sample, and across its diameter to take into account the non-uniformity of the sample. The thickness of the specimen was measured whilst in the sample holder to take into account any stretching of the film which may have occurred during the mounting. The measurements were made after the dispersive spectra of the sample had been obtained, since the use of the micrometer caused marking of the film surface, which may well have affected its dispersive properties.

Systemmatic measurement of the film thickness around the circumference of one of the samples showed that it was non-uniform, showing a variation of 0.0006 cm (5%) from one side of the sample to the other. The precision of the thickness measurement was found to be ±0.0001 cm (1%) when the thickness was measured 20 times at the same position. The measurements were 0.0135, 0.0135, 0.0135 0.0136, 0.0135, 0.0137, 0.0134, 0.0134, 0.0134, 0.0134, 0.0134, 0.0135, 0.0135, 0.0134, 0.0134, 0.0134, 0.0134, 0.0134, 0.0135 and

0.0135 cm. Hence the majority of the lack of precision involved in measuring the thickness was due to the non-uniformity of the sample, and not the precision of the measurement itself.

The displacement of the brightest fringe from zero path-difference, $\bar{x}$ of eqn. 8.8, was measured from chart interferograms, which were recorded for samples which had a small portion of the teflon cut away so that the non-dispersed Grand Maximum could be seen superimposed upon the dispersed interferograms of the teflon sample. Such a chart interferogram is shown in fig. 8.5, from which $\bar{x}$ was measured as 117±3 μm. The path-difference scale was determined by marking the chart every time the punch operated. This gave a path-difference scale with increments of 4 μm. This scale was interpolated to give the fraction of the 4 μm interval for the remaining displacement over the whole number of punch intervals.

The value of $\bar{x}$ was also calculated from actual distance measurements on the chart, which was converted to path-difference units by knowledge of the relative speeds of the moving mirror and the chart recorder. The half-sample interferogram of fig. 8.5 was recorded with a mirror drive speed of 2.5 μm per second (path-difference units) and a chart speed of 30 mm per minute. The separation of Grand Maximum and dispersed maximum on the chart was measured as 23.5±0.4 mm. $\bar{x}$ was thus calculated as 23.5x60x2.5/30 = 117.5 ±2.5 μm. The 0.4 mm is the standard error obtained for 10 chart recordings for the separation of Grand and dispersed maxima. The separations recorded were 23, 23.5, 24, 24.5, 24, 23, 23, 23, 23.5 and 23 mm, giving an average of 23.5 mm and a standard deviation of ±0.4 mm (2%).

The measured values for $\bar{x}$ and d were then read into the refractive index programme DCH0623, and the arrays of background and sample phases used to obtain the refractive index as a function of frequency. Fig. 8.6 and table 8.3 show the refractive index curve for a 0.0105 cm thick teflon sample, whose background and sample phases were shown in figs. 8.3 and 8.4. The refractive index curves were obtained by assuming that the phase-difference

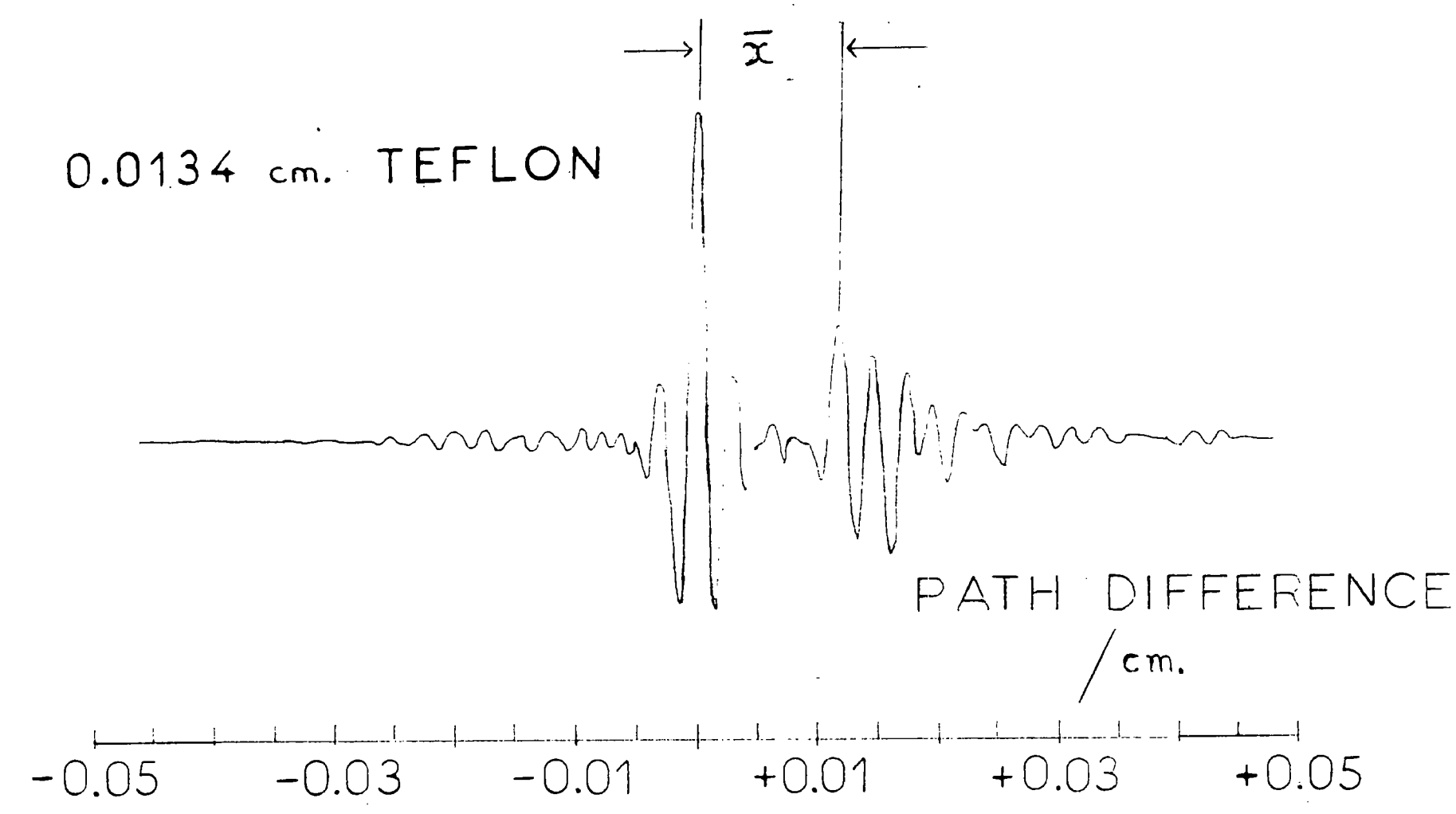

FIG. 8.5 HALF-SAMPLE INTERFEROGRAM

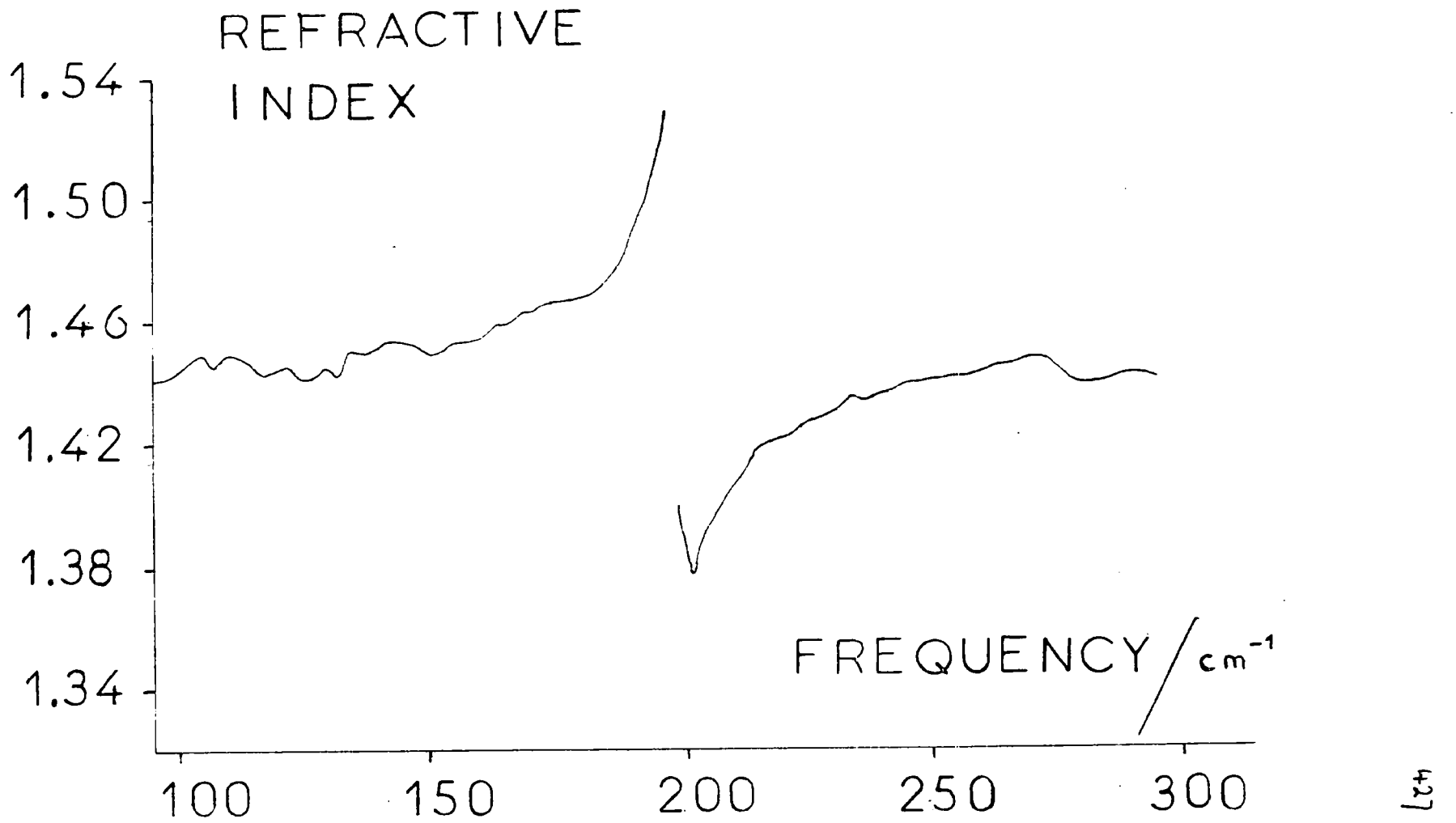

FIG. 8.6 0.0105 cm TEFLON REFRACTIVE INDEX

Table 8.3 Refractive index values for 0.0105 cm teflon

frequency /cm^{-1}	refractive index	frequency /cm^{-1}	refractive index
95.21	1.441	146.48	1.453
97.66	1.441	148.93	1.453
100.10	1.444	151.37	1.451
102.54	1.447	153.81	1.449
104.98	1.449	156.25	1.452
107.42	1.445	158.69	1.453
109.86	1.449	161.13	1.453
112.30	1.448	163.57	1.454
114.75	1.447	166.02	1.459
117.19	1.443	168.46	1.458
119.63	1.444	170.90	1.463
122.07	1.445	173.34	1.463
124.51	1.442	175.78	1.466
126.95	1.442	178.22	1.466
129.39	1.445	180.66	1.467
131.84	1.442	183.11	1.468
134.28	1.450	185.55	1.469
136.72	1.449	187.99	1.474
139.16	1.451	190.43	1.478
141.60	1.451	192.87	1.489
144.04	1.454	195.31	1.497

(continued)

Table 8.3 (continued)

frequency /cm^{-1}	refractive index	frequency /cm^{-1}	refractive index
197.75	1.512	249.02	1.439
200.20	1.528	251.46	1.440
202.64	1.399	253.91	1.440
205.08	1.378	256.35	1.441
207.52	1.391	258.79	1.441
209.96	1.397	261.23	1.442
212.40	1.404	263.67	1.443
214.84	1.409	266.11	1.445
217.29	1.417	268.55	1.445
219.73	1.420	271.00	1.447
222.17	1.421	273.44	1.447
224.61	1.423	275.88	1.444
227.05	1.426	278.32	1.440
229.49	1.428	280.76	1.439
231.93	1.429	283.20	1.439
234.38	1.432	285.64	1.440
236.82	1.435	288.09	1.441
239.26	1.434	290.53	1.442
241.70	1.436	292.97	1.442
244.14	1.436	295.41	1.441
246.58	1.438		

values $\Psi(\bar{\nu})$ of eqn. 8.8 can be replaced by the principal value of the phase-difference $\psi(\bar{\nu})$.

Table 8.4 shows the phase values for a 0.0134 cm thick sample of teflon. The value at 200.20 cm^{-1} showed a discontinuity, which resulted from the actual phase value of 3.34 ($=-3.02+2\pi$) being calculated as the principal phase value -3.02 by the programme DCH0690. Such discontinuities were easily removed by inspection, and subsequent replotting of the phase and refractive index spectra. Fig. 8.7 and table 8.5 show the corrected refractive index curve for the 0.0134 cm thick sample of teflon. Similarly table 8.6 shows the corrected path-difference values for a 0.0229 cm thick teflon sample. The figures in parenthesis are the values of the phase-difference within the principal value range. The phase-differences between 197.75 and 212.40 cm^{-1} have all been corrected by use of the $\pm m\pi$ factor of eqn. 8.8. This table shows that careful consideration of the phase-differences outside the principal value range needs to be taken. Fig. 8.8 and table 8.7 show the corrected refractive index values for this 0.0229 cm teflon sample. Prior knowledge of the shape of the dispersion curves for thinner teflon samples, where the phase-differences were always within the principal value range, enabled the correct phase values to be determined.

The discontinuities in the phase values were expected for the thicker samples as can be seen from eqn. 8.9. For phase-differences within the principal value range then the following inequality must hold;

$$|2(n(\bar{\nu})-\bar{n})d| < 1/2\bar{\nu}$$

However at $\bar{\nu}$ = 200.20 cm^{-1} and $n(\bar{\nu})$ = 1.493 for a teflon sample with d = 0.0229 cm and $\bar{n}$ = 1.419;

$$2(n(\bar{\nu})-\bar{n})d = 0.00339 \text{ cm}$$

and $1/2\bar{\nu}$ = 0.00250 cm

Hence $2(n(\bar{\nu})-\bar{n})d| \not< 1/2\bar{\nu}$ and the phase-difference would be expected to lie outside the range $-3.14<\psi(\bar{\nu})<+3.14$. From table 8.6 the phase value at 200.20 cm^{-1} was found to be 4.55 after correction.

Table 8.4 Phase values for 0.0134 cm teflon

frequency /cm^{-1}	phase /radians	frequency /cm^{-1}	phase /radians
95.21	-0.24	146.48	-0.16
97.66	-0.29	148.93	-0.18
100.10	-0.26	151.37	-0.18
102.54	-0.26	153.81	-0.17
104.98	-0.24	156.25	-0.15
107.42	-0.22	158.69	-0.06
109.86	-0.18	161.13	-0.08
112.30	-0.17	163.57	0.02
114.75	-0.17	166.02	0.07
117.19	-0.18	168.46	0.08
119.63	-0.21	170.90	0.12
122.07	-0.24	173.34	0.09
124.51	-0.25	175.78	0.12
126.95	-0.27	178.22	0.21
129.39	-0.32	180.66	0.30
131.84	-0.27	183.11	0.37
134.28	-0.22	185.55	0.52
136.72	-0.19	187.99	0.71
139.16	-0.17	190.43	0.87
141.60	-0.12	192.87	1.14
144.04	-0.15	195.31	1.54

(continued)

Table 8.4 (continued)

frequency /cm^{-1}	phase /radians	frequency /cm^{-1}	phase /radians
197.75	2.22	249.02	-0.98
200.20	3.34 (-3.02)	251.46	-0.89
202.64	0.41	253.91	-0.89
205.08	-2.56	256.35	-0.86
207.52	-2.96	258.79	-0.85
209.96	-2.60	261.23	-0.81
212.40	-2.33	263.67	-0.77
214.84	-2.10	266.11	-0.73
217.29	-1.82	268.55	-0.69
219.73	-1.65	271.00	-0.69
222.17	-1.52	273.44	-0.66
224.61	-1.44	275.88	-0.71
227.05	-1.33	278.32	-0.85
229.49	-1.28	280.76	-0.92
231.93	-1.25	283.20	-0.89
234.38	-1.22	285.64	-0.86
236.82	-1.16	288.09	-0.81
239.26	-1.10	290.53	-0.71
241.70	-1.07	292.97	-0.76
244.14	-1.02	295.41	-0.81
246.58	-0.98		

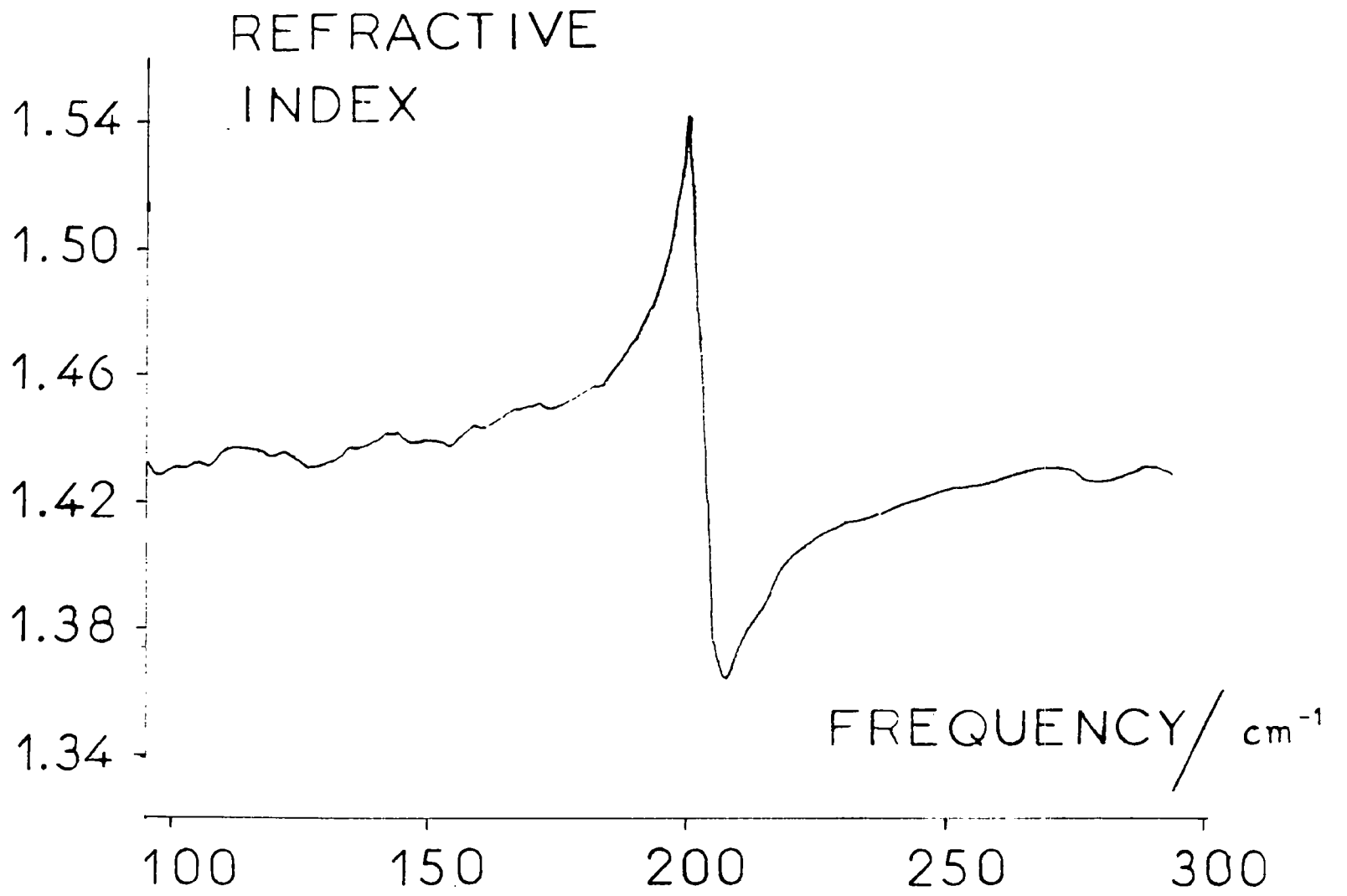

FIG. 8.7 0.0134 cm TEFLON REFRACTIVE INDEX

Table 8.5 Refractive index values for 0.1034 cm teflon

frequency /cm^{-1}	refractive index	frequency /cm^{-1}	refractive index
95.21	1.432	146.48	1.439
97.66	1.428	148.93	1.439
100.10	1.430	151.37	1.439
102.54	1.430	153.81	1.438
104.98	1.432	156.25	1.440
107.42	1.431	158.69	1.444
109.86	1.436	161.13	1.443
112.30	1.437	163.57	1.446
114.75	1.436	166.02	1.449
117.19	1.436	168.46	1.449
119.63	1.434	170.90	1.451
122.07	1.435	173.34	1.449
124.51	1.434	175.78	1.451
126.95	1.431	178.22	1.453
129.39	1.432	180.66	1.456
131.84	1.432	183.11	1.457
134.28	1.437	185.55	1.462
136.72	1.437	187.99	1.468
139.16	1.438	190.43	1.472
141.60	1.441	192.87	1.482
144.04	1.441	195.31	1.493

Table 8.5 (continued)

frequency /cm^{-1}	refractive index	frequency /cm^{-1}	refractive index
197.75	1.513	249.02	1.424
200.20	1.543	251.46	1.425
202.64	1.457	253.91	1.425
205.08	1.372	256.35	1.426
207.52	1.362	258.79	1.427
209.96	1.373	261.23	1.428
212.40	1.381	263.67	1.429
214.84	1.387	266.11	1.430
217.29	1.396	268.55	1.430
219.73	1.402	271.00	1.432
222.17	1.405	273.44	1.432
224.61	1.408	275.88	1.431
227.05	1.411	278.32	1.428
229.49	1.413	280.76	1.427
231.93	1.414	283.20	1.427
234.38	1.415	285.64	1.428
236.82	1.417	288.09	1.430
239.26	1.418	290.53	1.431
241.70	1.420	292.97	1.431
244.14	1.421	295.41	1.430
246.58	1.423		

Table 8.6 Phase values for 0.0229 cm teflon

frequency /cm^{-1}	phase /radians	frequency /cm^{-1}	phase /radians
95.21	-0.17	146.58	-0.11
97.66	-0.23	148.93	-0.10
100.10	-0.17	151.37	-0.08
102.54	-0.27	153.81	-0.04
104.98	-0.27	156.25	0.00
107.42	-0.26	158.69	0.09
109.86	-0.20	161.13	0.12
112.30	-0.19	163.57	0.13
114.75	-0.23	166.02	0.14
117.19	-0.24	168.46	0.21
119.63	-0.23	170.90	0.31
122.07	-0.25	173.34	0.46
124.51	-0.23	175.78	0.50
126.95	-0.20	178.22	0.64
129.39	-0.13	180.66	0.67
131.84	-0.18	183.11	0.87
134.28	-0.24	185.55	1.09
136.72	-0.28	187.99	1.33
139.16	-0.16	190.43	1.58
141.60	-0.18	192.87	1.97
144.04	-0.06	195.31	2.72

(continued)

Table 8.6 (continued)

frequency /cm^{-1}	phase /radians	frequency /cm^{-1}	phase /radians
197.75	3.38 (-2.90)	249.02	-1.25
200.20	4.55 (-1.73)	251.46	-1.14
202.64	3.96 (-2.32)	253.91	-1.06
205.08	3.29 (-2.99)	256.35	-0.98
207.52	-4.21 (2.07)	258.79	-0.96
209.96	-3.74 (2.54)	261.23	-0.90
212.40	-3.30 (2.98)	263.67	-0.84
214.84	-2.94	266.11	-0.81
217.29	-2.56	268.55	-0.75
219.73	-2.35	271.00	-0.65
222.17	-2.20	273.44	-0.72
224.61	-2.04	275.88	-0.85
227.05	-1.85	278.32	-1.05
229.49	-1.77	280.76	-1.16
231.93	-1.68	283.20	-1.20
234.38	-1.59	285.64	-1.10
236.82	-1.49	288.09	-0.98
239.26	-1.48	290.53	-0.86
241.70	-1.43	292.97	-0.93
244.14	-1.39	295.41	-0.98
246.58	-1.34		

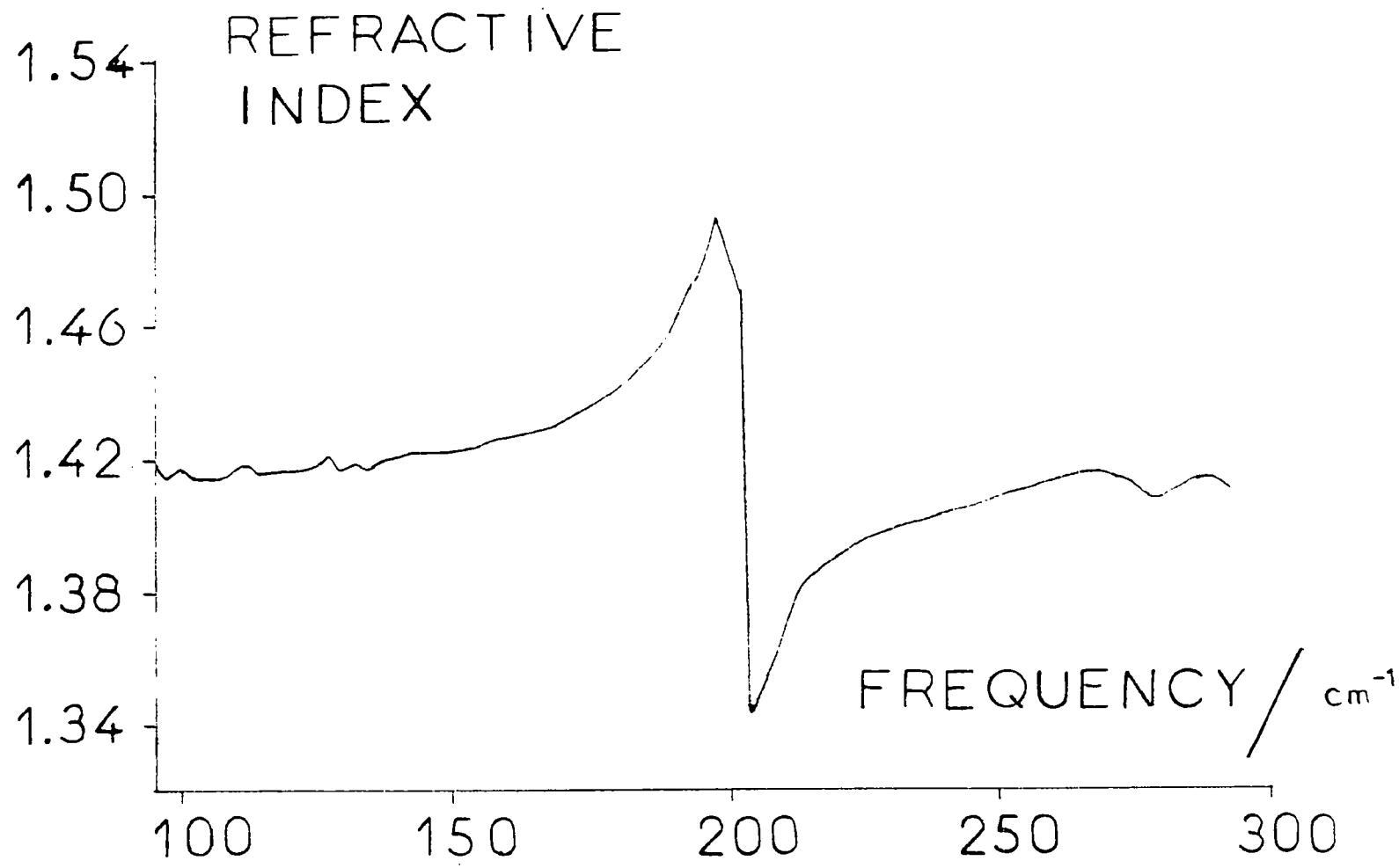

FIG. 8.8 0.0229 cm TEFLON REFRACTIVE INDEX

Table 8.7 Refractive index values for 0.0229 cm teflon

frequency /cm^{-1}	refractive index	frequency /cm^{-1}	refractive index
95.21	1.418	146.48	1.421
97.66	1.415	148.93	1.421
100.10	1.417	151.37	1.422
102.54	1.414	153.81	1.422
104.98	1.414	156.25	1.423
107.42	1.414	158.69	1.425
109.86	1.417	161.13	1.426
112.30	1.418	163.57	1.426
114.75	1.416	166.02	1.427
117.19	1.416	168.46	1.428
119.63	1.416	170.90	1.430
122.07	1.417	173.34	1.432
124.51	1.417	175.78	1.434
126.95	1.417	178.22	1.436
129.39	1.421	180.66	1.437
131.84	1.417	183.11	1.440
134.28	1.418	185.55	1.444
136.72	1.416	187.99	1.448
139.16	1.419	190.43	1.452
141.60	1.419	192.87	1.459
144.04	1.422	195.31	1.472

(continued)

Table 8.7 (continued)

frequency /cm^{-1}	refractive index	frequency /cm^{-1}	refractive index
197.75	1.474	249.02	1.406
200.20	1.493	251.46	1.408
202.64	1.483	253.91	1.409
205.08	1.470	256.35	1.410
207.52	1.344	258.79	1.411
209.96	1.353	261.23	1.412
212.40	1.361	263.67	1.413
214.84	1.376	266.11	1.414
217.29	1.382	268.55	1.415
219.73	1.386	271.00	1.415
222.17	1.389	273.44	1.414
224.61	1.392	275.88	1.413
227.05	1.395	278.32	1.410
229.49	1.397	280.76	1.409
231.93	1.398	283.20	1.409
234.38	1.399	285.64	1.410
236.82	1.400	288.09	1.412
239.26	1.402	290.53	1.413
241.70	1.403	292.97	1.413
244.14	1.404	295.41	1.412
246.58	1.405		

8.3 Reproducibility and precision of refractive index spectra

To determine the reproducibility of the refractive index curves ten spectra were recorded for the same teflon sample. Ten dispersive interferograms were recorded for a 0.0083 cm teflon sample, and ten background interferograms were recorded alternately with the sample tapes. This procedure required repositioning of the teflon sample for each interferogram. This ensured that the reproducibility of the refractive index curve was being calculated taking into account imprecise positioning of the sample in the beam. When all the dispersive interferograms had been recorded, then the same sample was used to obtain ten non-dispersive interferograms, so that the intensities obtained from refractive index and absorption curves could be compared. When these interferograms were completed the teflon sample was cut in half across a diameter, and the half-sample technique used to determine $\bar{x}$, the displacement of the brightest fringe. 10 determinations of $\bar{x}$ were made and the average was found to be 0.0073±0.0002 cm. The thickness d of the sample was measured using a micrometer, and was found to be 0.0083±0.0002 cm. The compound error for the mean refractive index $\bar{n}$ was calculated as 0.01, which gave the mean refractive index ($1+\bar{x}/2d$ in eqn. 8.8) as 1.44±0.01. The 10 refractive index curves were computed using this average value for the mean refractive index over the full band-width of the incident radiation.

Values for the refractive index at 97.66 cm^{-1} were used to calculate the precision for the refractive index at any frequency. The 10 refractive index values were 1.448, 1.446, 1.428, 1.400, 1.451, 1.476, 1.371, 1.454, 1.445, and 1.400 which gave an average of 1.440, and a standard deviation of ±0.033. These figures indicated that the phase values themselves were the major contributory factor to the errors involved in the refractive index calculation. The errors in mean level for the refractive index are small when compared with the errors involved in calculating the varying portion of the refractive index $(\phi(\bar{\nu})-\phi_0(\bar{\nu}))/4\pi\bar{\nu}d$.

The refractive index curves obtained from the first 5 dispersive

interferograms recorded for the 0.0083 cm teflon sample are shown in fig. 8.9 and table 8.8. These curves indicated that whilst the actual refractive index values can only be determined to a precision of ±0.03, the shapes of the curves matched very well, and indicated that the differences in refractive index caused by the absorption will be highly reproducible. (See under intensity calculation for the quantitative measurement of this refractive index difference across the dispersion.)

The effect of beam divergence within the interferometer upon the precision of the refractive index values was also calculated. As already mentioned a diaphragm of diameter 1.9 cm was used to restrict the cone of radiation to the size of the dispersive sample. The sample has a diameter of 3.0 cm, and hence the half-angle β of the cone of radiation incident upon the sample was calculated as $\tan^{-1}(0.55/15.0)$ giving $\beta = 1.9^{o}$. The radiation passing through the sample was presumed to be distributed uniformly over the whole conical solid angle, and does not pass uniformly through the sample. Chamberlain and Gebbie (212) replaced the thickness d of the sample in eqn. 8.8 by an average thickness d', determined by this maximum half-angle β for the cone of radiation incident upon the sample. The relationship between d and d' was given as;

$$d' = d\{1+1/4n(1-\sin\beta\cos\beta/\beta)\} \qquad 8.14$$

For $\beta=1.9^{o}$, $\cos\beta=0.9995$, $\sin\beta=0.0332$, $\beta=0.0332$ radians. Therefore d' = 1.00009 d for a typical refractive index value of 1.4. Now since;

$$n(\bar{\nu}) = 1 + \bar{x}/2d + 1/4\pi\bar{\nu}d\{\phi(\bar{\nu})-\phi_{o}(\bar{\nu})\}$$

For the 0.0083 cm teflon sample $\bar{x}$=0.0073 cm, therefore $\bar{n}$ becomes 1.43972, where it was originally 1.43976, before correction for the beam divergence. The correction of 0.00004 was not significant with respect to the precision for the refractive index of ±0.03 already calculated, and hence could be ignored.

The effect of beam divergence on the varying part of the refractive index $(\phi(\bar{\nu})-\phi_{o}(\bar{\nu}))/4\pi\bar{\nu}d$ was also determined. For a refractive index value determined at 200 cm^{-1}, and a typical phase difference, this varying part

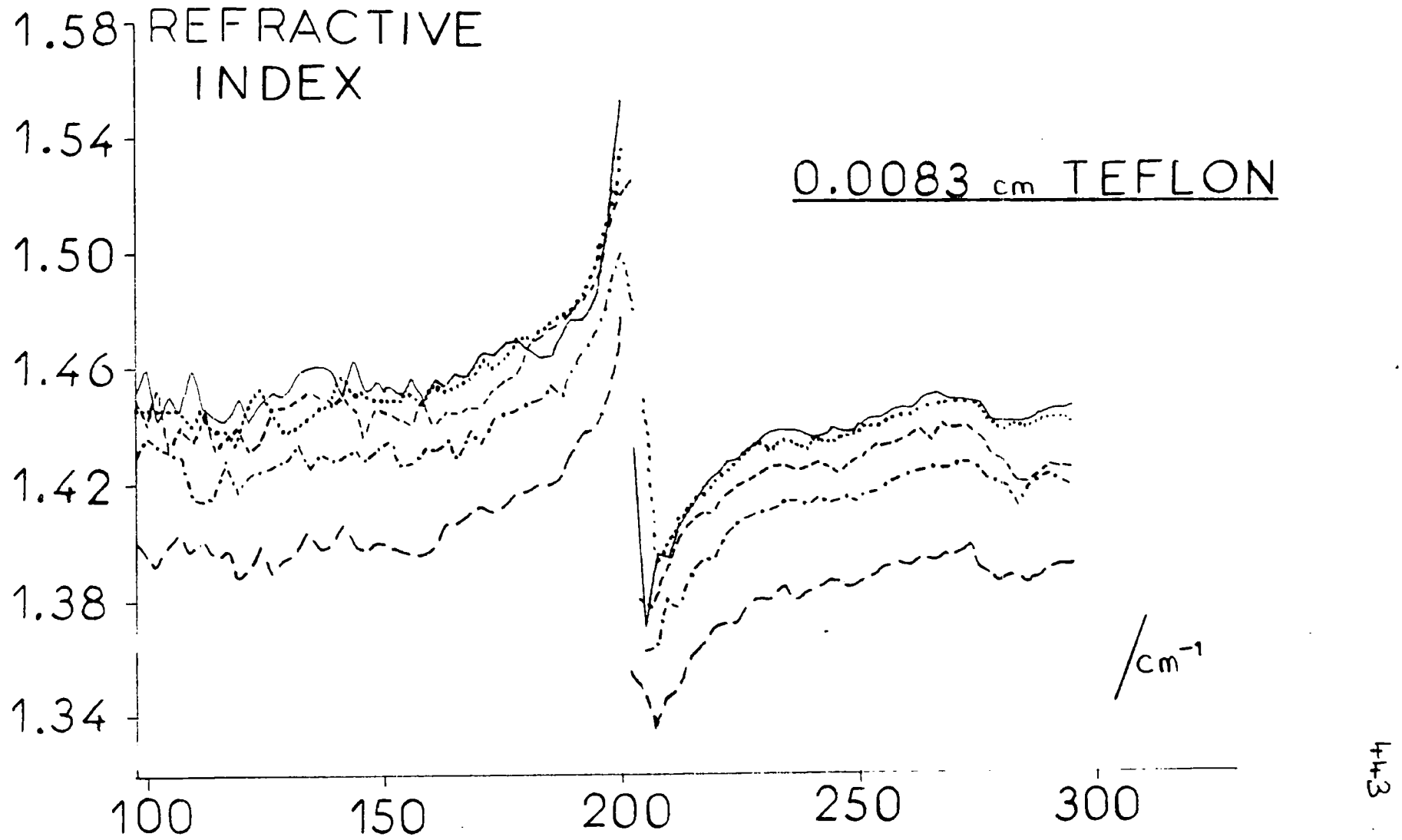

FIG. 8.9 REPRODUCIBILITY OF REFRACTIVE INDEX

Table 8.8 Reproducibilty of refractive index curves for 0.0083 cm teflon

frequency /cm^{-1}	refractive index				
97.66	1.448	1.446	1.428	1.399	1.451
100.10	1.459	1.458	1.435	1.397	1.439
102.54	1.441	1.444	1.433	1.390	1.453
104.98	1.450	1.446	1.431	1.398	1.431
107.42	1.445	1.445	1.429	1.403	1.439
109.86	1.439	1.459	1.415	1.397	1.435
112.30	1.447	1.440	1.414	1.400	1.445
114.75	1.443	1.439	1.415	1.394	1.431
117.19	1.442	1.439	1.427	1.397	1.436
119.63	1.449	1.432	1.417	1.387	1.439
122.07	1.440	1.448	1.422	1.391	1.432
124.51	1.448	1.452	1.424	1.399	1.435
126.95	1.451	1.445	1.426	1.388	1.446
129.39	1.450	1.446	1.427	1.393	1.437
131.84	1.457	1.449	1.433	1.396	1.439
134.28	1.460	1.451	1.426	1.403	1.442
136.72	1.460	1.451	1.429	1.398	1.446
139.16	1.458	1.449	1.428	1.399	1.447
141.60	1.450	1.457	1.429	1.406	1.450
144.04	1.461	1.452	1.431	1.400	1.446
146.48	1.451	1.451	1.428	1.396	1.437
148.93	1.455	1.446	1.432	1.400	1.445
151.37	1.449	1.453	1.433	1.399	1.444
153.81	1.449	1.451	1.426	1.398	1.442
156.25	1.456	1.451	1.427	1.396	1.441
158.69	1.450	1.447	1.432	1.396	1.449

Table 8.8 (continued)

frequency /cm^{-1}	refractive index				
161.13	1.454	1.456	1.431	1.398	1.440
163.57	1.454	1.452	1.434	1.406	1.443
166.02	1.457	1.454	1.427	1.406	1.444
168.46	1.457	1.456	1.437	1.409	1.446
170.90	1.464	1.462	1.433	1.412	1.446
173.34	1.464	1.460	1.442	1.410	1.452
175.78	1.468	1.463	1.443	1.412	1.455
178.22	1.468	1.470	1.446	1.417	1.457
180.66	1.466	1.470	1.447	1.417	1.465
183.11	1.472	1.469	1.449	1.420	1.463
185.55	1.475	1.473	1.453	1.419	1.463
187.99	1.477	1.475	1.450	1.422	1.470
190.43	1.479	1.480	1.460	1.432	1.476
192.87	1.487	1.483	1.466	1.437	1.476
195.31	1.496	1.490	1.472	1.438	1.484
197.75	1.511	1.507	1.490	1.451	1.510
200.20	1.551	1.534	1.498	1.477	1.518
202.64	1.432	1.400	1.479	1.354	1.523
205.08	1.370	1.449	1.362	1.348	1.380
207.52	1.395	1.389	1.363	1.336	1.378
209.96	1.394	1.399	1.379	1.346	1.388
212.40	1.408	1.404	1.377	1.350	1.398
214.84	1.410	1.414	1.388	1.358	1.405
217.29	1.418	1.417	1.393	1.364	1.409
219.73	1.422	1.419	1.393	1.369	1.409
222.17	1.426	1.427	1.403	1.371	1.415

Table 8.8 (continued)

frequency /cm^{-1}	refractive index				
224.61	1.428	1.428	1.406	1.372	1.418
227.05	1.432	1.432	1.408	1.378	1.420
229.49	1.435	1.434	1.410	1.380	1.423
231.93	1.437	1.431	1.411	1.380	1.425
234.38	1.437	1.435	1.413	1.384	1.426
236.82	1.437	1.433	1.414	1.380	1.424
239.26	1.436	1.432	1.412	1.382	1.425
241.70	1.435	1.438	1.414	1.383	1.427
244.14	1.438	1.434	1.414	1.385	1.426
246.58	1.437	1.436	1.414	1.386	1.424
249.02	1.437	1.437	1.413	1.384	1.427
251.46	1.441	1.440	1.416	1.385	1.428
253.91	1.442	1.440	1.417	1.388	1.432
256.35	1.443	1.441	1.419	1.390	1.433
258.79	1.445	1.444	1.421	1.392	1.434
261.23	1.445	1.444	1.423	1.391	1.436
263.67	1.449	1.446	1.424	1.394	1.438
266.11	1.450	1.447	1.425	1.393	1.435
268.55	1.448	1.448	1.425	1.395	1.440
271.00	1.449	1.448	1.426	1.395	1.439
273.44	1.448	1.449	1.426	1.398	1.439
275.88	1.447	1.446	1.423	1.390	1.436
278.32	1.441	1.440	1.420	1.388	1.430
280.76	1.441	1.438	1.419	1.386	1.428
283.20	1.441	1.440	1.412	1.388	1.431
285.64	1.441	1.439	1.418	1.387	1.430

became 0.143802 when beam divergence was taken into account, when it had been 0.143814 originally. This change of 0.00001 was once again not significant with respect to the precision of the curves already given. Thus the beam divergence was seen to have no effect upon the precision of the refractive index values determined.

8.4.1 Theory for intensity calculations

The integrated strength of absorption bands, and their relative positions determine the refractive index values in any spectral region. Various expressions have been used which relate the measured refractive index values to the integrated absorption strengths for associated bands. The use of these equations will be discussed in the following section.

The absorption coefficient $\alpha(\bar{\nu})$, and the refractive index can be related (225);

$$N(\bar{\nu}) = n(\bar{\nu}) - j\alpha(\bar{\nu})/4\pi\bar{\nu} \qquad 8.15$$

where $N(\bar{\nu})$ is the complex refractive index at wavenumber $\bar{\nu}$ cm^{-1}

$\alpha(\bar{\nu})$ is the absorption coefficient per cm at wavenumber $\bar{\nu}$ cm^{-1}

$n(\bar{\nu})$ is the real refractive index at wavenumber $\bar{\nu}$ cm^{-1}

The integrated absorption strength A_i of the ith absorption feature centred at wavenumber $\bar{\nu}_i$ has already been determined as (eqn. 4.1);

$$A_i = \int_i \alpha(\bar{\nu}).d\bar{\nu}$$

and has been used for calculation of band intensities from photometric measurements of $\alpha(\bar{\nu})$. (See section 4.2.)

The absorption coefficient per cm can be written as (226);

$$\alpha(\bar{\nu}) = 4\pi\bar{\nu}n(\bar{\nu})\kappa(\bar{\nu}) \qquad 8.16$$

where $\kappa(\bar{\nu})$ is the extinction coefficient at wavenumber $\bar{\nu}$ cm^{-1}

Substitution of 8.16 into 8.15 gives;

$$N(\bar{\nu}) = n(\bar{\nu}) - jn(\bar{\nu})\kappa(\bar{\nu})$$

$$N(\bar{\nu}) = n(\bar{\nu})(1-j\kappa(\bar{\nu})) \qquad 8.17$$

This equation shows that the real and im aginary parts of the refractive index are dependent, and are related through the extinction coefficient.

Consideration of particular models for the absorption processes have enabled explicit relationships between the real and immaginary parts in eqn. 8.17 to be determined. For a series of classical, damped, harmonic oscillators immersed in an isotropic medium $n(\bar{\nu})$ and $\alpha(\bar{\nu})$ could be determined by using Lorentzian type equations (226). The Claussius-Mosotti approximation (226,227) gave the real part of the refractive index $n(\bar{\nu})$ at wavenumber $\bar{\nu}$ cm^{-1} as;

$$n(\bar{\nu}) = n_V(\bar{\nu}) + \Sigma_i \, A_i/2\pi^2(1/(\bar{\nu}_i^2-\bar{\nu}^2)+\Gamma_i^2) \qquad 8.18$$

where $n_V(\bar{\nu})$ is the extrapolated contribution to the refractive index at wavenumber $\bar{\nu}$ cm^{-1} in the infrared region, which arises from resonances at wavenumbers higher than those within the infrared region. The postscript V indicates that resonances affecting the refractive index in the infrared often occur in the visible spectral region.

A_i is the integrated absorption strength, as already defined, for the i.th absorption band, which has a maximum absorption coefficient per cm $\alpha(\bar{\nu})$ at wavenumber $\bar{\nu}_i$ cm^{-1}.

$$\Gamma_i^2 = (\Delta\bar{\nu}_{\frac{1}{2}i}\bar{\nu})^2/(\bar{\nu}_i^2-\bar{\nu}^2) \qquad 8.19$$

$\Delta\bar{\nu}_{\frac{1}{2}i}$ is the total width at half maximum of the absorption coefficient per cm $\alpha(\bar{\nu})$ for the i.th band.

Γ_i^2 as given by eqn. 8.19 is a line shape term, which takes into account the finite widths of the absorption features in eqn. 8.18. Fig. 8.10 shows the variation of refractive index $n(\bar{\nu})$ at wavenumber $\bar{\nu}$ cm^{-1}, through the absorption band. The maximum and minimum of refractive index are clearly visible in the region of the anomolous dispersion around the band centre $\bar{\nu}_i$ cm^{-1}. The maximum refractive index occurs at $\bar{\nu}_i-\frac{1}{2}\Delta\bar{\nu}_{\frac{1}{2}i}$ cm^{-1}, and the minimum at $\bar{\nu}_i+\frac{1}{2}\Delta\bar{\nu}_{\frac{1}{2}i}$ cm^{-1}. The maximum refractive index difference, that is the difference between maximum and minimum refractive index, in the region of the absorption is known as the refraction amplitude Δ_i cm^{-1}.

Now $$\Delta_i = n(\bar{\nu}_i-\tfrac{1}{2}\Delta\bar{\nu}_{\frac{1}{2}i}) - n(\bar{\nu}_i+\tfrac{1}{2}\Delta\bar{\nu}_{\frac{1}{2}i}) \qquad 8.20$$

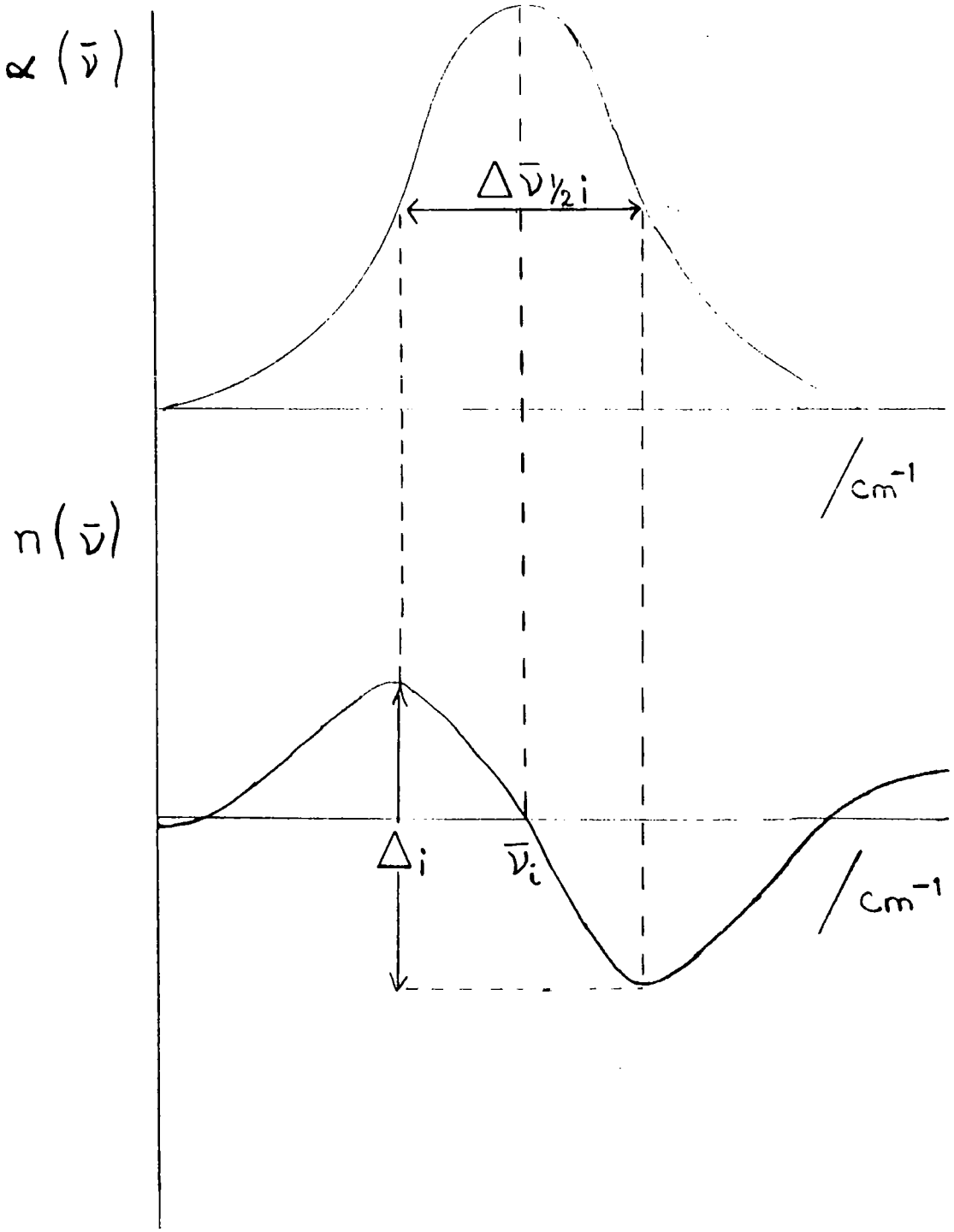

FIG. 8.10 REFRACTION AMPLITUDE

A simple equation for determining the integrated absorption strength has been obtained by assuming contributions from other infrared bands are negligible, then the sum over i bands, in eqn. 8.18, can be replaced by the integrated intensity for a single band.

$$n(\bar{\nu}) = n_V(\bar{\nu}) + A_i/2\pi^2\{(\bar{\nu}_i^2-\bar{\nu}^2)+\Gamma_i^2\} \qquad 8.21$$

Substituting for $n(\bar{\nu}_i-\frac{1}{2}\Delta\bar{\nu}_{\frac{1}{2}i})$ and $n(\bar{\nu}_i+\frac{1}{2}\Delta\bar{\nu}_{\frac{1}{2}i})$ from eqn. 8.21 into 8.20 gives;

$$\begin{aligned}\Delta_i = {} & n_V(\bar{\nu}_i-\tfrac{1}{2}\Delta\bar{\nu}_{\frac{1}{2}i}) - n_V(\bar{\nu}_i+\tfrac{1}{2}\Delta\bar{\nu}_{\frac{1}{2}i}) \\ & + A_i/2\pi^2\{(\bar{\nu}_i^2-(\bar{\nu}_i-\tfrac{1}{2}\Delta\bar{\nu}_{\frac{1}{2}i})^2) + \frac{\Delta\bar{\nu}_{\frac{1}{2}i}^2(\bar{\nu}_i-\Delta\bar{\nu}_{\frac{1}{2}i})^2}{(\bar{\nu}_i^2-(\bar{\nu}_i-\frac{1}{2}\Delta\bar{\nu}_{\frac{1}{2}i})^2)}\} \\ & - A_i/2\pi^2\{(\bar{\nu}_i^2-(\bar{\nu}_i+\tfrac{1}{2}\Delta\bar{\nu}_{\frac{1}{2}i})^2) + \frac{\Delta\bar{\nu}_{\frac{1}{2}i}^2(\bar{\nu}_i+\frac{1}{2}\Delta\bar{\nu}_{\frac{1}{2}i})^2}{(\bar{\nu}_i^2-(\bar{\nu}_i+\frac{1}{2}\Delta\bar{\nu}_{\frac{1}{2}i})^2)}\end{aligned} \qquad 8.22$$

By making the further reasonable assumption that;

$$n_V(\bar{\nu}_i-\tfrac{1}{2}\Delta\bar{\nu}_{\frac{1}{2}i}) = n_V(\bar{\nu}_i+\tfrac{1}{2}\Delta\bar{\nu}_{\frac{1}{2}i})$$

that is that the extrapolated value for the refractive index in the region of the infrared absorption, due to absorptions in the visible spectral region, was constant over the infrared absorption, then eqn. 8.22 can be simplified to give;

$$\begin{aligned}\Delta_i = {} & A_i/2\pi^2(\bar{\nu}_i\Delta\bar{\nu}_{\frac{1}{2}i}-\tfrac{1}{4}\Delta\bar{\nu}_{\frac{1}{2}i}^2) + \frac{\Delta\bar{\nu}_{\frac{1}{2}i}^2(\bar{\nu}_i-\Delta\bar{\nu}_{\frac{1}{2}i})^2}{(\bar{\nu}_i\Delta\bar{\nu}_{\frac{1}{2}i}-\frac{1}{4}\Delta\bar{\nu}_{\frac{1}{2}i}^2)} \\ & - 1/(-\bar{\nu}_i\Delta\bar{\nu}_{\frac{1}{2}i}-\tfrac{1}{4}\Delta\bar{\nu}_{\frac{1}{2}i}^2) + \frac{\Delta\bar{\nu}_{\frac{1}{2}i}^2(\bar{\nu}_i+\Delta\bar{\nu}_{\frac{1}{2}i})^2}{(-\bar{\nu}_i\Delta\bar{\nu}_{\frac{1}{2}i}-\frac{1}{4}\Delta\bar{\nu}_{\frac{1}{2}}^2)}\end{aligned} \qquad 8.23$$

If $\Delta\bar{\nu}_{\frac{1}{2}i} \ll \bar{\nu}_i$, that is the band width at half height is very much smaller than the wavenumber of maximum absorption coefficient, then $\Delta\bar{\nu}_{\frac{1}{2}i}^2$ is negligible with respect to $\bar{\nu}_1^2$.

By neglecting $\Delta\bar{\nu}_{\frac{1}{2}i}^2$ terms eqn. 8.23 becomes;

$$\begin{aligned}\Delta_i = {} & A_i/2\pi^2(\bar{\nu}_i\Delta\bar{\nu}_{\frac{1}{2}i} + \Delta\bar{\nu}_{\frac{1}{2}}(\bar{\nu}_i^2-2\bar{\nu}_i\Delta\bar{\nu}_{\frac{1}{2}i}+\tfrac{1}{4}\Delta\bar{\nu}_{\frac{1}{2}i}^2)/\bar{\nu}_i \\ & -1/(-\bar{\nu}_i\Delta\bar{\nu}_{\frac{1}{2}i} + \Delta\bar{\nu}_{\frac{1}{2}i}(\bar{\nu}_i^2+2\bar{\nu}_i\Delta\bar{\nu}_{\frac{1}{2}i}+\tfrac{1}{4}\Delta\bar{\nu}_{\frac{1}{2}i}^2))/\bar{\nu}_i\end{aligned} \qquad 8.24$$

On multiplying up and neglecting $\Delta\bar{\nu}_{\frac{1}{2}i}^{\,2}$ and $\Delta\bar{\nu}_{\frac{1}{2}i}^{\,3}$ terms this becomes;

$$\Delta_i = A_i/2\pi^2\{(\bar{\nu}_i\Delta\bar{\nu}_{\frac{1}{2}i}+\bar{\nu}_i\Delta\bar{\nu}_{\frac{1}{2}i})\} - A_i/2\pi^2\{(-\bar{\nu}_i\Delta\bar{\nu}_{\frac{1}{2}i}-\bar{\nu}_i\Delta\bar{\nu}_{\frac{1}{2}i})\} \quad 8.25$$

$$\Delta_i = A_i/2\pi^2(1/2\bar{\nu}_i\Delta\bar{\nu}_{\frac{1}{2}i} + 1/2\bar{\nu}_i\Delta\bar{\nu}_{\frac{1}{2}i}) \quad 8.26$$

$$\Delta_i = A_i/2\pi^2\bar{\nu}_i\Delta\bar{\nu}_{\frac{1}{2}i} \quad 8.27$$

$$A_i = \Delta_i 2\pi^2\bar{\nu}_i\Delta\bar{\nu}_{\frac{1}{2}i} \quad 8.28$$

Eqn. 8.28 gives the integrated absorption strength A_i in terms of the refraction amplitude Δ_i, the wavenumber of maximum absorption $\bar{\nu}_i$ and the half-band width $\Delta\bar{\nu}_{\frac{1}{2}i}$. These 3 quantities can readily be determined from the dispersion curve to give preliminary intensity measurements. The turning points of the refractive index curve can easily be determined by inspection, and the refraction amplitude and half-band width thus calculated. To determine the band centre the band was assumed to be symmetrical, so that the mean frequency for maximum and minimum refractive index was taken as the wavenumber of maximum absorption.

8.4.2. Preliminary intensity calculations for 0.0083 cm teflon

Table 8.9 shows the maximum and minimum refractive index observed for the 10 dispersive spectra of the 0.0083 cm teflon sample recorded as detailed in section 8.2. The calculated values for $\Delta\bar{\nu}_{\frac{1}{2}i}$ and Δ_i were used in eqn. 8.28 to calculate the absorption strengths for the 10 curves. The average absorption strength for the 202 cm^{-1} absorption was found to be 3 010 $\pm$860 cm^{-2}. The average half-band width was calculated as 4.8$\pm$1.4 cm^{-1}.

For comparison with the dispersion work 10 ratioed transmission spectra for the 0.0083 cm teflon sample were recorded and computed. Typical absorption curves are shown in fig. 8.11. The integrated absorption intensity for the 202 cm^{-1} teflon absorption was calculated as detailed in chapter 4. Table 8.10 shows the average of computer and planimeter intensity for each spectrum. The average intensity for the computer and planimeter intensities for the 10 absorption curves was 4 150$\pm$70 cm^{-2}. This value suggested that the preliminary intensity values from the dispersion curves were low.

Table 8.9 Refractive index/frequency data for 0.0083 cm teflon

index	n_{max}	$\bar{\nu}n_{max}$ /cm^{-1}	n_{min}	$\bar{\nu}n_{min}$ /cm^{-1}	$\bar{\nu}_i$ /cm^{-1}	$\Delta\bar{\nu}_{\frac{1}{2}}$ /cm^{-1}	Δ_i	$10^{-3}A_i$ /cm^{-2}
1	1.482	201.42	1.336	206.30	203.86	4.88	0.146	2.86
2	1.584	202.64	1.382	207.52	205.08	4.88	0.202	3.99
3	1.536	200.20	1.398	206.30	203.25	6.10	0.137	3.36
4	1.530	201.42	1.388	206.30	203.86	5.12	0.141	2.90
5	1.555	201.42	1.390	203.86	202.64	2.44	0.166	1.62
6	1.523	202.64	1.387	208.74	205.69	6.10	0.135	3.35
7	1.477	200.20	1.326	203.86	202.03	3.66	0.151	2.21
8	1.560	203.86	1.356	206.30	205.08	2.44	0.204	2.02
9	1.534	200.20	1.389	207.52	203.86	7.32	0.144	4.25
10	1.551	200.20	1.370	205.08	202.64	4.88	0.181	3.53

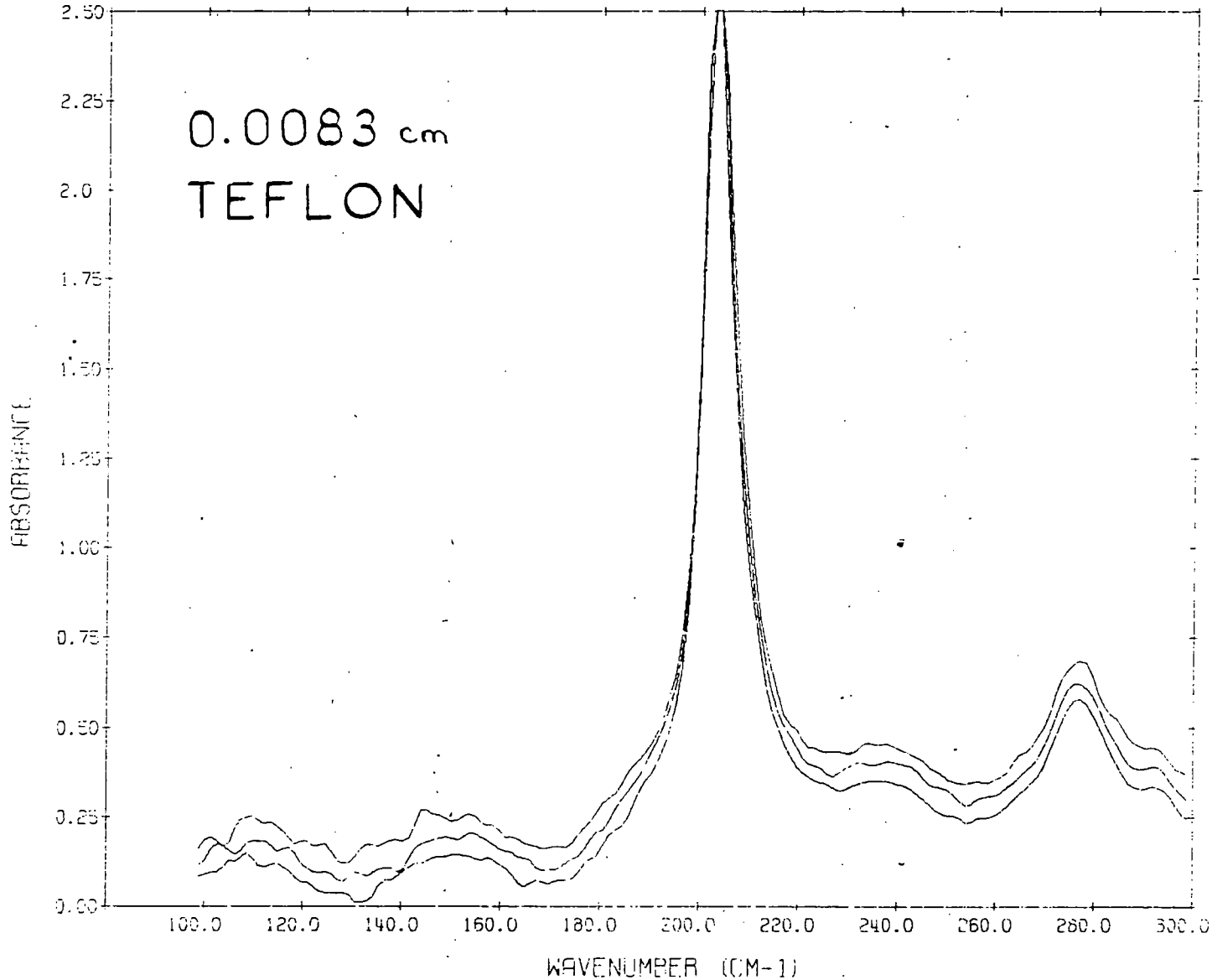

FIG. 8.11 REPRODUCIBILITY TRANSMISSION

Table 8.10 Transmission intensities for 0.0083 cm teflon

index	intensity /cm^{-2}
1	4250
2	3960
3	4200
4	4140
5	4130
6	4160
7	4210
8	4220
9	4110
10	4120

8.4.3. More sophisticated fitting techniques for intensity calculations

Eqn. 8.18 related the real refractive index $n(\bar{\nu})$ at wavenumber $\bar{\nu}$ cm^{-1} to the absorption strength A_i cm^{-2} for the various absorptions in the infrared region;

$$n(\bar{\nu}) = n_V(\bar{\nu}) + \Sigma_i \, A_i/2\pi^2 \, (1/(\bar{\nu}_i^{\,2}-\bar{\nu}^2)+\Gamma_i^{\,2} \qquad 8.18$$

If $\bar{\nu}'$ is taken to represent a wavenumber below that of the centre of resonance $\bar{\nu}_i$, and $\bar{\nu}''$ a wavenumber above $\bar{\nu}_i$ then;

$$n(\bar{\nu}')-n(\bar{\nu}'') = n_V(\bar{\nu}')-n_V(\bar{\nu}'')+\Sigma_i A_i/2\pi^2((\bar{\nu}_i^{\,2}-\bar{\nu}'^2)+\Gamma_i'^2) - \Sigma_i A_i/2\pi^2((\bar{\nu}_i^{\,2}-\bar{\nu}''^2)+\Gamma_i''^2) \qquad 8.29$$

By assuming that the extrapolated contribution to the refractive index from resonances from wavenumbers outside the infrared region remain constant over the region of resonance then;

$$n_V(\bar{\nu}') = n_V(\bar{\nu}'') \qquad 8.30$$

and when writing $n(\bar{\nu}')-n(\bar{\nu}'') = \delta(\bar{\nu}',\bar{\nu}'')$

then $$\delta(\bar{\nu}',\bar{\nu}'') = \Sigma_i A_i g_i(\bar{\nu}',\bar{\nu}'')/2\pi^2 \qquad 8.31$$

$$\text{where } g_i = 1/((\bar{\nu}_i^{\,2}-\bar{\nu}'^2)+\Gamma_i'^2) - 1/((\bar{\nu}_i^{\,2}-\bar{\nu}''^2)+\Gamma_i''^2) \qquad 8.32$$

Eqn. 8.31 represents the refractive index difference at wavenumbers either side of a central resonance at wavenumber $\bar{\nu}_i$ cm^{-1}, and indicates that this difference is due to the sum of all absorption strengths for resonances throughout the infrared region. The refractive index in the region of a resonance is due primarily to the resonance feature itself, but also contains contributions due to resonances $\bar{\nu}_j$, which have been separated out as below;

$$\delta(\bar{\nu}',\bar{\nu}'') = A_i g_i(\bar{\nu}',\bar{\nu}'')/2\pi^2 + \Sigma_{j\neq 1} A_j g_j(\bar{\nu}',\bar{\nu}'')/2\pi^2 \qquad 8.33$$

The sum term now represents the effect on the refractive index difference due to all infrared resonances, excepting that centred at wavenumber $\bar{\nu}_i$ cm^{-1}. The effect of resonances outside the infrared have already been considered in the term $n_V(\bar{\nu})$.

In certain circumstances, which are detailed below, the line

shape term Γ_i^2 can be neglected, and eqn. 8.33 simplifies to;

$$\delta(\bar{\nu}',\bar{\nu}'') = A_i f_i(\bar{\nu}',\bar{\nu}'')/2\pi^2 + \Sigma_{j\neq 1} A_j f_j(\bar{\nu}',\bar{\nu}'')/2\pi^2 \qquad 8.34$$

$$\text{where } f_i(\bar{\nu}',\bar{\nu}'') = 1/(\bar{\nu}_i^2-\bar{\nu}'^2) - 1/(\bar{\nu}_i^2-\bar{\nu}''^2) \qquad 8.35$$

This approximation was made when $\Delta\bar{\nu}_{\frac{1}{2}i}^2 \ll (\bar{\nu}_i^2-\bar{\nu}'^2)$, which was seen to make Γ_i^2 approach zero, since;

$$\Gamma_i'^2 = \Delta\bar{\nu}_{\frac{1}{2}i}^2\bar{\nu}'^2/(\bar{\nu}_i^2-\bar{\nu}'^2)$$

This was seen to occur when either (i) the resonance was very narrow i.e. $\Delta\bar{\nu}_{\frac{1}{2}i}$ small, or (ii) when the wavenumbers $\bar{\nu}'$ and $\bar{\nu}''$ were chosen so as to be far removed from the absorption feature. It was noted that eqn. 8.34 indicated that the refractive index difference would be expected to tend to infinity as $\bar{\nu}$ tends to $\bar{\nu}_i$, since $\bar{\nu}_i^2-\bar{\nu}'^2$ tends to zero. This limited use of eqn. 8.34 to refractive index differences far removed from the resonance, as detailed above.

For isolated resonances situated at wavenumber $\bar{\nu}_i$ the summation term in eqn. 8.34 was ignored, giving;

$$\delta(\bar{\nu}',\bar{\nu}'') = A_i f_i(\bar{\nu}',\bar{\nu}'')/2\pi^2 \qquad 8.36$$

when the line shape factor was ignored, or;

$$\delta(\bar{\nu}',\bar{\nu}'') = A_i g_i(\bar{\nu}',\bar{\nu}'')/2\pi^2 \qquad 8.37$$

when the line shape factor was included. The functions $f_i(\bar{\nu}',\bar{\nu}'')$ and $g_i(\bar{\nu}',\bar{\nu}'')$ were given in eqns. 8.35 and 8.32 respectively.

8.4.4 Sophisticated fitting techniques for 0.0083 cm teflon

Table 8.11 shows the values of $\bar{\nu}'$, $n(\bar{\nu}')$, $\bar{\nu}''$, $n(\bar{\nu}'')$, $10^2\delta(\bar{\nu}',\bar{\nu}'')$, $10^4 f_i(\bar{\nu}',\bar{\nu}'')$ and $10^4 g_i(\bar{\nu}',\bar{\nu}'')$ obtained for one dispersion curve of 0.0083 cm thick teflon. Fig. 8.12 shows the plot of $10^2\delta(\bar{\nu}',\bar{\nu}'')$ versus $10^4 f_i(\bar{\nu}',\bar{\nu}'')$, and $10^2\delta(\bar{\nu}',\bar{\nu}'')$ versus $10^4 g_i(\bar{\nu}',\bar{\nu}'')$. Eqn. 8.36 showed that the gradient of the best straight line through the points for $10^4 f_i(\bar{\nu}',\bar{\nu}'')$ would give $A_i/2\pi^2$. Therefore $A_i = 2\pi^2$ x gradient of the best straight line. The values of $10^2\delta(\bar{\nu}',\bar{\nu}'')$ against $10^4 f_i(\bar{\nu}',\bar{\nu}'')$ approximated to a straight line up to a value of 7×10^{-4} cm^2 for f_i, above which the line shape factor Γ_i^2 presumably

Table 8.11 Refractive index data for 0.0083 cm teflon

$\bar{\nu}'$ /cm^{-1}	$\bar{\nu}''$ /cm^{-1}	$n(\bar{\nu}')$	$n(\bar{\nu}'')$	$10^2\delta(\bar{\nu}',\bar{\nu}'')$	$10^4 f_i(\bar{\nu}',\bar{\nu}'')$ /cm^{-2}	$10^4 g_i(\bar{\nu}',\bar{\nu}'')$ /cm^{-2}
202.64	205.08	1.499	1.406	9.32	40.24	7.44
201.42	206.30	1.530	1.389	14.06	20.10	9.57
200.20	207.52	1.524	1.397	12.87	13.40	9.00
198.97	208.74	1.515	1.393	12.16	10.00	7.88
197.75	209.96	1.500	1.394	10.57	8.04	6.84
196.53	211.18	1.501	1.400	10.10	6.70	5.97
195.31	212.40	1.487	1.402	8.55	5.74	5.27
194.09	213.62	1.482	1.401	8.10	5.03	4.70
192.87	214.84	1.484	1.411	7.37	4.47	4.24
191.65	216.06	1.476	1.411	6.43	4.02	3.85
190.43	217.29	1.474	1.417	5.71	3.66	3.53
189.21	218.51	1.472	1.415	5.65	3.35	3.25
187.99	219.73	1.468	1.417	5.06	3.10	3.02
186.77	220.95	1.470	1.422	4.85	2.88	2.81

Table 8.11 (continued)

$\bar{\nu}'$ /cm^{-1}	$\bar{\nu}''$ /cm^{-1}	$n(\bar{\nu}')$	$n(\bar{\nu}'')$	$10^2\delta(\bar{\nu}',\bar{\nu}'')$	$10^4 f_i(\bar{\nu}',\bar{\nu}'')$ /cm^{-2}	$10^4 g_i(\bar{\nu}',\bar{\nu}'')$ /cm^{-2}
185.55	222.17	1.472	1.424	4.84	2.68	2.63
184.33	223.39	1.468	1.420	4.73	2.52	2.48
183.11	224.61	1.471	1.424	4.67	2.37	2.33
181.88	225.83	1.470	1.424	4.57	2.24	2.21
180.66	227.05	1.469	1.427	4.14	2.12	2.10
179.44	228.27	1.461	1.429	3.21	2.02	1.99
178.22	229.49	1.465	1.428	3.70	1.92	1.90
177.00	230.71	1.464	1.430	3.42	1.83	1.82
175.78	231.93	1.464	1.428	3.60	1.76	1.74
174.56	233.15	1.460	1.431	2.89	1.68	1.67
173.34	234.37	1.458	1.431	2.71	1.62	1.61
172.12	235.60	1.460	1.434	2.60	1.55	1.55
170.90	236.82	1.462	1.432	2.96	1.50	1.49
169.68	238.04	1.456	1.431	2.51	1.45	1.44

Table 8.11 (continued)

$\bar{\nu}'$ /cm^{-1}	$\bar{\nu}''$ /cm^{-1}	$n(\bar{\nu}')$	$n(\bar{\nu}'')$	$10^2\delta(\bar{\nu}',\bar{\nu}'')$	$10^4 f_i(\bar{\nu}',\bar{\nu}'')$ /cm^{-2}	$10^4 g_i(\bar{\nu}',\bar{\nu}'')$ /cm^{-2}
168.46	239.26	1.454	1.432	2.26	1.40	1.39
167.24	240.48	1.452	1.434	1.75	1.35	1.34
166.02	241.70	1.452	1.431	2.08	1.31	1.30
164.79	242.92	1.449	1.429	1.98	1.27	1.26
163.57	244.14	1.452	1.429	2.23	1.23	1.22
162.35	245.36	1.449	1.429	1.95	1.19	1.19
161.13	246.58	1.447	1.430	1.62	1.16	1.16
159.91	247.80	1.448	1.433	1.58	1.13	1.13
158.69	249.02	1.447	1.433	1.39	1.10	1.10
157.47	250.24	1.446	1.435	1.01	1.07	1.07
156.25	251.46	1.455	1.432	2.33	1.04	1.04
155.03	252.69	1.448	1.437	1.10	1.02	1.02

for symbols see text.

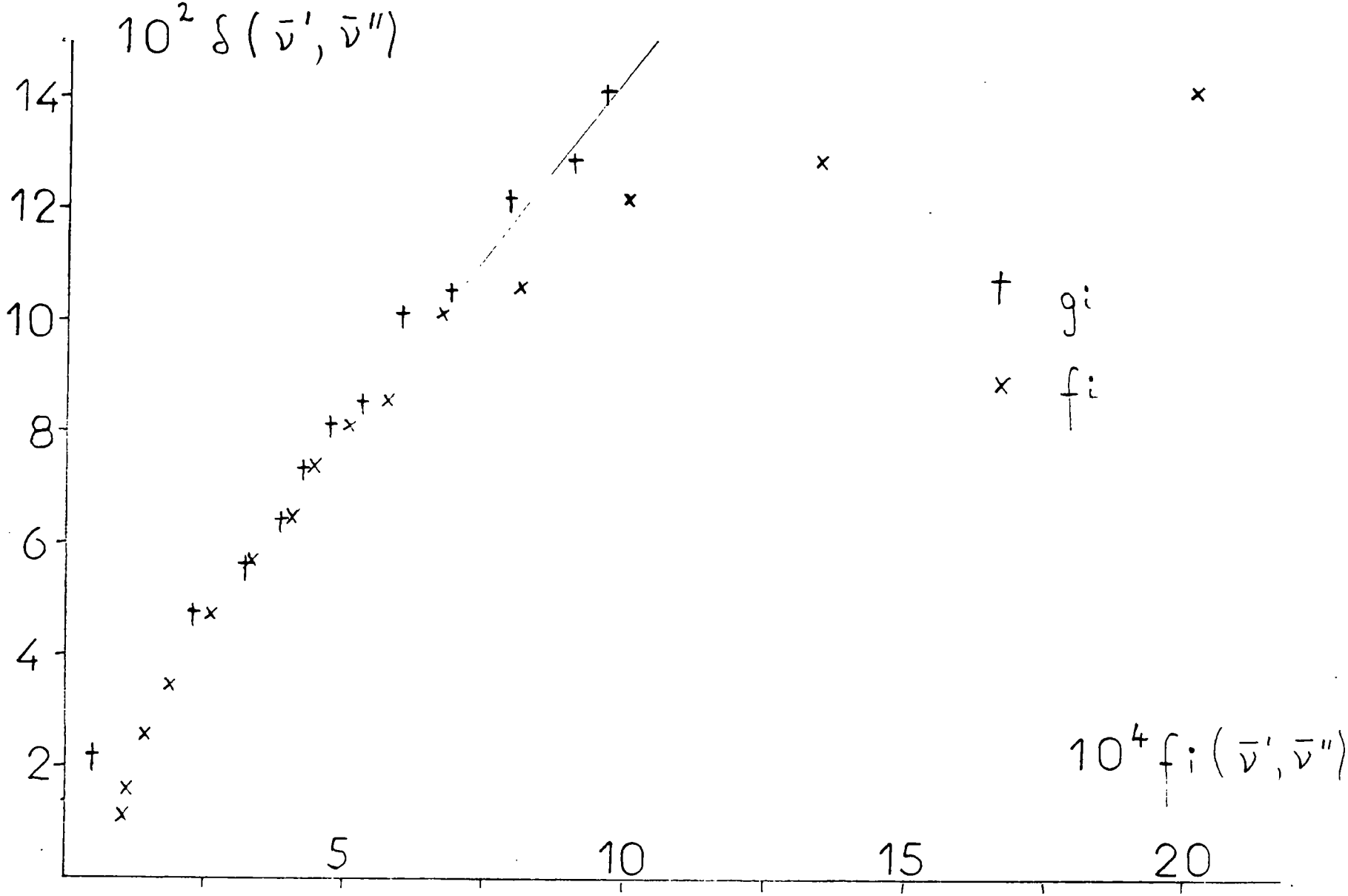

FIG. 8.12 $10^2\,\delta(\bar{\nu}', \bar{\nu}'') / 10^4 f_i(\bar{\nu}', \bar{\nu}'')$ AND $10^4 g_i(\bar{\nu}', \bar{\nu}'')$

becomes important. The wavenumber values corresponding to this value for f_i were 196.53 and 211.18 cm^{-1}. For this resonance the band centre was calculated as 203.86 cm^{-1}, and the half-band width as 4.88 cm^{-1} (see table 8.9). These figures gave $\bar{\nu}_i - \bar{\nu}' = 7.3\ cm^{-1}$, and indicated that the f_i function could only be used when $\bar{\nu}_i - \bar{\nu}' > 2\Delta\bar{\nu}_{\frac{1}{2}i}$.

Fig. 8.13 shows an expansion plot for $10^2\delta(\bar{\nu}',\bar{\nu}")$ against $10^4 g_i(\bar{\nu}',\bar{\nu}")$, for values of g_i between 0 and 7×10^{-4} cm^2. The best straight line through the data points had a gradient of 1.68×10^2 cm^{-2}. Hence the absorption coefficient A_i for the 202 cm^{-1} absorption was calculated as 3 320 cm^{-2}.

The simple linear least squares analysis programme BEERSLAW was adapted for use with the $\delta(\bar{\nu}',\bar{\nu}")$ versus $g_i(\bar{\nu}',\bar{\nu}")$ data to obtain the gradient of the best straight line. The values for $10^2\delta$ and $10^4 g_i$ for 40 values of $\bar{\nu}'$ and $\bar{\nu}"$ were firstly used to obtain the best straight line fit. The deviation of each data point from the computed best straight line was then analysed, and any data points, especially at the beginning or end of the array, which had large deviations were removed. The gradient of the best straight line for the truncated data set was then redetermined using the BEERSLAW programme. The truncation procedure was continued until the deviations of the individual data points from the computed best straight line fit became random throughout the array. By using this procedure it was hoped that the data points suited to the physical restraints of the model used in determining the relation between refractive index and integrated intensity would be chosen. The values for the absorption strengths of the 202 cm^{-1} teflon resonance, for the 10 dispersion curves, are given in table 8.12. The average value for the 10 curves was found to be 3 400±200 cm^{-2}.

The half-band widths measured from the dispersion curves were shown in table 8.9. The values shown were lower than those obtained for the transmission spectra for the same teflon sample. The average half-band width obtained with the transmission spectra was 9±1 cm^{-1}, as compared with the

Table 8.12 Intensities for 0.0083 cm teflon

index	intensity		
	$A_i = \Delta\bar{\nu}_{\frac{1}{2}}\bar{\nu}_i 2\pi^2\Delta_i$ /cm^{-2}	A_i (Γ_{disp}) /cm^{-2}	A_i (Γ_{tran}) /cm^{-2}
1	2860	3370 ± 60	3810 ± 70
2	3990	3130 ± 100	3960 ± 50
3	3360	3470 ± 40	3860 ± 60
4	2900	3410 ± 50	3830 ± 60
5	1620	3460 ± 70	3760 ± 80
6	3350	3590 ± 60	3770 ± 60
7	2210	3020 ± 90	3940 ± 70
8	2020	3490 ± 50	3850 ± 70
9	4250	3540 ± 40	3660 ± 50
10	3530	3410 ± 50	3810 ± 70

for symbols see text.

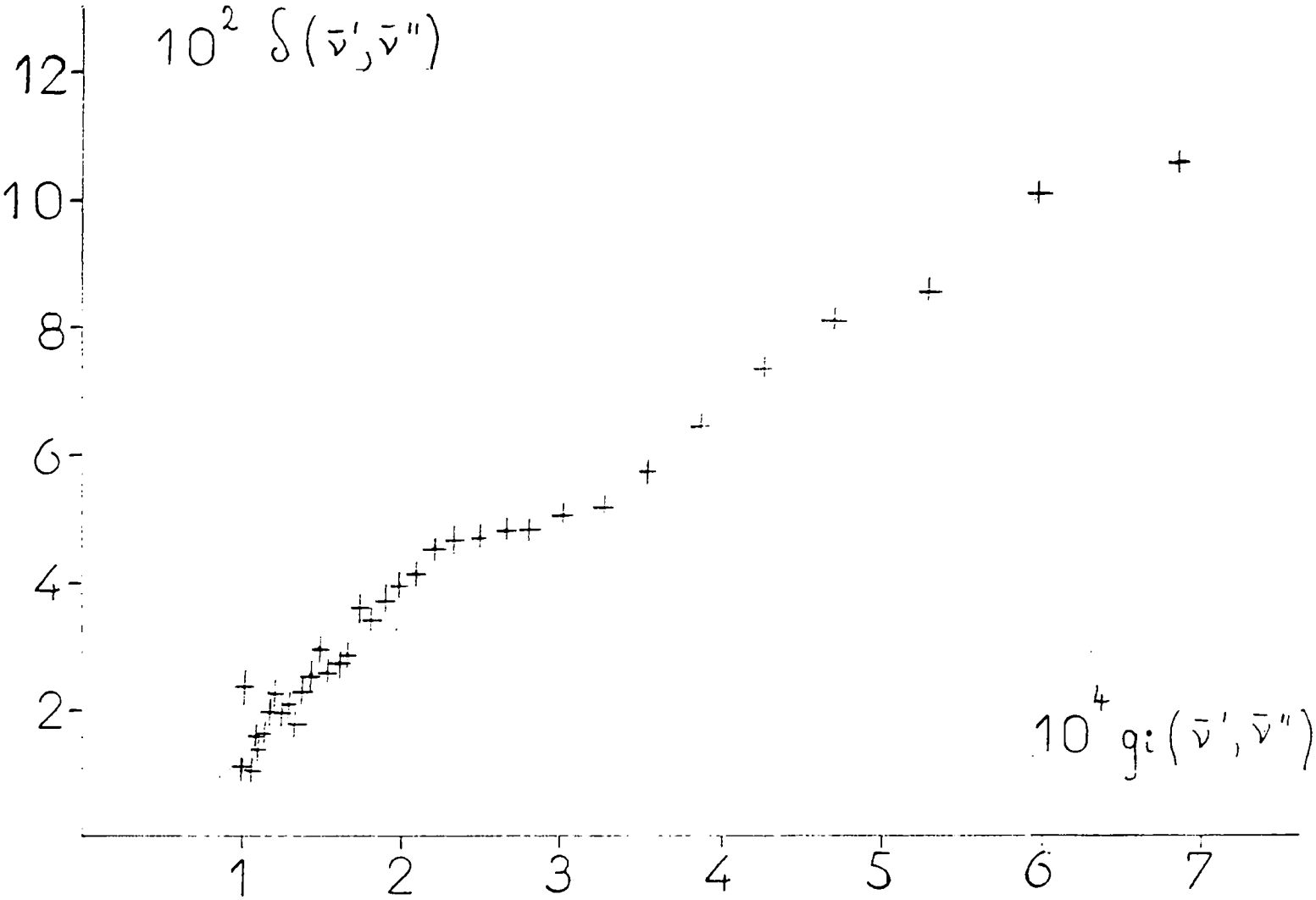

FIG. 8.13 $10^2\ \delta(\bar{\nu}',\bar{\nu}'') \;/\; 10^4\ g_i(\bar{\nu}',\bar{\nu}'')$

dispersion value of 4.8±1.4 cm^{-1}. This value of the half-band width from the transmission spectra was used to determine Γ_i^2, and eqn. 8.37 used to calculate the integrated intensity via the gradient of the best straight line for the $10^2\delta(\bar{\nu}',\bar{\nu}")$ versus $10^4 g_i(\bar{\nu}',\bar{\nu}")$ plot, and the truncation of arrays method as detailed above. The 10 values for the integrated intensity A_i determined are shown in table 8.12, and gave an intensity of 3 800±200 cm^{-2} as an average value. This large increase from the value of A_i, of 3 400±200 cm^{-2}, using the half-band widths as measured by dispersion, indicated the large effect the line shape function Γ_i^2 has on the calculated intensity. Since Γ_i^2 was a function of the half-band width, then the latter must be measured accurately. This was difficult in a dispersive spectrum, where the half-band width was obtained as the frequency difference between the turning points in the phase or refractive index curve. If these turning points are not observed on the phase curve then the feature is not being resolved. The return between turning points was not observed for many of our refractive index curves (see figs. 8.6 to 8.9), and this made determination of the half-band width difficult. It thus seems likely that a higher resolution is necessary. The resolution achieved from the refractive index curves appeared to be approximately one-half that achieved for the maximum mirror displacement of 0.0208 cm with a transmission spectrum. No further tests have been undertaken, but it appears that twice the interferogram length is required in the dispersive mode to obtain equivalent resolution to that in the non-dispersive mode.

Chamberlain and Gebbie (212) obtained a value of A_i = 4 710 cm^{-2} for the 202 cm^{-1} band of 0.0075 cm teflon. This value is larger than the 3 400±200 cm^{-2} value obtained from our 0.0083 cm samples. The intensities of the teflon would not be expected to be dependent upon the thickness, but only on the composition of the sample. The optical quality of the samples is an important consideration in the far-infrared spectral region. The interferogram could be significantly modified by effects additional to those of a purely absorptive or dispersive sample, by such factors as varying sample thickness,

which has already been seen to occur in section 8.2, and undulating surfaces. This degradation of the interferogram leads to a phase spectrum not related in the expected way to the true refractive index spectrum, and hence giving false intensity values. The effects of this problem on the intensity would be very difficult to estimate.

The nature of the sample is also an important consideration for these far-infrared spectra. The important low frequency bands for synthetic polymers are rarely due to lattice modes as for crystalline materials, but often arise from internal vibrational modes, particularly those of twisting and deformation motions. (228). Teflon is a partially crystalline polymer, where the 202 cm^{-1} band arises from the CF_2 rocking mode in the crystalline regions (212). Thus, if the crystallinity of the various teflon samples varies, then the intensity of the 202 cm^{-1} absorption would be expected to vary. If the crystallinity falls then the intensity will fall due to the decreased crystallinity, but will rise to a smaller extent due to the increase in general background absorption from the amorphous regions of the sample. The latter absorptions arise from various conformations of the polymer unit, each of which have their own absorptions, giving broad and indefinite absorptions.

Teflon has associated with it a further problem if it is to be used as an intensity standard, as it can exist in more than one crystalline form (228). The change of crystalline form is accomplished by a change in pitch of the CF_2 helix. The two different crystalline forms correspond to different rotational isomers, which will presumably have different spectra. A further problem is that the film is unlikely to be isotropic, and hence the absorption intensity will depend upon the direction of propogation of the radiation in relation to the axes of the specimen. Thus the differences in intensity for the two different teflon samples are easily accountable.

Chamberlain obtained a 15 cm^{-1} separation of the turning points of the refractive index curve in the region of the 202 cm^{-1} absorption, which corresponded to a half-band width of 15 cm^{-1}. In this work the turning points

were found to be 9±1 cm^{-1} apart for the 0.0083 cm sample, thus indicating that the absorptions of the two samples vary greatly presumably due to the effects detailed above.

The difference in intensities for the dispersive and non-dispersive modes, obtained in this work, for the same teflon sample is much more worrying than the differences for our work and that of Chamberlain. At present no real explanation can be offered for this intensity difference, and more work is clearly necessary in this area. A value of A_1 = 4 200±100 cm^{-2} was obtained using the transmission method, and 3 400±200 cm^{-2} obtained using the dispersion method. The effects of crystallinity were clearly not responsible for the intensity differences here as the same sample was used for both sets of intensity measurements. Intensity differences due to anisotropy of the sample cannot be eliminated, because no special care was taken in orienting the sample when it was transferred from the dispersive arm of the interferometer to the transmission sample position. However these effects would be expected to be small and not sufficient to give the intensity variation necessary. It thus appeared that these effects on the intensity were mainly due to the methods of computation of the intensity, rather than to differences in the sample.

8.5 Advantages and disadvantages of intensity measurements from refractive index determinations

An alternative to the calculation of intensities from absorption curves has been sought, because of the difficulties in fitting a baseline to the absorption profile, as noted in chapter 4. When absorption bands are either broad, or not clearly resolved from other neighbours, i.e. when the wings of the band are not clearly observable, then it is difficult to fit a baseline to the band to enable the area under the baseline to be determined. The refractive index method for intensity calculation eliminates the necessity of fitting a baseline.

The dispersive method has the disadvantage that the intensity is not a simple function of the refractive index. In fact a model has to be

assumed, where the absorbing species is approximated to a series of classical oscillators (see section 8.4.1). The relationship between refractive index and absorption intensity was developed through an empirical equation from the model of the harmonic oscillarors. Thus the calculation of intensity depended upon the applicability of the model to the particular situation under consideration. The intensity of the band is a function of the refractive index differences in the region of the i.th band, as seen in section 8.4.1. For overlapping bands all of the refractive index difference in the region of the i.th band is not due to the i.th band. Hence, if the experimental refractive index difference is used to calculate the intensity of the i.th band without taking into account the intensity of other bands in the region, then the intensity of the i.th band calculated will be too high. The sophisticated fitting techniques, detailed in section 8.4.3, were designed to overcome this problem, since only the points about the band centre are taken to give the intensity. The linearity of the $\delta(\bar{\nu}',\bar{\nu}'')$ against $g_i(\bar{\nu}',\bar{\nu}'')$ plots was used as an internal test to show that the neighbouring bands were not contributing significantly to the refractive index difference under consideration. Thus the data was used at gradually increasing frequencies from the band centre, until the effects of neighbouring bands, causing the plot to be non-linear, were first noticed. The data was then truncated. This truncation technique, using the linearity of the graph, was sometimes made difficult when the line shape term was significant, and caused lack of linearity at frequencies near the band centre. For overlapping bands an iterative process for summation of contributions to the refractive index difference from individual bands will have to be developed.

Since the intensities measured by dispersion methods were smaller than those measured by transmission measurements on the same sample, then it appears that overestimation of band intensities, due to refractive indices being affected by neighbouring bands, was not causing significant problems in the measurement of intensities by the dispersive method.

The dispersive intensities place serious doubts upon the accuracy of transmission intensities, and suggested that the values for the latter may well have been too large. This indicated that the baseline drawn for these bands was, in fact, too low. This could have been caused by the proximity of the band at 277 cm^{-1}. This once again highlights the difficulty of baseline positioning for transmission intensity measurements.

Thus it appeared that the dispersive method gave the more accurate intensity values, as against the transmission method. The inaccuracy of the transmission method was due to difficulty in the positioning of the baseline. An initial disadvantage of the dispersive method was that much more numerical calculation was necessary than for the transmission method, where calculation of the intensity from the area under the absorption curve was simple. However once a computer programme had been written to calculate $\delta(\bar{\nu}',\bar{\nu}'')$ and $g_i(\bar{\nu}',\bar{\nu}'')$ functions, then the intensity values were easily determined by a least squares analysis fit. The truncation technique was tedious and time-consuming if attempted in batch-mode, but was relatively simple with an interactive computer terminal.

The uncertainty of the dispersive method (A_i = 3 400±200 cm^{-2}) was greater than that for the transmission method (A_i = 4 200±100 cm^{-2}) for the calculation of intensities, presumably mainly due to the greater degree of numerical manipulation necessary in the former technique. However, this would be overshadowed by the dispersive method giving a more accurate value for the 'true' intensity. It should be noted here that these conclusions do not in any way invalidate the intensity calculations determined using the non-dispersive mode earlier in this study. This is the case because the intensities were all carried out using the same methods of baseline fitting, and hence they are internally consistent, but perhaps are not valid for consideration with intensities from other systems as has been pointed out earlier (see section 4.2).

CHAPTER 9

LIQUID PHASE REFRACTIVE INDEX MEASUREMENTS

This chapter describes the work involved in the design, construction and development of a cell for measuring the refractive index spectrum of liquids in the far-infrared region.

9.1 Previous work

Chamberlain, Gibbs and Gebbie (225) developed their modular interferometer, which was originally designed for absorption measurements, for the determination of liquid phase refractive indices. They maximised the energy throughput of the modulated term of the interferogram by cutting down the number of boundary surfaces in the dispersive arm. In their dispersive interferometer the liquid specimen was not placed between plane-par allel transparent plates, but was a gravity held layer on the horizontal surface of the fixed mirror. The specimen was separated from the remainder of the evacuated interferometer by a thin vacuum window of 'melinex' or polypropylene.

The FS-720 interferometer used in this laboratory was not suitable for such modification, especially in that it was considered inadvisable to turn the instrument through the 90^{o} necessary to make the dispersive arm of the interferometer vertical, hence making the mirror surface in that arm horizontal. The FS-720 instrument, with its heavy metal casing, was designed for the 4 arms surrounding the beam-splitter module to be horizontal. The possibility of using a 45^{o} mirror in the dispersive arm, so that the plane of the instrument could be left horizontal and yet a horizontal fixed mirror was considered, but after taking into account the further disadvantages of the free liquid layer, was discounted.

The gravity held layer could cause problems due to absorption from the vapour present in the space between the surface of the liquid layer and the vacuum window. For liquids with strong vapour absorptions this would be a serious problem, especially when the resulting absorption bands were narrow, which would cause derivative refractive index changes on top of the major absorptions. These problems would not, however, be as serious as those encountered for the ratioed transmission spectra, since for the refractive

index curves the phase value for sample and background are subtracted, rather than being ratioed. Chamberlain and Gebbie (225) filled the space above the liquid with dry air, which of course became saturated with the vapour of the liquid. They maintained that the latter was not generally troublesome.

A further disadvantage of the liquid layer was that each liquid had a minimum layer thickness, which is determined by the surface tension and viscosity of the liquid. Thus for strongly absorbing liquids the capillary layer thickness may well cause the phase values to pass outside the principal value range, with the consequent problems, as given by the conditions of eqn. 8.9. To obtain further indications as to the viability of such a gravity held liquid surface, an interferometer has been operated in this mode in this laboratory. Some preliminary refractive index work has been made using a Chamberlain and Gebbie type cube interferometer on loan from Salford University/ National Physics Laboratory. A schematic diagram of this interferometer is shown as fig. 9.1.

For the liquid layer to be plane-parallel it was essential, for such a system, that the mirror on which the liquid was placed was exactly horizontal. With the Salford/ N.P.L. modular interferometer this adjustment was made by altering the tilt of the whole instrument by turning levelling screws attached to the base of the main beam-splitter cube. This proved to be a very difficult operation with the coarse pitch screws that are necessary to support the weight of the whole instrument. The alignment for a horizontal mirror was obtained as follows. The source module was removed from the top of the beam-splitter module, and a metal ring with cotton thread cross-wires was placed in the position formerly occupied by the lens. A 100 W lamp was placed near the cross-wires so that they were brightly illuminated. A small quantity of carbon tetrachloride was then inserted into the cell so that a thin liquid layer was formed. Carbon tetrachloride was chosen because it is transparent to visible radiation, has a low viscosity, and is volatile, so that it can be easily flushed from the cell module. The tilt of the instrument

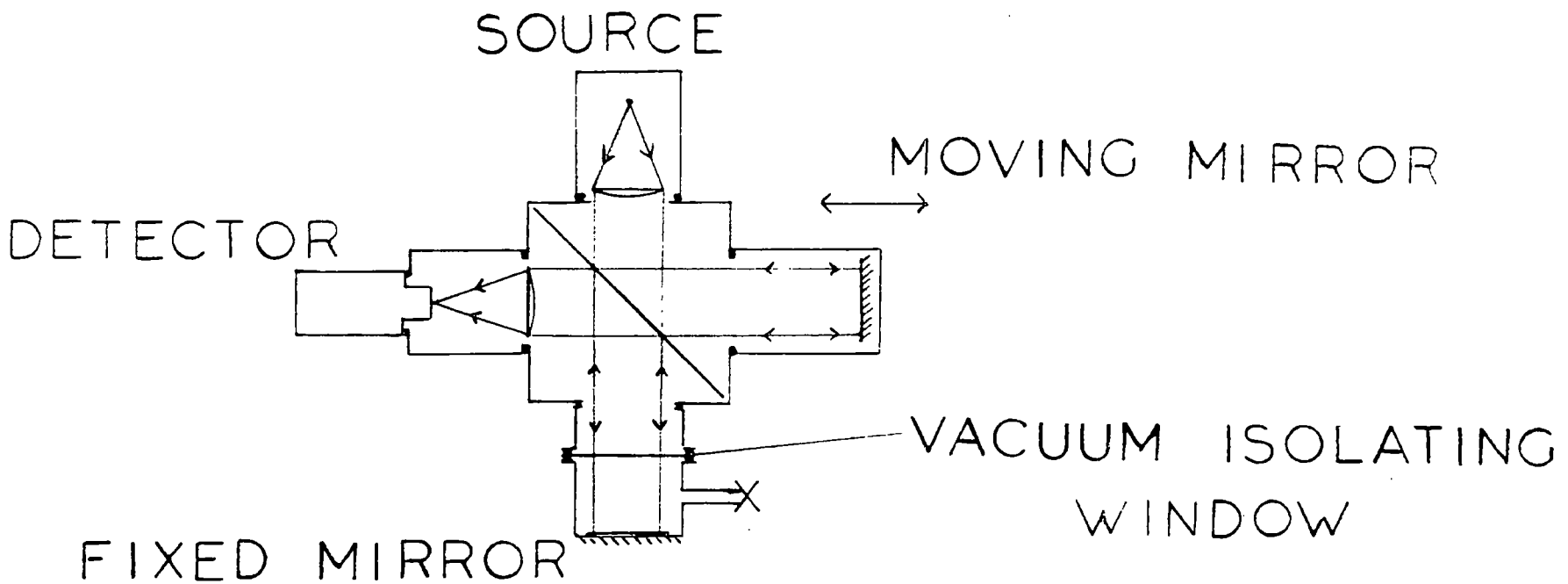

FIG. 9.1 SALFORD/N.P.L INTERFEROMETER

was then adjusted carefully, so that the images of the cross-wires formed at the mirror and the liquid surface, appeared to be coincident, thus indicating that the liquid layer was plane-parallel. This adjustment was sometimes found to be difficult because, even with a weakly absorbing liquid, the image of the cross-wires from the mirror itself was very weak.

The optical alignment for mutual normality of the fixed and moving mirrors was made by making adjustments to the tilt of the moving mirror module against the beam-splitter module, via an oversize 'O' ring. Adjustments were possible by means of the bolts retaining the module against the compression of the 'O' ring seal between the two modules. This adjustment was difficult as the pitch of the retaining bolts was very coarse, and made fine adjustments to the optical alignment almost impossible. This difficulty indicated that any system for refractive index measurement should have fine calipers for mirror movement, as in the FS-720 interferometer.

The free liquid surface in the Salford system caused further problems in that the noise level of the recorded interferograms was very high. Much lower signal-to-noise ratios were obtained with the Salford interferometer than for the FS-720. This high noise level was presumably caused by vibration of the liquid surface at a frequency equal to the vibration of the source modulator. In the design for a refractive index cell it was hoped to trap the liquid layer between mirror surface and a thin plastic film, in an effort to overcome the difficulties of the free liquid film and the necessary adjustments to the optical alignment for such a film.

9.2 Viability tests for the refractive index cell

The following tests were carried out using the FS-720 interferometer, by placing various samples in the fixed mirror arm. It was firstly noticed that even very thin samples of teflon significantly reduced the depth of modulation observed in the asymmetric interferogram. The quality, Q decreased from 0.54 for a 0.0105 cm teflon sample, through 0.49 for a 0.0134 cm sample, to 0.34 for a 0.0229 cm sample. The quantity Q, as defined by Chamberlain

(225), represents the magnitude of modulation in the interferogram, relative to the background level;

$$Q_J = (J(0) - J_o)/J_o \qquad 9.1$$

where $J(0)$ is the interferogram level at the dispersed maximum

J_o is the mean interferogram level

The contrast C_J (225) for an interferogram determines the signal-to-noise ratio in the computed spectrum;

$$C_J = J_{max} - J_{min} \qquad 9.2$$

where J_{max} is the interferogram level at maximum intensity

J_{min} is the interferogram level at minimum intensity.

When a 3mm piece of high density polyethylene was placed over the whole of the fixed mirror, then the quality of the interferogram fell to 0.33 and a contrast of 24% (with an asymmetry of 3% of the contrast). The quality for the interferogram from the empty instrument was 0.8 and the contrast 60%. The Grand Maximum was displaced by 27 units on the drive counter i.e. 0.0270 cm by insertion of the 0.3 cm sample of polythene. The calipers of the fixed mirror were then adjusted to give the maximum modulation, and after adjustment the quality was unchanged at 0.33, but the contrast had been increased to 25% (with the asymmmetry remaining at 3%).

Attempts were made to compensate for the dispersion of the sample in the fixed mirror arm, by placing a similar sample in the moving mirror arm. The dispersed maximum now occurred within 1 unit of the drive from the position of undispersed Grand Maximum (i.e within 0.0100 cm of the original position). Thus the dispersion of the second window was compensating the dispersion of the first. The polythene samples were positioned only by use of plasticine mounts, and hence it was difficult to place the samples so that they were normal to the radiation beam. This misalignment probably accounted for the fact that the dispersed maximum position was not quite returned to the position of Grand Maximum for the empty instrument. Initially the quality of the compensated interferogram was low, and was found to be 0.28 with a

contrast of 19% and an asymmetry of 5%. By carefully repositioning the compensating sample, thequality of the interferogram was increased to 0.44 and the contrast to 31%, with an asymmetry of 2%. The interferogram immediately around the Grand Maximum was seen to be different to that obtained with an empty instrument. This was probably due to the slight difference in optical path through the two plates.

An attempt was made to regain maximum modulation for a sample in the fixed arm by compensating with a wire mesh in the moving mirror arm. It was hoped that the energy in the moving mirror arm could be decreased to more nearly match the residual energy in the fixed mirror arm. This hopefully would result in beams of approximately equal amplitudes interfering with a high degree of modulation, relative to the mean interferogram level, rather than a high mean level with little depth of modulation, which would be expected to occur for beams of mis-matched energy. The attempt with the grid was unsuccessful, presumably because the attenuation of the beam in the moving mirror arm was occurring by a different process with the wire mesh, than in the attenuation of the sample in the fixed mirror arm due to the dispersion there. The grid was simply blocking off some of the beam, and hence cutting down the energy in the beam, whereas the teflon sheet was actually absorbing specific regions of the radiation.

The radiation beam diameter was restricted by use of a diaphragm with a diameter of 1 cm, which was placed at the exit of the source module. This enabled studies to be made of the radiation incident at the centre of the mirrors. This enabled pieces of polythene to be placed against the mirror sufaces, which ensured that they were normal to the beams. The whole of the radiation beam passed through both polythene samples by use of the diaphragm. With this experimental set-up the quality was 0.83 and the contrast 61%, with no observable asymmetry, for the interferometere with no sample. With the sample inserted the quality was 0.54 and the contrast 36% with no noticeable asymmetry. Similar tests were carried out whilst not using the diaphragm to

restrict the diameter of the radiation beam. It was found much more difficult to retrieve the original interferogram quality, and the asymmetry was never fully removed. The best interferogram had a quality of 0.43 and a contrast of 34% with 4.4% asymmetry. The inability to remove the asymmetry was probably caused by the divergence of the beam, which became more serious when the edges of the sample were used to disperse the radiation beam.

A 1.5 cm diameter hole was cut in one of the 0.3 cm thick polythene samples, in an attempt to discover if a small 'sample out' interferogram could be obtained to give a zero path-difference marker on the interferogram record. This would mean that the displacement of the dispersed maximum could be measured directly from the chart record, to enable the mean level of the refractive index curve to be fixed accurately. With the 1.5 cm hole positioned at the edge of the mirror the zero path-difference interferogram had a quality Q of 0.1 ($J(0) = 55\%$, $J_0 = 50\%$), which was thought to be ample for its purpose. Thus a mirror surface of about 2 cm^2 gave a zero path-difference Grand Maximum of ample modulation to allow calculation of the diplacement of the dispersed maximum. This knowledge was utilised in the design of the cell (see section 9.3), where a zero path-difference mirror was employed.

To test for the viability of the ratioing out of the liquid retaining window, a spectrum was recorded where a piece of 0.0134 cm teflon was placed behind a sample of 0.3 cm polythene in the fixed mirror arm. The ratioed absorption spectrum was computed, and, as expected, was very noisy due to the ratioing process, with very little energy throughput. The refractive index curve for the teflon sample was also computed by subtracting the phase values for the polythene background. This refractive index curve showed a definite rise and fall through the teflon absorption in the 200 cm^{-1} region. The noise level for the refractive index curve was lower than that for the absorption spectrum, presumably due to the subtraction of background from sample in the former case, and the ratioing of sample by background in the latter case. When the energy was low the former will obviously result in

higher signal-to-noise ratios. The refractive index curve showed an increase in noise level to the high frequency side of the band, and the shape of the refractive index feature was a little different from that of the original teflon curves obtained with no polythene 'window'. No background (polythene) absorption was observed in this region (200-300 cm^{-1}), and so the change in refractive index curve shape was not due directly to the polythene absorption. The half-band width of the teflon absorption seemed to be increased when the refractive index curve was recorded with a polythene window. The polythene must have been affecting the light rays in such a way that the phase changes recorded were not only due to the dispersive properties of the sample. Possibly multiple reflections were taking place, both in the polythene window and in the air gap between the polythene and the teflon.

0.0134 cm teflon refractive index curves were also recorded behind 0.076 cm polythene 'windows'. The quality of the refractive index curves did not greatly increase, suggesting that the thickness of the polythene window did not affect the modulation depth in the interferograms significantly. It was considered possible that reflection from the front surface of the polythene could be causing the loss of modulation. The percentage of incident radiation which is reflected R for a material of refractive index n_1 in a medium of refractive index n_2 can be calculated from (229);

$$R = ((n_2-n_1)/n_2+n_1)^2 \qquad 9.3$$

For polythene n_1 = 1.51 and for a vacuum n_2 = 1. Thus 4% of the incident radiation would be expected to be reflected whilst 96% would be transmitted. It thus seemed unlikely that the 4% of reflected radiation was causing the degradation of the interferogram.

As the interferograms for tetrabromoethane (213) showed a very strong reflection peak, and the reflection for tetrabromoethane was calculated as only 6% from eqn. 9.3, then it appeared that the small percentage loss due to reflection may we l have caused some of the degradation of our teflon interferograms.It was decided that we should search for the reflection

peak from the front surface of a polythene sample. This interferogram maximum would occur when the moving mirror and the front surface of the sample were equidistant from the beam-splitter. No such peak could be found after repeated searches. This was considered to be due to the poor optical quality of the surface of the polythene sample, indicating that the surface was not as flat as that of a liquid layer. Similarly no reflection peak could be detected for a 0.0134 cm sample. This indicated that the samples used for the intensity work described in chapter 8 were not of sufficiently high optical quality to remove boundary effects between different samples, and in fact different orientations of the same sample.

As much reflected light in the visible region was observed with the polythene samples in the interferometer beam, then it was concluded that much of the incident radiation was being scattered rather than reflected, and that this factor alone probably accounted for the degradadtion of the interferograms.

As expected, measurements of expanded chart interferograms for the teflon with polythene sample showed that the displacement of the dispersed maximum from zero path-difference was equal to the sum of the displacement of the dispersed maxima for the teflon and polythene singly.

$$\bar{x}_{\text{polythene + teflon}} = \bar{x}_{\text{polythene}} + \bar{x}_{\text{teflon}} \qquad 9.4$$

Thus for a cell arrangement, where a liquid layer is contained by a window, then $\bar{x}_{\text{liquid}}$ can be calculated once $\bar{x}_{\text{window}}$ has been determined for a separate determination for an empty cell. For a cell window of thickness, t and refractive index n_w containing a liquid sample of thickness, d and refractive index n_l, then for an empty cell;

$$\bar{x}_{\text{empty cell}} = \bar{x}_{\text{window}} + \bar{x}_{\text{air}} \qquad 9.5$$

and since $\bar{x} = 2(n-1)t$

then $$\bar{x}_{\text{empty cell}} = 2(n_w-1)t + 2(n_{\text{air}}-1)d \qquad 9.6$$

if n_{air} is taken as 1 then;

$$\bar{x}_{\text{empty cell}} = 2(n_w - 1)t \qquad 9.7$$

with a full cell;

$$\bar{x}_{\text{full cell}} = \bar{x}_{\text{window}} + \bar{x}_{\text{liquid}}$$

$$= 2(n_w - 1)t + 2(n_l - 1)d \qquad 9.8$$

Thus $$\bar{x}_{\text{liquid}} = \bar{x}_{\text{full cell}} - \bar{x}_{\text{empty cell}} \qquad 9.9$$

The thickness of the liquid layer, d could be calculated from an interference pattern for an empty cell, or with a micrometer screw gauge to measure the thickness of the spacer used to determine the thickness of the liquid sample.

Polypropylene seemed to be a suitable choice for the window material on optical considerations, because a 0.0010 cm thick sample showed no refractive index changes in the region 40 - 400 cm^{-1}. With such a thin sample only one interferogram was detectable, indicating that the dispersive and non-dispersive interferograms were superimposed. Thus the mean level of refractive index could not be calculated for such a thin sample.

These tests indicated that a cell could be designed to enable the refractive index of a liquid to be measured. The cell would involve a vertical sample of the liquid held between a fixed mirror surface and a thin film of transparent material such as polypropylene. The tests have shown that it should be possible to remove the background phase of the window material from the phase obtained from the interferograms. It has also been shown that the displacement of the Grand Maximum for the liquid sample can be calculated from that for the whole cell. A method of calculating the displacement via a 'sample out' zero path-difference marker has also been discussed.

9.3 Design and construction of the liquid refractive index cell

The main concern in this design of the refractive index module was that it should be easily interchangeable with the standard fixed mirror mounting block of the FS-720 interferometer. This would make the FS-720 system easily interchangeable from transmission to refractive index measurements. The cell was thus designed to fit into the existing circular mounting in

in the beam-splitter module, using the existing bolt holes. The vacuum seal, necessary to allow the instrument to be evacuated but yet allow the refractive index cell itself to be at atmospheric pressure, was to be designed as an integral but separate part of the module. This allowed the cell to be removed from the interferometer without the remainder of the instrument having to be returned to atmospheric pressure.

The size of the mirror was required to be at a maximum to maximise the energy throughput. Thus the cell was to be designed to have the same dimensions as the original mirror. It has already been shown that the zero path-difference mirror should have an area of 2 cm^2 to give a clearly observable Grand Maximum in the reference spectrum. This area could be taken near the circumference of the mirror, as in the tests. The mirror surface for the cell itself was designed to be circular to give the maximum possible area for given dimensions, and to be offset from the centre of the interferometer beam. The layout of the mirror surfaces can be seen from fig. 9.2, which shows the layout of the two mirrors A and B relative to the cell top window clamping ring C, and the screen for blanking off the reference mirror D, in the refractive index module casing E. The main mirror surface has a diameter of 5.2 cm, giving an area of about 27 cm^2, as opposed to the original mirror diameter of 7.7 cm, giving an area of about 47 cm^2. The mirror surfaces were to be lapped and polished together to ensure that the reference mirror gave a true reading. The mirror surfaces needed to be non-corrosive for the various liquids used, and to have high reflectivity, which would not be affected by 'pitting' due to reaction with any of the liquids. Gold was the obvious choice for mirror surface on grounds of non-reactivity and reflectivity. The surface of the mirror was a layer of chromium on the glass base to give a hard surface which could be highly polished. The chromium layer was then flashed with a very thin layer of gold, which acted as an anchor for the deposit of a slightly thicker layer of gold by electrolysis. This was then very carefully polished to give the final surface.

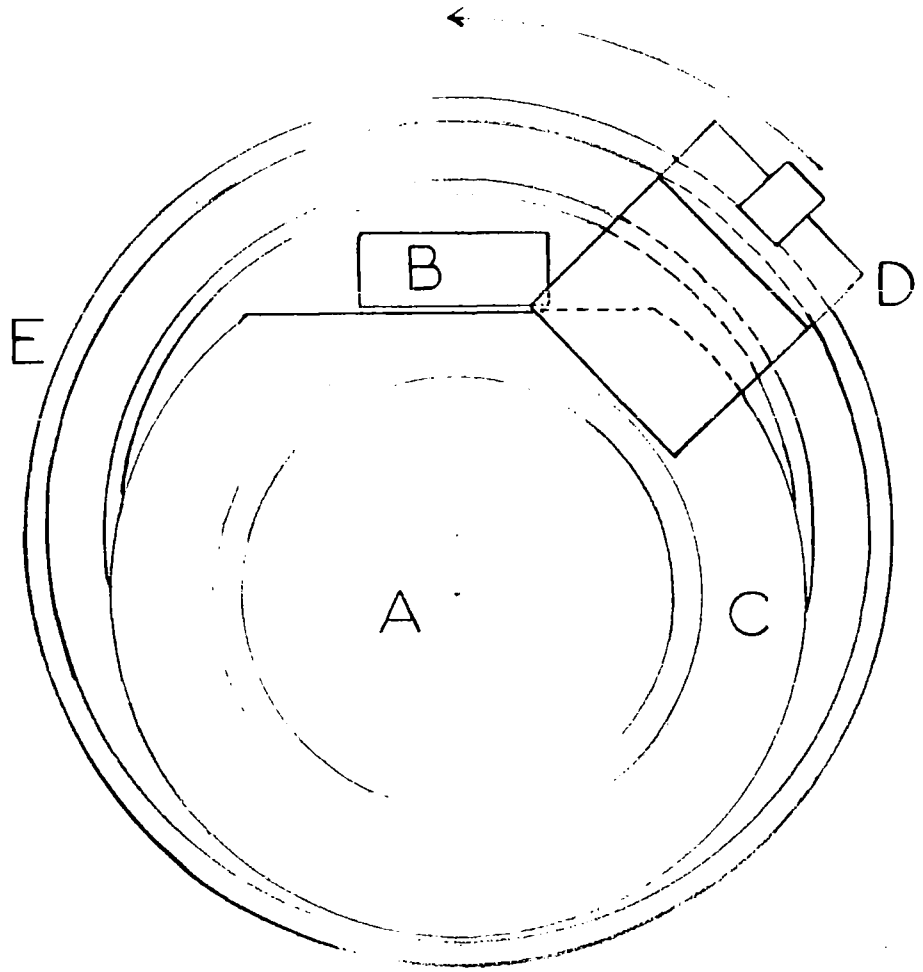

Key;

A main mirror

B reference mirror

C cell top window clamping ring

D screen for blanking off the reference mirror

E refractive index module casing

FIG. 9.2 FRONT VIEW OF MIRROR SURFACES

To allow for easy alignment of the refractive index cell, the mirror mounting was supported on two caliper adjustments with coarse and fine screws, as for the original fixed mirror. These calipers were at the back of the cell, and were easily adjustable even when the interferometer was evacuated, since the cell itself was at atmospheric pressure.

9.3.1 Vacuum window

The vacuum window was designed to fit ac ross the access port to the beam-splitter module. The vacuum window was to be made of the thinnest possible beam-splitter material which could sustain the vacuum without bursting. It was envisaged that a grid would be necessary to support the vacuum window, and prevent too much bulging and subsequent rupture. Thus some sort of clamping system was necessary to hold the window material in place. The original design for the window support is shown in fig. 9.3. In this design the film was held in the right-angled retaining ring by a tightly stretched 'O' ring D. The film retaining ring was tightened against the cell support ring C by 4 small screws. When these were tightened then the 'O' ring seal was compressed, thus gripping the film more tightly. The film was to be supported on a wire grid on a circular ring. The ring was to support the force on it by the wires being pressed up against the interferometer casing. The pressure of the vacuum caused the film to buckle as expected, but the wire grid was unable to withstand the pressure and the glue seal between the ring and the 0.02 cm diameter grid wires sheared, and the vacuum window gave way. The grid was then redesigned, and made much more substantial. A circular ring was drilled and slotted to take the grid wires, which were increased to 0.05 cm diameter. The wires were then soldered into the ring, to make a much more rigid assembly than the original.

However, this design still proved inadequate because the vacuum in the interferomter could only be maintained at 0.10 Torr, whereas for the transmission work with the normal interferometer the pressure could be maintained at 0.01 Torr. Great care had to be taken when the instrument was being pumped down as the melinex film tended to pull through the film retaining

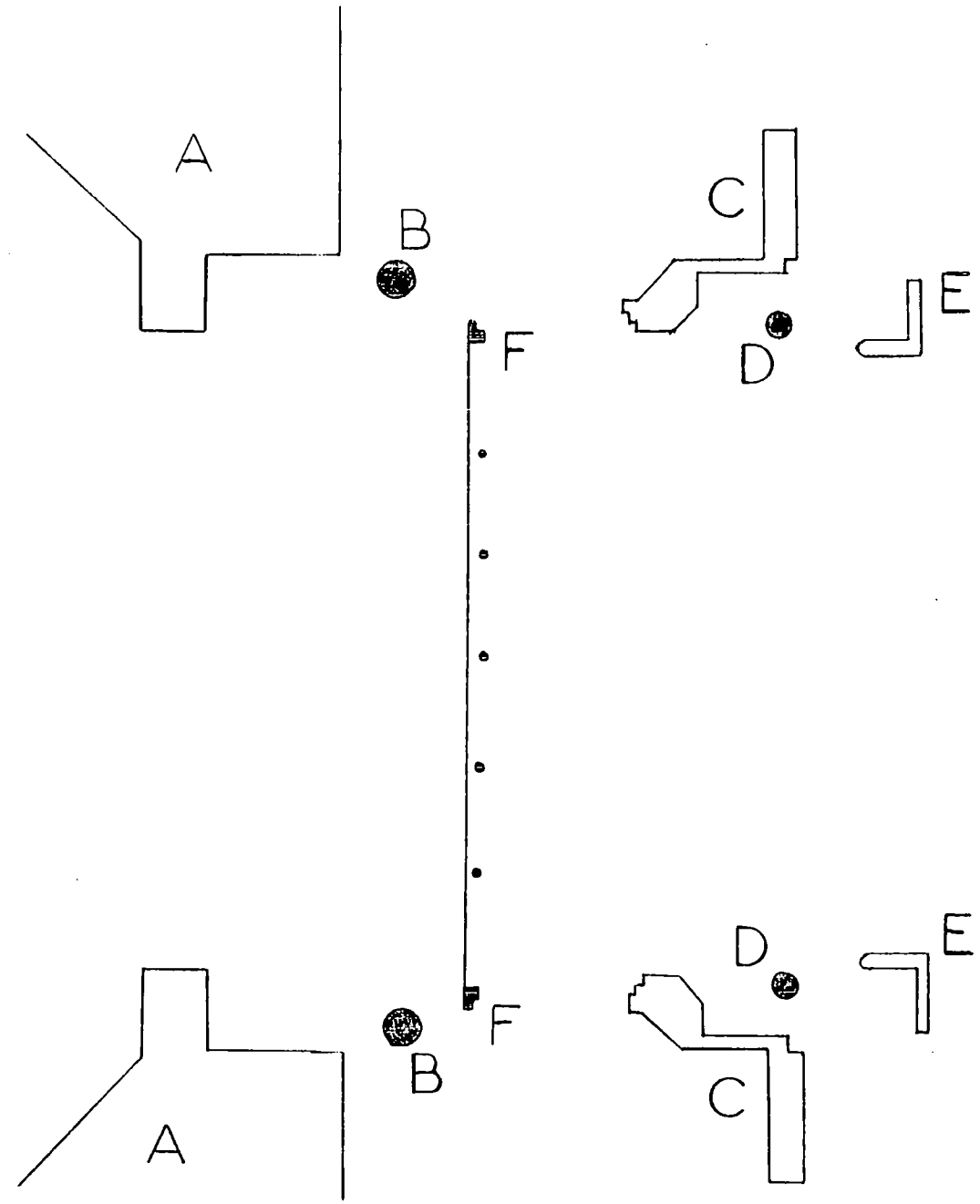

Key;

A interferometer casing

B main seal '0' ring

C cell support ring

D film retaining '0' ring

E circular film retaining ring

F grid support ring

FIG. 9.3 ORIGINAL VACUUM WINDOW SUPPORT

ring D. Various thicknesses of film material were tried in the holder, and it was found that the thinner films retained the vacuum better. This was presumably the case, because the 'O' ring could retain the flexible films better, since they had to be folded into the right-angle groove of the film retaining ring. The thinnest film could not be used without bursting was the 50 gauge film, since the 25 gauge material burst if the pumping down operation was not taken very carefully.

Attempts were made to stick the films to the flat surface of the film retaining ring. As both the surface of the ring and the film were very flat then they were both etched by scratching with a pin to assist with the sticking. 400 gauge material was used for these tests, since it was possible to scratch the surface of this film without tearing. Evostick contact adhesive was tried firstly. The film was stretched in a film-stretcher so that the surface could be easily scratched. The surface of the film and the retaining ring were smeared with a thin layer of glue, which was then allowed to dry until it was tacky. The ring was then placed on the film in the stretching device and pressure applied by placing a few books on the ring. The glue was then allowed to dry for 16 hours, and then the film and ring was carefully cut from the remainder of the film, and the assembly placed in the interferometer. The vacuum was gradually increased and the film began to bulge. This bulging caused the evostick bond to stretch, and eventually a ridge was formed and leakage thus began to occur. The vacuum could only be decreased to about 0.5 Torr with this system, and thus the evostick sticking system was not suitable. The failure of the evostick seemed to be due to its flexibility. Araldite was used as this seemed to be a much more rigid glue. Using the same etching and sticking technique the 400 gauge film was stuck to the film retaining ring. This bond was tested in the interferometer, but sheered away all round the film holder almost as soon as the vacuum pump was switched on. Thus the sticking techniques failed.

The film holder was then redesigned as shown in fig. 9.4. The

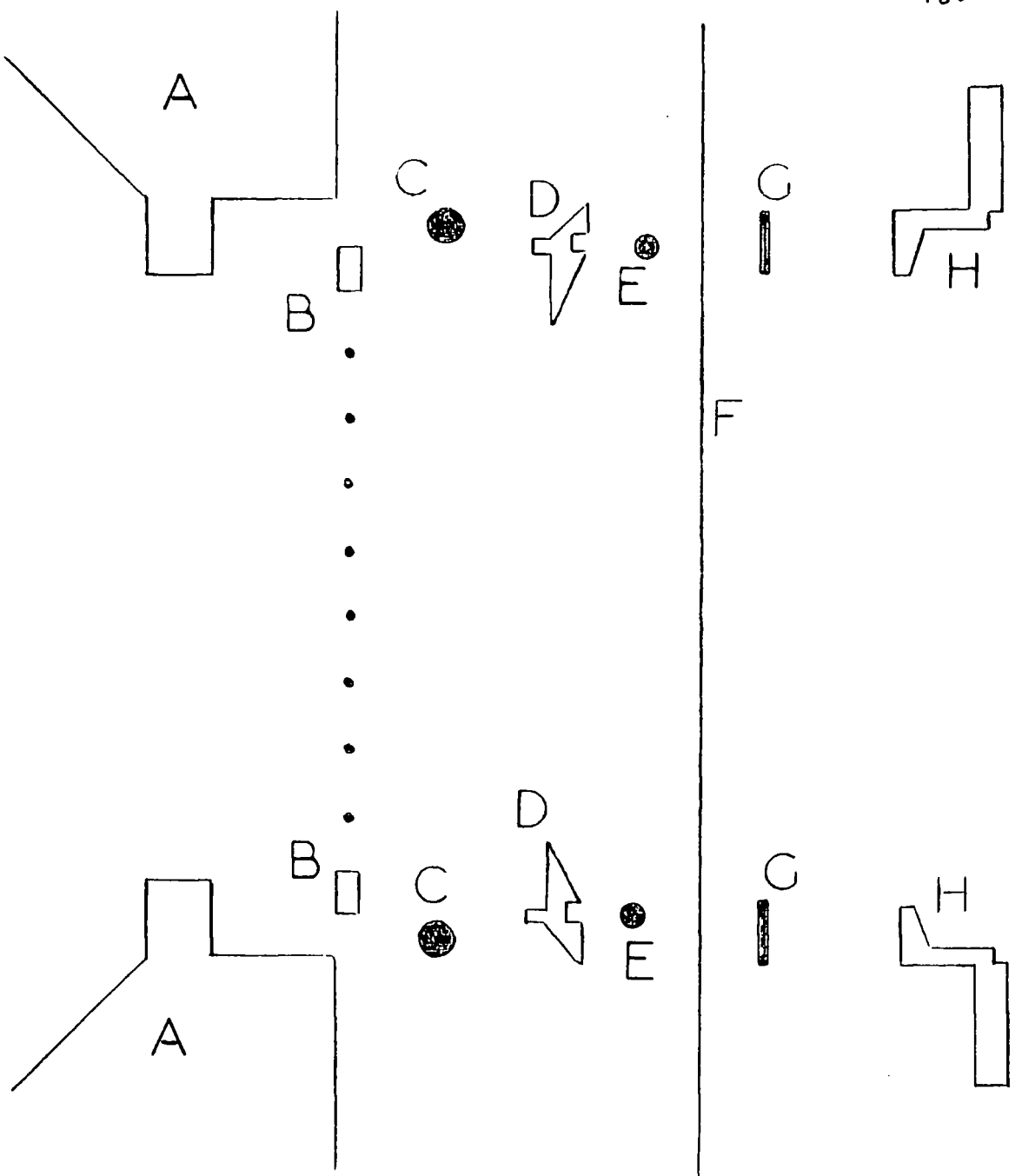

Key;

A interferometer casing

B vacuum film support grid

C vacuum seal 'O' ring

D grid support ring

E film retaining 'O' ring

F vacuum film

G neoprene rubber gasket

H cell housing ring

FIG. 9.4 SIDE VIEW — VACUUM WINDOW SUPPORT

major change was that the vacuum film F was now supported between an 'O' ring E and a circular neoprene rubber gasket G, which were then compressed by the cell housing ring H, which is bolted to the interferometer casing A. In this system the 'O' ring was of harder material than the neoprene gasket, and so when the system was tightened the 'O' ring compressed the gasket and formed a groove in this gasket to make a solid seal which would hopefully hold the film very tightly. With this design as the vacuum inside the interferometer increased then the grid support ring D was compressed towards the interferometer, which made the seal more effective. The grid support ring was shaped towards the centre so as to follow the contour of the stretched film after it had been bowed under the vacuum. The film support grid was necessary with a 50 gauge beam-splitter to prevent too great a bowing of the film, which became almost hemispherical under the high vacuum. The grid support of crossed- wires with a spacing of 1.5 cm between the wires prevented too great a bowing of the film. It was hoped that the series of small bowed hemispheres caused by the grid would effect the interferometer beam less than one large bowed hemisphere over the whole of the mirror surface.

9.3.2 Refractive index cell construction

The refractive index cell was to consist of the mirror as the back window and a thin stretched film as the front window. Thus the design problem was to discover some system by which the stretched film could be held tightly over the mirror surface. The system designed was that as shown in fig. 9.5. The top window film was held between two circular metal rings C and G by means of an 'O' ring D. The cell spacer , to determine the path-length of the cell, was placed between the lower plate G and the film E, which was stretched using the film stretcher. The second plate C, containing the 'O' ring D was placed at the other side of the film, and then the 3 retaining screws tightened to clamp the two rings together. The film was then carefully cut around the outside edge of the rings. The cell window top plate A was then tightened against the two film retaining rings. This whole assembly

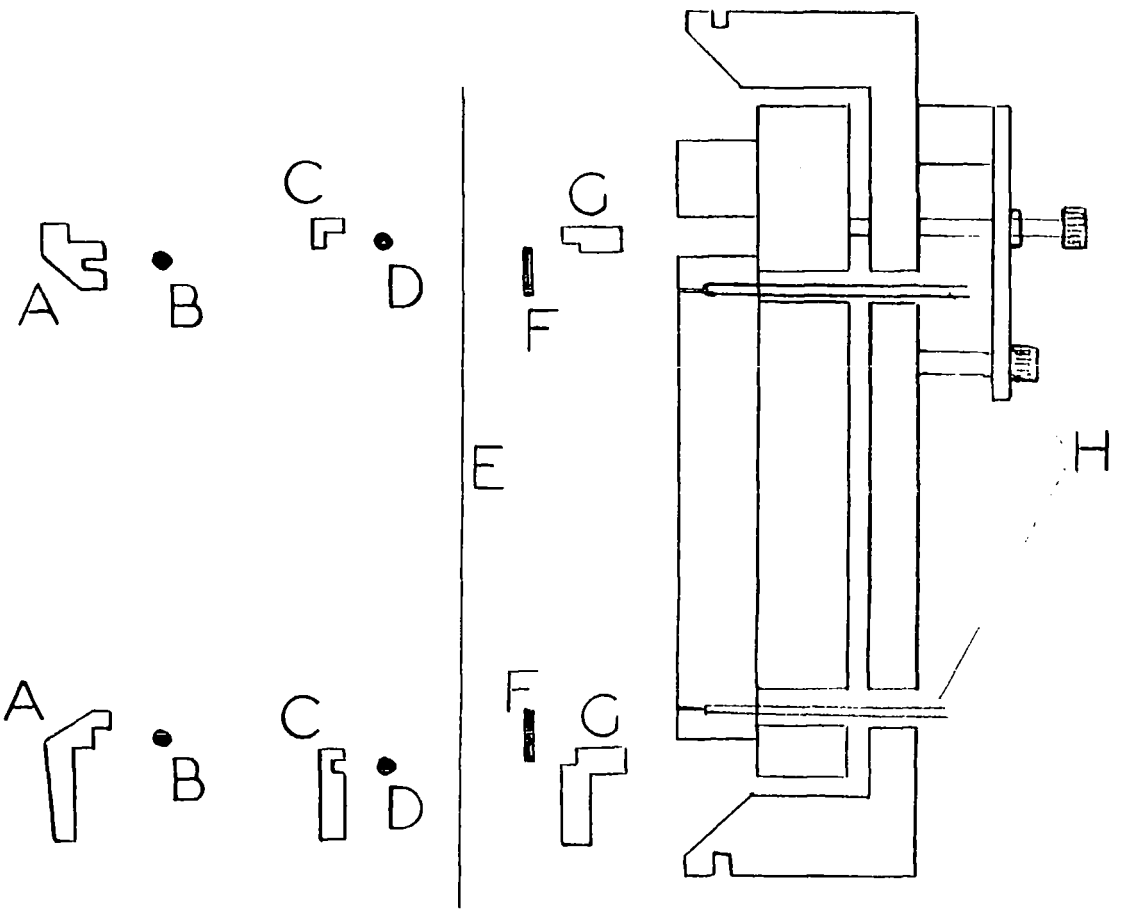

Key;

A cell window top plate

B 'O' ring to seal film against the spacer

C film retaining top plate

D film retaining 'O' ring

E top window film

F cell spacer

G film retaining bottom plate

H liquid entry and exit ports

FIG. 9.5 SIDE VIEW REFRACTIVE INDEX CELL

was then to be clamped over the mirror block and retained by 3 screws through from the back of the cell block. These 3 retaining screws pulled down the 'O' ring B, which sealed the window film against the spacer and the spacer against the mirror surface. An enlargement of the film retaining rings is given in fig. 9.6, where the key is the same as that used in fig. 9.5. This figure shows clearly the sealing of the film against the mirror surface.

The cell could be filled and flushed through two capillary tubes made from teflon, which was used because of its lack of reactivity. These tubes were connected to two holes drilled through the glass mirror. These holes were just inside the spacer so that the whole cell would be filled by a flow of liquid through the entry and exit ports. The connections between the glass and the teflon tubes was a glued joint into the glass block, where the drilled hole was slightly enlarged to take the diameter of the teflon tube. The ends of the teflon tube away from the cell had nickel luer fittings attached to fit the standard glass luers used for filling the Beckman FS-01 cells.

A flushing port was provided in the refractive index module, so that the space in the interferometer beam between the vacuum window and the top window of the cell could be purged with dry nitrogen gas. This was positioned so that the nitrogen flow hits the steel base of the mirror and then flowed into the air space.

9.4 Use of the refractive index cell

The cell was firstly tested by placing the vacuum window in position and then pumping down the instrument carefully. With the 25 gauge film the film was distorted very badly over the metal grid and the stretching was such that the interferometer could only be pumped down once using the same film. The film burst on starting the pumping on any subsequent occa sion. The 50 gauge film did not distort nearly so badly as the 25 gauge, and the interferometer could be pumped down repeatedly if the pumping was done in a controlled fashion. The base pressure obtained was typically 0.02 Torr,

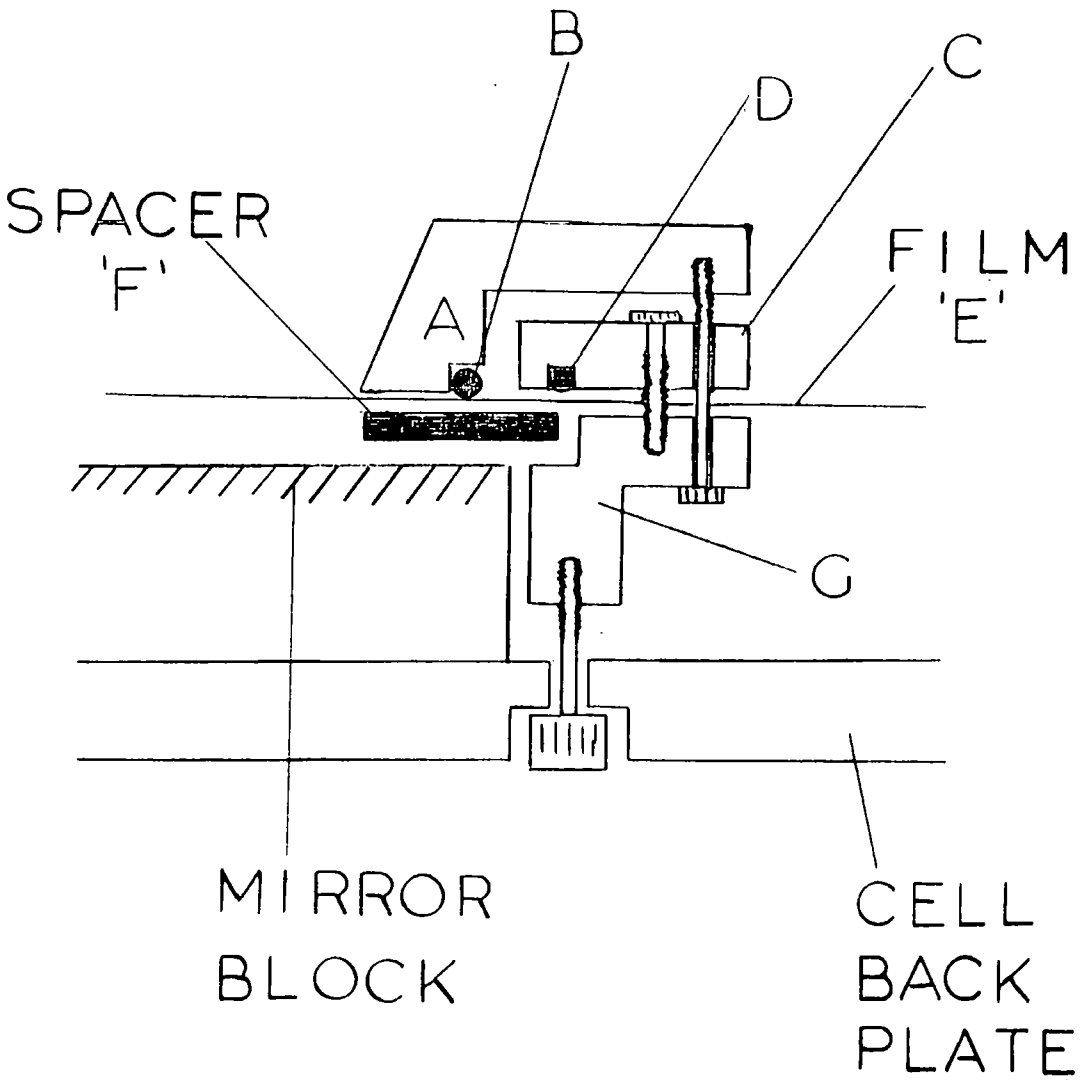

FIG. 9.6 ENLARGEMENT OF WINDOW RETAINING RINGS

which was almost as good as that (0.01 Torr) in the conventional fully enclosed interferometer.

To test the effect of the window material on the intensity of radiation in the beam the following experiments were performed. With the instrument at atmospheric pressure a level of 60% on the chart recorder was obtained with the standard fixed mirror in place. The fixed mirror was then removed, and as expected the interferogram mean level was recorded as 31%, due to reflection only being possible at the moving mirror. A fresh 50 gauge film was placed in the film holder and clamped into the instrument. With this film in place the level on the chart recorder was 45%, due to reflection from the undistorted vacuum film. The refractive index cell with a 400 gauge top window film and a 400 gauge spacer was then placed in position, and the interferogram level was seen to rise further to 54%. These figures indicated that about 46% of the radiation in the fixed mirror arm was reflected at the vacuum window before it was disturbed from its plane parallel state by the pumping process. Presumably this reflection loss will be increased when the film is distorted by the pumping process, and this loss is obviously considerable. When the cell was placed in position a further 9% of radiation was returned to the detector. This indicated that only about 4% of the radiation in the fixed mirror arm was being reflected at the mirror surface of the cell, if it was assumed that the percentage reflection at the first mirror surface was the same as that at the vacuum window, which seems likely. This indicated that the modulation in the interferograms obtained from the refractive index cell would be small. Thus it seemed likely that the alignment of the mirror would be critical if any useful interferogram was to be produced. This study also indicated that some way of increasing the percentage of radiation in the fixed mirror arm which was being reflected at the cell mirror had to be found.

Attempts were then initiated to observe interferograms using the refractive index cell in its present form as experimental time was becoming short. The method used for alignment of the cell was as detailed below.

1. The alignment of the basic interferometer was carefully checked by observing the interferogram with the interferometer in the symmetric mode. The methods of alignment were detailed in chapter 2. The source/ beam-splitter/ moving mirror alignments were all carefully checked before the fixed mirror block was removed from the instrument.

2. The fixed mirror block was then completely removed by taking out the 3 long retaining bolts. The circular ring mounting was likewise removed by taking out the 3 short bolts which attached it to the beam-splitter module.

3. The vacuum seal 'O' ring (C in fig. 9.4) was then carefully greased to ensure a good seal. This 'O' ring was then placed in position in its groove on the grid support ring D. The film retaining 'O' ring was then greased very slightly and placed in the groove on the face of the grid support ring. This 'O' ring must be only lightly greased or the vacuum film was pulled through the grid. A little grease was found to assist with the formation of the vacuum seal. A very thin layer of grease was then spread on the face of the neoprene rubber gasket G, and a piece of the 50 gauge melinex film (20 cm x 20 cm) carefully placed over this gasket. The thin layer of grease was used to form an attraction of the gasket for the film thus enabling the film to be positioned more easily before the retaining ring was fastened in place.

4. The vacuum window support was then assembled and placed in position as follows. The grid ring B was placed in position at the rear of the grid support ring D, which was then placed in position in the circular aperture in the beam-splitter module. The vacuum film attached to the neoprene rubber gasket was then placed in position with the neoprene gasket outermost. The cell housing ring H was then pressed up against the neoprene gasket, and then held in place by the 3 short retaining bolts in the original holes in the beam-splitter module. These bolts were tightened gradually in turn to ensure that the film was not crinkled as it was tightened.

5. The vacuum pump was then set in motion and the vacuum of the system checked before any further alignments were made.

6. The refractive index cell was then placed in position, and clamped in this position by use of the 3 flanges with small retaining bolts.

7. The flow of purging nitrogen was then started, and the cell was then ready for use.

9.5 Typical results

The actual testing of the cell itself was initiated by recording interferograms for the empty cell. Firstly the use of the zero path-difference mirror was tested. The refractive index cell was attached, and aligned as detailed in section 9.4. The cell was set up with a 400 gauge top window a nominally 0.1 cm spacer. The interferograms recorded with the reference mirror both covered and uncovered are shown in fig. 9.7. A 50 gauge vacuum window was used throughout these studies. The dispersed interferogram of the top window, due to reflection from the cell mirror is denoted by the letter A in the figure. The zero path-difference interferogram from the reference mirror is denoted by the letter B. The displacement of the Grand Maximum was measured as approximately 0.0160 cm, the scale being determined by marking the chart at 0.0080 cm intervals as the interferogram was recorded. The chart was marked every tenth time the punch operated.

It was soon noticed that the empty cell interferograms were far more complicated than might have been expected. This complexity was considered to be due to internal reflections within the cell. Several empty cell interferograms were recorded to study the effects of these internal reflections on the interferograms. Fig. 9.8 shows the interferogram recorded for the refractive index cell with a 400 gauge (0.010 cm) beam-splitter material top window, and a spacer of nominally 0.1 cm thickness. The dispersed interferogram is denoted by the letter A, and the zero path-difference reflection by the letter B. Two more interferogram signatures were clearly seen in this trace and are denoted by the letters C and D in the figure. The two 'extra' interferograms occurred at path-differences shorter than zero path-difference. Interferogram C was thought to be due to reflection from the bottom surface of the

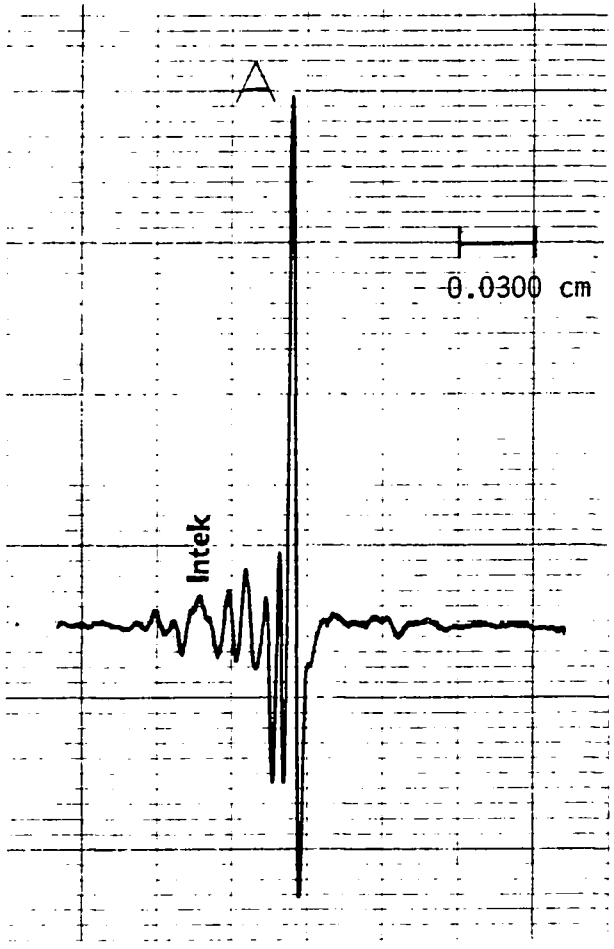

(a) Reference mirror covered

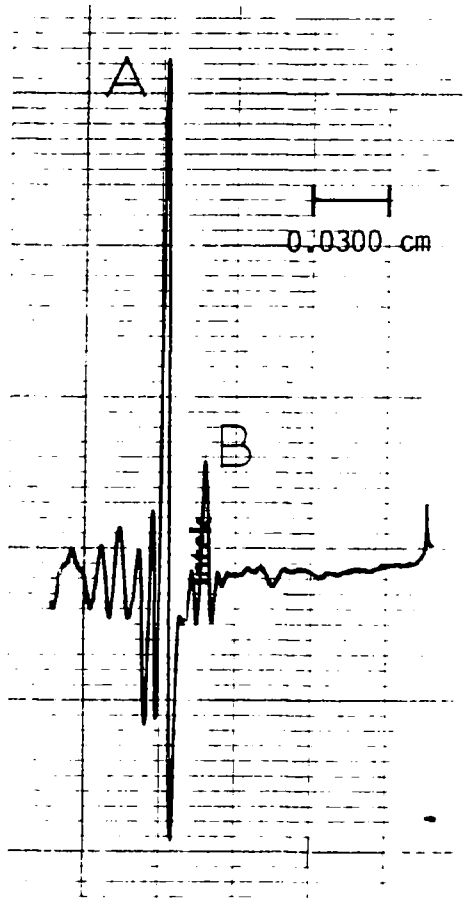

(b) Reference mirror uncovered

494

FIG. 9.7 USE OF THE REFERENCE MIRROR

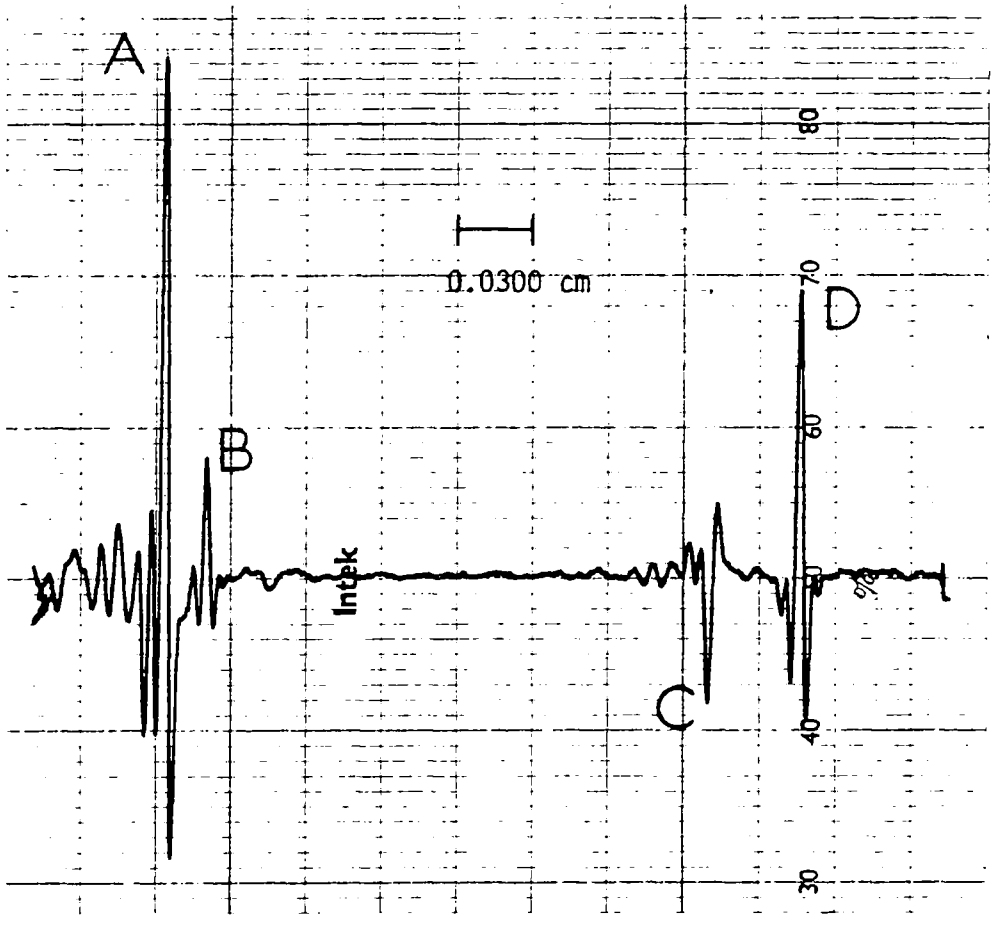

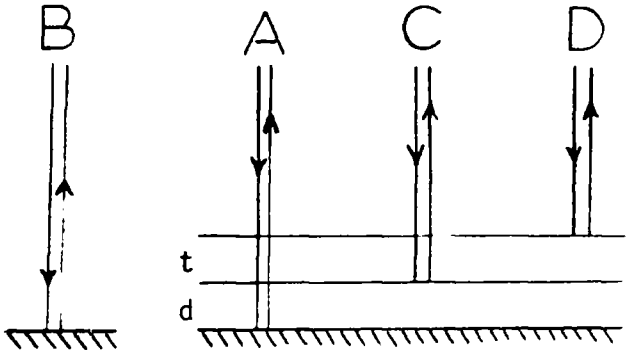

$t = 0.0100$ cm

$d = 0.1068$ cm

$\bar{x}_w = 0.0153$ cm

FIG. 9.8 EMPTY CELL INTERFEROGRAM

cell window. Likewise interferogram D was thought to be due to reflection at the top surface of the cell window. The inset in figure 9.8 shows schematically the various reflections occurring in the cell. A phase change of π radians would be expected where reflection occurred at a boundary surface from a less optically dense medium to a more optically dense medium. Thus a phase change of π radians would be expected for reflection at the main mirror surface and also at the reference mirror. These reflections gave rise to the signatures A and B in the interferogram trace. Such a phase change would also be expected for reflection at the top surface of the cell window for interferogram D. A phase change of π radians would not be expected for reflection at the bottom surface of the top window, and hence this interferogram signature was seen to be inverted relative to the other 3 signatures on the chart.

An expanded interferogram was recorded so that measurements of the displacement of the various interferogram signatures could be made, to assist with the assignment of the interferogram signatures. The displacement of the dispersed interferogram was measured as 0.0153 cm, which gave $\bar{x}_{window}$ directly as $\bar{x}_W$ = 0.0153 cm. The displacement of interferogram D from zero path-difference was measured as 0.2337 cm. If the assignments were correct, then this displacement would be twice the sum of the window thickness t, and the cell pathlength d. Thus 2(d+t) = 0.2337, i.e. d+t = 0.1168 cm. The displacement of interferograms C and D was measured as 0.0353 cm. This displacement was the sum of 2t + $\bar{x}_W$, and hence 2t was calculated as 0.0200 cm, and the window thickness as 0.0100 cm, which was correct for the 400 gauge material used. The cell pathlength was then calculated since d+t = 0.1168cm, giving d = 0.1068 cm for the pathlength of the cell, which again corresponded well for the nominal 0.1 cm spacer used. These measurements thus indicated that the assignments for the interferogram signatures were correct. The signatures were also seen to enable accurate calculation of the cell pathlength. A disadvantage of the many signatures was that the empty cell interferograms would not be useable as a background for the liquid samples, and would necessitate use of

liquid samples of different thicknesses to obtain refractive index curves for liquids.

Further empty cell interferograms were recorded with a 0.010 cm film as the top window and also as the cell spacer. Fig. 9.9 shows the interferogram obtained, for this cell with the reference mirror covered. In this case further signatures were observed due to the short pathlength of the cell. Signature A was once again the major dispersed interferogram, C the reflection from the lower surface of the top window, and D the reflection from the top surface of the window film. Measurements of the displacements of these signatures gave A to D as 0.0620 cm ($= \bar{x}_w + 2(d+t)$), C to D was 0.0390 cm ($= \bar{x}_w + 2t$). Thus 2d was calculated as 0.0620-0.0390, giving d = 0.0115 cm for the pathlength of the cell. A to E was measured as 0.0240 cm and so signature E was assigned to the first internal reflection in the cell air gap, since 2d was determined as 0.0230 above. Signature F was assigned to a double pass through the top window after reflection at the mirror (as shown in the inset to fig. 9.9). A to F was measured as 0.0620 cm ($= \bar{x}_w + 2t + 2d$ = 0.0390 + 0.0230 = 0.0620 cm). Signature G was assigned to the complete double pass of the air gap and window, since F to G was measured as 0.0220 cm (2d = 0.0230 cm).

The refractive index cell was then set up with a nominal 0.1 cm pathlength and 0.01 cm film thickness. The empty cell interferogram is shown as fig. 9.10. The reflections are lettered as previously, and the corresponding reflections are shown in the inset. These reflections gave a pathlength d of 0.0993 cm, top window thickness of 0.0104 cm, and $\bar{x}_w$ of 0.0153 cm. (B to A = 0.0153 cm = $\bar{x}_w$, E to F = 0.0360 cm = $\bar{x}_w + 2t$; 2t = 0.0207 cm; t = 0.0104, B to E = 0.2345 cm = $2d + 2t + \bar{x}_w$; 2d = 0.1985; d = 0.0993 cm). Fig. 9.11 shows the interferogram obtained when the refractive index cell was filled with cyclohexane. The expanded chart of fig. 9.12, with the reference mirror uncovered, gave A to B = 0.0980 cm. A to B will be $\bar{x}_w + \bar{x}_{cyclohexane}$, and so $\bar{x}_{cyclohexane}$ can be calculated as 0.0980 - 0.0153 = 0.0727 cm. The displacement

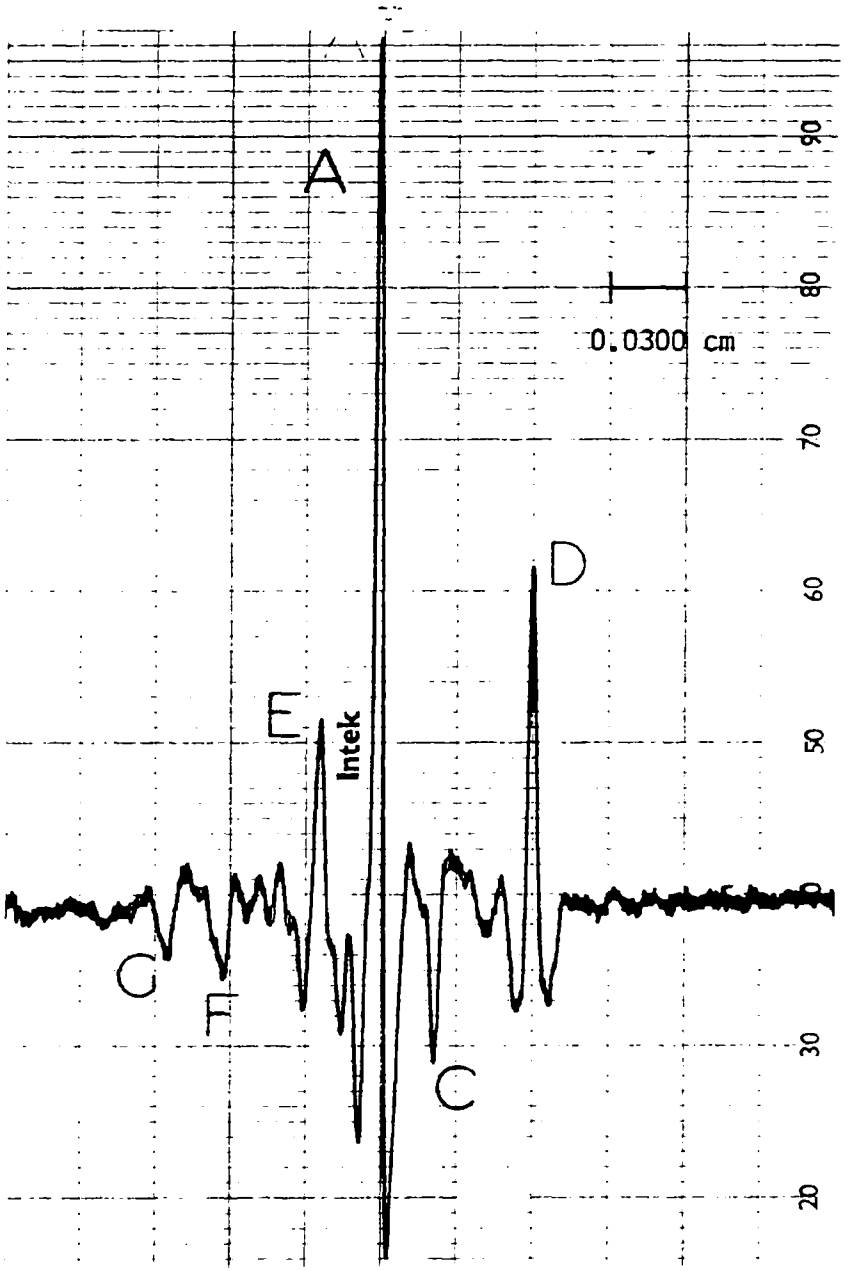

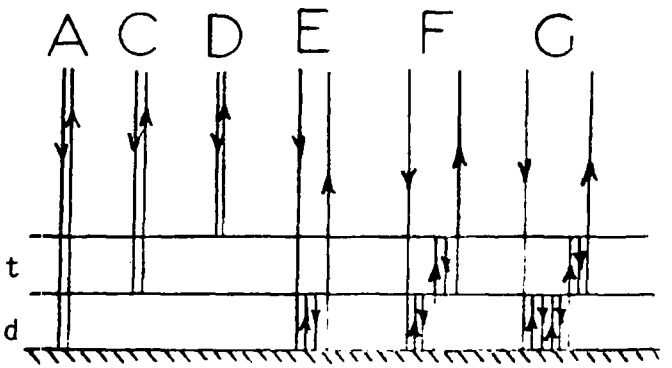

$\bar{x}_w + t = 0.0390$ cm

$d = 0.0115$ cm

FIG. 9.9 EMPTY CELL INTERFEROGRAM

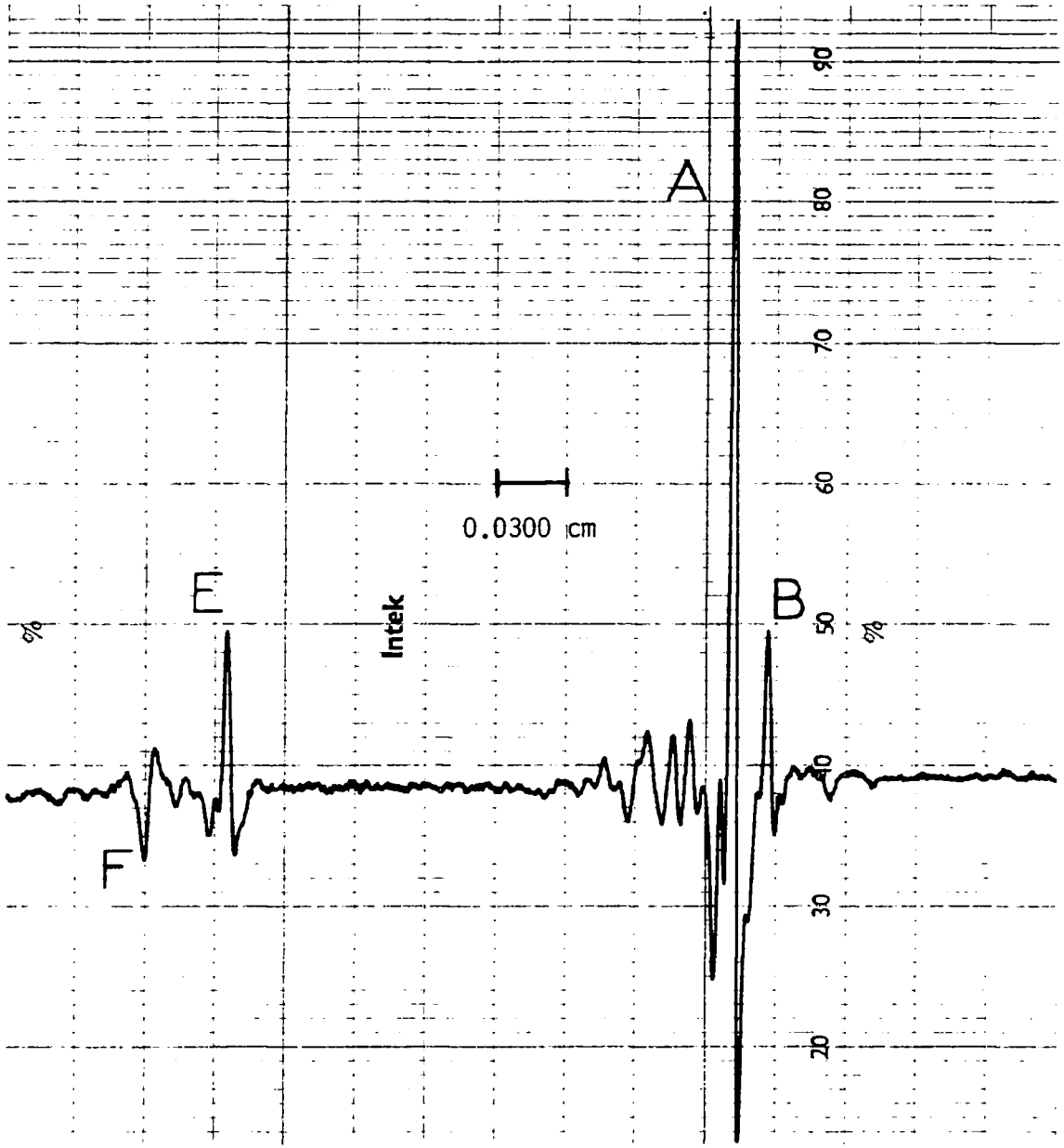

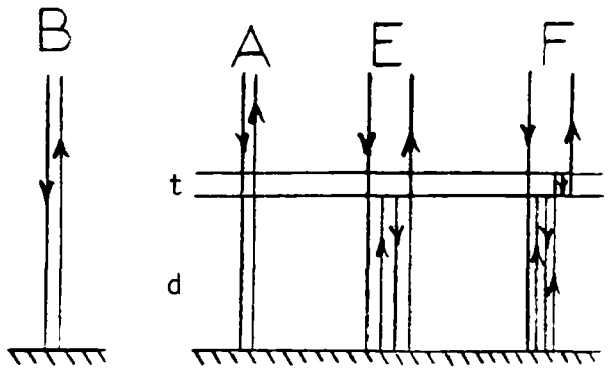

t = 0.0104 cm

d = 0.0993 cm

$\bar{x}_w$ = 0.0153 cm

FIG. 9.10 EMPTY CELL INTERFEROGRAM

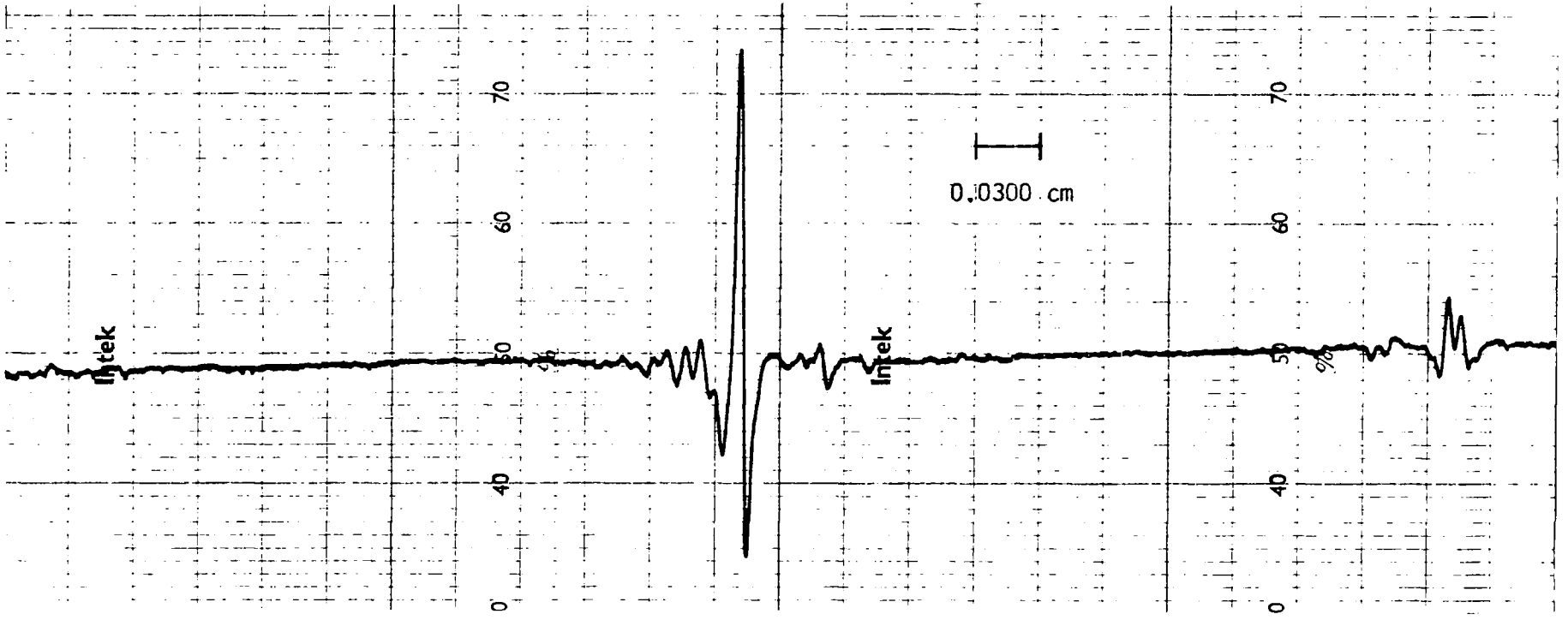

500

FIG. 9.11 DISPERSIVE CYCLOHEXANE INTERFEROGRAM

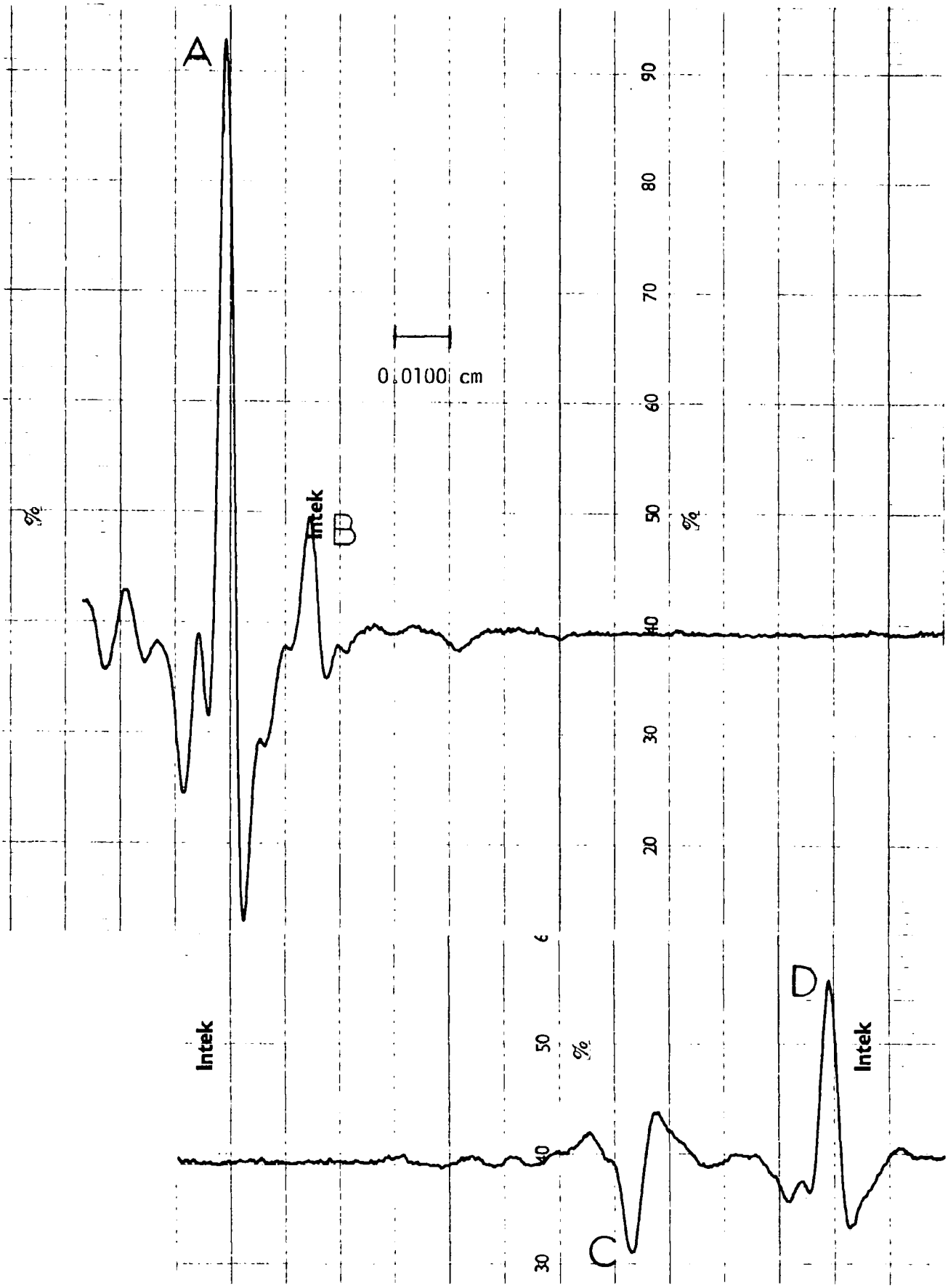

FIG. 9.12

EMPTY CELL INTERFEROGRAM

C to D was measured as 0.0360 cm (= $\bar{x}_w$ + 2t, and since $\bar{x}_w$ = 0.0153 then t = 0.0104 cm), which gave 0.0104 cm as the top window thickness, which agreed well with the determination from the empty cell. B to C was measured as 0.200 cm (= 2d; d = 0.100), which gave the sample thickness as 0.100 cm, which indicated that the cyclohexane had caused slight bulging of the cell window, as the air gap was measured as 0.0993 cm for the empty cell.

The refractive index programme DCH0623 was then used to compute the refractive index as a function of frequency from the 0.100 cm of cyclohexane and empty cell interferograms. Table 9.1 shows the refractive index as a function of frequency, and as expected the refractive index showed very little variation with frequency over the range studied, for this non-absorbing cyclohexane sample. The mean refractive index between 40 and 240 cm^{-1} was calculated as 1.4013.

Various interferograms were recorded for chloroform, carbon disulphide and carbon tetrachloride. Many problems were experienced with cell leakage and high signal-to-noise ratios, and it was found very difficult to obtain interferograms with sufficient modulation for any results to be achieved. No attempts were made to couple the dispersive interferometer to the more sensitive cooled detector, but this would be necessary to obtain good results with the more absorbing liquids. However the small amount of work achieved after the testing had been completed indicated that the system could be successfully used for the determination of refractive index spectra for liquids in the far-infrared region.

Table 9.1 Refractive index values for cyclohexane

$\bar{\nu}$ /cm^{-1}	n	$\bar{\nu}$ /cm^{-1}	n
39.1	1.4007	136.7	1.4021
44.0	1.4060	141.6	1.4006
48.8	1.4029	146.5	1.4010
53.7	1.4042	151.4	1.4009
58.6	1.4010	156.3	1.4013
63.5	1.4011	161.1	1.4012
68.4	1.4024	166.0	1.4010
73.2	1.4019	170.9	1.4006
78.1	1.4035	175.8	1.4007
83.0	1.4012	180.7	1.4008
87.9	1.4013	185.6	1.4010
92.8	1.4009	190.4	1.4006
97.7	1.4015	195.3	1.4008
102.5	1.4026	200.2	1.3997
107.4	1.4014	205.1	1.4013
112.3	1.4012	210.0	1.4011
117.2	1.4003	214.8	1.4007
122.1	1.4009	219.7	1.4005
127.0	1.4018	224.6	1.4003
131.8	1.4011	229.5	1.4012

References

1. J.E. Chamberlain, A.E. Costley and H.A. Gebbie; Spectrochim. Acta 23A, 2255 (1967).
2. N.E. Hill; Proc. Phys. Soc. 82, 723 (1963).
3. J.Ph. Poley; J. Appl. Sci. 4B, 337 (1965).
4. M. Davies, G.W.F. Pardoe, J.E. Chamberlain and H.A. Gebbie; Trans. Far. Soc. 64, 847 (1968).
5. J.P. Kettle and A.P. Price; J. Chem. Soc. Far. Trans II 68, 1309 (1972).
6. G.W.F. Pardoe; Trans. Far. Soc. 66, 2699 (1970).
7. S.G. Kroon and J. van der Elsken; Chem. Phys. Lett. 1, 285 (1967).
8. G.W. Chantry; 'Submillimetre Spectroscopy', Academic Press (1971).
9. F.B.J. Fourier; 'Theorie Analitique de la Chaleur', (1882).
10. H.A. Gebbie and R.Q. Twiss; Rep. Prog. Phys. 29, 729 (1966).
11. J.D. Strong; 'Concepts of Classical Optics', Freeman, San Francisco (1958).
12. R.J. Bell; 'Introductory Fourier Transform Spectroscopy', Academic Press (1971).
13. D.C. Champency; 'Fourier Transforms and their Physical Applications', Techniques of Physics Series, Academic Press (1973).
14. M. Nelkon and P. Parker; 'Advanced Level Physics', Heinemann (1966).
15. D.H. Martin and E. Puplett; Infrared Phys. 10, 105 (1969).
16. P. Fellgett; J. Phys. Radium 19, 187 (1958).
17. P. Fellgett; J. de Physique C2 28, 165 (1967).
18. H.A. Gebbie; Applied Optics 8, 501 (1969).
19. P. Jacquinot; Rep. Prog. Phys. 23, 267 (1960).
20. K.D. Möller and W.G. Rothschild; 'Far-Infrared Spectroscopy', Wiley-Interscience (1971).
21. H. Zahl and M. Golay; Rev. Sci. Instr. 17, 511 (1946).
22. M. Golay; Rev. Sci. Instr. 18, 357 (1947).
23. G.W. Chantry and J. Chamberlain; 'Far infrared spectra of Polymers', Chapter 20 of 'Polymer Science', A.D. Jenkins, North-Holland (1972).

24. Y. Yamada, A. Mitsuishi and H. Yoshinaga; J. Opt. Soc. Am. 52, 17 (1962).

25. K.D. Möller and R.V. McKnight; J. Opt. Soc. Am. 53, 760 (1963).

26. K.D. Möller and R.V. McKnight; J. Opt. Soc. Am. 55, 1075 (1965).

27. G.W. Brownson; PhD Thesis, Durham University (1974).

28. J. Yarwood; 'Absolute Intensity Measurements in the Region 10 - 600 cm^{-1}', Beckman-RIIC Ltd. (1970).

29. J.W. Cooley and J.W. Tukey; Mathematics of Computation 19, 295 (1965).

30. P.L. Richards; J. Opt. Soc. Am. 54, 1474 (1964).

30a. S. Cantarano and G.V. Pallotino; Electronic Engineering, 57 (Sept. 1970).

31. M.L. Forman; J. Opt. Soc. Am. 56, 978 (1966).

32. L. Mertz; Infrared Phys. 7, 17 (1967).

33. E.V. Loewenstein; Appl. Opt. 2, 491 (1963).

34. M.L. Forman, W.H. Steel and G.A. Vanasse; J. Opt.Soc. Am. 56, 59 (1966).

35. M.J. Connes; Rev. Opt. 40, 45, 116, 171, 231 (1961).

36. E.O. Brigham and R.E. Morrow; IEEE Trans. Audio Electraccoust. AU-15(2), 63 (1967).

37. J. Connes; Aspen. Int. Conf. on Fourier Spectrosc., G.A. Vanasse, A.T. Stair,Jr. and D.J. Baker, AFCRL-71-0019, 5 Jan. 1971, Spec. Rep. No. 114.

38. H.G. Jerrard and D.B. McNeill; 'A Dictionary of Scientific Units', Chapman and hall (1964).

39. 'Instruction Manual for the Fourier Spectrophotometer FS-720', Research and Industrial Instruments Company (now Beckman-RIIC Ltd.) (1968).

40. V.I. Malisek and M. Miler; 'Vibration Spectroscopy', Iliffe, Butterworth (1971).

41. M.J. French and J.L. Wood; J. Chem Phys. 49, 2358 (1968).

42. W.F. Edgell, J. Lyford, R. Wright, W.M. Risen and A. Watts; J. Am. Chem. Soc. 92, 2240 (1970).

43. W.F. Edgell, A.T. Watts, J. Lyford and W.M. Risen; J. Am. Chem. Soc. 88, 1815 (1966).

44. M.K. Wong, W.J. McKinney and A.I. Popov; J. Phys. Chem. 75, 56 (1971).

45. B.W. Maxey and A.I. Popov; J. Am. Chem. Soc. 91, 20 (1969).

46. P.R. Handy and A.I. Popov; Spectrochim. Acta 28A, 1545 (1972).

47. W.F. Edgell; 'Ions and Ion Pairs in Organic Reactions', ed. M. Szwarc, Wiley Interscience, Vol. 1, Chap. 4.

48. J.C. Evans and G. Y-S. Lo; J. Phys. Chem. 69, 3223 (1965).

49. J.P. Badiali, H. Cachet, A. Cyrot and J.C. Lestrade; J.C.S. Faraday II 69, 1339 (1973).

50. J.P. Badiali, H. Cachet, A. Cyrot and J.C. Lestrade; 'Molecular Motion in Liquids', ed. J. Lascombe, Reidel, Dordrecht (1974), p. 173.

51. J.P. Badiali, H. Cachet, P. Canard, A. Cyrot and J.C. Lestrade; Compt. Rend. C 273, 199 (1971).

52. J.P. Badiali, H. Cachet and J.C. Lestrade; Ber. Bungsenges. Phys. Chem. 75, 297 (1971).

53. W.F. Edgell and A.T. Watts; 'Abstracts, Symposium on Molecular Structure and Spectroscopy', Ohio State University (1965).

54. J. Overend; 'Infrared Spectroscopy and Molecular Structure'; ed. M.M. Davies, Elsevier (1963).

55. J. Topping; 'Errors of Observation and their Treatment', The Institute of Physics and the Physical Society Monographs for Students, Chapman and Hall Ltd., London (1969).

56. International Critical Tables.

57. J.L. Hollenberg and D.A. Dows; J. Chem. Phys. 34, 1061 (1961).

58. J.L. Hollenberg and D.A. Dows; J. Chem. Phys. 37, 1300 (1962).

59. G. Herzberg; 'Molecular Spectra and Molecular Structure, Vol. II, Infrared and Raman Spectra of Polyatomic Molecules', D. van Nostrand (1964).

60. I. Harada and T. Shimanouchi; J. Chem Phys. 55, 3605 (1971).

61. 'Infrared and Ultraviolet Sampling Accessories, 'Specac '75''; Spectroscopic Accessory Company (1975).

62. H. Yamada and W.B. Person; J. Chem. Phys. 38, 1253 (1963).

63. K. Szczepaniak and W.B. Person; Spectrochim. Acta 28A, 15 (1972).

64. E.B. Wilson Jr.; Phys. Rev. 45, 706 (1934).

65. F.C. Strong; Appl. Spectrosc. 23, 593 (1969).

66. J. Pitha and R.N. Jones; Can. J. Chem. 44, 3031 (1966).

67. K.S. Seshadii and R.N. Jones; Spectrochim. Acta 19, 1013 (1963).

68. R.L. Goodstein; 'Complex Functions', McGraw-Hill (1970).

69. M.R. Spiegel; 'Theory and Problems of Advanced Calculus', McGraw-Hill (1963).

70. J. Pitha and R.N. Jones; 'Optimization Methods for fitting curves to Infrared Band Envelopes - Computer Programs', National Research Council of Canada, NRC Bulletin No. 12 (1968).

71. G.W. Chantry, H.A. Gebbie, B. Lassier and G. Wyllie; Nature 214, 163 (1967).

72. G.W. Chantry and H.A. Gebbie; Nature 208, 378 (1965).

73. L.E. Strong and C.A. Kraus; J. Am. Chem. Soc. 72, 166 (1950).

74. I. Harada and T. Shimanouchi; J. Chem. Phys. 44, 2016 (1966).

75. I. Harada and T. Shimanouchi; J. Chem. Phys. 46, 2708 (1967).

76. T. Miyazawa and N. Nakamaru; J. Chem. Phys. 52, 5972 (1970).

77. Encyclpedia Britannica 22, 281 (1963).

78. R.E. Kirk and D.F. Other (Eds.); 'Encyclopedia of Chemical Technology' 3, 191 (1949).

79. P. Datta and G.M. Borrow; J. Chem. Phys. 48, 4662 (1968).

80. B.J. Bulkin; Helv. Chim. Acta 52, 1348 (1969).

81. S.R. Jain and S. Walker; J. Phys. Chem. 75, 2942 (1971).

82. B.W. Maxey and A.I. Popov; J. Am. Chem. Soc. 89, 2230 (1967).

83. W.J. McKinney and A.I. Popov; J. Phys. Chem. 74, 535 (1970).

84. J.L. Wuepper and A.I. Popov; J. Am. Chem. Soc. 91, 4352 (1969).

85. K. Koya, Y. Kanazawa and H. Shimizu; J. Molec. Spectrosc. 47, 107 (1973).

86. Covington and Dickinson; 'Physical Chemistry of Organic Solvent Systems', Plenum.

87. G.J. Janz and R.P.T. Tomkins; 'Nonaqueous Electrolytes Handbook', Vol. II.

88. R.C. Paul, P. Singh and S.L. Chadna; Ind. J. Chem. 9, 1160 (1971).

89. C.F. Tweeney and L.E. Hughes; 'Chambers Technical Dictionary', (1964).

90. C.C. Addison, D.W. amos, D. Sutton and W.H.H. Hoyle; J. Chem. Soc. A, 808 (1967).

91. J.M. Kolthoff and J.F. Coetzee; J. Am. Chem. Soc. 79, 870 (1957).

92. J.E. Prue and P.J. Sherrington; Trans. Far. Soc. 57, 1795 (1961).

93. H.E. Zaugg; J. Am. Chem. Soc. 82, 2903 (1960).

94. P.G. Sears, E.D. Wilhoit and L.R. Dawson; J. Phys. Chem. 59, 373 (1955).

95. P.G. Sears, G.R. Lester and L.R. Dawson; J. Phys. Chem. 60, 1433 (1956).

96. A.D. Buckingham; Dis. Far. Soc. 24, 151 (1957).

97. I.M. Kolthoff and J.F. Coetzee; J. Am. Chem. Soc. 79, 1852 (1957).

98. 'Solubilities of Inorganic Compounds', Edited by Seidell, Van Nostrand, New York (1940).

99. A.J. Parker; Chem. Rev. 69, 1 (1969).

100. J.A. Geddes and C.A. Kraus; Trans. Far. Soc. 32, 585 (1936).

101. G.S. Hooper and C.A. Kraus; J. Am. Chem. Soc. 56, 2265 (1934).

102. D.T. Copenhafer and C.A. Kraus; J. Am. Chem. Soc. 73, 4557 (1951).

103. C.A. Kraus and R.A. Vingee; J. Am. Chem. Soc. 56, 511 (1934).

104. F.M. Batson and C.A. Kraus; J. Am. Chem. Soc. 56, 2017 (1934).

105. C.A. Kraus; J. Phys. Chem. 60, 129 (1956).

106. M. Szwarc (Ed.); 'Ions and Ion Pairs in Organic Reactions', Vol. I.

107. W.R. Gilkerson and K.K. Strivastava; J. Phys. Chem. 64, 1485 (1960).

108. H. Sadek and R.M. Fuoss; J. Am. Chem. Soc. 76, 5897 (1954).

109. D.S. Berns and R.M. Fuoss; J. Am. Chem. Soc. 82, 5585 (1960).

110. E. Hirsch and R.M. Fuoss; J. Am. Chem. Soc. 82, 1018 (1960).

111. M.A. Caplan and R.M. Fuoss; J. Phys. Chem. 68, 1177 (1964).

112. H. Sadek and R.M. Fuoss; J. Am. Chem. Soc. 81, 4511 (1959).

113. D.N. Bhattacharya, C.L. Lee, J. Smid and M. Szwarc; J. Phys. Chem. 69, 608 (1965).

114. R.M. Fuoss and E. Hirsh; J. Am. Chem. Soc. 82, 1013 (1966).

115. F.H. Healey and A.E. Martell; J. Am. Chem. Soc. 73, 3296 (1951).

116. P.H. Flaherty and K.H. Stern; J. Am. Chem. Soc. 80, 1034 (1958).

117. R.M. Fuoss; J. Am. Chem. Soc. 81, 2659 (1959).

118. J.J. Padova; 'Modern aspects of Electrochemistry No. 7', Vol. I, Edited by B.E. Conway and J.O'M. Bockris, Butterworths. Chap. 1.

119. E. Price; 'The Chemistry of Non-Aqueous Solvents', Vol. I Edited by Lagowski, Academic Press (1966).

120. H. Sadek and R.M. Fuoss; J. Am. Chem. Soc. 76, 5905 (1954).

121. H. Sadek and R.M. Fuoss; J. Am. Chem. Soc. 76, 5902 (1954).

122. F.M. Sacks and R.M. Fuoss; J. Am. Chem. Soc. 75, 5172 (1953).

123. R.C. Miller and R.M. Fuoss; J. Am. Chem. Soc. 75, 3076 (1953).

124. H. Sadek and R.M. Fuoss; J. Am. Chem. Soc. 72, 301 (1950).

125. M.J. McDowell and C.A. Kraus; J. Am. Chem. Soc. 73, 3293 (1951).

126. M.B. Reynolds and C.A. Kraus; J. Am. Chem. Soc. 70, 1709 (1948).

127. D.L. Fowler and C.A. Kraus; J. Am. Chem. Soc. 62, 2237 (1940).

128. R.M. Fuoss; J. Am. Chem. Soc. 80, 5059 (1958).

129. R.M. Fuoss and C.A. Kraus; J. Am. Chem. Soc. 55, 3614 (1953).

130. R.M. Fuoss and C.A. Kraus; J. Am. Chem. Soc. 57, 1 (1935).

131. W.F. Luder, P.B. Kraus, C.A. Kraus and R.M. Fuoss; J. Am Chem Soc. 58, 255 (1936).

132. S. Winstein, E. Clippinger, A.H. Fainberg and G.C. Robinson; J. Am. Chem. Soc. 76, 2597 (1954).

133. C. Carvajal, K.J. Tölle, J. Smid and M. Szwarc; J. Am. Chem. Soc. 87, 5548 (1965).

134. J.L. Wueppur and A.I. Popov; J. Am. Chem. Soc. 92, 1493 (1970).

135. B.W. Maxey and A.I. Popov; J. Inorg. Nucl. Chem. 32, 1029 (1970).

136. W.F. Edgell and J. Lyford; J. Am. Chem. Soc. 93, 6407 (1971).

137. M.K. Wong and A.I. Popov; J. Inorg. and Nucl. Chem. 34, 3615 (1972).

138. L.G. Savedoff; J. Am. Chem. Soc. 88, 664 (1966).

139. P. Beronius, U. Isacsson and A.M. Nilson; Acta Chem. Scand. 24, 189 (1970).

140. J.C. Boubel and J.J. Delpuech; Mol. Phys. 27, 113 (1974).

141. T.D. Westmoreland, N.S. Bhacca, J.D. Wander and H.C. Day; J. Am. Chem. Soc. 95, 2019 (1973).

142. B. Kingston and M.C.R. Symons; J. Chem. Soc. Far. Trans. 69, 978 (1973).

143. M.S. Greenberg, R.L. Bodner and A.I. Popov; J. Phys. Chem. 77, 2449 (1973).

144. R.H. Erlich, M.S. Greenberg and A.I. Popov; Spectrochim. Acta 29A, 543 (1973).

145. M. Herlem and A.I. Popov; J. Am. Chem. Soc. 94, 1431 (1972).

146. R.H. Erlich and A.I. Popov; J. Am. Chem. Soc. 93, 5620 (1971).

147. R.H. Erlich, E. Roach and A.I. Popov; J. Am. Chem. Soc. 92, 4989 (1970).

148. R.L. Bodner, M.S. Greenberg and A.I. Popov; Spectrosc. Lett. 5, 489 (1972).

149. E.T. Roach, P.R. Handy and A.I. Popov; Inorg. Nucl. Chem. Lett. 9, 359 (1973).

150. R.H. Erlich, M.S. Greenberg and A.I. Popov; Spectrochim. Acta 29A, 543 (1973).

151. E.B. Baker and A.I. Popov; J. Phys. Chem. 76, 2403 (1972).

152. B.W. Maxey and A.I. Popov; J. Am. Chem. Soc. 90, 4470 (1968).

153. H. Cachet, I. Epelboin and J.C. Lestrade; Electrochim. Acta 11, 1759 (1966).

154. H. Cachet, F.F. Hanna, J.C. Lestrade and J. Pouget; J. de Physique 2, 285 (1974).

155. J.P. Badiali, H. Cachet and J.C. Lestrade; Electrochim. Acta 16, 731 (1971).

156. E.A. Cavell and E. Sheikh; J. C. S. Far. II 69, 317 (1973).

157. J.C. Lestrade, J.P. Badiali and H. Cachet; 'Dielectric and Related Processes', ed. M.M. Davies, Specialist Periodical Reports, Chemical Society 2, 6 (1975).

158. H. Cachet, F.F. Hanna and J. Pouget; J. Chim. Phys. 71, 1322 (1974).

159. E.A. Cavell and P.C. Knight; J.C.S. Far. II 68, 765 (1972).

160. M.M. Davies and G. Williams; Trans. Far. Soc. 56, 1619 (1960).

161. C.N. Banwell; 'Fundamentals of Molecular Spectroscopy', McGraw-Hill (1966).

162. Birnbaum and Maryott; J. Chem. Phys. 36, 2026 (1962).

163. Gebbie and Stone; Proc. Phys. Soc. 82, 543 (1963).

164. Kaufmann and Thaddeus; J. Chem. Phys. 45, 877 (1966).

165. P.W. Atkins; 'Molecular Quantum Mechanics', Vol. I, Clarendon Press (1970).

166. P.W. Atkins; 'Molecular Quantum Mechanics', Vol. II, Clarendon Press (1970)

167. W.J. Driscol; 'Progress in Infrared Spectroscopy', Vol. I, S. Zymanski (ed.) (1962).

168. B. Crawford; J. Chem. Phys. 29, 1042 (1958).

169. J. Overend; 'Infrared Spectroscopy and Molecular Structure', Ed. M.M. Davies, Elsevier (1963).

170. C. Barker and J. Yarwood; Faraday Symposium of the Chemical Society, No. 11, (Dec. 1976).

171. P. Debye; 'Polar Molecules', Dover Publishers (1929).

172. A. Gerschel, I. Darmon and C. Brot; Mol. Phys. 23, 317 (1973).

173. G.J. Davies, G.W.F. Pardoe, J. Chamberlain and H.A. Gebbie; Trans. Far. Soc. 64, 847 (1968).

174. M. Evans; J. C. S. Faraday II 71, 2051 (1975).

175. M. Evans; J. C. S. Faraday II 72, 727 (1976).

176. M. Evans; Spectrochim. Acta 32A, 1253 (1976).

177. M. Evans; Spectrochim. Acta 32A, 1259 (1976).

178. M. Evans; Molec. Phys. 29, 1345 (1975).

179. H.S. Gabelnick and H.L. Strauss; J. Chem. Phys. 46, 396 (1967).

180. M. Davies, G.W.F. Pardoe, J. Chamberlain and H.A. Gebbie; Chem. Phys. Lett. 2, 411 (1968).

181. T.G. Paker and A.M. North; Trans. Far. Soc. 67, 2234 (1971).

182. G.J. Davies, J. Chamberlain and M. Davies; J. C. S. Faraday II 69, 1223 (1973).

183. G.J. Davies and J. Chamberlain; J. C. S. Faraday II 69, 1739 (1973).

184. M. Evans and G.J. Davies; J. C. S. Faraday II 72, 1206 (1976).

185. M. Evans; J. C. S. Faraday II 69, 763 (1973).

186. M. Evans; J. C. S. Faraday II 71, 71 (1975).

187. S. Glasstone; 'Theoretical Chemistry', Van Nostrand (1966).

188. T. Duncan; 'Advanced Physics, Fields, Waves and Atoms', J. Murray (1975).

189. K. Bauge and J.W. Smith; J. Chem. Soc., 4244 (1964).

190. J. Yarwood (ed.); 'Spectroscopy and Structure of Molecular Complexes', Plenum (1973).

191. M.J. Wooten; 'Electrochemistry', Vol. 3, ed. G.J. Hills, Specalist Periodical Reports, The Chemical Society (1973).

192. E.A.S. Cavell and M.A. Sheikh; J. C. S. Faraday II 71, 474 (1975).

193. H. Cachet, F.F. Hanna and J. Pouget; J. Chim. Phys. 71, 285 (1974).

194. H. Cachet, F.F. Hanna and J. Pouget; J. Chim. Phys. 71, 1546 (1974).

195. H. Cachet and J.C. Lestrade; Bull. Soc. Chim. Belg. 85, 481 (1976).

196. E. Grunwald, S. Highsmith and T.P. I; 'Ions and Ion Pairs in Organic Reactions', Vol. II, ed. M. Szwarc, J. Wiley (1974).

197. S.G. Kroon and J. Van der Elsken; Chem. Phys. Lett. 1, 285 (1967).

198. H. Dandy, V. Volterra and T.A. Litovitz; 'Faraday symposium No. 6, The Chemical Society (1972).

199. R.G. Gordon; J. Chem. Phys. 38, 1724 (1963).

200. A. Gerschel, I. Darmon and C. Brot; Molec. Phys. 23, 317 (1972).

201. M. Davies, G.F. Pardoe, J. Chamberlain and H.A. Gebbie; Trans Far. Soc. 66, 273 (1970).

202. I. Darmon, A. Gerschel and C. Brot; Chem. Phys. Lett. 8, 454 (1971).

203. A.I. Baise; Chem. Phys. Lett. 9, 627 (1971).

204. C.F. Böttcher; 'The theory of Electrical Polarisation', Elsevier (1952).

205. E.A. Moelwyn-Hughes; 'Physical Chemistry', Pergamon (1961).

206. M.K. Wong and A.I. Popov; J. Inorg. Nucl. Chem. 33, 1203 (1971).

207. E.E. Ferguson and I.Y. Chang; J. Chem. Phys. 34, 628 (1961).

208. E.E. Ferguson; J. Chim. Phys. 61, 257 (1964).

209. J. Chamberlain, J.E. Gibbs and H.A. Gebbie; Nature 198, 874 (1963).

210. J. Chamberlain, F.D. Finlay and H.A. Gebbie; Applied Optics 4, 1382 (1965).

211. J. Chamberlain and H.A. Gebbie; Nature 208, 480 (1965).

212. J. Chamberlain and H.A. Gebbie; Applied Optics 5, 393 (1966).

213. J. Chamberlain, A.E. Costley and H.A. Gebbie; Spectrochim. Acta 23A, 2255 (1967).

214. J. Chamberlain, H.A. Gebbie, G.W.F. Pardoe and M. Davies; Chem. Phys. Lett. 1, 523 (1968).

215. M. Davies, G.W.F. Pardoe, J. Chamberlain and H.A. Gebbie; Trans. Far. Soc. 64, 847 (1968).

216. J. Chamberlain, A.E. Costley and H.A. Gebbie; Spectrochim. Acta 25A, 9 (1969).

217. E.E. Bell; Japan. J. Appl. Phys. 4, Suppl. 1, 412 (1965).

218. E.E. Bell; Infrared Phys. 6, 57 (1966).

219. E.E. Russell and E.E. Bell; Infrared Phys. 6, 75 (1966).

220. E.E. Russell and E.E. Bell; J. Opt. Soc. Am. 57, 341 (1967).

221. E.E. Russell and E.E. Bell; J. Opt. Soc. Am. 57, 343 (1967).

222. R. Sanderson; Appl. Opt. 6, 1527 (1967).

223. E.E. Bell; J. Phys. 28, C2-18 (1967).

224. G.A. Vanasse and H. Sakai; 'Progress in Optics', Vol. 6, ed. E. Wolf, North-Holland (1967).

225. J. Chamberlain, J.E. Gibbs and H.A. Gebbie; Infrared Phys. 9, 185 (1969).

226. J. Chamberlain; J. Quant. Spectrosc. Radiat. Transfer 7, 151 (1967).

227. S.A. Korff and G. Brett; Rev. Mod. Phys. 4, 471 (1932).

228. H.A. Willis; private communication.

229. R.S. Longhurst; 'Geometrical and Physical Optics', Longman (1973).

A1 Listings of computer programmes and input data

A1.1 FTRAN4 Fourier transformation programme

```
C
C PROGRAMME FTRAN4  COLIN PARKER  UNIVERSITY OF DURHAM
C
C
C FS720 TRANSMISSION SPECTRA COMPUTATION
C
C COMPLETE AUTOCORRELATION METHOD WITH COOLEY-TUKEY TRANSFORMATION ROUTINE
C
      IMPLICIT REAL*4(A-H,O,V-Z),INTEGER*4(J-N,P-U)
C
      DIMENSION A(4096),C(4096),P(2048),B(2048),F(1),G(1),H(50)
      DIMENSION O(2048),V(11),I(15),ZX(20)
      DIMENSION E(2048)
C
      COMMON A,C,B,D
C
  100 FORMAT(I4,2XF5.2,2XF7.2,2XF7.2,2X11,2X11,2X11,2X11,2X11,2X11)
  101 FORMAT(3I2,3XA4,1XA4)
  102 FORMAT(4F6.3)
  103 FORMAT(I3)
  104 FORMAT(1HO,I4,2XF5.2,2(2XF7.2),6(2XI1))
  105 FORMAT(1H ,3I2,3XA4,1XA4)
  106 FORMAT(1H ,4F6.3)
  107 FORMAT(1HO'FS720 TRANSMISSION SPECTRA COMPUTATION USING FTRAN3')
  140 FORMAT(20A4)
  200 FORMAT(1H ,' RATIO SAMPLE/BACKGROUND TRANSFORMED ELEMENTS')
  201 FORMAT(1H ,10F12.4)
C
C
      READ(8,103) NSETS
   11 IF(NSETS)13,13,12
   12 I(7)=0
      I(9)=0
C
C
      READ(8,100) N,ESINT,FREQL,FREQH,IOPUT,NSIG,NABS,NOUT,NCARD,NOPN
C N=NUMBER OF POINTS TO BE TRANSFORMED (I4) MAXIMUM=2048
C ESINT=SAMPLING INTERVAL IN MICRONS (TOTAL PATH DIFFERENCE UNITS)
C FREQL=LOWER FREQUENCY LIMIT IN CM-1
C FREQH=UPPER FREQUENCY LIMIT IN CM-1
C IOPUT=NUMBER OF OUTPUT POINTS PER RESOLUTION (=1 TO 5 ONLY)
C NSIG = SIGNAL TO INDICATE WHETHER RATIO IS REQUIRED
C       = 1 FOR RATIOED SPECTRUM
C       = 2 FOR SINGLE BEAM SPECTRUM
C NABS = SIGNAL TO INDICATE HOW RATIOED SPECTRUM IS TO BE PLOTTED
C       = 1 FOR ABSORBANCE SPECTRUM
C       = 0 FOR TRANSMITTANCE
C NOUT = SIGNAL TO DETERMINE WHAT DATA IS LISTED
C      (=0 FOR NORMAL LISTING)
C      (=1 FOR SPECTRA ONLY)
C      (=2 FOR FULL DATA LISTING FOR ERROR SEARCHING)
C NCARD= SIGNAL TO INDICATE IF SPECTRAL CARD OUTPUT IS REQUIRED
C      (=0 GIVES NO CARD OUTPUT)
C      (=1 GIVES RATIOED SPECTRUM ON CARDS)
C      (=2 GIVES SINGLE SPECTRUM ON CARDS)
```

```
C NORM = SIGNAL TO INDICATE IF NORMALISATION OF THE BACKGROUND AND
C        SAMPLE SPECTRA IS REQUIRED
C     (=0 NORMALISATION OCCURS)
C     (=1 GIVES NO NORMALISATION)
C
C
      READ(8,101)I(11),I(12),I(13),I(14),I(15)
C I(11)=DAY(NUMERIC)
C I(12)=MONTH(NUMERIC)
C I(13)=YEAR(NUMERIC)
C I(14)=SAMPLE TAPE REFERENCE NUMBER
C I(15)=BACKGROUND TAPE REFERENCE NUMBER
C
C
      READ(8,102)(V(J),J=3,6)
C V(3)=SAMPLE COURSE GAIN SETTING
C V(4)=SAMPLE FINE GAIN SETTING
C V(5)=BACKGROUND COURSE GAIN SETTING
C V(6)=BACKGROUND FINE GAIN SETTING
C
C
      READ(8,140) ZX
C ZX=TITLE OF SPECTRA
      IF(NOUT.EQ.1) GO TO 28
      WRITE(6,107)
      WRITE(6,140) ZX
      WRITE(6,104) N,FSINT,FREQL,FREQH,IOPUT,NSIG,NABS,NCLT,NCARD,NORM
      WRITE(6,105)(I(J),J=11,15)
      WRITE(6,106)(V(J),J=3,6)
   28 I(7)=I(7)+1
      Z=FLOAT(N)
      PI=3.14159265
      CALL TPREAD(N,NOUT)
C READS IN BINARY DATA FROM TAPE
      CALL SUBDH(N,Z,M,NOUT)
C REDUCES,AUTOCORRELATES,NORMALISES AND APPODISES THE INTERFEROGRAM
      J=N/2
      L=J
      K=N/4
      Z=Z/2.0
      CALL SUBTM(N,NOUT)
C COOLEY-TUKEY TRANSFORMATION ROUTINE
      IF(NSIG.EQ.1) GO TO 31
      II=3
      GO TO 133
   31 IF(I(7).GT.1) GO TO 40
      DO 3 M=1,J
    3 D(M)=A(M)
C STORES BACKGROUND TRANSFORMED ELEMENTS IN ARRAY D
      GO TO 28
C GOES BACK TO PICK UP SAMPLE TAPE AND LIKEWISE TRANSFORMS
   40 DO 41 M=1,J
   41 E(M)=A(M)
C STORES SAMPLE TRANSFORMED ELEMENTS IN ARRAY E
      DO 42 M=1,J
   42 A(M)=C(M)
      II=1
  133 CALL SUBPT(I(9),I(7),Z,FSINT,FREQL,FREQH,IOPUT,I(14),I(15),V(3),
     1V(4),V(5),V(6),I(11),I(12),I(13),ZX,NABS,NOUT,NCARD,NORM)
C PLOTTING ROUTINE
```

```
      IF(II.EQ.2) GO TO 43
      IF(II.EQ.3) GO TO 113
      DO 44 M=1,J
   44 A(M)=E(M)
      II=2
      GO TO 133
   43 DO 4 M=1,J
    4 A(M)=E(M)/D(M)
C RATIOES SAMPLE TO BACKGROUND
      IF(NOUT.NE.2) GO TO 202
      WRITE(6,200)
      WRITE(6,201)(A(M),M=1,J)
  202 CONTINUE
      II=3
      GO TO 133
  113 NSETS=NSETS-1
      GO TO 11
   13 CALL EXIT
      END
      SUBROUTINE SUBDH(N,Z,M,NOUT)
C
C REDUCES, AUTOCORRELATES, NORMALISES AND APODISES THE INTERFEROGRAM
C
      IMPLICIT REAL*4(A-H,O,V-Z),INTEGER*4(I-N,P-U)
C
      DIMENSION A2(4500)
C
      COMMON A(4096),C(4056),B(2048),D(2048)
C
  100 FORMAT(1H ,I3,1X,'POINTS SHORT')
  101 FORMAT(1X,10F12.2)
  102 FORMAT(/54H   REDUCED INTERFEROGRAM                                    )
  103 FORMAT(/54H  AUTOCORRELATED INTERFEROGRAM                              )
  104 FORMAT(1H ,'FINAL DATA SET AFTER APODISATION LENGTH=',I4)
  105 FORMAT(/54H  NORMALISED INTERFEROGRAM                                  )
  106 FORMAT(1X,20F6.3)
  108 FORMAT(1H ,'TAPE TOO SHORT BEFORE MAXIMUM')
  109 FORMAT(1H ,'TAPE TOO SHORT AFTER MAXIMUM')
  111 FORMAT(1X,10F12.6)
  113 FORMAT(1HO,' N-POINTED INTERFEROGRAM')
  114 FORMAT(1H ,20F6.0)
  201 FORMAT(1H ,'AVERAGE=',F8.2)
C
C
      MM=1
      CALL AMX(MM,M,J,AMAX)
      T=N/2
      L=J-T
      LL=J+T
      KK=0
      L7=L
      IF(L.LT.0) GO TO 19
      GO TO 18
   19 WRITE(6,108)
      L=-L
      A1=A(1)
      L1=L+1
      L2=L+2
      WRITE(6,100) L
      DO 21 J=1,M
```

```
   21 A2(J)=A(J)
      DO 25 K=1,M
   25 A(K)=0.0
      DO 20 LLL=1,LL
   20 A(LLL)=A1
      LL3=2
      DO 23 K=L2,M
      A(K)=A2(LL3)
   23 LL3=LL3+1
      KK=1
   18 IF(M.LT.LL) GO TO 22
      IF(KK.EQ.1) GO TO 17
      GO TO 26
   22 DO 24 K=M,LL
   24 A(K)=A(M)
      WRITE(6,109)
      LL1=LL-M
      WRITE(6,100) LL1
      IF(KK.EQ.1) GO TO 17
   26 DO 15 K=1,N
   15 A(K)=A(K+L7)
   17 IF(NOUT.NE.2) GO TO 117
      WRITE(6,113)
      WRITE(6,114)(A(K),K=1,N)
  117 AVE=0.0
      DO 27 K=1,N
   27 AVE=AVE+A(K)
      AVE=AVE/(N+1)
      WRITE(6,201) AVE
   13 DO 3 K=1,N
      C(K)=A(K)-AVE
    3 CONTINUE
      IF(NOUT.EQ.1) GO TO 50
      WRITE(6,102)
      WRITE(6,101)(C(K),K=1,N)
   50 CONTINUE
      DO 4 K=1,N
      ASUM=0.0
      DO 5 KK=1,N
      K1=KK+K-1
      IF(K1-N) 6,6,7
    7 K1=K1-N
    6 ASUM=ASUM+C(KK)*C(K1)
    5 CONTINUE
      A(K)=ASUM
    4 CONTINUE
      IF(NOUT.NE.2) GO TO 51
      WRITE(6,103)
      WRITE(6,101)(A(K),K=1,N)
   51 CONTINUE
      CALL AMX(MM,N,J,AMAX)
      DO 8 K=1,N
      A(K)=A(K)/AMAX
    8 CONTINUE
      IF(NOUT.NE.2) GO TO 52
      WRITE(6,105)
      WRITE(6,111)(A(K),K=1,N)
   52 CONTINUE
      DO 10 K=1,T
      APOD=COS(3.141593*(K-1)/(N-2))**2
```

```
      A(K)=A(K)*APOD
      A(N-K+2)=A(N-K+2)*APOD
   10 CONTINUE
      A(1+T)=0.0
      DO 11 K=1,N
      C(K)=0.0
   11 CONTINUE
      IF(NOUT.NE.2) GO TO 53
      WRITE(6,104) N
      WRITE(6,102)(A(K),K=1,N)
   53 CONTINUE
      RETURN
      END
      SUBROUTINE AMX(MM,M,J,AMAX)
C
C SUBROUTINE TO DETERMINE MAXIMUM VALUES
C
      COMMON A(4096),C(4096),B(2048),D(2048)
C
  200 FORMAT(3H J=,I4)
 1000 FORMAT(1H ,7(E10.4,2X))
C
C
      AMAX=0
      DO 1 K=1,M
      IF(A(K)-AMAX) 1,1,2
    2 AMAX=A(K)
      J=K
    1 CONTINUE
      WRITE(6,200) J
      L=-3
      DO 3 IQ=1,7
      KK=J+L
      C(IQ)=A(KK)
      L=L+1
    3 CONTINUE
      WRITE(6,1000) (C(IQ),IQ=1,7)
      RETURN
      END
      SUBROUTINE SUBTM(NMAX,NOUT)
C
C SUBROUTINE FOR TRANSFORMATION OF DATA TO GIVE SPECTRAL OUTPUT
C      THIS PROGRAM MAKES USE OF A TECHNIQUE DUE TO J.W.COOLEY AND J.W.
C      TUKEY (MATH. OF COMPUTATION,VOL 19,PG.295,1965). MODIFICATIONS TO
C      THIS TECHNIQUE HAVE BEEN MADE SO THAT FOURIER ELEMENTS COME OUT
C      IN A NORMAL ORDER. THE APPROPRIATE SINES AND COSINES MAKE USE OF
C      INTERNAL MACHINE SUBROUTINES. FOR REDUCTION OF 8192 INPUT POINTS
C      TO 8192 OUTPUT POINTS, THE TIME IS ABOUT 1 MINUTE.
C      IF THIS DIMENSION IS USED, THERE IS LITTLE ROOM FOR OTHER
C      CALCULATION, HOWEVER IT CAN OPERATE ON TAPES WHERE ORIGINAL DATA
C      HAS BEEN PRETREATED AND OUTPUT MAY ALSO BE A SEPERATE PROGRAM.
C
      DIMENSION TR1(4096),TI1(4096),TR2(2048),TI2(2048)
C
      COMMON TK1,TI1,TR2,TI2
C
  100 FORMAT(26H TRANSFORMATION COMPLETED )
  101 FORMAT(42H ERROR CAUSED BY INVALID CONTROL PARAMETER)
  102 FORMAT(1H ,10(E12.4)
  104 FORMAT(22H TRANSFORMED ELEMENTS )
```

```
  110 FORMAT(7H IHALF=,I3)
C
C
C       SETTING OF CONSTANTS THAT DO NOT CHANGE DURING PROGRAM
C       NMAX=NUMBER OF POINTS TO BE PROCESSED = 2
C       IHALF USED TO KEEP TRACK OF N
C       KHALF USED TO DETERMINE WHERE PARTIAL SUMS ARE TO BE STORED
C       DURING EACH PASS
        JHALF=NMAX/2
        IHALF=NMAX/2
        KHALF=NMAX/4
        PI=3.14159265
C CLEARS ARRAY TI1READY FOR COMPUTATION
        DO 10 I=1,NMAX
   10   TI1(I)=0.0
C       CHECK TO SEE IF N PASSES HAVE BEEN MADE
   34   IF(IHALF)999,65,37
C       SETTING OF CONSTANTS FOR EACH PASS
C       WR,WI ARE THE REAL AND IMAGINARY PARTS OF EXP(2*PI*J*K/NMAX)
C       RESPECTIVELY AND = 1,0 AT THE START OF EACH PASS
   37   JP=0
        WR=1.0
        WI=0.0
C       I AND L ARE THE REAL INDICES OF THE LOCATIONS TO WHICH THE PARTIAL
C         SUMS WOULD BE TRANSFERRED IF TR1,TI1,TR2,TI2 WERE OF
C       EQUAL LENGTH. TR2,TI2 NEEDED FOR AUXILLARY STORAGE
        DO 81 I=1,JHALF
        L=I+JHALF
C       JK=J*K AND DETERMINES PROPER FREQUENCIES DURING PASS
        IF(IHALF-1)38,38,39
   38   JK=I-1
        ANG=    PI*FLOAT(JK)/FLOAT(JHALF)
        WR=COS(ANG)
        WI=SIN(ANG)
        GO TO 48
   39   IMOD=I-(I/IHALF)*IHALF
        IF(IMOD)999,46,41
   41   JK=I-IMOD
        IF(JK-JP)999,48,43
   43   ANG=    PI*FLOAT(JK)/FLOAT(JHALF)
        JP=JK
        WR=COS(ANG)
        WI=SIN(ANG)
C       IP AND IQ ARE THE LOCATIONS OF PREVIOUSLY CALCULATED PARTIAL SUMS
C       STORED IN TR1,TI2 WHICH ARE TO BE USED IN PRESENT PARTIAL
C       SUM. THE RESULTS ARE TEMPORARILY STORED IN TR1,TI1,TR2,TI2
C       DEPENDING IN RELATION OF I TO KHALF
   48   IP=JK+I
        IQ=IP+IHALF
C       I AND IQ ARE INDICES OF TR2,TI2 WHERE RESULTS OF PARTIAL SUMS ARE
C       STORED AND CORRESPOND TO I AND L RESPECTIVELY FOR
C       I LESS THAN OR EQUAL TO KHALF
        IF(I-KHALF)51,51,53
   51   IQ=I+KHALF
        AR=TR1(IP)
        AI=TI1(IP)
        BR=TR1(IQ)*WR-TI1(IQ)*WI
        BI=TR1(IQ)*WI+TI1(IQ)*WR
        TR2(I)=AR+BR
        TI2(I)=AI+BI
```

```
      TR2(IU)=AR-BR
      TI2(IU)=AI-BI
      GO TO 81
C      FURTHER CALCULATIONS DURING THIS PASS AND HENCE MAY BE USED
C      FOR TEMPORARY STORAGE OF RESULTS CORRESPONDING TO I AND L
C      RESPECTIVELY FOR I GREATER THAN KHALF
   53 IL=I-KHALF
      IU=IL+JHALF
      AR=TR1(IP)
      AI=TI1(IP)
      BR=TR1(IQ)*WR-TI1(IQ)*WI
      BI=TR1(IQ)*WI+TI1(IQ)*WR
      TR1(IL)=AR+BR
      TI1(IL)=AI+BI
      TR1(IU)=AR-BR
      TI1(IU)=AI-BI
   81 CONTINUE
C      STORES PARTIAL SUMS JUST CALCULATED (TR1,TI1,TR2,TI2) IN TR1,TI1
C      IN THE PROPER ORDER PRIOR TO NEXT PASS
      JJJ=KHALF+1
      DO 83 IK=JJJ,JHALF
      JJMK=IK-KHALF
      JJPK=IK+KHALF
      JJPJ=IK+JHALF
      TR1(IK)=TR1(JJMK)
      TI1(IK)=TI1(JJMK)
      TR1(JJPJ)=TR1(JJPK)
      TI1(JJPJ)=TI1(JJPK)
      TR1(JJMK)=TR2(JJMK)
      TI1(JJMK)=TI2(JJMK)
      TR1(JJPK)=TR2(IK)
   83 TI1(JJPK)=TI2(IK)
C      RESETS IHALF AS A COUNTER FOR N
      IHALF=IHALF/2
      WRITE(6,110) IHALF
      GO TO 34
   65 CONTINUE
      IF(NOUT.EQ.1) GO TO 107
      GO TO 108
  107 WRITE(6,106)
      GO TO 50
  108 WRITE(6,104)
      WRITE(6,102)(TR1(J),J=1,JHALF)
      WRITE(6,100)
      GO TO 50
  999 WRITE(6,101)
   50 RETURN
      END
      SUBROUTINE SUBPT(I9,I7,Z,FSINT,FREQL,FREQH,IOPUT,I14,I15,V3,V4,
     1V5,V6,I11,I12,I13,ZX,NABS,NCUT,NCARD,NORM)
C
C SUBROUTINE FOR PLOTTING OUT SPECYRAL DATA IN A FORM WHICH CAN BE
C RECOGNISED AS A SPECTRUM
C
      IMPLICIT  REAL*4(A-H,O,V-Z), INTEGER*4(J-N,P-U)
C
      DIMENSION AA(4000),BB(4000)
      DIMENSION H(50),I(15),G(1),F(1),V(11),ZX(20)
C
      COMMON A(4096),C(4096)
```

```
C
C
  100 FORMAT(1H1,'FS720 SPECTRA COMPILATION USING FSTRAN3')
  101 FORMAT(1H ,'NO NORMALISATION EFFECTED')
  102 FORMAT(1H0,' NUMBER OF POINTS TRANSFORMED = ',I4,5X,' SAMPLING INT
     1ERVAL = ',F5.2,'  MICRONS')
  103 FORMAT(1H0,' LOWER FREQUENCY LIMIT = ',F7.2,'  CM-1 ',5X,' UPPER F
     1REQUENCY LIMIT = ',F7.2,'  CM-1 ')
  104 FORMAT(1H0,' IOPUT = ',I1)
  105 FORMAT(1H0,' TAPES ',A4,' AND ',A4,9X,A4,'/',A4)
  106 FORMAT(1H0,' SAMPLE GAIN = ',F6.3,15X,' BACKGROUND GAIN = ',F6.3)
  107 FORMAT(1H0,' DATE = ',I2,1X,I2,1X,I2)
  108 FORMAT(1H0,' NABS = ',I1,5X,' NOUT = ',I1,5X,' NCARD = ',I1,5X,' N
     1ORM = ',I1)
  109 FORMAT(1H0,' THEORETICAL RESOLUTION LIMIT = ',F5.2,'  CM-1')
  112 FORMAT(1H ,' SAMPLE SPECTRUM ')
  113 FORMAT(1H ,' BACKGROUND SPECTRUM')
  114 FORMAT(55H  ABSOLUTE TRANSMITTANCE RATIO OF SAMPLE/BACKGROUND.    )
  115 FORMAT(55H  I(9)=4,AN ERROR HAS OCCURRED.                         )
  116 FORMAT(22H SAMPLE TAPE REF NO = A5)
  117 FORMAT(26H BACKGROUND TAPE REF NO = A5)
  118 FORMAT(21H NORMALISING FACTOR =, F10.6)
  122 FORMAT(17H FREQ  AMPLITUDE )
  124 FORMAT(20H FREQ  TRANSMITTANCE)
  127 FORMAT(17H FREQ  ABSORBANCE)
  140 FORMAT(1H0,20A4)
  189 FORMAT(5(F7.2,F7.4,1X))
  190 FORMAT(5I5)
  191 FORMAT(1X 'HAS PUNCHED CARD OUTPUT')
  200 FORMAT(1H1,5X,' I9 = ',I3)
  201 FORMAT(1H ,' FREQUENCY INCREMENT = ',F8.4)
  400 FORMAT(16H LARGEST VALUE=,F10.6)
  500 FORMAT(1H ,' HAS NORMALISED ARRAY ')
  503 FORMAT(1H ,10F12.4)
  550 FORMAT(1H ,' BACKGROUND ARRAY OVER REQUIRED RANGE ')
  556 FORMAT(1H ,' SAMPLE ARRAY OVER REQUIRED RANGE')
  557 FORMAT(1H ,' RATIOED ARRAY OVER REQUIRED RANGE')
  558 FORMAT(1H ,10F12.4)
  600 FORMAT(1H ,' K = ',I4,10X,' Q = ',I4)
  800 FORMAT(1H ,' SQUARE-ROOTED RATIOED ELEMENTS ')
  801 FORMAT(1H1)
C
C
      IF(I9.GE.1) GO TO 3
      WRITE(6,100)
      WRITE(6,105) I14,I15,I14,I15
      WRITE(6,107) I11,I12,I13
      WRITE(6,140) ZX
      N20=INT(Z)
      N20=2*N20
      WRITE(6,102) N20,FSINT
      WRITE(6,103) FREQL,FREQH
      WRITE(6,104) IOPUT
      V100=V3+V4
      V101=V5+V6
      WRITE(6,106) V100,V101
      WRITE(6,108) NABS,NOUT,NCARD,NORM
      AN20=FLOAT(N20)
      AN2=AN20/2.0
      AN21=AN20*FSINT
```

```
      AN21=AN21/1000.0
      AN22=1.0/AN21
      WRITE(6,109) AN22
    3 I9=1+I9
      IF(NOUT.NE.2) GO TO 1000
      WRITE(6,200) I9
 1000 CONTINUE
      IF(NOUT.EQ.2) GO TO 1004
      WRITE(6,801)
 1004 CONTINUE
      V(7)=1
      IF(I9.EQ.4) GO TO 26
      DATA H/1.0,2*9.0,1.0,5.0,60.0,30.0,2*4.0,30.0,60.0,5.0,7.0,105.0,
     135.0,5.0,1.0,2*9.0,1.0,5.0,35.0,105.0,7.0,6.0,189.0,27.0,4.0,8.0,
     184.0,56.0,2*7.0,56.0,84.0,8.0,4.0,27.0,108.0,6.0,16.0,2*81.0,
     1128.0,16.0,128.0,4*125.0/
      K=41
      L=1
      DO 120 Q=2,5
      DO 121 IX=2,Q
      C(10*Q+IX)=-H(L)/H(K)
      C(10*Q-IX)=H(1+L)/H(K)
      C(30*Q+IX)=H(2+L)/H(K)
      C(30*Q-IX)=-H(3+L)/H(K)
      L=4+L
      K=1+K
  121 CONTINUE
  120 CONTINUE
      DATA I/1,2,3,5,4,0/
      GI=7*FSIN
      GI=5000.0/GI
C GI IS THE INCREMENTAL FREQUENCY FOR THE SPECTRAL ARRAY
      FI=5000.0/FSIN
      X=FREQL/GI
      K=INT(X)
      Y=FREQH/GI
      Y=Y+0.5
      Q=INT(Y)
      IF(NOUT.NE.2) GO TO 1001
      WRITE(6,600) K,Q
 1001 CONTINUE
C PRODUCES AN ARRAY Q-K FOR INTERPOLATION OF SPECTRAL DATA
      Y=0
      IK=K
      L=Q
      IF(NOUT.NE.2) GO TO 554
      GO TO (551,552,553),I9
  551 WRITE(6,555)
      GO TO 555
  552 WRITE(6,556)
      GO TO 555
  553 WRITE(6,557)
  555 WRITE(6,558) (A(M),M=IK,L)
  554 IF(NORM.EQ.1) GO TO 13
      DO 10 M=IK,L
      IF(A(M).LT.Y) GO TO 10
      Y=A(M)
   10 CONTINUE
      WRITE(6,400) Y
C CALCULATES LARGEST A(M) IN ARRAY FROM I TO L FOR NORMALISATION
```

```
      Y=1/Y
   15 DO 11 M=IK,L
      IF(I9.EQ.3) GO TO 51
      A(M)=A(M)*Y
      GO TO 11
   51 IF (A(M))53,53,54
   53 A(M)=0.0
      GO TO 11
   54 A(M)=SQRT(A(M))
   11 CONTINUE
      IF(I9.EQ.3) GO TO 700
      WRITE(6,500)
      IF(NOUT.NE.2) GO TO 14
      GO TO 701
  700 IF(NOUT.NE.2) GO TO 14
      WRITE(6,800)
  701 WRITE(6,503)(A(M),M=IK,L)
      GO TO 14
   13 IF(I9.NE.3) GO TO 216
      DO 211 M=IK,L
      IF(A(M))214,214,215
  214 A(M)=0.0
      GO TO 211
  215 A(M)=SQRT(A(M))
  211 CONTINUE
  213 IF(NOUT.NE.2) GO TO 216
      WRITE(6,800)
      WRITE(6,503)(A(M),M=IK,L)
  216 CONTINUE
      WRITE(6,101)
   14 CONTINUE
   26 GO TO(4,2,5,6),I9
    2 WRITE(6,112)
      GO TO 300
    4 WRITE(6,113)
      GO TO 300
    5 WRITE(6,114)
      GO TO 300
    6 WRITE(6,115)
  300 GO TO (9,8),I9
      GO TO 48
    8 WRITE(6,116) I14
      GO TO 48
    9 IF(NOUT.NE.2) GO TO 1002
      WRITE(6,117) I15
   48 IF(NOUT.NE.2) GO TO 1002
      WRITE(6,201) GI
 1002 CONTINUE
      IF(NORM.EQ.1) GO TO 303
      IF(I9.EQ.3) GO TO 303
      WRITE(6,118) Y
  303 IF(I9.NE.3) GO TO 43
      CALL SUBCOR(V3,V4,V5,V6,V(7))
      IF(NABS.EQ.1) GO TO 63
      WRITE(6,124)
      GO TO 50
   63 WRITE(6,127)
      CALL SUBLPL
      GO TO 34
   43 WRITE(6,122)
```

```
   50 CALL SUBLP
   34 P=10*IOPUT
      R=30*IOPUT
      G(1)=FLOAT(IOPUT)
      G(1)=GI/G(1)
C GI IS THE FREQ INCREMENT WHICH RESULTS IF IOPUT >1
      JJ=0
      DO 61 MI=K,Q
      DO 62 IK=1,IOPUT
      JJ=JJ+1
      X=FLOAT(MI)
      X=X*GI
      IF(X.GT.FI) GO TO 35
C FI IS THE ALIAS FREQUENCY
      IF(IK.GT.1) GO TO 27
      F(1)=A(1+MI)
      F(1)=F(1)*V(7)
      GO TO 29
   27 Y=FLOAT(IK)
      Y=Y-1
      Y=Y*G(1)
      X=X+Y
      IF(MI.EQ.0) GO TO 351
C CHECKS FOR END OF ARRAY K-Q
      Y=A(MI)*C(P+IK)
      E=A(1+MI)*C(P-IK)
      Y=Y+E
      E=A(2+MI)*C(R+IK)
      Y=Y+E
      E=A(3+MI)*C(R-IK)
      F(1)=Y+E
      F(1)=F(1)*V(7)
   29 AA(JJ)=X
      BB(JJ)=F(1)
C INTERPOLATING COEFFICIENTS C USED TO GIVE CORRECTED AMPLITUDES F(1)
C AT THE NEW FREQUENCY INTERVAL G(1)
   62 CONTINUE
   61 CONTINUE
  351 QQ=Q-K
      QQ=QQ*IOPUT
      IF(I9.EQ.3) GO TO 28
      GO TO 25
   28 IF(NABS.EQ.1)GO TO 64
      GO TO 25
   64 CALL SUBGPL(AA,BB,I9,NCARD,NOUT,QQ)
      GO TO 350
   25 CALL SUBGP(AA,BB,I9,NCARD,NOUT,QQ)
  350 WRITE(6,190) Q,K,QQ,IOPUT
      IF(NCARD.EQ.0) GO TO 35
      GO TO (301,302),NCARD
  301 IF(I9.EQ.3) GO TO 302
      GO TO 35
  302 WRITE(7,189)(AA(JJ),BB(JJ),JJ=1,QQ)
      WRITE(7,192)
  192 FORMAT(1HQ)
      WRITE(6,191)
   35 RETURN
      END
      SUBROUTINE SUBLPL
C
```

```
C ABSORBANCE SPECTRUM SET-UP
C
      DIMENSION CHAR(101),XNUM(11)
C
      DATA DOT,DIV/1H.,1H+/
      DATA XNUM/0.00,0.25,0.50,0.75,1.00,1.25,1.50,1.75,2.00,2.25,2.50/
C
  100 FORMAT(1H ,17X,101A1)
  101 FORMAT(16X,F4.2,10(6X,F4.2))
C
C
      WRITE(6,101) XNUM
      DO 90 K=1,101
   90 CHAR(K)=DOT
      DO 91 IZ=1,21
      IK=1
      IK=IK+5*(IZ-1)
   91 CHAR(IK)=DIV
      WRITE(6,100) CHAR
      RETURN
      END
      SUBROUTINE SUBGPL(X,Y,IS,NCARD,MOUT,MM6)
C
C ABSORBANCE SPECTRUM PLOT
C
      DIMENSION CHAR(101)
      DIMENSION X(1),Y(1)
C
      DATA BLANK,PLOT,PLUS/1H ,1H.,1H+/
C
  103 FORMAT(1X,F6.2,3X,F6.4,2X,101A1)
C
C
      DO 10 L=1,MM6
      Y(L)=1.0/Y(L)
      Y(L)=ALOG(Y(L))
      IF(NOUT.EQ.1) GO TO 105
      DO 92 K=2,101
   92 CHAR(K)=BLANK
      CHAR(1)=PLUS
      I=((Y(L)*40)+0.5)
      IF(I.GT.100) GO TO 3
      IF(I.LT.1) GO TO 5
      GO TO 4
    3 I=101
      GO TO 4
    5 I=2
    4 CHAR(I)=PLOT
      WRITE(6,103) X(L),Y(L),CHAR
  105 CONTINUE
   10 CONTINUE
   11 RETURN
      END
      SUBROUTINE TPREAD(N,NOUT)
C
C      TAPE READ SUBROUTINE
C
      DIMENSION A(4096)
C
      COMMON A
```

```
C
    3 FORMAT(1H ,20E6.0)
    4 FORMAT(1HC,' DATA FROM TAPE ')
  100 FORMAT(20E4.0)
  102 FORMAT(19H NO OF DATA POINTS=,I4)
C
C
      I=1
   10 K=I+19
      READ(5,100)(A(J),J=I,K)
      DO 50 J=I,K
      IF(A(J)) 20,50,50
   50 CONTINUE
      I=I+20
      GO TO 10
   20 M=J-1
   21 WRITE(6,102) M
      IF(NOUT.NE.2) GO TO 1
      WRITE(6,4)
      WRITE(6,3)(A(K),K=1,M)
    1 CONTINUE
      RETURN
      END
      SUBROUTINE SUBLP
C
C TRANSMISSION SPECTRUM SET-UP
C
      DIMENSION CHAR(101),XNUM(11)
C
      DATA DOT,DIV/1H.,1H+/
      DATA XNUM/0.0,0.1,0.2,0.3,0.4,0.5,0.6,0.7,0.8,0.9,1.0/
C
  100 FORMAT(1H ,17X,101A1)
  101 FORMAT(17X,F3.1,10(7X,F3.1))
C
C
      WRITE(6,101) XNUM
      DO 90 K=1,101
   90 CHAR(K)=DOT
      DO 91 IZ=1,21
      IK=1
      IK=IK+5*(IZ-1)
   91 CHAR(IK)=DIV
      WRITE(6,100) CHAR
      RETURN
      END
      SUBROUTINE SUBGP(X,Y,IS,NCARD,NOUT,MM6)
C
C TRANSMISSION SPECTRUM PLOT
C
      DIMENSION X(1),Y(1)
      DIMENSION CHAR(102)
C
      DATA BLANK,PLOT,PLUS/1H ,1H*,1H+/
C
  103 FORMAT(F7.2,2X,F6.4,3X,102A1)
C
C
      DO 10 L=1,MM6
      DO 92 K=2,102
```

```
   92 CHAR(K)=BLANK
      CHAR(1)=PLUS
      I=((Y(L))*100)+1.5
      IF(I.GT.100) GO TO 3
      IF(I.LT.1) GO TO 5
      GO TO 4
    3 I=102
      GO TO 4
    5 I=1
    4 CHAR(I)=PLOT
      WRITE(6,103) X(L),Y(L),CHAR
   10 CONTINUE
  105 CONTINUE
      RETURN
      END
      SUBROUTINE SUBCOR(V3,V4,V5,V6,V7)
C
C      GAIN CORRECTION CALCULATION
C
  101 FORMAT(1H ,' GAIN CORRECTION FACTOR = ',F12.4)
C
C
      GSAM=V3+V4*10.0
      GBKG=V5+V6*10.0
      DGAIN=GSAM-GBKG
      IF(DGAIN)5,7,7
    5 DGAIN=-DGAIN
    7 VP=DGAIN/20.0
      VP=VP*2.3025851
      VP=EXP(VP)
      V7=1.0/VP
      WRITE(6,101) V7
      RETURN
      END
```

A1.2 Dispersive Fourier transformation programme

```
C
C
C
C FOURIER TRANSFORMATION PROGRAMME FOR EITHER NON-DISPERSIVE OR
C DISPERSIVE INTERFEROGRAMS.
C THE INTERFEROGRAMS ARE MADE SYMMETRICAL BY THE USE OF A PHASE
C ERROR CALCULATION AND THESE PHASE VALUES CAN BE RECOVERED
C FOR THE DISPERSIVE INTERFEROGRAMS
C
C
      DIMENSION NW(20)
     .DIMENSION B(4100)
     -DIMENSION V(11),I(15),ZX(20)
      REAL*4 A(12)C0),IC(12CCC)
  101 FORMAT(I4,F4.1,2F6.1,I3,I3,I4,2I2,I4)
  102 FORMAT(1H ,I4,F4.1,2F6.2,I3,I3.I4,I3,2I3,I4)
  120 FORMAT(20I4)
  140 FORMAT(20A4)
  141 FORMAT(3I2,3XA4,1XA4)
  142 FORMAT(4F6.3)
  151 FORMAT(3I2)
  212 FORMAT(6I2)
  998 READ(9,212,END=999) NCARD,NOUT,NCOR,NORM,NPCRD,NREAD
C NCARD= INTEGER DECIDING WHETHER CARD OUTPUT IS PRODUCED
C       =0 GIVES CARD OUTPUT
C       =1 GIVES NO CARD OUTPUT
C NOUT =INTEGER DECIDING WHETHER CARD OUTPUT OF RATIOED SPECTRUM IS PRODUCED
C       =0 GIVES LINE PRINTER PLUS CARD OUTPUT IF NCARD=0
C       =1 GIVES CARD OUTPUT ONLY
C NCOR =1 PRODUCES A SPECTRUM CORRECTED FOR GAIN SETTINGS
C NORM = INTEGER DECIDING WHETHER NORMALISATION IS CARRIED OUT
C       =0 NO NORMALISATION
C       =1 GIVES NORMALISATION
C NPCRD=1 GIVES CARD + LINE PRINTER OUTPUT FOR PHASE
C       =0 GIVES LINE PRINTER ONLY
C NREAD=0 DOES NOT READ EXTRA DATA CARD
C       =1 READS EXTRA DATA CARD
      IF(NREAD-1)156,155,156
  155 READ(9,151) MINT,MPHAS,NOSPEC
  156 READ(9,101) N,SI,FLOW,FHIGH,I9,I8,N2,IP,IAP
C N = NUMBER OF POINTS
C SI= SAMPLING INTERVAL IN MICRONS
C FLOW= LOWER FREQUENCY LIMIT IN RECIPROCAL CENTIMETRES
C FHIGH= UPPER FREQUENCY LIMIT IN RECIPROCAL CENTIMETRES
C I9= INTEGER CONSTANT DETERMINING NUMBER OF POINTS PER RESOLUTION (1-5 ONLY)
C I8= NUMBER OF TAPES TO BE PROCESSED (I8=1 FOR SINGLE TAPE,=2 FOR RATIO)
C N2= NUMBER OF POINTS TO BE USED IN DETERMINATION OF PHASE CORRECTION FUNCTION
C IP=0 COMPUTATION OF SPECTRUM FROM ONE-SIDED (COSINE) TRANSFORM
C IP=1 COMPUTATION OF SPECTRUM FROM DOUBLE-SIDED (POWER) TRANSFORM
C IAP=0 TRANSFORMATION OCCURS WITHOUT APODISATION
C IAP=1 TRANSFORMATION OF APODISED INTERFEROGRAM OCCURS
      READ(9,141)I(11),I(12),I(13),I(14),I(15)
C I(11)= DAY(NUMERIC)
C I(12)= MONTH(NUMERIC)
C I(13)= YEAR(NUMERIC)
```

```
C I(14)= SAMPLE TAPE REFERENCE NUMBER (ALPHANUMERIC)
C I(15)= BACKGROUND TAPE REFERENCE NUMBER (ALPHANUMERIC)
      READ(5,142)(V(J),J=3,6)
C V(3)= COURSE GAIN SETTING FOR SAMPLE
C V(4)= FINE GAIN SETTING FOR SAMPLE
C V(5)= COURSE GAIN SETTING FOR BACKGROUND
C V(6)= FINE GAIN SETTING FOR BACKGROUND
      READ(8,140) ZX
C ZX= TITLE OF SPECTRUM
      WRITE(6,102)N,SI,FLOW,FHIGH,IS,IB,N2,IP,IAP
      DO 17 I7=1,18
      NN=N*(I7-1)
      N1=NN/N
      NCNT=21
      IF(NINT-1)153,152,153
  153 DO 14 M=1,6000
      IF(NCNT.LE.20) GO TO 1002
      READ(8,120) NW
      NCNT=1
 1002 IN=NW(NCNT)
      NCNT=NCNT+1
      IF(IN) 2,2,1
    1 MPN2=M+N2
      M1=M+NN
      IA(M1)=IN
   14 CONTINUE
  152 DO 163 M=1,6000
      IF(NCNT.LE.20) GO TO 161
      READ(8,120) NW
      NCNT=1
  161 IN=NW(NCNT)
      NCNT=NCNT+1
      IF(IN) 2,2,162
  162 MPN2=M+N2
      M1=M+NN
      IA(M1)=IN
  163 CONTINUE
    2 AMAX=0.0
      L=NN+1
      LL=M+NN
      WRITE(6,122)
  122 FORMAT(1H ,'DATA FROM IN PLT TAPE')
      WRITE(6,121)(IA(K),K=L,LL)
  121 FORMAT(1H ,2CF6.0)
      M=M-1
      AVA=0.0
      DO 31 K=1,M
      K1=K+NN
      AVA=AVA+IA(K1)
      IF(IA(K1)-AMAX) 31,31,43
   43 AMAX=IA(K1)
      J=K1
   31 CONTINUE
      AVA=AVA/FLOAT(M)
      DO 3 K=1,M
      K1=K+NN
    3 IA(K1)=IA(K1)-AVA
  194 WRITE(6,110) J,M,AVA
  110 FORMAT(1H1,'ZERO PATH LOCATION IS',I6,/' TOTAL NO OF DATA POINTS
     1 IS ',I5,/' AVERAGE VALUE OF INPUT ARRAY',F6.0)
```

```
      K2=K+NN
      WRITE(6,170) K2
  170 FORMAT(I5)
      DO 6 K=K2,12000
      IA(K)=IA(K2)
    6 CONTINUE
C COPIES MIDDLECF INTERFEROGRAM TO ARRAY IC
C THERE MUST BE N/2 POINTS EITHER SIDE OF ZERO PATH
      IM=J-N/2
      IN=J+N/2
      K=1+NN
      WRITE(6,171) IM,IN,K
  171 FORMAT(3I5)
      DO 26 J=IM,IN
      IC(K)=IA(J)
   26 K=K+1
      NK=NN+1
      NJ=NN+N
      DO 27 JI=NK,NJ
   27 IA(JI)=0.0
      WRITE(6,171) NK,NJ
      DO 28 JJ=NK,NJ
   28 IA(JJ)=IC(JJ)
C IA NOW CONTAINS ARRAY I------N ONLY -INFEDUCEDFORM
      WRITE(6,125)
  125 FORMAT(1H ,'INTERFEROGRAM REDUCED TO SIZE REQUIRED BY N VALUE')
      WRITE(6,121)(IA(JJ),JJ=NK,NJ)
C NOW FINDS CENTRE OF DF TRUNCATED ARRAY SO THAT CENTRE MAY BE COPIED INTO B
      AMAX=0.0
      DO 36 K=1,N
      K1=K+NN
      IF(IA(K1)-AMAX) 36,36,35
   35 AMAX=IA(K1)
      J=K1
   36 CONTINUE
      WRITE(6,110) J
      N3=N2/2
      DO 4 K=1,N2,1
      KK=J-N3+K-1
      B(K)=IA(KK)
    4 CONTINUE
      CALL SLIDE(B,N3)
      WRITE(6,5)
    5 FORMAT(1H ,'DATA USED IN CORRECTION FUNCTION')
      WRITE(6,8)(B(K),K=1,N2,1)
    8 FORMAT(1H ,8F10.4)
      IF(NPHAS.GT.0) GO TO 197
      CALL PHASE2(B,N2,M1,NRORD)
      GO TO 198
  197 CALL PHASE3(B,N2,M1,NRORD)
  198 IF(NOSPEC.EQ.1) GO TO 999
      IFSET=-1
      CALL FFT(B,M1,IFSET)
      CALL SLIDE(B,N3)
      RN=N3/4.0
      DO 12 K=1,N2,1
      KK=K-(N3+1)
      RKK=KK
      Z=EXP(-0.5*((RKK/RN)**2))
      B(K)=B(K)*Z
```

```
   12 CONTINUE
      WRITE(6,22)
   22 FORMAT(1H ,'CORRECTION FUNCTION')
      WRITE(6,8)(B(K),K=1,N2,1)
      CALL CONVOL(IA,B,N,N2,NN)
      AMAX=0.0
      DO16 K=1,N
      K1=K+NN
      IF(K.GT.M) IA(K1)=0.0
      IF(IA(K1)-AMAX) 16,16,15
   15 AMAX=IA(K1)
      J=K1
   16 CONTINUE
      WRITE(6,110)J,M
      JL=J-10
      JLL=J+10
      WRITE(6,8)(IA(K),K=JL,JLL,1)
      CALL SORT(IA,N,J,NN)
      WRITE(6,103)
  103 FORMAT(/25H SORTED INTERFEROGRAM   )
      K3=1+NN
      K4=N+NN
      WRITE(6,8)(IA(K),K=K3,K4)
      IFSET=1
      JJ=J-NN
      MM=2*JJ-M
      IF(MM) 19,50,50
   19 MMJ=M-JJ
      DO 51 K=J,MMJ,1
      IA(K+NN)=0.0
   51 CONTINUE
      GO TO 53
   50 NMJ=N-JJ
      NJM=N+JJ-M
      DO 52 K=NMJ,NJM,1
      IA(K+NN)=0.0
   52 CONTINUE
   53 CONTINUE
      IF(NN-N) 38,17,38
   38 DO 18 K=1,N
      K1=K+N
   18 IA(K1)=0
   17 CONTINUE
      IF(IAP-1)7,10,7
   10 IT= ((N/2)+1)
      RN=N-2
      DO 11 K=2,IT
      KK=N-K+2
      RK=K-1
      APOD=COS(3.14159*RK/RN)**2
      IA(K)=IA(K)*APOD
      IA(KK)=IA(KK)*APOD
      IA(K+N)=IA(K+N)*APOD
      IA(KK+N)=IA(KK+N)*APOD
   11 CONTINUE
    7 RN4=N
      DO 23 K=1,12,1
      RN4=RN4/2.0
      IF(RN4.GE.1.0) M1=K
   23 CONTINUE
```

```
      L3=2*N
      CALL FFT(IA,M1,IRSET)
      CALL OPPUT(IA,N,SI,FLOW,FHIGH,I9,I8,IP,NCARD,NOUT,NCOP,
     1I(12),I(13),I(14),I(15),I(11),V(3),V(4),V(5),V(6),ZX,NORM)
      GO TO 998
  999 CALL EXIT
      END
      SUBROUTINE OPPUT(IA,N,SI,FLOW,FHIGH,I9,I8,IP,NCARD,NOUT,NCOP,
     1I12,I13,I14,I15,I11,V3,V4,V5,V6,ZX,NORM)
      DIMENSION H(5 ),I(15),G(1),F(1),V(11),ZX(2 )
      DIMENSION AA(4200),BB(4100)
      REAL*4IA(1)
      KS=3
      L3=2*N
  107 FORMAT(1H ,'NORMALISING FACTOR=',F12.4)
  110 FORMAT(10F10.2)
      DELF=10000.0/(SI*N)
      MM=1.0+FLOW/DELF
      M=1.0+FHIGH/DELF
      WRITE(6,119) MM,M,DELF
  119 FORMAT(//2I4,F10.4)
      N2=N/2
      DO 70 K=2,N2,1
      KK=(N-K+2)
      SAMR=(IA(K)+IA(KK))/2.0
      BKDI=(IA(K)-IA(KK))/2.0
      BKDR=(IA(K+N)+IA(KK+N))/2.0
      SAMI=(IA(K+N)-IA(KK+N))/2.0
      IA(K)=SAMR
      IA(KK)=SAMI
      IA(K+N)=BKDR
      IA(KK+N)=BKDI
   70 CONTINUE
      DO 9 K=1,N2,1
      KK=N2+K
      IA(KK)=IA(KK+1)
      IA(KK+N)=IA(KK+N+1)
      IF(K-N2) 8,9,8
    9 IA(KK)=0.0
      IA(KK+N)=0.0
    8 CONTINUE
      DO 3 J2=1,I8
        NN=N*(J2-1)
      SAMAXR=0.0
      SAMINR=0.0
      SAMAXI=0.0
      SAMINI=0.0
      DO 4 K=1,N2,1
      KK=N-K+1
      SAMR=IA(K+NN)
      SAMI=IA(KK+NN)
      IF(SAMR-SAMAXR) 60,60,61
   61 SAMAXR=SAMR
      IP1=K
   60 IF(SAMR-SAMINR) 62,63,63
   62 SAMINR=SAMR
      IP2=K
   63 IF(SAMI-SAMAXI) 64,64,65
   65 SAMAXI=SAMI
      IP3=K
```

```
 64 IF(SAMI-SAMINI)66,4,4
 66 SAMINI=SAMI
    IP4=K
  4 CONTINUE
    WRITE(6,111) SAMAXR,SAMINR,SAMAXI,SAMINI
111 FORMAT(1H ,'COS MAX=',F1 .2,'COS MIN=',F1 .2,'SIN MAX=',F10.2,'SIN
   * MIN=',F10.2)
    WRITE(6,112) IP,IP1,IP2,IP3,IP4
112 FORMAT(1H ,I1,10X,I5,12X,I5,12X,I5,12X,I5)
  3 CONTINUE
    IF(IP-1) 6,5,6
  5 DO 7 K=1,N2,1
    KK=N-K+1
    IA(K)=SQRT(IA(K)**2+IA(KK)**2)
    IA(K+N)=SQRT(IA(K+N)**2+IA(KK+N)**2)
  7 CONTINUE
  6 DO 15 JJ=1,IE
    N=N*(JJ-1)
    NNN=0
    GO TO 30
 32 CONTINUE
    K1=N+N-JJ
    IA(K1)=AMAX
 15 CONTINUE
    N5=N+3
    N4=N+N2
    WRITE(6,115)
115 FORMAT(/54H  SAMPLE      ARRAY K=3,N2                                  )
    WRITE(6,110)(IA(K),K=3,N2)
    WRITE(6,116)
116 FORMAT(/54H  BACKGROUND ARRAY K=N+3,N2+N                               )
    WRITE(6,110)(IA(K),K=N5,N4)
    GO TO 11
 46 IF(NORM.EQ.0) GO TO 43
    GO TO 42
 43 DO 29 K=3,N2
    K1=N+N-1
    K2=N+N-2
    K3=K+N
    SAM=IA(K3)
    BKG=IA(K)
    IA(K)=SAM/BKG
 29 CONTINUE
    GO TO 600
 42 DO 28 K=3,N2
    K1=N+N-1
    K2=N+N-2
    K3=K+N
    BKG=IA(K)/IA(K1)
    SAM=IA(K3)/IA(K2)
    IA(K)=SAM/BKG
 28 CONTINUE
600 WRITE(6,172)
172 FORMAT(1H )
    WRITE(6,117)
117 FORMAT(/54H  RATIOED ARRAY K=3,N2                                      )
    WRITE(6,110)(IA(K),K=3,N2)
    WRITE(6,92) ZX
 92 FORMAT(20A4)
    NN=0
```

```
      NNN=1
      GO TO 30
   33 CONTINUE
       V8=1/IA(K1)
       V9=1/IA(K2)
       V10=1.0/AMAX
      CALL SUBCOR(V8,V9,V10,V3,V4,V5,V6,V7,NORM)
      GO TO 72
   11 WRITE(6,96) NORM,AMAX, IA(K1)
   96 FORMAT(I3,2F10.3)
      WRITE(6,310)
  310 FORMAT(1H1,'BACKGROUND SPECTRUM')
      NN5=0
      MM5=MM
      M5=M
      II8=1
  304 CALL SUBLP
      JJ=0
      NN5=NN5+1
      WRITE (6,401) MM5,M5,I9,NN5
  401 FORMAT(4I5)
      NN7=N*(II8-1)
      DO 25 K=MM5,M5,I9
      JJ=JJ+1
      KK1=K-NN7
      FREQ=DELF*(KK1-1)
      IF(NORM.EQ.0) GO TO 31
      AMP=IA(K)/IA(K1)
      GO TO 37
   31 AMP=IA(K)
   37 AA(JJ)=FREQ
      BB(JJ)=AMP
   25 CONTINUE
      MM6=M5-MM5
      CALL SUBGP(AA,BB,NCARD,NOUT,I9,MM6)
      IF(II8-1)139,139,303
  303 IF(NN5-1)305,305,306
  305 MM5=MM+N
      M5=M+N
      II8=II8+1
      WRITE(6,311)
  311 FORMAT(1H1,'SAMPLE SPECTRUM')
      GO TO 304
  306 GO TO 46
   72 JJ=0
      WRITE(6,172)
      WRITE(6,92) ZX
      CALL SUBLP
      WRITE(6,401) MM,M,I9
      DO 73 K=MM,M,I9
      JJ=JJ+1
      FREQ=DELF*(K-1)
      IF(NORM.EQ.0) GO TO 38
      AMP=IA(K)/AMAX
      AMP=AMP*V7
      GO TO 39
   38 AMP=IA(K)*V7
   39 AA(JJ)=FREQ
      BB(JJ)=AMP
   73 CONTINUE
```

```
      MM6=M-MM
      CALL SUBGP(AA,BB,NCARD,NOUT,I9,MM6)
      GO TO 139
   30 AMAX=0.0
      M1=MM
      M2=M
   50 DO 26 L=M1,M2
   51 K=L+NN
      IF(IA(K)-AMAX) 26,26,27
   27 AMAX=IA(K)
   26 CONTINUE
      WRITE(6,107)AMAX
      IF(NNN) 32,32,33
  139 NQ=(M-MM)/I9
      GO TO(301,302),NCARD
  302 WRITE(6,192) NQ
      WRITE(6,191)
      WRITE(7,188) ZX
      WRITE(7,189)(AA(JJ),BB(JJ),JJ=1,NQ)
  188 FORMAT(20A4)
  189 FORMAT(5(F7.2,F7.4,1X))
  191 FORMAT(1X ' HAS PUNCHED CARDS')
  192 FORMAT(1X ' NO OF OUTPUT POINTS='I4)
  301 RETURN
      END
      SUBROUTINE SUBCOR(V8,V9,V10,V3,V4,V5,V6,V7,NORM)
      IF(NORM.EQ.0) GO TO 20
      XNC=V8/(V9*V10)
      WRITE(6,100) XNC
  100 FORMAT(1H ,26H NORMALISATION CORRECTION=,F10.4)
      GO TO 21
   20 XNC=1.0
      WRITE(6,102)
  102 FORMAT(1H ,26H NO NORMALISTION EFFECTED )
   21 GSAM=V3+V4*10.0
      GBKG=V5+V6*10.0
      DGAIN=GSAM-GBKG
      IF(DGAIN)5,7,7
    5 DGAIN=-DGAIN
    7 VP=DGAIN/20.0
      VP=VP*2.3025851
      VP=EXP(VP)
      VX=1.0/VP
      V7=XNC*VX
      WRITE(6,101) VP,VX,V7
  101 FORMAT(1H ,3HVP=,F12.4,3HVX=,F12.4,3HV7=,F12.4)
      RETURN
      END
      SUBROUTINE PHASE2(B,NN,M,NPORD)
C  DIMENSION OF B MUST BE AT LEAST 3*NN.
C  THE NN POINTS USED FORM REGION ABOUT THE Z.P.C. POSITION.
C  PHASE FUNCTION CONTAINS NN POINTS.
C  NN MUST BE A BINARY POWER.
      DIMENSION B(1),C(4100)
      IFSET=1
      RN=NN
      DO 1 K=1,12,1
      RN=RN/2.0
      IF(RN.GE.1.0) M=K
    1 CONTINUE
```

```
      DO 2 K=1,NN,1
      KK=K+NN
      B(KK)=0.0
    2 CONTINUE
      CALL FFT(B,M,IFSET)
      DO 3 K=1,NN,1
      KK=K+NN
      WRITE(6,105) B(KK),B(K)
      Z=ATAN2(B(KK),B(K))
      B(K)=COS(Z)
      B(KK)=SIN(Z)
      C(K)=Z
    3 CONTINUE
      IF(NPCRD) 107,106,107
  107 WRITE(6,108)
  108 FORMAT(1X 'HAS PUNCHED CARDS')
      WRITE(7,110) ((C(K)),K=1,NN)
  110 FORMAT(10F5.2)
  106 CONTINUE
      WRITE(6,101)
  101 FORMAT(/54H PHASE FUNCTION FROM COS FUNCTION                    )
      WRITE(6,105)((C(K)),K=1,NN)
  105 FORMAT(1H ,10F5.2)
      RETURN
      END
      SUBROUTINE PHASE3(B,NN,M,NPCRD)
      DIMENSION B(1),C(4100)
      IFSET=1
      RN=NN
      DO 1 K=1,12,1
      RN=RN/2.0
      IF(RN.GE.1.0) M=K
    1 CONTINUE
      DO 2 K=1,NN,1
      KK=K+NN
      B(KK)=0.0
    2 CONTINUE
      CALL FFT(B,M,IFSET)
      DO 3 K=1,NN,1
      KK=K+NN
      Z=ATAN2(B(KK),B(K))+3.14159/2.0
      B(K)=COS(Z)
      B(KK)=SIN(Z)
      C(K)=Z
    3 CONTINUE
      IF(NPCRD) 107,106,107
  107 WRITE(6,108)
  108 FORMAT(1X 'HAS PUNCHED CARDS')
      WRITE(7,110) ((C(K)),K=1,NN)
  110 FORMAT(10F5.2)
  106 CONTINUE
      WRITE(6,101)
  101 FORMAT(/54H PHASE FUNCTION FROM COS FUNCTION                    )
      WRITE(6,105)((C(K)),K=1,NN)
  105 FORMAT(1H ,10F5.2)
      RETURN
      END
      SUBROUTINE SLICE(A,N)
C   THIS SUBROUTINE SLICES THE LAST N POINTS OF THE ARRAY A CONTAINING
C   2*N POINTS TO THE BEGINING OF THE ARRAY.
```

```
      DIMENSION A(1)
      WRITE(6,2)N
    2 FORMAT(1H1,15HCALLED SLIDE N=,I4)
      DO 1 K=1,N,1
      KK=K+N
      Z=A(K)
      A(K)=A(KK)
      A(KK)=Z
    1 CONTINUE
      RETURN
      END
      SUBROUTINE FFT(A,M,IFSET)
      DIMENSION A(1)
      N=2**M
      NV2=N/2
      NM1=N-1
      J=1
      IF(IFSET) 6,6,7
    6 FN=N
      DO 8 K=1,N
      A(K)=A(K)/FN
      A(K+N)=-A(K+N)/FN
    8 CONTINUE
    7 DO 1 I=1,NM1
      IR=I
      II=I+N
      IF(I.GE.J) GO TO 2
      JR=J
      JI=J+N
      T=A(JR)
      TI=A(JI)
      A(JR)=A(IR)
      A(JI)=A(II)
      A(IR)=T
      A(II)=TI
    2 K=NV2
    3 IF(K.GE.J) GO TO 1
      J=J-K
      K=K/2
      GO TO 3
    1 J=J+K
      PI=3.14159265358979
      DO 4 L=1,M
      LE=2**L
      LE1=LE/2
      RLE=LE
      RLE=RLE/2.0
      U=1.0
      V=0.0
      W=SIN(PI/RLE)
      X=COS(PI/RLE)
      DO 4 J=1,LE1
      DO 5 I=J,N,LE
      IR=I
      II=I+N
      IP=I+LE1
      IPR=IP
      IPI=IP+N
      T=A(IPR)*U-A(IPI)*V
      TI=A(IPR)*V+A(IPI)*U
```

```
      A(IPR)=A(IR)-1
      A(IPI)=A(II)-TI
      A(IP)=A(IR)+T
      A(II)=A(II)+TI
    5 CONTINUE
      E=U*X-V*W
      F=U*W+V*X
      U=E
      V=F
    4 CONTINUE
      WRITE(6,9) M
    9 FORMAT(1H ,13HCALLED FFT M=,I6)
      RETURN
      END
      SUBROUTINE CONVCL(A,B,N,MM,N1)
C       NN IS THE NUMBER OF POINTS IN THE FUNCTION A.
C       MM IS THE NUMBER OF POINTS IN THE FUNCTION B.
C       ARRAY A MUST HAVE DIMENSION .GE. (NN+MM)
C       NN.GE.MM.
      DIMENSION A(1),B(1)
      J=N1+1
      N3=NN+N1
      DO 2 K=J,N3,1
      TOT=0.0
      DO 3 KK=1,MM,1
      KR=K+KK-1
      TOT=TOT+A(KR)*B(KK)
    3 CONTINUE
      A(K)=TOT
    2 CONTINUE
      N4=1+N1
      WRITE(6,9)
      WRITE(6,8)(A(K),K=N4,N3)
    8 FORMAT(1H ,1(F8.2)
    9 FORMAT(/54H  CONVOLVED INTERFEROGRAM                              )
      WRITE(6,5)NN,MM
    5 FORMAT(1H1,17HCONVCL CALLED NN=,I4,6H  MM=,I4)
      RETURN
      END
      SUBROUTINE SORT(A,N,J,NN)
      DIMENSION A(1)
C       J MUST BE .LE. N.
      L=0
      K=NN+1
      K2=J
    1 Z=A(K)
      A(K)=A(K2)
      L=L+1
    2 IF(K-K2) 3,5,6
    3 KK=NN+N-(J-K)+1
    4 ZZ=A(KK)
      A(KK)=Z
      Z=ZZ
      K=KK
      L=L+1
      GO TO 2
    5 IF(L.EQ.N) GO TO 7
      K2=K2+1
      K=NN+K2-(J-1)
      GO TO 1
```

```
    6 KK=NN+K-J+1
      GO TO 4
    7 CONTINUE
      WRITE(6,8)J,N,NN
    8 FORMAT(1H ,'SORT CALLED J=',I4,'N=',I4,'NN=',I4)
      END
C SUBROUTINE USED TO SET UP LINE PRINTER SO THAT DATA CAN BE OBTAINED  IN
C SPECTRAL FORM
      SUBROUTINE SUBLP
      DIMENSION CHAR(101),XNUM(11)
      DATA DOT,DIV/1H.,1H+/
      DATA XNUM/0.0,0.1,0.2,0.3,0.4,0.5,0.6,0.7,0.8,0.9,1.0/
      WRITE(6,101) XNUM
  101 FORMAT(17X,F3.1,10(7X,F3.1))
      DO 90 K=1,101
   90 CHAR(K)=DOT
      DO 91 IZ=1,21
      IK=1
      IK=IK+5*(IZ-1)
   91 CHAR(IK)=DIV
      WRITE(6,100) CHAR
  100 FORMAT(1H ,17X,101A1)
      RETURN
      END
      SUBROUTINE SUBGP(X,Y,NCARD,NCL1,I9,MM6)
      DIMENSION X(1),Y(1)
      DIMENSION CHAR(101)
      DATA BLANK,PLOT,PLUS/1H ,1H*,1H+/
      IF(NOUT.EQ.1) GO TO 11
      DO 25 L=1,MM6,I9
      DO 92 K=2,101
   92 CHAR(K)=BLANK
      CHAR(1)=PLUS
      I=((Y(L))*100)+0.5
      IF(I.GT.100) GO TO 3
      IF(I.LT.1) GO TO 5
      GO TO 4
    3 I=101
      GO TO 4
    5 I=2
    4 CHAR(I)=PLOT
   25 WRITE(6,103)  X(L),Y(L),CHAR
  103 FORMAT(1X,F6.2,3X,F6.4,3X,101A1)
   11 RETURN
      END
```

A1.3 DCH0623 Refractive index programme

```
C
C
C
C PROGRAMME TO PROCESS DISPERSIVE(PHASE)SPECTRA FROM FS720,CALCULATES
C AVERAGE PHASE FUNCTIONS AND  REFRACTIVE INDEX/FREQUENCY CURVE  BY
C METHOD  OF CHAMBERLAIN AND GERBIE
      DIMENSION PHASO(4100,6),PHASS(4100,6),SPHASO(4100),
     1APHASO(4100),APHASS(4100),FREQ(4100),ZX(4100),SPHASS(4100),
     1DIFPHS(4100),RFINDX(4100)
      DIMENSION Y(4100),A(4100,6),B(4100,6),C(4100),D(4100)
      DIMENSION BPHAS(4100)
      DIMENSION ZT(20)
   15 FORMAT(1H1)
   40 FORMAT(1X 'BACKGROUND PHASE/FREQ CURVE K=',I2)
   41 FORMAT(1X ' SAMPLE PHASE/FREQ CURVE K=',I2)
   86 FORMAT(1X'SAMPLE PHASE/FREQ CURVE')
   87 FORMAT(1X'BACKGROUND PHASE/FREQ CURVE')
  100 FORMAT(5I3)
  101 FORMAT(2I3,I4,7I3)
  102 FORMAT(10F5.2)
  103 FORMAT(//'CALCULATION OF REFRACTIVE INDEX FROM PHASE SPECTRUM')
  104 FORMAT(1H ,10F6.2)
  105 FORMAT(1H ,F7.2,9XF5.2,9XF5.2,3XI3)
  106 FORMAT(/'FREQ(CM-1) PHASE(SAMPLE) PHASE(BKG)  J')
  107 FORMAT(/'FREQ(CM-1) PHASE DIFFERENCE  4PIXPATHLXFREQ  N(COMPUTED)
     1 J')
  108 FORMAT(F7.2,12XF7.3,3XF8.3,10XF8.4,5XI3)
  109 FORMAT(I3,5E10.5)
  110 FORMAT(1H ,17X,101A1)
  111 FORMAT(1H ,'COMPUTATION FOR SOLUTION R.I. VALUES')
  113 FORMAT(1X,F7.2,1X,F8.4,1X,101A1)
  115 FORMAT(1H1)
  116 FORMAT(1H1,'REFRACTIVE INDEX/ FREQUENCY CURVE')
  117 FORMAT(20A4)
  211 FORMAT(1H ,'CUT OF RANGE')
  221 FORMAT(17X,F5.3,10(5X,F5.3))
  301 FORMAT(1H ,6X,F6.4)
  302 FORMAT(F5.3)
  303 FORMAT(1H ,6X,F5.3)
      WRITE(6,103)
      READ(5,100) NSETS,NOPH,NOSPH,NPHM,NCARD
C NSETS= NUMBER OF SETS OF DATA
C NOPH= INTEGER DECIDING HOW OUTPUT DATA IS DISPLAYED
C      =1 GIVES PHASE CURVE FOR EACH DATA SET PLUS AVERAGE
C     =2 GIVES AVERAGE PHASE CURVE ONLY
C     =3 GIVES NO PHASE CURVES
C NOSPH= DETERMINES WHERE PHASE VALUES ARE READ FROM
C       =0 READS FROM INPUT DEVICE 5 (=*SOURCE*)
C       =1 READS BACKGROUND PHASE FROM FILE 7 AND SAMPLE PHASE FROM FILE 9
C NPHM= SIGNAL TO INDICATE SYSTEM ON WHICH COMPUTATION IS BEING CARRIED OUT
C      =0 CALCULATION FOR A PURE LIQUID OR A SOLID
C      =1 CALCULATION FOR A SOLUTION
   20 READ(5,101) NBKG,NDIS,NA,NC,NSIG1,NSIG2,NSIG3,NPHAS
C NBKG= NUMBER OF PHASE BACKGROUNDS
C NDIS= NUMBER OF PHASE SAMPLES
```

```
C NN= NUMBER OF POINTS
C NO= NUMBER OF RUNS WITH DIFFERENT MEAN REFRACTIVE INDEX VALUES
C NSIG1= SAMPLING INTERVAL IN MICRONS
C NSIG2= SIGNAL TO DETERMINE SPACING OF PLOTTED REFRACTIVE INDEX
C       =0 GIVES NO SPACING
C       =1 GIVES SPACING FOR COMPARISON OF CURVES WITH DIFFERENT NUMBERS OF POINTS
C NOTE ONLY FOR 512 POINTS AND OVER
C NSIG3= SIGNAL TO INDICATE WHETHER REFRACTIVE INDEX CALCULATION IS REQUIRED
C       =0 GIVES REFRACTIVE INDEX PLOT
C       =1 GIVES ONLY PHASE SPECTRA
C NPHAS= SIGNAL TO INDICATE IF INSTRUMENT BACKGROUND IS TO BE READ IN
C  FOR SOLUTION COMPUTATIONS
C  =1 READS BACKGROUND
      NM=NN/2
      Z=3.1416
      IF(NOSPH) 510,510,501
  510 DO 1 K=1,NBKG
    1 READ(5,102)(PHASO(J,K),J=1,NN)
      DO 2 K=1,NDIS
    2 READ(5,102)(PHASS(J,K),J=1,NN)
      IF(NPHAS.EQ.1) GO TO 550
      GO TO 16
  501 DO 502 K=1,NBKG
  502 READ(7,102)(PHASO(J,K),J=1,NN)
      DO 503 K=1,NDIS
  503 READ(9,102)(PHASS(J,K),J=1,NN)
      IF(NPHAS.EQ.1) GO TO 550
      GO TO 16
  550 READ(5,102)(BPHAS(J),J=1,NN)
      DO 552 K=1,NBKG
      DO 551 J=1,NN
  551 PHASO(J,K)=PHASO(J,K)-BPHAS(J)
  552 CONTINUE
      DO 553 K=1,NDIS
      DO 554 J=1,NN
  554 PHASS(J,K)=PHASS(J,K)-BPHAS(J)
  553 CONTINUE
   16 IF(NO) 11,12,13
   13 READ(5,109)OM,RMEAN,PATHL1,FREQL,FREQH,PATHL2
C OM= INTEGER NUMBER OF RADIANS FOR CONNECTING UP BRANCHES OF PHASE CURVES
C RMEAN= MEAN VALUE OF REFRACTIVE INDEX CORRECTED FOR SAMPLING ERRORS AT
C           ZERO PATH DIFFERENCE
C PATHL1= PATHLENGTH IN CENTIMETRES (FOR SOLUTION COMPUTATIONS THIS IS
C  THE PATHLENGTH OF THE SOLUTION)
C FREQL= LOWER LIMIT OF COMPUTATION IN RECIPROCAL CENTIMETRES
C FREQH= UPPER LIMIT OF COMPUTATION IN RECIPROCAL CENTIMETRES
C PATHL2= PATHLENGTH OF THE SOLVENT BACKGROUND (ONLY REQUIRED FOR
C  SOLUTION COMPUTATIONS)
      READ(5,117) ZT
C ZT= HEADING
      DO 4 J=1,NN
      SPHASO(J)=0.0
      DO 5 K=1,NBKG
      SPHASO(J)=SPHASO(J)+PHASO(J,K)
    5 APHASO(J)=SPHASO(J)/NBKG
    4 CONTINUE
      WRITE(6,104)(APHASO(J),J=1,NN)
      DO 6 J=1,NN
      SPHASS(J)=0.0
      DO 7 K=1,NDIS
```

```
      SPHASS(J)=SPHASS(J)+PHASS(J,K)
    7 APHASS(J)=SPHASS(J)/NDIS
    6 CONTINUE
      WRITE(6,104)(APHASS(J),J=1,NN)
C ALIAS FREQUENCY =1/2*SAMPLING INTERVAL
      ASFREQ=10000.000/(2.0*NSIG1)
      DFREQ=ASFREQ/NM
      FREQ(1)=0.0
      DO 8 J=2,NM
    8 FREQ(J)=FREQ(J-1)+DFREQ
      M=INT(FREQL)
      MM=INT(FREQH)
      M1=M*NM/ASFREQ
      M2=MM*NM/ASFREQ
      WRITE(6,15)
      JJ=0
      DO 37 J=M1,M2
      JJ=JJ+1
   37 Y(JJ)=FREQ(J)
      GO TO (34,35,33),NOPH
   34 KK=0
      DO 31 K=1,NBKG
      KK=KK+1
      WRITE(6,115)
      WRITE(6,40) K
      CALL SETUP
      JJ=0
      DO 55 J=M1,M2
      JJ=JJ+1
   55 A(JJ,KK)=PHASO(J,K)
      CALL PAPLOT(A,Y,M1,M2,KK)
   31 CONTINUE
      KK=0
      DO 32 K=1,NDIS
      KK=KK+1
      WRITE(6,115)
      WRITE(6,41) K
      CALL SETUP
      JJ=0
      DO 75 J=M1,M2
      JJ=JJ+1
   75 B(JJ,KK)=PHASS(J,K)
      CALL PAPLOT(B,Y,M1,M2,KK)
   32 CONTINUE
      WRITE(6,115)
   35 WRITE(6,87)
      CALL SETUP
      JJ=0
      DO 85 J=M1,M2
      JJ=JJ+1
   85 C(JJ)=APHASO(J)
      CALL PHPLOT(C,Y,M1,M2)
      WRITE(6,115)
      WRITE(6,86)
      CALL SETUP
      JJ=0
      DO 95 J=M1,M2
      JJ=JJ+1
   95 D(JJ)=APHASS(J)
      CALL PHPLOT(D,Y,M1,M2)
```

```
   33 WRITE(6,115)
      WRITE(6,106)
      WRITE(6,105)(FREQ(J),APHASS(J),APHASO(J),J,J=M1,M2)
      IF(NSIG3.EQ.1) GO TO 12
      IF(NPHM.EQ.1) GO TO 402
      ZZ=4.0*Z*PATHL1
      DO 14 J=M1,M2
      ZX(J)=ZZ*FREQ(J)
      DIFPHS(J)=APHASS(J)-APHASO(J)
   14 REINDX(J)=1.0+RMEAN+(DIFPHS(J)/ZX(J))
      GO TO 401
  402 ZZ=4.0*Z
      DO 403 J=M1,M2
      ZX(J)=ZZ*FREQ(J)
      DIFPHS(J)=2.0*(APHASS(J)/PATHL1)-APHASO(J)/PATHL2
  403 REINDX(J)=1.0+RMEAN+(DIFPHS(J)/ZX(J))
  401 WRITE(6,111)
      WRITE(6,107)
      WRITE(6,108)(FREQ(J),DIFPHS(J),ZX(J),REINDX(J),J,J=M1,M2)
C TO SET UP LINE PRINTR TO OBTAIN DATA IN SPECTRAL FORM
      DATA DOT,DIV/1H.,1H+/
      AMAX=0.0
      DIMENSION CHAR(101),X(11)
      DO 201 J=M1,M2
      IF(REINDX(J)-AMAX) 201,201,202
  202 AMAX=REINDX(J)
  201 CONTINUE
      WRITE(6,301) AMAX
      AMIN=2.0
      DO 203 J=M1,M2
      IF(REINDX(J)-AMIN) 204,203,203
  204 AMIN=REINDX(J)
  203 CONTINUE
      WRITE(6,301) AMIN
      RDIFF=AMAX-AMIN
      WRITE(6,301) RDIFF
      IF(RDIFF.GT.0.4) GO TO 205
      IF(RDIFF.GT.0.2) GO TO 217
      IF(RDIFF.GT.0.1) GO TO 206
      IF(RDIFF.GT.0.05) GO TO 207
      GO TO 208
  207 R=0.1
      GO TO 210
  206 R=0.2
      GO TO 210
  208 R=0.05
      GO TO 210
  217 R=0.4
      GO TO 210
  205 WRITE(6,211)
      GO TO 300
  210 ADIFF=RDIFF/2.0
      CLINE=AMIN+ADIFF
      LLINE=INT(CLINE*100.0)
      DLINE=LLINE
      ALINE=CLINE/100.0
      WRITE(6,303) ALINE
      WRITE(6,302) R
      AINC=R/10.0
      Q=R/2.0+AINC
```

```
      DO 220 K=1,11
      AK=K
  220 X(K)=ALINE-Q+AINC*AK
      WRITE(6,116)
      WRITE(6,117) ZT
      WRITE(6,221)(X(K),K=1,11)
      DO 90 K=1,101
   90 CHAR(K)=DOT
      DO 91 IZ=1,11
      IK=1
      IK=IK+10*(IZ-1)
   91 CHAR(IK)=DIV
      WRITE(6,110) CHAR
      DO 25 J=M1,M2
      DATA BLANK,PLOT,PLUS/1H ,1H*,1H+/
      DO 92 M=2,101
   92 CHAR(M)=BLANK
      CHAR(1)=PLUS
      N=INT(100.0/R)
      ABASE=(((ALINE-R/2.0)*N)-1.0)
      L=REINDX(J)*N-ABASE
      IF(L.GT.100) GO TO 123
      IF(L.LT.1) GO TO 125
      GO TO 124
  123 L=101
      GO TO 124
  125 L=1
  124 CHAR(L)=PLOT
      IF(NSIG2) 12,357,358
  358 IF((NN-2048).EQ.0) GO TO 359
      GO TO 360
  359 WRITE(6,370)
  370 FORMAT(1H )
  360 IF((NN-1024).EQ.0) GO TO 361
      GO TO 362
  361 WRITE(6,370)
      WRITE(6,370)
      WRITE(6,370)
  362 IF((NN-512).EQ.0) GO TO 363
      GO TO 357
  363 WRITE(6,370)
      WRITE(6,370)
      WRITE(6,370)
      WRITE(6,370)
      WRITE(6,370)
      WRITE(6,370)
      WRITE(6,370)
      WRITE(6,370)
  357 WRITE(6,113)(FREQ(J),REINDX(J),CHAR)
   25 CONTINUE
      IF(NCARD.EQ.0) GO TO 26
      WRITE(8,27)((FREQ(J),REINDX(J)),J=M1,M2)
   27 FORMAT(5(F6.2,F6.4,3X))
   26 CONTINUE
  300 NO=NC-1
      GO TO 16
   12 NSETS=NSETS-1
      IF(NSETS)11,11,20
   11 CALL EXIT
      END
      SUBROUTINE SETUP
```

```
      DIMENSION ALINE(65)
      DIMENSION XNUM(7)
      DATA XNUM/-3.0,-2.0,-1.0,0.0,1.0,2.0,3.0/
      DATA BLANK,DOT,PLUS,STAR/1H ,1H.,1H+,1H*/
   52 FORMAT(65A1)
   53 FORMAT(1H ,F4.1,6(6X,F4.1))
      WRITE (6,53) XNUM
      DO 51 K=1,65
   51 ALINE(K)=DOT
      DO 57 K=3,63,5
   57 ALINE(K)=PLUS
      WRITE(6,52) ALINE
      RETURN
      END
      SUBROUTINE PAPLOT(Z1,Y,M1,M2,K)
      DIMENSION Z1(4100,1),Y(4100)
      DIMENSION N(4100)
      DIMENSION ALINE(65)
      DATA BLANK,DOT,PLUS,STAR/1H ,1H.,1H+,1H*/
   54 FORMAT(1H ,2X,65A1,6X,F7.2,2X,F8.4)
      M3=M2-M1
      M4=1+M3
      DO 70 K1=1,M4
      N(K1)=0
      IF(Z1(K1,K).GT.3.14) GO TO 71
      GO TO 70
   71 Z1(K1,K)=Z1(K1,K)-6.28
      N(K1)=1
   70 CONTINUE
      DO 1 JJ=1,M4
      DO 53 M=1,65
   53 ALINE(M)=BLANK
      ALINE(31)=DOT
      M=INT((Z1(JJ,K)+3.14159)*10.0)
      IF(M.GT.65) GO TO 60
      IF(M.LT.1) GO TO 61
      GO TO 62
   60 M=65
      GO TO 62
   61 M=1
   62 IF(N(JJ).EQ.1) GO TO 63
      GO TO 64
   63 ALINE(M)=DOT
      GO TO 1
   64 ALINE(M)=STAR
    1 WRITE(6,54) ALINE,Z1(JJ,K),Y(JJ)
      RETURN
      END
      SUBROUTINE PPPLOT(Z1,Y,M1,M2)
      DIMENSION Z1(4100),Y(4100)
      DIMENSION N(4100)
      DIMENSION ALINE(65)
      DATA BLANK,DOT,PLUS,STAR/1H ,1H.,1H+,1H*/
   54 FORMAT(1H ,2X,65A1,6X,F7.2,2X,F8.4)
      M3=M2-M1
      M4=1+M3
      DO 70 K1=1,M4
      N(K1)=0
      IF(Z1(K1).GT.3.14) GO TO 71
      GO TO 70
```

```
   71 Z1(K1)=Z1(K1)-6.28
      N(K1)=1
   70 CONTINUE
      DO 1 JJ=1,M4
      DO 53 M=1,65
   53 ALINE(M)=BLANK
      ALINE(31)=DOT
      M=INT((Z1(JJ)+3.14159)*10.0)
      IF(M.GT.65) GO TO 60
      IF(M.LT.1) GO TO 61
      GO TO 62
   60 M=65
      GO TO 62
   61 M=1
   62 IF(N(JJ).EQ.1) GO TO 63
      GO TO 64
   63 ALINE(M)=DOT
      GO TO 1
   64 ALINE(M)=STAR
    1 WRITE(6,54) ALINE,Z1(JJ),Y(JJ)
      RETURN
      END
```

A1.4 GPLOT3 Spectra plotting programme

```
C
C
C
C  GPLOT3
C
C  GRAPH PLOTTER ROUTINE TO GIVE VARIBLE  X AND Y  AXES PLUS MULTIPLE
C  BAND PLOTTING ON SINGLE SHEET
C
C
      DOUBLE PRECISION Z
C
      DIMENSION X(5000),  Y(5000),XX(5000,5),YY(5000,5)
      DIMENSION XAXIS(50),YAXIS(11),YYAXIS(11),TITLE(20)
      DIMENSION YNAXIS(11)
C
      DATA YAXIS/'0.0','0.1','0.2','0.3','0.4','0.5','0.6','0.7','0.8',
     X'0.9','1.0'/
      DATA YYAXIS/'0.00','0.25','0.50','0.75','1.00','1.25','1.50',
     X'1.75','2.0','2.25','2.50'/
C
    1 FORMAT(20A4)
    2 FORMAT(I3,I3,F5.1,I3)
    3 FORMAT(I3)
    4 FORMAT (2I3)
    5 FORMAT(1HO,' NSETS = ',I3)
    6 FORMAT(1HO,2CA4)
    7 FORMAT(1HO,' NCURVE = ',I3,5X,' NS = ',I1,5X,' XSCALE = ',F5.1)
    8 FORMAT(1HO,' DATA AS READ IN ')
    9 FORMAT(1H ,(5(3X,F9.2,F8.4)))
   11 FORMAT(5(F7.2,F7.4,1X))
   12 FORMAT(1HO,' NA = ',I1,5X,' NOLT = ',I1)
   13 FORMAT(1HO,' DATA FOR PLOTTING ')
   14 FORMAT(1HO,' XSCALE = ',F6.2)
   16 FORMAT(F7.2,F7.4)
 1001  FORMAT (//1H ,10X,6HX-AXIS/19H STARTING POINT     ,F10.2/
     C  1H ,18HFINISHING POINT    ,F10.2)
 1002  FORMAT (//1H ,I10,15H POINTS TO PLOT/)
 1003 FORMAT(1HO,' SSJ = ',F6.2,5X,' JJ = ',I3)
C
C
      READ(5,3) NSETS
C NSETS= NUMBER OF SERIES OF CURVES TO PLOT
C NOT OPERATIVE AS YET - SET EQUAL TO 1
C
C
  102 READ(5,1)(TITLE(I),I=1,20)
      READ(5,2) NCURVE,NS,XSCALE,XS1
C NCURVE= NUMBER OF CURVES PER PLOT
C
C NS=1 GIVES ABSORBANCE SCALE FROM 0 TO 1
C NS=2 GIVES ABSORBANCE SCALE FROM 0 TO 2.5
C
C XSCALE= FREQUENCY INTERVAL PER INCH OF GRAPH PLOT
C XS1=0 GIVES STRAIGHT-FORWARD WAVENUMBER SCALE
C XS1=1 GIVES ROUNDED OFF WAVENUMBER SCALE
```

```
C
C
      READ(5,4) NA,NOUT
C
C      NA=1 READS IN TRANSMITTANCE DATA IN INCREASING WAVENUMBER ORDER AND
C      PLOTS TRANSMITTANCE SPECTRUM
C      NA=2 READS IN ABSORBANCE DATA IN INCREASING WAVENUMBER ORDER AND PLOTS
C      ABSORBANCE SPECTRUM
C      NA=3 READS IN TRANSMITTANCE DATA IN INCREASING WAVENUMBER ORDER AND
C      PLOTS ABSORBANCE SPECTRUM
C      NA=4 READS IN DCH05277 DATA AND PLOTS ABSORBANCE SPECTRUM
C      NA=5 PLOTS ABSORBANCE SPECTRUM WITH NEPER METRE +2 MOLE -1 SCALE
C      NA=6 PLOTS ABSORBANCE WITH NEPER METRE -1 SCALE
C      NA=7 READS IN ABSORBANCE DATA IN DECREASING WAVENUMBER ORDER AND
C      CONVERTS TO INCREASING WAVENUMBER ORDER
C
C NOUT=0 GIVES NORMAL DATA LISTING
C NOUT=1 GIVES ADDITIONAL DATA FOR ERROR SEARCHING
C
C
      IF(NA.EQ.5) GO TO 500
      IF(NA.EQ.6) GO TO 580
      GO TO 501
  500 READ(5,451) PATHL,CONC
C     PATHL=PATHLENGTH (CM)
C     CONC=CONCENTRATION (MOLES CM -3)
  451 FORMAT(E12.3,E12.3)
      CONC=CONC*1000000.0
      PATHL=PATHL/100.0
      WRITE(6,452) PATHL,CONC
  452 FORMAT(1HO,' PATHLENGTH = ',E12.3,' METRE      ',5X,' CONCENTRATION
     1 = 'E12.3,' MOLES METRES -3 ')
      CL=PATHL*CONC
      WRITE(6,453) CL
  453 FORMAT(1HO,' CL = ',E12.3,' MOLES METRE -2 ')
      GO TO 501
  580 READ(5,480) PATHL
C     PATHL= PATHLENGTH  (CM)
  480 FORMAT(E12.3)
      PATHL=PATHL/100.0
      WRITE(6,481) PATHL
  481 FORMAT(1HO,'PATHLENGTH = ',E12.3,' METRE')
      CL=PATHL
  501 IF(NOUT.EQ.0) GO TO 49
      WRITE(6,6)(TITLE(I),I=1,20)
      WRITE(6,5) NSETS
      WRITE(6,7) NCURVE,NS,XSCALE
      WRITE(6,12) NA,NOUT
   49 CONTINUE
      IF(NOUT.EQ.0) GO TO 248
      WRITE(6,8)
  248 CONTINUE
      DO 50 J=1,NCURVE
      IF(NA.NE.4) GO TO 115
      K=1
  100 READ(8,16,END=15)(X(K),Y(K))
      IF(NOUT.EQ.0) GO TO 17
      WRITE(6,9)(X(K),Y(K))
   17 CONTINUE
      IF(X(K).EQ.0.0) GO TO 18
```

```
      GO TO 19
   18 NP=K-1
      GO TO 15
   19 K=K+1
      GO TO 100
   15 NA=3
      GO TO 350
  115 L=1
      M=5
   10 READ(8,11,END=101)(X(K),Y(K),K=L,M)
      IF(NOUT.EQ.0) GO TO 48
      WRITE(6,9)(X(K),Y(K),K=L,M)
   48 CONTINUE
      DO 20 I=L,M
      IF(X(I).EQ.0.0) GO TO 25
      GO TO 20
   25 NP=I-1
      GO TO 101
   20 CONTINUE
      L=L+5
      M=L+4
      GO TO 10
  101 CONTINUE
      WRITE(6,999) NP
  999 FORMAT(1HO,' NP = ',I4)
      GO TO (150,250,350,450,350,350,450),NA
  450 DO 26 K=1,NP
      XX(K,J)=X(NP-K+1)
   26 YY(K,J)=Y(NP-K+1)
      GO TO 50
  150 DO 126 K=1,NP
      XX(K,J)=X(K)
      YY(K,J)=Y(K)
  126 IF(YY(K,J).GT.1.0) YY(K,J)=1.0
      GO TO 50
  250 DO 226 K=1,NP
      XX(K,J)=X(K)
      YY(K,J)=Y(K)
  226 CONTINUE
      IF(NOUT.EQ.0) GO TO 50
      WRITE(6,9)(XX(K,J),YY(K,J),K=1,NP)
      GO TO 50
  350 DO 326 K=1,NP
      XX(K,J)=X(K)
      Y(K)=1.0/Y(K)
      Y(K)=ALOG(Y(K))
      IF(NA.EQ.5) GO TO 336
      IF(NA.EQ.6) GO TO 336
      GO TO(330,331),NS
  330 IF(Y(K).GT.1.0000) GO TO 329
  331 IF(Y(K).GT.2.5000) GO TO 327
      IF(Y(K).LT.0.0000) GO TO 328
      GO TO 336
  327 Y(K)=2.5000
      GO TO 336
  328 Y(K)=0.0000
      GO TO 336
  329 Y(K)=1.0000
  336 YY(K,J)=Y(K)
  326 CONTINUE
```

```
      BBFREQ=BFREQ/XSCALE
      JBFREQ=INT(BBFREQ+1.0)
      JBFREQ=JBFREQ*JXSCAL
      SFREQ=FLOAT(JSFREQ)
      BFREQ=FLOAT(JBFREQ)
   80 SSJ=(BFREQ-SFREQ)/XSCALE
      JJ=INT(SSJ+0.5)
      DO 60 K=1,JJ
   60 XAXIS(K)=SFREQ+XSCALE*(K)
      WRITE(6,1001) SFREQ,BFREQ
      WRITE(6,1002) NP
      WRITE(6,1003) SSJ,JJ
C HAS CALCULATED THE XAXIS VALUES TO BE PLOTTED ACCORDING TO DATA
C  DRAWS AND LABELS BOX
      CALL PAXIS(2.0,1.0,'                    ',-17,-SSJ,0.0,SFREQ,XSCALE,
     1-1.0)
      IF(NA.EQ.1) GO TO 72
      CALL PAXIS(2.0,10.0,'           ',-10,-9.0,270.0,0.0,0.1111,0.9)
      GO TO 73
   72 CALL PAXIS(2.0,10.0,'              ',-13,-9.0,270.0,0.0,0.1111,0.9)
   73 CALL PAXIS(2.0+SSJ,10.0,'      ',5,-SSJ,180.0,0.0,XSCALE,-1.0)
      CALL PAXIS(2.0+SSJ,1.0,1H ,1.0,-9.0,90.0,SFREQ,0.1111,-0.9)
      GO TO (70,69,69,69,68,67),NA
   69 CALL PSYMB(1.2,4.62,-0.18,10HABSORBANCE,90.0,10)
      GO TO 71
   70 CALL PSYMB(1.2,4.62,-0.18,13HTRANSMITTANCE,90.0,13)
      GO TO 71
   68 CALL PSYMB(0.7,4.62,-0.18,22HWAVENUMBER METRE +2 MOLE -1,90.0,22)
      GO TO 71
   67 CALL PSYMB(0.7,4.62,-0.18,14HWAVENUMBER METRE -1,90.0,14)
   71 CALL PSYMB(2.0,10.25,-0.2,TITLE,0.0,80)
      SSJ1=SSJ/2.0
      CALL PSYMB(SSJ1+1.0,0.3,-0.18,17HWAVENUMBER (CM-1),0.0,17)
      YJ=0
      JJ7=JJ+1
      DO 32 J=1,JJ
      Z=XAXIS(J)
      CALL PFNMBR((YJ*0.1)+2.2,0.75,0.13,Z,0.0,'F6.1 *')
   32 YJ=YJ+10
      IF(NA.EQ.5) GO TO 163
      IF(NA.EQ.6) GO TO 163
      GO TO(61,62), NS
   61 DO 40 I=1,11
   40 CALL PSYMB(1.60,(I*0.9)+0.03,-0.13,YAXIS(I),0.0,3)
      CALL PLTOFS(SFREQ,XSCALE,0.0,0.1111,2.0,1.0)
      GO TO 63
   62 DO 41 I=1,11
   41 CALL PSYMB(1.50,(I*0.9)+0.03,-0.13,YYAXIS(I),0.0,4)
      CALL PLTOFS(SFREQ,XSCALE,0.0,0.2777,2.0,1.0)
      GO TO 63
  163 AMAX=AMAX/10.0
      IAMAX=INT(AMAX+1.0)
      AMAX=FLOAT(IAMAX)
      AMAX=AMAX*10.0
      YS=AMAX/10.0
      WRITE(6,91) YS
   91 FORMAT(1HO,' YS = ',F10.2)
      DO 700 J=1,11
  700 YNAXIS(J)=YS*(J-1)
      WRITE(6,741)(YNAXIS(J),J=1,11)
```

```
741 FORMAT(1H0,(6F10.2))
    DO 730 J=1,11
    Z=YNAXIS(J)
730 CALL PENNBR(0.9,(J*0.9)+0.03,-0.13,Z,0.0,'F6.1 *')
    AMAX1=AMAX/9.0
    CALL PLTOFS(SFREQ,XSCALE,0.0,AMAX1,2.0,1.0)
 63 CALL PENUP(2.0,1.0)
    NN=04
    DO 33 J=1,NCURVE
    IF(NA.NE.7) GO TO 160
    CALL PLINE(XX(1,J),YY(1,J),NP,1,5,NN,1.0)
    GO TO 161
160 CALL PLINE(XX(1,J),YY(1,J),NP,1,0,0,1.0)
161 NN=NN+01
 33 CONTINUE
    CALL PLTEND
    NSETS=NSETS-1
    IF(NSETS) 103,103,102
103 CALL EXIT
    END
```

```
   50 CONTINUE
      DO 51 J=1,NCURVE
      DO 21 K=1,NP
      IF(YY(K,J).LT.0.0) GO TO 27
      GO TO 21
   27 YY(K,J)=0.0
   21 CONTINUE
      IF(NOUT.EQ.0) GO TO 51
      WRITE(6,9)(XX(K,J),YY(K,J),K=1,NP)
   51 CONTINUE
      GO TO (600,600,600,600,621,621,600),NA
  621 DO 430 J=1,NCURVE
      DO 431 K=1,NP
      YY(K,J)=YY(K,J)/CL
  431 CONTINUE
      WRITE(6,997)(YY(K,J),K=1,NP)
  997 FORMAT(1HO,5(5X,E12.3))
      AMAX=0.0
      DO 440 K=1,NP
      IF(YY(K,J).GT.AMAX) GO TO 441
      GO TO 440
  441 AMAX=YY(K,J)
  440 CONTINUE
  430 CONTINUE
      IF(NA.EQ.6) GO TO 739
      WRITE(6,442) AMAX
  442 FORMAT(1HO,' MAXIMUM ABSORBANCE = ',E12.3,' NEPER METRE +2 MOLE -1
     1')
      GO TO 740
  739 WRITE(6,742) AMAX
  742 FORMAT(1HO,'MAXIMUM ABSORBANCE = ',E12.3,'NEPER METRE -1')
  740 WRITE(6,13)
      DO 436 J=1,NCURVE
  436 WRITE(6,443)(XX(K,J),YY(K,J),K=1,NP)
  443 FORMAT(1HO,(5X,5(F8.3,E10.3,5X)))
      GO TO 47
  600 IF(NOUT.EQ.0) GO TO 47
      WRITE(6,13)
      DO 46 J=1,NCURVE
      WRITE(6,9)((XX(K,J),YY(K,J)),K=1,NP)
   46 CONTINUE
   47 CONTINUE
C  NB. ALL DATA SETS TO BE PLOTTED  ARE TO BE OF THE SAME LENGTH AND
C      START  AT THE  SAME FREQUENCY
C DETERMINES CONVENIENT STARTING AND FINISHING FREQUENCIES FOR PLOTTING
      SFREQ=XX(1,1)
      BFREQ=XX(NP,1)
      IF(XSI.EQ.0) GO TO 80
      T=BFREQ-SFREQ
      T=T/15.0
      T=T/10.0
      IT=INT(T+1.0)
      IT=IT*10
      T=FLOAT(IT)
      XSCALE=T
      WRITE(6,14) XSCALE
      SSFREQ=SFREQ/XSCALE
      JSFREQ=INT(SSFREQ)
      JXSCAL=INT(XSCALE+0.5)
      JSFREQ=JSFREQ*JXSCAL
```

A1.5 RIINTEN Intensities from refractive index programme

```
C
C
C
C PROGRAMME TO COMPUTE INTENSITIES, DELTA, FI, GI FROM R.I. DATA
      DIMENSION DELT(100),FFI(100),FGI(100)
      READ(8,7) NSETS,NSIG
C NSETS= NUMBER OF FREQUENCY REFRACTIVE INDEX PAIRS
      NS=NSETS
      CONST3=1.0
C NSIG=1 FI CALCULATED
C      =2 GI CALCULATED
    7 FORMAT(2I3)
      READ(8,2) FREQI
      IF(NSIG.EQ.1) GO TO 6
      READ(8,2) HALF
C HALF= HALF-BAND WIDTH
      J=0
      READ(8,90) CONST1,CONST2
   90 FORMAT(2E7.1)
    6 READ(8,1) RDX1,RDX2
    1 FORMAT(2F8.5)
      READ(8,2) FREQ1,FREQ2
    2 FORMAT(3F8.4)
      RDIFF=RDX1-RDX2
      A=3.14159**2
      A=A*2
      A=A*RDIFF
      IF(NSIG.EQ.2) GO TO 20
      BK=FREQI**2-FREQ1**2
      BL=FREQ2**2-FREQI**2
      GO TO 21
   20 TOR1=HALF*FREQ1
      TOR1=TOR1**2
      BK=FREQI**2-FREQ1**2
      TOR1=TOR1/BK
      BK=BK+TOR1
      BL=FREQ2**2-FREQI**2
      TOR2=HALF*FREQ2
      TOR2=TOR2**2
      TOR2=TOR2/BL
      BL=BL+TOR2
   21 BK=1.0/BK
      BL=1.0/BL
      B=BK+BL
      AI=A/B
      WRITE(6,4) RDX1,RDX2,FREQ1,FREQI,FREQ2
    4 FORMAT(1HO,'RDX1=',F8.5,'  RDX2=',F8.5,/'FREQ1= ',F8.4,'  FREQI= '
     1,F8.4,'  FREQ2= ',F8.4)
      IF(NSIG.EQ.2) GO TO 11
      WRITE(6,10) RDIFF,B
   10 FORMAT(1H ,'DELTA= ',F8.5,'  FI= ',E10.3)
      GO TO 13
   11 WRITE(6,12) RDIFF,B
   12 FORMAT(1H ,'DELTA= ',F8.5,'  GI= ',E10.3)
   13 WRITE(6,3) AI
```

```
  3 FORMAT(1H ,'ABSOLUTE INTENSITY= ',E10.3,' CM-2')
    J=J+1
    DELT(J)=RDIFF*CONST1
    IF(NSIG.EQ.2) GO TO 30
    FFI(J)=B*CONST2
    GO TO 31
 30 FGI(J)=B*CONST2
    NSETS=NSETS-1
    IF(NSETS.GT.0) GO TO 6
 31 IF(NSIG.EQ.2) GO TO 50
    DO 41 J=1,NS
 41 WRITE(7,40) DELT(J),CONST3
    DO 42 J=1,NS
 42 WRITE(7,40) FFI(J),CONST3
    GO TO 5
 40 FORMAT(2E12.4)
 50 DO 51 J=1,NS
 51 WRITE(7,40) DELT(J),CONST3
    DO 52 J=1,NS
 52 WRITE(7,40) FGI(J),CONST3
  5 CALL EXIT
    END
```

A1.6 Data input listings

```
PROGRAMME CHK6:FTRAN3

    PRIVATE DISK  MTS567


DEVELOPMENT OF FTRAN1
PROGRAMME TO COMPUTE TRANSMISSION SPECTRA FROM INTERFEROGRAM DATA
THIS VERSION IS DIMENSIONED FOR 2048 POINT TAPES


NORMALISED OR NON-NORMALISED SINGLE BEAM SPECTRA ARE PLOTTED
RATIOED SPECTRUM CALCULATED FROM NON-NORMALISED TRANSFORMED ELEMENTS


INPUT/OUTPUT DEVICES
    5=TAPE INPUT=FILENAME (EG CRA1(1,2[illegible]))
    8=CARD INPUT=*SOURCE*
    6=PRINTER OUTPUT=*SINK*
    7=CARD OUTPUT=*PUNCH*


READ(8) NSETS(I3)

    NSETS=NUMBER OF DATA SETS


READ(8) N(I4),FSINT(2X,F5.2),FREQL(2X,F7.2),FREQH(2X,F7.2),IOPUT(2X,I1),
    NSIG(2X,I1),NABS(2X,I1),NOUT(2X,I1),NCARD(2X,I1),NORM(2X,I1)

    N=NUMBER OF POINTS TO BE TRANSFORMED

    FSINT=SAMPLING INTERVAL IN MICRONS

    FREQL=LOWER FREQUENCY LIMIT IN CM-1

    FREQH=UPPER FREQUENCY LIMIT IN CM-1

    IOPUT=NUMBER OF OUTPUT POINTS PER RESOLUTION
    (1 TO 5 ONLY)

    NSIG=1 FOR RATIOED SPECTRUM
        =2 FOR SINGLE SPECTRUM

    NABS=1 RATIOED ABSORBANCE SPECTRUM IS PLOTTED
        =0 RATIOED TRANSMITTANCE SPECTRUM IS PLOTTED

    NOUT=0 GIVES NORMAL LISTING OF INTERMEDIATE DATA
        =1 GIVES SPECTRA ONLY
        =2 GIVES FULL LISTING FOR ERROR SEARCHING
```

```
      NCARD=0 GIVES NO CARD OUTPUT
           =1 GIVES CARD OUTPUT OF RATIOED SPECTRUM
           =2 GIVES CARD OUTPUT OF SINGLE SPECTRUM
        (SPECTRAL CARD OUTPUT IN FORMAT 5(F7.2,F7.4,1X) GIVING FREQUENCY (CM-1)
         AND EITHER TRANSMITTANCE OR ABSORBANCE DATA)

      NORM=0 GIVES NORMALISED SINGLE SPECTRA
          =1 GIVES NON-NORMALISED SINGLE SPECTRA


READ(8) I(J),J=11,13(3I2),I(J),J=14,15(3X,A4,1X,A4)

      I(11)=DAY(NUMERIC)

      I(12)=MONTH(NUMERIC)

      I(13)=YEAR(NUMERIC)

      I(14)=SAMPLE TAPE REFERENCE NUMBER

      I(15)=BACKGROUND TAPE REFERENCE NUMBER.


READ(8) V(J),J=3,6(4F6.3)

      V(3)=SAMPLE COURSE GAIN SETTING

      V(4)=SAMPLE FINE GAIN SETTING

      V(5)=BACKGROUND COURSE GAIN SETTING

      V(6)=BACKGROUND FINE GAIN SETTING


READ(8) ZX(20A4)

      ZX=TITLE OF SPECTRUM


READ(5) M(ARRAY)(20F4.0)

      M=VALUES OF INTERFEROGRAM FUNCTION FROM TAPE
      (BACKGROUND TAPE READ IN FIRST AND THEN SAMPLE TAPE)


      READS IN DATA FROM THE TAPE FILE,REDUCES THE ARRAY DATA TO THE NECESSARY
      NUMBER OF POINTS EITHER SIDE OF ZERO PATH DIFFERENCE,REPEATS THE FIRST
      OR LAST DATA POINT IF TAPE IS TOO SHORT BEFORE OR AFTER THE MAXIMUM.
      AUTOCORRELATES,NORMALISES AND APODISES THE INTERFEROGRAM; COOLEY-TUKEY
      TRANSFORMS,NORMALISES AND PLOTS THE BACKGROUND AND SAMPLE SINGLE SPECTRA.
      RATIOS SAMPLE TO BACKGROUND AND PLOTS RATIOED SPECTRUM AS EITHER
      TRANSMITTANCE OR ABSORBANCE
```

```
PROGRAMME CHK6:DCH0623

    PUBLIC DISK


PROGRAMME TO PROCESS DISPERSIVE (PHASE) SPECTRA


C. BARKER

CALCULATES AVERAGE PHASE FUNCTIONS AND REFRACTIVE INDEX / FREQUENCY CURVE
BY THE METHOD OF CHAMBERLAIN AND GEBBIE


INPUT/OUTPUT DEVICES
    5=CARD INPUT=*SOURCE*
    7=BACKGROUND PHASE FILENAME
    9=SAMPLE PHASE FILENAME
    6=LINE PRINTER OUTPUT=*SINK*


READ(5)NSETS(I3),NOPH(I3),NOSPH(I3),NPHM(I3),NAVER(I3)

    NSETS=NUMBER OF SETS OF DATA

    NOPH=1 GIVES PHASE CURVE FOR EACH DATA SET PLUS AVERAGE
        =2 GIVES AVERAGE PHASE CURVE ONLY
        =3 GIVES NO PHASE CURVES

    NOSPH=0 READS PHASE FROM INPUT DEVICE 5 (=*SOURCE*)
         =1 READS BACKGROUND PHASE FROM FILE 7 AND SAMPLE PHASE FROM FILE 9

    NPHM=0 CALCULATION FOR A PURE LIQUID OR A SOLID
        =1 CALCULATION FOR A SOLUTION

    NAVER= NOT USED AS YET


READ(5) NBKG(I3),NDIS(I3),NN(I4),ND(I3),NSIG1(I3),NSIG2(I3),NSIG3(I3),NPHAS(I3
        NBPHA(I3)

    NBKG=NUMBER OF PHASE BACKGROUNDS

    NDIS=NUMBER OF SAMPLE PHASES

    NN=NUMBER OF POINTS

    NC=NUMBER OF RUNS WITH DIFFERENT MEAN REFRACTIVE INDEX VALUES

    NSIG1=SAMPLING INTERVAL IN MICRONS
```

```
      NSIG2=0 GIVES SINGLE SPACING OF POINTS IN REFRACTIVE INDEX CURVE
           =1 GIVES SPACING OF POINTS FOR COMPARISON OF CURVES WITH DIFFERENT
            NUMBERS OF POINTS

      NSIG3=0 GIVES REFRACTIVE INDEX PLOT
           =1 GIVES ONLY PHASE SPECTRA

      NPHAS=1 READS IN INSTRUMENT BACKGROUND FOR SOLUTION COMPUTATIONS
           =0 DOES NOT READ IN BACKGROUND


IF NOSPH=0 (READING PHASES FROM *SOURCE*
READ(5)(PHASO(J,K),J=1,NN)(10F5.2)

      PHASO=ARRAY OF BACKGROUND PHASES


READ(5)(PHASS(J,K),J=1,NN)(10F5.2)

      PHASS=ARRAY OF SAMPLE PHASES.


IF NOSPH=1 (READING PHASES FROM FILES)
READ(7)(PHASO(J,K),J=1,NN)(10F5.2)

      PHASO=ARRAY OF BACKGROUND PHASES


READ(9)(PHASS(J,K),J=1,NN)(10F5.2)

      PHASS=ARRAY OF SAMPLE PHASES


IF NPHAS=1 (READING IN INSTRUMENT BACKGROUND PHASE FOR SOLUTION WORK)
READ(5)(BPHAS(J),J=1,NN)(10F5.2)

      BPHAS=ARRAY OF INSTRUMENT BACKGROUND PHASES


IF NO IS POSITIVE
READ(5) OM(I3),RMEAN(F10.5),PATHL1(F10.5),FREQL(F10.5),FREQH(F10.5),
        PATHL2(F10.5)
      OM= INTEGER NUMBER OF RADIANS FOR JOINING UP BRANCHES OF PHASE CURVES

      RMEAN=MEAN VALUE OF REFRACTIVE INDEX CORRECTED FOR SAMPLING ERRORS AT
            ZERO PATH DIFFERENCE

      PATHL1=PATHLENGTH IN CENTIMETRES (FOR SOLUTION COMPUTATIONS THIS IS THE
             PATHLENGTH OF THE SOLUTION)

      FREQL=LOWER FREQUENCY OF COMPUTATION IN CM-1

      FREQH=UPPER LIMIT OF COMPUTATION IN CM-1

      PATHL2=PATHLENGTH OF SOLVENT BACKGROUND (ONLY REQUIRED FOR SOLUTION
             COMPUTATIONS)
```

```
READ(5) ZT(20A4)
    ZT=HEADING
```

```
PROGRAMME CHK6:FTRAN4

PUBLIC DISK VERSION OF FTRAN3



PROGRAMME CHK6:GPLOT3

    PUBLIC DISK

CURRENT PLOTTING PROGRAMME

THIS VERSION IS DIMENSIONED FOR 500 POINTS


INPUT/OUTPUT DEVICES
    5=*SOURCE* =CARD INPUT
    6=*SINK* =PRINTER OUTPUT
    8=-A = FILE CONTAINING FREQUENCY/TRANSMITTANCE OR ABSORBANCE DATA
    9=-XX = OUTPUT FILE FOR *OURPLOT INFORMATION


READ(5) NSETS(I3)

    NSETS=NUMBER OF SERIES OF CURVES TO PLOT
      NOT OPERATIVE AS YET - SET EQUAL TO 1


READ(5)(TITLE(I),I=1,20)(20A4)

    TITLE(I),I=1,20 = TITLE OF SPECTRUM


READ(5) NCURVE(I3),NS(I3),XSCALE(F5.1),XS1(I3)

    NCURVE=NUMBER OF CURVES PER PLOT

    NS=1 GIVES ABSORBANCE SCALE FROM 0 TO 1
      =2 GIVES ABSORBANCE SCALE FROM 0 TO 2.5

    XSCALE=FREQUENCY INTERVAL PER INCH OF GRAPH PLOT
      NOT REQUIRED WHEN XS1 = 1

    XS1=0 GIVES STRAIGHT-FORWARD WAVENUMBER SCALE WITH SCALE FACTOR DEPENDANT
      UPON XSCALE
       =1 GIVES ROUNDED-OFF WAVENUMBER SCALE, XSCALE IS CALCULATED DEPENDING
      UPON THE FREQUENCY RANGE OF THE DATA
```

```
READ(5)NA(I3),NOUT(I3)
```

=1 READS IN TRANSMITTANCE DATA IN INCREASING WAVENUMBER ORDER AND PLOTS TRANSMITTANCE SPECTRUM
=2 READS IN ABSORBANCE DATA IN INCREASING WAVENUMBER ORDER AND PLOTS ABSORBANCE SPECTRUM

=3 READS IN TRANSMITTANCE DATA IN INCREASING WAVENUMBER ORDER AND PLOTS ABSORBANCE SPECTRUM

=4 READS IN DCH05277 DATA AND PLOTS ABSORBANCE SPECTRUM

=5 PLOTS ABSORBANCE SPECTRUM WITH NEPER METRE+2 MOLE-1 SCALE (READING IN TRANSMITTANCE (FTRAN3) DATA)

=6 PLOTS ABSORBANCE SPECTRUM WITH NEPER METRE-1 SCALE (READING IN TRANSMITTANCE (FTRAN3) DATA)

=7 READS IN ABSORBANCE DATA IN DECREASING WAVENUMBER ORDER AND PLOTS INCREASING WAVENUMBER ORDER

NOUT=0 GIVES NORMAL DATA LISTING
=1 GIVES ADDITIONAL DATA FOR ERROR SEARCHING

```
IF NA EQUALS 5 (PLOTTING NEPER METRE+2 MOLE-1 SCALE)
READ(5) PATHL(E12.3), CONC(E12.3)
```

PATHL= PATHLENGTH (CM)

CONC= CONCENTRATION OF ABSORBING SUBSTANCE (MOLES CM-3)

```
IF NA EQUALS 6 (PLOTTING NEPER METRE-1 SCALE)
READ(5) PATHL(E12.3)
```

PATHL= PATHLENGTH (CM)

```
IF NA EQUALS 4 (READING DCH 5277 DATA)
READ(8)(X(K),Y(K))(F7.2,F7.4)
```

X(K)=FREQUENCY (CM-1)

Y(K)=TRANSMITTANCE

```
IF NA NOT EQUAL TO 4
READ(8)(X(K),Y(K),K=L,M)(5(F7.2,F7.4,1X))
```

X(K)=FREQUENCY IN CM-1

Y(K)=ABSORBANCE OR TRANSMITTANCE

READS IN EITHER ABSORBANCE OR TRANSMISSION DATA (5 PER CARD EXCEPT WITH NA=4 R
FOR DCH05277 DATA) AND PLOTS ABSORBANCE OR TRANSMISSION DATA AS INCREASING W
SCALES OF ABSORBANCE AVAILABLE ARE 2.5 AND 1.0 ABSORBANCE UNITS
ALSO PLOTS ABSORBANCE SPECTRUM WITH NEPER METRE+2 MOLE-1 SCALE
OR NEPER METRE-1 SCALE

```
789
790
791
792
793       PROGRAMME CHK6:DCH 69
794
795           PRIVATE DISK  MTS967
796
797
798       DEVELOPMENT OF CH5K:DCH0590
799       PROGRAMME TO TRANSFORM DISPERSIVE (ASYMMETRIC) INTERFEROGRAMS
800       THIS VERSION IS DIMENSIONED FOR 4096 POINT TAPES
801
802
803       INPUT/OUTPUT DEVICES
804           5=TAPE INPUT=FILENAME (EG CBA1(1,20))
805           6=PRINTER OUTPUT=*SINK*
806           7=CARD OUTPUT=*PUNCH*
807           8=CARD INPUT=*SOURCE*
808
809
810
811       READ(8) NCARD(I2),NOUT(I2),NCOR(I2),NORM(I2),NPCRD(I2),NREAD(I2)
812
813           NCARD=  GIVES CARD OUTPUT OF SPECTRUM
814                   (FORMAT 5(F7.2,F7.4,1X))
815                =1 GIVES NC CARD OUTPUT
816
817           NOUT=0 GIVES LINE PRINTER+CARD OUTPUT IF NCARD=0
818                =1 GIVES CARD OUTPUT ONLY
819
820           NCOR=1 PRODUCES A SPECTRUM CORRECTED FOR GAIN SETTINGS
821
822           NORM=0 GIVES NO NORMALISATION
823                =1 GIVES NORMALISATION
824
825           NPCRD=1 GIVES CARD AND LINE PRINTER OUTPUT FOR PHASE
826                 =0 GIVES LINE PRINTER ONLY
827
828           NREAD=0 DO NOT READ EXTRA DATA CARD
829                 =1 READS EXTRA DATA CARD
830
831
832       WHEN NREAD=1
833       READ(8) NINT(I2),NPHAS(I2),NOSPEC(I2)
834
835           NINT=  READS INTERFEROGRAM FROM FILE 5
836                =1 READS INTERFEROGRAM FROM 8
837
838           NPHAS=  CALCULATION OF PHASE FOR AMPLITUDE MODULATION
839                =1 CALCULATION OF PHASE FOR PHASE MODULATION
840
841           NSPEC=0 GIVES SPECTRUM PLOT
842                =1 TERMINATES PROGRAMME AFTER PHASE VALUES HAVE BEEN DETERMINED
843
```

```
READ(8) N(I4),SI(F4.1),FLOW(F6.1),FHIGH(F6.1),I9(I3),I8(I3),N2(I4),
        IP(I3),IAP(I3)

    N=NUMBER OF POINTS

    SI=SAMPLING INTERVAL MICRONS

    FLOW=LOWER FREQUENCY LIMIT IN CM-1

    FHIGH=UPPER FREQUENCY LIMIT IN CM-1

    I9=NUMBER OF POINTS PER RESOLUTION (1-5 ONLY)

    I8=NUMBER OF TAPES TO BE PROCESSED
      =1 FOR SINGLE TAPE
      =2 FOR RATIO

    N2=NUMBER OF POINTS USED FOR DETERMINATION OF PHASE CORRECTION FUNCTION

    IP=0 GIVES COMPUTATION OF SPECTRUM FROM ONE-SIDED (COSINE) TRANSFORM
      =1 GIVES COMPUTATION OF SPECTRUM FROM TWO-SIDED (POWER) TRANSFORM

    IAP=0 TRANSFORMATION OCCURS WITHOUT APODISATION
       =1 TRANSFORMATION OF APODISED INTERFEROGRAM


READ(8) I(J),J=11,13(3I2),I(J),J=14,15(3X,A4,1X,A4)

    I(11)=DAY(NUMERIC)

    I(12)=MONTH(NUMERIC)

    I(13)=YEAR(NUMERIC)

    I(14)=SAMPLE TAPE REFERENCE NUMBER

    I(15)=BACKGROUND TAPE REFERENCE NUMBER


READ(8) V(J),J=3,6(4F6.3)

    V(3)=SAMPLE COURSE GAIN SETTING

    V(4)=SAMPLE FINE GAIN SETTING

    V(5)=BACKGROUND COURSE GAIN SETTING

    V(6)=BACKGROUND FINE GAIN SETTING

READ(8) ZX(20A4)

    ZX=TITLE OF SPECTRUM

READ(5) M(ARRAY)(2(F4.0)
```

M=VALUES OF INTERFEROGRAM FUNCTION FROM TAPE
(BACKGROUND TAPE READ IN FIRST AND THEN SAMPLE TAPE)

A2.1

566

Offprinted from the *Journal of The Chemical Society, Faraday Transactions II*, 1975, vol. 71.

Vibrational Spectroscopic Studies on Ion–Molecule Interactions in Non-aqueous Solvents

Part 1.—Far Infrared Studies on Tetra-n-butylammonium Chloride in Benzene

BY COLIN BARKER AND JACK YARWOOD*

Department of Chemistry,
University of Durham, Durham City DH1 3LE

Received 2nd December, 1974

The far infrared absorption of solutions of tetra-n-butylammonium chloride in benzene has been examined as a function of concentration and temperature. Part of the absorption (both for liquid and solid solutions) arises from severely perturbed benzene molecules which must, therefore, be involved in " solvation " of ion aggregates. The whole spectrum is thought to arise from vibrations of the solvated, or maybe solvent separated, ion aggregates and from the collisions of severely polarised benzene molecules. The benzene perturbation is further reflected by the intensity enhancement of the ν_{16} (e_{1u}) band. The concentration dependence of the band intensity shows clearly that the ion aggregates are " breaking up " as the concentration is lowered.

Evans and Lo[1] published some far infrared spectra of tetra-alkylammonium salts in benzene and attributed bands in the 70–100 cm^{-1} region to vibrations of ion-pairs or associated ion pairs in solution. The band positions were sensitive to the anion used and the shifts observed agreed quite well with those expected using simple considerations of anion mass. No consideration of the part played by the solvent was mentioned although if the salt dissolves at all then, clearly, solvation must occur. These results were later considered in the light of results obtained for various salts in polar solvents by French and Wood.[2] From the lack of solvent dependence of the band observed for $Na^+BPh_4^-$ it was concluded that the solvent was not involved in the mechanism giving rise to absorption (even in highly solvating solvents such as pyridine and piperidine). More recently[3-8] it has been shown that the origin of the bands which arise in the spectra of solutions of metal salts in polar solvents is related to the motions of the solvated cation, and that such spectra *are* solvent dependent [3] (but largely anion independent). However, very little further work has been published on the origin of these far infrared bands in " poorly solvating " media, although models have recently been proposed [9-13] to explain the dielectric relaxation of tetra-alkylammonium ions in non-polar solvents. Evans and Lo [1] pointed out that their spectra showed an asymmetry to low frequency which suggested the presence of unresolved bands. This was rationalised in terms of a planar rhombic model of a " double " ion pair cluster with 3 infrared active modes, only one of which could be positively identified in the spectrum. It is, however, established [14] that, at the concentrations used (0.05 mol dm^{-3}), the ions are likely to form clusters containing up to 15 ion pairs, hence that the model used was unrealistically simple. As part of a new programme of research on ion–ion and ion–molecule interactions we carried out at detailed study of these absorptions as a function of solvent, concentration, phase and temperature for a variety of salts. Our major objective is to throw additional light on the nature and origin of these bands. We further hope to construct

a dynamic model which will satisfactorily explain the observed phenomena in terms of the co-operative motions of the ions and solvent in the liquid phase. This paper describes the data for tetra-n-butylammonium chloride in the non-polar solvent benzene and shows in particular the enhanced value of the information collected by careful work in this very low frequency region using modern interferometric equipment and proper data handling techniques.

EXPERIMENTAL

B.D.H. AnalaR benzene was used as solvent. It was dried over molecular sieves for at least two days before use. A Karl-Fischer titration showed $<0.001\%$ by weight of water in the benzene solvent. The tetra-n-butylammonium chloride used was purchased from Eastman-Kodak Ltd. This salt was kept over calcium chloride in a dessicator and was used without further purification. The solutions were made by weighing out the required amount of salt in a 10 cm^3 volumetric flask and then making up to the mark with dried benzene. The solutions were made up as quickly as possible since the salt is deliquescent. Some solutions were kept over molecular sieves for a few days and the spectra recorded show the same intensities as those solutions without molecular sieves. The amount of water in these solutions was small (about 0.1–0.2%) and did not noticeably affect the recorded spectra. The spectra show no time dependence over a period of a week.

The spectra were recorded using a Beckman-RIIC FS 720 Fourier spectrometer giving tape output of the digitised interferogram. The spectra were obtained in the conventional transmission mode over the range 20–250 cm^{-1} using a 50 gauge (12.5 μm polyethylene terephthalate) beam-splitter together with a white lens and 50 μm black polythene filter. Sufficient data points were recorded to give a resolution of 1.2 cm^{-1} before apodisation for the double-sided interferogram, and a time of recording of 35 min for each background and sample tape. The spectra were computed using our Cooley-Tukey Fourier Transform program on the NUMAC IBM 360/67 computer. The 1024 points transformed gave a resolution of approximately 2 cm^{-1} after apodisation. The time of computation was typically 160 s for a ratioed spectrum. The spectra illustrated are ratioed absorbance spectra, corrected for gain differences, of solutions of tetrabutylammonium chloride in benzene against pure benzene solvent background. The intensities were determined from the areas under the absorption bands which were measured by using a planimeter after drawing the " best " baseline by eye. As these bands are very broad the positioning of the baseline has a critical effect on the intensity computed. We fitted baselines by comparison of the profiles of the absorption bands from different concentrations so that the high and low frequency limits of the absorption could be determined; this method should give consistency over all the spectra measured. The ratioed transmission spectrum was also obtained on cards and the areas under the absorption bands calculated using a simple integrator program with a linear baseline. The " computed " and measured areas compared favourably and any differences were always within the limits of the precision of the measurements. A precision check was conducted by making up five solutions of 0.5 mol dm^{-3} concentration of tetrabutylammonium chloride in benzene and recording four spectra of each solution, refilling the cell for each run. The computed intensities of these 20 runs were then treated statistically, giving a root mean square deviation for the intensity and a coefficient of variation of $\pm 6.5\%$. (The " coefficient of variation " is defined as 100 times the root mean square deviation divided by the mean value.) This precision is depicted by the error bar on the concentration graph (fig. 6.).

RESULTS AND DISCUSSION

Fig. 1 shows the spectra of $Bu^n_4N^+Cl^-$ in benzene solution at several different concentrations between 0.3 and 0.7 mol dm^{-3}. The asymmetry to low frequency of the band centred at about 115 cm^{-1} is clearly evident. Our spectra are more clearly defined than those previously published, especially on the low frequency side, and there is no doubt that a distinct asymmetry does occur. This asymmetry, and

the extreme band width, account for the difference between our $\bar{\nu}_{max}$ and the published data (see table 1). Although they are not considered specifically here, we also have spectra of $Bu^n_4N^+$ salts with other anions which confirm the $\bar{\nu}_{max}$ pattern with in-

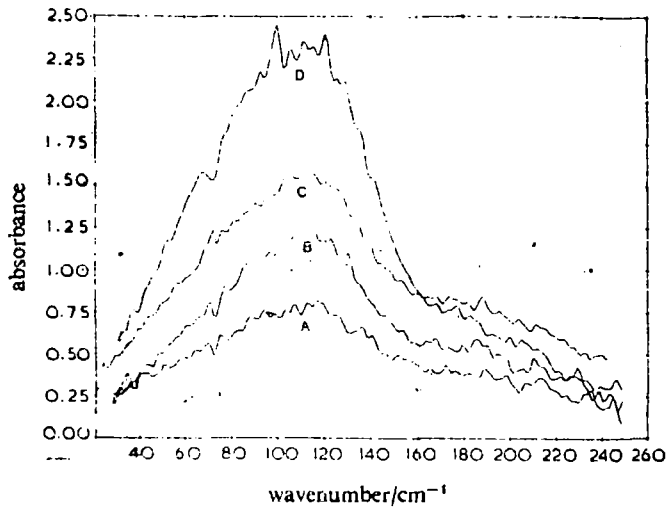

FIG. 1.—Spectrum of $Bu^n_4N^+Cl^-$ in benzene at various concentrations (A) 0.3 mol dm^{-3}, (B) 0.4 mol dm^{-3}, (C) 0.5 mol dm^{-3}, (D) 0.7 mol dm^{-3}. Pathlength is 0.2 mm in each case.

creasing mass. The band at 115 cm^{-1} therefore probably arises from some sort of ion aggregate and from a " vibration " (or other phenomenon) in which both cation and anion take part. Our spectra are ratioed against the same pathlength of benzene so that, at least at first sight, they should not be affected by benzene " collisional " absorption in this region [15] (table 1). To further investigate the possibility of there being two bands in this region we decided to cool the solutions, thereby reducing the band widths and (hopefully) separating the absorptions.

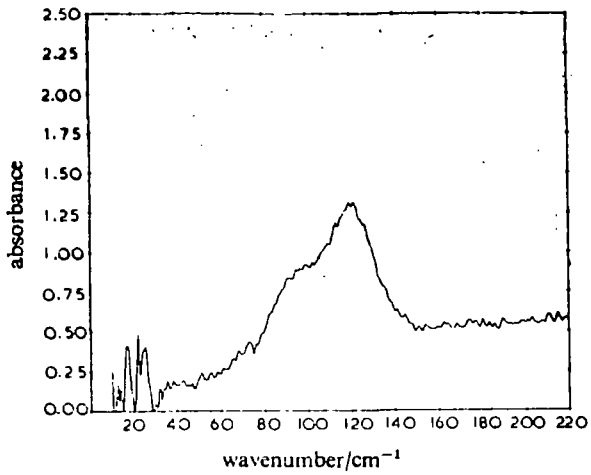

FIG. 2.—$Bu^n_4N^+Cl^-$ in solid benzene at −20°C (obtained by ratioing at the same pathlength). The concentration is 0.75 mol dm^{-3}.

Fig. 2 shows the spectrum of a 0.75 mol dm^{-3} solution at 253 K ratioed against solid benzene at the same pathlength. The ion aggregate band is still present, of course, when the solutions is frozen and there is clearly another band centred at about 93 cm^{-1}. For the solid material " collisional " bands are converted into translational

TABLE 1.—SPECTRAL PARAMETERS FOR LOW FREQUENCY ABSORPTIONS OF SOLUTIONS OF $Bu^n_4N^+Cl^-$ IN BENZENE

	benzene "collisional" band			ion aggregate band		
	$\tilde{\nu}_{max}$/ cm^{-1}	$\Delta\tilde{\nu}_{\frac{1}{2}}$/ cm^{-1}	B_i/ $dm^3\ mol^{-1}\ cm^{-2}$	$\tilde{\nu}_{max}$/ cm^{-1}	$\Delta\tilde{\nu}_{\frac{1}{2}}$/ cm^{-1}	B_i/ $dm^3\ mol^{-1}\ cm^{-2}$
liquid benzene ($T = +20°C$)	75 ± 2	80 ± 5	45			
lit.[15] ($T = +27°C$)	70	90	40			
crystalline benzene ($T = -20°C$)	88 ± 2	42 ± 2	54			
lit.[15] ($T = -100°C$)	97	20	31			
liquid solution ($T = +20°C$) (1.04 mol dm^{-3} $Bu^n_4N^+Cl^-$ in benzene)	74 ± 2	82 ± 5	(800)[a]	115 ± 2	52 ± 2	(5000)[a]
lit.[1] (room temperature)				120 ± 3	—	—
crystalline solution ($T = -20°C$) (0.7 mol dm^{-3} $Bu_4N^+Cl^-$ in benzene)	93 ± 1	22 ± 2	116	119 ± 1	27 ± 2	(2420)[a]

[a] Intensity varies with concentration.

lattice modes. One of the strongest lattice modes of crystalline benzene [15-17] is centred near 90 cm^{-1} (depending on the temperature and the method of sample preparation [17]). The band width of this lattice mode also appears to be very variable but is normally found to be between 20 and 40 cm^{-1}. We have attempted to separate these two bands for both liquid and solid spectra and some typical best fits to the

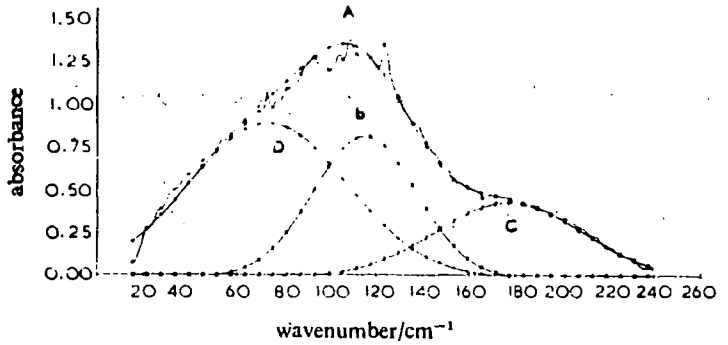

FIG. 3.—Typical " best " fit to a sum of three gaussian bands for the far infrared spectrum of $Bu^n_4N^+Cl^-$ in liquid benzene. ×, actual spectrum; A, total computed band envelope; B, band at ~115 cm^{-1}; C, band at ~181 cm^{-1}; D, band at 79 cm^{-1}).

observed overall profile are given in fig. 3 and 4. The results we have obtained for the separated bands are included in table 1. It may be seen that the obvious conclusion is that the second band at about 75 cm^{-1} is due to a *perturbed* " collisional " or lattice band of the benzene molecule, either in the liquid or the solid phase, and

this strongly implies that the benzene solvent molecules are very much involved in the aggregate giving rise to the band at 115 cm^{-1}. This is no ordinary " solvent " effect. The concentration of solvent molecules is typically more than twenty times that of the ions in solution and a very severe perturbation must occur for the benzene spectrum to be so pronounced. Table 1 shows that the integrated intensity of the benzene " collisional " band is perturbed by at least a factor of six in the liquid phase

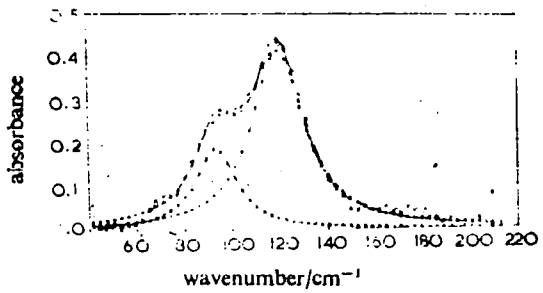

FIG. 4.—Typical best fit to a pair of lorentzian bands for the far infrared spectrum of $Bu^n_4N^+Cl^-$ in solid benzene.

(based on the total benzene concentration). This must involve either an extremely powerful mode of " solvation " or possibly an " aggregate " which *includes* solvent molecules. In other words, it appears as though the ions may be " solvent separated " in the ion cluster. Ion-induced forces between the salt and the solvent will be operative and these will result in entirely different electrical field fluctuations when the benzene molecules collide, either with other solvent molecules or with the ions themselves. A simple ion-induced dipole calculation shows that the " extra " benzene absorption can be accounted for if the ion and the benzene molecule have interaction distances of between 1.2 Å and 1.9 Å giving perturbed intensity values for

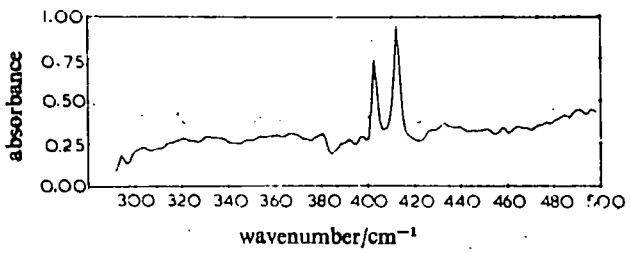

FIG. 5—Spectrum of frozen solution of $Bu^n_4N^+Cl^-$ in benzene showing perturbed ν_{16} band at 403, 416 cm^{-1}.

the collisional benzene band of 800 to 50 $dm^3\ mol^{-1}\ cm^{-2}$. These distances are fairly short (compared with the sum of the van der Waals radii of the ion and molecule concerned) and provide support for the theory that the benzene molecules are severely perturbed by strong ion–molecule electrostatic interactions. We have confirmed using the $Bu^n_4N^+Br^-$ and $Ag^+ClO_4^-$ salts that the band at 75 cm^{-1} is still present even though these salts have ion aggregate bands at different frequencies (i.e. the ion aggregate bands are shifted but the extra " benzene " band remains at the same position with the same relative intensity).

It seemed to us, that, if the benzene molecule is perturbed in this way, then there ought also to be some perturbation of the internal modes.

Such a perturbation has been found for the $\nu_{16}(e_{2u})$ band which is observed as a doublet at 403, 418 cm^{-1} in the spectrum of crystalline benzene [18] (the splitting is caused by the lifting of the degeneracy in the crystalline material [18]). This band is apparently too weak to be observed in glassy benzene or in the liquid.

It is, of course, formally forbidden for the isolated molecule but allowed by the site symmetry of the crystal.[18] Fig. 5 shows the spectrum of the frozen salt solution ratioed against the same thickness of crystalline benzene. The perturbation in intensity is of the order of 100% while the band positions are hardly moved at all. The presence of this perturbed ν_{16} band serves to confirm the presence of crystalline material (as opposed to a glass) in the cell as well as supporting the far infrared evidence for a severely perturbed solvent molecule. We have not so far confirmed an intensity enhancement of the ν_{16} band in the *liquid* phase. This is due to the very low intensity of the band in the first instance. It seems likely from the very small difference in position and splitting pattern of the ν_{16} band that the nature and symmetry of the benzene crystal is not drastically altered by the dissolved ions, although there is clearly a large electronic perturbation. This particular mode is a CCC out of plane rocking mode [19] and it is the *only* internal mode whch we have found to be severely perturbed. This implies that the cation interacts with the benzene molecule in a way which affects out of plane rocking modes of the ring. This might be expected to be the case for a strong electrostatic interaction with the $p\pi$-bonding orbitals of the benzene and would appear not to be the expected behaviour for a donor-acceptor interaction of the benzene--$Bu_4^nN^+$ system,[20, 21] in which case perturbation of the totally symmetric modes of benzene would be expected. The implication is that the anion and cation in solution are closely associated with one another, as indicated by the freezing point measurements.[14]

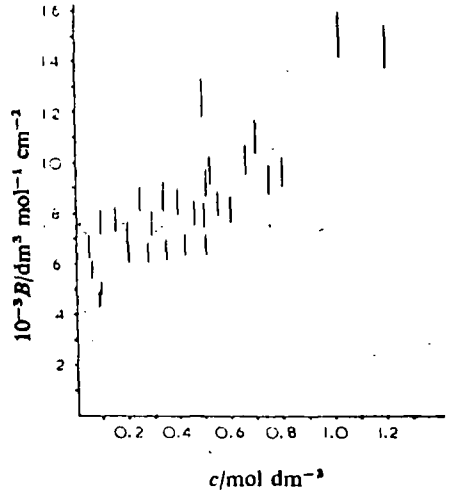

FIG. 6—Intensity against concentration plot for tetra-n-butylammonium chloride in benzene at 291 K (low frequency absorption).

We have further attempted to investigate the results of such ion aggregation on the far infrared spectrum by studying the effects of dilution. In this region of the spectrum (with our present optics and detector) we are only able to study benzene solutions of up to about 2 mm pathlength. This means that our lower concentration limit is about 0.05 mol dm^{-3}. The question is whether or not Beer's Law is obeyed,

since this ought to give some indication as to whether there is clear evidence that the aggregates are breaking up on dilution. If the absolute intensities for vibrations of clusters of *different* sizes are the same (or roughly so) then a ten or twenty-fold dilution is expected to lead to a decrease in the total band intensity since the number of ion–ion vibrations decreases as the clusters break up. On the other hand, if Beer's Law is obeyed this means that ion–ion vibrations in a large cluster have a smaller inherent intensity than those smaller clusters. Fig. 6 shows that Beer's Law is, in fact, not obeyed and represents further strong evidence for the solvating ability of the benzene molecules. However, we have since shown (unpublished, preliminary data) that, for concentrations in the 0.1–0.45 mol dm^{-3} range the $Bu^n_4N^+Br^-$ band in benzene *does* obey Beer's Law quite well. The bromide salt is less deliquescent than the chloride salt and we have tried to find out whether the increase in intensity with concentration (fig. 6) is possibly due to the presence of (very small) amounts of water in the solutions. To this end we have added very small concentrations of distilled water to our solutions and measured the intensity of the (total) low frequency band. The results are shown in table 2.

TABLE 2.—EFFECT OF ADDED WATER ON INTENSITY OF LOW FREQUENCY BAND FOR $Bu^n_4N^+Cl$ IN BENZENE SOLUTIONS

% water[a] (by volume)	$10^{-3}B$/dm^3 mol^{-1} cm^{-2}
0.16	11.35
0.38	10.66
0.44	10.37
0.73	10.57
1.19	10.67

[a] Concentrations monitored using the Karl-Fischer method.

It is obvious from the table that the intensity of the band is not increased by even large concentrations of water and may, in fact, be decreased slightly as would be expected if the tetrabutylammonium salt is now being solvated by water rather than benzene. We have little doubt that the solution process for these tetra-alkylammonium salts is affected by the small amounts of water present but the evidence is that the observed deviations from Beers Law are not caused by water in the solutions.

We are now proposing to study this and similar salts in a range of polar and non-polar solvents (e.g., dioxan, chloroform, carbon tetrachloride and tetrahydrofuran) with the object of studying differences in the band shape and intensity behaviour in media of different solvating ability. We are also proposing to compare these spectra with those which are thought to arise from the libration of a solvated cation (usually a metal cation) and attempt to correlate the spectral and dynamic parameters with the nature of solvent action. Some efforts will be directed towards casting further light on the origin of the band which arises to the high energy side of the ion aggregate band (at about 200 cm^{-1} on fig. 1). This is certainly a real band and it appears to have a counterpart in the spectra of Li^+ and Na^+ ions in solvents such as acetone and tetrahydrofuran. The band does appear fairly sensitive to the anion used and could be a " solvated anion " phenomenon. However, this requires more extensive investigation.

Finally, with the installation of a polarizing optical arrangement [22] and a liquid helium cooled detector we shall be able to reach lower concentrations of salt and approach more closely the " ion pair " situation.

Meanwhile, this work shows how valuable information on the nature and extent of solvated ion aggregation may be obtained using very far infrared spectroscopy.

C. B. thanks S.R.C. for a C.A.S.E. studentship (granted in collaboration with Beckman-RIIC Ltd). Thanks are also due to S.R.C. for an equipment grant to purchase the far infrared interferometer.

[1] J. C. Evans and G. Y. S-Lo, *J. Phys. Chem.*, 1965, **69**, 3223.
[2] M. J. French and J. L. Wood, *J. Chem. Phys.*, 1968, **49**, 2358.
[3] W. F. Edgell, J. Lyford, R. Wright, W. Risen and A. Watts, *J. Amer. Chem. Soc.*, 1970, **92**, 2240.
[4] W. F. Edgell, A. T. Watts, J. Lyford and W. M. Risen, *J. Amer. Chem. Soc.*, 1966, **88**, 1815.
[5] M. K. Wong, W. J. McKinney and A. I. Popov, *J. Phys. Chem.*, 1971, **75**, 56.
[6] B. W. Maxey and A. I. Popov, *J. Amer. Chem. Soc.*, 1969, **91**, 20.
[7] P. R. Handy and A. I. Popov, *Spectrochim. Acta*, 1972, **28A**, 1545.
[8] W. F. Edgell, *Ions and Ion Pairs in Organic Reactions*, ed. M. Szwarc (Wiley Interscience, New York, 1972), vol. 1, chap. 4.
[9] J. P. Badiali, H. Cachet, A. Cyrot and J. C. Lestrade, *J.C.S. Faraday II*, 1973, **69**, 1339.
[10] J. P. Badiali, H. Cachet, A. Cyrot and J. C. Lestrade, *Molecular Motion in Liquids*, ed. J. Lascombe (Reidel, Dordrecht, 1974), p. 179.
[11] J. P. Badiali, H. Cachet, P. Canard, A. Cyrot and J. C. Lestrade, *Compt. rend. C*, 1971, **273**, 199.
[12] H. Cachet, F. F. Hanna and J. Pouget, *J. Chim. phys.*, to be published.
[13] J. P. Badiali, H. Cachet and J. C. Lestrade, *Ber. Bunsenges. phys. Chem.*, 1971, **75**, 297.
[14] D. T. Copenhafer and C. A. Kraus, *J. Amer. Chem. Soc.*, 1951, **73**, 4557.
[15] G. W. Chantry, H. A. Gebbie, B. Lassier and G. Wyllie, *Nature*, 1967, **214**, 163.
[16] I. Harada and T. Shimanouchi, *J. Chem. Phys.*, 1967, **46**, 2708.
[17] I. Harada and T. Shimanouchi, *J. Chem. Phys.*, 1971, **55**, 3605.
[18] J. L. Hollenberg and D. A. Dows, *J. Chem. Phys.*, 1961, **34**, 1061; 1962, **37**, 1300.
[19] G. Herzberg, *Molecular Spectra and Molecular structure, II. Infrared and Raman Spectra of Polyatomic Molecules* (Van Nostrand, New York, 1945), p. 118.
[20] E. E. Ferguson and I. Y. Chang, *J. Chem. Phys.*, 1961, **34**, 628.
[21] E. E. Ferguson, *J. Chim. phys.*, 1964, **61**, 257.
[22] D. H. Martin and E. Puplett, *Infrared Phys.*, 1969, **10**, 105.

PRINTED IN GREAT BRITAIN AT
THE UNIVERSITY PRESS
ABERDEEN

Faraday Symposium 11—11/11—Barker—1A

11/11

Studies of Ion-ion and Ion-molecule Interactions using Far-infrared Interferometry

BY COLIN BARKER AND JACK YARWOOD*

Department of Chemistry, University of Durham, Durham City, DH1 3LE

Received 11*th August*, 1976

The far-infrared spectra of tetra-n-butylammonium halides in benzene, chloroform and carbon tetrachloride are interpreted with the aid of a dynamic model based on the stochastically modulated oscillator theory of Kubo. Although the model is not necessarily unique for this particular (and complicated) system, it does enable a reasonable interpretation of the observed band frequencies, widths and intensities and their variation (or otherwise) with changes of salt, solvent and temperature. All the data are consistent with situations in which the ion-pair (or aggregate) vibrations are stochastically, but relatively slowly, modulated by interaction with the surrounding solvent molecules. The perturbation of the solvent molecules, mainly by dipole-induced dipole interaction, is shown to be severe. There is also evidence of strong coupling of the solvent " collision mode " and the ion-pair vibration and that the latter is strongly overdamped by a high Langevin friction constant. The implications of this work for the interpretation of data obtained at lower frequencies are considered to centre on the large solvent-solute interaction and this large microscopic viscosity coefficient.

The far-infrared (submillimetre) absorption by electrolyte solutions has been examined both directly[1–3] and indirectly[4,5] (using high frequency microwave measurements). Recent work in our laboratory[6] has been aimed at a comprehensive quantitative study of a range of tetra-alkylammonium salts in (supposedly) poorly solvating media in an effort to throw further light on the nature and origin of these absorptions. In this paper we examine the possibility of constructing a dynamic model for the ion-pairs (or aggregates) which will allow us to interpret the experimental data in a meaningful way and which will (hopefully) provide further insight into the vibrational and relaxational behaviour of the system. We also consider here the ways in which our model may be developed and tested, and the similarities and differences between this and other models—particularly ones used to interpret " dielectric " (microwave) data.[4,5,7–12]

EXPERIMENTAL

The measurements were made using a Beckman-R.I.I.C. Ltd., FS720 interferometer and fixed pathlength cells of stainless steel with high density polyethylene windows. A Beckman-R.I.I.C. Ltd. variable temperature cell holder (VLT-2) and temperature controller were used for measurements between 285 and 350 K. The tetra-n-butylammonium salts were purchased from Eastman-Kodak Ltd. They were dried (when necessary) and the water content of the solutions was monitored by the Karl-Fischer method. The solvents were either " AnalaR " or " Spectro " grades and were dried over molecular sieves immediately prior to use.

The spectra shown here are ratioed absorbance spectra (corrected for gain differences) of the appropriate solution against pure solvent background. The spectral resolution is $\sim$2.5 cm^{-1}. Our methods of estimating the precision of the data, of constructing a meaning-

ful " base line " (for intensity measurements) and of checking on the effects of small amounts of water in the solutions have been published previously.[3]

RESULTS

Typical spectra of $Bu_4^nN^+Cl^-$ in the three solvents used and of $Bu_4^nN^+Br^-$ in benzene are shown in fig. 1–4 together with the decomposition (for $Bu_4^nN^+Cl^-$ solutions) into their separate components.[3] The resulting band frequencies, half-widths and intensities are given in table 1. Our initial interpretations of these spectra have already been published[3] but, since any model which is constructed must at least be consistent with the experimental data, it is appropriate here to summarise the principal features of the observed spectra.

(*a*) The band system (for $Bu_4^nN^+Cl^-$ solutions, at least) can be decomposed into three separate bands (called A, B and C for convenience) each of which appears to be consistent (both statistically and phenomenologically) with the (assumed) Gaussian profile.[13]

(*b*) The three bands are of distinctly different widths and intensities and these parameters are to some degree (see discussion below) dependent on variables such as salt, concentration and temperature. However, the main features of the spectra remain essentially unchanged for a given anion (but change when the anion is changed). In particular, the spectra are to a large extent *solvent independent.*

(*c*) The assignments[5] of bands A and B to phenomena associated with solvent (ν_s) and ion-aggregate (ν_{cA}) (ion-pair in dilute solution) respectively is fairly straightforward. Thus, ν_s corresponds to a (perturbed) collision mode[14] of the non-polar solvent while ν_{cA} is taken as a vibration of anion against cation in an ionic aggregate—whose exact nature, in concentrated solutions, is somewhat obscure.

The assignment of band C is more difficult but we shall see that our model points to a reasonable interpretation in terms of a combination band of $\nu_s + \nu_{cA}$ (see below).

THEORETICAL CONSIDERATIONS

Previous models[5,7–9] relating to the relaxation of a system of solvated ions have been aimed at interpreting data collected[4,5,7–12] at much lower frequencies (typically between 100 Hz and 300 GHz i.e., up to 10 cm^{-1}) on the dipolar relaxation of the perturbed solvent and of the ion-pairs (or aggregates of ion-pairs). As pointed out by Lestrade *et al.*,[5] the relaxation (or other) phenomena which are observed depend on the frequency of the radiation used in the experiment and so in the far-infrared region (at frequencies corresponding to > 1000 GHz) we expect to " see " phenomena which are characterised by relaxation times in the 0.1–1.0 ps region. Nevertheless, it is valid to observe that microwave measurements lead to relaxation times for the ionic aggregate lifetime (τ_1 in Lestrade's notation)[7] and for the elapsed time between ionic collisions (τ_s) of the order of 100–300 ps.[5,7–9] This means that, as far as the far-infrared region is concerned, the ion-pairs can be treated as though they are quasi-stationary. This is one of the assumptions inherent in the treatment given below. The other major assumption is that the vibrational mode considered is that of a solvent-surrounded ion-pair (see fig. 5). Except in very dilute solution this is unlikely to be realistic, of course, but we note that the spectra vary little over the concentration range studied down to 0.05 M. Further, we have now studied (with the aid of a polarising optical system and a cryogenic detector[6,15]) some of these systems down below 0.01 M without any major spectral changes. So there may be some empirical justification for considering an ion-pair in pseudo-isolation.

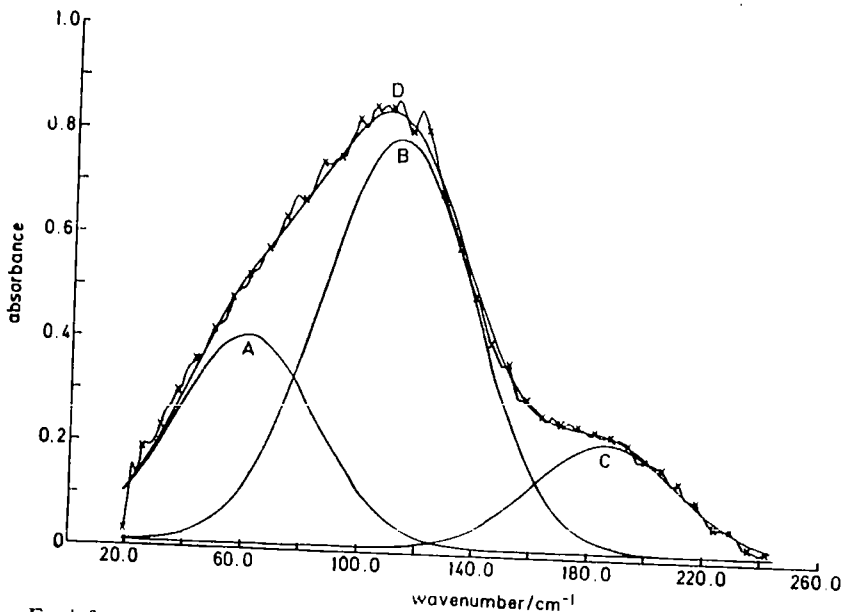

FIG. 1.—Far-infrared spectrum of $Bu_4^nN^+Cl^-$ in benzene. X, observed spectrum; A, ν_s band at ~65 cm^{-1}; B, ν_{cA} band at ~115 cm^{-1}; C, $\nu_s + \nu_{cA}$ band at ~185 cm^{-1}; D, total computed band envelope.

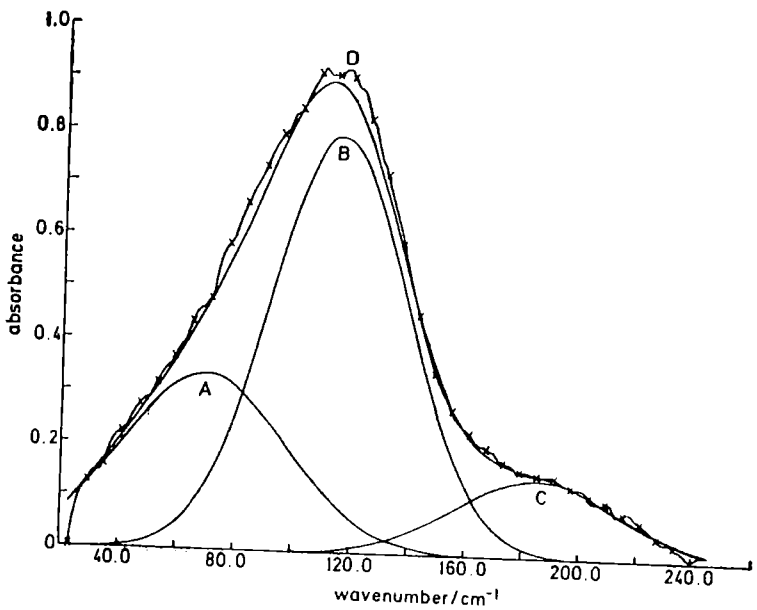

FIG. 2.—Far-infrared spectrum of $Bu_4^nN^+Cl^-$ in carbon tetrachloride. X, observed spectrum; A, ν_s band at ~70 cm^{-1}; B, ν_{cA} band at ~120 cm^{-1}; C, $\nu_s + \nu_{cA}$ at ~185 cm^{-1}; D, total computed band envelope.

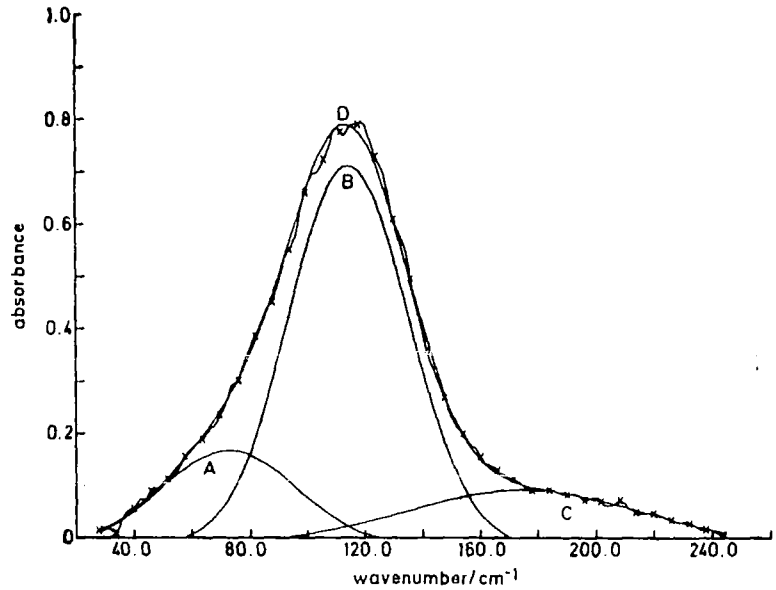

FIG. 3.—Far-infrared spectrum of $Bu_4^nN^+Cl^-$ in chloroform. X, observed spectrum; A, ν_s band at ~70 cm^{-1}; B, ν_{cA} band at ~120 cm^{-1}; C, $\nu_s + \nu_{cA}$ band at ~180 cm^{-1}; D, total computed band envelope.

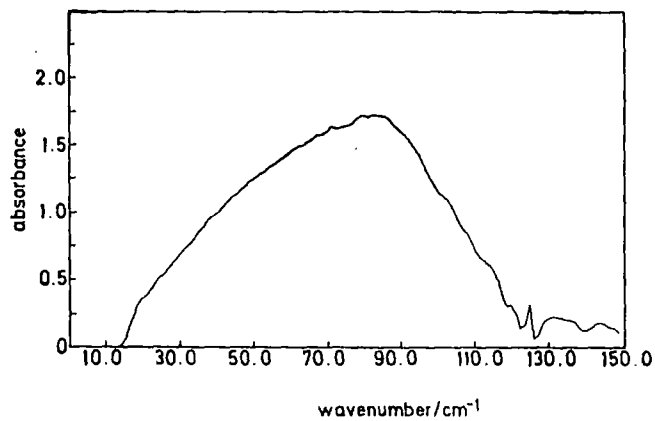

FIG. 4.—Far-infrared spectrum of $Bu_4^nN^+Br^-$ in benzene. Bands A and B are now very much closer together and absorption in 150 cm^{-1} region is very small.

The observed spectra and initial interpretation[3] (see above) point to the need to consider a stable vibrating ion-pair (with a lifetime which is long compared with the vibrational period) whose solvation shell of surrounding solvent molecules is considerably perturbed by interactions with the charged species.

Consider (fig. 5) a representative solvent molecule (S) at radial distance R from the ion-pair CA (of finite length r_{cA}). A multipole expansion[16] of the potential at S due to the ion-pair is,

$$V(R, \theta) = + \frac{Qr_{cA}\cos\theta}{R^2} + \frac{Qr_{cA}^3}{8R^4}(5\cos^3\theta - \cos\theta) + \ldots \qquad (1)$$

TABLE 1.—FAR-INFRARED SPECTRAL PARAMETERS OF $Bu_4^nN^+X^-$ SOLUTIONS IN ORGANIC SOLVENTS

			Band " A " (ν_s)			Band " B " (ν_{cA})			Band " C " ($\nu_s + \nu_{Cs}$)		
salt	solvent	temp./K	$\tilde{\nu}_{max}$/cm^{-1}	$\Delta\tilde{\nu}_{\frac{1}{2}}$/cm^{-1}	intensity[a]	$\tilde{\nu}_{max}$/cm^{-1}	$\Delta\tilde{\nu}_{\frac{1}{2}}$/cm^{-1}	intensity[a]	$\tilde{\nu}_{max}$/cm^{-1}	$\Delta\tilde{\nu}_{\frac{1}{2}}$/cm^{-1}	intensity[a]
$Bu_4^nN^+Cl^-$	C_6H_6	285–305	75 ± 3	56 ± 2	2400	118 ± 2	52 ± 3	3800	182 ± 2	60 ± 10	~1400
		305–328	73 ± 2	58 ± 2	2600	117 ± 2	54 ± 2	3900	181 ± 2	54 ± 5	~1200
		328–350	75 ± 5	62 ± 3	3300	118 ± 2	52 ± 5	4200	180 ± 3	55 ± 5	~1500
		293	73 ± 4[b]	72 ± 8[b]	6300[b]	118 ± 3[b]	53 ± 4[b]	5800[b]	181 ± 6[b]	72 ± 19[b]	3500[b]
$Bu_4^nN^+Cl^-$	CCl_4	293	75 ± 6	64 ± 6	3700	114 ± 2	50 ± 2	7200	184 ± 3	80 ± 15	2500
$Bu_4^nN^+Cl^-$	$CHCl_3$	293	70 ± 7	50 ± 11	1800	116 ± 2	52 ± 4	7500	175 ± 7	84 ± 16	1500
$Bu_4^nN^+Br^-$	C_6H_6	293	65 ± 4	75 ± 4	3300	78 ± 2	56 ± 3	1900	—[c]	—[c]	—[c]
$Bu_4^nN^+Br^-$	$CHCl_3$	293	65 ± 5	—	3900[d]	80 ± 5	—	3900[d]	—[c]	—[c]	—[c]

a Intensities have ±10–15% error in all cases. They are based on total solvent (band " A ") or total solute (bands " B " and " C ") concentrations. The units are dm^3 mol^{-1} cm^{-2}.

b Data at 293 K are averages over whole range of concentration from 0.05 to 0.8 M. Variable temperature data at 0.25 M.

c Band not intense enough to measure. *d* total band intensity of ν_s and ν_{cA}.

where Q is the electronic charge. If $R \gg r_{cA}$ then the 1st term (dipole term) in (1) is dominant, and it will be a reasonable approximation to consider the solute-solvent interaction to be controlled mainly by dipole-induced dipole interactions. For a polarisable ion the dipole moment is,[14]

$$\mu_{cA} = Qr_{cA} - \frac{Q\alpha_{cA}}{r_{cA}^2} \tag{2}$$

and, for the tetrabutylammonium halides, μ_{cA} is expected[12,17] to be about $30 - 36 \times 10^{-30}$C m. Thus, the dipole induced in a typical solvent molecule

$$\mu_s' = \alpha_s E \tag{3}$$

(where the field strength is given[18] by $E = -\text{grad}\,\{V(R, \theta\}$ gives rise to a potential energy of interaction

$$U_{dp-indp} = -\tfrac{1}{2}\alpha_s E^2 \tag{4}$$

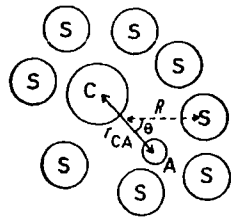

FIG. 5.—The ion-pair and surrounding solvent molecules. Parameters needed for the calculation of the dipole induced in a representative solvent molecule by a point dipole μ_{cA}.

where α_s is the polarisability of the solvent molecule. It should be noted that for benzene the polarisability is distinctly anisotropic,[19,31] and this may result in orientational effects around an ion-pair. The results of applying eqn (3) and (4) will, of course, be to calculate significant dipole induced interactions between the ion-pair and solvent.

We now have to note that, due to the motions of the solvent molecules, and also due to the vibration of the ion-pair, the dipole-induced dipole interaction of eqn (4) is time dependent. In particular, it will depend on $r_{cA}(t)$ and $R(t)$ and, since in the simplest case (2) reduces to $\mu_{cA} = Qr_{cA}$, it then follows from (1), (3) and (4) that $U_{dp-indp}$ is proportional to the square of the total ion-pair-solvent distance (see ref. 18, p. 126). However, if $R(t)$ is taken to be a slowly varying function of t (for the simplest case) then we can write,

$$U_{dp-indp} = k(t)\, r_{cA}^2. \tag{5}$$

(However, see discussion section for details of possible deviation from this simplified expression for U.) $k(t)$ then represents the time dependence of the interaction potential and is a complicated function which depends on (i) the relative orientations and separation of the solvent and ion-pair (ii) the (possibly anisotropic)[19] polarisability of the solvent molecules. Thus, as $k(t)$ fluctuates, the ion-pair vibration suffers a stochastic modulation which will, of course, in principle affect the spectrum.

The ion-pair vibration may now be treated using the general formalism developed by Kubo[20] for calculating the spectral line shape (or associated relaxation function) of a randomly modulated oscillator. (This treatment has recently been successfully applied[21,22] to the case of a weak hydrogen-bond vibration in a " bath " of surrounding solvent molecules.)

The Hamiltonian for the vibration of the ion-pair is written as

$$\begin{aligned}\mathscr{H} &= \tfrac{1}{2}p_{cA}^2/m + \tfrac{1}{2}m\, r_{cA}^2\, \omega_{cA}^2 + kr_{cA}^2 \\ &= \tfrac{1}{2}p_{cA}^2/m + \tfrac{1}{2}m\, r_{cA}^2\, \{\omega_{cA}^2 + 2k/m\}\end{aligned} \tag{6}$$

where m is the reduced mass, given[23] for a contact ion-pair as,

$$m = \frac{M_c(M_A + M_s + M_c),}{(M_A + M_s)} \tag{7}$$

the subscripts C, A and S referring to cation, anion and solvent respectively. We may now regard the operator (6) as a stochastic operator written as,

$$\mathscr{H}(t) = \tfrac{1}{2}p_{cA}^2/m + \tfrac{1}{2}m\, r_{cA}^2\, \omega^2(t)$$

where the effective time dependent oscillator frequency, $\omega(t)$, is obviously given by

$$\begin{aligned}\omega(t) &= \left[\omega_{cA}^2 + \frac{2k(t)}{m}\right]^{\frac{1}{2}} \\ &\simeq \omega_{cA} + \frac{k(t)}{m\omega_{cA}} + \ldots .\end{aligned} \tag{8}$$

Thus $\omega(t) = \omega_0 + \omega_1(t)$ where $\omega_0 = \omega_{cA}$ and $\omega_1(t) = k(t)/m\omega_{cA}$ in our case.

The transition dipole relaxation function, $\varphi(t)$, of the oscillator is given[20] by,

$$\varphi(t) = \langle \exp\,(\mathrm{i}\int_0^t k(t')\mathrm{d}t')\rangle \tag{9}$$

is easily calculated from the spectral distribution, $I(\omega)$ since the transition dipole moment autocorrelation function is

$$\langle \mu(0)\cdot\mu(t)\rangle = |\mu^2|\exp(-\mathrm{i}\omega_{cA}t)\varphi(t) \tag{10}$$

and

$$I(\omega) = |\mu^2|\int_{-\infty}^{+\infty} \exp[\mathrm{i}(\omega - \omega_{cA})t]\varphi(t)\mathrm{d}t. \tag{11}$$

Although the calculation of $\varphi(t)$ is easy (see fig. 6), in order to proceed further with the interpretation in terms of the molecular properties of the system it is necessary to know the form and distribution of the stochastic process, $k(t)$, of eqn (8). Although expressions for $k(t)$ are complicated (and we do not believe that, with the present quality of spectral data, band fitting is justified) we do have some *experimental* evidence as to the probable source and properties of this process.

We first note that the observed spectral distribution of r_{cA} and its associated $\varphi(t)$ (fig. 6) are well-approximated by Gaussian functions with relaxation times of about 0.4 ps. In the slow modulation limit[20,22] (i.e., for a $k(t)$ process which is slow compared the rate of decay of the dipole moment relaxation function $\varphi(t)$) the spectral distribution follows the statistical distribution of $k(t)$—which would, in that case, be Gaussian. Further, we note that the band profile is expected[22] to be Gaussian (by the central limit theorem[24]) if the number of near neighbour solvent molecules is large. Since it is unlikely that benzene molecules are rigidly " bound " to the ion-pair in this case, it is doubtful if the solvation number concept[5,25] means very much for these solutions. However, the tetralkylammonium ions are known[26] to have effective ionic sizes (without solvation shell) of 4–5 Å and the number of benzene near neighbours is estimated to be about 20–30. However, $k(t)$ is clearly not a stationary

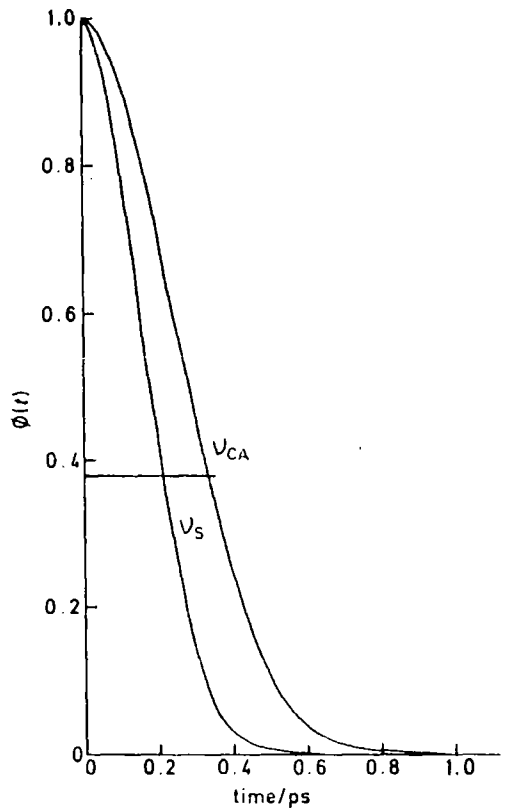

FIG. 6.—Relaxation functions $\varphi(t)$, of the ν_s and ν_{cA} vibrations in the Gaussian approximation.

process. In the liquid phase we know that the solvent molecules collide with the ion-pair (or aggregates) and with each other. Indeed, we see the effects of these collisions in the " A " band of the observed spectrum. So one component of $k(t)$ will fluctuate at the solvent collision rate and another component will fluctuate at the solvent-ion collision rate. Since the motion of the ions is rather slow it is principally these motions of the solvent molecules which lead to the variation of k with time. Thus the collision mode of the solvent may be treated as a stochastic process. If the change in R caused by collisions is ΔR then

$$R(t) = R_0 + \Delta R(t) \tag{12}$$

and, since the effect on ω_{cA} is through dipole-induced dipole[16,18] interactions,

$$k(t) = C'R^{-6} = C'(R_0 + \Delta R)^{-6}. \tag{13}$$

Expansion of (13) gives terms in ΔR, ΔR^2, etc. which, when used to modify the Hamiltonian, will lead to terms in $r_{cA}^2 \cdot \Delta R$, $r_{cA}^2 \cdot \Delta R^2$, etc. These will lead, in principle, to coupling of the collisional (ν_s) and ion-pair (ν_{cA}) modes. The resulting effect, which is expected to be large because ν_s and ν_{cA} are very similar in frequency, is that a band at $\approx \bar{\nu}_s + \bar{\nu}_{cA}$ is predicted. The presence of a band very close to $\bar{\nu}_s + \bar{\nu}_{cA}$ in our spectra—a band without any other obvious explanation—provides strong support for the general validity of our model and the preceding theoretical considerations.

DISCUSSION

Clearly, the principal observed spectral features are adequately explained with the aid of the model of the electrolyte/solvent system which is outlined above. This model is based on a stochastically modulated ion-pair vibration, the modulation being provided by the surrounding solvent molecules, which are themselves severely perturbed by the effects of dipole-induced dipole interactions. Nevertheless, it is useful to consider the data in rather more detail in order to investigate more closely the nature of the molecular processes involved in giving rise to these spectra. Consider first the " A " band (ν_s). The results in benzene solution show that both the width of this band and its intensity increase with increasing temperature, while the band centre remains fairly constant (with a slight tendency to show a high frequency shift but the scatter of data is too high for this tendency to be confirmed). These results are, of course, what is expected if the band is due to collisions of the solvent molecules. For example, Pardoe[27] found that collision bands of non-polar solvents increase slowly with an increase in temperature (in contrast to the behaviour of the " librational " band[27-29] of a polar solvent which decreases rapidly in frequency as the temperature is increased). Thus, our data strongly support the idea that band " A " is caused by solvent molecules translating against one another (and against the ions in solution), the large perturbation being due to the greatly enhanced fluctuating electrical fields caused by changes in the solvent-ion distances. Although *any* solvent might be expected to show this effect, a correlation is expected between the size of these fluctuating fields (and hence spectral intensity) and the polarisability. It is clear from table 1 that, indeed, the largest " A " band intensity occurs for benzene, which is known to have high polarisability.[30,31] (Since carbon tetrachloride also has a high polarisability[31] it appears that the anisotropy of the polarisability of benzene does play an important role.) The data for carbon tetrachloride and chloroform show some interesting features in that the ν_s band frequency is virtually solvent independent. Carbon tetrachloride shows[14] a collisional band at 44 cm^{-1} in the pure liquid, while chloroform shows[32] an absorption maximum at ~35 cm^{-1}. Of course, the situation is complicated in chloroform by the presence of permanent solvent dipoles and the possibility[33] of specific solvation of the anion, but it appears that interaction with the ion-pairs (of aggregates) in solution is so strong that this produces virtually the same " effective " collisional frequency of the perturbed solvent molecules. This may be related to the change in viscosity[27,34] of the medium on going from solvent to solution (some of the solutions are highly viscous[34] especially at the higher concentrations) but in that case, it is surprising that benzene does not show the same effect.

The results in benzene show that this band is strongly anion dependent, the frequency and intensity of the band decreasing somewhat on going from Cl^- to Br^- (table 1). This implies that the effects of ion-solvent interaction are smaller for the bromide salt. Such effects depend, of course, on the " effective " dipole moment of the ion-pair (μ_{cA} of eqn (2)) and some such values have been calculated from dielectric data.[12,17,35] Since the effective interionic distance is expected to be greater for the bromide salt the effective dipole moment should be greater. Comparison of the observed dipole moment data[33] for the corresponding $Bu_3^nNH^+X^-$ (X = Cl, Br, I) salts shows that this is indeed the case. However, the exact nature of the species present (and their electrical properties) depends on the extent of ionic aggregation so it is difficult at this stage to be sure of the effects to be expected. Measurements of the far-infrared spectra at much lower concentrations[15] should throw further light on this problem (and remove possible effects due to gross viscosity changes).

Considering now the " B " band (designated ν_{cA}) we see from table 1 that the

most obvious feature of the data is the almost total invariability of the spectral parameters for a given salt. The band centre and width remain constant (within the experimental error) over a concentration range of 0.8–0.05 M and a temperature range of nearly 70 K for three different solvents. (There is a suspected tendency to show some increase in intensity as a function of increasing temperature but this effect, if real, is small.) On the other hand, there is a considerable shift of ν_{cA} on changing the anion and this is roughly in proportion to the increase in effective reduced mass.[1,2,23] The data serve to confirm that this band is due to an internal mode (or modes) of the ion-pair or aggregate. They also enable us to confirm that the principal effect of the presence of these ions is, as expected, a large dipole-induced dipole effect on the surrounding solvent molecules. Within the framework of the stochastic model outlined above, we might expect that this vibration would be sensitive to both temperature and solvent since we have treated the collisions of the solvent as a stochastic process—giving rise to $k(t)$ of eqn (5)—and these processes are obviously dependent on temperature and microscopic solvent properties (the solvent properties are usually[20,21] characterised by a " friction constant ", β, obtained by using the Langevin equation of motion for the displacement coordinate, r_{cA} (i.e., $\ddot{r}_{cA} + \beta\dot{r}_{cA} + \omega_{cA}^2 r_{cA} = F(t)$). Such a friction constant (or damping factor) will be temperature- and solvent-dependent). However, it is easily shown that, in the classical (high temperature) approximation, the root-mean-square amplitude of the oscillator Δ (equivalent to $\langle k^2\rangle^{1/2}$ in the slow modulation limit and measured by the band width in this approximation) is proportional to $T^{1/2}$ so over a range of 70 K the effect is unlikely to be large. The damping factor, β, being a viscosity coefficient, is exponentially dependent on temperature and should also change from one solvent to another. The fact that little or no change occurs in the band profile with temperature or solvent strongly supports the assertion that one is dealing with the slow modulation limit: this is further rationalized as follows. It seems that β is so large[34] for the concentrations studied so far that the vibrational mode ν_{cA} is heavily overdamped[20,21] ($\beta/2\omega_{cA} \gg 1$). Since the amplitude of the modulation $\langle k^2\rangle^{1/2}$ is also large we see that the slow modulation limit ($\Delta \cdot \beta/2\omega^2_{cA} \gg 1$ in this notation[20,21]) arises as a natural consequence of the combined high viscosity and rapid rate of vibrational relaxation.[22] We note here that the mean vibrational lifetime measured by the rate of decay of $\varphi(t)$—see fig. 6—has a time constant of ~0.4 ps. This is comparable with the rate of collision of the solvent molecules, of course, and means that the rate of modulation of the environment of the ion-pair oscillator is a considerably slower process than the rate of solvent-solvent collisions. It is known from dielectric studies[5,7] that the time between ion-ion collisions is of the order of 200 ps and it is possible that it is this quasi-static situation of the solute particles which leads to the slow modulation limit. What is clear is that the variation of $k(t)$ (eqn (5)) is slow compared with the decay of $\varphi(t)$ and that this is caused (as far as the model is concerned) principally by a very high viscosity coefficient β. Our current studies are aimed at collecting more accurate data at reduced concentrations and extending the solvent and temperature range so that some of these ideas may be further tested.

As we have already pointed out, the band " C " in the spectrum is explained within the framework of our model as a combination band of $\nu_s + \nu_{cA}$ which arises through strong coupling of the solvent collisional and ion-pair vibrational motions. Interestingly, the band is very weak in (or absent from) the spectra of $Bu_4^nN^+Br^-$ solutions (fig. 4) but one can only speculate at the present time as to why this is. Only an investigation of salts with a range of anions will indicate whether or not there is a strong anion dependence of the intensity of this band.

Finally, it is interesting to consider what aspects of the model described and the

conclusions drawn here have a bearing on models used to interpret microwave data on similar solutions. Two points emerge which need to be carefully considered in relation to the data obtained at lower frequencies. These are: (i) the very severe perturbation of the solvent molecules and their large induced dipole moments; (ii) the very large viscosity coefficient—arising very probably from the large macroscopic viscosity of the solutions. Both these effects are likely to be important in the microwave region of the spectrum and indeed have been, at least implicitly, taken into account.[5,7–11] The real value of this work may well be that we have shown a combination of studies in different frequency regions leads to a better understanding of the fundamental resonant and relaxation processes involved in the behaviour of similar or identical systems.

The help of Dr G. N. Robertson (University of Cape Town) with the theoretical aspects of this paper is gratefully acknowledged. Thanks are also due to Beckman-R.I.I.C. Ltd. for their continued support (through the C.A.S.E. scheme) and to the S.R.C. for the C.A.S.E. award (to C. B.) and equipment grants. We are grateful to Dr. R. N. Jones for copies of the N.R.C. band fitting programmes.

[1] J. C. Evans and G. Y. S-Lo, *J. Phys. Chem.*, 1965, **69**, 3223.
[2] M. J. French and J. L. Wood, *J. Chem. Phys.*, 1968, **49**, 2358.
[3] C. Barker and J. Yarwood, *J.C.S. Faraday II*, 1975, **71**, 1322.
[4] H. Cachet, F. F. Hanna and J. Pouget, *J. Chim. Phys.*, 1974, **71**, 285, 1546.
[5] J-C. Lestrade, J. P.-Badiali and H. Cachet, *Dielectric and Related Processes*, ed. M. M. Davies (Specialist Periodical Reports, Chemical Society, London, 1975), **2**, pp. 6–50.
[6] C. Barker, *Ph.D. thesis*, (University of Durham, 1976).
[7] J. P. Badiali, H. Cachet, A. Cryot and J-C. Lestrade, *J.C.S. Faraday II*, 1973, **69**, 1339.
[8] J. P. Badiali, H. Cachet, A. Cryot and J-C. Lestrade, *Molecular Motions in Liquids*, ed. J. Lascombe (Reidel, Dordrecht, 1974), p. 179.
[9] J. P. Badiali, H. Cachet, P. Canard, A. Cryot and J-C. Lestrade, *Compt. rend. C*, 1971, **283**, 199.
[10] E. A. Cavell and M. Azam Sheikh, *J.C.S. Faraday II*, 1973, **69**, 315.
[11] E. A. Cavell and P. C. Knight, *J.C.S. Faraday II*, 1972, **68**, 765.
[12] M. M. Davies and G. Williams, *Trans. Faraday Soc.*, 1960, **56**, 1619.
[13] J. Pitha and R. N. Jones, *Canad. J. Chem.*, 1966, **44**, 3031; 1967, **45**, 2347.
[14] M. M. Davies, *Molecular Motions in Liquids*, ed. J. Lascombe (Reidel, Dordrecht, 1974), p. 615 and references contained therein.
[15] P. L. James, *M.Sc. thesis*, (University of Durham, 1976).
[16] E. A. Moelwyn-Hughes, *Physical Chemistry* (Pergamon, London, 1961), pp. 303–4.
[17] C. A. Kraus, *J. Phys. Chem.*, 1956, **60**, 129.
[18] C. J. F. Böttcher, *Theory of Electric Polarisation* (Elsevier Amsterdam, 1952), Chap. 5.
[19] Landolt-Börnstein, *Zahlenwerte und Funktionen* (Springer, Berlin, 1951) Band 1/3.
[20] R. Kubo in *Fluctuation, Relaxation and Resonance in Magnetic Systems*, ed. D. Ter Haar (Oliver and Boyd, London, 1962), pp. 23–68.
[21] J. Yarwood and G. N. Robertson, *Mol. Phys.*, 1977, in press; *Nature*, 1975, **257**, 41.
[22] S. Bratos, *J. Chem. Phys.*, 1975, **63**, 3499; S. Bratos, J. Rios and Y. Guissani, *J. Chem. Phys.*, 1970, **52**, 439.
[23] W. F. Edgell, *Ions and Ion Pairs in Organic Reactions*, ed. M. Szwarc (Wiley-Interscience, New York, 1972), Vol. 1, Chap 4.
[24] G. A. P. Wylie, ref. (20), p. 7.
[25] J. P. Badiali, H. Cachet and J-C. Lestrade, *J. Chim. Phys.*, 1967, **64**, 1350.
[26] M. J. Wootten, *Electrochemistry*, ed. G. J. Hills (Specialist Periodical Report, The Chemical Society, London, 1973), Chap. 2, and references therein.
[27] G. W. F. Pardoe, *Trans. Faraday Soc.*, 1970, **66**, 2699.
[28] M. Davies, G. W. F. Pardoe, J. E. Chamberlain and H. A. Gebbie, *Trans. Faraday Soc.*, 1968, **64**, 847.
[29] M. Evans, *J.C.S. Faraday II*, 1975, **71**, 2051 and references quoted therein.
[30] G. J. Davies, J. Chamberlain and M. Davies, *J.C.S. Faraday II*, 1973, **69**, 1223.

[31] H. A. Stuart, *Molekülstruktur* (Springer, Berlin, 1967), p. 416–20.
[32] S. R. Jain and S. Walker, *J. Phys. Chem.*, 1971, **75**, 2942.
[33] P. Bacelon, J. Corset and C. de Loze, *J. Chim. Phys.*, 1973, **70**, 1145.
[34] K. F. Denning and J. A. Plambeck, *Canad. J. Chem.*, 1972, **50**, 1600.
[35] J. A. Geddes and C. A. Kraus, *Trans. Faraday Soc.*, 1936, **32**, 585.